

# Demonstration of cooling by the Muon Ionization Cooling Experiment

<https://doi.org/10.1038/s41586-020-1958-9>

MICE collaboration\*

Received: 22 July 2019

Accepted: 13 December 2019

Published online: 5 February 2020

Open access

The use of accelerated beams of electrons, protons or ions has furthered the development of nearly every scientific discipline. However, high-energy muon beams of equivalent quality have not yet been delivered. Muon beams can be created through the decay of pions produced by the interaction of a proton beam with a target. Such ‘tertiary’ beams have much lower brightness than those created by accelerating electrons, protons or ions. High-brightness muon beams comparable to those produced by state-of-the-art electron, proton and ion accelerators could facilitate the study of lepton–antilepton collisions at extremely high energies and provide well characterized neutrino beams<sup>1–6</sup>. Such muon beams could be realized using ionization cooling, which has been proposed to increase muon-beam brightness<sup>7,8</sup>. Here we report the realization of ionization cooling, which was confirmed by the observation of an increased number of low-amplitude muons after passage of the muon beam through an absorber, as well as an increase in the corresponding phase-space density. The simulated performance of the ionization cooling system is consistent with the measured data, validating designs of the ionization cooling channel in which the cooling process is repeated to produce a substantial cooling effect<sup>9–11</sup>. The results presented here are an important step towards achieving the muon-beam quality required to search for phenomena at energy scales beyond the reach of the Large Hadron Collider at a facility of equivalent or reduced footprint<sup>6</sup>.

## High-quality muon beams

Fundamental insights into the structure of matter and the nature of its elementary constituents have been obtained using beams of charged particles. The use of time-varying electromagnetic fields to produce sustained acceleration was pioneered in the 1930s<sup>12–14</sup>. Since then, high-energy and high-brightness particle accelerators have delivered electron, proton and ion beams for applications ranging from the search for new phenomena in the interactions of quarks and leptons to the study of nuclear physics, materials science and biology.

Muon beams can be created using a proton beam striking a target to produce a secondary beam comprising many particle species including pions, kaons and muons. The pions and kaons decay to produce additional muons, which are captured by electromagnetic beamline elements to produce a tertiary muon beam. Capture must be realized on a timescale compatible with the muon lifetime at rest, 2.2  $\mu$ s. Without acceleration, the energy and intensity of the muon beam is limited by the energy and intensity of the primary proton beam and the efficiency with which muons are captured.

Accelerated high-brightness muon beams have been proposed as a source of neutrinos at neutrino factories and for the delivery of multi-TeV lepton–antilepton collisions at muon colliders<sup>1–6</sup>. Muons have attractive properties for the delivery of high-energy collisions. The muon is a fundamental particle with mass 207 times that of the electron. This high mass results in suppression of synchrotron radiation, potentially enabling collisions between beams of muons and

antimuons at energies far in excess of those that can be achieved in an electron–positron collider, such as the proposed International Linear Collider<sup>15</sup>, the Compact Linear Collider<sup>16</sup>, the Circular Electron–Positron Collider<sup>17</sup> and the electron–positron option of the Future Circular Collider<sup>18</sup>. The virtual absence of synchrotron radiation makes it possible to build a substantially smaller facility with the same or greater physics reach.

The energy available in collisions between the constituent gluons and quarks in proton–proton collisions is considerably less than the energy of the proton beam because the colliding quarks and gluons each carry only a fraction of the proton’s momentum. Muons carry the full energy of the beam, making muon colliders attractive for the study of particle physics beyond the energy reach of facilities such as the Large Hadron Collider<sup>19</sup>.

Most of the proposals for accelerated muon beams exploit the proton-driven muon-beam production scheme outlined above and use beam cooling to increase the brightness of the tertiary muon beam before acceleration and storage to ensure sufficient luminosity or beam current. Four cooling techniques are in use at particle accelerators: synchrotron radiation cooling<sup>20</sup>, laser cooling<sup>21</sup>, stochastic cooling<sup>22</sup> and electron cooling<sup>23</sup>. In each case, the time required to cool the beam is long compared to the muon lifetime. Frictional cooling of muons, in which muons are electrostatically accelerated through an energy-absorbing medium at energies significantly below 1 MeV, has been demonstrated but with low efficiency<sup>24–26</sup>.

\*A list of participants and their affiliations appears at the end of the paper.

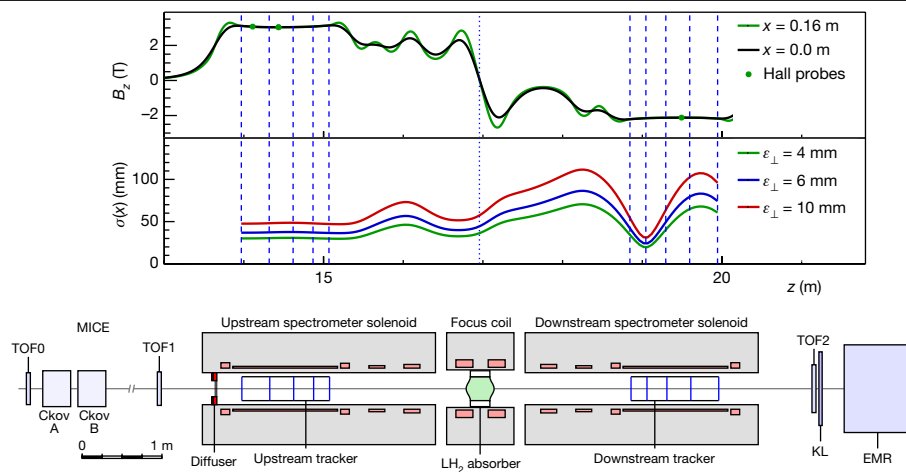


**Fig. 1 | The MICE apparatus, the calculated magnetic field and the nominal horizontal width of the beam.** The modelled field,  $B_z$ , is shown on the beam axis (black line) and at 160 mm from the axis (green line) in the horizontal plane. The readings of Hall probes situated at 160 mm from the beam axis are also shown. Vertical lines indicate the positions of the tracker stations (dashed

lines) and the absorber (dotted line). The nominal r.m.s. beam width,  $\sigma(x)$ , is calculated assuming a nominal input beam and using linear beam transport equations. See text for the description of the MICE apparatus. TOF0, TOF1 and TOF2 are time-of-flight detector stations; KL is a lead-scintillator pre-shower detector; EMR is the Electron–Muon Ranger.

The technique demonstrated in this study, ionization cooling<sup>7,8</sup>, is based on a suitably prepared beam passing through an appropriate material (the absorber) and losing momentum through ionization. Radio-frequency cavities restore momentum only along the beam direction. Passing the muon beam through a repeating lattice of material and accelerators causes the ionization cooling effect to build up in a time much shorter than the muon lifetime<sup>9–11</sup>. Acceleration of a muon beam in a radio-frequency accelerator has recently been demonstrated<sup>27</sup>, and reduced beam heating, damped by the ionization cooling effect, has been observed<sup>28</sup>. Ionization cooling has not been demonstrated so far. Experimental validation of the technique is important for the development of muon accelerators. The international Muon Ionization Cooling Experiment (MICE; <http://mice.iit.edu>) was designed to demonstrate transverse ionization cooling, the realization of which is presented here.

The brightness of a particle beam can be characterized by the number of particles in the beam and the volume occupied by the beam in position–momentum phase space. The phase-space volume occupied by the beam and the phase-space density of the beam are conserved quantities in a conventional accelerator without cooling. The phase space considered here is the position and momentum transverse to the direction of travel of the beam,  $\mathbf{u} = (x, p_x, y, p_y)$ , where  $x$  and  $y$  are coordinates perpendicular to the beam line, and  $p_x$  and  $p_y$  are the corresponding components of the momentum. The  $z$  axis is the nominal beam axis.

The normalized root-mean-square (r.m.s.) emittance is conventionally used as an indicator of the phase-space volume occupied by the beam<sup>29</sup>, but this quantity is not conserved when scraping or optical aberrations affect the edge of the beam. The distribution of amplitudes<sup>30,31</sup> is used here to study effects in the core of the beam. The amplitude of a particle is the distance of the particle from the beam centroid in normalized phase space, and is a conserved quantity in a conventional accelerator without cooling. The phase-space density of the beam is also directly studied using a  $k$ -nearest-neighbour technique<sup>32</sup>.

### MICE cooling apparatus

The MICE collaboration has built a tightly focusing solenoid lattice, absorbers and instrumentation to demonstrate the ionization cooling of muons. A schematic of the apparatus is shown in Fig. 1.

A transfer line<sup>33–35</sup> brought a beam, composed mostly of muons, from a target<sup>36</sup> in the ISIS synchrotron<sup>37</sup> to the cooling apparatus. The central momentum of the muons could be tuned between  $140 \text{ MeV } c^{-1}$  and  $240 \text{ MeV } c^{-1}$  ( $c$ , speed of light in vacuum). A variable-thickness brass and tungsten diffuser allowed the emittance of the incident beam to be varied between 4 mm and 10 mm.

The tight focusing (low  $\beta$  function) and large acceptance required by the cooling section was achieved using 12 superconducting solenoids. The solenoids were contained in three warm-bore modules cooled by closed-cycle cryocoolers. The upstream and downstream modules (spectrometer solenoids) were identical, each containing three coils to provide a uniform field region of up to 4 T within the 400-mm-diameter warm bore for momentum measurement, as well as two ‘matching’ coils to match the beam to the central pair of closely spaced ‘focus’ coils, which focus the beam onto the absorber. The focus coils were designed to enable peak on-axis fields of up to 3.5 T within one module with a 500-mm-diameter warm bore containing the absorbers.

For the experiment reported here the focus coils were operated in ‘flip’ mode with a field reversal at the centre. Because the magnetic lattice was tightly coupled, the cold mass-suspension systems of the modules were designed to withstand longitudinal cold-to-warm forces of several hundred kN, which could arise during an unbalanced quench of the system. At maximum field, the inter-coil force on the focus coil cold mass was of the order of 2 MN. The total energy stored in the magnetic system was of the order of 5 MJ and the system was protected by both active and passive quench-protection systems. The normal charging and discharging time of the solenoids was several hours. The entire magnetic channel was partially enclosed by a 150-mm-thick soft-iron return yoke for external magnetic shielding. The magnetic fields in the tracking volumes were monitored during operation using calibrated Hall probes.

One of the matching coils in the downstream spectrometer solenoid was not operable owing to a failure of a superconducting lead. Although this necessitated a compromise in the lattice optics and acceptance, the flexibility of the magnetic lattice was exploited to ensure a clear cooling measurement.

The amplitude acceptance of approximately 30 mm, above which particles scrape, was large compared to that of a typical accelerator. Even so, considerable scraping was expected and observed for the highest-emittance beams. Ionization cooling cells with even larger acceptances, producing less scraping, have been designed<sup>9–11</sup>.

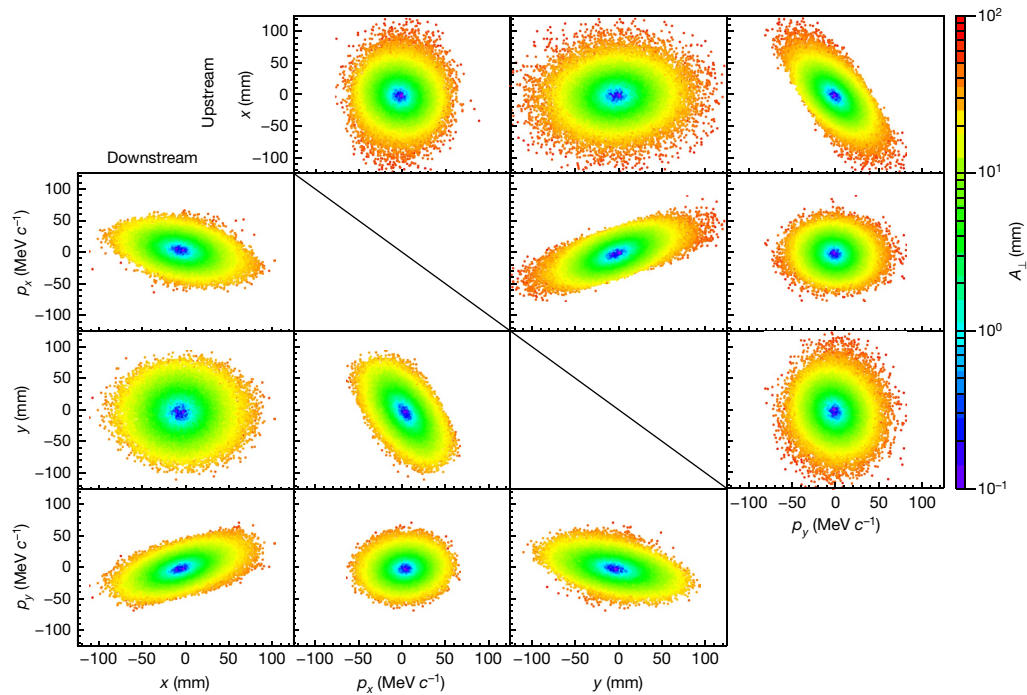


**Fig. 2 | Beam distribution in phase space for the 6–140 Full LH2 setting of MICE.** Measured beam distribution in the upstream tracker (above the diagonal) and in the downstream tracker (below the diagonal). The measured coordinates of the particles are coloured according to the amplitude  $A_{\perp}$  of the particle.

The magnetic lattice of MICE, shown in Fig. 1, was tuned so that the focus of the beam was near the absorber, resulting in a small beam width and large angular divergence. The tight focusing, corresponding to a nominal transverse  $\beta$  function of around 430 mm at the centre of the absorber, yielded an optimal cooling performance.

Materials with low atomic number, such as lithium and hydrogen, have a long radiation length relative to the rate of energy loss, and consequently better cooling performance, making them ideal absorber materials. Therefore, cooling by both liquid-hydrogen and lithium hydride absorbers was studied.

The liquid hydrogen was contained within a 22-l vessel<sup>38</sup> in the warm bore of the focus coil. Hydrogen was liquefied by a cryocooler and piped through the focus coil module into the absorber body. When filled, the absorber presented  $349.6 \pm 0.2$  mm of liquid hydrogen along the beam axis with a density of  $0.07053 \pm 0.00008$  g cm<sup>-3</sup> (all uncertainties represent the standard error). The liquid hydrogen was contained between a pair of aluminium windows covered by multi-layer insulation. A second pair of windows provided a secondary barrier to protect against failure of the primary containment windows. These windows were designed to be as thin as possible so that any scattering in them would not cause substantial heating. The total thickness of all four windows on the beam axis was  $0.79 \pm 0.01$  mm.

The lithium hydride absorber was a disk of thickness  $65.37 \pm 0.02$  mm with a density of  $0.6957 \pm 0.0006$  g cm<sup>-3</sup>. The isotopic composition of the lithium used to produce the absorber was 95% <sup>6</sup>Li and 5% <sup>7</sup>Li. The cylinder had a thin coating of parylene to prevent ingress of water or oxygen. Configurations with the empty liquid-hydrogen containment vessel and with no absorber were also studied.

## MICE beam instrumentation

Detectors placed upstream and downstream of the apparatus measured the momentum, position and species of each particle entering and leaving the cooling channel in order to reconstruct the full four-dimensional phase space, including the angular momentum introduced by the solenoids. Particles were recorded by the apparatus

one at a time, which enabled high-precision instrumentation to be used and particles other than muons to be excluded from the analysis. Each ensemble of muons was accumulated over a number of hours. This is acceptable because space-charge effects are not expected at a neutrino factory and in a muon collider they become important only at very low longitudinal emittance<sup>39</sup>. Data-taking periods for each absorber were separated by a period of weeks owing to operational practicalities. The phase-space distribution of the resulting ensemble was reconstructed using the upstream and downstream detectors. The emittance reconstruction in the upstream detector system is described in ref. <sup>40</sup>.

Upstream of the cooling apparatus, two time-of-flight (TOF) detectors<sup>41</sup> measured the particle velocity. A complementary velocity measurement was made upstream by the threshold Cherenkov counters Ckov A and Ckov B<sup>42</sup>. Scintillating fibre trackers, positioned in the uniform-field region of each of the two spectrometer solenoids, measured the particle position and momentum upstream and downstream of the absorber<sup>43,44</sup>. Downstream, an additional TOF detector<sup>45</sup>, a mixed lead-scintillator pre-shower detector and a totally active scintillator calorimeter, the Electron–Muon Ranger<sup>46,47</sup>, identified electrons produced by muon decay and allowed cross-validation of the measurements made by the upstream detectors and the trackers.

Each tracker consisted of five planar scintillating-fibre stations. Each station comprised three views; each view was composed of two layers of 350- $\mu$ m-diameter scintillating fibres positioned at an angle of 120° with respect to the other views. The fibres were read out by cryogenic visible-light photon counters<sup>48</sup>. The position of a particle crossing the tracker was inferred from the coincidence of signals from the fibres, and the momentum was calculated by fitting a helical trajectory to the signal positions, with appropriate consideration for energy loss and scattering in the fibres.

Each TOF detector was constructed from two orthogonal planes of scintillator slabs. Photomultiplier tubes at each end of every TOF detector slab were used to determine the time at which a muon passed through the apparatus with a 60-ps resolution<sup>41</sup>. The momentum resolution of particles with a small helix radius in the tracker was improved

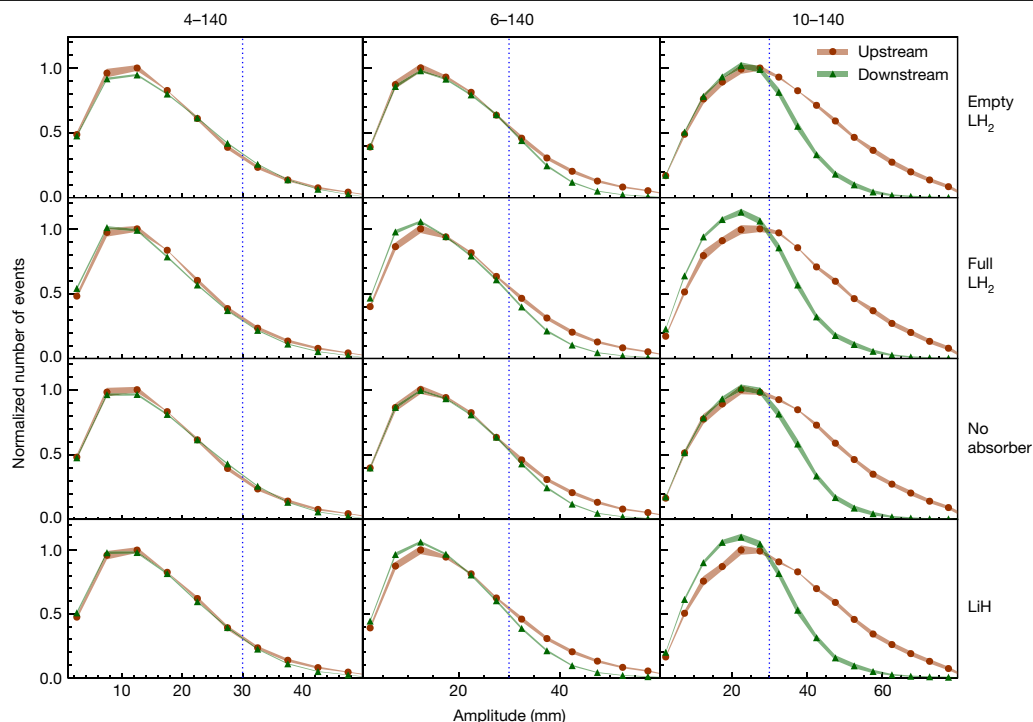


**Fig. 3 | Muon amplitudes measured by MICE.** The measured upstream distributions are shown by red circles while the downstream distributions are shown by green triangles. Both upstream and downstream distributions are normalized to the bin with the most entries in the upstream distribution (see text). Coloured bands show the estimated standard error, which is dominated

by systematic uncertainties. Vertical lines indicate the approximate channel acceptance above which scraping occurs. The number of events in each sample is listed in Extended Data Table 2. Data for each experimental configuration were accumulated in a single discrete period.

by combining the TOF measurement of velocity with the measurement of momentum in the tracker.

A detailed Monte Carlo simulation of the experiment was performed to study the resolution and efficiency of the instrumentation and to determine the expected performance of the cooling apparatus<sup>49,50</sup>. The simulation was found to give a good description of the data<sup>40</sup>.

### Demonstration of cooling

The data presented here were taken using beams with a nominal momentum of  $140 \text{ MeV } c^{-1}$  and a nominal normalized r.m.s. emittance in the upstream tracking volume of 4 mm, 6 mm and 10 mm; these settings are denoted as ‘4–140’, ‘6–140’ and ‘10–140’, respectively. Beams with a higher emittance have more muons at high amplitudes and occupy a larger region in phase space. For each beam setting, two samples were considered for the analysis. The ‘upstream sample’ contained particles identified as muons by the upstream TOF detectors and tracker, for which the muon trajectory reconstructed in the upstream tracker was fully contained in the fiducial volume and for which the reconstructed momentum fell within the range  $135 \text{ MeV } c^{-1}$  to  $145 \text{ MeV } c^{-1}$  (which is considerably higher than the momentum resolution of the tracker,  $2 \text{ MeV } c^{-1}$ ). The ‘downstream sample’ was the subset of the upstream sample for which the reconstructed muons were fully contained in the fiducial volume of the downstream tracker. Each of the samples had between 30,000 and 170,000 events. Examples of the phase-space distributions of the particles in the two samples are shown in Fig. 2. The strong correlations between  $y$  and  $p_x$  and between  $x$  and  $p_y$  are due to the angular momentum introduced by the solenoidal field. The shorter tails along the semi-minor axis compared to the semi-major axis in these projections arise from scraping in the diffuser.

The distributions of amplitudes in the upstream and downstream samples for each of the 4–140, 6–140 and 10–140 datasets are shown in Fig. 3. The nominal acceptance of the magnetic channel is also

indicated. A correction has been made to account for the migration of events between amplitude bins due to the detector resolution and to account for inefficiency in the downstream detector system (see Methods). Distributions are shown for the measurements with an empty liquid-hydrogen vessel (‘Empty  $\text{LH}_2$ ’), with a filled liquid-hydrogen vessel (‘Full  $\text{LH}_2$ ’), with no absorber (‘No absorber’) and with the lithium hydride absorber (‘LiH’). The distributions were normalized to allow a comparison of the shape of the distribution between different absorbers. Each pair of upstream and downstream amplitude distributions is scaled by  $1/N_{\text{max}}^u$ , where  $N_{\text{max}}^u$  is the number of events in the most populated bin in the upstream sample.

The behaviour of the beam at low amplitude is the key result of this study. For the ‘No absorber’ and ‘Empty  $\text{LH}_2$ ’ configurations, the number of events with low amplitude in the downstream sample is similar to that observed in the upstream sample. For the 6–140 and 10–140 configurations for both the ‘Full  $\text{LH}_2$ ’ and the ‘LiH’ samples, the number of events with low amplitude is considerably larger in the downstream sample than in the upstream sample. This indicates an increase in the number of particles in the beam core when an absorber is installed, which is expected if ionization cooling takes place. This effect can occur only because energy loss is a non-conservative process.

A reduction in the number of muons at high amplitude is also observed, especially for the 10–140 setting. Whereas part of this effect arises owing to migration of muons into the beam core, a substantial number of high-amplitude particles outside the beam acceptance intersected the beam pipe or fell outside the fiducial volume of the downstream tracker. The beam pipe was made of materials with higher atomic number than those of the absorber materials, so interactions in the beam pipe tended to be dominated by multiple Coulomb scattering, leading to beam loss.

A  $\chi^2$  test was performed to determine the confidence with which the null hypothesis that for the same input beam setting, the amplitude distributions in the downstream samples of the ‘Full  $\text{LH}_2$ ’ and ‘Empty  $\text{LH}_2$ ’

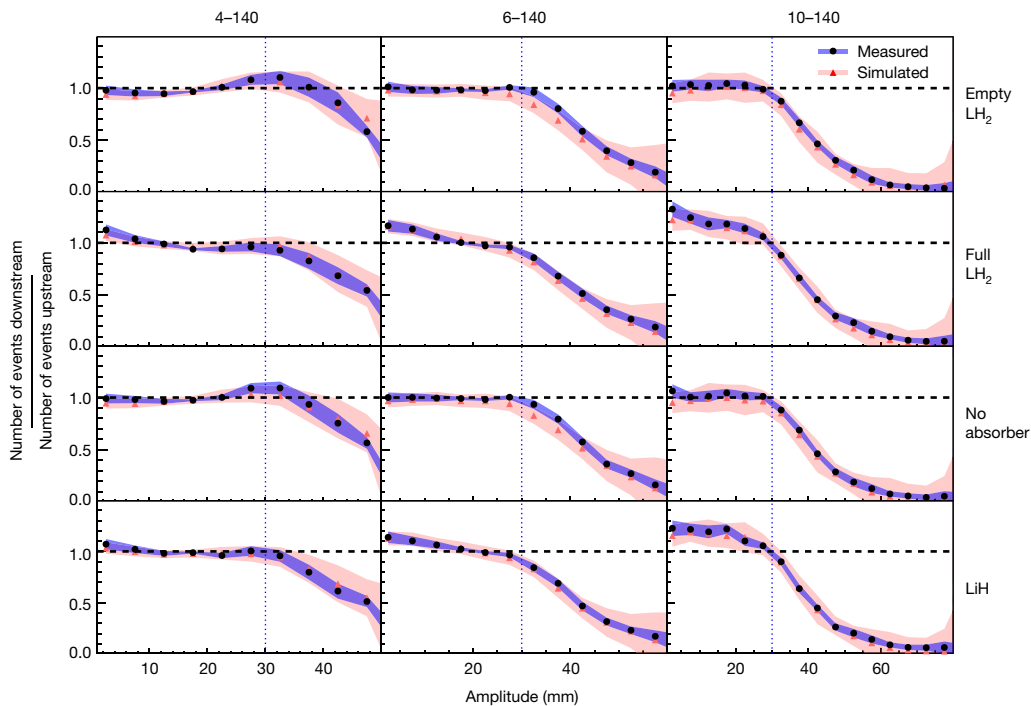


**Fig. 4 | Downstream-to-upstream ratio of number of events in MICE.** A ratio greater than unity in the beam core, which is evidence of ionization cooling, is observed in the data obtained with the 6–140 and 10–140 beams with both the full  $\text{LH}_2$  absorber and the  $\text{LiH}$  absorber. The effect predicted from the simulation is shown in red and that measured is shown in black. The

corresponding shading shows the estimated standard error, which is dominated by systematic uncertainty. Vertical lines indicate the channel acceptance above which scraping occurs. The number of events in each sample is listed in Extended Data Table 2. Data for each experimental configuration were accumulated in a single discrete period.

configurations are compatible, and the amplitude distributions in the downstream samples of the ‘ $\text{LiH}$ ’ and ‘No absorber’ configurations are compatible. The test was performed on the uncorrected distributions using only statistical uncertainties. Systematic effects are the same for the pairs of distributions tested, and cancel. Assuming that this null hypothesis is correct, the probability of observing the effect seen in the data is considerably lower than  $10^{-5}$  for each beam setting and for each ‘Full  $\text{LH}_2$ ’–‘Empty  $\text{LH}_2$ ’ and ‘ $\text{LiH}$ ’–‘No absorber’ pair; therefore, the null hypothesis was rejected.

The fractional increase in the number of particles with low amplitude is most pronounced for the 10–140 beams. High-amplitude beams have high transverse emittance,  $\varepsilon_{\perp}$ , and a larger transverse momentum relative to the stochastic increase in transverse momentum due to scattering, so they undergo more cooling. For the magnet settings and beams studied here, heating due to multiple Coulomb scattering becomes dominant over ionization cooling at an emittance of around 4 mm. As a result, only modest cooling is observed for the 4–140 setting in both the ‘Full  $\text{LH}_2$ ’ and ‘ $\text{LiH}$ ’ configurations.

The ratios of the downstream to the upstream amplitude distributions are shown in Fig. 4. In the ‘No absorber’ and ‘Empty absorber’ configurations, the ratios are consistent with 1 for amplitudes of less than 30 mm, confirming the conservation of amplitude in this region, irrespective of the incident beam. Above 30 mm the ratios drop below unity, indicating that at high amplitude there are fewer muons downstream than upstream, as outlined above. The presence of the absorber windows does not strongly affect the amplitude distribution. For the 6–140 and 10–140 datasets, the addition of liquid-hydrogen or lithium hydride absorber material causes the ratios to rise above unity for the low-amplitude particles that correspond to the beam core. This indicates an increase in the number of particles in the beam core and demonstrates ionization cooling.

The density in phase space is an invariant of a symplectic system; therefore, an increase in phase-space density is also an unequivocal

demonstration of cooling. Figure 5 shows the normalized density of the upstream and downstream samples,  $\rho_i(\mathbf{u}_i)/\rho_0$ , as a function of  $\alpha$ , the fraction of the upstream sample that has a density greater than or equal to  $\rho_i$ . This is known as the quantile distribution. To enable comparison between different beam configurations, the densities for each configuration have been normalized to the peak density in the upstream tracker,  $\rho_0$ . To enable comparison between the upstream and downstream distributions, the fraction of the sample is always relative to the total number of events in the upstream sample. The transmission is the fraction of the beam for which the density in the downstream tracker reaches zero. For the ‘No absorber’ and ‘Empty  $\text{LH}_2$ ’ cases, the downstream density in the highest-density regions is indistinguishable from the upstream density. A small amount of scraping is observed for the 4–140 and 6–140 beams. More substantial scraping is observed for the 10–140 beam. In all cases, for ‘Full  $\text{LH}_2$ ’ and ‘ $\text{LiH}$ ’ the phase-space density increases, and the increase is greater for higher-emittance beams. These observations demonstrate the ionization cooling of the beam when an absorber is installed. In the presence of an absorber, beams with larger nominal emittance show a greater increase in density than those with a lower nominal emittance.

## Conclusions

Ionization cooling has been unequivocally demonstrated. We have built and operated a section of a solenoidal cooling channel and demonstrated the ionization cooling of muons using both liquid hydrogen and lithium hydride absorbers. The effect has been observed through the measurement of both an increase in the number of small-amplitude particles (Figs. 3, 4) and an increase in the phase-space density of the beam (Fig. 5). The results are well described by simulations (Fig. 4). This demonstration of ionization cooling is an important advance in the development of high-brightness muon beams. The seminal results presented in this paper encourage further development of high-brightness

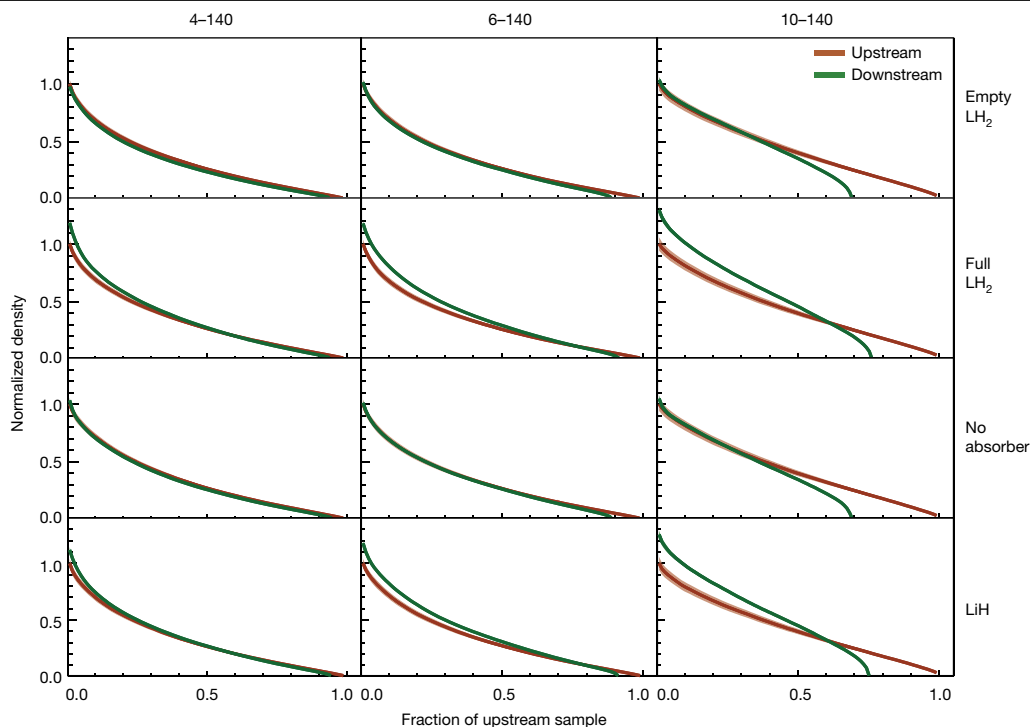


**Fig. 5 | Normalized quantile distribution of the beam density in MICE.**

Upstream and downstream quantiles are indicated by orange and green lines, respectively, as a function of the fraction of the upstream sample. For each configuration, the density is normalized to the highest-density region in the

upstream sample. The estimated standard error is indicated by the thickness of the coloured bands and is dominated by systematic uncertainty. The number of events in each sample is listed in Extended Data Table 2. Data for each experimental configuration were accumulated in a single discrete period.

muon beams as a tool for the investigation of the fundamental properties of matter.

## Online content

Any methods, additional references, Nature Research reporting summaries, source data, extended data, supplementary information, acknowledgements, peer review information; details of author contributions and competing interests; and statements of data and code availability are available at <https://doi.org/10.1038/s41586-020-1958-9>.

- Neuffer, D. V. & Palmer, R. B. A high-energy high-luminosity  $\mu^+\mu^-$  collider. *AIP Conf. Proc.* **356**, 344–358 (1996).
- Geer, S. Neutrino beams from muon storage rings: characteristics and physics potential. *Phys. Rev. D* **57**, 6989–6997 (1998).
- Alsharo'a, M. M. et al. Recent progress in neutrino factory and muon collider research within the Muon Collaboration. *Phys. Rev. Accel. Beams* **6**, 081001 (2003).
- Palmer, R. B. Muon colliders. *Rev. Accel. Sci. Tech.* **7**, 137–159 (2014).
- Boscolo, M. et al. Low emittance muon accelerator studies with production from positrons on target. *Phys. Rev. Accel. Beams* **21**, 061005 (2018).
- Neuffer, D. & Shiltsev, V. On the feasibility of a pulsed 14 TeV c.m.e. muon collider in the LHC tunnel. *J. Instrum.* **13**, T10003 (2018).
- Skrinsky, A. N. & Parkhomchuk, V. V. Cooling methods for beams of charged particles. *Sov. J. Part. Nucl.* **12**, 223–247 (1981).
- Neuffer, D. Principles and applications of muon cooling. *Part. Accel.* **14**, 75–90 (1983).
- Rogers, C. T. et al. Muon front end for the neutrino factory. *Phys. Rev. Accel. Beams* **16**, 040104 (2013).
- Stratakis, D. & Palmer, R. B. Rectilinear six-dimensional ionization cooling channel for a muon collider: a theoretical and numerical study. *Phys. Rev. Accel. Beams* **18**, 031003 (2015).
- Neuffer, D. et al. Final cooling for a high-energy high-luminosity lepton collider. *J. Instrum.* **12**, T07003 (2017).
- Lawrence, E. O. & Livingston, M. S. The production of high speed protons without the use of high voltages. *Phys. Rev.* **38**, 834 (1931).
- Lewis, G. N., Livingston, M. S. & Lawrence, E. O. The emission of alpha-particles from various targets bombarded by deuterons of high speed. *Phys. Rev.* **44**, 55–56 (1933).
- R. Wideröe. Das Betatron. *Z. Angew. Phys.* **5**, 187–200 (1953).
- Behnke, T. et al. *The International Linear Collider Technical Design Report – Volume 1: Executive Summary* (ILC, 2013).
- Burrows, P. N. et al. (eds) *The Compact Linear Collider (CLIC): 2018 Summary Report* (CERN, 2018).
- CEPC Study Group. *CEPC Conceptual Design Report: Volume 1 – Accelerator*. (IHEP, 2018).
- Abada, A. et al. FCC-ee: the lepton collider. *Eur. Phys. J. Spec. Top.* **228**, 261–623 (2019).
- Myers, S. The Large Hadron Collider 2008–2013. *Int. J. Mod. Phys. A* **28**, 1330035 (2013).
- Lee, S. Y. *Accelerator Physics* 3rd edn (World Scientific, 2012).
- Schröder, S. et al. First laser cooling of relativistic ions in a storage ring. *Phys. Rev. Lett.* **64**, 2901–2904 (1990).
- Möhl, D., Petrucci, G., Thorndahl, L., & van der Meer, S. Physics and technique of stochastic cooling. *Phys. Rep.* **58**, 73–119 (1980).
- Parkhomchuk, V. V. & Skrinsky, A. N. Electron cooling: 35 years of development. *Phys. Uspekhi* **43**, 433–452 (2000).
- Mühlbauer, M. et al. Frictional cooling: experimental results. *Hyperfine Interact.* **119**, 305–310 (1999).
- Abramowicz, H. et al. A muon collider scheme based on frictional cooling. *Nucl. Instrum. Methods Phys. Res. A* **546**, 356–375 (2005).
- Taqqi, D. Compression and extraction of stopped muons. *Phys. Rev. Lett.* **97**, 194801 (2006).
- Bae, S. et al. First muon acceleration using a radio frequency accelerator. *Phys. Rev. Accel. Beams* **21**, 050101 (2018).
- Mori, Y. et al. Neutron source with emittance recovery internal target. In *Proc. of the 23rd Particle Accelerator Conference (JACoW, 2009)*; <http://accelconf.web.cern.ch/AccelConf/PAC2009/papers/th4gac04.pdf>.
- Penn, G. & Wurtele, J. S. Beam envelope equations for cooling of muons in solenoid fields. *Phys. Rev. Lett.* **85**, 764–767 (2000).
- Holzer, E. B. Figure of merit for muon cooling – an algorithm for particle counting in coupled phase planes. *Nucl. Instrum. Methods Phys. Res. A* **532**, 270–274 (2004).
- Rogers, C. *Beam Dynamics in an Ionisation Cooling Channel*. PhD thesis, Imperial College London (2008).
- Drielsma, F. *Measurement of the Increase in Phase Space Density of a Muon Beam through Ionization Cooling*. PhD thesis, Univ. Geneva (2018).
- Bogomilov, M. et al. The MICE muon beam on ISIS and the beam-line instrumentation of the Muon Ionization Cooling Experiment. *J. Instrum.* **7**, P05009 (2012).
- Adams, D. et al. Characterisation of the muon beams for the Muon Ionisation Cooling Experiment. *Eur. Phys. J. C* **73**, 2582 (2013).
- Bogomilov, M. et al. Pion contamination in the MICE muon beam. *J. Instrum.* **11**, P03001 (2016).
- Booth, C. N. et al. The design and performance of an improved target for MICE. *J. Instrum.* **11**, P05006 (2016).
- Thomason, J. W. G. The ISIS Spallation Neutron and Muon Source – the first thirty-three years. *Nucl. Instrum. Methods Phys. Res. A* **917**, 61–67 (2019).
- Bayliss, V. et al. The liquid-hydrogen absorber for MICE. *J. Instrum.* **13**, T09008 (2018).
- Stratakis, D., Palmer, R. B. & Grote, D. P. Influence of space-charge fields on the cooling process of muon beams. *Phys. Rev. Accel. Beams* **18**, 044201 (2015).

40. Blackmore, V. et al. First particle-by-particle measurement of emittance in the Muon Ionization Cooling Experiment. *Eur. Phys. J. C* **79**, 257 (2019).
41. Bertoni, R. et al. The design and commissioning of the MICE upstream time-of-flight system. *Nucl. Instrum. Methods Phys. Res. A* **615**, 14–26 (2010).
42. Cremaldi, L. et al. A Cherenkov radiation detector with high density aerogels. *IEEE Trans. Nucl. Sci.* **56**, 1475–1478 (2009).
43. Ellis, M. et al. The design, construction and performance of the MICE scintillating fibre trackers. *Nucl. Instrum. Methods Phys. Res. A* **659**, 136–153 (2011).
44. Dobbs, A. et al. The reconstruction software for the MICE scintillating fibre trackers. *J. Instrum.* **11**, T12001 (2016).
45. Bertoni, R. et al. *The Construction of the MICE TOF2 Detector*. MICE Technical Note 254 (2010); <http://mice.iit.edu/micenotes/public/pdf/MICE0286/MICE0286.pdf>.
46. Adams, D. et al. Electron–Muon Ranger: performance in the MICE Muon Beam. *J. Instrum.* **10**, P12012 (2015).
47. Asfandiyarov, R. et al. The design and construction of the MICE Electron–Muon Ranger. *J. Instrum.* **11**, T10007 (2016).
48. Petroff, M. D. & Stapelbroek, M. G. Photon-counting solid-state photomultiplier. *IEEE Trans. Nucl. Sci.* **36**, 158–162 (1989).
49. Agostinelli, S. et al. GEANT4: a simulation toolkit. *Nucl. Instrum. Methods Phys. Res. A* **506**, 250–303 (2003).
50. Asfandiyarov, R. et al. MAUS: the MICE Analysis User Software. *J. Instrum.* **14**, T04005 (2019).

**Publisher's note** Springer Nature remains neutral with regard to jurisdictional claims in published maps and institutional affiliations.



**Open Access** This article is licensed under a Creative Commons Attribution 4.0 International License, which permits use, sharing, adaptation, distribution and reproduction in any medium or format, as long as you give appropriate credit to the original author(s) and the source, provide a link to the Creative Commons license, and indicate if changes were made. The images or other third party material in this article are included in the article's Creative Commons license, unless indicated otherwise in a credit line to the material. If material is not included in the article's Creative Commons license and your intended use is not permitted by statutory regulation or exceeds the permitted use, you will need to obtain permission directly from the copyright holder. To view a copy of this license, visit <http://creativecommons.org/licenses/by/4.0/>.

© The Author(s) 2020

#### MICE collaboration

**M. Bogomilov<sup>1</sup>, R. Tsenov<sup>1</sup>, G. Vankova-Kirilova<sup>1</sup>, Y. P. Song<sup>2</sup>, J. Y. Tang<sup>2</sup>, Z. H. Li<sup>3</sup>, R. Bertoni<sup>4</sup>, M. Bonesini<sup>4</sup>, F. Chignoli<sup>4</sup>, R. Mazza<sup>4</sup>, V. Palladino<sup>5</sup>, A. de Bari<sup>6</sup>, D. Orestano<sup>7</sup>, L. Tortora<sup>7</sup>, Y. Kuno<sup>8</sup>, H. Sakamoto<sup>8,34</sup>, A. Sato<sup>8</sup>, S. Ishimoto<sup>9</sup>, M. Chung<sup>10</sup>, C. K. Sung<sup>10</sup>, F. Filthaut<sup>11,12</sup>, D. Jokovic<sup>13</sup>, D. Maletic<sup>13</sup>, M. Savic<sup>13</sup>, N. Jovancevic<sup>14</sup>, J. Nikolov<sup>14</sup>, M. Vretenar<sup>15</sup>, S. Ramberger<sup>15</sup>, R. Asfandiyarov<sup>16</sup>, A. Blondel<sup>16</sup>, F. Drielsma<sup>16</sup>, Y. Karadzhev<sup>16</sup>, S. Boyd<sup>17</sup>, J. R. Greis<sup>17</sup>, T. Lord<sup>17</sup>, C. Pidcott<sup>17,35</sup>, I. Taylor<sup>17,36</sup>, G. Charnley<sup>18</sup>, N. Collomb<sup>18</sup>, K. Dumbell<sup>18</sup>, A. Gallagher<sup>18</sup>, A. Grant<sup>18</sup>, S. Griffiths<sup>18</sup>, T. Hartnett<sup>18</sup>, B. Martlew<sup>18</sup>, A. Moss<sup>18</sup>, A. Muir<sup>18</sup>, I. Mullacraane<sup>18</sup>, A. Oates<sup>18</sup>, P. Owens<sup>18</sup>, G. Stokes<sup>18</sup>, P. Warburton<sup>18</sup>, C. White<sup>18</sup>, D. Adams<sup>19</sup>, V. Bayliss<sup>19</sup>, J. Boehm<sup>19</sup>, T. W. Bradshaw<sup>19</sup>, C. Brown<sup>19,20</sup>, M. Courthold<sup>19</sup>, J. Govans<sup>19</sup>, M. Hills<sup>19</sup>, J.-B. Lagrange<sup>19</sup>, C. Macwaters<sup>19</sup>, A. Nichols<sup>19</sup>, R. Preece<sup>19</sup>, S. Ricciardi<sup>19</sup>, C. Rogers<sup>19\*</sup>, T. Stanley<sup>19</sup>,**

**J. Tarrant<sup>19</sup>, M. Tucker<sup>19</sup>, S. Watson<sup>19,37</sup>, A. Wilson<sup>19</sup>, R. Bayes<sup>21,38</sup>, J. C. Nugent<sup>21</sup>, F. J. P. Soler<sup>21</sup>, G. T. Chatzitheodoridis<sup>21,22,23</sup>, A. J. Dick<sup>22,23</sup>, K. Ronald<sup>22,23</sup>, C. G. Whyte<sup>22,23</sup>, A. R. Young<sup>22,23</sup>, R. Gamet<sup>24</sup>, P. Cooke<sup>24</sup>, V. J. Blackmore<sup>25</sup>, D. Colling<sup>25</sup>, A. Dobbs<sup>25,39</sup>, P. Dornan<sup>25</sup>, P. Franchini<sup>25</sup>, C. Hunt<sup>25,40</sup>, P. B. Jurj<sup>25</sup>, A. Kurup<sup>25</sup>, K. Long<sup>25</sup>, J. Martyniak<sup>25</sup>, S. Middleton<sup>25,41</sup>, J. Pasternak<sup>25</sup>, M. A. Uchida<sup>25,42</sup>, J. H. Cobb<sup>26</sup>, C. N. Booth<sup>27</sup>, P. Hodgson<sup>27</sup>, J. Langlands<sup>27</sup>, E. Overton<sup>27,43</sup>, V. Pec<sup>27</sup>, P. J. Smith<sup>27</sup>, S. Wilbur<sup>27</sup>, M. Ellis<sup>20,44</sup>, R. B. S. Gardener<sup>20</sup>, P. Kyberd<sup>20</sup>, J. J. Nebrensky<sup>20</sup>, A. DeMello<sup>28</sup>, S. Gourlay<sup>28</sup>, A. Lambert<sup>28</sup>, D. Li<sup>28</sup>, T. Luo<sup>28</sup>, S. Prestemon<sup>28</sup>, S. Virostek<sup>28</sup>, M. Palmer<sup>29</sup>, H. Witte<sup>29</sup>, D. Adey<sup>30,45</sup>, A. D. Bross<sup>30</sup>, D. Bowring<sup>30</sup>, A. Liu<sup>30,46</sup>, D. Neuffer<sup>30</sup>, M. Popovic<sup>30</sup>, P. Rubinov<sup>30</sup>, B. Freemire<sup>31,46</sup>, P. Hanlet<sup>31,47</sup>, D. M. Kaplan<sup>31</sup>, T. A. Mohaya<sup>31,47</sup>, D. Rajaram<sup>31</sup>, P. Snopok<sup>31</sup>, Y. Torun<sup>31</sup>, L. M. Cremaldi<sup>32</sup>, D. A. Sanders<sup>32</sup>, D. J. Summers<sup>32</sup>, L. R. Coney<sup>33,48</sup>, G. G. Hanson<sup>33</sup> & C. Heidt<sup>33</sup>**

<sup>1</sup>Department of Atomic Physics, St Kliment Ohridski University of Sofia, Sofia, Bulgaria.

<sup>2</sup>Institute of High Energy Physics, Chinese Academy of Sciences, Beijing, China.

<sup>3</sup>Sichuan University, Chengdu, China.

<sup>4</sup>Sezione INFN Milano Bicocca, Dipartimento di Fisica G. Occhialini, Milan, Italy.

<sup>5</sup>Sezione INFN Napoli and Dipartimento di Fisica, Università Federico II, Complesso Universitario di Monte S. Angelo, Naples, Italy.

<sup>6</sup>Sezione INFN Pavia and Dipartimento di Fisica, Pavia, Italy.

<sup>7</sup>INFN Sezione di Roma Tre and Dipartimento di Matematica e Fisica, Università Roma Tre, Rome, Italy.

<sup>8</sup>Osaka University, Graduate School of Science, Department of Physics, Toyonaka, Japan.

<sup>9</sup>High Energy Accelerator Research Organization (KEK), Institute of Particle and Nuclear Studies, Tsukuba, Japan.

<sup>10</sup>UNIST, Ulsan, South Korea.

<sup>11</sup>Nikhef, Amsterdam, The Netherlands.

<sup>12</sup>Radboud University, Nijmegen, The Netherlands.

<sup>13</sup>Institute of Physics, University of Belgrade, Belgrade, Serbia.

<sup>14</sup>Faculty of Sciences, University of Novi Sad, Novi Sad, Serbia.

<sup>15</sup>CERN, Geneva, Switzerland.

<sup>16</sup>DPNC, Section de Physique, Université de Genève, Geneva, Switzerland.

<sup>17</sup>Department of Physics, University of Warwick, Coventry, UK.

<sup>18</sup>STFC Daresbury Laboratory, Daresbury, Cheshire, UK.

<sup>19</sup>STFC Rutherford Appleton Laboratory, Harwell Oxford, Didcot, UK.

<sup>20</sup>Brunel University, Uxbridge, UK.

<sup>21</sup>School of Physics and Astronomy, The University of Glasgow, Glasgow, UK.

<sup>22</sup>SUPA and Department of Physics, University of Strathclyde, Glasgow, UK.

<sup>23</sup>Cockcroft Institute, Daresbury Laboratory, Daresbury, UK.

<sup>24</sup>Department of Physics, University of Liverpool, Liverpool, UK.

<sup>25</sup>Department of Physics, Blackett Laboratory, Imperial College London, London, UK.

<sup>26</sup>Department of Physics, University of Oxford, Oxford, UK.

<sup>27</sup>Department of Physics and Astronomy, University of Sheffield, Sheffield, UK.

<sup>28</sup>Lawrence Berkeley National Laboratory, Berkeley, CA, USA.

<sup>29</sup>Brookhaven National Laboratory, Upton, NY, USA.

<sup>30</sup>Fermilab, Batavia, IL, USA.

<sup>31</sup>Illinois Institute of Technology, Chicago, IL, USA.

<sup>32</sup>University of Mississippi, Oxford, MS, USA.

<sup>33</sup>University of California, Riverside, CA, USA.

<sup>34</sup>Present address: RIKEN 2-1 Horosawa, Wako, Japan.

<sup>35</sup>Present address: Department of Physics and Astronomy, University of Sheffield, Sheffield, UK.

<sup>36</sup>Present address: Defence Science and Technology Laboratory, Salisbury, UK.

<sup>37</sup>Present address: ATC, Royal Observatory Edinburgh, Edinburgh, UK.

<sup>38</sup>Present address: Laurentian University, Sudbury, Ontario, Canada.

<sup>39</sup>Present address: OPERA Simulation Software, Kidlington, UK.

<sup>40</sup>Present address: CERN, Geneva, Switzerland.

<sup>41</sup>Present address: School of Physics and Astronomy, University of Manchester, Manchester, UK.

<sup>42</sup>Present address: Cavendish Laboratory, Cambridge, UK.

<sup>43</sup>Present address: Arm, Sheffield, UK.

<sup>44</sup>Present address: Westpac Group, Sydney, New South Wales, Australia.

<sup>45</sup>Present address: Institute of High Energy Physics, Chinese Academy of Sciences, Beijing, China.

<sup>46</sup>Present address: Euclid Techlabs, Bolingbrook, IL, USA.

<sup>47</sup>Present address: Fermilab, Batavia, IL, USA.

<sup>48</sup>Present address: European Spallation Source ERIC, Lund, Sweden.

\*e-mail: [chris.rogers@stfc.ac.uk](mailto:chris.rogers@stfc.ac.uk)

### Characterization of beam brightness

In particle accelerators, the average beam brightness  $\bar{B}$  is defined as the beam current,  $I$ , passing through a transverse phase-space volume  $\mathcal{V}_4$  (ref. <sup>31</sup>)

$$\bar{B} = \frac{I}{\mathcal{V}_4} \quad (1)$$

The normalized r.m.s. emittance is often used as an indicator of the phase-space volume occupied by the beam and is given by<sup>29</sup>

$$\varepsilon_{\perp} = \frac{\sqrt[4]{|V|}}{m_{\mu}c} \quad (2)$$

where  $m_{\mu}$  is the muon mass and  $|V|$  is the determinant of the covariance matrix of the beam in the transverse phase space  $\mathbf{u} = (x, p_x, y, p_y)$ . The covariance matrix has elements  $v_{ij} = \langle u_i u_j \rangle - \langle u_i \rangle \langle u_j \rangle$ . The distribution of individual particle amplitudes also describes the volume of the beam in phase space.

The amplitude is defined by<sup>30</sup>

$$A_{\perp} = \varepsilon_{\perp} R^2(\mathbf{u}, \langle \mathbf{u} \rangle) \quad (3)$$

where  $R^2(\mathbf{u}, \mathbf{v})$  is the square of the distance between two points,  $\mathbf{u}$  and  $\mathbf{v}$ , in the phase space, normalized to the covariance matrix:

$$R^2(\mathbf{u}, \mathbf{v}) = (\mathbf{u} - \mathbf{v})^T V^{-1} (\mathbf{u} - \mathbf{v}) \quad (4)$$

The normalized r.m.s. emittance is proportional to the mean of the particle amplitude distribution. In the approximation that particles travel near the beam axis, and in the absence of cooling, the particle amplitudes and the normalized r.m.s. emittance are conserved quantities. If the beam is well described by a multivariate Gaussian distribution, then  $R^2$  is distributed according to a  $\chi^2$  distribution with four degrees of freedom, so the amplitudes are distributed according to

$$f(A_{\perp}) = \frac{A_{\perp}}{4\varepsilon_{\perp}^2} \exp\left(\frac{-A_{\perp}}{2\varepsilon_{\perp}}\right) \quad (5)$$

The rate of change of the normalized transverse emittance as the beam passes through an absorber is given approximately by<sup>8,29,31</sup>

$$\frac{d\varepsilon_{\perp}}{dz} \approx -\frac{\varepsilon_{\perp}}{\beta^2 E_{\mu}} \left| \frac{dE_{\mu}}{dz} \right| + \frac{\beta_{\perp} (13.6 \text{ MeV } c^{-1})^2}{2\beta^3 E_{\mu} m_{\mu} X_0} \quad (6)$$

where  $\beta c$  is the muon velocity,  $E_{\mu}$  is the muon energy,  $|dE_{\mu}/dz|$  is the mean energy loss per unit path length,  $X_0$  is the radiation length of the absorber and  $\beta_{\perp}$  is the transverse betatron function at the absorber<sup>29</sup>. The first term of this equation describes ‘cooling’ by ionization energy loss and the second term describes ‘heating’ by multiple Coulomb scattering. Equation (6) implies that there is an equilibrium emittance for which the emittance change is zero.

If the beam is well described by a multivariate Gaussian distribution both before and after cooling, then the downstream and upstream amplitude distributions  $f^d(A_{\perp})$  and  $f^u(A_{\perp})$  are related to the downstream and upstream emittances  $\varepsilon_{\perp}^d$  and  $\varepsilon_{\perp}^u$  by

$$\frac{f^d(A_{\perp})}{f^u(A_{\perp})} = \left( \frac{\varepsilon_{\perp}^u}{\varepsilon_{\perp}^d} \right)^2 \exp\left[ -\frac{A_{\perp}}{2} \left( \frac{1}{\varepsilon_{\perp}^d} - \frac{1}{\varepsilon_{\perp}^u} \right) \right] \quad (7)$$

In the experiment described in this paper, many particles do not travel near the beam axis. These particles experience effects from

optical aberrations, as well as geometrical effects such as scraping, in which high-amplitude particles outside the experiment’s aperture are removed from the beam. Scraping reduces the emittance of the ensemble and selectively removes those particles that scatter more than the rest of the ensemble. Optical aberrations and scraping introduce a bias in the change in r.m.s. emittance that occurs because of ionization cooling. In this work the distribution of amplitudes is studied. To expose the behaviour in the beam core, independently of aberrations affecting the beam tail,  $V$  and  $\varepsilon_{\perp}$  are recalculated for each amplitude bin, including particles that are in lower-amplitude bins and excluding particles that are in higher-amplitude bins. This results in a distribution that, in the core of the beam, is independent of scraping effects and spherical aberrations.

The change in phase-space density provides a direct measurement of the cooling effect. The  $k$ -nearest-neighbour algorithm provides a robust non-parametric estimator of the phase-space density of the muon ensemble<sup>32,34,52</sup>. The separation of pairs of muons is characterized by the normalized squared distance,  $R_{ij}^2(\mathbf{u}_i, \mathbf{u}_j)$ , between muons with positions  $\mathbf{u}_i$  and  $\mathbf{u}_j$ . A volume  $\mathcal{V}_{ik}$  is associated with each particle, which corresponds to the hypersphere that is centred on  $\mathbf{u}_i$  and intersects the  $k$ th nearest particle (that is, the particle that has the  $k$ th smallest  $R_{ij}$ ). The density,  $\rho_i$ , associated with the  $i$ th particle is estimated by

$$\rho_i(\mathbf{u}_i) = \frac{k}{n} \frac{1}{|V|^{1/2} \mathcal{V}_{ik}} = \frac{2k}{n\pi^2} \frac{1}{|V|^{1/2} R_{ik}^4} \quad (8)$$

where  $n$  is the number of particles in the ensemble. An optimal value for  $k$  is used,  $k = n^{4/(4+d)} = \sqrt{n}$ , with phase-space dimension  $d = 4$  (ref. <sup>32</sup>).

### Data taking and reconstruction

Data were buffered in the front-end electronics and read out after each target actuation. Data storage was triggered by a coincidence of signals in the photomultiplier tubes (PMTs) serving a single scintillator slab in the upstream TOF station closest to the cooling channel (TOF1). The data recorded in response to a particular trigger are referred to as a ‘particle event’.

Each TOF station was composed of a number of scintillator slabs that were read out using a pair of PMTs, one mounted at each end of each slab. The reconstruction of the data began with the search for coincidences in the signals from the two PMTs serving any one slab in a TOF plane. Such coincidences are referred to as ‘slab hits’. ‘Space points’ were then formed from the intersection of slab hits in the  $x$  and  $y$  projections of each TOF station separately. The position and time at which a particle giving rise to the space point crossed the TOF station were then calculated using the slab position and the times measured in each of the PMTs. The relative timing of the two upstream TOF stations (TOF0 and TOF1) was calibrated relative to the measured time taken for electrons to pass between the two TOF detectors, on the assumption that they travelled at the speed of light.

Signals in the tracker readout were collected to reconstruct the helical trajectories (‘tracks’) of charged particles in the upstream and downstream trackers (TKU and TKD, respectively). Multiple Coulomb scattering introduced significant uncertainties in the reconstruction of the helical trajectory of tracks with a bending radius of less than 5 mm. For this class of track, the momentum was deduced by combining the tracker measurement with the measurements from nearby detectors. The track-fitting quality was characterized by the  $\chi^2$  per degree of freedom

$$\chi_{\text{df}}^2 = \frac{1}{n} \sum_i \frac{\delta x_i^2}{\sigma_i^2} \quad (9)$$

where  $\delta x_i$  is the distance between the fitted track and the measured signal in the  $i$ th tracker plane,  $\sigma_i$  is the resolution of the position measurement in the tracker planes and  $n$  is the number of planes that had



a signal used in the track reconstruction. Further details of the reconstruction and simulation may be found in ref. <sup>50</sup>.

### Beam selection

Measurements made in the instrumentation upstream of the absorber were used to select the input beam. The input beam (the upstream sample) was composed of events that satisfied the following criteria:

- Exactly one space point was found in TOF0 and TOF1 and exactly one track in TKU.
- The track in TKU had  $\chi_{df}^2 < 8$  and was contained within the 150-mm fiducial radius over the full length of TKU.
- The track in TKU had a reconstructed momentum in the range 135–145 MeV  $c^{-1}$ , corresponding to the momentum acceptance of the cooling cell.
- The time-of-flight between TOF0 and TOF1 was consistent with that of a muon, given the momentum measured in TKU.
- The radius at which the track in TKU passed through the diffuser was smaller than the diffuser aperture.

The beam emerging from the cooling cell (the downstream sample) was characterized using the subset of the upstream sample that satisfied the following criteria:

- Exactly one track was found in TKD.
- The track in TKD had  $\chi_{df}^2 < 8$  and was contained within the 150-mm fiducial radius of TKD over the full length of the tracker.

The same sample-selection criteria were used to select events from the simulation of the experiment, which included a reconstruction of the electronics signals expected for the simulated particles.

### Calculation of amplitudes

The amplitude distributions obtained from the upstream and downstream samples were corrected for the effects of the detector efficiency and resolution and for the migration of events between amplitude bins. The corrected number of events in a bin,  $N_i^{\text{corr}}$ , was calculated from the raw number of events,  $N_j^{\text{raw}}$ , using

$$N_i^{\text{corr}} = E_i \sum_j S_{ij} N_j^{\text{raw}} \quad (10)$$

where  $E_i$  is the efficiency correction factor and  $S_{ij}$  accounts for the detector resolution and event migration.  $E_i$  and  $S_{ij}$  were estimated from the simulation of the experiment. The uncorrected and corrected amplitude distributions for a particular configuration are shown in Extended Data Fig. 1. The correction is small relative to the ionization cooling effect, which is clear even in the uncorrected distributions.

It can be seen from equation (7) that in the limit of small amplitudes, and in the approximation that the beam is normally distributed in the phase-space variables, the ratio of the number of muons is equal to the ratio of the square of the emittances,

$$\lim_{A_{\perp} \rightarrow 0} \frac{f^d(A_{\perp})}{f^u(A_{\perp})} = \left( \frac{\varepsilon_{\perp}^u}{\varepsilon_{\perp}^d} \right)^2 \quad (11)$$

The ratio of  $f^d$  to  $f^u$  in the lowest-amplitude bin of Fig. 3, which is an approximation to this ratio, is listed in Extended Data Table 1.

### Data availability

The unprocessed and reconstructed data that support the findings of this study are publicly available on the GridPP computing Grid at <https://doi.org/10.17633/rd.brunel.3179644> (MICE unprocessed data) and <https://doi.org/10.17633/rd.brunel.5955850> (MICE reconstructed data). Source data for Figs. 3–5 and Extended Data Fig. 1 are provided with the paper.

Publications using MICE data must contain the following statement: “We gratefully acknowledge the MICE collaboration for allowing us access to their data. Third-party results are not endorsed by the MICE collaboration.”

### Code availability

The MAUS software<sup>50</sup> that was used to reconstruct and analyse the MICE data is available at <https://doi.org/10.17633/rd.brunel.8337542>. The analysis presented here used MAUS version 3.3.2.

51. Reiser, M. in *Theory and Design of Charged Particle Beams* 51–103 (John Wiley & Sons, 2008).
52. Mack, Y. P. & Rosenblatt, M. Multivariate k-nearest neighbor density estimates. *J. Multivar. Anal.* **9**, 1–15 (1979).

**Acknowledgements** The work described here was made possible by grants from the Science and Technology Facilities Council (UK), the Department of Energy and the National Science Foundation (USA), the Istituto Nazionale di Fisica Nucleare (Italy), the European Union under the European Union’s Framework Programme 7 (AIDA project, grant agreement number 262025; TIARA project, grant agreement number 261905; and EuCARD), the Japan Society for the Promotion of Science, the National Research Foundation of Korea (number NRF-2016R1A5A1013277), the Ministry of Education, Science and Technological Development of the Republic of Serbia, the Institute of High Energy Physics/Chinese Academy of Sciences fund for collaboration between the People’s Republic of China and the USA, and the Swiss National Science Foundation in the framework of the SCOPES programme. We gratefully acknowledge all sources of support. We are grateful for the support given to us by the staff of the STFC Rutherford Appleton and Daresbury laboratories. We acknowledge the use of Grid computing resources deployed and operated by GridPP in the UK, <http://www.gridpp.ac.uk/>.

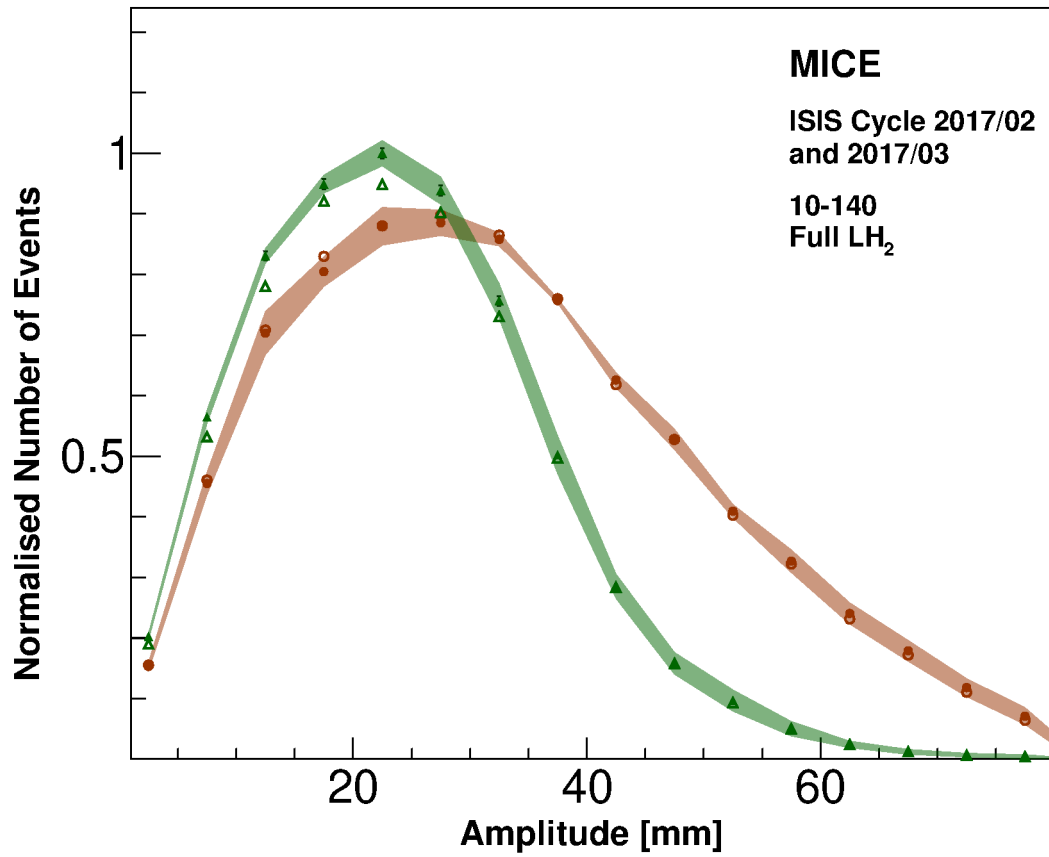
**Author contributions** All authors contributed considerably to the design or construction of the apparatus or to the data taking or analysis described here.

**Competing interests** The authors declare no competing interests.

### Additional information

**Correspondence and requests for materials** should be addressed to C.R.

**Reprints and permissions information** is available at <http://www.nature.com/reprints>.



**Extended Data Fig. 1 | Corrected and uncorrected amplitude distributions for the 10–140 ‘LH2 full’ configuration.** The uncorrected data are shown by open points and the corrected data by filled points. Orange circles correspond

to the upstream distribution and green triangles to the downstream distribution. Shading represents the estimated total standard error. Error bars show the statistical error and for most points are smaller than the markers.

**Extended Data Table 1 | Ratio of number of muons downstream to number of muons upstream having an amplitude of less than 5 mm**

	4-140	6-140	10-140
LH2 empty	$0.98 \pm 0.005 \pm 0.05$	$1.01 \pm 0.006 \pm 0.05$	$1.02 \pm 0.02 \pm 0.05$
LH2 full	$1.12 \pm 0.009 \pm 0.05$	$1.16 \pm 0.009 \pm 0.05$	$1.32 \pm 0.02 \pm 0.07$
None	$0.99 \pm 0.006 \pm 0.05$	$1.00 \pm 0.005 \pm 0.05$	$1.06 \pm 0.02 \pm 0.06$
LiH	$1.07 \pm 0.008 \pm 0.05$	$1.14 \pm 0.01 \pm 0.05$	$1.23 \pm 0.03 \pm 0.07$

Uncertainties denote standard error; statistical uncertainty is followed by the total uncertainty.

# Article

**Extended Data Table 2 | Number of events in the samples shown in Fig. 3–5**

	4-140		6-140		10-140	
	Upstream	Downstream	Upstream	Downstream	Upstream	Downstream
LH2 empty	163508	153813	158520	140981	123067	85082
LH2 full	71823	67640	117383	107329	82371	62660
None	91804	86877	172606	153809	54195	37436
LiH	87514	82682	98443	89875	43423	32715

## Journal Pre-proofs

New Insights from Cross-correlation Studies between Solar Activity Indices and Cosmic-ray Flux during Forbush Decrease events

Mihailo Savić, Nikola Veselinović, Aleksandar Dragić, Dimitrije Maletić, Dejan Joković, Vladimir Udovičić, Radomir Banjanac, David Knežević

PII: S0273-1177(22)00913-9  
DOI: <https://doi.org/10.1016/j.asr.2022.09.057>  
Reference: JASR 16285

To appear in: *Advances in Space Research*

Accepted Date: 27 September 2022

Please cite this article as: Savić, M., Veselinović, N., Dragić, A., Maletić, D., Joković, D., Udovičić, V., Banjanac, R., Knežević, D., New Insights from Cross-correlation Studies between Solar Activity Indices and Cosmic-ray Flux during Forbush Decrease events, *Advances in Space Research* (2022), doi: <https://doi.org/10.1016/j.asr.2022.09.057>

This is a PDF file of an article that has undergone enhancements after acceptance, such as the addition of a cover page and metadata, and formatting for readability, but it is not yet the definitive version of record. This version will undergo additional copyediting, typesetting and review before it is published in its final form, but we are providing this version to give early visibility of the article. Please note that, during the production process, errors may be discovered which could affect the content, and all legal disclaimers that apply to the journal pertain.

© 2022 Published by Elsevier B.V. on behalf of COSPAR.





# New Insights from Cross-correlation Studies between Solar Activity Indices and Cosmic-ray Flux during Forbush Decrease events

Mihailo Savić<sup>a</sup>, Nikola Veselinović<sup>a,\*</sup>, Aleksandar Dragić<sup>a</sup>, Dimitrije Maletić<sup>a</sup>, Dejan Joković<sup>a</sup>, Vladimir Udovičić<sup>a</sup>, Radomir Banjanac<sup>a</sup>, David Knežević<sup>a</sup>

<sup>a</sup>*Institute of Physics Belgrade, University of Belgrade, Pregrevica 118, 11080 Belgrade, Serbia*

Received 1 May 2013; Received in final form 10 May 2013; Accepted 13 May 2013;  
Available online 15 May 2013

## Abstract

Observed galactic cosmic ray intensity can be subjected to a transient decrease. These so-called Forbush decreases are driven by coronal mass ejection induced shockwaves in the heliosphere. By combining in-situ measurements by space borne instruments with ground-based cosmic ray observations, we investigate the relationship between solar energetic particle flux, various solar activity indices, and intensity measurements of cosmic rays during such an event. We present cross-correlation study done using proton flux data from the SOHO/ERNE instrument, as well as data collected during some of the strongest Forbush decreases over the last two completed solar cycles by the network of neutron monitor detectors and different solar observatories. We have demonstrated connection between the shape of solar energetic particles fluence spectra and selected coronal mass ejection and Forbush decrease parameters, indicating that power exponents used to model these fluence spectra could be valuable new parameters in similar analysis of mentioned phenomena. They appear to be better predictor variables of Forbush decrease magnitude in interplanetary magnetic field than coronal mass ejection velocities.

© 2022 COSPAR. Published by Elsevier Ltd All rights reserved.

**Keywords:** Cosmic rays; Forbush decrease; Solar energetic particles; Solar activity

## 1. Introduction

Cosmic rays (CRs) are high-energy charged particles that arrive at Earth from space, mainly originating from outside of our Solar system. CRs are modulated in the heliosphere (Heber, B. et al., 2006) due to interaction with the interplanetary magnetic field (IMF) frozen in a constant stream of charged particles from Sun - the solar wind (SW). Transients in the heliosphere additionally modulate CRs. One type of transients are interplanetary coronal mass ejections (ICMEs), closely related to coronal mass ejections (CMEs).

ICMEs interact with SW, and as the speed of particles in ICME is different than the speed of SW particles, a bow shock

can be created, affecting the CR flux (Belov et al., 2014). This interaction between ICMEs and residual solar wind can be one of the causes of short-term depression in CR flux, detectable at Earth (Subramanian, P. et al., 2009). Such transient decrease in observed flux is known as a Forbush decrease (FD), a type of CR flux modulation that has been studied extensively since its initial discovery in the 1930s (Gopalswamy (2016) and references therein). There are two clearly distinguishable classes of Forbush decreases: recurrent and non-recurrent. Non-recurrent FDs, typically caused by ICMEs (Dumbović, M. et al., 2012), are mostly characterized by a sudden offset, which lasts about a day, followed by a gradual recovery phase within several days (Cane, 2000). Due to ICME sub-structures (the sheath and the associated shock and magnetic cloud) FD can have one or two-step profile, which depends on transit of one or both structures to the observer (Richardson & Cane, 2011). Recurrent FDs

\*Corresponding author: Email: veselinovic@ipb.ac.rs

have different profile, with gradual onset and decrease and symmetrical recovery caused by high-speed streams from coronal holes (Melkumyan et al., 2019). In this paper we will focus on non-recurrent ICME induced FDs.

Apart from FD profile, one of the main parameters that is used to describe a Forbush decrease is its magnitude. The effect is not the same for all CR particles, as it depends on their rigidity. Rigidity is defined as  $R \equiv B\rho = p/q$ , where  $\rho$  is gyroradius of the particle due to magnetic field  $B$ ,  $p$  is particle momentum, and  $q$  is its charge. The higher the rigidity of a particle, the less it is affected by heliospheric inhomogeneities, hence the reduction in flux is less pronounced.

Another phenomenon that can accompany violent events on the Sun is emission of fast-moving particles, commonly known as solar energetic particles (SEP). The occurrence of such particles is typically related to eruptions on the surface of the Sun, which can be characterized by bursts of X-rays - solar flares (SF), and/or emission of coronal plasma - already mentioned CMEs. When excess of these solar energetic particles with high energy penetrates the geomagnetic field, it can cause a sudden and brief increase in measured CR flux at Earth - a ground level enhancement (GLE). Because GLEs can be harmful to human infrastructures (potentially damaging power lines, satellites in orbit, etc.), they have been studied in detail for decades.

Variations of CR flux have been monitored at Earth for decades using ground and underground-based detectors, primarily neutron monitors (NM) (Belov et al., 2001; Koldobskiy et al., 2019) and muon detectors (de Mendonça et al., 2016; Veselinović et al., 2015). Different types of ground-based detectors complement each other in terms of their CR energy domain (Veselinović et al., 2017), muon detectors being sensitive to energies higher than those detectable by NMs. In addition, CR flux is also (especially in the last couple of decades) directly measured in space using space-borne instruments (Dumbović et al., 2020; Freiherr von Forstner et al., 2020). In the MeV energy range most space probe particle detectors are sensitive to, enhancement of SEP flux can enshroud CR flux, thus making a task of establishing decoupled event-integrated energy spectra (or spectral fluences) for SEP and CRs a laborious task (Koldobskiy, S. et al., 2021; Bruno, A. & Richardson, I. et al., 2021).

Many authors have studied the connection between SFs, CMEs/ICMEs and SEP, consequential effects on the geomagnetic field and compound effect of the IMF and geomagnetic field disturbances on CRs. Most relevant for our analysis is work that studied connection between different FD and ICME parameters (Belov et al. (2001); Belov (2008); Papaioannou et al. (2020) and references therein), which has among other, shown significant correlation between CME speeds and FD magnitudes. More precisely, CME speeds have been established as the best predictor variables of FD magnitudes for primary CR particles with 10 GV rigidity detected at Earth. Also of interest is the work that studied the connection between the disturbance of geomagnetic field and CR flux measured at Earth (Alhassan et al., 2021; Badruddin et al., 2019), where a significant correlation between FD magnitude and different geomagnetic parameters due to common solar or interplanetary origin

has been established.

SF, CME/ICME, SEP and FD events are very often related processes that occur either simultaneously or in succession, in which case can be thought of as different components of one more complex event. CMEs (along with their interplanetary counterparts ICMEs) have been recognized as the main driver of FDs, while on the other hand there has been plenty of evidence for the relationship between CMEs with SEP. Namely, there are two different known mechanism for SEP acceleration: acceleration during magnetic-reconnection events usually resulting in solar flares (which produce short impulsive SEP events), and acceleration caused by CME induced shock waves (which result in gradual SEP events) (Reames, 1999). For this study the second class is of interest. Another type of closely related events that are important for this analysis are energetic storm particle (ESP) events, which represent particles accelerated locally by interplanetary shocks driven by fast CMEs (Desai & Giacalone, 2016). Even though details of the mechanism and the precise role of CME induced shock in the evolution of SEP events are not fully understood (Anastasiadis et al., 2019), we believe that analysis of how SEP/ESP events relate to CME, geomagnetic and FD events could provide some valuable new insight. We are especially interested in, and will concentrate the most on, the possibility of the last of these connections. To do so, we have decided to look into the shape of SEP/ESP fluence spectra and analyze how it relates to different CME, geomagnetic and especially FD parameters.

It should be noted that different mentioned types of events, even when related, do not need to occur at the same place nor at the same time. This is due to the fact that SEP travel along magnetic field lines, while CME/ICME shocks travel mostly directly away from the Sun. Furthermore, modulation of primary CR, detected as FD upon their arrival at Earth, can happen anywhere in the heliosphere. Hence, in general case, detection of these events should not necessarily be simultaneous. However, we believe that for the class of events selected for this analysis we can assume that they occur and are detected within a certain time window. We will elaborate more on this in section 2.3.

The article is structured as follows: first we list various sources of data and justify the selection of solar cycle 23 and 24 FD events to be used in the analysis; then we describe parametrization of SEP events (involving calculation and parametrization of SEP fluence spectra); finally we perform correlative analysis between established SEP parameters and various CME, FD and geomagnetic indices and discuss the observed dependencies.

## 2. Data

Sources of SEP proton flux, various solar and space weather parameters, as well as ground CR measurements and different FD parameters used in this study are listed below. Different criteria for FD event selection are also described.

### 2.1. Solar energetic particle flux data

The source for SEP flux data was the ERNE instrument (Torsti et al., 1995) onboard the Solar and Heliospheric Ob-

servatory (SOHO). Instrument consists of two separate particle detectors. The Low-Energy Detector (LED) and the High-Energy Detector (HED). Former covers ion fluxes and count rates in the 1.3 – 13 MeV/nucleon energy range, and latter ion fluxes and count rates in the 13 – 130 MeV/nucleon energy range. Both ranges are separated in ten energy channels. SOHO has been making in-situ observation from Lagrangian point L1 for the last three solar cycles (data available at [https://omniweb.gsfc.nasa.gov/ftpbrowser/flux\\_spectrum\\_m.html](https://omniweb.gsfc.nasa.gov/ftpbrowser/flux_spectrum_m.html)). ERNE data for solar cycles 23, 24 and current cycle 25 allows the study of variations of proton fluences in SEP events during this period (Paassilta, Miikka et al., 2017; Belov et al., 2021). Higher channels are more correlated with measured CR flux (Veselinović, Nikola et al., 2021) and it appears as if flux in these channels is a mixture of CR and energetic proton fluxes of particles with the same energy. Important feature of HED detector is that, due to rather large geometric factor, during large intensity proton events SOHO/ERNE data have been subject to saturation effects in higher energy channels (Valtonen & Lehtinen, 2009; Miteva et al., 2020).

## 2.2. IZMIRAN directory of Forbush decreases

IZMIRAN database is an online repository developed at the Institute of Terrestrial Magnetism, Ionosphere and Radiowave Propagation (IZMIRAN) at Moscow Troitsk, Russia. It contains an extensive list of Forbush decreases and various parameters from solar, space weather, cosmic ray and geomagnetic measurements, spanning from the late 1950s (<http://spaceweather.izmiran.ru/eng/dbs.html>). Database has been compiled from a number of sources, such as measurements by ground-based detectors, instruments mounted on various satellites, as well as public data provided by different agencies specializing in monitoring solar, space and atmospheric weather and geomagnetism. Extensive list of sources and data repositories used to compile this database are referenced in a number of publications listed on the IZMIRAN internet site (IZMIRAN Space Weather Prediction Center, 2016).

We have decided to use IZMIRAN database as our primary source of data for Forbush decrease parameters as well as for selected variables, parameters and indices that describe associated space weather and geomagnetic phenomena. Selection of parameters pertinent to our analysis was mostly based on previous work by other authors (i.e. Belov (2008); Lingri et al. (2016)), where they established which quantities are most relevant in these types of studies.

Chosen parameters fall into three categories (abbreviations to be used throughout the text are given in parentheses). First category are FD related parameters - Forbush decrease magnitude for 10 GV rigidity primary particles ( $M$ ) and Forbush decrease magnitude for 10 GV rigidity primary particles corrected for magnetospheric effect using  $Dst$  index ( $M_M$ ). These magnitudes are determined using global survey method (GSM). GSM combines measurements from a world-wide network of neutron monitors (NMs), takes into account different anisotropies, disturbances of atmospheric and geomagnetic origin, as well as apparatus-specific features, and produces an estimated hourly

variation of CR flux outside Earth's atmosphere and magnetosphere (Belov et al., 2018). Specifically, correction for magnetospheric effect takes into account the fact that geomagnetic disturbances affect the effective cutoff threshold rigidities and effective asymptotic directions of primary particles for different NM stations (Belov et al., 2005).

Second group of parameters used from IZMIRAN database are CME and SW related parameters - the average CME velocity between the Sun and the Earth, calculated using the time of the beginning of the associated X-ray flare ( $V_{mean}$ ), the average CME velocity between the Sun and the Earth, calculated using the time of the beginning of the associated CME observations ( $V_{meanC}$ ) and maximal hourly solar wind speed in the event ( $V_{max}$ ). Izmiran DB authors have matched detected FD events with associated CMEs using a SOHO LASCO CME catalog (Belov et al., 2014). Catalog includes a comprehensive list of CME events along with some of most relevant parameters, i.e. speeds calculated by tracking CME leading edge (as described in Yashiro et al. (2004), further sources available at [https://cdaw.gsfc.nasa.gov/CME\\_list/catalog\\_description.htm](https://cdaw.gsfc.nasa.gov/CME_list/catalog_description.htm)).

Final group of parameters from IZMIRAN database used in this analysis are related to geomagnetic field - maximal  $Kp$  index in the event ( $Kp_{max}$  - based on data from NOAA Space Weather Prediction Center, <https://www.swpc.noaa.gov/products/planetary-k-index>), maximal 3-hour  $Ap$  index in the event ( $Ap_{max}$  - defined as the mean value of the variations of the terrestrial magnetic field, derived from  $Kp$  index) and minimal  $Dst$  index in the event ( $Dst_{min}$  - calculated using data provided by World Data Center for Geomagnetism, Kyoto, <http://wdc.kugi.kyoto-u.ac.jp/dstdir/index.html>).

## 2.3. Selection of FD events

Time interval used for this analysis was dictated by the period of operation of SOHO/ERNE device, which was commissioned in December 1995 (data available from June 1996) and is still operational. That coincides with the beginning of solar cycle 23 and lasts through cycle 24, so we considered all FD events that occurred in this period, concentrating on events with magnitudes for 10 GV particles larger 4% in the analysis. There are several reasons for such magnitude cut, primary reason being that even though we often reference neutron monitor data in the analysis, CR related research in our laboratory is mainly based on muons detectors, which are generally less sensitive to FDs of smaller magnitude and GLE events. Additionally, it is known that all larger FDs (i.e. with magnitudes greater than 5%) are caused by CMEs (Belov, 2008). Since we use CME speed as a reference parameter in the analysis, introducing such cut made event selection simpler, as practically all considered FD events would have an associated CME. Finally, CME speed is less reliably determined in the case of weaker CME events (Yashiro et al., 2004).

One important step in the event selection procedure is to make sure that for each global event both proton flux increase detected by SOHO/ERNE and FD are related to the same CME. As mentioned in the introduction, detection of these separate



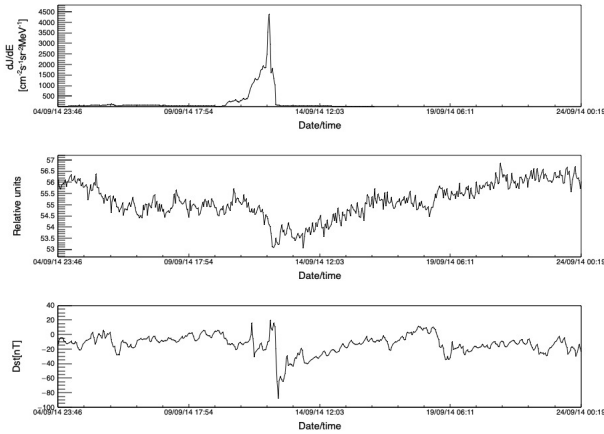


Fig. 1: Time series of hourly data for the same time interval around FD event of 12 September 2014: proton flux in the 1.3 – 1.6 MeV channel (top), Athens neutron monitor count rate (middle), and  $Dst$  index (bottom).

events is not necessarily simultaneous. However, we have checked the direction of CMEs/ICMEs for all events for which such information was available, and in all these cases they moved directly toward Earth. This would imply that detection of the increase of energetic particles, Forbush decrease and geomagnetic storm associated with a given CME should be detectable within a relatively small time window. To illustrate this, on Figure 1 we have shown time series for proton flux (in one selected energy channel), CR flux and  $Dst$  index for one such event. Furthermore, because of large magnitudes of FDs selected for the analysis, we believe it to be the case for all events.

Another important point is that we cannot say with certainty what is the exact origin of detected proton flux solely based on SOHO/ERNE data. They could be of solar origin (SEP), particles accelerated locally at shock in interplanetary space (ESP) or combination of both. For the sake of simplicity we have decided to use the somewhat more general term SEP for energetic particles, having mentioned limitation of its use in mind.

As determination of SEP fluence is not a straightforward procedure (as explained in more detail in section 3.1), from the initial set of events we discarded all for which fluence value was difficult to determine or had a large uncertainty due to overlap and unclear separation of proton flux time series of successive events. That set was then further reduced based on the quality of FD identification flag assigned to each event in the IZMIRAN database, taking into account only events where identification was confident or reliable enough. Applying mentioned selection criteria resulted in the final set of 21 events, presented in Table 1 with some of the parameters of interest.

### 3. Parametrization of SEP fluence energy spectra

Parametrization procedure for any of the selected FD events can be broken down into two steps: 1 - calculation of SEP fluence in different energy channels and 2 - determination of power exponents for SEP fluence spectra.

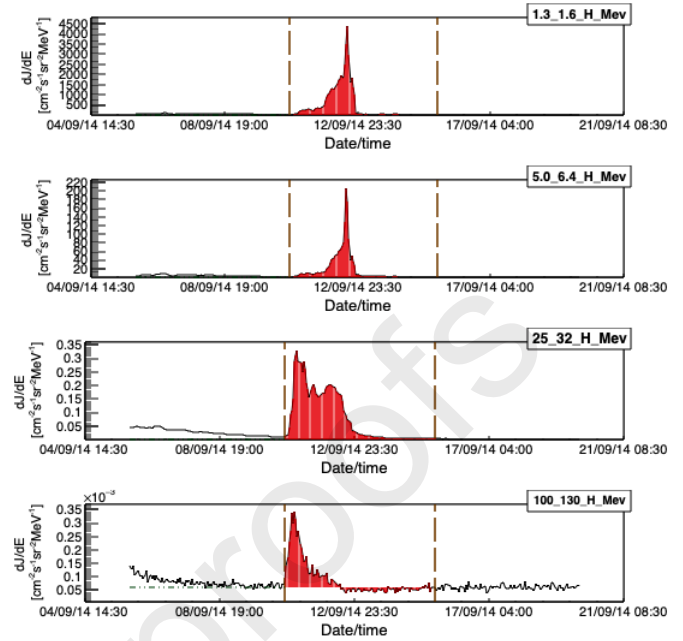


Fig. 2: Solar proton flux for four selected energy channels during FD event of 12 September 2014. Vertical dashed lines indicate integration interval, horizontal dashed line indicates the baseline value, while areas shaded red correspond to result of the integration used to calculate the SEP fluence.

#### 3.1. SEP fluence calculation

SEP fluence is calculated by integrating SOHO/ERNE proton flux time series in separate energy channels over time period associated with a given FD event. First step in this procedure is to determine this time period (and hence integration boundaries) as precisely as possible. Most more energetic events we considered for this analysis have a strong SF associated with them. This may lead to a complex picture, as FD event of interest often occurs in the middle of a turbulent period where additional FDs (sometimes associated with other CMEs) precede or follow it. As a consequence, clear separation of successive events and determination of optimal integration boundaries may not be simple nor straightforward. To make this procedure more reliable, we have used IZMIRAN database and neutron monitor data (courtesy of the Neutron Monitor Database (Neutron Monitor Database, 2022)) in parallel with SOHO/ERNE proton time series, trying to identify prominent features in all three sources, so we could separate events of interest in all energy channels as clearly as possible.

Baseline for integration was determined based on a data interval of at least one (but preferably several) days, where proton flux was negligibly different from zero relative to the flux during the event. If possible, time interval before the event was taken for the calculation of baseline unless there was a preceding disturbance, in which case quiet interval following the event was taken instead. Integration of fluence for several selected SOHO/ERNE energy channels for the event of 12 September 2014 is shown on Figure 2. Integration interval is indicated with vertical dashed lines and baseline value with a horizontal dashed line.

Table 1: Forbush decrease events from solar cycles 23 and 24 selected for the analysis, along with some of the FD, CME and geomagnetic field parameters of interest

Date/Time	$M$ [%]	$M_M$ [%]	X flare	$V_{mean}$ [km s <sup>-1</sup> ]	$V_{meanC}$ [km s <sup>-1</sup> ]	$V_{max}$ [km s <sup>-1</sup> ]	$Kp_{max}$	$Ap_{max}$	$Dst_{min}$ [nT]
2001.09.29 09:40:00	4.3	4.4	M 1.0/	852.0	831	694.0	5.33	56.0	-56.0
2001.10.11 17:01:00	7.0	6.9	M 1.4/2F	766.0	769	572.0	6.0	80.0	-71.0
2001.10.21 16:48:00	5.4	7.3	X 1.6/2B	855.0	858	677.0	7.67	179.0	-187.0
2001.11.24 05:56:00	9.2	9.8	M 9.9/	1323.0	1366	1024.0	8.33	236.0	-221.0
2002.04.17 11:07:00	6.2	7.0	M 1.2/SF	742.0	745	611.0	7.33	154.0	-127.0
2002.09.07 16:36:00	4.6	5.1	C 5.2/SF	860.0	863	550.0	7.33	154.0	-181.0
2003.10.30 16:19:00	14.3	9.4	X10.0/2B	2109.0	2140	1876.0	9.0	400.0	-383.0
2003.11.20 08:03:00	4.7	6.8	M 3.2/2N	854.0	872	703.0	8.67	300.0	-422.0
2004.07.26 22:49:00	13.5	14.4	M 1.1/1F	1279.0	1290	1053.0	8.67	300.0	-197.0
2004.09.13 20:03:00	5.0	5.3	M 4.8/SX	945.0	948	613.0	5.33	56.0	-50.0
2005.05.15 02:38:00	9.5	12.2	M 8.0/SX	1207.0	1231	987.0	8.33	236.0	-263.0
2006.12.14 14:14:00	8.6	9.6	X3.4/4B	1154.0	1165	955.0	8.33	236.0	-146.0
2011.02.18 01:30:00	5.2	4.7	X2.2/	579.0	579	691.0	5.0	48.0	-30.0
2011.08.05 17:51:00	4.3	4.8	M 9.3/	1089.0	1104	611.0	7.67	179.0	-115.0
2011.10.24 18:31:00	4.9	6.5	-	-	633	516.0	7.33	154.0	-147.0
2012.03.08 11:03:00	11.7	11.2	X5.4/	1187.0	1188	737.0	8.0	207.0	-143.0
2012.07.14 18:09:00	6.4	7.6	X 1.4/	822.0	834	667.0	7.0	132.0	-127.0
2013.06.23 04:26:00	5.9	5.3	M 2.9/	832.0	844	697.0	4.33	32.0	-49.0
2014.09.12 15:53:00	8.5	5.9	X1.6/2B	893.0	897	730.0	6.33	94.0	-75.0
2015.06.22 18:33:00	8.4	9.1	M2.6/	1027.0	1040	742.0	8.33	236.0	-204.0
2017.09.07 23:00:00	6.9	7.7	X9.3/	-	1190	817.0	8.33	236.0	-124.0

One interesting feature that can be observed in SOHO/ERNE data time series is that in some cases proton flux in the highest energy channels can dip below the baseline after the initial increase. For a number of events such behavior is even more pronounced, where in extreme cases it can happen that no flux increase is observed, but rather just the decrease. We believe this indicates that the highest energy channels have non-negligible contribution of low-energy cosmic rays, which can increase uncertainty for fluence calculation. We will refer to this again when discussing fluence spectra in section 3.2.

To make fluence calculation procedure more reliable we have assigned a quality flag to each event, based on our estimate of the uncertainty of integration, and decided on a quality cut we deemed acceptable for further analysis. As mentioned in section 2.3, 21 events have passed this criterium. Even then, for a number of events calculated fluence proved to be sensitive to small variations of integration boundaries, which makes it especially difficult to give a reliable estimate of the error for the integration procedure and should be kept in mind when discussing the results.

### 3.2. Determination of SEP fluence spectra power exponents

Fluence energy spectra for all selected events were formed using values for different energy channels, calculated as explained in the previous section. The choice of parameters to be used to describe their shape and characteristics depends on the analytic expression used to model the spectrum. In general, during a SEP event spectra exhibit a characteristic "bend"

or a "knee", which is not so straightforward to describe theoretically. Various expressions were proposed to model this observed feature (Ellison & Ramaty, 1985; Mottl et al., 2001), out of which we have decided to use the following double power law one (Band et al., 1993; Zhao et al., 2016), as we feel it is well suited for our analysis:

$$\frac{dJ}{dE} = \begin{cases} E^{-\alpha} \exp\left(-\frac{E}{E_b}\right) & E \leq (\beta - \alpha)E_b, \\ E^{-\beta} [(\beta - \alpha)E_b]^{\beta - \alpha} \exp(\alpha - \beta) & E > (\beta - \alpha)E_b, \end{cases} \quad (1)$$

where  $E_b$  is knee energy at which the break occurs, while  $\alpha$  and  $\beta$  are power-law exponents that describe energy ranges below and above the break respectively, and consequently are variables we chose to parametrize the SEP event.

These power-law exponents obtained by fitting fluence spectra with Expression 1 can be very sensitive to variation of knee energy, so some care needs to be taken in order to determine  $E_b$  as accurately as possible.

Determination of knee energy using "by eye" method proved to be uncertain enough for us to decide on using a more quantitative approach, which is based on the fact that knee energy generally depends on the integral fluence of the event (as described in Nymmik (2013) and Miroshnichenko & Nymmik (2014)). In accordance with this, we firstly determined the knee energy "by eye", plotted it against integral fluence and then fitted this dependence with a power function in the form of  $E_b = aJ^b$  (Figure 3), where  $E_b$  is the knee energy,  $J$  integral fluence, and  $a$  and  $b$  are fit parameters. We then used these fit parameters to deter-

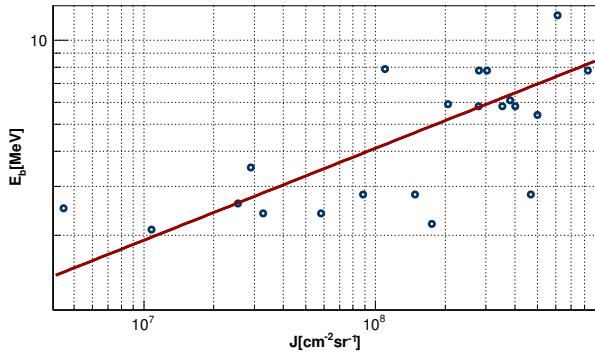


Fig. 3: "Knee" energy dependence on SEP fluence (integrated over full energy range) for selected events. Power function fit is indicated by the red line.

mine  $E_b$  for each event. In several cases where there has been some overlap of proton flux time series profiles associated with different successive events, small correction for integral fluence was introduced, which also affected the knee energy value.

Fluence spectra were then fitted with expression given in Equation 1, using thusly calculated knee energy. On Figure 4 we can see two characteristic examples that illustrate how well this expression actually models the fluence spectrum during a SEP event. In case of 11 October 2001 event (Figure 4a) we see that the theoretical model fits the experimental data reasonably well, except for some small disagreement in the highest energy channels (feature we believe can be explained by our assumption that there is a non-negligible contribution of low-energy CR in this energy range). On the other hand, for a number of events with greater SEP flux higher energy channels tend to get saturated (as mentioned in section 2.1). This in turn leads to an underestimated fluence and consequently poorer fit in this energy range, as can be seen for the 24 November 2001 event shown on Figure 4b. Contribution of flux in these high-energy channels to integral fluence is very small, so this underestimated value does not significantly affect the value of knee energy or uncertainty of the exponent  $\alpha$ . However, the uncertainty of exponent  $\beta$  is more significantly affected and for this reason in further analysis we will rely on exponent  $\alpha$  more for the parametrization of fluence spectra.

#### 4. Correlative analysis

We have performed correlative analysis between power exponents chosen to parametrize SEP fluence and selected parameters from Izmiran database. The results are presented in Table 2. Worth noting is the slightly lower statistics for  $V_{mean}$  due to exclusion of two events for which this parameter was not available.

Strong correlation between FD magnitude for particles with 10 GV rigidity ( $M$ ) and mean CME ( $V_{meanC}$ ,  $V_{mean}$ ) and maximum SW ( $V_{max}$ ) velocities illustrates the important role these parameters have in driving FD events, as has been discussed in detail by several authors (i.e. Belov et al. (2014)). On the other hand, correlation between these velocities and parameter  $M_M$

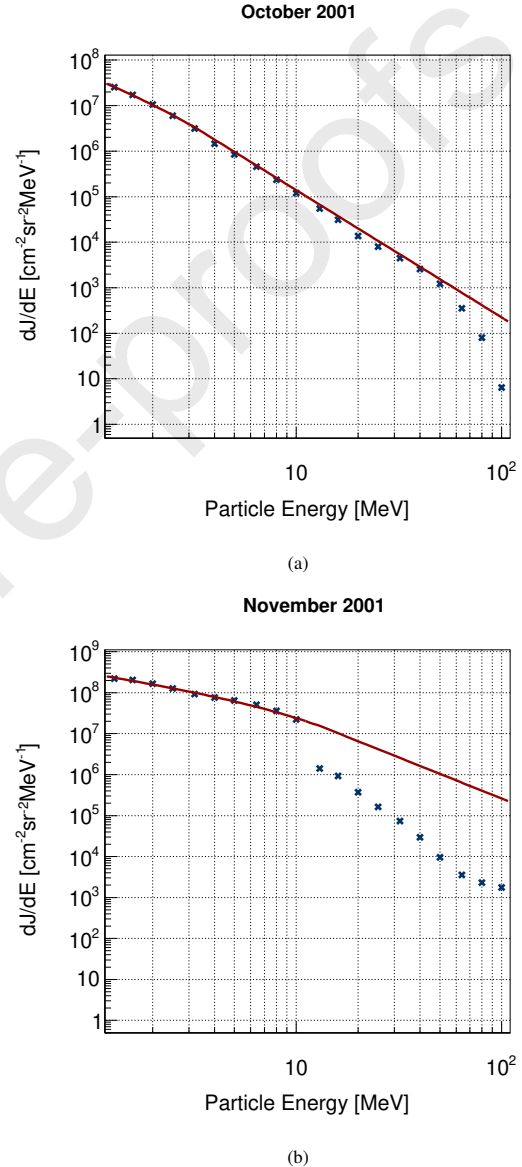


Fig. 4: SEP fluence energy spectra for the: (a) 11 October 2001 event, (b) 24 November 2001 event. Red lines indicate the double power law fit.

Table 2: Correlation coefficients ( $r$ ) between SEP fluence spectra power exponents and selected FD, CME and geomagnetic field indices

	$\alpha$	$\beta$	$M$	$M_M$	$V_{meanC}$	$V_{mean}$	$V_{max}$	$Kp_{max}$	$Ap_{max}$	$Dst_{min}$
$\alpha$	1.00	0.96	0.67	0.64	0.77	0.75	0.66	0.40	0.53	-0.40
$\beta$	0.96	1.00	0.67	0.67	0.72	0.70	0.60	0.44	0.50	-0.38
$M$	0.67	0.67	1.00	0.84	0.79	0.79	0.79	0.53	0.65	-0.41
$M_M$	0.64	0.67	0.84	1.00	0.57	0.57	0.53	0.69	0.69	-0.46
$V_{meanC}$	0.77	0.72	0.79	0.57	1.00	1.00	0.92	0.61	0.77	-0.58
$V_{mean}$	0.75	0.70	0.79	0.57	1.00	1.00	0.92	0.62	0.78	-0.60
$V_{max}$	0.66	0.60	0.79	0.53	0.92	0.92	1.00	0.49	0.71	-0.58
$Kp_{max}$	0.40	0.44	0.53	0.69	0.61	0.62	0.49	1.00	0.94	-0.78
$Ap_{max}$	0.53	0.50	0.65	0.69	0.77	0.78	0.71	0.94	1.00	-0.87
$Dst_{min}$	-0.40	-0.38	-0.41	-0.46	-0.58	-0.60	-0.58	-0.78	-0.87	1.00

is noticeably smaller.  $M_M$  is FD magnitude for particles with 10 GV rigidity corrected for magnetospheric effect (using  $Dst$  index), so we could approximate it as an estimated measure of the FD magnitude in interplanetary magnetic field.

If we now look at how SEP fluence spectra power exponents relate to other parameters in Table 2, we observe the best correlation with mean CME velocities, while it is somewhat smaller with maximum SW velocity. Correlation with FD magnitude ( $M$ ) is smaller than for CME velocities, however interestingly the correlation with the corrected FD magnitude ( $M_M$ ) appears larger than in the case of CME velocities. One possible explanation for this could be that the shape of SEP fluence spectrum is more related to CR disturbance induced in interplanetary magnetic and less to one induced in geomagnetic field. What could support this assumption further is the fact that we observe smaller correlation between  $\alpha$  and  $\beta$  exponents and geomagnetic indices  $Kp_{max}$ ,  $Ap_{max}$  and  $Dst_{min}$  than between these indices and CME velocities.

It should be said that even though SEP fluence spectra power exponents are not directly measured independent variables, the procedure to calculate them is relatively simple, while procedure used to calculate FD magnitudes (using GSM approach) is somewhat less straightforward and accessible. Hence, these exponents could be used to give a first estimate of Forbush decrease magnitudes outside atmosphere and magnetosphere. Having this in mind, we could conclude that SEP fluence power exponents could be better predictor variables (in the sense described above) of FD magnitude in interplanetary space than CME velocities are, while they are less reliable predictor variables of FD magnitude observed at Earth. If true, this could possibly lead us a small step closer to empirically decoupling the effects of IMF and geomagnetic fields on CR.

To further examine how FD magnitude corrected for magnetospheric effects is related to the shape of SEP fluence spectra, we have analyzed their dependence, which is plotted on Figure 5. Both power exponents exhibit similar dependence, but only plot for  $\alpha$  is shown, as it has considerably smaller uncertainty (as mentioned in section 3.2) and we believe it to be a more reliable parameter. We can see that the graph is fairly linear, as could be expected based on the correlation coefficients, but on closer inspection it appears as if there are two separate classes of events with somewhat different behavior. If we loosely di-

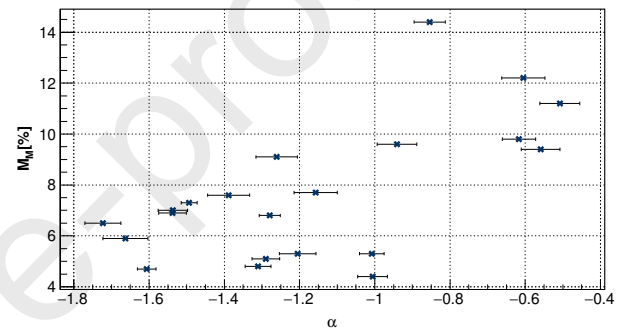


Fig. 5: Dependence of FD magnitude for particles with 10 GV rigidity corrected for magnetospheric effects ( $M_M$ ) on power exponent  $\alpha$ .

vide all FD events into low-magnitude set (with  $M_M$  less than 6%) and high-magnitude set (with  $M_M$  greater or equal to 6%), we can observe much weaker dependence of corrected FD magnitude on power exponent  $\alpha$  for the first class than for the second one.

To check if this observation is well founded, we look into the correlation coefficients for these two separate classes, which are shown in Table 3.

We can see that correlation coefficients for these two sets are indeed very different. While in case of FDs with  $M_M$  equal or greater than 6% we observe an even larger correlation than before between power exponents  $\alpha$  and  $\beta$  and both FD magnitude and corrected FD magnitude (approaching the values of correlation coefficients for CME velocities), coefficients for FDs with  $M_M$  less than 6% have very different values, correlation even being negative. Although statistics for this second set of events is rather small (and hence the uncertainty for correlation coefficients might be large), it appears that the assumption about two classes of events does stand. What is more, we observe a similarly drastic difference in correlation coefficients between FD magnitudes and mean CME velocities (with little to none correlation for events with  $M_M < 6\%$ ), also pointing to the existence of two separate classes of events. This could need to be further confirmed using larger statistics, i.e. by including FD events with magnitudes smaller than 4%.

Table 3: Correlation coefficients ( $r$ ) between FD magnitudes for particles with 10 GV rigidity (uncorrected  $M$  and corrected for magnetospheric effect  $M_M$ ) and SEP fluence spectra power exponents, selected FD, CME and geomagnetic field indices for particles with  $M_M \geq 6\%$  (left) and particles with  $M_M < 6\%$  (right)

	$M_M \geq 6\%$					$M_M < 6\%$				
	$\alpha$	$\beta$	$V_{meanC}$	$V_{mean}$	$V_{max}$	$\alpha$	$\beta$	$V_{meanC}$	$V_{mean}$	$V_{max}$
$M$	0.82	0.76	0.84	0.85	0.78	-0.55	-0.25	-0.08	-0.10	0.62
$M_M$	0.77	0.76	0.52	0.49	0.55	-0.38	0.01	0.23	0.19	0.17

## 5. Conclusions

We analyzed the connection between CME, SEP and FD events, investigating how the shape of SEP fluence spectra during the global disturbance relates to different CME and FD parameters typically used in such analysis. We fitted SEP fluence spectra with double power law and used power exponents ( $\alpha$  and  $\beta$ ) from these fits to parametrize the shape of SEP fluence spectra.

By the means of correlative analysis we investigated the connection between SEP fluence spectra power exponents and selected CME and SW parameters (mean CME and maximum SW velocities), as well as selected FD parameters (magnitude for 10 GV particles and magnitude for 10 GV particles corrected for magnetospheric effect) and various parameters of geomagnetic activity ( $Kp$ ,  $Ap$  and  $Dst$  indices).

We observed largest correlation between power exponents and CME velocities. The correlation between power exponents and FD magnitude ( $M$ ) is significant yet smaller than in case of mean CME velocities ( $V_{meanC}$ ,  $V_{mean}$ ) and FD magnitude. On the other hand, the correlation between FD magnitude corrected for magnetospheric effects ( $M_M$ ) and power exponents is larger than between these magnitudes and mean CME velocities.

The dependence of corrected FD magnitude on power exponent  $\alpha$  possibly indicates two separate classes of events in terms of corrected magnitude value, rough boundary being corrected FD magnitude value of 6%. Events with corrected FD magnitude larger than 6% show increased correlation with power exponent  $\alpha$ , while for the set of events with this magnitude smaller than 6% correlation even has opposite sign. Similarly considerable difference between two classes of events can be observed in correlations of mean CME velocities and corrected FD magnitude. Even taking into account smaller number of events used in the analysis, this could be an indication of these two groups of events exhibiting different behavior.

With everything considered, we believe we have demonstrated an important connection of the shape of SEP fluence spectra with CME and FD events, and that power exponents  $\alpha$  and  $\beta$  can be valuable new parameters to be used in the future study of mentioned phenomena. They seem to be better predictor variables of FD magnitude (and hence CR disturbance) in interplanetary magnetic field than CME velocities, especially in the case of events where FD magnitude corrected for magnetospheric effect is larger than 6%.

## 6. Acknowledgments

The authors acknowledge funding provided by the Institute of Physics Belgrade, through the grant by the Ministry of Edu-

cation, Science and Technological Development of the Republic of Serbia.

OMNI data was made available by NASA/GSFC's Space Physics Data Facility's OMNIWeb service. Data from the SOHO experiment, an international collaboration between ESA and NASA, was kindly provided by ERNE team from Turku University, Finland. Neutron monitor data is available online through the use of excellent NEST tool, provided by the Neutron Monitor Database. We would also like to express our gratitude to the cosmic ray group at the IZMIRAN Space Weather Prediction Center at Pushkov Institute of Terrestrial Magnetism, Ionosphere and Radio Wave Propagation of the Russian Academy of Sciences for kindly providing catalogue of Forbush-effects and interplanetary disturbances.

Finally, we would like to thank the Reviewers for constructive comments and useful suggestions that significantly contributed to the quality of the manuscript.

## References

- Alhassan, J. A., Okike, O., & Chukwude, A. E. (2021). Testing the effect of solar wind parameters and geomagnetic storm indices on galactic cosmic ray flux variation with automatically-selected forbush decreases. *Research in Astronomy and Astrophysics*, 21(9), 234. URL: <https://doi.org/10.1088/1674-4527/21/9/234>. doi:10.1088/1674-4527/21/9/234.
- Anastasiadis, A., Lario, D., Papaioannou, A., Kouloumvakos, A., & Vourlidas, A. (2019). Solar energetic particles in the inner heliosphere: status and open questions. *Philosophical Transactions of the Royal Society A: Mathematical, Physical and Engineering Sciences*, 377(2148), 20180100. URL: <https://royalsocietypublishing.org/doi/abs/10.1098/rsta.2018.0100>. doi:10.1098/rsta.2018.0100.
- Badruddin, B., Aslam, O. P. M., Derouich, M., Asiri, H., & Kudela, K. (2019). Forbush decreases and geomagnetic storms during a highly disturbed solar and interplanetary period, 4–10 september 2017. *Space Weather*, 17(3), 487–496. URL: <https://agupubs.onlinelibrary.wiley.com/doi/abs/10.1029/2018SW001941>. doi:<https://doi.org/10.1029/2018SW001941>.
- Band, D., Matteson, J., Ford, L., Schaefer, B., Palmer, D., Teegarden, B., Cline, T., Briggs, M., Pacias, W., Pendleton, G., Fishman, G., Kouveliotou, C., Meegan, C., Wilson, R., & Lestrade, P. (1993). BATSE Observations of Gamma-Ray Burst Spectra. I. Spectral Diversity. *Astrophysical Journal*, 413, 281–292. doi:10.1086/172995.
- Belov, A. (2008). Forbush effects and their connection with solar, interplanetary and geomagnetic phenomena. *Proceedings of the International Astronomical Union*, 4(S257), 439–450. doi:10.1017/S1743921309029676.
- Belov, A., Abunin, A., Abunina, M., Eroshenko, E., Oleneva, V., Yanke, V., Papaioannou, A., Mavromichalaki, H., Gopalswamy, N., & Yashiro, S. (2014). Coronal mass ejections and non-recurrent forbush decreases. *Solar Physics*, 289, 3949–3960. doi:10.1007/s11207-014-0534-6.
- Belov, A., Baisultanova, L., Eroshenko, E., Mavromichalaki, H., Yanke, V., Pchelkin, V., Plainaki, C., & Mariatos, G. (2005). Magnetospheric effects in cosmic rays during the unique magnetic storm on november 2003. *Journal of Geophysical Research: Space Physics*, 110(A09S20). doi:<https://doi.org/10.1029/2005JA011067>.
- Belov, A., Eroshenko, E., Oleneva, V., Struminsky, A., & Yanke, V. (2001). What determines the magnitude of forbush decreases? *Advances in Space*

- Research, 27(3), 625–630. URL: <https://www.sciencedirect.com/science/article/pii/S0273117701000953>. doi:[https://doi.org/10.1016/S0273-1177\(01\)00095-3](https://doi.org/10.1016/S0273-1177(01)00095-3).
- Belov, A., Eroshenko, E., Yanke, V., Oleneva, V., Abunin, A., Abunina, M., Papaioannou, A., & Mavromichalaki, H. (2018). The Global Survey Method Applied to Ground-level Cosmic Ray Measurements. *Solar Physics*, 293(4), 649–650. doi:10.1007/s11207-018-1277-6.
- Belov, A., Papaioannou, A., Abunina, M., Dumbovic, M., Richardson, I. G., Heber, B., Kuhl, P., Herbst, K., Anastasiadis, A., Vourlidis, A., Eroshenko, E., & Abunin, A. (2021). On the rigidity spectrum of cosmic-ray variations within propagating interplanetary disturbances: Neutron monitor and SOHO/EPHIN observations at ~1–10 GV. *The Astrophysical Journal*, 908(1), 5. URL: <https://doi.org/10.3847/1538-4357/abd724>. doi:10.3847/1538-4357/abd724.
- Bruno, A., & Richardson, I. G. (2021). Empirical model of 10–130 mev solar energetic particle spectra at 1 au based on coronal mass ejection speed and direction. *Solar Physics*, 296(36). URL: <https://doi.org/10.1007/s11207-021-01779-4>. doi:10.1007/s11207-021-01779-4.
- Cane, H. (2000). Coronal mass ejections and forrush decreases. *Space Science Reviews*, 93(1), 55–77. URL: <https://doi.org/10.1023/A:1026532125747>. doi:10.1023/A:1026532125747.
- Desai, M., & Giacalone, J. (2016). Large gradual solar energetic particle events. *Living Reviews in Solar Physics*, 13(3). doi:10.1007/s41116-016-0002-5.
- Dumbovic, M., Vrsnak, B., Guo, J., Heber, B., Dissauer, K., Carcaboso, F., Temmer, M., Veronig, A., Podladchikova, T., Möstl, C., Amerstorfer (Rollett), T., & Kirin, A. (2020). Evolution of coronal mass ejections and the corresponding forrush decreases: Modeling vs. multi-spacecraft observations. *Solar Physics*, 295(104). doi:10.1007/s11207-020-01671-7.
- Dumbović, M., Vršnak, B., Čalogović, J., & Zupan, R. (2012). Cosmic ray modulation by different types of solar wind disturbances. *A&A*, 538, A28. URL: <https://doi.org/10.1051/0004-6361/201117710>. doi:10.1051/0004-6361/201117710.
- Ellison, D. C., & Ramaty, R. (1985). Shock acceleration of electrons and ions in solar flares. *Astrophysical Journal*, 298, 400–408. doi:10.1086/163623.
- Freiher von Forstner, J. L., Guo, J., Wimmer-Schweingruber, R. F., Dumbović, M., Janvier, M., Démoulin, P., Veronig, A., Temmer, M., Papaioannou, A., Dasso, S., Hassler, D. M., & Zeitlin, C. J. (2020). Comparing properties of icme-induced forrush decreases at earth and mars. *Journal of Geophysical Research: Space Physics*, 125(3), e2019JA027662. URL: <https://agupubs.onlinelibrary.wiley.com/doi/abs/10.1029/2019JA027662>. doi:<https://doi.org/10.1029/2019JA027662>. E2019JA027662 10.1029/2019JA027662.
- Gopalswamy, N. (2016). History and development of coronal mass ejections as a key player in solar terrestrial relationship. *Geoscience Letters*, 3(8), 18pp. URL: <https://doi.org/10.1186/s40562-016-0039-2>. doi:10.1186/s40562-016-0039-2.
- Heber, B., Fichtner, H., & Scherer, K. (2006). Solar and heliospheric modulation of galactic cosmic rays. *Space Science Reviews*, 125(1), 81–91. URL: <https://doi.org/10.1007/s11214-006-9048-3>. doi:10.1007/s11214-006-9048-3.
- IZMIRAN Space Weather Prediction Center (2016). Izmiran space weather prediction center. URL: <http://spaceweather.izmiran.ru/eng/about.html> [Online; accessed 29-January-2022].
- Koldobskiy, S. A., Bindi, V., Corti, C., Kovaltsov, G. A., & Usoskin, I. G. (2019). Validation of the neutron monitor yield function using data from ams-02 experiment, 2011–2017. *Journal of Geophysical Research: Space Physics*, 124(4), 2367–2379. URL: <https://agupubs.onlinelibrary.wiley.com/doi/abs/10.1029/2018JA026340>. doi:<https://doi.org/10.1029/2018JA026340>.
- Koldobskiy, S., Raukunen, O., Vainio, R., Kovaltsov, G. A., & Usoskin, I. (2021). New reconstruction of event-integrated spectra (spectral fluences) for major solar energetic particle events. *Astronomy and Astrophysics*, 647, A132. URL: <https://doi.org/10.1051/0004-6361/707202040058>. doi:10.1051/0004-6361/707202040058.
- Lingri, D., Mavromichalaki, H., Belov, A., Eroshenko, E., Yanke, V., Abunin, A., & Abunina, M. (2016). Solar activity parameters and associated forrush decreases during the minimum between cycles 23 and 24 and the ascending phase of cycle 24. *Solar Physics*, 291, 1025–1041. doi:10.1007/s11207-016-0863-8.
- Melkumyan, A., Belov, A., Abunina, M., Abunin, A., Eroshenko, E., Oleneva, V., & Yanke, V. (2019). On recurrent Forrush Decreases. In A. Lagutin, I. Moskalenko, & M. Panasyuk (Eds.), *Journal of Physics Conference Series* (p. 012009). IOP Publishing, Bristol, United Kingdom volume 1181 of *Journal of Physics Conference Series*. doi:10.1088/1742-6596/1181/1/012009.
- de Mendonça, R. R. S., Braga, C. R., Echer, E., Lago, A. D., Munakata, K., Kuwabara, T., Kozai, M., Kato, C., Rockenbach, M., Schuch, N. J., Jassar, H. K. A., Sharma, M. M., Tokumaru, M., Duldig, M. L., Humble, J. E., Evenson, P., & Sabbah, I. (2016). THE TEMPERATURE EFFECT IN SECONDARY COSMIC RAYS (MUONS) OBSERVED AT THE GROUND: ANALYSIS OF THE GLOBAL MUON DETECTOR NETWORK DATA. *The Astrophysical Journal*, 830(2), 88. URL: <https://doi.org/10.3847/0004-637x/830/2/88>. doi:10.3847/0004-637x/830/2/88.
- Miroshnichenko, L., & Nymmik, R. (2014). Extreme fluxes in solar energetic particle events: Methodological and physical limitations. *Radiation Measurements*, 61, 6–15. URL: <https://www.sciencedirect.com/science/article/pii/S1350448713003806>. doi:<https://doi.org/10.1016/j.radmeas.2013.11.010>.
- Miteva, R., Samwel, S. W., Zabunov, S., & Dechev, M. (2020). On the flux saturation of SOHO/ERNE proton events. *Bulgarian Astronomical Journal*, 33, 99.
- Mottl, D. A., Nymmik, R. A., & Sladkova, A. I. (2001). Energy spectra of high-energy SEP event protons derived from statistical analysis of experimental data on a large set of events. In M. S. El-Genk, & M. J. Bragg (Eds.), *Space Technology and Applications International Forum - 2001* (pp. 1191–1196). AIP Publishing LLC., New York volume 552 of *American Institute of Physics Conference Series*. doi:10.1063/1.1358071.
- Neutron Monitor Database (2022). Neutron Monitor Database. URL: <https://www.nmdb.eu/>.
- Nymmik, R. (2013). Charge states of heavy ions, as determined from the parameters of solar energetic particle spectra. *Bulletin of the Russian Academy of Sciences: Physics*, 77, 490–492. doi:10.3103/S1062873813050419.
- Paasilta, Miikka, Raukunen, Osku, Vainio, Rami, Valtonen, Eino, Papaioannou, Athanasios, Siipola, Robert, Riihonen, Esa, Dierckx, Mark, Crosby, Norma, Malandraki, Olga, Heber, Bernd, & Klein, Karl-Ludwig (2017). Catalogue of 55–80 mev solar proton events extending through solar cycles 23 and 24. *J. Space Weather Space Clim.*, 7, A14. URL: <https://doi.org/10.1051/swsc/2017013>. doi:10.1051/swsc/2017013.
- Papaioannou, A., Belov, A., Abunina, M., Eroshenko, E., Abunin, A., Anastasiadis, A., Patsourakos, S., & Mavromichalaki, H. (2020). Interplanetary coronal mass ejections as the driver of non-recurrent forrush decreases. *The Astrophysical Journal*, 890(2), 101. URL: <https://doi.org/10.3847/1538-4357/ab6bd1>. doi:10.3847/1538-4357/ab6bd1.
- Reames, D. V. (1999). Particle acceleration at the sun and in the heliosphere. *Space Science Reviews*, 90(3), 413–491. doi:<https://doi.org/10.1023/A:1005105831781>.
- Richardson, I. G., & Cane, H. V. (2011). Galactic Cosmic Ray Intensity Response to Interplanetary Coronal Mass Ejections/Magnetic Clouds in 1995 - 2009. *Solar Physics*, 270(2), 609–627. doi:10.1007/s11207-011-9774-x.
- Subramanian, P., Antia, H. M., Dugad, S. R., Goswami, U. D., Gupta, S. K., Hayashi, Y., Ito, N., Kawakami, S., Kojima, H., Mohanty, P. K., Nayak, P. K., Nonaka, T., Oshima, A., Sivaprasad, K., Tanaka, H., & S. C. Tonwar (The GRAPES-3 collaboration) (2009). Forrush decreases and turbulence levels at coronal mass ejection fronts. *A&A*, 494(3), 1107–1118. URL: <https://doi.org/10.1051/0004-6361/200809551>. doi:10.1051/0004-6361/200809551.
- Torsti, J., Valtonen, E., Lumme, M., Peltonen, P., Eronen, T., Louhola, M., Riihonen, E., Schultz, G., Teittinen, M., Ahola, K., Holmlund, C., Kellhä, V., Leppälä, K., Ruuska, P., & Strömmer, E. (1995). Energetic particle experiment erne. *Solar Physics*, 162(1-2), 505–531. URL: <https://doi.org/10.1007/BF00733438>. doi:10.1007/BF00733438.
- Valtonen, E., & Lehtinen, I.-V. (2009). Solar energetic particle fluences from soho/erne. *Acta Geophysica*, 57, 116–124. doi:10.2478/s11600-008-0056-4.
- Veselinović, N., Dragić, A., Maletić, D., Joković, D., Savić, M., Banjanac, R., Udovičić, V., & Aničin, I. (2015). Cosmic rays muon flux measurements at Belgrade shallow underground laboratory. In L. Trache, D. Chesneau, & C. Alexandru Ur (Eds.), *Exotic Nuclei and Nuclear/Particle Astrophysics (V) From Nuclei to Stars: Carpathian Summer School of Physics 2014* (pp. 421–425). AIP Publishing LLC., New York volume 1645 of *American Institute*

- 715 of *Physics Conference Series*. doi:10.1063/1.4909614.
- 716 Veselinović, N., Dragić, A., Savić, M., Maletić, D., Joković, D., Banjanac, R.,  
717 & Udovičić, V. (2017). An underground laboratory as a facility for stud-  
718 ies of cosmic-ray solar modulation. *Nuclear Instruments and Methods in*  
719 *Physics Research Section A: Accelerators, Spectrometers, Detectors and As-*  
720 *sociated Equipment*, 875, 10–15. URL: <https://www.sciencedirect.com/science/article/pii/S0168900217309634>. doi:<https://doi.org/10.1016/j.nima.2017.09.008>.
- 723 Veselinović, Nikola, Savić, Mihailo, Dragić, Aleksandar, Maletić, Dim-  
724 itrije, Banjanac, Radomir, Joković, Dejan, Knezević, David, & Udovičić,  
725 Vladimir (2021). Correlation analysis of solar energetic particles and sec-  
726 ondary cosmic ray flux. *Eur. Phys. J. D*, 75(6), 173. URL: <https://doi.org/10.1140/epjd/s10053-021-00172-x>. doi:10.1140/epjd/  
727 s10053-021-00172-x.
- 729 Yashiro, S., Gopalswamy, N., Michalek, G., St. Cyr, O. C., Plunkett, S. P.,  
730 Rich, N. B., & Howard, R. A. (2004). A catalog of white light coro-  
731 nal mass ejections observed by the soho spacecraft. *Journal of Geophys-*  
732 *ical Research: Space Physics*, 109(A7). doi:[https://doi.org/10.1029/  
733 2003JA010282](https://doi.org/10.1029/2003JA010282).
- 734 Zhao, L., Zhang, M., & Rassoul, H. K. (2016). DOUBLE POWER LAWS  
735 IN THE EVENT-INTEGRATED SOLAR ENERGETIC PARTICLE SPEC-  
736 TRUM. *The Astrophysical Journal*, 821(1), 62. URL: [https://doi.org/  
737 10.3847/0004-637x/821/1/62](https://doi.org/10.3847/0004-637x/821/1/62). doi:10.3847/0004-637x/821/1/62.

**Declaration of interests**

The authors declare that they have no known competing financial interests or personal relationships that could have appeared to influence the work reported in this paper.

The authors declare the following financial interests/personal relationships which may be considered as potential competing interests:





# The SHiP experiment at the proposed CERN SPS Beam Dump Facility

SHiP Collaboration\*

Received: 16 December 2021 / Accepted: 18 April 2022 / Published online: 26 May 2022  
© The Author(s) 2022

**Abstract** The Search for Hidden Particles (SHiP) Collaboration has proposed a general-purpose experimental facility operating in beam-dump mode at the CERN SPS accelerator to search for light, feebly interacting particles. In the baseline configuration, the SHiP experiment incorporates two complementary detectors. The upstream detector is designed for recoil signatures of light dark matter (LDM) scattering and for neutrino physics, in particular with tau neutrinos. It consists of a spectrometer magnet housing a layered detector system with high-density LDM/neutrino target plates, emulsion-film technology and electronic high-precision tracking. The total detector target mass amounts to about eight tonnes. The downstream detector system aims at measuring visible decays of feebly interacting particles to both fully reconstructed final states and to partially reconstructed final states with neutrinos, in a nearly background-free environment. The detector consists of a 50 m long decay volume under vacuum followed by a spectrometer and particle identification system with a rectangular acceptance of 5 m in width and 10 m in height. Using the high-intensity beam of 400 GeV protons, the experiment aims at profiting from the  $4 \times 10^{19}$  protons per year that are currently unexploited at the SPS, over a period of 5–10 years. This allows probing dark photons, dark scalars and pseudo-scalars, and heavy neutral leptons with GeV-scale masses in the direct searches at sensitivities that largely exceed those of existing and projected experiments. The sensitivity to light dark matter through scattering reaches well below the dark matter relic density limits in the range from a few MeV/ $c^2$  up to 100 MeV-scale masses, and it will be possible to study tau neutrino interactions with unprecedented statistics. This paper describes the SHiP experiment baseline setup and the detector systems, together with performance results from prototypes in test beams, as it was prepared for the 2020 Update of the European Strategy for Particle Physics. The expected detector performance from simulation is summarised at the end.

## 1 Introduction

The SHiP Collaboration has proposed a general-purpose intensity-frontier facility operating in beam-dump mode at the CERN SPS accelerator to search for feebly interacting GeV-scale particles, here referred to as hidden sector (HS) particles, and to perform measurements in neutrino and in flavour physics. The SPS accelerator with its present performance is capable of delivering an annual yield of up to  $4 \times 10^{19}$  protons on target in slow extraction of one second long spills of de-bunched beam at 400 GeV/c, while still respecting the beam requirements of the HL-LHC and the existing SPS beam facilities. The slow extraction of de-bunched beam is motivated by the need to control the combinatorial background, and to dilute the large beam power deposited on the beam-dump target. Yields of  $\mathcal{O}(10^{18})$  charmed hadrons,  $\mathcal{O}(10^{16})$  tau leptons, and  $\mathcal{O}(10^{21})$  photons above 100 MeV are expected within the acceptance of the detectors in five years of nominal operation. The unprecedented yields offer a unique opportunity to complement the world-wide program of searches for New Physics with the help of a new intensity-frontier facility that is complementary to the high-energy and the precision frontiers.

The SHiP experiment is designed to both search for decay signatures of models with HS particles, such as heavy neutral leptons (HNL) [1], dark photons (DP) [2], dark scalars (DS), etc, by full reconstruction and particle identification of Standard Model (SM) final states, and to search for LDM scattering signatures by the direct detection of recoil of atomic electrons (or nuclei) in a high-density medium [3]. The experiment is also optimised to make measurements on tau neutrinos and on neutrino-induced charm production by all three species of neutrinos.

The proposal was submitted in the form of an Expression of Interest to the CERN SPS and PS committee in 2013 (CERN-SPSC-2013-024/SPSC-EOI-010). Following the recommendation of the committee, the SHiP Collaboration proceeded with the preparation of the Technical Proposal (TP) on the detectors and on the proposed SPS experimen-

\*e-mail: [Richard.Jacobsson@cern.ch](mailto:Richard.Jacobsson@cern.ch)

\*e-mail: [Antonia.Di.Crescenzo@cern.ch](mailto:Antonia.Di.Crescenzo@cern.ch)

tal facility, together with an extensive report on the Physics Case, submitted in 2015 (CERN-SPSC-2015-016/SPSC-P-350, CERN-SPSC-2015-040/SPSC-P-350-ADD-2 and [4, 5]). The review of the TP concluded with a recommendation to proceed with a three-year Comprehensive Design Study, under the auspices of the CERN Physics Beyond Colliders (PBC) initiative, with the goal of submitting a proposal for the SHiP detector and the SPS Beam Dump Facility (BDF) to the 2020 European Strategy for Particle Physics Update (ESPPU) (CERN-SPSC-2019-010/SPSC-SR-248, CERN-SPSC-2019-049/SPSC-SR-263, CERN Yellow Reports CYRM-2020-002).

The 2020 ESPPU (CERN-ESU-014) recognised the BDF/SHiP proposal as one of the front-runners among the new facilities investigated within CERN's Physics Beyond Collider initiative. With regards to the cost of the baseline design of the facility, the project could not, as of 2020, be recommended for construction considering the overall recommendations of the Strategy.

In line with the ESPPU recommendations and in view of the importance of the CERN injector complex as a provider of physics programmes complementary to CERN's primary large-scale research facility, and the strong motivation behind the BDF/SHiP proposal, a continued study programme was launched in 2020. The renewed effort has initially focused on reviewing the layout of the facility and the most suitable site, including reuse of existing experimental areas at the CERN SPS, with the goal of significantly reducing the cost of the facility (CERN-SPSC-2022-009) and allow implementation to start in CERN's Long Shutdown 3. This effort is accompanied by a re-optimisation of the experiment in order to allow integration into the alternative areas, while preserving the original physics scope and sensitivity.

The present paper describes in detail the detector and summarises the results of the detector studies and the main per-

formance parameters as it was prepared for the 2020 ESPPU. More details on the physics sensitivity of the experiment can be found in Refs. [1–3].

## 2 Overview of the experiment

The SHiP experiment would be served by a new, short, dedicated beam line branched off the existing SPS transfer line to the CERN North Area. The current layout of the SPS Beam Dump Facility [5] with the SHiP experimental area is shown in Fig. 1, and the current layout of the SHiP experiment in Fig. 2.

The setup consists of a high-density proton target located in the target bunker [7–9], followed by a hadron stopper and a muon shield [10]. The target is made of blocks of a titanium-zirconium doped molybdenum alloy (TZM) in the region of the largest deposit of energy, followed by blocks of pure tungsten. The total target depth is twelve interaction lengths over 1.4 m. The high atomic numbers and masses of the target material maximises the production of charm, beauty and photons as sources of HS particles, and the short interaction length ensures a high level of stopping power for pions and kaons to reduce the neutrino background.

To control the beam-induced background from muons, the flux in the detector acceptance must be reduced from  $\mathcal{O}(10^{11})$  Hz ( $> 1$  GeV) to less than  $\mathcal{O}(10^5)$  Hz. Despite the aim to cover the long lifetimes associated with the HS particles, the detector volume should be situated as close as possible to the proton target due to the relatively large production angles of the HS particles. Hence, the muon flux should be reduced over the shortest possible distance. To this end, an active muon shield entirely based on magnetic deflection has been developed. The first section of the muon shield starts within the target complex shielding assembly,

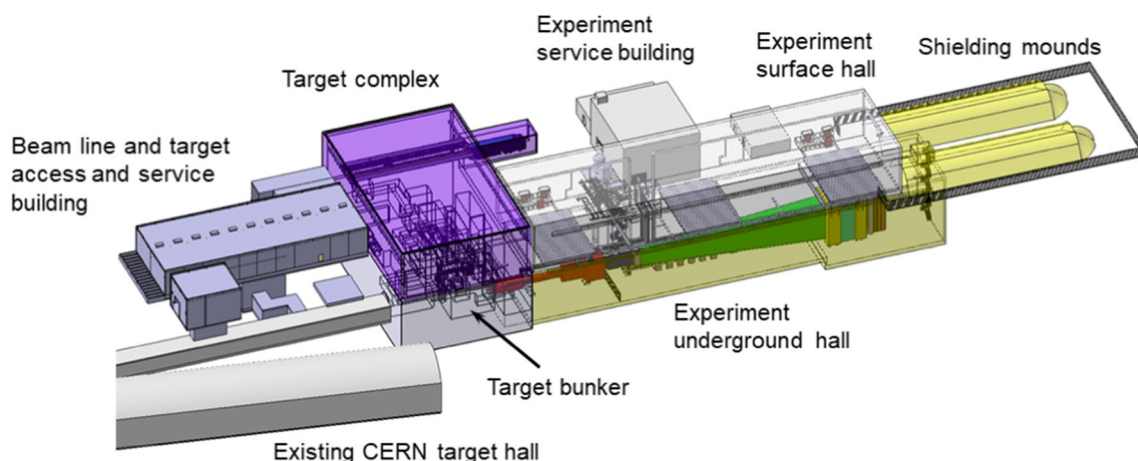


**Fig. 1** Overview of the SPS Beam Dump Facility with the SHiP experimental area

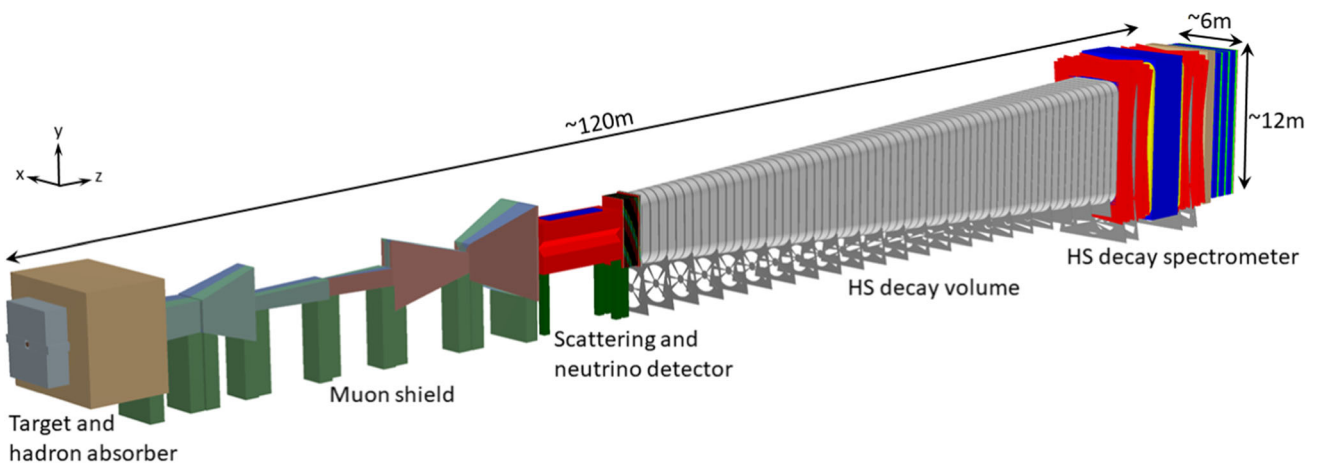


**Fig. 2** Overview of the SHiP experiment as implemented in the GEANT4-based [6] physics simulation

**Table 1** Summary of the physics models and final states ( $\ell = e, \mu, \tau$ ) that the SND and the HSDS detectors are sensitive to (HNL=Heavy Neutral Lepton, DP=Dark Photon, DS=Dark Scalar, ALP=Axion-Like Particle, LDM=Light Dark Matter)

	Physics model	Final state
HSDS	HNL, SUSY neutralino	$\ell^\pm \pi^\mp, \ell^\pm K^\mp, \ell^\pm \rho^\mp (\rho^\mp \rightarrow \pi^\mp \pi^0)$
	DP, DS, ALP (fermion coupling), SUSY sgoldstino	$\ell^+ \ell^-$
	DP, DS, ALP (gluon coupling), SUSY sgoldstino	$\pi^+ \pi^-, K^+ K^-$
	HNL, SUSY neutralino, axino	$\ell^+ \ell^- \nu$
	ALP (photon coupling), SUSY sgoldstino	$\gamma \gamma$
SND	SUSY sgoldstino	$\pi^0 \pi^0$
	LDM	Electron, proton, hadronic shower
	$\nu_\tau, \bar{\nu}_\tau$ measurements	$\tau^\pm$
	Neutrino-induced charm production ( $\nu_e, \nu_\mu, \nu_\tau$ )	$D_s^\pm, D^\pm, D^0, \bar{D}^0, \Lambda_c^+, \bar{\Lambda}_c^-$

one metre downstream of the target. This first section consists of a magnetic coil which magnetises the hadron stopper with a dipole field of  $\sim 1.6$  T over 4.5 m. The rest of the muon shield consists of six free-standing magnets, each 5 m long, located in the upstream part of the experimental hall.

The SHiP detector consists of two complementary apparatuses, the Scattering and Neutrino Detector (SND) and the Hidden Sector Decay Spectrometer (HSDS). The SND will search for scattering of LDM and perform the neutrino measurements. It also provides normalisation of the yield for the HS particle search. The HSDS is designed to reconstruct the decay vertex of a HS particle, measure its invariant mass and provide particle identification of the decay products in an environment of extremely low background. The SND and the HSDS detectors have been designed to be sensitive to as many physics models and final states as possible, summarised in Table 1.

The muon shield and the SHiP detector systems are housed in an  $\sim 120$  m long underground experimental hall at a depth of  $\sim 15$  m.

### 3 Muon shield

The free-standing magnetic muon shield [10, 11] is one of the most critical and challenging subsystems of SHiP. The baseline design relies on air-cooled warm magnets made from cold-rolled grain-oriented (CRGO) steel for an optimal compromise between a high field gradient and low input power, the latter required to reduce the space required for the coils. The technology studies indicate that it is safe to assume an average field of 1.7 T including the magnetic-core packing factor. The optimisation of the muon shield [11, 12] has been performed with machine learning using a Bayesian optimisation algorithm and fully simulated muons from the beam-dump target by GEANT4 [6]. Under the assumption that the muon shield is composed of six magnets whose geometry is described by a total of 42 parameters, the algorithm simultaneously minimises the muon background rate in the HSDS and the total mass of the shield magnet yokes. The input parameters describing the muon flux out of the target in the simulation were tuned to measured data with a 400 GeV pro-

ton beam, as discussed in [13]. The current design consists of about 600 individual packs of sheets with 50 mm thickness, the largest with transverse dimensions of  $6.6 \times 3.8 \text{ m}^2$  and weighing about 8 tonnes. In total, the muon shield has an overall weight of about 1400 tonnes. The baseline for the coil consists of 9 mm isolated stranded copper wire consolidated using an elastic compound. A table-size prototype has already been constructed and tested.

## 4 Scattering and neutrino detector

### 4.1 Overview

SND aims at performing measurements with neutrinos and to search for LDM. The detection of tau neutrinos and the observation for the first time of tau anti-neutrinos pose a challenge for the design of the detector, which has to fulfill conflicting requirements: a large target mass to collect enough statistics, an extremely high spatial accuracy to observe the short-lived tau lepton and a magnetic field to disentangle neutrinos from anti-neutrinos. The optimisation of the SND layout also had to take into account constraints given by the location and the muon flux. The overall layout, as implemented in simulation, is shown in Fig. 3.

SND consists of a  $\sim 7 \text{ m}$  long detector inserted in a magnet [14] providing a 1.2 T horizontal magnetic field, followed by a muon identification system. The hourglass shape of the magnet is driven by the profile of the area in the transverse plane which is cleared from the bulk of the muon flux, which in turn defines the allowed region for the detector. The neutrino flux and neutrino energy decrease with larger polar angles and this produces a radial dependence of the neutrino interaction yield, favouring the development of a narrow and long emulsion target.

The magnet hosts the emulsion target, interleaved with target tracker planes, and a downstream tracker. The emulsion target has a modular structure: the unit cell consists of an emulsion cloud chamber (ECC) made of tungsten plates interleaved with nuclear emulsion films, followed by a compact emulsion spectrometer (CES) for the momentum and charge sign measurement of particles produced in neutrino interactions. The ECC bricks are arranged in walls alternated with target tracker planes, providing the time stamp of the interactions occurring in the target. The downstream tracker is made of three target tracker planes separated by  $\sim 50 \text{ cm}$  air gaps. It is used to measure the charge and momentum of muons exiting the target region, thus extending significantly the detectable momentum range of the CES. The downstream tracker planes also help to connect the tracks in the emulsion films with the downstream SND muon identification system.

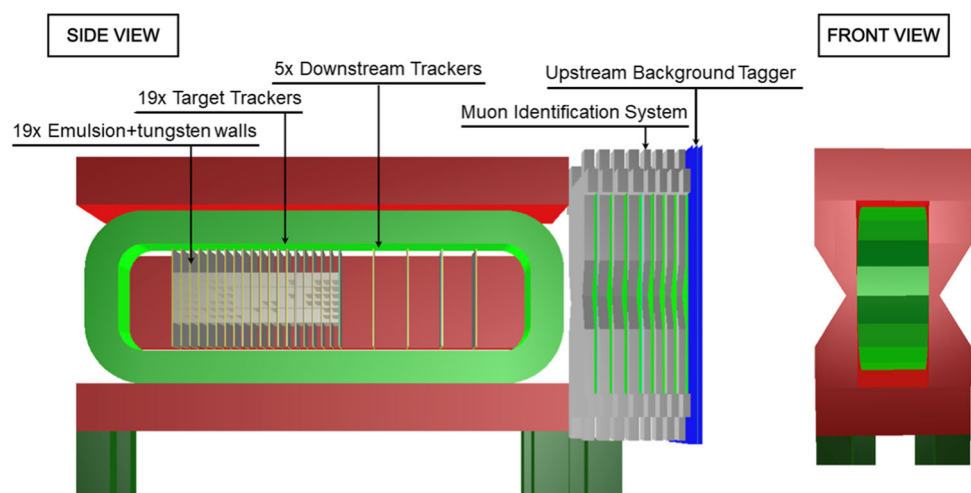
The SND muon identification system is made of a sequence of iron filters and resistive plate chamber (RPC) planes, totalling about two metres in length. As neutrino interactions in the iron can generate background for the HS decay search through the production of long-lived neutral particles entering the downstream HSDS decay volume and mimicking signal events, the downstream part of the muon identification system also acts as an HSDS upstream background tagger (UBT).

### 4.2 SND emulsion target

The emulsion target is in the current baseline made of 19 emulsion brick walls and 19 target tracker planes. The walls are divided in  $2 \times 2$  cells, each with a transverse size of  $40 \times 40 \text{ cm}^2$ , containing ECC and a CES as illustrated in Fig. 4.

The ECC technology makes use of nuclear emulsion films interleaved with passive absorber layers to build up a tracking device with sub-micrometric position and milliradian angular

**Fig. 3** Schematic layout of the Scattering and Neutrino Detector (SND)



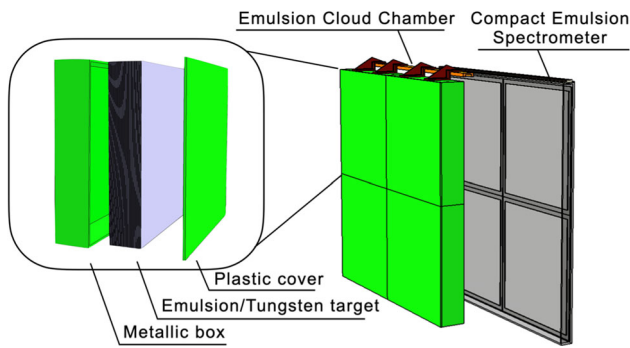


**Fig. 4** Layout of the emulsion target and closeup view of one emulsion brick wall of four cells, each containing an ECC and a CES

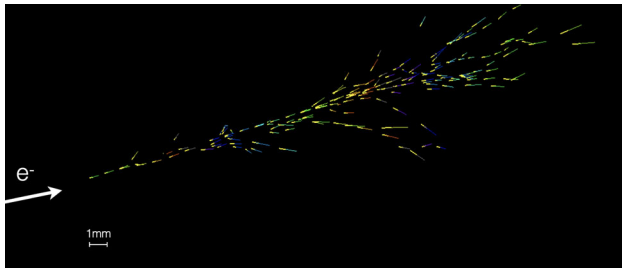


**Fig. 5** Simulated electromagnetic shower induced in an ECC by a 6 GeV/c electron. The picture shows the  $e^+e^-$ -track segments reconstructed in the emulsion films

resolution, as demonstrated by the OPERA experiment [15]. The technique allows detecting tau leptons [16] and charmed hadrons [17] by disentangling their production and decay vertices. It is also suited for LDM detection through the direct observation of the scattering off electrons in the absorber layers. The high spatial resolution of the nuclear emulsion allows measuring the momentum of charged particles through the detection of multiple Coulomb scattering in the passive material [18], and identifying electrons by observing electromagnetic showers in the brick [19]. Nuclear emulsion films are produced by Nagoya University in collaboration with the Fuji Film Company and by the Slavich Company in Russia.

An ECC brick is made of 36 emulsion films with a transverse size of  $40 \times 40 \text{ cm}^2$ , interleaved with 1 mm thick tungsten layers. Tungsten has been chosen in place of lead as in the OPERA experiment for its higher density and for its shorter radiation length and smaller Molière radius in order to improve the electromagnetic-shower containment. The resulting brick has a total thickness of  $\sim 5 \text{ cm}$ , corresponding to  $\sim 10 X_0$ , and a total weight of  $\sim 100 \text{ kg}$ . The overall target weight with 19 walls of  $2 \times 2$  bricks is about 8 tonnes. With the estimated background flux, the emulsion films must be replaced twice a year in order to keep the integrated amount of tracks to a level that does not spoil the reconstruction performance. The films are analysed by fully automated optical microscopes [20, 21]. The scanning speed, measured in terms of film surface per unit time, was significantly increased in

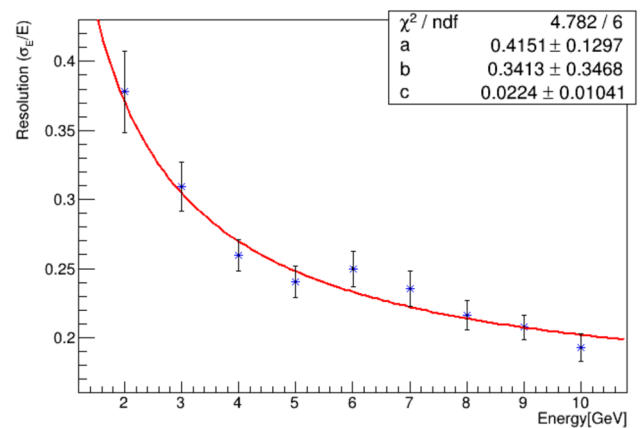


**Fig. 6** Energy resolution for electrons using the ECC as sampling calorimeter, as estimated with MC simulations. The function  $\sigma_E/E = \sqrt{(a/\sqrt{E})^2 + (b/E)^2 + c^2}$  was used for the fit

recent years [22–25]. The current scanning speed and the availability of several tens of microscopes within the collaboration makes it possible to scan the whole emulsion film surface over a time scale of six months.

The performance of the ECC in terms of electromagnetic shower identification and energy measurement was studied with Monte Carlo (MC) simulations for different electron energies. The ECC can be used as a sampling calorimeter, with the number of track segments being proportional to the energy of the electron (see Fig. 5). A new approach based on machine learning techniques was developed and an energy better than 25% was achieved for energies higher than 4 GeV, as reported in Fig. 6.

The CES modules aim at measuring the electric charge of hadrons produced in tau lepton decays, thus providing the unique feature of disentangling  $\nu_\tau$  and  $\bar{\nu}_\tau$  charged-current interactions also in their hadronic decay channels. It complements the use of the ECC in the momentum measurement for hadrons and soft muons which are emitted at large angles and which do not reach the downstream tracker. The basic structure of the CES is made of three emulsion films interleaved by two layers of low density material. The emulsion films belonging to the CES will need more frequent replacements than those of the ECCs since reconstruction requires a lower level of background tracks. The replacement frequency is part of the current investigations. The CES concept was demonstrated in 2008 [26]. A new version with air gaps was designed and tested in 2017 at the CERN PS. The air gap was made by a 15 mm-thick poly(methyl methacrylate) (PMMA) hollow spacer placed between consecutive emulsion films. Different emulsion-film prototypes were tested in order to identify the support for the emulsion which minimises local deformations. Results show that the use of a 500  $\mu\text{m}$ -thick glass base induces deformations on the emulsion surface which are five times smaller than the 175  $\mu\text{m}$ -

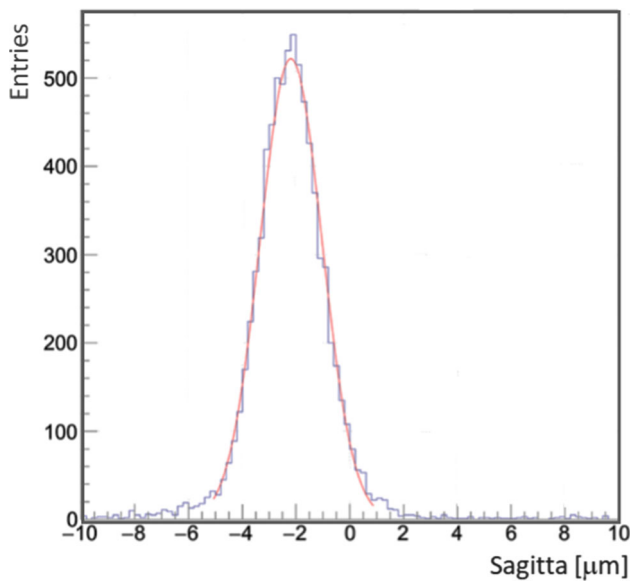


**Fig. 7** Measured sagitta for 10 GeV/c pions in a CES prototype tested in 2017 at the CERN PS

thick PMMA base typically used. Results obtained with the CES made with a glass base are very promising. The distributions of the measured sagitta along the  $x$ -axis for 1 and 10 GeV/c pions show gaussian peaks with  $\sigma$  of 10.2  $\mu\text{m}$  and 1.15  $\mu\text{m}$ , respectively (Fig. 7). A momentum resolution of  $\sim 30\%$  up to 10 GeV/c momenta was achieved for the first time.

#### 4.3 SND target tracker and downstream tracker

A system of electronic detectors in combination with the ECCs is needed in order to time stamp the events reconstructed inside the bricks and to connect the emulsion tracks to those reconstructed in the downstream tracker and in the SND muon identification system.

In the baseline configuration, the SND employs 19 target tracker planes within the emulsion target, with the first one acting as a veto for charged particles entering the emulsion target. The three additional downstream tracker planes located immediately after the emulsion target measure momentum and charge for long tracks, in particular muons. The distance between two downstream tracker planes is 50 cm without any material interposed between them.

The baseline technology for the SND tracker systems consists of a scintillating-fibre tracker (SciFi). Its main characteristics are: high granularity tracking with a spatial resolution of 50  $\mu\text{m}$  over a surface of  $\sim 1 \text{ m}^2$ , single plane time resolution of 400 ps, high detection efficiency of  $>99.5\%$ , and insensitivity to magnetic field. The active detector planes are composed of six fibre layers glued together to form fibre mats of  $\sim 1.5 \text{ mm}$  thickness. The fibre mats are glued on supports

made of carbon fibre honeycomb structures, forming large detector surfaces with dead-zones of less than 500  $\mu\text{m}$  along the borders with adjacent fibre mats. The total thickness of an  $x - y$  plane is less than 15 mm. The spatial resolution has been measured to be 36  $\mu\text{m}$  by LHCb.

The active area of each plane is  $917 \times 1440 \text{ mm}^2$ . The dimensions exceed those of the ECC and CES in order to track particles emitted at large angles in several consecutive walls downstream of the ECC in which the interaction occurred. Additionally, a signal-cluster shape analysis allows a modest single-hit angular resolution which helps to resolve possible combinatorial ambiguities.

#### 4.4 SND muon identification system

The SND muon identification system is designed to identify with high efficiency the muons produced in neutrino interactions and  $\tau$  decays occurring in the emulsion target. The system consists of eight hadron filters of iron interleaved with tracking planes instrumented with RPCs, plus three additional downstream layers based on multigap resistive plate chamber (MRPC) planes. The MRPC planes also act as the upstream background tagger for the HS decay searches, and is described in Sect. 5.3.1. The four most upstream iron layers are 15 cm thick. The downstream layers are 10 cm thick in order to have a better tracking performance.

Each RPC plane is made of three gaps with an active area of  $1900 \times 1200 \text{ mm}^2$  each. The RPC planes are read out by means of orthogonal-strip panels with  $\sim 1 \text{ cm}$  pitch. The overall transverse dimension of one plane is  $4290 \times 2844 \text{ mm}^2$ . The planes are staggered by  $\pm 10 \text{ cm}$  to compensate for the acceptance loss due to the dead areas between adjacent gaps in the same plane. Due to the significant rate of beam-induced particles impinging on the muon system, the RPCs will be operated in avalanche mode.

The front-end boards house two ASICs with eight input channels each, performing amplification and discrimination of signals, and an on-board FPGA for data time-stamping, zero suppression and serialization. Each RPC plane are read out by 38 boards. The current option for the ASICs is the FEERIC chip [27], developed by the ALICE Collaboration.

Five prototype RPC detectors, each consisting of a 2 mm-wide gas gap with 2 mm-thick Bakelite electrodes and an active area of  $1900 \times 1200 \text{ mm}^2$ , were constructed and used in CERN H4 beam line for the SHiP muon-spectrum and charm-production measurements in July 2018 [13]. The chambers, read out by two panels of orthogonal copper strips with a pitch of 10.625 mm were operated in avalanche mode with a standard gas mixture of  $\text{C}_2\text{H}_2\text{F}_4/\text{C}_4\text{H}_{10}/\text{SF}_6$  in volume ratios of 95.2%/4.5%/0.3%, respectively. As shown in Fig. 8, the chambers showed efficiencies above 98%.

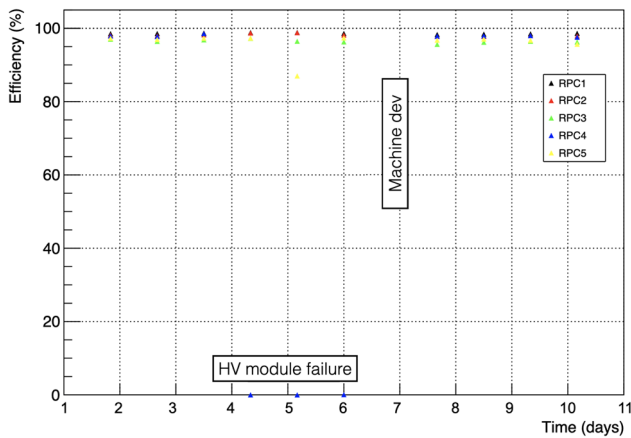


**Fig. 8** Efficiency of the five RPC stations used in the muon-flux and charm-production measurement. During the run, RPC chamber 4 suffered a problem with the high-voltage module during three days and SPS had a day of machine development studies

## 5 Hidden sector decay spectrometer

### 5.1 Overview

HS particles are typically endowed with long lifetimes compared to most unstable SM particles, making the beam-dump configuration with a large fiducial volume particularly suitable. The decay volume of SHiP is located immediately downstream of the SND at  $\sim 45$  m from the centre of the proton target. The geometry and dimensions of the detector volume that define the decay acceptance have been obtained by an optimisation based on a wide range of physics models and particle masses, the performance of the muon shield, and the  $5\text{ m} \times 10\text{ m}$  aperture of SHiP's spectrometer. The resulting decay volume delineates a pyramidal frustum with a length of 50 m and upstream dimensions of  $1.5\text{ m} \times 4.3\text{ m}$ .

The signature of a HS particle decay consists of an isolated decay vertex within the decay volume and no associated activity in the tagger system surrounding the decay volume. For fully reconstructed signal decays, where all particles coming from the decaying hidden particle are reconstructed in the spectrometer, the total momentum vector of the decay vertex extrapolates back to the proton interaction region. In partially reconstructed final states with one or more missing particles, e.g. as in one of the decay modes of heavy neutral leptons,  $\text{HNL} \rightarrow \mu^+ \mu^- \nu$ , the total momentum vector of the decay vertex extrapolates back to a larger region around the proton interaction region. Particle identification of the decay products is used in order to further suppress background and to allow characterising a signal and associating it with physics models.

The search for visible decays requires an extremely low and well-controlled background environment with a highly redundant detector system. The dominant sources of back-

ground are neutrino-induced and muon-induced inelastic interactions in the detector or surrounding materials, and random combinations of reconstructed residual muons. Backgrounds originating from cosmic muons have been demonstrated to be negligible (CERN-SPSC-2015-016/SPSC-P-350).

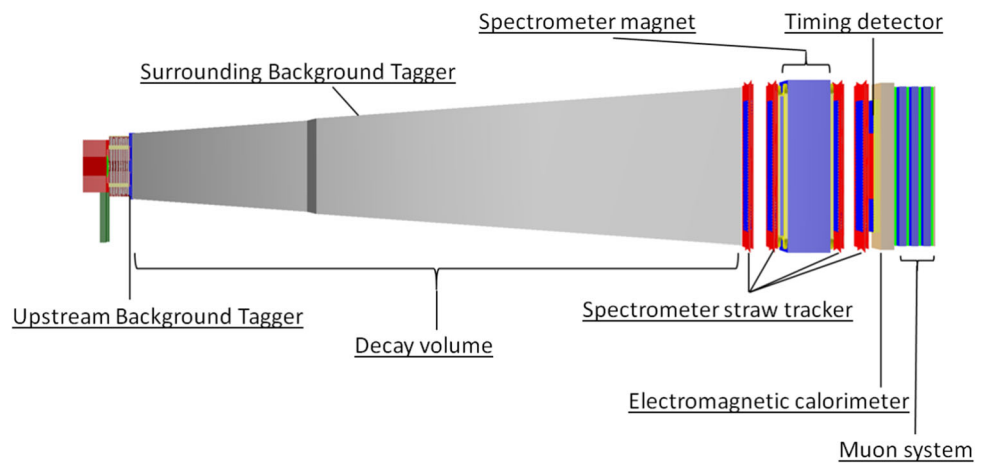
In order to suppress the background from neutrinos interacting with air in the fiducial volume, the decay volume is maintained at a pressure of  $< 10^{-3}$  bar by means of a vacuum vessel. In this configuration, neutrino interactions mainly occur in the vessel walls. Neutral long-lived background particles from these neutrino interactions that decay in the decay volume can be rejected by the reconstructed impact parameter at the beam-dump target. The impact parameter at the proton target is very powerful in rejecting all background sources to fully reconstructed final states. Partially reconstructed final states are more challenging to discriminate from the background since they require a looser criterion on the impact parameter. To further ensure that signal candidates are not produced by neutrino or muon interactions in the upstream SND or in the decay volume walls, the decay volume is completely covered by a high-efficiency background tagger system which is capable of detecting the charged particles produced in the interactions of muons and neutrinos. Requiring no local activity in the background tagger in time with the decay candidate is very efficient in suppressing residual background events in the partially reconstructed modes. Timing coincidence with high resolution is used to reject background from fake decay vertices formed by random combinations of muon tracks. The particle identification system provides further background rejection.

The various sub-systems of the HSDS are indicated in Fig. 9 and are described in details in the following.

### 5.2 HSDS vacuum vessel and magnet

In order to avoid material between the decay volume and the spectrometer straw tracker (Sect. 5.4), the HSDS vacuum vessel logically consists of two connected parts, the volume in which a decay vertex is accepted and the spectrometer section (Fig. 10). The spectrometer section runs through the spectrometer magnet and includes four tracker stations, two stations upstream and two downstream of the magnet. An upstream and a downstream end-cap close off the ends of the vacuum vessel. The two sections and the end-caps are connected by bolted flanges. To ensure that signal candidates are not produced by neutrino or muon interactions in the upstream SND or the walls of the vacuum vessel, the decay volume is completely covered by the high-efficiency upstream background tagger (UBT) (Sect. 5.3.1) and a surrounding background tagger (SBT) (Sect. 5.3.2) which are capable of detecting the charged particles produced in the interactions.

**Fig. 9** Schematic layout of the HS Decay Spectrometer (HSDS)



The decay-volume wall structure has been optimised [28] in order to be as thin and light as possible, and to incorporate the SBT liquid-scintillator detector in compartments with dimensions of  $0.80 \times 1.20 - 1.5 \text{ m}^2$ . The final design consists of a double-wall structure with an internal skeleton of azimuthal beams and longitudinal strengthening members entirely based on S355JO(J2/K2)W Corten steel.

The spectrometer section of the vacuum volume is constructed from austenitic stainless steel and is mechanically supported by the magnet yoke. The tracker is inserted into the vacuum by a top-loader system including a flange and cover. This results in a total vacuum-vessel volume of  $\sim 2040 \text{ m}^3$ .

The vacuum volume downstream end-cap is located just behind the last tracker station upstream of the timing and the particle identification detectors. The baseline design of both the upstream and downstream end-caps is based on a flat panel weld from a vertical stack of extruded profiles of aluminium alloy of type 6060. The material budget is equivalent to 0.8 radiation lengths in order to minimise the risk of neutrino and muon interactions in the upstream end-cap and not spoil the calorimeter performance after the downstream end-cap.

The HSDS magnet is based on a warm conventional magnet, see Fig. 10. It is required to have a physics aperture of  $5 \times 10 \text{ m}^2$  and provide a vertical bending power of about  $\sim 0.65 \text{ Tm}$  over the distance between the upstream and the downstream tracking stations. As the magnet aperture is limited in the horizontal plane by the region cleared from the beam-induced muon flux, the choice of the horizontal field orientation is motivated by the shorter field gap. The coils are made from a square-shape hollow aluminum conductor with transverse dimensions of  $50 \times 50 \text{ mm}^2$  and a bore hole of 25 mm for water cooling. The yoke is built from packs of 50 mm thick sheets of AISI 1010 steel. The pack is assembled in a brick-laying fashion around the corners. In terms of aperture, 100 mm has been reserved all around the physics aperture to accommodate the vacuum vessel and its anchor-

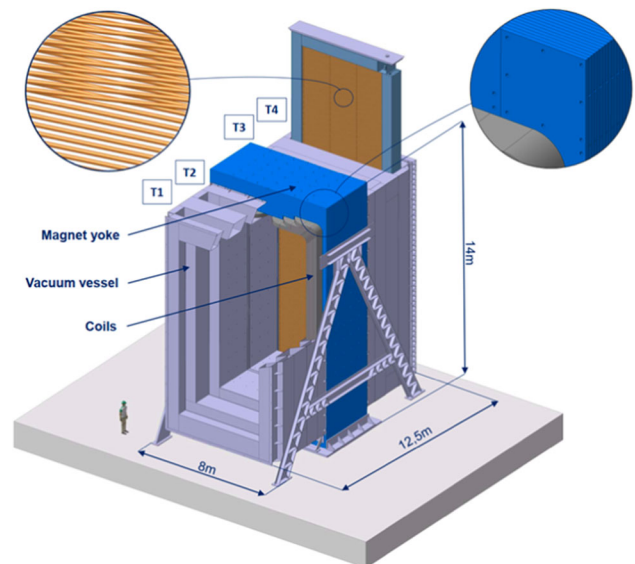


**Fig. 10** Layout of the spectrometer section, with the four top openings in the vacuum vessel for the insertion of the straw tracker stations (T1–T4), and the surrounding spectrometer magnet. The top-left magnified view illustrates the orientation of the tracker straw tubes, and the top right zooms on the magnet yoke plates with through-holes for assembling with rods

ing within the yoke. The result is a 1155-tonne yoke with two vertical coil packs of 25 tonnes each. Simulations show that the required magnetic performance can be obtained with a current density of  $1.5 \text{ A/mm}^2$  and an excitation current of 3000 A, resulting in a total power consumption of  $\sim 1.1 \text{ MW}$ .

### 5.3 HSDS background taggers

#### 5.3.1 UBT

The UBT covers the front-cap window of the vacuum vessel and is designed to tag the time and position of charged particles produced by neutrino interactions in the passive material



of the SND muon identification system. A good time resolution, around 300 ps, is needed. Having a position resolution of the order of a few millimeters, this system also provides position information for muon tracks, complementing the RPCs in the SND muon identification. The envisaged technology is similar to the technology used in the HSDS timing detector based on MRPCs described in Sect. 5.5.2, but given the less stringent requirements on the time resolution, a multi-gap RPC structure with only two gas gaps of 1 mm width is sufficient. To cover the HSDS vacuum vessel entrance window, each tagger plane is made of five MRPC modules (of about  $2070 \times 1020 \text{ mm}^2$ ) arranged vertically with an overlap of 10 cm in order to create layers without dead regions.

This technology has been successfully tested [29,30] and is being used in the framework of other projects [31]. Experimental tests performed with a single MRPC with an active area of  $1.5\text{--}1.2 \text{ m}^2$  have shown 90% efficiency on the whole surface (limited by the pick-up electrode, which covers 90% of the detector active area), and about 300 ps time resolution.

### 5.3.2 SBT

The SBT must be capable of detecting charged particles either entering the vacuum vessel side walls from outside, or produced in inelastic interactions of muons and neutrinos in the vessel walls. The baseline option to cover the top-, the bottom-, and the side-walls of the vacuum vessel is using a state-of-the-art liquid scintillator (LS-SBT) consisting of linear alkylbenzene (LAB) together with 2.0 g/l diphenyl-oxazole (PPO) as the fluorescent. This technology provides a high detection efficiency and good time resolution at a reasonable cost.

The LS-SBT is sub-divided into individual cells integrated into the support structure of the vacuum vessel. This results in cell sizes of 80 cm in the longitudinal direction, and between  $\sim 80 \text{ cm}$  and  $\sim 150 \text{ cm}$  in the azimuthal direction, depending on the location along the vacuum vessel. The thickness of the liquid-scintillator layer volume is about 30 cm, varying slightly along the length of the vacuum vessel, making up a total volume of  $\sim 300 \text{ m}^3$ .

Each cell of the SBT is read out by two wavelength-shifting optical modules (WOM) made from PMMA tubes (length: 23 cm, diameter: 6 cm, wall thickness: 3 mm) that are dip-coated with a wavelength-shifting dye (77.31% toluene, 22.29% paraloid B723, 0.13% bis-MSB and 0.27% p-terphenyl [32]). The WOMs absorb scintillation light in the range of 340–400 nm. The re-emitted photons with wavelengths above 400 nm are guided by the WOM tube to a ring of 40 SiPMs, each with a  $3 \times 3 \text{ mm}^2$  area, directly coupled to the WOM tube (see Fig. 11). There are  $O(4000)$  WOMs for the whole SBT. Beam test measurements in 2017 demonstrated the principle with a small-scale prototype of WOM-equipped liquid-scintillator cell [33]. Combining two WOM

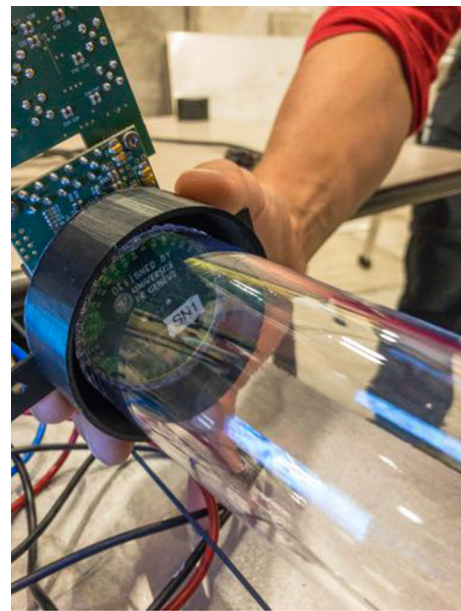


**Fig. 11** Coupling of the SBT wavelength-shifting optical module (WOM) tube to a 40-SiPM ring-array printed circuit board

signals, a time resolution of 1 ns and a homogeneity of the detector response over the detector volume within 20% are achieved. Further beam tests in 2018 and 2019 with a prototype of  $120 \times 80 \times 30 \text{ cm}^3$  (see Fig. 12) achieved a detection efficiency for charged particles depositing at least 45 MeV, corresponding to a minimum-ionising particle passing about 30 cm of liquid scintillator, close to 99.9% for distances between the passing particle and the WOM up to about 60 cm (see Fig. 13). Tests with a small-scale cell using a liquid scintillator purified by  $\text{Al}_2\text{O}_3$  columns as e.g. described in [34] were performed and show an increase of 20% in light yield compared to measurements with an unpurified liquid scintillator. GEANT4-based photon-transport simulations show that covering the cell walls with acrylic  $\text{BaSO}_4$ -coating is expected to increase the detected light yield by a factor of about five. As a result, the detection technique is well-suited to achieve 99.9% detection efficiency over large-area liquid-scintillator filled cells for energy depositions even below 45 MeV.

### 5.4 HSDS straw tracker

The main element of the HSDS is the straw tracker designed to accurately reconstruct the decay vertex, the mass, and the impact parameter of the hidden particle trajectory with respect to the proton interaction region. The precision of the extrapolated tracks must be well matched with the segmentation of the downstream timing detector.

The straw tracker design consists of two tracking telescopes located in the vacuum vessel, upstream and down-



**Fig. 12** Experimental setup of the SBT liquid-scintillator cell prototype, equipped with four WOMs (at positions labelled A, B, C, D) at DESY electron test beam in 2019

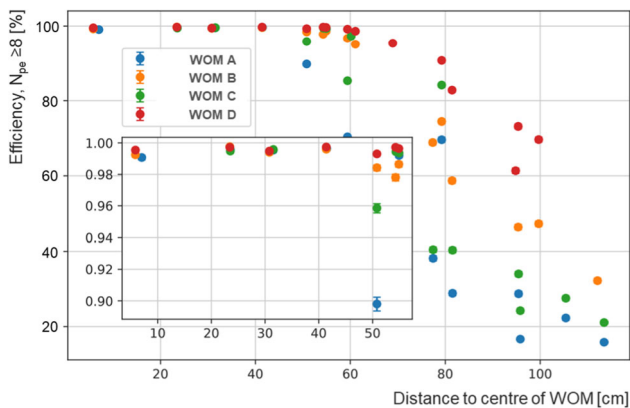


**Fig. 13** Detection efficiency by single SBT WOM for muons as a function of the distance between the muon beam and the WOM. A, B, C, D refer to the four WOMs positioned as indicated in Fig. 12. The insert shows the relevant region magnified

stream of the magnet, and each composed of two tracking stations. The four stations are identical with a nominal acceptance of 5 m in width and 10 m in height, and are based on 20 mm diameter ultralight drift tubes inspired by the NA62 design [35]. The cathode is constructed from 36  $\mu\text{m}$  thick PET film coated with 50 nm Cu and 20 nm Au. The anode is made of an Au-plated tungsten wire. As a consequence of the vertical bending of the spectrometer magnet, the straw tubes are oriented horizontally and have a length of 5 m. Background simulations indicate that, for the chosen straw dimensions, the expected straw hit rates will remain everywhere below 10 kHz. Each station contains four views, in a Y-U-V-Y arrangement, where U and V are stereo views with straws rotated by a small angle  $\pm\theta_{\text{stereo}}$  around the Z-axis with respect to the Y-measuring straws. In the baseline,

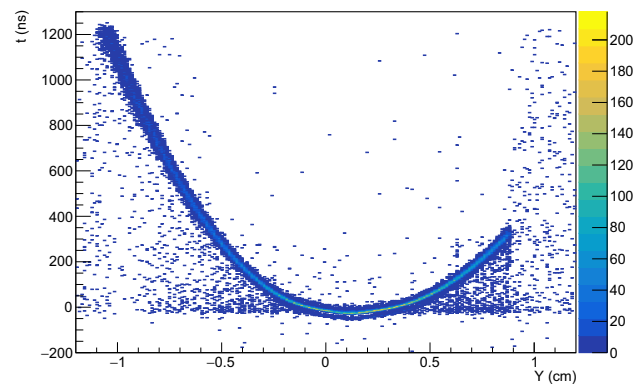


**Fig. 14** Measured drift time versus Y position of the reconstructed particle trajectory with the 20 mm diameter straw-tube prototype with a large wire eccentricity (2.05 mm). The Y axis is vertical, perpendicular to the wire axis X and to the particle beam axis Z

$\theta_{\text{stereo}} = 5^\circ$ . In total, the four views consist of about 4000 straw tubes which, together with services, are mounted on a frame. The frame, hung from a cover plate, is lowered into the vacuum vessel through openings in the roof of the vessel (Fig. 10). Straw tube elongation and relaxation effects present a serious challenge to the mechanics, which, if neglected, would result in an evolving and possibly excessive sagging of the straws. Three mechanical designs have been developed. The first one includes a constant-force spring to maintain the wire under the desired tension while accommodating the evolving straw elongation of several centimeters with the help of an expandable frame. The second scheme utilizes a straw suspension mechanism based on carbon fibres. The third one is inspired by the self-supporting design of the PANDA straw tracker [36].

A 2 m long prototype straw was manufactured, with a 30  $\mu\text{m}$  diameter anode, and its performance was characterised in a test run with beam in the CERN SPS North area as a function of the wire eccentricity at nominal conditions (2.2 kV,  $\sim 1.05$  bar pressure, 70% Ar / 30% CO<sub>2</sub>). The tracks were externally measured by a silicon-strip telescope made of 8 single-sided sensors [37] and a 2.5 cm thick plastic scintillator for defining the start time. Figure 14 shows the measured drift time versus the vertical position of the extrapolated track at the straw for a 2.05 mm artificially induced wire eccentricity. As shown in Fig. 15, a straw hit resolution of  $<120 \mu\text{m}$  is achievable with high hit efficiency over most of the straw diameter, independently of the wire eccentricity.

### 5.5 HSDS timing detector

The timing detector covers the 50 m<sup>2</sup> physics aperture of the vacuum vessel end-cap window (Fig. 16). Its purpose is to provide information on the coincidence of the charged particles originating from a decay candidate. At the expected rate of fully reconstructed residual background muons of

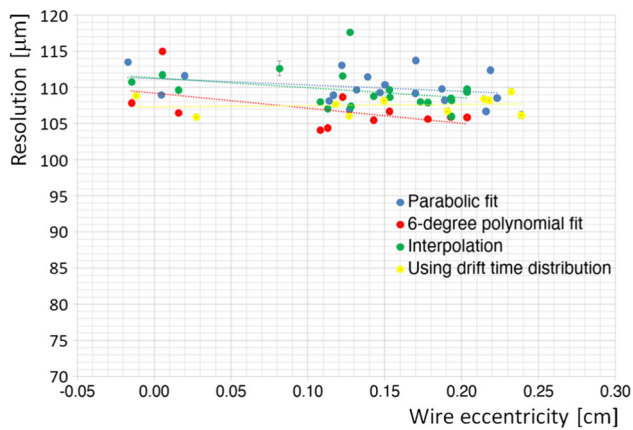


**Fig. 15** Measured spatial resolution for the 20 mm diameter straw tube prototype as a function of the artificially induced wire eccentricity. Four different analysis methods of the spatial resolution are compared (see CERN-THESIS-2020-218). The lines are the results of linear fits

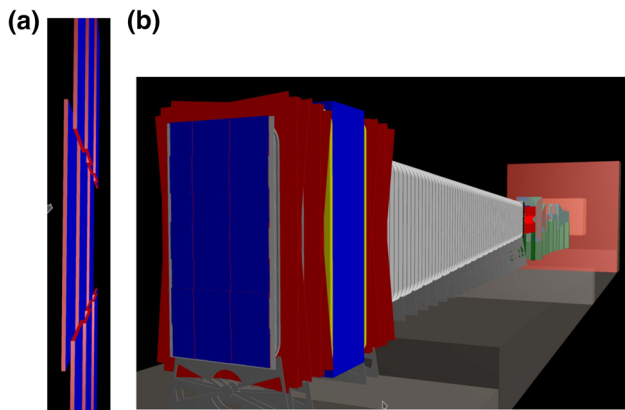


**Fig. 16** Side view (a) and downstream view (b) of the HSDS timing detector from the geometry implemented in the GEANT4-based [6] physics simulation

$\sim 25$  kHz, a hit time resolution of  $< 100$  ps is required in order to provide sufficient rejection of combinatorial events. Two technologies are currently being considered: scintillating bars and MRPCs.

### 5.5.1 Scintillator-based option

The scintillator option uses EJ200 plastic bars read out by large-area SiPMs. The material for the scintillator plastic was chosen by the requirement on the timing resolution. EJ200 is found to have the right combination of light output, attenuation length (3.8 m) and fast timing (rise time of 0.9 ns and decay time of 2.1 ns). The emission spectrum peaks at 425 nm, perfectly matching the SiPMs spectral response. The number of photons generated by a minimum-ionising particle crossing 1 cm of scintillator is  $\mathcal{O}(10^4)$ . The bars are wrapped in an aluminum foil, and a black plastic stretch film on top, to ensure opacity.

The  $5 \text{ m} \times 10 \text{ m}$  aperture is built from three columns, each with 182 rows of plastic bars with dimensions  $168 \text{ cm} \times 6 \text{ cm} \times 1 \text{ cm}$ . A 0.5 cm overlap between columns and a 1 cm overlap between bars in the same column provide means of cross-calibration during time alignment. Each bar is read out on both sides by a matrix of eight  $6 \text{ mm} \times 6 \text{ mm}$  SiPMs. The signals from the eight SiPMs are summed to form a single channel, hence making up 1092 channels which are subsequently digitized by a DAQ module based on the SAMPIC ASIC.

A 22-bar (44 channels) prototype array with 1.68 m long bars has been successfully operated at the CERN PS test beam [38]. The resolution was demonstrated to be  $\sim 80$  ps over the whole  $2.1 \text{ m}^2$  area of the prototype.

### 5.5.2 MRPC-based option

In the MRPC option, the end-cap window of the vacuum vessel is covered by 35 modules, each with two stacked MRPC chambers, arranged in a matrix 7 (vertically)  $\times$  5 (horizontally). The active areas of the modules are overlapped by 10 cm (vertically and horizontally) in order to create a layer without dead regions.

The MRPCs use a novel concept [39,40] in the construction of the chambers, in which the glass stack and High-Voltage (HV) electrodes are confined within a permanently sealed plastic box. PMMA is used for the frame and polycarbonate (PC) is used for the covers. The box is equipped only with gas and HV feed-throughs (Fig. 17a). This facilitates construction and allows operation with a low gas flow of a few  $\text{cm}^3/(\text{min} \times \text{m}^2)$ .

Each MRPC chamber has six gas gaps defined by seven 1 mm thick float glass electrodes of about  $1550 \times 1250 \text{ mm}^2$  separated by 0.3 mm nylon mono-filaments. The glass has a bulk resistivity of  $\approx 4 \times 10^{12} \Omega \text{cm}$  at  $25^\circ \text{C}$ . The HV electrodes are made up of a semi-conductive layer based on an acrylic paint with sheet resistivity of around  $100 \text{ M}\Omega/\square$  that is applied to the outer surface of the outermost glasses with airbrush techniques.

The two MRPCs chambers are read out in parallel by a readout strip plane which is based on a 1.6 mm Flame Retardant 4 (FR4) printed circuit board located between the two chambers. The readout plane is equipped with 41 copper strips with 29 mm width, 30 mm pitch and 1600 mm length. Two ground planes, located on the top and bottom of the dual MRPC stack complete the readout planes. The complete structure is housed in an aluminum box that provides the necessary electromagnetic insulation and mechanical rigidity. A schematic of the inner structure of the module is shown in Fig. 17a. The module operates in a open gas loop with a mixture of 97.5%  $\text{C}_2\text{H}_2\text{F}_4$  and 2.5%  $\text{SF}_6$  at a pressure a few millibars below the atmospheric pressure. In this way, the

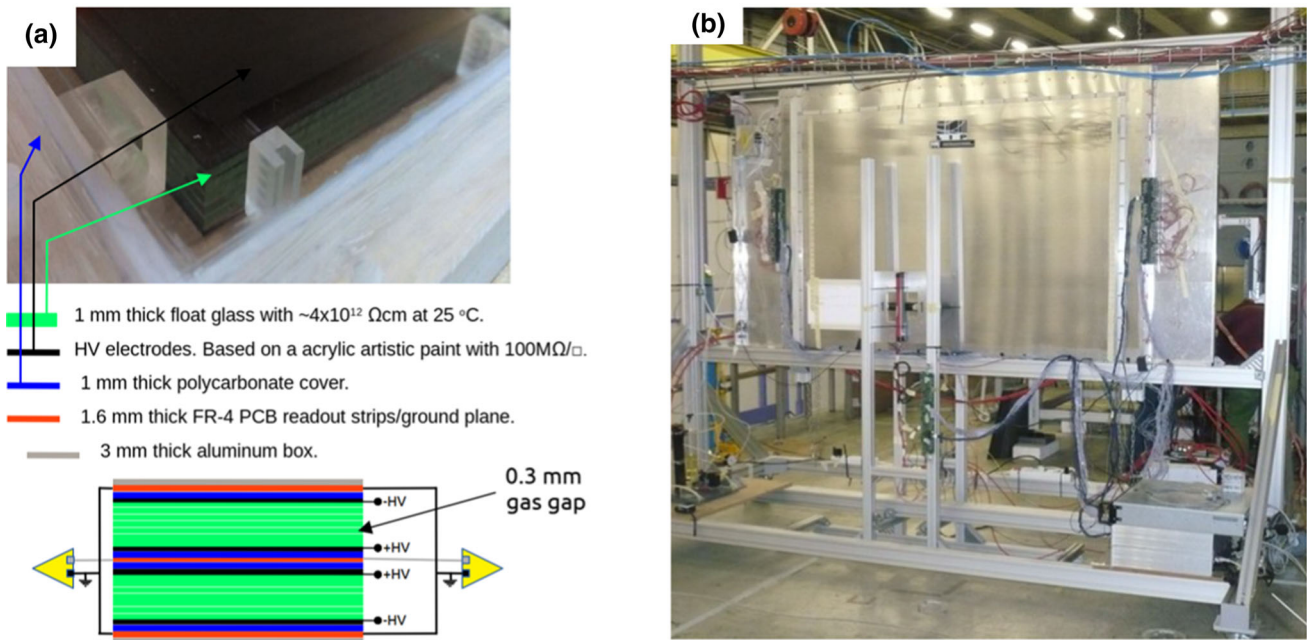


**Fig. 17** **a** Detailed photograph of one of the MRPCs together with a sketch of the internal structure of the module. **b** Experimental setup at the T9 beam line (CERN East Area), where the MRPC was exposed to negative pions of 8 GeV/c

width of the gaps is correctly defined with the help of the compression exerted by atmospheric pressure.

The MRPC signals from both sides of each strip are fed to fast front-end electronics [41] capable of measuring time and charge in a single channel. The resulting signals are read out by the “TRB3” board [42] equipped with 128 multi-hit TDC (TDC-in-FPGA technology) channels with a time precision better than 20 ps RMS.

A complete prototype was exposed to 8 GeV negative pions in the T9 beam line (CERN East Area) (Fig. 17b). Time resolution and detection efficiency were measured at various positions over the active area. Figure 18 shows the time resolution and efficiency as a function of the horizontal position (for a vertical position of 500 mm) and vertical position (for a horizontal position of 725 mm) respectively without noticeable dependence on the position. The measurements demonstrate a time resolution of 54 ps and an efficiency of 98%. More details on the beam time results can be found in [43].

### 5.6 HSDS electromagnetic calorimeter

Apart from providing electron and photon identification and discriminating between hadrons and muons, the electromagnetic calorimeter should be capable of measuring the shower angle with a resolution of  $\sim 5$  mrad to reconstruct two-photon final states. In the baseline configuration, SHiP is not equipped with a hadron calorimeter. The longitudinal segmentation of the electromagnetic calorimeter, with the

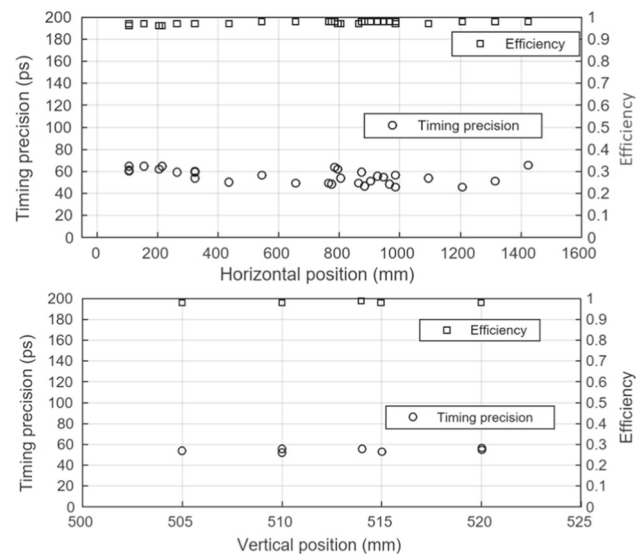


**Fig. 18** Time resolution and efficiency as a function of the horizontal and vertical position on the MRPC prototype

shower energy being sampled every  $0.5 X_0$ , provides sufficient electron/hadron separation.

The electromagnetic calorimeter is based on the “Split-Cal” concept [44]. It consists of a longitudinally segmented lead sampling calorimeter with a total sampling depth of  $20 X_0$ . The lead absorber plates are  $0.5 X_0$  thick, i.e. 0.28 cm, thus leaving space for 40 sampling layers. Most sampling layers are equipped with scintillating plastic bars read out

by WLS fibres with a relatively coarse spatial segmentation. The scintillator planes are 0.56 cm thick.

Three sampling layers, each with a thickness of 1.12 cm, are equipped with high resolution detectors providing a spatial segmentation of  $\sim 200 \mu\text{m}$ . They are located at a depth of  $3 X_0$  and at the shower maximum in order to accurately measure the barycentres of the transverse shower profile. The shower direction is determined from the three measurements of the barycentres. For the high-resolution layers, it is foreseen to use micro-pattern detectors, such as micro-megas.

To increase the lever arm for the angular measurement, the calorimeter is mechanically split in two parts in the longitudinal direction with an air gap of 1 m between the first  $3 X_0$  and the remaining  $17 X_0$ . With a few mm transverse shower-position resolution in the high-precision layers, the target angular resolution is of the order of a few mrad.

The principal challenge in achieving a good angular resolution, along with high efficiency for the photon reconstruction, is the presence of shower satellites due to long tails in the transverse shower shape. The shower profiles were measured with a prototype at an electron beam test at CERN in order to tune the simulation and optimise the layout. The test setup is shown in Fig. 19, while the experimental result comparing data and simulation at different shower depths is shown in Fig. 20.

### 5.7 HSDS muon system

The muon system provides identification of muons with an efficiency of  $> 95\%$  in the momentum range of  $\sim 5\text{--}100 \text{ GeV}/c$  with a mis-identification rate of  $\sim 1\text{--}2\%$ .

As shown in Fig. 21, the muon system is comprised of four stations of active layers interleaved by the three muon filters. The four stations are 6 m wide and 12 m high. The amount of material of the calorimeter system corresponds to  $6.7$  interaction lengths ( $\lambda_I$ ). The muon filters are 60 cm thick iron walls, corresponding to  $3.4 \lambda_I$  each. A muon with normal incidence must have an energy of at least of 2.6 GeV to reach the first muon station and at least 5.3 GeV to reach the last muon station. The multiple scattering of muons in the material of the calorimeter and the muon filters drives the granularity of the system. Simulation studies show that a readout granularity of  $\sim 10 \text{ cm}$  in the transverse directions is adequate for the momentum range of interest.

The rate expected in the muon detector is between 1 and 6 MHz, depending on the station, mostly caused by the beam-induced muon background. Simulation studies show that the rate is dominated by very low momentum ( $< 100 \text{ MeV}/c$ ) electrons, positrons and photons produced by inelastic and electromagnetic interactions of muons with the material of the detector. Most of the hits are concentrated in the first muon station. The second and third stations see very low rates while the fourth station sees an almost uniform illumination originating from very low momentum particles surrounding the system. To shield the last muon station against hits arising from muon interactions with the surrounding material, including the cavern walls, a thin ( $\sim 10 \text{ cm}$ ) layer of iron is located downstream of the last station. The hit rate from real muons is subdominant and does not exceed  $\sim 300 \text{ kHz}$ , being concentrated on the sides of stations.

The detectors of the muon system cover the total surface of  $\sim 288 \text{ m}^2$ . Scintillating bars and scintillating tiles with direct SiPM readout were investigated as options for SHiP. All

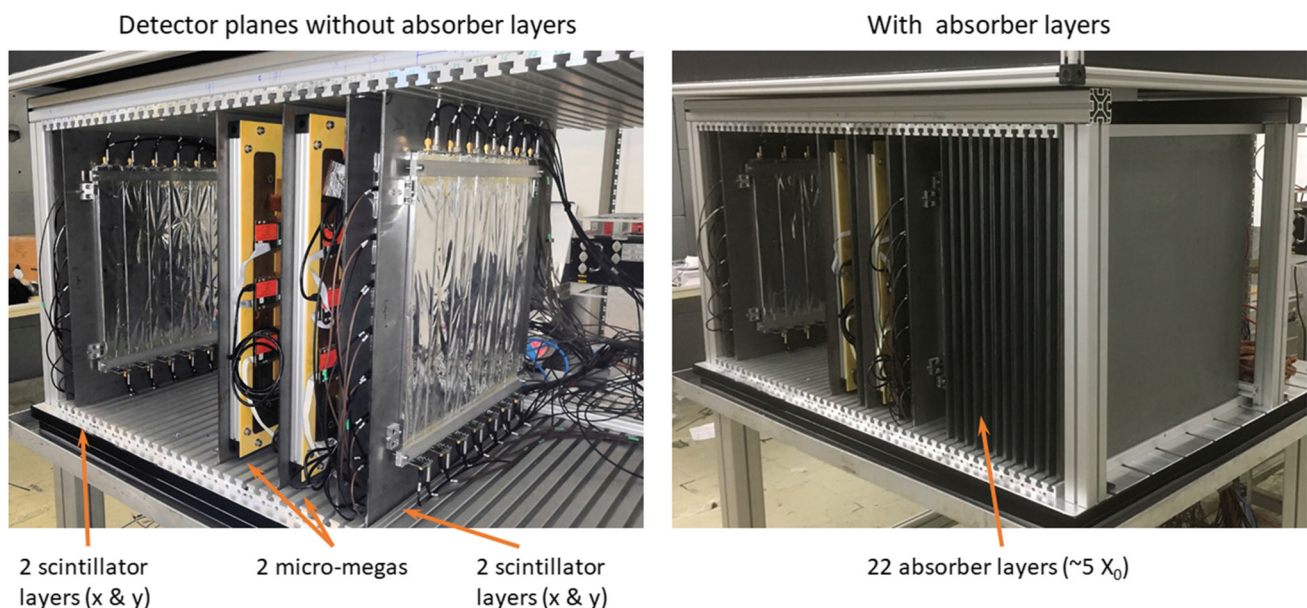


**Fig. 19** Test beam setup for the electromagnetic calorimeter measurements of the shower profiles

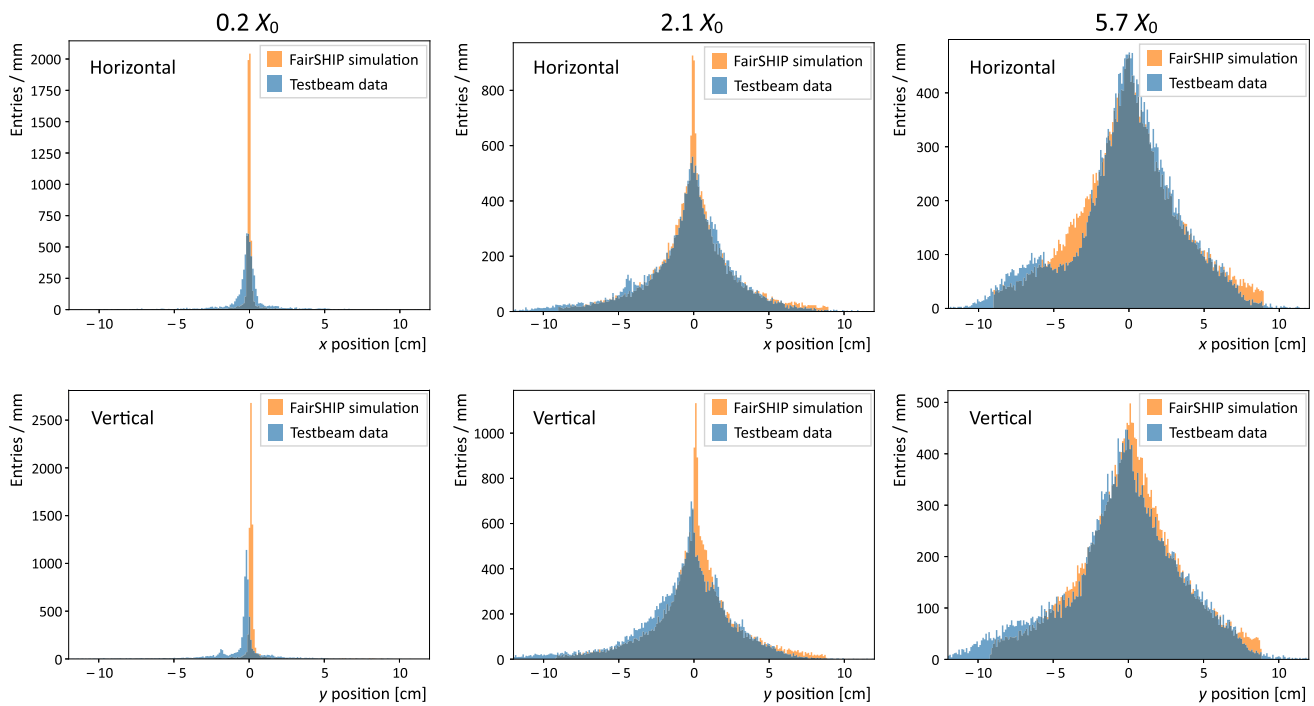


**Fig. 20** Measured and simulated transverse electromagnetic-shower distribution with 5 GeV electrons from the CERN PS at different calorimeter depths. The small discrepancies between simulation and data are mostly due to known issues of the prototype read-out

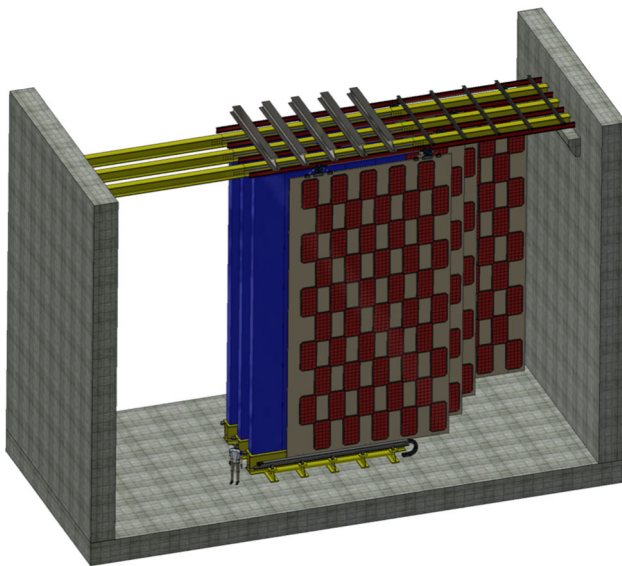


**Fig. 21** Conceptual layout of the HSDS muon system made of four stations

details of these works, including performance results from beam tests, can be found in [45,46].

## 6 Common detector electronics and online system

The design of the SHiP front-end electronics and readout system is characterised by a relatively small data throughput,

no radiation to the electronics, and mostly trivial powering and cooling. The complexity lies in the collection of data from a relatively high number of channels spread out over a very large detector, and in the event building with a very wide range of times-of-flight.

Figure 22 shows an overview of the electronics and read-out system. The system has two main subsystems: the control distribution, data transport and concentration (CTC) system; and the timing and fast control (TFC) system. Downstream of the front-end (FE) electronics, the system is composed of cascaded FE concentrators which fan-in and fan-out the CTC and the TFC networks. The FE links are based on 4 LVDS copper pairs carrying physics data at 400 Mbits/s, 40 MHz clock, fast commands and slow control at 40 Mbits/s, and status monitoring at 40 Mbits/s, respectively. Figure 23 shows a photo of a prototype of the FE concentrator. Downstream of the FE concentrator chain of each subsystem (called partition), the last concentrator is interfaced with a front-end host (FEH) computer for data readout, slow control and monitoring, and with the TFC master for the clock and synchronous commands, as shown in Fig. 22. The design strategy is to base the system as much as possible on FPGAs, including the FE electronics.

The architecture does not comprise a hardware trigger. The FEH computers format the data and forward them to the event filter farm (EFF). For every SPS cycle, a computer in the EFF is assigned to collect the partition data, to extract the physics events candidates and to build the

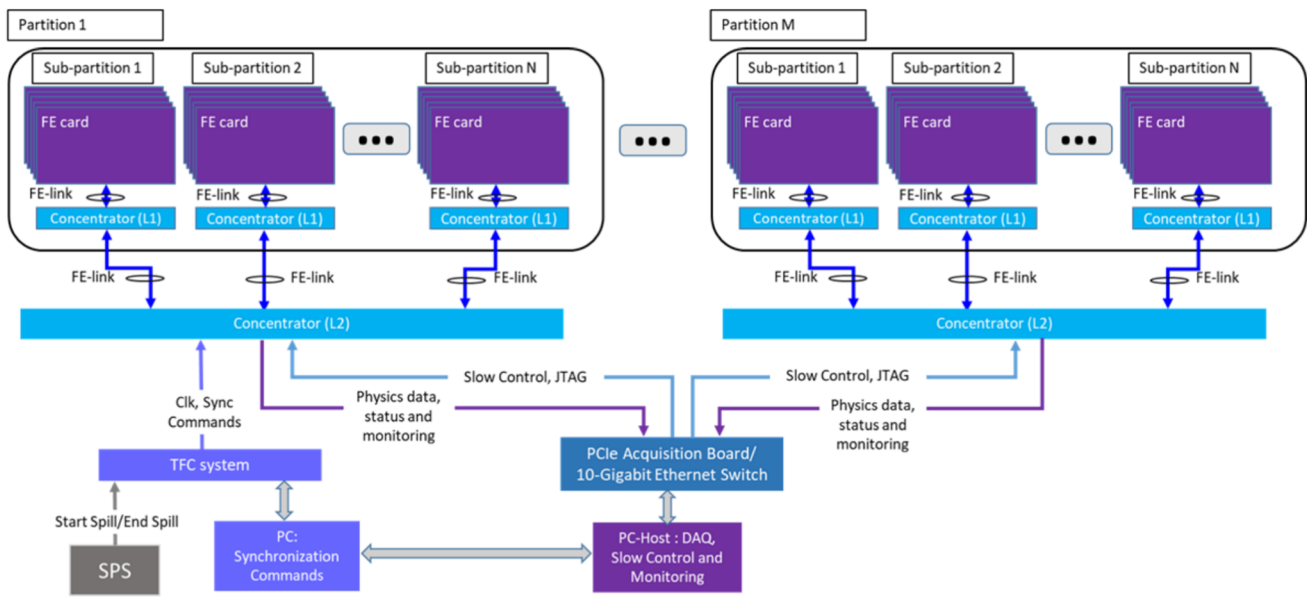


Fig. 22 Global scheme of the SHiP electronics and readout system

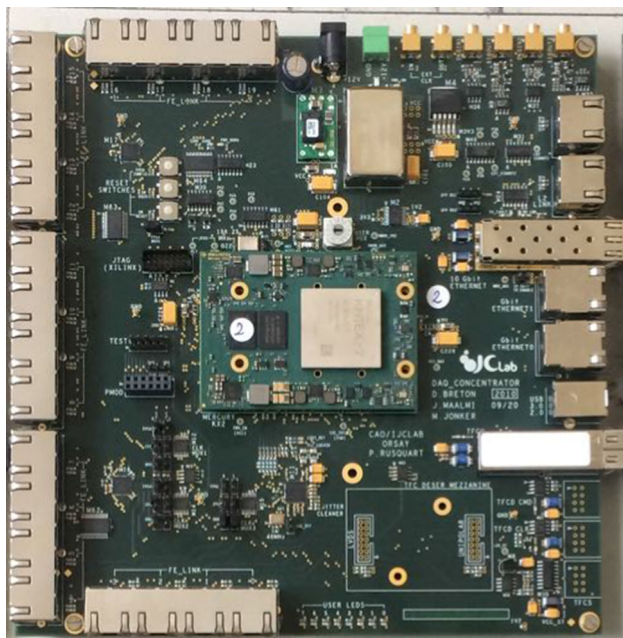


Fig. 23 Prototype of the SHiP FE concentrator board

## 7 Simulation and reconstruction

The SHiP experiment relies on an accurate simulation of the background components, in particular related to combinatorial events from muons, and muon and neutrino deep inelastic scattering (DIS) in the material of the detector. The design of the muon shield also relies on an accurate knowledge of the muon spectrum. The SHiP software framework for simulation, reconstruction, and analysis is based on the FairRoot package [47] and is called FairShip. The FairShip code is largely a specialisation of the generic C++ base classes provided by FairRoot, mainly profiting from the methods to describe the detector geometry, implement detector classes, and performing simulation and reconstruction. The framework incorporates GEANT4 [6] to trace particles through the target and the experimental setup, PYTHIA8 [48] for the primary proton fixed-target interaction, PYTHIA6 [49] for muon deep inelastic scattering, and the GENIE [50] MC generator for interactions of neutrinos. In addition some specific auxiliary libraries needed by SHiP are included, like GENFIT [51] for reconstruction of tracks. The steering of the simulation flow, and the main parts of the reconstruction and analysis are based on Python classes and functions.

For background studies and detector optimisation, a total of  $6.5 \times 10^{10}$  protons on target have been simulated with an energy cut of 10 GeV for transporting particles after the hadron absorber. This simulation was run with strongly enhanced muon production from QED processes, such that for the studies of muon-induced backgrounds, the sample corresponds to  $6.5 \times 10^{12}$  protons on target. In addition, a total

events. The EFF performs reconstruction and event triggering after the final event building with data from complete SPS cycles. The FEH and EFF computers are based on commodity PCs.

With the baseline detector, it is estimated that about 300 concentrator boards will be required together with a total of 25 DAQ links, 12 FEH and 42 EFF computers.

of  $1.8 \times 10^9$  protons on target have been simulated with an energy cut of 1 GeV. Heavy flavour production is both a source of signal and background. Dedicated samples of charm and beauty hadrons corresponding to about  $10^{11}$  protons on target have been produced. These simulation samples give sufficient statistics after the muon shield for the background determination to be extrapolated to full run of SHiP with  $2 \times 10^{20}$  protons on target with good statistical accuracy and such that any rare contribution to the muon flux is subdominant.

In order to produce a background sample of muon DIS events that is equivalent to what is expected for the full run of SHiP, the muon samples from the simulations above were used to produce DIS events with the cross-section boosted such that every muon interacts according to the material distribution of the experimental setup.

For neutrino DIS, the neutrino spectra from the simulated minimum bias, and charm and beauty samples were used to produce a sample of neutrino interactions in the material of the detector with the help of the GENIE generator that is equivalent to seven times the full run of SHiP, again by making every neutrino interact according to the material distribution of the experimental setup.

The validity of the FairShip prediction of the particle fluxes has been verified by comparing to the data from the CHARM beam-dump experiment at CERN [52] (see PhD thesis F. Bergsma, University of Amsterdam, 1990). The most realistic cross-check of FairShip has been performed in summer 2018 in a dedicated experiment at the CERN SPS [13]. It has directly measured the rate and momentum of muons produced by 400 GeV/c protons dumped on a replica of the SHiP target, and found a very good agreement between the prediction by the simulation and the measured spectrum.

The production and decays of the various HS particles have been implemented in FairShip. PYTHIA8 is predominantly used to generate the different signal processes. For particles, and background, produced from the decays of charm and beauty hadrons, the effect of cascade production of charm and beauty from secondary hadrons is accounted for. For decays to hadronic final states, fragmentation is handled by PYTHIA8.

## 8 Expected detector performance

The SHiP detector performance has been studied in detail with the help of the full MC FairShip framework supported by the measurements done in test beam on the detector prototypes. The physics performance of the experiment is anchored in a highly efficient background suppression, provided by the target design, hadron stopper and the muon shield. The background suppression in the HS decay search is further guaranteed by the vacuum volume and the back-

ground taggers. The overall detector concept provides sensitivity to as many decay modes as possible to ensure model-independent searches.

In addition to improving present constraints on many models by several orders of magnitude, SHiP's decay spectrometer allows distinguishing between different models, and, in a large part of the parameter space, measure parameters that are relevant for model building and cosmology. These features make the SHiP experiment a unique discovery tool for HS particles. Moreover, together with the direct search for LDM, and neutrino physics, SHiP represents a wide scope general-purpose beam-dump experiment.

### 8.1 SND performance

The nuclear emulsion technology combined with the information provided by the SND muon identification system makes it possible to identify the three different neutrino flavours in the SND detector. The neutrino flavour is determined through the flavour of the primary charged lepton produced in neutrino charged-current interactions. The muon identification is also used to distinguish between muons and hadrons produced in the  $\tau$  decay and, therefore, to identify the  $\tau$  decay channel. In addition, tracking in the SND magnetic spectrometer will allow for the first time to distinguish between  $\nu_\tau$  and  $\bar{\nu}_\tau$  by measuring the charge of  $\tau$  decay products. The charge sign of hadrons and muons is measured by the CES, the downstream tracker, and by the muon identification system.

The neutrino fluxes produced in the beam dump have been estimated with FairShip, including the contribution from cascade production in the target. The number of charged-current deep inelastic scattering (CC DIS) interactions in the neutrino target is evaluated by convoluting the generated neutrino spectrum with the cross-section provided by the GENIE [50] Monte Carlo generator. The expected number of CC DIS in the target of the SND detector is reported in the first column of Table 2.

With  $2 \times 10^{20}$  protons on target, more than  $\sim 2 \times 10^5$  neutrino-induced charmed hadrons are expected, as reported

**Table 2** Expected CC DIS interactions in the SND assuming  $2 \times 10^{20}$  protons on target

	CC DIS interactions	CC DIS w. charm prod.
$N_{\nu_e}$	$8.6 \times 10^5$	$5.1 \times 10^4$
$N_{\nu_\mu}$	$2.4 \times 10^6$	$1.1 \times 10^5$
$N_{\nu_\tau}$	$2.8 \times 10^4$	$1.5 \times 10^3$
$N_{\bar{\nu}_e}$	$1.9 \times 10^5$	$9.8 \times 10^3$
$N_{\bar{\nu}_\mu}$	$5.5 \times 10^5$	$2.2 \times 10^4$
$N_{\bar{\nu}_\tau}$	$1.9 \times 10^4$	$1.1 \times 10^3$



in the second column of Table 2. The total charm yield exceeds the samples available in previous experiments by more than one order of magnitude. No charm candidate from electron neutrino interactions was ever reported by any previous experiment. Consequently, all the studies on charm physics performed with neutrino interactions will be improved, and some channels inaccessible in the past will be explored. This includes the double charm production cross-section [53,54] and the search for pentaquarks with charm quark content [55]. Charmed hadrons produced in neutrino interactions are also important to investigate the strange-quark content of the nucleon. The samples available at SHiP will also allow to significantly constrain the  $\nu_\tau$  magnetic moment and test lepton flavour violation in the neutrino sector.

The SND can also probe existence of LDM ( $\chi$ ) by detecting the electromagnetic showers initiated by the recoil electrons coming from elastic scattering of LDM in the SND. The SND ECC bricks, interleaved with the SND target tracker planes, act as sampling calorimeters with five active layers per radiation length,  $X_0$ , and a total depth of  $10 X_0$ . The configuration allows reconstructing a sufficient portion of the shower produced by the recoil electron to determine the particle angle and energy. In addition, the micro-metric accuracy of the nuclear emulsions provides crucial topological discrimination of LDM interactions against neutrino-induced background events.

Neutrino events with only one reconstructed outgoing electron at the primary vertex constitute background in the LDM searches, mimicking the signature  $\chi e^- \rightarrow \chi e^-$ . The GENIE Monte Carlo generator, interfaced with FairShip, has been employed for a full simulation to provide an estimate of the expected background for  $2 \times 10^{20}$  protons on target. After imposing a selection optimised for the signal, the residual neutrino background amounts to 230 events. All results of this study and the SHiP sensitivity to LDM are reported in [3].

In order to further reduce the background from neutrino events, and consolidate a possible LDM signal, it has been envisaged to alternatively operate SHiP with slowly extracted spills of bunched beam instead of uniformly de-bunched beam. Using the timing capability of the SND target tracker allows rejecting the neutrino background based on the difference in the time of flight. Figure 24 shows the region of discrimination assuming the  $4\sigma$  SPS bunch length of 1.5 ns and a bunch spacing of 25 ns and 5 ns, and 40 m distance between the beam-dump target and the detector. Currently, this mode of operation would only be used in order to consolidate a signal. Further studies are needed to determine if this mode of operation could also work for the HS decay search.

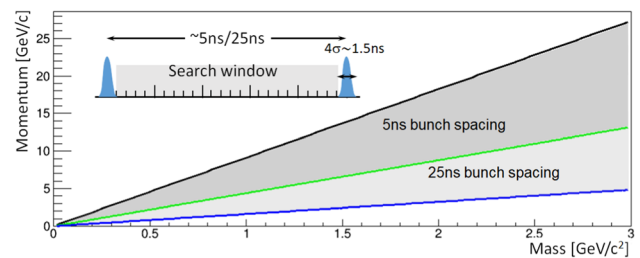


**Fig. 24** Mass-momentum region in which it is possible to discriminate an LDM scattering signature from a neutrino interaction using slow extraction of bunched beam in the SPS and a time-of-flight measurement. The figures assumes a bunch structure with 5 ns respectively 25 ns bunch spacing and 1.5 ns ( $4\sigma$ ) bunch length, and a distance of 40 m between the target and the detector

## 8.2 HSDS performance

The broad range of signals to which the SHiP experiment is sensitive can be classified into two main categories: fully and partially reconstructed decays. The former category refers to decays where there are at least two charged particles and no invisible final state particles, examples are  $DP \rightarrow \mu^\pm \mu^\mp$  and  $HNL \rightarrow \mu^\pm \pi^\mp$ . The latter category refers to decays with at least two charged particles and at least one invisible particle in the final state, e.g.  $HNL \rightarrow \mu^\pm \mu^\mp \nu$ . In all cases, the experimental signature consists of an isolated vertex with a total momentum vector that extrapolates accurately back to the proton interaction region for fully reconstructed final states, and with a slightly wider distribution of impact parameters for partially reconstructed final states (see Fig. 25).

### 8.2.1 Tracking performance

A key goal of the SHiP experiment is to determine the mass of a potential hidden sector candidate with a high degree of accuracy. The mass resolution of an HNL candidate with mass  $1 \text{ GeV}/c^2$  reconstructed through the decay  $HNL \rightarrow \mu^\pm \pi^\mp$  is shown in Fig. 25. The dependence of the mass resolution as a function of the mass of the HS particle for decays to both fully and partially reconstructed modes is also shown.

Accurate vertex and momentum resolution are also critical to suppress backgrounds. As HS particle candidates originate from the target, the impact parameter of the reconstructed candidate with respect to the proton interaction region ( $IP_{\text{target}}$ ) offers excellent discriminating power against backgrounds. In addition, signal tracks originate from a common vertex in contrast to backgrounds arising from random combinations of tracks. Therefore, the distance of closest approach (DOCA) between tracks can also be used to suppress backgrounds. The distributions of  $IP_{\text{target}}$  and DOCA

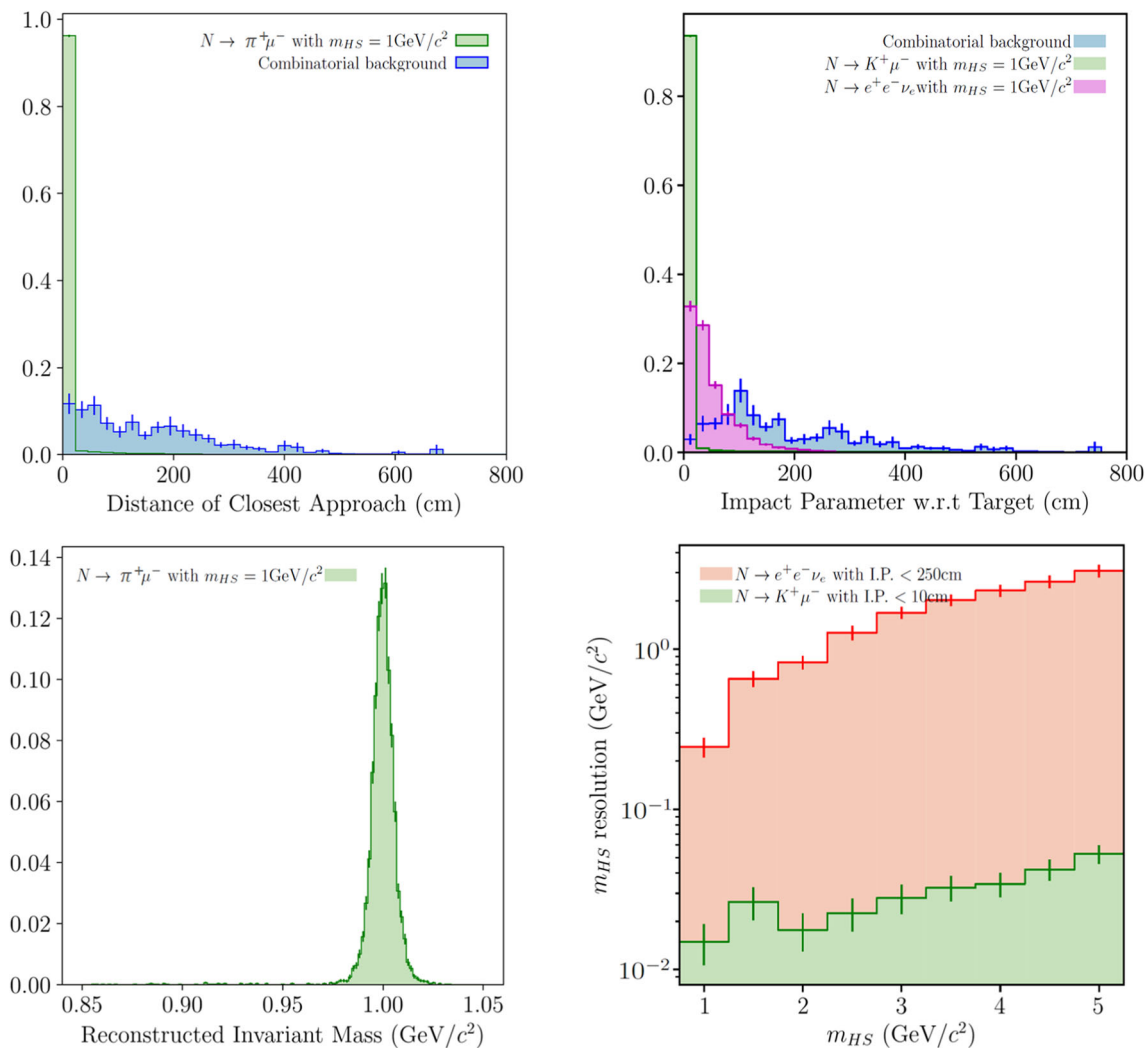


**Fig. 25** Examples of detector performance showing key reconstructed observables for an HNL candidate of  $m_{HS} = 1\text{GeV}/c^2$  decaying to fully reconstructed modes and to partially reconstructed modes with neutrinos. For the distance of closest approach (top-left) and impact parameter (IP) with respect to the proton interaction region (top-right),

both the signal (green and pink) and combinatorial background (blue) distributions are shown. Details on the combinatorial background can be found in Sect. 8.2.2. All distributions are normalised to unit area. Bottom-left shows the reconstructed invariant mass and bottom-right the mass resolution as a function of the HNL mass

for typical signals and combinatorial background are shown in Fig. 25.

### 8.2.2 Background rejection

In order to maximise SHiP's sensitivity, the background in the HSDS decay volume should be reduced to a negligible level. A common set of loose selection criteria are applied to all HS particle searches to suppress the background (Table 3). The selection criteria preserves close to 100% of the signal efficiency in fully reconstructed modes, as can be seen with the example of  $1\text{GeV}/c^2$  HNLs in Fig. 25.

There are three main sources of background that can mimic the signature of HS particles: random combinations

of residual muons within the same proton spill, muon DIS and neutrino DIS. The background from cosmics has been proven to be negligible.

- **Muon combinatorial:** The expected rate of residual muons that enter the fiducial volume of the HSDS, or back-scatter in the cavern and traverse the SHiP spectrometer, is  $26.3 \pm 3.6\text{kHz}$ . After applying the acceptance and selection cuts listed in Table 3, together with a cut of  $<25$  on the sum of hits in all tracking stations and no hit in the SBT/UBT, about  $10^8$  pairs of muons are expected for the partially reconstructed topology in the lifetime of the experiment. Under the assumption of a flat time structure for the 1 s proton spills, these are suppressed to a level of  $10^{-2}$  muon pairs in  $2 \times 10^{20}$  protons on target by requiring the muons to

coincide in a time window of 340 ps, corresponding to  $> 2.5$  times the time resolution of the HSDS timing detector. In reality, non-uniformity in the spill structure and the probability of this background can be measured by relaxing the timing criterion. A fast high-resolution spill structure monitor is also under study. The information from the monitor will be recorded with the data to have a continuous measure of this background probability. At the same time, significant progress has also been made in the context of BDF to improve the SPS spill structure, and studies of new techniques are underway.

- **Muon DIS:** Muons interacting inelastically in the floor and walls of the cavern, and in the material upstream of the vacuum vessel, can produce particles that enter the decay volume and mimic the signal. We expect about  $2 \times 10^8$  muon DIS interactions in the proximity of the vacuum vessel for  $2 \times 10^{20}$  protons on target. Samples of background corresponding to the expected number of DIS interactions have been generated (see Sect. 7). No events remain after applying the pre-selection in Table 3 and the detector information from the SBT and the UBT. To further investigate the background suppression it is assumed that the background taggers' veto and the pointing criteria factorize. This results in an upper limit of  $6 \times 10^{-4}$  expected background events for  $2 \times 10^{20}$  protons on target.

- **Neutrino DIS:** The dominant source of this background comes from neutrino DIS in the proximity of the decay volume, roughly corresponding to  $3.5 \times 10^7$  interactions from  $2 \times 10^{20}$  protons on target. In order to avoid irreducible background from neutrinos interacting with the air molecules inside the vessel, a level of vacuum below  $10^{-2}$  bar is necessary. The background from neutrino scattering in the floor and the walls of the cavern was studied and found to be negligible. A large sample, corresponding roughly to seven times the planned proton yield of  $2 \times 10^{20}$  protons on target was generated (see Sect. 7). By applying the selection cuts listed in Table 3 together with the background tagger information and timing, we expect  $< 0.1$  background events for the fully reconstructed signal and 6.8 background events for the partially reconstructed signal. This background consists of photon conversions in the material. It can be easily eliminated by requiring an invariant mass of the pair to be larger than  $100 \text{ MeV}/c^2$ .

As Table 4 shows, in the design of the SHiP experiment, much attention has been given to the identification of possible sources of background and to the means to reduce the background with a high level of redundancy for a broad spectrum of searches for visible decays of Hidden Sector particles. The redundancy of the selection criteria also allows determining the background directly from data and, in case of signal evidence, to perform cross checks that minimise the probability of false positives.

**Table 3** Pre-selection criteria used for the background rejection and the sensitivity estimates in the analysis of HS particle decays

Requirement	Value
Track momentum	$> 1.0 \text{ GeV}/c$
Track pair distance of closest approach	$< 1 \text{ cm}$
Track pair vertex position in decay volume	$> 5 \text{ cm}$ from inner wall
Impact parameter w.r.t. target (fully reconstructed)	$< 10 \text{ cm}$
Impact parameter w.r.t. target (partially reconstructed)	$< 250 \text{ cm}$

**Table 4** Expected background in the search for HS particle decays at 90% CL for  $2 \times 10^{20}$  protons on target after applying the pre-selection, the timing, veto, and invariant mass cuts. The neutrino-induced background is given separately for fully and partially reconstructed background modes

Background source	Expected events
Neutrino DIS	$< 0.1$ (fully)/ $< 0.3$ (partially)
Muon DIS (factorisation)	$< 6 \times 10^{-4}$
Muon combinatorial	$1.2 \times 10^{-2}$

## 9 Conclusions

While the energy frontier is investigated at the LHC and the precision frontier is pursued at LHCb, Belle II, NA62 and elsewhere, the intensity frontier remains under-explored. In the wake of the Higgs discovery, the SHiP collaboration identified a unique opportunity to pursue a new path of direct searches for a large class of feebly interacting particles, including light dark matter, by developing a novel type of beam-dump facility at the CERN SPS. The SPS is currently under-exploited and can provide a yield of protons to explore the interesting parameters space of HS particles that greatly surpasses existing facilities.

SHiP has since instigated a number of pioneering developments that make it possible to construct a large-scale, high-precision detector operating in beam-dump mode with  $4 \times 10^{19}$  protons per year at  $400 \text{ GeV}/c$  and in an environment of extremely low background. The detector setup is capable of reconstructing the decay vertex of a HS particle, measuring its invariant mass and providing particle identification of the decay products. Detailed full MC simulations have demonstrated that SHiP can suppress the expected background level in the search for visible decays to below 0.1 event at 90% C.L. in  $2 \times 10^{20}$  protons on target, equivalent to five years of operation at nominal intensity. It has also sensitivity to explore new parameter ranges of light dark matter and tau neutrino physics through scattering signatures in a dedicated set of sub-detectors with an emulsion target. This puts SHiP in an outstanding position world-wide to make a break-through in the range of particle masses and couplings that is not acces-

sible to the energy and precision frontier experiments, and potentially find the particles that lead to neutrino masses and oscillations, explain the baryon asymmetry of the universe, and shed new light on the properties of dark matter.

All of SHiP's sub-systems have addressed the most relevant technological challenges and undertaken genuine programs of prototyping to validate their performance with beam tests of small scale prototypes. The results have been used in the full simulation of the expected physics performance. In the 2020 Update of the European Strategy for Particle Physics, the preparatory evaluation of experiments complementary to the high energy frontier singled out SHiP at the SPS Beam Dump Facility as a major potential player in the future search for feebly interacting particles (CERN-PBC-REPORT-2018-003 and [56]). With regards to the cost of the baseline design of the facility, the project could not, as of 2020, be recommended for construction considering the overall recommendations of the Strategy. Hence, with the feasibility of the facility and the detector proven, CERN and the SHiP collaboration are focusing efforts on reviewing the design of the facility and possible alternative locations at the SPS (CERN-SPSC-2022-009), with the aim to significantly reduce the implementation cost, and enable start of construction in CERN's Long Shutdown 3, while preserving the original physics reach. The detector concept developed for the SND is also being deployed at the LHC (CERN-LHCC-2021-003/LHCC-P-016) in order to make measurements with neutrinos, in particular from charm production, in an unexplored range of energy and a range of pseudorapidity that is inaccessible to the other LHC experiments, as well as search for light dark matter.

**Acknowledgements** All work related to this publication was performed between 2014 and 2020. The SHiP Collaboration wishes to thank the Castaldo company (Naples, Italy) for their contribution to the development studies of the decay vessel. We also wish to thank the groups from INFN/University of Bologna and Laboratori Nazionali dell'INFN di Frascati for developing the scintillating tile-based option for the hidden sector muon system. The support from DFG, Germany, is acknowledged. The support from the National Research Foundation of Korea with Grant Numbers of 2018R1A2B2007757, 2018R1D1A3B07050649, 2018R1D1A1B07050701, 2017R1D1A1B03036042, 2017R1A6A3A01075752, 2016R1A2B4012302, and 2016R1A6A3A11930680 is acknowledged. The support from the Russian Foundation for Basic Research, Grant 17-02-00607, and the support from the TAEK of Turkey are acknowledged. The work was carried out with financial support from the Ministry of Education and Science of the Russian Federation in the framework of the Competitiveness Enhancement Program of NUST "MISIS", implemented by a governmental decree dated 16th of March 2013, No 2. We would like to thank Andrea Merli, Nicola Neri and Marco Petruzzo (Milano University) for making available a complete silicon strip telescope, with readout and reconstruction software, that allowed us to perform test beam measurements with our prototype straws.

**Data Availability Statement** This manuscript has no associated data or the data will not be deposited. [Authors' comment: Data sharing not applicable - no new data generated.]

**Open Access** This article is licensed under a Creative Commons Attribution 4.0 International License, which permits use, sharing, adaptation, distribution and reproduction in any medium or format, as long as you give appropriate credit to the original author(s) and the source, provide a link to the Creative Commons licence, and indicate if changes were made. The images or other third party material in this article are included in the article's Creative Commons licence, unless indicated otherwise in a credit line to the material. If material is not included in the article's Creative Commons licence and your intended use is not permitted by statutory regulation or exceeds the permitted use, you will need to obtain permission directly from the copyright holder. To view a copy of this licence, visit <http://creativecommons.org/licenses/by/4.0/>.  
Funded by SCOAP<sup>3</sup>.

## References

1. C. Ahdida, (SHiP) et al., JHEP **04**, 077 (2019). [arXiv:1811.00930](https://arxiv.org/abs/1811.00930)
2. C. Ahdida et al. (SHiP), Eur. Phys. J. C **81**, 451 (2021). [arXiv:2011.05115](https://arxiv.org/abs/2011.05115)
3. C. Ahdida et al. (SHiP), JHEP **04**, 199 (2021). [arXiv:2010.11057](https://arxiv.org/abs/2010.11057)
4. S. Alekhin, Rep. Prog. Phys. **79**, 124201 (2016)
5. C. Ahdida et al., J. Instrum. **14**, P03025 (2019)
6. S. Agostinelli et al., Nucl. Instr. Methods A **508**, 250 (2003)
7. E. Lopez Sola et al., Phys. Rev. Accel. Beams **22**, 123001 (2019)
8. E. Lopez Sola et al., Phys. Rev. Accel. Beams **22**, 113001 (2019)
9. K. Kershaw et al., JINST **13**, P10011 (2018). [arXiv:1806.05920](https://arxiv.org/abs/1806.05920)
10. A. Akmete et al. (SHiP), JINST **12**, P05011 (2017). [arXiv:1703.03612](https://arxiv.org/abs/1703.03612)
11. A. Baranov, E. Burnaev, D. Derkach, A. Filatov, N. Klyuchnikov, O. Lantwin, F. Ratnikov, A. Ustyuzhanin, A. Zaitsev (SHiP), J. Phys. Conf. Ser. **934**, 012050 (2017)
12. C. Ahdida et al. (SHiP), JINST **14**, P11028 (2019). [arXiv:1909.04451](https://arxiv.org/abs/1909.04451)
13. C. Ahdida et al. (SHiP), Eur. Phys. J. C **80**, 284 (2020)
14. C. Ahdida et al. (SHiP), (2019). [arXiv:1910.02952](https://arxiv.org/abs/1910.02952)
15. R. Acquafredda et al., JINST **4**, P04018 (2009)
16. N. Agafonova et al. (OPERA), Phys. Rev. Lett. **120**, 211801 (2018). [Erratum: Phys. Rev. Lett. **121**(13), 139901 (2018)]. [arXiv:1804.04912](https://arxiv.org/abs/1804.04912)
17. N. Agafonova et al. (OPERA), Eur. Phys. J. C **74**, 2986 (2014). [arXiv:1404.4357](https://arxiv.org/abs/1404.4357)
18. N. Agafonova et al. (OPERA), New J. Phys. **14**, 013026 (2012). [arXiv:1106.6211](https://arxiv.org/abs/1106.6211)
19. N. Agafonova, (OPERA) et al., JHEP **06**, 151 (2018). [arXiv:1803.11400](https://arxiv.org/abs/1803.11400)
20. L. Arrabito et al., Nucl. Instrum. Methods A **568**, 578 (2006). [arXiv:physics/0604043](https://arxiv.org/abs/physics/0604043)
21. N. Armenise et al., Nucl. Instrum. Methods A **551**, 261 (2005)
22. A. Alexandrov et al., JINST **10**, P11006 (2015)
23. A. Alexandrov et al., JINST **11**, P06002 (2016)
24. A. Alexandrov et al., Sci. Rep. **7**, 7310 (2017)
25. A. Alexandrov, G. De Lellis, V. Tioukov, Sci. Rep. **9**, 2870 (2019)
26. C. Fukushima, M. Kimura, S. Ogawa, H. Shibuya, G. Takahashi, K. Kodama, T. Hara, S. Mikado, Nucl. Instrum. Methods A **592**, 56 (2008)
27. P. Dupieux, B. Joly, F. Jouve, S. Manen, R. Vandaele (ALICE), JINST **9**, C09013 (2014)
28. A. Miano, A. Fiorillo, A. Salzano, A. Prota, R. Jacobsson, Arch. Civ. Mech. Eng. **21**, 3 (2021)
29. J. Machado et al., J. Instrum. **10**, C01043 (2015)
30. A. Blanco et al., J. Instrum. **10**, C02034 (2015)
31. A. Blanco et al., J. Instrum. **9**, C09027 (2014)
32. D. Hebecker et al., EPJ Web Conf. **116**, 01006 (2016)

33. M. Ehlert, A. Hollnagel, I. Korol, A. Korzenev, H. Lacker, P. Mermod, J. Schliwinski, L. Shihora, P. Venkova, M. Wurm, *JINST* **14**, P03021 (2019). [arXiv:1812.06460](https://arxiv.org/abs/1812.06460)
34. J. Benziger et al., *Nucl. Instrum. Methods A* **587**, 277 (2008). [arXiv:0709.1503](https://arxiv.org/abs/0709.1503)
35. N. Azorskiy, L. Glonti, Y. Gusakov, V. Elsha, T. Enik, S. Kakurin, V. Kekelidze, E. Kislov, A. Kolesnikov, D. Madigozhin et al., *Nucl. Instrum. Methods Phys. Res. Sect. A Accel. Spectrom. Detect. Assoc. Equip.* **824**, 569 (2016). *Frontier Detectors for Frontier Physics: Proceedings of the 13th Pisa Meeting on Advanced Detectors*
36. W. Erni, I. Keshelashvili, B. Krusche, M. Steinacher, Y. Heng, Z. Liu, H. Liu, X. Shen, Q. Wang, H. Xu et al., *Eur. Phys. J. A* **49** (2013)
37. A. Abba, F. Caponio, M. Citterio, S. Coelli, J. Fu, M. Lazzaroni, A. Merli, M. Monti, N. Neri, M. Petruzzo et al., *J. Instrum.* **12**, C03060 (2017)
38. C. Betancourt, A. Korzenev, P. Mermod, N. Serra (SHiP), *Nucl. Instrum. Methods A* **979**, 164398 (2020)
39. A. Blanco, J. Adamczewski-Musch, K. Boretzky, P. Cabanelas, L. Cartegni, R.F. Marques, P. Fonte, J. Fruehauf, D. Galaviz, M. Heil et al., *J. Instrum.* **10**, C02034 (2015)
40. L. Lopes, A. Alves, P. Assis, A. Blanco, N. Carolino, M. Cerda, R. Conceição, O. Cunha, C. Dobrigkeit, M. Ferreira et al., *J. Instrum.* **14**, C07002 (2019)
41. D. Belver et al., *IEEE Trans. Nucl. Sci.* **57**, 2848 (2010)
42. A. Neiser et al., *J. Instrum.* **8**, C12043 (2013)
43. G. De Lellis, *J. Instrum.* **14**, C06009 (2019)
44. W.M. Bonivento (SHiP), *JINST* **13**, C02041 (2018)
45. W. Baldini, A. Blondel, A. Calcaterra, R. Jacobsson, A. Khotjantsev, Y. Kudenko, V. Kurochka, G. Lanfranchi, A. Mefodiev, O. Mineev et al., *J. Instrum.* **12**, P03005 (2017)
46. A. Balla, B. Buonomo, V. Cafaro, A. Calcaterra, F. Cardelli, A. Ceccucci, P. Ciambrone, V. Cicero, D.D. Giovenale, C.D. Giulio et al., *J. Instrum.* **17**, P01038 (2022)
47. M. Al-Turany, D. Bertini, R. Karabowicz, D. Kresan, P. Malzacher, T. Stockmanns, F. Uhlig, *J. Phys. Conf. Ser.* **396**, 022001 (2012)
48. T. Sjöstrand, S. Ask, J.R. Christiansen, R. Corke, N. Desai, P. Ilten, S. Mrenna, S. Prestel, C.O. Rasmussen, P.Z. Skands, *Comput. Phys. Commun.* **191**, 159 (2015). [arXiv:1410.3012](https://arxiv.org/abs/1410.3012)
49. T. Sjöstrand, S. Mrenna, P.Z. Skands, *JHEP* **05**, 026 (2006). [arXiv:hep-ph/0603175](https://arxiv.org/abs/hep-ph/0603175)
50. C. Andreopoulos et al., *Nucl. Instrum. Methods A* **614**, 87 (2010). [arXiv:0905.2517](https://arxiv.org/abs/0905.2517)
51. J. Rauch, T. Schlüter, **608**, 012042 (2015)
52. J. Dorenbosch, J.V. Allaby, U. Amaldi, G. Barbiellini, C. Berger, F. Bergsma, A. Capone, W. Flegel, L. Lanceri, M. Metcalf et al. (CHARM Collaboration), *Phys. Lett. B* **166**, 473 (1985)
53. A. Kayis-Topaksu et al. (CHORUS), *Phys. Lett. B* **539**, 188 (2002)
54. I. Abt et al. (HERA-B), *Eur. Phys. J. C* **52**, 531 (2007). [arXiv:0708.1443](https://arxiv.org/abs/0708.1443)
55. G. De Lellis, A.M. Guler, J. Kawada, U. Kose, O. Sato, F. Tramontano, *Nucl. Phys. B* **763**, 268 (2007)
56. J. Jaeckel, M. Lamont, C. Vallée, *Nat. Phys.* **16**, 393 (2020)

### SHiP Collaboration\*

C. Ahdida<sup>44</sup>, A. Akmete<sup>48</sup>, R. Albanese<sup>15,c,e</sup>, J. Alt<sup>7</sup>, A. Alexandrov<sup>15,32,34,c</sup>, A. Anokhina<sup>39</sup>, S. Aoki<sup>18</sup>, G. Arduini<sup>44</sup>, E. Atkin<sup>38</sup>, N. Azorskiy<sup>29</sup>, J. J. Back<sup>54</sup>, A. Bagulya<sup>32</sup>, F. Baaltasar Dos Santos<sup>44</sup>, A. Baranov<sup>40</sup>, F. Bardou<sup>44</sup>, G. J. Barker<sup>54</sup>, M. Battistin<sup>44</sup>, J. Bauche<sup>44</sup>, A. Bay<sup>46</sup>, V. Bayliss<sup>51</sup>, A. Y. Berdnikov<sup>37</sup>, Y. A. Berdnikov<sup>37</sup>, C. Betancourt<sup>47</sup>, I. Bezshyiko<sup>47</sup>, O. Bezshyyko<sup>55</sup>, D. Bick<sup>8</sup>, S. Bieschke<sup>8</sup>, A. Blanco<sup>28</sup>, J. Boehm<sup>51</sup>, M. Bogomilov<sup>1</sup>, I. Boiarska<sup>3</sup>, K. Bondarenko<sup>27,55</sup>, W. M. Bonivento<sup>14</sup>, J. Borburgh<sup>44</sup>, A. Boyarsky<sup>27,55</sup>, R. Brenner<sup>43</sup>, D. Breton<sup>4</sup>, A. Brignoli<sup>6</sup>, V. Büscher<sup>10</sup>, A. Buonauro<sup>47</sup>, S. Buontempo<sup>15</sup>, S. Cadeddu<sup>14</sup>, M. Calviani<sup>44</sup>, M. Campanelli<sup>53</sup>, M. Casolino<sup>44</sup>, N. Charitonidis<sup>44</sup>, P. Chau<sup>10</sup>, J. Chauveau<sup>5</sup>, A. Chepurinov<sup>39</sup>, M. Chernyavskiy<sup>32</sup>, K.-Y. Choi<sup>26</sup>, A. Chumakov<sup>2</sup>, M. Climescu<sup>10</sup>, A. Conaboy<sup>6</sup>, L. Congedo<sup>12,a</sup>, K. Cornelis<sup>44</sup>, M. Cristinziani<sup>11</sup>, A. Crupano<sup>13</sup>, G. M. Dallavalle<sup>13</sup>, A. Datwyler<sup>47</sup>, N. D'Ambrosio<sup>16</sup>, G. D'Appollonio<sup>14,b</sup>, R. de Asmundis<sup>15</sup>, J. De Carvalho Saraiva<sup>28</sup>, G. De Lellis<sup>15,34,44,c</sup>, M. de Magistris<sup>15,g</sup>, A. De Roeck<sup>44</sup>, M. De Serio<sup>12,a</sup>, D. De Simone<sup>47</sup>, L. Dedenko<sup>39</sup>, P. Dergachev<sup>34</sup>, A. Di Crescenzo<sup>44,15,c,\*</sup>, L. Di Giulio<sup>44</sup>, C. Dib<sup>2</sup>, H. Dijkstra<sup>44</sup>, V. Dmitrenko<sup>38</sup>, L. A. Dougherty<sup>44</sup>, A. Dolmatov<sup>33</sup>, S. Donskov<sup>35</sup>, V. Drohan<sup>55</sup>, A. Dubreuil<sup>45</sup>, O. Durhan<sup>48</sup>, M. Ehlert<sup>6</sup>, E. Elikkaya<sup>48</sup>, T. Enik<sup>29</sup>, A. Etenko<sup>33,38</sup>, O. Fedin<sup>36</sup>, F. Fedotovs<sup>52</sup>, M. Ferrillo<sup>47</sup>, M. Ferro-Luzzi<sup>44</sup>, K. Filippov<sup>38</sup>, R. A. Fini<sup>12</sup>, H. Fischer<sup>7</sup>, P. Fonte<sup>28</sup>, C. Franco<sup>28</sup>, M. Fraser<sup>44</sup>, R. Fresa<sup>15,f,e</sup>, R. Froeschl<sup>44</sup>, T. Fukuda<sup>19</sup>, G. Galati<sup>12,a</sup>, J. Gall<sup>44</sup>, L. Gatignon<sup>44</sup>, G. Gavrilo<sup>36</sup>, V. Gentile<sup>15,34,c</sup>, B. Goddard<sup>44</sup>, L. Golinka-Bezshyiko<sup>55</sup>, A. Golovatiuk<sup>15,c</sup>, V. Golovtsov<sup>36</sup>, D. Golubkov<sup>30</sup>, A. Golutvin<sup>52,34</sup>, P. Gorbounov<sup>44</sup>, D. Gorbunov<sup>31</sup>, S. Gorbunov<sup>32</sup>, V. Gorkavenko<sup>55</sup>, M. Gorshenkov<sup>34</sup>, V. Grachev<sup>38</sup>, A. L. Grandchamp<sup>46</sup>, E. Graverini<sup>46</sup>, J.-L. Grenard<sup>44</sup>, D. Grenier<sup>44</sup>, V. Grichine<sup>32</sup>, N. Gruzinskii<sup>36</sup>, A. M. Guler<sup>48</sup>, Yu. Guz<sup>35</sup>, G. J. Haefeli<sup>46</sup>, C. Hagner<sup>8</sup>, H. Hakobyan<sup>2</sup>, I. W. Harris<sup>46</sup>, E. van Herwijnen<sup>34</sup>, C. Hessler<sup>44</sup>, A. Hollnagel<sup>10</sup>, B. Hosseini<sup>52</sup>, M. Hushchyn<sup>40</sup>, G. Iaselli<sup>12,a</sup>, A. Iuliano<sup>15,c</sup>, R. Jacobsson<sup>44,\*</sup>, , D. Joković<sup>41</sup>, M. Jonker<sup>44</sup>, I. Kadenko<sup>55</sup>, V. Kain<sup>44</sup>, B. Kaiser<sup>8</sup>, C. Kamiscioglu<sup>49</sup>, D. Karpenkov<sup>34</sup>, K. Kershaw<sup>44</sup>, M. Khabibullin<sup>31</sup>, E. Khalikov<sup>39</sup>, G. Khaustov<sup>35</sup>, G. Khoraiuli<sup>10</sup>, A. Khotyantsev<sup>31</sup>, Y. G. Kim<sup>23</sup>, V. Kim<sup>36,37</sup>, N. Kitagawa<sup>19</sup>, J.-W. Ko<sup>22</sup>, K. Kodama<sup>17</sup>, A. Kolesnikov<sup>29</sup>, D. I. Kolev<sup>1</sup>, V. Kolosov<sup>35</sup>, M. Komatsu<sup>19</sup>, A. Kono<sup>21</sup>, N. Kononova<sup>32,34</sup>, S. Kormannshaus<sup>10</sup>, I. Korol<sup>6</sup>, I. Korol'ko<sup>30</sup>, A. Korzenev<sup>45</sup>, E. Koukovini Platia<sup>44</sup>, S. Kovalenko<sup>2</sup>, I. Krasilnikova<sup>34</sup>, Y. Kudenko<sup>31,38,d</sup>, E. Kurbatov<sup>40</sup>, P. Kurbatov<sup>34</sup>, V. Kurochka<sup>31</sup>, E. Kuznetsova<sup>36</sup>, H. M. Lacker<sup>6</sup>, M. Lamont<sup>44</sup>, O. Lantwin<sup>47,34</sup>, A. Lauria<sup>15,c</sup>, K. S. Lee<sup>25</sup>, K. Y. Lee<sup>22</sup>, N. Leonardo<sup>28</sup>, J.-M. Lévy<sup>5</sup>, V. P. Loschiavo<sup>15,e</sup>, L. Lopes<sup>28</sup>, E. Lopez Sola<sup>44</sup>, F. Lyons<sup>7</sup>, V. Lyubovitskij<sup>2</sup>, J. Maalmi<sup>4</sup>, A.-M. Magnan<sup>52</sup>, V. Maleev<sup>36</sup>, A. Malinin<sup>33</sup>, Y. Manabe<sup>19</sup>, A. K. Managadze<sup>39</sup>, M. Manfredi<sup>44</sup>, S. Marsh<sup>44</sup>, A. M. Marshall<sup>50</sup>, A. Mefodev<sup>31</sup>, P. Mermod<sup>45</sup>, A. Miano<sup>15,c</sup>, S. Mikado<sup>20</sup>, Yu. Mikhaylov<sup>35</sup>, A. Mikulenko<sup>27</sup>, D. A. Milstead<sup>42</sup>, O. Mineev<sup>31</sup>, M. C. Montesi<sup>15,c</sup>, K. Morishima<sup>19</sup>, S. Movchan<sup>29</sup>,

Y. Muttoni<sup>44</sup>, N. Naganawa<sup>19</sup>, M. Nakamura<sup>19</sup>, T. Nakano<sup>19</sup>, S. Nasybulin<sup>36</sup>, P. Ninin<sup>44</sup>, A. Nishio<sup>19</sup>, B. Obinyakov<sup>33</sup>, S. Ogawa<sup>21</sup>, N. Okateva<sup>32,34</sup>, J. Osborne<sup>44</sup>, M. Ovchynnikov<sup>27,55</sup>, N. Owtscharenko<sup>11</sup>, P. H. Owen<sup>47</sup>, P. Pacholek<sup>44</sup>, B. D. Park<sup>22</sup>, A. Pastore<sup>12</sup>, M. Patel<sup>52,34</sup>, D. Pereyma<sup>30</sup>, A. Perillo-Marcione<sup>44</sup>, G. L. Petkov<sup>1</sup>, K. Petridis<sup>50</sup>, A. Petrov<sup>33</sup>, D. Podgrudkov<sup>39</sup>, V. Poliakov<sup>35</sup>, N. Polukhina<sup>32,34,38</sup>, J. Prieto Prieto<sup>44</sup>, M. Prokudin<sup>30</sup>, A. Prota<sup>15,c</sup>, A. Quercia<sup>15,c</sup>, A. Rademakers<sup>44</sup>, A. Rakai<sup>44</sup>, F. Ratnikov<sup>40</sup>, T. Rawlings<sup>51</sup>, F. Redi<sup>46</sup>, A. Reghunath<sup>6</sup>, S. Ricciardi<sup>51</sup>, M. Rinaldesi<sup>44</sup>, Volodymyr Rodin<sup>55</sup>, Viktor Rodin<sup>55</sup>, P. Robbe<sup>4</sup>, A. B. Rodrigues Cavalcante<sup>46</sup>, T. Roganova<sup>39</sup>, H. Rokujo<sup>19</sup>, G. Rosa<sup>15,c</sup>, O. Ruchayskiy<sup>3</sup>, T. Ruf<sup>44</sup>, V. Samoylenko<sup>35</sup>, V. Samsonov<sup>38</sup>, F. Sanchez Galan<sup>44</sup>, P. Santos Diaz<sup>44</sup>, A. Sanz Ull<sup>44</sup>, O. Sato<sup>19</sup>, E. S. Savchenko<sup>34</sup>, J. S. Schliwinski<sup>6</sup>, W. Schmidt-Parzefall<sup>8</sup>, M. Schumann<sup>7</sup>, N. Serra<sup>47,34</sup>, S. Sgobba<sup>44</sup>, O. Shadura<sup>55</sup>, A. Shakin<sup>34</sup>, M. Shaposhnikov<sup>46</sup>, P. Shatalov<sup>30,34</sup>, T. Shchedrina<sup>32,34</sup>, L. Shchutska<sup>46</sup>, V. Shevchenko<sup>33,34</sup>, H. Shibuya<sup>21</sup>, L. Shihora<sup>6</sup>, S. Shirobokov<sup>52</sup>, A. Shustov<sup>38</sup>, S. B. Silverstein<sup>42</sup>, S. Simone<sup>12,a</sup>, R. Simoniello<sup>10</sup>, M. Skorokhvatov<sup>38,33</sup>, S. Smirnov<sup>38</sup>, G. Soares<sup>28</sup>, J. Y. Sohn<sup>22</sup>, A. Sokolenko<sup>55</sup>, E. Solodko<sup>44</sup>, N. Starkov<sup>32,34</sup>, L. Stoel<sup>44</sup>, M. E. Stramaglia<sup>46</sup>, D. Sukhonos<sup>44</sup>, Y. Suzuki<sup>19</sup>, S. Takahashi<sup>18</sup>, J. L. Tastet<sup>3</sup>, P. Teterin<sup>38</sup>, S. Than Naing<sup>32</sup>, I. Timiryasov<sup>46</sup>, V. Tioukov<sup>15</sup>, D. Tommasini<sup>44</sup>, M. Torii<sup>19</sup>, D. Treille<sup>44</sup>, R. Tsenov<sup>1,29</sup>, S. Ulin<sup>38</sup>, E. Ursov<sup>39</sup>, A. Ustyuzhanin<sup>40,34</sup>, Z. Uteshev<sup>38</sup>, L. Uvarov<sup>36</sup>, G. Vankova-Kirilova<sup>1</sup>, F. Vannucci<sup>5</sup>, P. Venkova<sup>6</sup>, V. Venturi<sup>44</sup>, I. Vidulin<sup>39</sup>, S. Vilchinski<sup>55</sup>, Heinz Vincke<sup>44</sup>, Helmut Vincke<sup>44</sup>, C. Visone<sup>15,c</sup>, K. Vlasik<sup>38</sup>, A. Volkov<sup>32,33</sup>, R. Voronkov<sup>32</sup>, S. van Waasen<sup>9</sup>, R. Wanke<sup>10</sup>, P. Wertelaers<sup>44</sup>, O. Williams<sup>44</sup>, J.-K. Woo<sup>24</sup>, M. Wurm<sup>10</sup>, S. Xella<sup>3</sup>, D. Yilmaz<sup>49</sup>, A. U. Yilmazer<sup>49</sup>, C. S. Yoon<sup>22</sup>, Yu. Zaytsev<sup>30</sup>, A. Zelenov<sup>36</sup>, J. Zimmerman<sup>6</sup>

<sup>1</sup> Faculty of Physics, Sofia University, Sofia, Bulgaria

<sup>2</sup> Universidad Técnica Federico Santa María and Centro Científico Tecnológico de Valparaíso, Valparaíso, Chile

<sup>3</sup> Niels Bohr Institute, University of Copenhagen, Copenhagen, Denmark

<sup>4</sup> LAL, Univ. Paris-Sud, CNRS/IN2P3, Université Paris-Saclay, Orsay, France

<sup>5</sup> LPNHE, IN2P3/CNRS, Sorbonne Université, Université Paris Diderot, 75252 Paris, France

<sup>6</sup> Humboldt-Universität zu Berlin, Berlin, Germany

<sup>7</sup> Physikalisches Institut, Universität Freiburg, Freiburg, Germany

<sup>8</sup> Universität Hamburg, Hamburg, Germany

<sup>9</sup> Forschungszentrum Jülich GmbH (KFA), Jülich, Germany

<sup>10</sup> Institut für Physik and PRISMA Cluster of Excellence, Johannes Gutenberg Universität Mainz, Mainz, Germany

<sup>11</sup> Universität Siegen, Siegen, Germany

<sup>12</sup> Sezione INFN di Bari, Bari, Italy

<sup>13</sup> Sezione INFN di Bologna, Bologna, Italy

<sup>14</sup> Sezione INFN di Cagliari, Cagliari, Italy

<sup>15</sup> Sezione INFN di Napoli, Naples, Italy

<sup>16</sup> Laboratori Nazionali dell'INFN di Gran Sasso, L'Aquila, Italy

<sup>17</sup> Aichi University of Education, Kariya, Japan

<sup>18</sup> Kobe University, Kobe, Japan

<sup>19</sup> Nagoya University, Nagoya, Japan

<sup>20</sup> College of Industrial Technology, Nihon University, Narashino, Japan

<sup>21</sup> Toho University, Funabashi, Chiba, Japan

<sup>22</sup> Physics Education Department & RINS, Gyeongsang National University, Jinju, South Korea

<sup>23</sup> Gwangju National University of Education, Gwangju, South Korea

<sup>24</sup> Jeju National University, Jeju, South Korea

<sup>25</sup> Korea University, Seoul, Korea

<sup>26</sup> Sungkyunkwan University, Suwon-si, Gyeong Gi-do, South Korea

<sup>27</sup> University of Leiden, Leiden, The Netherlands

<sup>28</sup> LIP, Laboratory of Instrumentation and Experimental Particle Physics, Lisbon, Portugal

<sup>29</sup> Joint Institute for Nuclear Research (JINR), Dubna, Russia

<sup>30</sup> Institute of Theoretical and Experimental Physics (ITEP) NRC “Kurchatov Institute“, Moscow, Russia

<sup>31</sup> Institute for Nuclear Research of the Russian Academy of Sciences (INR RAS), Moscow, Russia

<sup>32</sup> P.N. Lebedev Physical Institute (LPI RAS), Moscow, Russia

<sup>33</sup> National Research Centre “Kurchatov Institute“, Moscow, Russia

<sup>34</sup> National University of Science and Technology “MISIS“, Moscow, Russia

<sup>35</sup> Institute for High Energy Physics (IHEP) NRC “Kurchatov Institute“, Protvino, Russia

- <sup>36</sup> Petersburg Nuclear Physics Institute (PNPI) NRC “Kurchatov Institute“, Gatchina, Russia
- <sup>37</sup> St. Petersburg Polytechnic University (SPbPU), St. Petersburg, Russia
- <sup>38</sup> National Research Nuclear University (MEPhI), Moscow, Russia
- <sup>39</sup> Skobeltsyn Institute of Nuclear Physics of Moscow State University (SINP MSU), Moscow, Russia
- <sup>40</sup> Yandex School of Data Analysis, Moscow, Russia
- <sup>41</sup> Institute of Physics, University of Belgrade, Serbia
- <sup>42</sup> Stockholm University, Stockholm, Sweden
- <sup>43</sup> Uppsala University, Uppsala, Sweden
- <sup>44</sup> European Organization for Nuclear Research (CERN), Geneva, Switzerland
- <sup>45</sup> University of Geneva, Geneva, Switzerland
- <sup>46</sup> École Polytechnique Fédérale de Lausanne (EPFL), Lausanne, Switzerland
- <sup>47</sup> Physik-Institut, Universität Zürich, Zurich, Switzerland
- <sup>48</sup> Middle East Technical University (METU), Ankara, Turkey
- <sup>49</sup> Ankara University, Ankara, Turkey
- <sup>50</sup> H.H. Wills Physics Laboratory, University of Bristol, Bristol, UK
- <sup>51</sup> STFC Rutherford Appleton Laboratory, Didcot, UK
- <sup>52</sup> Imperial College London, London, UK
- <sup>53</sup> University College London, London, UK
- <sup>54</sup> University of Warwick, Warwick, UK
- <sup>55</sup> Taras Shevchenko National University of Kyiv, Kyiv, Ukraine
- <sup>a</sup> Università di Bari, Bari, Italy
- <sup>b</sup> Università di Cagliari, Cagliari, Italy
- <sup>c</sup> Università di Napoli “Federico II“, Naples, Italy
- <sup>d</sup> Also at Moscow Institute of Physics and Technology (MIPT), Moscow Region, Russia
- <sup>e</sup> Consorzio CREATE, Naples, Italy
- <sup>f</sup> Università della Basilicata, Potenza, Italy
- <sup>g</sup> Università di Napoli Parthenope, Naples, Italy

# Space Weather



## RESEARCH ARTICLE

10.1029/2020SW002712

### Key Points:

- Correction of meteorological effects on muon component of secondary cosmic rays significantly extends the usability of muon monitors
- A new method for modeling of meteorological effects utilizing multivariate analysis and machine learning techniques is presented
- Correction efficiency of the best performing algorithm is greater than for other commonly used methods

### Correspondence to:


M. Savić,  
[msavic@ipb.ac.rs](mailto:msavic@ipb.ac.rs)

### Citation:

Savić, M., Maletić, D., Dragić, A., Veselinović, N., Joković, D., Banjanac, R., et al. (2021). Modeling meteorological effects on cosmic ray muons utilizing multivariate analysis. *Space Weather*, 19, e2020SW002712. <https://doi.org/10.1029/2020SW002712>

Received 30 DEC 2020  
 Accepted 13 JUL 2021

## Modeling Meteorological Effects on Cosmic Ray Muons Utilizing Multivariate Analysis

M. Savić<sup>1</sup> , D. Maletić<sup>1</sup>, A. Dragić<sup>1</sup>, N. Veselinović<sup>1</sup>, D. Joković<sup>1</sup>, R. Banjanac<sup>1</sup>, V. Udovičić<sup>1</sup>, and D. Knežević<sup>1</sup>

<sup>1</sup>Institute of Physics Belgrade, University of Belgrade, Belgrade, Serbia

**Abstract** Correction of meteorological effects on muon component of secondary cosmic rays significantly extends the usability of muon monitors. We propose a new data driven empirical method for correction of meteorological effects on muon component of secondary cosmic rays, based on multivariate analysis. Several multivariate algorithms implemented in Toolkit for Multivariate Data Analysis with ROOT framework are trained and then applied to correct muon count rate for barometric and temperature effects. The effect of corrections on periodic and aperiodic cosmic ray variations is analyzed and compared with integral correction method, as well as with neutron monitor data. The best results are achieved by the application of linear discriminant method, which increases sensitivity of our muon detector to cosmic ray variations beyond other commonly used methods.

**Plain Language Summary** Primary cosmic rays are energetic particles that arrive at Earth from space. On their journey toward Earth they are affected by the solar wind (a stream of charged particles emanating from the sun), which has information about various solar processes embedded in it. In top layers of the atmosphere primary cosmic rays interact with nuclei of air molecules and produce large number of secondary particles that propagate toward Earth's surface. These secondary particles preserve information about variations of primary cosmic rays, which allows for the study of solar processes using Earth based detectors. One type of secondary particles that can be detected on the ground are muons. However, muons are affected by the conditions in the atmosphere, which can disturb the information about variations of primary cosmic rays. That is why it is important to model these atmospheric effects on cosmic ray muons as well as possible so they can be corrected for. In this study, we present a new method for modeling and correction of atmospheric effects on cosmic ray muons, that is based on multivariate analysis utilizing machine learning algorithms. This method increases sensitivity of our muon detector to cosmic ray variations beyond other commonly used methods.

## 1. Introduction

Meteorological effects on muon component of secondary cosmic rays have been known and studied for almost a century. A number of meteorological parameters contribute to variation of muon flux in the atmosphere, but two are the most significant: atmospheric pressure and atmospheric temperature.

Aperiodic fluctuations of intensity, discovered in the very early cosmic ray measurements, were eventually attributed to the variation of atmospheric pressure by Myssowsky & Tuwim (1926) (associated effect dubbed *barometric*), while *temperature effect* has been discovered more than a decade later and has two components: *negative* (first quantitatively described by Blackett, 1938) and *positive* (suggested by Forró, 1947). Barometric effect represents variation of muon flux due to variation of the mass of the absorber (air column) above the detector. Negative temperature effect is a consequence of dependence of effective height of muon generation level on the atmospheric temperature, resulting in longer muon path and increased probability of decay with higher temperature. Positive temperature effect has to do with positive correlation between atmospheric temperature and air density, decreasing the probability of nuclear interactions and increasing the probability of decay of muon-generating pions with the increase of temperature.

In order to study variations of primary cosmic rays (CR) using Earth based muon detectors, it is of the utmost importance to describe these meteorological effects as precisely as possible so they can be corrected for. A precise correction for meteorological effects significantly increases sensitivity of muon detectors to CR variations, making them a more usable counterpart to neutron monitors (the other widely used type of

© 2021. The Authors.

This is an open access article under the terms of the [Creative Commons Attribution-NonCommercial-NoDerivs License](https://creativecommons.org/licenses/by-nc-nd/4.0/), which permits use and distribution in any medium, provided the original work is properly cited, the use is non-commercial and no modifications or adaptations are made.



ground based cosmic ray detectors), as muon detectors are normally responsive to higher energy primary cosmic rays. Additionally, muon monitors have a unique application in diagnostics of the atmosphere, allowing for prediction of atmospheric temperatures provided a good model of meteorological effects is available (Belov et al., 1987; Kohno et al., 1981).

Several empirical and theoretical models of meteorological effects have been proposed over the years, based on which corrections can be performed. Even though full set of meteorological effects is larger, in this analysis we will concentrate on the correction of temperature and barometric effect only, so results can be more easily compared to other methods.

Some of the most commonly used methods for temperature correction are: method of effective level of generation, introduced by Duperier (1949), integral method, developed by Feinberg (1946), Dorman (1954), and others (Maeda & Wada, 1954; Wada, 1962), method of mass-averaged temperature developed by Dvornikov et al. (1976), and method of effective temperature (mostly applicable to underground detectors) (Barrett et al., 1952).

Each of these methods have their own advantages, but in this study, we have decided to use the integral method as a reference against which to compare the results of our analysis. Main reason being is that it is derived from the theory of meteorological effects, which involves the most detailed analysis, as well as it being the least approximative. According to this approach, relative variation of muon count rate due to the temperature effect can be expressed as:

$$\left(\frac{\delta I}{I}\right)_{temp} = \int_0^{h_0} \alpha(h) \cdot \delta T(h) \cdot dh, \quad (1)$$

where  $\alpha$  is temperature coefficient density function,  $\delta T$  is temperature variation and  $h_0$  is atmospheric depth of the observation level expressed in  $g/cm^2$ . Temperature coefficient density function is calculated theoretically, while temperature variation is calculated relative to some reference temperature for the period, usually mean temperature. In practical application, integration in Equation 1 is substituted with a sum, taking into account some finite number of isobaric levels.

Analysis of barometric effect is also included in the theory of meteorological effects, but barometric coefficient is rarely calculated theoretically. Most commonly it is determined using linear regression, assuming linear dependence between atmospheric pressure and muon flux:

$$\left(\frac{\delta I}{I}\right)_{pres} = \beta \cdot \delta P, \quad (2)$$

where  $\beta$  is barometric coefficient, and  $\delta P$  represents atmospheric pressure variation.

Each of the mentioned methods is at least in some part approximative, so the idea behind this work is to introduce a new empirical method for correction of meteorological effects that would be data driven, assuming as little as possible upfront. Other advantages of such approach are that it does not depend on the design of the detector, location of the site or topology of the surrounding terrain (as these would ideally be factored in by the model), and that it can be applied in near-real time. Additionally, proposed method can be used in the analysis and potential correction of temperature effect of neutron component of cosmic rays, as part of detected neutrons can originate from cosmic ray muons captured in the nuclei of the shielding of a neutron monitor detector (Dorman, 2004). Finally, in principle it can easily be generalized to take wider set of meteorological parameters into account.

As the presented problem is multidimensional, involving a relatively large number of correlated variables, we have decided to employ multivariate analysis, relying on machine learning techniques. In some recent work (Morozova et al., 2017; Savic et al., 2019) decorrelation of atmospheric variables and numerical modeling has been successfully applied to the study of interaction of cosmic rays with Earth's atmosphere, so utilizing adaptive and flexible machine learning methods could possibly yield further improvement, potentially revealing additional dependencies and taking higher order effects into account. This approach involves application of a number of multivariate algorithms, more or less rooted in statistical machine learning, to our problem and comparing their consistency and effectiveness with selected reference results.

Large part of variations observed in continuous cosmic ray measurements can be attributed to different space weather phenomena, due to modulation of primary cosmic rays in the heliosphere. In terms of temporal properties, they can be classified as periodic or aperiodic. We will test how newly introduced methods for correction of meteorological effects affect the sensitivity for detection of both periodic as well as aperiodic variations of muon flux of nonterrestrial origin, and how it ultimately compares to the sensitivity of neutron monitors.

## 2. Data

For the analysis of meteorological effects both muon flux and meteorological data are needed. Muon flux was measured experimentally in the Low Background Laboratory at the Institute of Physics Belgrade, while meteorological data is a combination of modeled atmospheric temperature profiles, and atmospheric pressure and ground level temperature measured locally.

### 2.1. CR Muon Data

Low Background Laboratory (LBL) is located on the grounds of the Institute of Physics Belgrade. Geographical coordinates for the laboratory are  $44^{\circ}51'N$  and  $20^{\circ}23'E$ , with elevation of 75 m and geomagnetic cutoff rigidity of 5.3 GV. Detector system is comprised of a  $100 \times 100 \times 5$  cm plastic scintillator with accompanying read-out electronics. Median energy for the detector system is  $(59 \pm 2)$  GeV (Veselinović et al., 2017), with muon flux of  $(1.37 \pm 0.06) \times 10^{-2}$  per  $\text{cm}^2$  s. Electron contamination determined for a previously used experimental setup was  $\sim 24\%$  (Dragić et al., 2008), and is assumed to be comparable for the current one (Joković, 2011). More detailed description of the laboratory and the experimental setup can be found elsewhere (Dragić et al., 2011). Native muon count rate data has time resolution of 5 min, but hour sums are also frequently used in analysis.

Continuous cosmic ray muon flux measurements have been ongoing in LBL since 2002, current setup being utilized since 2009. Data are available to public via an online interface on the Belgrade Cosmic Ray Station internet site (Low Background Laboratory for Nuclear Physics, 2020).

As with any long-term measurement, some shorter interruptions and inconsistencies are unavoidable, hence when choosing the interval to be used for the analysis we decided to use a one-year period from June 1, 2010 to May 31, 2011, where measurements had the most continuity and consistency. Additionally, using a one-year period should remove any potential bias, primarily due to annual temperature variation.

### 2.2. Meteorological Data

Meteorological parameters needed for the analysis come from two sources: Atmospheric temperature profile data are produced by an atmospheric numerical model, while atmospheric pressure and ground temperature data come from local measurements.

Meteorological balloon soundings above Belgrade done by Republic Hydro-meteorological Service of Serbia (RHMZ, 2020) are not frequent enough for the purposes of this analysis, so modeled data for atmospheric temperature profile are used instead. Several numerical atmospheric models can provide such data. In this work, we have chosen Global Forecast System (GFS) produced by National Centers for Environmental Prediction (GFS, 2020), which has been found to be in best agreement with balloon soundings done above Belgrade. Comparison was done where soundings data were available, as described in our previous study (Savić et al., 2019). GFS provides a large number of modeled atmospheric parameters among which are atmospheric temperatures for different isobaric levels. Modeled data sets are being produced four times per day (at hours 00:00, 06:00, 12:00, and 18:00). In addition, analysis data are also available, reprocessed *post festum* and taking into account real data measured by world network of meteorological services. In this analysis, we have been using such reprocessed atmospheric temperatures for the following isobaric levels: 10, 20, 30, 50, 70, 100, 150, 200, 250, 300, 350, 400, 450, 500, 550, 600, 650, 700, 750, 800, 850, 900, 925, and 975 mb. Data are available with spatial resolution of  $0.5^{\circ}$  of geographical longitude/latitude, so coordinates closest to the laboratory coordinates were chosen. Data were then interpolated with cubic spline, similar as in Berkova et al. (2012), and sampled in finer time resolution needed for the analysis.

Atmospheric pressure and ground temperature data are compiled from different meteorological stations in and around Belgrade, and then interpolated as described in more detail elsewhere (Savic et al., 2016). Finally, unique time series of combined modeled and measured meteorological data, with finest time resolution of 5 min, is assembled to be used in the analysis.

### 3. Methodology

The use of machine learning has seen an unprecedented expansion in the last decade. The main strength of such approach being that it does not assume any a priori model, but is data driven and thus able to potentially discover hidden dependencies. This is especially true when applied to large data sets with many correlated variables. In this study, we want to establish whether such approach would yield any improvements when applied to the problem of meteorological effect on cosmic ray muons.

To test this, we have decided to use toolkit for multivariate analysis (TMVA) package which provides a ROOT-integrated environment for application of multivariate classification and regression techniques (Hoecker et al., 2007). The package has been developed for the use in high-energy physics and contains implementation of a number of supervised learning algorithms, which utilize training and testing procedures on a sample data set to determine the mapping function. Mapping function maps the input parameters to output target value, trying to model the actual functional dependence (“target” function) as accurately as possible. The structure of the mapping function is algorithm specific, and can be a single global function or a set of local models. Trained algorithm is then applied to the full data set and provides either a signal/background separation (in case of classification) or prediction of target value (in case of regression).

For us, the later application is especially interesting. The idea is to train the mapping function, using meteorological parameters as input variables, and muon count rate as the regression target, and use trained function to produce the predicted target output for a larger data set. In principle, implementation of this procedure is specific for different analysis frameworks. TMVA provides template code for the training and application of multivariate methods, where optimal parameters obtained in the training/testing phase are stored in “weight” files to be used in the application phase. Thusly predicted muon count rate would ideally contain only variations related to meteorological effects, while the residual difference between modeled and measured muon count rate would contain variations of non-meteorological origin. We would apply this procedure for a number of algorithms implemented in TMVA, compare their performance and efficiency based on several criteria, and finally suggest the methods best suited for the modeling, and ultimately the correction, of meteorological effects.

Corrected muon count rate would be calculated according to the following equation:

$$N_{\mu}^{(corr)} = \Delta N_{\mu} + \langle N_{\mu} \rangle, \quad (3)$$

where

$$\Delta N_{\mu} = N_{\mu}^{(mod)} - N_{\mu} \quad (4)$$

is the difference between the modeled and measured muon count rate.

Not all machine learning methods are equally suited for all types of problems and selection of the optimal method for a particular application is rarely straightforward. The efficiency of different algorithms depends on a number of factors: Whether they are used for classification or regression, is correlation between parameters linear or nonlinear, what is the general complexity of the problem and required level of optimization, and so on. One can only assume the efficiency of any given algorithm upfront but there is no clear general rule which one will perform best in a particular situation. Often, several algorithms with specific strengths and weaknesses can be applied to the same problem and only through analysis of the final result the optimal one can be determined. For this reason, in our analysis we have decided to indiscriminately include the largest number of algorithm classes available in TMVA, and only after extensive parallel testing narrow the selection down to the optimal one.

We will briefly describe different classes of multivariate methods available in TMVA, as well as list specific algorithms that were chosen as representative for each class. First class are methods based on probability

density estimation (PDE) techniques, where actual probability density function is estimated based on the available data. Here we have selected to test two specific multidimensional implementations, somewhat similar in nature: PDE range-search (PDE-RS) and k-nearest neighbor (KNN) algorithms. Examples of use of this approach for multivariate regression are scarce, but the success with which PDERS was applied in classification problems in high-energy physics (Carli & Koblitz, 2003) motivated its use here. Second class are methods based on function discriminant analysis. These methods are widely used for dimensionality reduction and classification. Here, we selected the linear discriminant (LD) algorithm which shares some similarities in the approach with principal component analysis (PCA), in that it maps a space of potentially correlated input variables onto a smaller space of uncorrelated variables, but in addition to PCA it also maximizes the separation between output classes, making it a natural choice for application to our problem. Algorithms that employ higher order functions were also tested, but as could be expected performed more poorly. Application of artificial neural networks (ANN) to multivariate regression problems has seen expansion in recent years, where ANN methods often perform better than more straightforward regression techniques, especially if some degree of nonlinearity is present. Even though the dependence of cosmic ray muon flux on atmospheric temperatures is linear, we felt it is certainly worth investigating how ANN methods would perform when applied to this problem, and if any additional hidden dependence would be revealed. We have chosen to apply the MLP, as it is the fastest and most flexible available ANN algorithm in TMVA. Finally, method of boosted regression trees (BDT) employs a larger number (*forest*) of binary decision trees, which split the phase space of input variables based on a yes/no decision to a series of sequential cuts applied, so to predict a specific value of the output variable. They have been very successfully applied to classification problems in high-energy physics (Lalchand, 2020), but can also be used for multivariate regression with the similar rationale as for the ANN. We have selected two representative algorithms for testing: boosted decision tree (BDT) and gradient boosted decision tree (BDTG).

In this analysis, the procedure is applied to correction of barometric and temperature effect but it is easy to see how it can be extended to include more atmospheric variables, especially as such data is readily available from atmospheric numerical models.

### 3.1. Training Procedure

For the training/testing data subset we have selected data for the 10 geomagnetically quietest days of each month (list provided by GFZ German Research Center for Geosciences, GFZ Potsdam, 2020), as we expect variations due to meteorological effects to be more pronounced here. This subset was then further split into training and testing data set, where 70% of randomly selected data was used for training while remaining 30% was used for testing. Data time resolution used was 5 min as it gave us a larger statistics for training.

There is a number of settings that can be manipulated for each of the multivariate algorithms used. They vary from some basic parameters, to selection of different subalgorithms or various options that can be turned on or off. For each algorithm, we have selected the optimal set of parameters. The criterium for optimal performance was minimizing the average quadratic deviation of the modeled output versus the target value. Also, where allowed by the algorithm, input variables were decorrelated prior to further processing.

Table 1 shows the values of average quadratic deviation for the modeled output (modeled muon count rate) versus the target value (measured muon count rate) for different algorithms. First two columns refer to the training data subset while second two columns refer to the testing data subset. First and third column represent average quadratic deviation defined as  $(\sum(f_{MVA} - f_{target})^2)^{1/2}$  (where  $f_{MVA}$  and  $f_{target}$  represent modeled and measured count rates, respectively), while second and fourth columns represent truncated average quadratic deviation which takes into account 90% of data with least deviation. As previously mentioned, the criterium for selection of optimal parameters for every algorithm is the minimal value of average quadratic deviation for the test data subset.

### 3.2. Algorithm Performance Analysis

All presented multivariate algorithms have no built in knowledge about the studied effect, so in addition to quantitative test mentioned in the section above, we introduce some qualitative analysis designed to estimate the integrity of modeled data. Prime concern here would be to test whether the suggested procedure

**Table 1**  
*Average Quadratic Deviation for Selected Multivariate Methods*

Method	Training		Testing	
	Average deviation (counts/5 min)	Truncated deviation (counts/5 min)	Average deviation (counts/5 min)	Truncated average (counts/5 min)
PDERS	234	185	258	201
KNN	224	177	233	185
LD	286	225	284	223
MLP	228	180	234	186
BDT	219	182	237	188
BDTG	223	174	236	187

Abbreviations: BDT, boosted decision tree; BDTG, gradient boosted decision tree; KNN, k-nearest neighbor; LD, linear discriminant.

for the correction of barometric and temperature effect (PT correction) removes these meteorological effects only, while leaving all other features nonperturbed. To this end, we will analyze several distributions of modeled data, compare them with raw and reference PT corrected data (obtained using the integral method) and look for possible anomalous features.

First, we will look into structure of distributions of difference between modeled and measured muon count rate as a function of measured count. We want to make comparison between these distributions in the training phase (for the test data subset) and after the trained algorithm was applied to the full data set. We would expect these distributions to be consistent, and appearance of some new structures or strong trends would point to some perturbation in the application phase. We have selected two examples to illustrate the difference in consistency of application of trained algorithms—BDTG and PDERS, their distributions shown in Figure 1.

We can see that distributions for BDTG algorithm for test data subset (Figure 1a) and full data set (Figure 1b) are fairly similar, and any structures and trends in the test distributions are mostly well replicated in the full data set distributions (different statistics taken into account). This is the case for most applied algorithms except for PDERS, where some dependence of the count rate, negligible for the test data distribution (Figure 1c), exists for the full data set distribution (Figure 1d).

Another, more important feature, is that for some algorithms distributions we analyzed in the previous paragraph are not smooth, but rather display some structures. To get further insight into these structures, for all featured methods we plotted distributions of modeled muon count rate along with the distribution of raw count rate on the same graph, as shown in Figure 2.

In order to better understand shapes of distributions and any structures observed in plots in Figure 2, it would be helpful to compare them to equivalent plots for muon count rates corrected for pressure and temperature effects using a well-established reference method. However, before we take a look at these distributions, we will first briefly describe procedures used to obtain reference PT correction.

Temperature and barometric effect are typically corrected for independently, where one of several methods mentioned in Section 1 is used for temperature correction, and barometric coefficient for pressure correction is determined empirically. Integral method for correction of temperature effect is widely accepted as the most accurate one. It is based on the theory of meteorological effects and takes complete atmospheric temperature profile and relevant processes into account. Most thorough description of the theory of meteorological effects is given by Dorman (2004), where temperature coefficient density function  $\alpha(h)$  in Equation 1 is given in its integral form. In order to be applied, this function is then calculated through integration, substituting parameters specific to the location of the experiment. Temperature coefficient density functions for the location of Low Background Laboratory for Nuclear Physics were calculated using Monte Carlo integration technique. In order to determine barometric coefficient, temperature corrected muon data were plotted as a function of atmospheric pressure (using entries for 10 geomagnetically quietest days

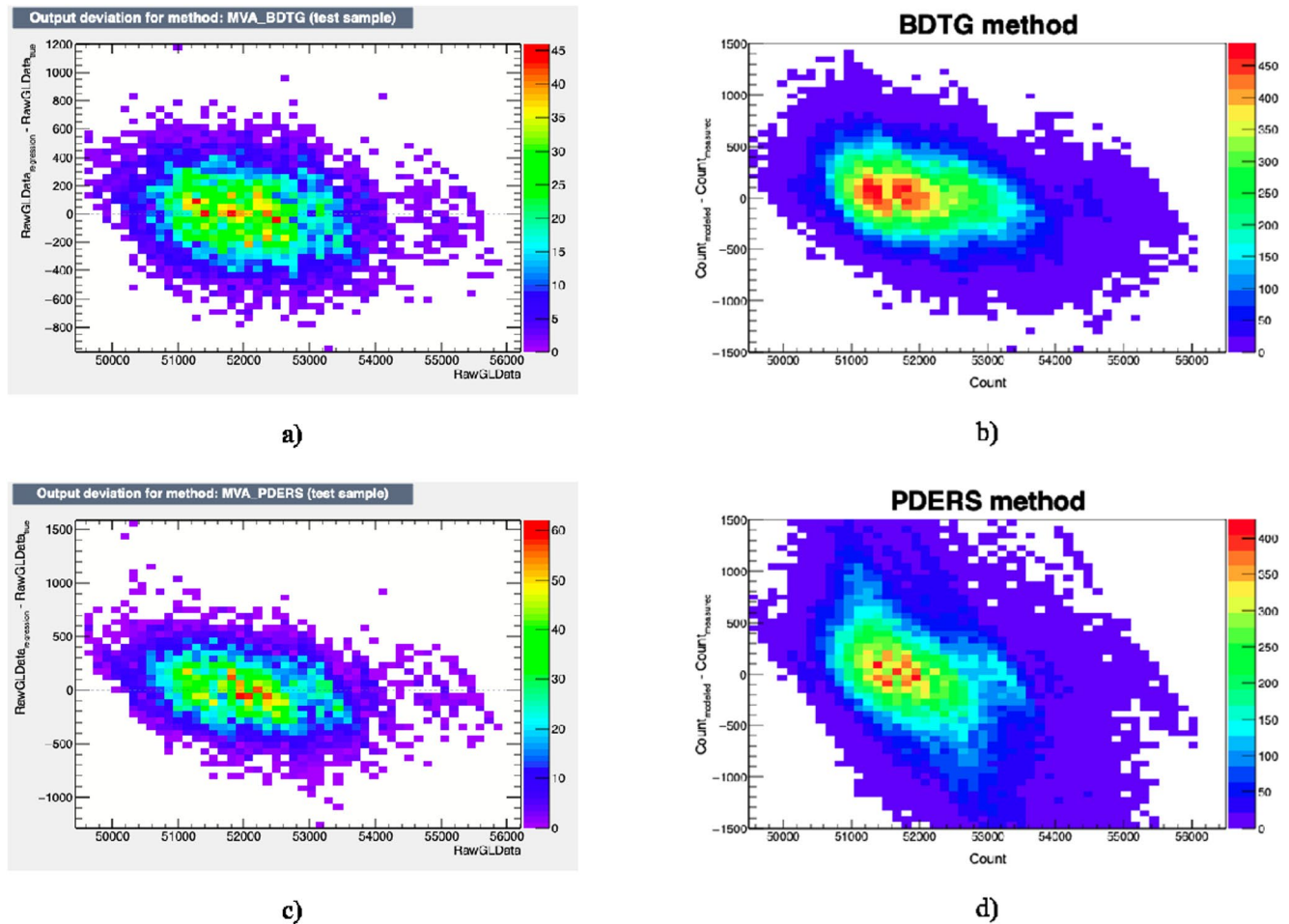


**Figure 1.** Distribution of difference between modeled (regression) and measured (true) muon count rate as a function of measured muon count rate for: (a) gradient Boosted decision tree (BDTG)—test data set, (b) BDTG—full data set, (c) PDERS—test data set, and (d) PDERS—full data set.

of each month only), coefficient determined via linear regression separately for each calendar year. Both procedures are presented in greater detail in our previous work (Savic et al., 2016).

Distributions equivalent to ones shown in Figures 1 and 2 were plotted for reference pressure and temperature corrected data, as shown in Figure 3. The analog for the modeled muon count rate is calculated from the variation due to pressure and temperature effects calculated based on the integral method. It is worth pointing out that distributions for reference PT corrected data are noticeably less smooth, which can be mostly attributed to lower statistics used as only hour summed data was available for this correction.

Based on these plots, we can conclude that we should not expect a significant deviation between raw and corrected data and that corresponding distributions should not have any characteristic structures. Most plots in Figure 2 are consistent with this expectation, however, some structures can be observed in KNN plots, and to a degree in BDT plots, while distribution plotted for PDERS algorithm does not have these structures but appears to somewhat deviate from raw data distribution.

Another insight into performance and consistency of different multivariate algorithms when applied to the modeling of meteorological parameters can be gathered by the way of spectral analysis of PT corrected data. Pressure and temperature corrected muon count rate was determined for all selected algorithms using modeled data, as described in Section 3. Since some gaps exist in our muon data, Lomb-Scargle algorithm was used to obtain the power spectra, as it is less sensitive to uneven data sampling (Press et al., 2007). Figure 4 shows power spectra for raw and muon count rates corrected for pressure and temperature effects using integral and two illustrative examples of multivariate methods. Full spectrum as well as selected interval

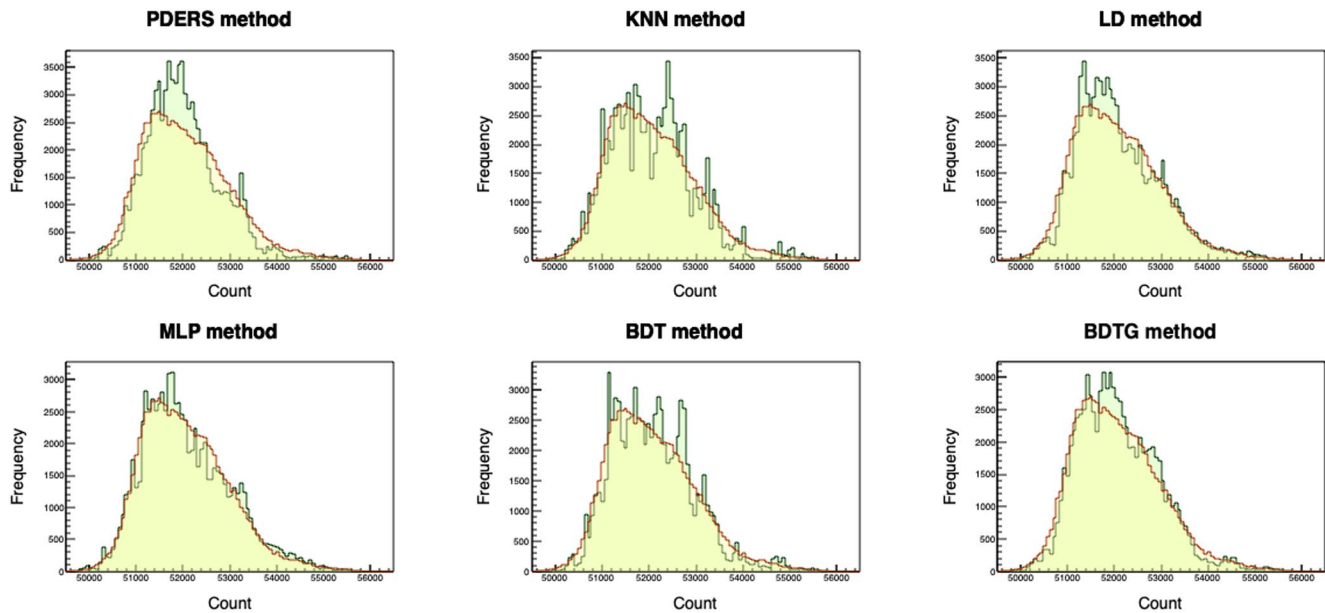


**Figure 2.** Comparison between distributions of raw (yellow) and muon count rate modeled by selected multivariate methods (green).

of frequencies around the periodicity of one day are shown, red dashed line indicating significance level of 0.01.

If integral method is again used as a reference, we can see that thus obtained PT correction does not remove daily variation, but rather makes it more pronounced. This should not come as a surprise, as only smaller part of the diurnal variation can be attributed to meteorological effects (Quenby & Thambyahpillai, 1960), while larger part is of nonmeteorological origin. Hence, removing variation due to atmospheric pressure would make daily variation more prominent. LD, and to a degree BDT/BDTG methods, have an effect on daily variation similar to the integral method, but for BDT method (bottom right in Figure 4) we observe emergence of some frequencies with significant power that cannot be associated with any known periodicity of cosmic rays, and probably have artificial origin. Such features are even more pronounced for the remaining multivariate algorithms, where in addition an over-reduction of power frequency corresponding to diurnal variation to can be observed. Over-reduction of daily variation coupled with introduction of artificial variations with significant powers points to possible inadequateness or overtraining of some of the multivariate methods.

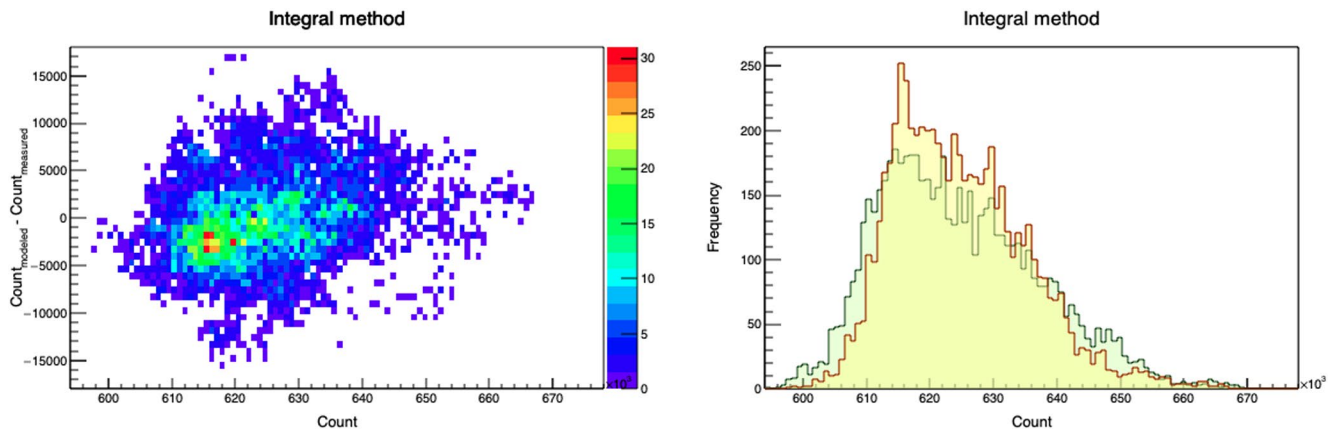


**Figure 3.** Distribution of difference between muon count rate calculated from the variation due to pressure and temperature effect using integral method and measured muon count rate as a function of measured muon count rate (left), and comparison between distributions of raw (yellow) and calculated muon count rate (green) shown on the right.

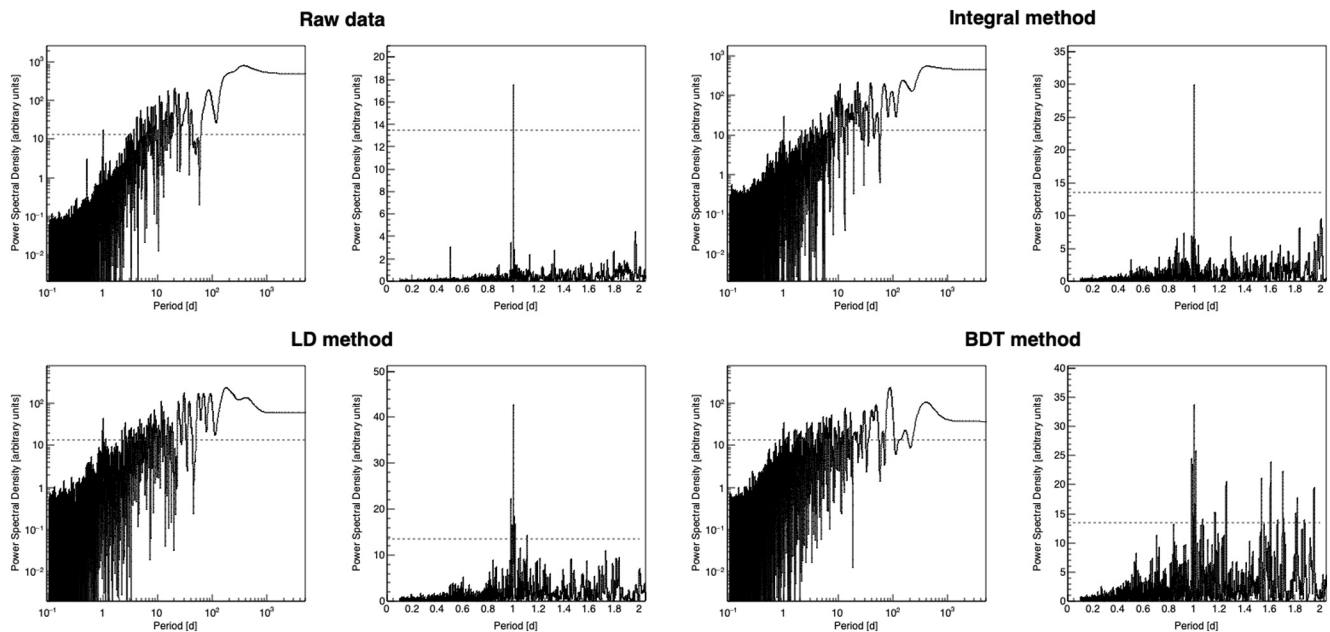


**Figure 4.** Power spectra for raw data (top left), PT corrected data using integral method (top right), and PT corrected data using selected multivariate methods (second row). For each method, both full spectrum and a range of frequencies around periodicity of one day are shown. Significance level of 0.01 is indicated by the red dashed line.

The effect on annual variation is difficult to determine based on the spectral analysis as period of only one year is analyzed, but we will introduce some quantitative tests in the next section that will help us with this estimate.

## 4. Results

We will use two criteria to estimate the efficiency of newly introduced methods for PT corrections. One will rely on the effectiveness with which the multivariate algorithms remove the annual variation and reduce variance, while the other will be based on the effect the correction has on detection sensitivity for aperiodic events, such as Forbush decreases (Forbush, 1937). In both cases, we will compare the results with the ones obtained by the integral method.

### 4.1. Effects of PT Correction on Periodic CR Variations

Significant part of the annual variation of cosmic ray muon flux can be attributed to the variation of atmospheric temperature (Hess, 1940). As mentioned before, the effectiveness with which this effect is corrected for will affect the detector sensitivity to variations of primary cosmic rays of non-atmospheric origin.

We will examine time series for pressure and temperature corrected data and compare them with raw and pressure corrected time series, especially taking note of how PT correction affects the annual variation. In order to estimate this effect, we fit the time series (except for raw data) with sine function with a period of one year. The amplitude of pressure corrected data determined from such fit will be used as an estimate of the annual muon flux variation, and serve as a reference against which to compare the effect of PT correction by different methods. In Figure 5 time series for raw, pressure corrected and pressure and temperature corrected data are shown. For the sake of simplicity, not all time series for data PT corrected using multivariate algorithms are shown, but rather only characteristic ones. Table 2 shows values for the annual variation amplitude for pressure and PT corrected time series, as well as possibly more informative reduction of annual variation calculated relative to the amplitude of the pressure corrected muon flux.

While, time series in Figure 5 for data PT corrected using integral, LD and BDTG methods do not seem to have some unexpected fluctuations, that is not the case for MLP method, where one can observe some



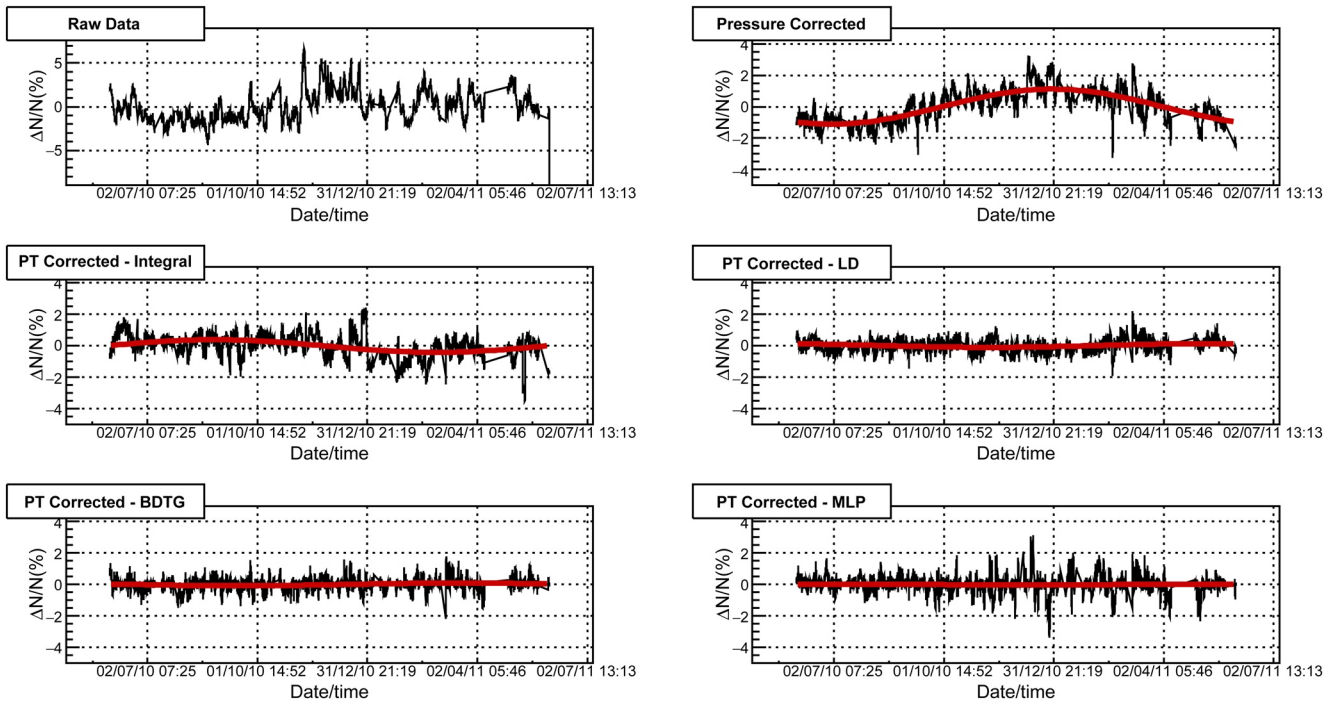


**Figure 5.** Muon count rate time series for the period from June 1, 2010 to May 31, 2011: raw data (top left), pressure corrected data (top right), PT corrected data using integral method (second row left) and data PT corrected using selected multivariate methods.

data that appears to deviate from the mean more significantly than what would be intuitively expected. For remaining multivariate algorithms this is even more the case. In order to try and quantify this visual comparison, we will analyze the effect corrections have on standard deviation of the data. If calculated relative to the mean muon flux for the whole period, standard deviation would be sensitive to the residual annual variation. To make standard deviation independent of the seasonal variation, we used a moving ten-day window to determine the mean value and then calculated the standard deviation relative to it.

Figure 6 shows distributions of relative variation of muon flux in respect to the moving window mean value for raw data and PT corrected data using integral, LD and MLP methods. It is based on these distributions that standard deviation was determined and results are presented in Table 3. Comparing standard deviations for PT corrected muon flux obtained by multivariate methods with the one obtained by the integral method, we can see that for LD, BDT, and BDTG algorithms they have comparable values. The difference is somewhat larger in the case of MLP, which is in accordance with features observed in Figure 6, while it is significantly larger for the remaining algorithms. This indicates that PT correction performed using KNN and PDERS (and possibly MLP) algorithms probably introduces some artificial features into PT corrected muon flux data.

One way to evaluate the effectiveness of different algorithms in reduction of the seasonal variation even better, would be to compare the PT corrected muon data to pressure corrected time series for selected neutron monitor detectors. The reasoning is based on a well-known fact that meteorological effects on the neutron component of secondary cosmic rays are dominated by the barometric effect. Temperature effect does exist for the secondary cosmic ray neutrons, but whether calculated theoretically (Dorman, 2004) or determined experimentally (Kaminer et al., 1965), it is still an order of magnitude smaller than for the muon component and typically not corrected for in neutron monitor data. Based on this, we

**Table 2**  
*Amplitude and Reduction of the Amplitude of Annual Variation Relative to Pressure Corrected Data (P Corrected) for PT Corrected Data (Using Integral and Selected Multivariate Methods)*

Method	Amplitude (%)	Relative reduction (% of P corrected)
P corrected	$1.11 \pm 0.09$	/
Integral	$0.40 \pm 0.03$	$64 \pm 6$
PDERS	$0.09 \pm 0.02$	$92 \pm 3$
KNN	$0.24 \pm 0.04$	$79 \pm 5$
LD	$0.11 \pm 0.03$	$90 \pm 4$
MLP	$0.03 \pm 0.01$	$98 \pm 2$
BDT	$0.12 \pm 0.03$	$89 \pm 4$
BDTG	$0.086 \pm 0.009$	$92 \pm 2$

Abbreviations: BDT, boosted decision tree; BDTG, gradient boosted decision tree; KNN, k-nearest neighbor; LD, linear discriminant.

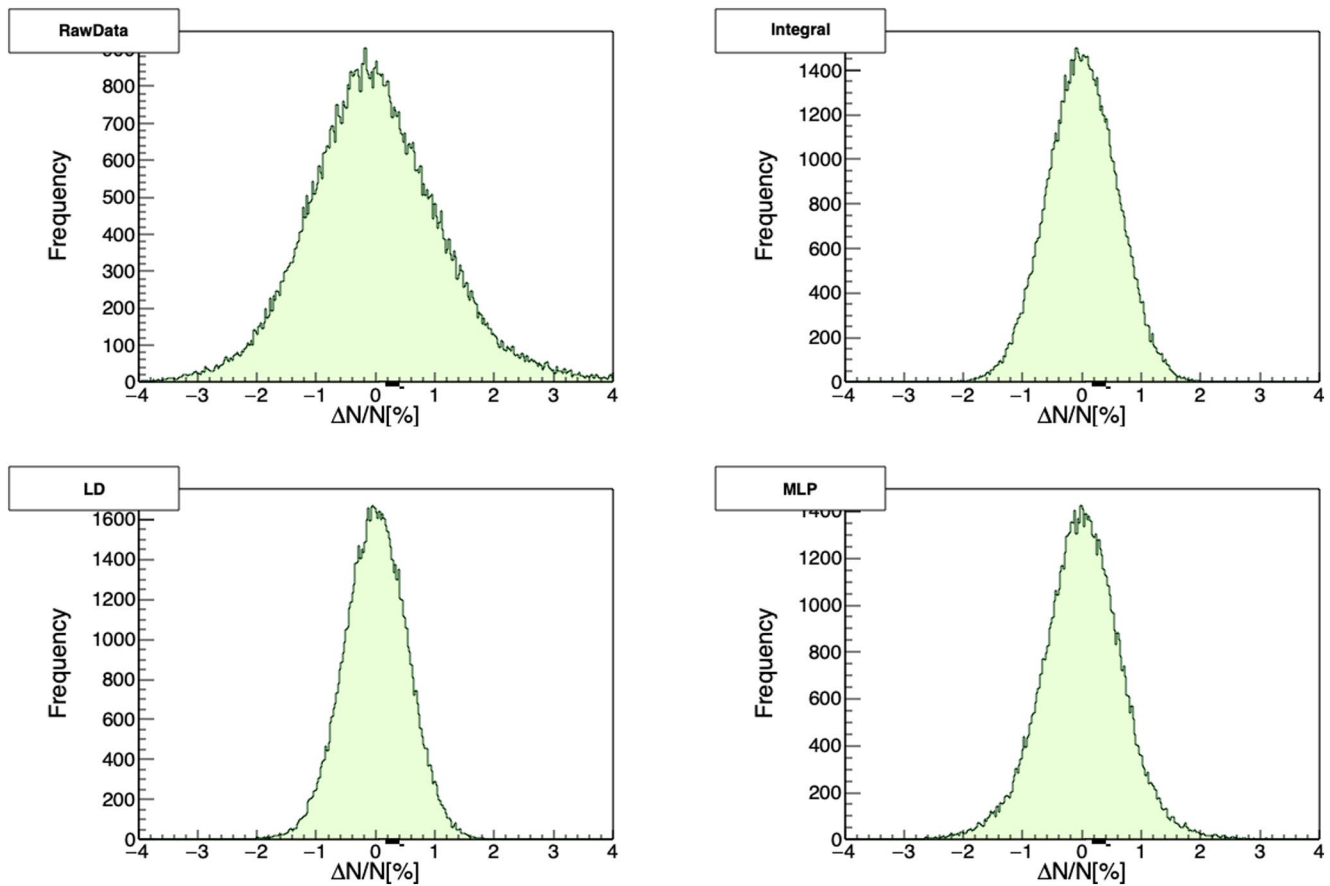


**Figure 6.** Relative variation of muon count rate calculated in respect to mean count in the ten-day moving window, for raw data (top left), PT corrected using integral method (top right), and data PT corrected using selected multivariate methods (second row).

believe pressure corrected neutron monitor data to be (in the first approximation) independent from meteorological effects, and hence a good reference for the evaluation of effectiveness of different methods for PT corrections of muon flux data.

For this comparison, we have chosen neutron monitors located in Athens and Rome, as they had the most consistent operation in the period we use for the analysis. Respective geomagnetic cutoff rigidities for these neutron monitors are 8.53 and 6.27 GV. Pressure and efficiency corrected relative neutron count rate was acquired via Neutron Monitor Database (NEST, 2020), presented for the said period in Figure 7. As for the muon flux data, relative neutron count rate time series were fitted with sinusoidal function, with a period of one year, to obtain the amplitude used as an estimate of the annual variation. Neutron monitors are more sensitive to lower energy secondaries than muon detectors so their time series can exhibit larger variations, which in turn can affect the fitting algorithm. However, in this case the fits seem to be dominantly affected by the relatively stable period between June and November 2010, hence we believe them to be a reliable estimate of the seasonal variation amplitude. Thus acquired annual variation amplitude for Rome neutron monitor is  $(0.29 \pm 0.01)\%$ , while for the Athens neutron monitor it is  $(0.17 \pm 0.05)\%$ .

**Table 3**

*Standard Deviation of Relative Variation of Muon Count Rate for Raw and Data Corrected for Pressure and Temperature Effect (Using Integral and Selected Multivariate Methods)*

Method	Raw	Integral	PDERS	KNN	LD	MLP	BDT	BDTG
Relative deviation (%)	1.117	0.592	0.990	0.785	0.533	0.687	0.607	0.551

Abbreviations: BDT, boosted decision tree; BDTG, gradient boosted decision tree; KNN, k-nearest neighbor; LD, linear discriminant.

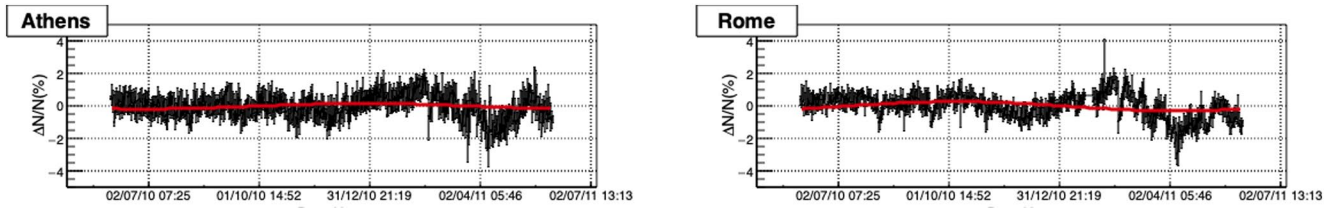


**Figure 7.** Relative neutron count rate time series for the period from June 1, 2010 to May 31, 2011 for Athens (left) and Rome (right) neutron monitors.

Comparing these values with the ones in Table 2, we see that methods KNN, LD, and BDT yield the most similar results. PDERS and MLP seem to underestimate the annual variation, while the integral method estimates a somewhat larger value.

Observed overall poor performance of KNN and PDERS algorithms could possibly be explained by the fact that these algorithms perform best when applied to problems involving strong nonlinear correlations, and are less efficient when dependencies between variables are dominantly linear (Hoecker et al., 2007). Additionally, these algorithms typically need a large training sample, so possibly statistics in our analysis was inadequate. However, artificial neural networks (such as MLP) should in principle be well suited for multivariate linear regression, and perform better than observed results suggest. Most likely, using minimization of the average quadratic deviation as a sole criterium for the selection of optimal parameters in the training phase may lead to overtraining (Montgomery et al., 2006), and additional qualitative criteria (i.e., ones introduced here) and more careful parameter control should also be used. BDT and BDTG algorithms performed reasonably well even though they are not optimized for treatment of linear multivariate problems, however, spectral analysis indicates a further improvement can be made. Additionally, all algorithms would probably benefit from a longer data interval of several years being used.

#### 4.2. Effects of PT Correction on Aperiodic CR Variations

As mentioned before, apart from increasing sensitivity of muon detectors to periodic variations of primary cosmic rays, correcting raw muon flux data for meteorological parameters also affects detector sensitivity to aperiodic events which occur due to heliospheric modulation of primary cosmic rays. Here, we will analyze the effect PT correction, performed by application of different multivariate algorithms, has on detection of Forbush decrease events. We have chosen to concentrate on Forbush decreases as our muon detector is much less sensitive to other aperiodic events, such as ground level enhancements (GLE).

Forbush decrease (FD) events are typically characterized by their amplitude, so it could be a natural choice for a parameter to be used as a measure of detection sensitivity. However, another requirement for definition of sensitivity could be that detected signal significantly deviates from random fluctuations. That is, why we have decided to use the ratio of the amplitude to the standard deviation of muon flux, or relative amplitude, as an estimate of sensitivity to aperiodic events, rather than the actual amplitude. As we primarily focus on the magnitude of Forbush decreases, when we mention an FD event in the following text it mainly refers to the decrease phase and not the recovery phase.

To determine the amplitude, we have used a method proposed by Barbashina et al. (2009). The idea is to make the result independent from different trends leading up to, and following the actual FD. To do this, two intervals are defined: one  $i$  days before the onset of the FD, where  $i$  can have value  $(1, \dots, n)$  days, and the other  $p$  days after the end of the decrease, where  $p$  can have value  $(1, \dots, m)$  days. These intervals are then detrended using fit parameters obtained from linear regression. Mean count is determined for the detrended time series before the onset of FD for  $j$  days (where  $j = 1, \dots, i$ ), and for the detrended time series during recovery stage for  $q$  days (where  $q = 1, \dots, p$ ). Thus, in total we obtain  $n!$  values for mean detrended count before the onset of FD, and  $m!$  values for mean detrended count for the recovery stage. FD amplitude estimate is then calculated for each combination of “before” and “after” values according to the following formula:

$$A_{ij}^{pq} = \frac{\langle I_{before}^{(i,j)} \rangle - \langle I_{after}^{(p,q)} \rangle}{\langle I_{before}^{(i,j)} \rangle} \times 100\%, \quad (5)$$

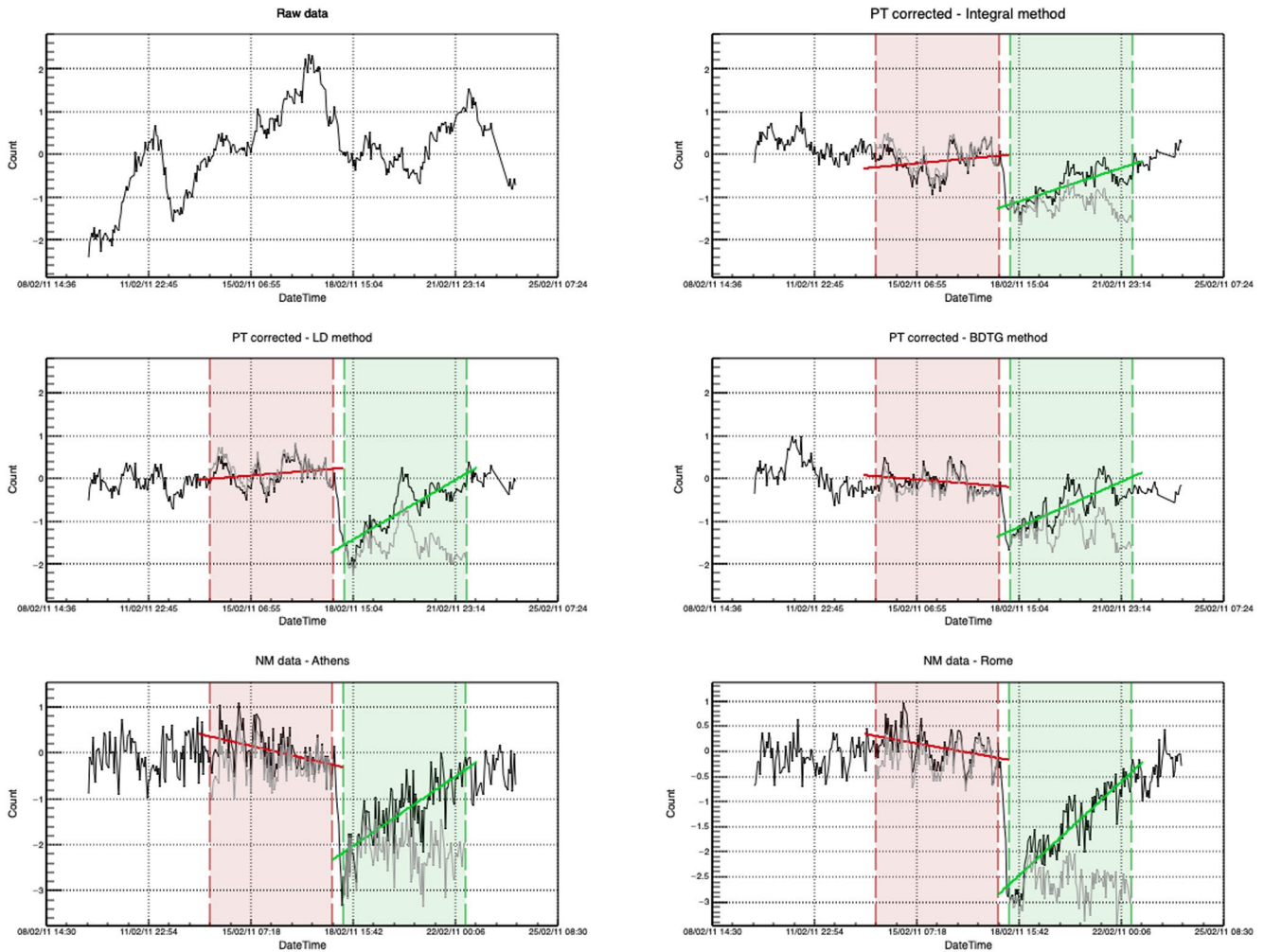


**Figure 8.** Time series for the interval around Forbush decrease of February 18, 2011: raw muon data (top left), PT corrected muon data using integral (top right), linear discriminant (center left) and gradient boosted decision tree (center right) methods, and neutron monitor data for Athens (bottom left) and Rome (bottom right) neutron monitors. Interval leading into (red) and following the Forbush decrease (FD) (green) are highlighted, as well as detrended intervals used to determine FD amplitude (gray).

where  $I_{before}$  and  $I_{after}$  are respective values for mean detrended count for intervals before the onset and after the end of the Forbush decrease. Finally, FD amplitude is calculated as the average of individual  $A_{ij}^{pq}$  values, rms deviation from the mean of the distribution used as an error estimate.

During the one-year period we used for the analysis there was a large number of Forbush events, but most of them had rather small amplitudes. We have analyzed several, however, here we will focus on the one with the largest magnitude as the results are most easily interpreted. The event is a Forbush decrease that occurred on February 18, 2011 in relation to X2.2 solar flare, and according to IZMIRAN space weather database (IZMIRAN, 2020) had 10 GV rigidity particle variation magnitude of 5.4. In Figure 8, we have shown plots that represent procedure described in the previous paragraph, applied to PT corrected datasets using integral method and selected multivariate algorithms. Procedure is also applied to pressure and efficiency corrected data for Athens and Rome neutron monitors, raw data also presented for reference. On the plots, interval leading into the onset of FD is indicated by red dashed lines, while recovery interval after the decrease is indicated by green dashed lines. We have chosen the lengths of both intervals to be four days ( $n = m = 4$ ). Linear fits are represented by solid red and green lines, respectively, while detrended intervals are plotted using gray lines. Amplitudes and relative amplitudes calculated from the differences of means of detrended intervals are shown in Table 4.

**Table 4**  
*Amplitudes and Relative Amplitudes for the Forbush Decrease of February 18, 2011 for PT Corrected Muon Data and Selected Neutron Monitors*

Method/NM monitor	Integral	LD	BDTG	Athens	Rome
FD amplitude (%)	1.38 ± 0.14	1.96 ± 0.18	1.10 ± 0.13	1.97 ± 0.15	2.68 ± 0.15
Relative FD amplitude	4.31 ± 0.44	7.09 ± 0.65	4.78 ± 0.56	5.30 ± 0.40	8.65 ± 0.48

Abbreviations: BDTG, gradient boosted decision tree; FD, Forbush decrease; LD, linear discriminant.

We see that relative amplitudes for this Forbush decrease, calculated based on data corrected for pressure and temperature using LD and BDTG algorithms, have sensitivity that is comparable or better than the sensitivity of integral method, even approaching the sensitivity of reference neutron monitors in the case of LD algorithm. However, when LD algorithm is concerned, such result can be at least in part explained by the fact that the calculated absolute FD amplitude is larger than expected for a muon detector. We would expect this value to be comparable to the value calculated based on the integral method. The reason for this discrepancy could be systematic, but also could be somewhat related to features of the studied FD event. Ideally, we should extend this analysis to more events, but selected time period was relatively calm in terms of solar activity, and February 2011 event was the only significant one with magnitude for 10 GV rigidity particles larger than five. Preliminary analysis done on Forbush decrease events of larger magnitude, that are outside the period used for analysis in this work, does show somewhat smaller effect for LD method, so that could be one of the focuses in the continuation of this work. We have excluded plots for the remaining multivariate algorithms as the results were either poorer (in the case of BDT and MLP) or inconsistent (in the case of PDERS and KNN).

## 5. Conclusions

We have selected a number of multivariate algorithms included in the TMVA package to apply for the correction of barometric and temperature effect on cosmic ray muons. Optimal parameters were determined for each algorithm based on the average quadratic deviation of modeled from measured data. Different distributions of modeled data for training phase and after the application of trained methods were compared to estimate the performance of selected algorithms. Pressure and temperature correction was done and spectral analysis performed to further test the algorithm consistency. The effect of the correction was analyzed for long-term (annual) and short-term (Forbush decrease) cosmic ray variations. In both cases, the efficiency of multivariate algorithms was compared to integral method and pressure corrected neutron monitor data.

Multidimensional probability density estimator algorithms (PDERS and KNN) appear not to be well suited for the modeling of pressure and temperature effect, most likely due to highly linear correlations between variables. MLP seems to have underperformed, while methods based on boosted decision trees (particularly BDTG) proved to be more successful, especially when effect on aperiodic variations was concerned. It should be expected that both MLP and BDT(G) methods can be improved if a longer period is used for analysis and parameters beyond average quadratic deviation of modeled data are used for algorithm optimization during training phase. Out of presented algorithms, LD proved to be the most consistent and effective in removing the pressure and temperature effects. In terms of the effect of PT correction on annual and aperiodic variations, this method matched or outperformed the integral method, while the effect it had on aperiodic effects was somewhat overestimative. This could give us grounds to assume at least part of the temperature effect is not taken into account by the integral method, and that there could be room for further improvement in modeling of meteorological effects beyond what theory currently provides.

## Data Availability Statement

Raw muon count rate data set used in this study are publicly available online on the Belgrade Cosmic Ray Station site (<http://www.cosmic.ipb.ac.rs/>). Modeled atmospheric temperature data are available online on the NOAA GFS page (<https://www.ncdc.noaa.gov/data-access/model-data/model-datasets/global-forecast->

system-gfs). Latest atmospheric pressure and ground temperature data are available online on the site of Republic Hydro-meteorological Service of Serbia (<http://www.hidmet.gov.rs/>). List of international geomagnetically quiet days can be downloaded from the GFZ site (<https://www.gfz-potsdam.de/en/kp-index/>). Neutron monitor data can be accessed online via NEST browser interface (<http://www01.nmdb.eu/nest/>).

## Acknowledgments

The authors acknowledge funding provided by the Institute of Physics Belgrade, through the grant by the Ministry of Education, Science and Technological Development of the Republic of Serbia.

## References

- Barbashina, N., Dmitrieva, A., Kompaniets, K., Petrukhin, A., Timashkov, D., Shutenko, V., et al. (2009). Specific features of studying Forbush decreases in the muon flux. *Bulletin of the Russian Academy of Sciences: Physics*, 73, 343–346. <https://doi.org/10.3103/S1062873809030198>
- Barrett, P. H., Bollinger, L. M., Cocconi, G., Eisenberg, Y., & Greisen, K. (1952). Interpretation of cosmic-ray measurements far underground. *Reviews of Modern Physics*, 24, 133–178. <https://doi.org/10.1103/RevModPhys.24.133>
- Belov, A., Blokh, Y., Dorman, L., & Rogovaya, S. (1987). The temperature diagnostics of the atmosphere allowing for the temperature of the near-surface layer. *International Cosmic Ray Conference*, 4, 263.
- Berkova, M., Belov, A., Eroshenko, E., & Yanke, V. (2012). Temperature effect of muon component and practical questions of how to take into account in real time. *Astrophysics and Space Sciences Transactions*, 8, 41–44. <https://doi.org/10.5194/astra-8-41-2012>
- Blackett, P. M. S. (1938). On the instability of the Barytron and the temperature effect of cosmic rays. *Physical Review*, 54, 973–974. <https://doi.org/10.1103/PhysRev.54.973>
- Carli, T., & Koblitz, B. (2003). A multi-variate discrimination technique based on range-searching. *Nuclear Instruments and Methods in Physics Research Section A: Accelerators, Spectrometers, Detectors and Associated Equipment*, 501, 576–588. [https://doi.org/10.1016/S0168-9002\(03\)00376-0](https://doi.org/10.1016/S0168-9002(03)00376-0)
- Dorman, L. I. (1954). On the temperature effect of the hard component of cosmic rays. *Reports of Academy of Sciences of USSR (DAN SSSR)*, 95, 49–52.
- Dorman, L. I. (2004). *Cosmic rays in the Earth's atmosphere and underground*. Springer. Retrieved from <https://books.google.rs/books?id=mKlv68WBU5kC>
- Dragić, A., Joković, D., Banjanac, R., Udovičić, V., Panić, B., Puzović, J., & Aničin, I. (2008). Measurement of cosmic ray muon flux in the Belgrade ground level and underground laboratories. *Nuclear Instruments and Methods in Physics Research Section A: Accelerators, Spectrometers, Detectors and Associated Equipment*, 591(3), 470–475.
- Dragic, A. L., Udovicic, V. I., Banjanac, R., Jokovic, D. R., Maletic, D. M., Veselinovic, N. B., et al. (2011). The new set-up in the Belgrade low-level and cosmic-ray laboratory. *Nuclear Technology & Radiation Protection*, 26(3), 181–192. <https://doi.org/10.2298/NTRP1103181D>
- Duperier, A. (1949). The meson intensity at the surface of the Earth and the temperature at the production level. *Proceedings of the Physical Society Section A*, 62(11), 684–696. <https://doi.org/10.1088/0370-1298/62/11/302>
- Dvornikov, V. M., Krestyannikov, Y. Y., & Sergeev, A. (1976). Determination of the mass-average temperature on the cosmic ray intensity data. *Geomagnetism and Aeronomy*, 16, 923–925.
- Feinberg, E. L. (1946). On the nature of cosmic ray barometric and temperature effects. *Reports of Academy of Sciences of USSR (DAN SSSR)*, 53, 421–424. <https://doi.org/10.1038/157421a0>
- Forbush, S. E. (1937). On the effects in cosmic-ray intensity observed during the recent magnetic storm. *Physical Review*, 51, 1108–1109. <https://doi.org/10.1103/PhysRev.51.1108.3>
- Forró, M. (1947). Temperature effect of cosmic radiation at 1000-m water equivalent depth. *Physical Review*, 72, 868–869. <https://doi.org/10.1103/PhysRev.72.868>
- GFS. (2020). Retrieved from <https://www.ncdc.noaa.gov/data-access/model-data/model-datasets/global-forecast-system-gfs>
- GFZ Potsdam. (2020). Retrieved from <https://www.gfz-potsdam.de/en/kp-index/>
- Hess, V. F. (1940). On the seasonal and the atmospheric temperature effect in cosmic radiation. *Physical Review*, 57, 781–785. <https://doi.org/10.1103/PhysRev.57.781>
- Hoecker, A., Speckmayer, P., Stelzer, J., Therhaag, J., von Toerne, E., Voss, H., & Zemla, A. (2007). *Tmva—Toolkit for multivariate data analysis*. Ithaca, NY: Cornell University.
- IZMIRAN. (2020). Retrieved from <http://spaceweather.izmiran.ru/eng/dbs.html>
- Joković, D. (2011). *Detekcija i spektroskopija miona iz kosmičkog zračenja plastičnim scintilacionim detektorima (Detection and spectroscopy of cosmic ray muons with plastic scintillation detectors) (Doctoral dissertation)*. Faculty of Physics, University of Belgrade. Retrieved from <http://www.cosmic.ipb.ac.rs/documents/jokovic-thesis.pdf>
- Kaminer, N. S., Ilgatch, S. F., & Khadakhanova, T. S. (1965). Temperature effect of the cosmic ray neutron component. In *Proceedings of the 9th International Cosmic Ray Conference* (Vol. 1, p. 486).
- Kohno, T., Imai, K., Inue, A., Kodama, M., & Wada, M. (1981). Estimation of the vertical profile of atmospheric temperature from cosmic-ray components. In *Proceedings of the 17th International Cosmic Ray Conference* (Vol. 10, p. 289).
- Lalchand, V. (2020). Extracting more from boosted decision trees: A high energy physics case study. In *33rd Annual Conference on Neural Information Processing Systems* (Vol. 1).
- Low Background Laboratory for Nuclear Physics. (2020). Retrieved from <http://www.cosmic.ipb.ac.rs/>
- Maeda, K., & Wada, M. (1954). Atmospheric temperature effect upon the cosmic ray intensity at sea level. *Journal of the Scientific Research Institute*, 48, 71–79.
- Montgomery, D. C., Peck, E. A., & Vining, G. G. (2006). *Introduction to linear regression analysis* (4th ed.). Hoboken, NJ: Wiley & Sons.
- Morozova, A. L., Blanco, J. J., & Ribeiro, P. (2017). Modes of temperature and pressure variability in midlatitude troposphere and lower stratosphere in relation to cosmic ray variations. *Space Weather*, 15(5), 673–690. <https://doi.org/10.1002/2016SW001582>
- Myssowsky, L., & Tuwim, L. (1926). Unregelmäßige intensitätsschwankungen der höhenstrahlung in geringer seehöhe. *Zeitschrift für Physik*, 39, 146–150. <https://doi.org/10.1007/BF01321981>
- NEST. (2020). Retrieved from <http://www01.nmdb.eu/nest/>
- Press, W. H., Teukolsky, S. A., Vetterling, W. T., & Flannery, B. P. (2007). *Numerical recipes 3rd edition: The art of scientific computing* (3rd ed.). New York: Cambridge University Press.
- Quenby, J. J., & Thambyahpillai, T. (1960). Atmospheric temperature effects on the solar daily variation of cosmic ray intensity. *The Philosophical Magazine: A Journal of Theoretical Experimental and Applied Physics*, 5(54), 585–600. <https://doi.org/10.1080/14786436008241210>
- RHMZ. (2020). Retrieved from <http://www.hidmet.gov.rs/index-eng.php>

- Savic, M., Dragic, A., Veselinovic, N., Udovicic, V., Banjanac, R., Jokovic, D., & Maletic, D. (2016). Effect of pressure and temperature corrections on muon flux variability at ground level and underground. In *25th European cosmic ray Symposium*.
- Savic, M. R., Dragic, A. L., Maletic, D. M., Veselinovic, N. B., Banjanac, R. M., Jokovic, D. R., & Udovicic, V. I. (2019). A novel method for atmospheric correction of cosmic-ray data based on principal component analysis. *Astroparticle Physics*, *109*, 1–11. <https://doi.org/10.1016/j.astropartphys.2019.01.006>
- Veselinović, N., Dragić, A., Savić, M., Maletić, D., Joković, D., Banjanac, R., & Udovičić, V. (2017). An underground laboratory as a facility for studies of cosmic-ray solar modulation. *Nuclear Instruments and Methods in Physics Research Section A: Accelerators, Spectrometers, Detectors and Associated Equipment*, *875*, 10–15. <https://doi.org/10.1016/j.nima.2017.09.008>
- Wada, M. (1962). Atmospheric effects on the cosmic-ray meson intensity. *Journal of the Physical Society of Japan Supplement*, *17*, 508. <https://doi.org/10.1143/jpsj.17.1805>

# Sensitivity of the SHiP experiment to light dark matter



## The SHiP collaboration

C. Ahdida,<sup>44</sup> A. Akmete,<sup>48</sup> R. Albanese,<sup>14,59,61</sup> A. Alexandrov,<sup>14,32,34,59</sup> A. Anokhina,<sup>39</sup>  
 S. Aoki,<sup>18</sup> G. Arduini,<sup>44</sup> E. Atkin,<sup>38</sup> N. Azorskiy,<sup>29</sup> J.J. Back,<sup>54</sup> A. Bagulya,<sup>32</sup>  
 F. Baaltasar Dos Santos,<sup>44</sup> A. Baranov,<sup>40</sup> F. Bardou,<sup>44</sup> G.J. Barker,<sup>54</sup> M. Battistin,<sup>44</sup>  
 J. Bauche,<sup>44</sup> A. Bay,<sup>46</sup> V. Bayliss,<sup>51</sup> G. Bencivenni,<sup>15</sup> A.Y. Berdnikov,<sup>37</sup>  
 Y.A. Berdnikov,<sup>37</sup> M. Bertani,<sup>15</sup> C. Betancourt,<sup>47</sup> I. Bezshyiko,<sup>47</sup> O. Bezshyyko,<sup>55</sup>  
 D. Bick,<sup>8</sup> S. Bieschke,<sup>8</sup> A. Blanco,<sup>28</sup> J. Boehm,<sup>51</sup> M. Bogomilov,<sup>1</sup> I. Boiarska,<sup>3</sup>  
 K. Bondarenko,<sup>27,57</sup> W.M. Bonivento,<sup>13</sup> J. Borburgh,<sup>44</sup> A. Boyarsky,<sup>27,55</sup> R. Brenner,<sup>43</sup>  
 D. Breton,<sup>4</sup> V. Büscher,<sup>10</sup> A. Buonauro,<sup>47</sup> L. Buonocore,<sup>47</sup> S. Buontempo,<sup>14</sup>  
 S. Cadettu,<sup>13</sup> A. Calcaterra,<sup>15</sup> M. Calviani,<sup>44</sup> M. Campanelli,<sup>53</sup> M. Casolino,<sup>44</sup>  
 N. Charitonidis,<sup>44</sup> P. Chau,<sup>10</sup> J. Chauveau,<sup>5</sup> A. Chepurnov,<sup>39</sup> M. Chernyavskiy,<sup>32</sup>  
 K.-Y. Choi,<sup>26</sup> A. Chumakov,<sup>2</sup> P. Ciambione,<sup>15</sup> V. Cicero,<sup>12</sup> L. Congedo,<sup>11,56</sup>  
 K. Cornelis,<sup>44</sup> M. Cristinziani,<sup>7</sup> A. Crupano,<sup>14,59</sup> G.M. Dallavalle,<sup>12</sup> A. Datwyler,<sup>47</sup>  
 N. D'Ambrosio,<sup>16</sup> G. D'Appollonio,<sup>13,58</sup> R. de Asmundis,<sup>14</sup> J. De Carvalho Saraiva,<sup>28</sup>  
 G. De Lellis,<sup>14,34,44,59</sup> M. de Magistris,<sup>14,63</sup> A. De Roeck,<sup>44</sup> M. De Serio,<sup>11,56</sup>  
 D. De Simone,<sup>47</sup> L. Dedenko,<sup>39</sup> P. Dergachev,<sup>34</sup> A. Di Crescenzo,<sup>14,59</sup> L. Di Giulio,<sup>44</sup>  
 N. Di Marco,<sup>16</sup> C. Dib,<sup>2</sup> H. Dijkstra,<sup>44</sup> V. Dmitrenko,<sup>38</sup> L.A. Dougherty,<sup>44</sup>  
 A. Dolmatov,<sup>33</sup> D. Domenici,<sup>15</sup> S. Donskov,<sup>35</sup> V. Drohan,<sup>55</sup> A. Dubreuil,<sup>45</sup>  
 O. Durhan,<sup>48</sup> M. Ehlert,<sup>6</sup> E. Elikkaya,<sup>48</sup> T. Enik,<sup>29</sup> A. Etenko,<sup>33,38</sup> F. Fabbri,<sup>12</sup>  
 O. Fedin,<sup>36</sup> F. Fedotovs,<sup>52</sup> G. Felici,<sup>15</sup> M. Ferrillo,<sup>47</sup> M. Ferro-Luzzi,<sup>44</sup> K. Filippov,<sup>38</sup>  
 R.A. Fini,<sup>11</sup> P. Fonte,<sup>28</sup> C. Franco,<sup>28</sup> M. Fraser,<sup>44</sup> R. Fresa,<sup>14,62,61</sup> R. Froeschl,<sup>44</sup>  
 C. Frugiuele,<sup>65</sup> T. Fukuda,<sup>19</sup> G. Galati,<sup>14,59</sup> J. Gall,<sup>44</sup> L. Gatignon,<sup>44</sup> G. Gavrilo,<sup>36</sup>  
 V. Gentile,<sup>14,59</sup> B. Goddard,<sup>44</sup> L. Golinka-Bezshyyko,<sup>55</sup> A. Golovatiuk,<sup>14,59</sup>  
 V. Golovtsov,<sup>36</sup> D. Golubkov,<sup>30</sup> A. Golutvin,<sup>52,34</sup> P. Gorbounov,<sup>44</sup> D. Gorbunov,<sup>31</sup>  
 S. Gorbunov,<sup>32</sup> V. Gorkavenko,<sup>55</sup> M. Gorshenkov,<sup>34</sup> V. Grachev,<sup>38</sup> A.L. Grandchamp,<sup>46</sup>



E. Graverini,<sup>46</sup> J.-L. Grenard,<sup>44</sup> D. Grenier,<sup>44</sup> V. Grichine,<sup>32</sup> N. Gruzinskii,<sup>36</sup>  
 A.M. Guler,<sup>48</sup> Yu. Guz,<sup>35</sup> G.J. Haefeli,<sup>46</sup> C. Hagner,<sup>8</sup> H. Hakobyan,<sup>2</sup> I.W. Harris,<sup>46</sup>  
 E. van Herwijnen,<sup>34</sup> C. Hessler,<sup>44</sup> A. Hollnagel,<sup>10</sup> B. Hosseini,<sup>52</sup> M. Hushchyn,<sup>40</sup>  
 G. Iaselli,<sup>11,56</sup> A. Iuliano,<sup>14,59</sup> R. Jacobsson,<sup>44</sup> D. Joković,<sup>41</sup> M. Jonker,<sup>44</sup> I. Kadenko,<sup>55</sup>  
 V. Kain,<sup>44</sup> B. Kaiser,<sup>8</sup> C. Kamiscioglu,<sup>49</sup> D. Karpenkov,<sup>34</sup> K. Kershaw,<sup>44</sup>  
 M. Khabibullin,<sup>31</sup> E. Khalikov,<sup>39</sup> G. Khaustov,<sup>35</sup> G. Khorauli,<sup>10</sup> A. Khotyantsev,<sup>31</sup>  
 Y.G. Kim,<sup>23</sup> V. Kim,<sup>36,37</sup> N. Kitagawa,<sup>19</sup> J.-W. Ko,<sup>22</sup> K. Kodama,<sup>17</sup> A. Kolesnikov,<sup>29</sup>  
 D.I. Kolev,<sup>1</sup> V. Kolosov,<sup>35</sup> M. Komatsu,<sup>19</sup> A. Kono,<sup>21</sup> N. Konovalova,<sup>32,34</sup>  
 S. Kormannshaus,<sup>10</sup> I. Korol,<sup>6</sup> I. Korol'ko,<sup>30</sup> A. Korzenev,<sup>45</sup> V. Kostyukhin,<sup>7</sup>  
 E. Koukovini Platia,<sup>44</sup> S. Kovalenko,<sup>2</sup> I. Krasilnikova,<sup>34</sup> Y. Kudenko,<sup>31,38,60</sup>  
 E. Kurbatov,<sup>40</sup> P. Kurbatov,<sup>34</sup> V. Kurochka,<sup>31</sup> E. Kuznetsova,<sup>36</sup> H.M. Lacker,<sup>6</sup>  
 M. Lamont,<sup>44</sup> G. Lanfranchi,<sup>15</sup> O. Lantwin,<sup>47,34</sup> A. Lauria,<sup>14,59</sup> K.S. Lee,<sup>25</sup> K.Y. Lee,<sup>22</sup>  
 J.-M. Lévy,<sup>5</sup> V.P. Loschiavo,<sup>14,61</sup> L. Lopes,<sup>28</sup> E. Lopez Sola,<sup>44</sup> V. Lyubovitskij,<sup>2</sup>  
 J. Maalmi,<sup>4</sup> A. Magnan,<sup>52</sup> V. Maleev,<sup>36</sup> A. Malinin,<sup>33</sup> F. Maltoni,<sup>12,57,64</sup> Y. Manabe,<sup>19</sup>  
 A.K. Managadze,<sup>39</sup> M. Manfredi,<sup>44</sup> S. Marsh,<sup>44</sup> A.M. Marshall,<sup>50</sup> O. Mattelaer,<sup>64</sup>  
 A. Mefodev,<sup>31</sup> P. Mermoud,<sup>45</sup> A. Miano,<sup>14,59</sup> S. Mikado,<sup>20</sup> Yu. Mikhaylov,<sup>35</sup>  
 D.A. Minstead,<sup>42</sup> O. Mineev,<sup>31</sup> A. Montanari,<sup>12</sup> M.C. Montesi,<sup>14,59</sup> K. Morishima,<sup>19</sup>  
 S. Movchan,<sup>29</sup> Y. Muttoni,<sup>44</sup> N. Naganawa,<sup>19</sup> M. Nakamura,<sup>19</sup> T. Nakano,<sup>19</sup>  
 S. Nasybulin,<sup>36</sup> P. Ninin,<sup>44</sup> A. Nishio,<sup>19</sup> A. Novikov,<sup>38</sup> B. Obinyakov,<sup>33</sup> S. Ogawa,<sup>21</sup>  
 N. Okateva,<sup>32,34</sup> B. Opitz,<sup>8</sup> J. Osborne,<sup>44</sup> M. Ovchynnikov,<sup>27,55</sup> N. Owtscharenko,<sup>7</sup>  
 P.H. Owen,<sup>47</sup> P. Pacholek,<sup>44</sup> A. Paoloni,<sup>15</sup> B.D. Park,<sup>22</sup> A. Pastore,<sup>11</sup> M. Patel,<sup>52,34</sup>  
 D. Pereyma,<sup>30</sup> A. Perillo-Marccone,<sup>44</sup> G.L. Petkov,<sup>1</sup> K. Petridis,<sup>50</sup> A. Petrov,<sup>33</sup>  
 D. Podgrudkov,<sup>39</sup> V. Poliakov,<sup>35</sup> N. Polukhina,<sup>32,34,38</sup> J. Prieto Prieto,<sup>44</sup>  
 M. Prokudin,<sup>30</sup> A. Prota,<sup>14,59</sup> A. Quercia,<sup>14,59</sup> A. Rademakers,<sup>44</sup> A. Rakai,<sup>44</sup>  
 F. Ratnikov,<sup>40</sup> T. Rawlings,<sup>51</sup> F. Redi,<sup>46</sup> S. Ricciardi,<sup>51</sup> M. Rinaldesi,<sup>44</sup>  
 Volodymyr Rodin,<sup>55</sup> Viktor Rodin,<sup>55</sup> P. Robbe,<sup>4</sup> A.B. Rodrigues Cavalcante,<sup>46</sup>  
 T. Roganova,<sup>39</sup> H. Rokujo,<sup>19</sup> G. Rosa,<sup>14,59</sup> T. Rovelli,<sup>12,57</sup> O. Ruchayskiy,<sup>3</sup> T. Ruf,<sup>44</sup>  
 V. Samoylenko,<sup>35</sup> V. Samsonov,<sup>38</sup> F. Sanchez Galan,<sup>44</sup> P. Santos Diaz,<sup>44</sup>  
 A. Sanz Ull,<sup>44</sup> A. Saputi,<sup>15</sup> O. Sato,<sup>19</sup> E.S. Savchenko,<sup>34</sup> J.S. Schliwinski,<sup>6</sup>  
 W. Schmidt-Parzefall,<sup>8</sup> N. Serra,<sup>47,34</sup> S. Sgobba,<sup>44</sup> O. Shadura,<sup>55</sup> A. Shakin,<sup>34</sup>  
 M. Shaposhnikov,<sup>46</sup> P. Shatalov,<sup>30,34</sup> T. Shchedrina,<sup>32,34</sup> L. Shchutka,<sup>46</sup>  
 V. Shevchenko,<sup>33,34</sup> H. Shibuya,<sup>21</sup> S. Shirobokov,<sup>52</sup> A. Shustov,<sup>38</sup> S.B. Silverstein,<sup>42</sup>  
 S. Simone,<sup>11,56</sup> R. Simoniello,<sup>10</sup> M. Skorokhvatov,<sup>38,33</sup> S. Smirnov,<sup>38</sup> J.Y. Sohn,<sup>22</sup>  
 A. Sokolenko,<sup>55</sup> E. Solodko,<sup>44</sup> N. Starkov,<sup>32,34</sup> L. Stoel,<sup>44</sup> M.E. Stramaglia,<sup>46</sup>  
 D. Sukhonos,<sup>44</sup> Y. Suzuki,<sup>19</sup> S. Takahashi,<sup>18</sup> J.L. Tastet,<sup>3</sup> P. Teterin,<sup>38</sup>  
 S. Than Naing,<sup>32</sup> I. Timiryasov,<sup>46</sup> V. Tioukov,<sup>14</sup> D. Tommasini,<sup>44</sup> M. Torii,<sup>19</sup>  
 N. Tosi,<sup>12</sup> F. Tramontano,<sup>14,59</sup> D. Treille,<sup>44</sup> R. Tsenov,<sup>1,29</sup> S. Ulin,<sup>38</sup> E. Ursov,<sup>39</sup>  
 A. Ustyuzhanin,<sup>40,34</sup> Z. Uteshev,<sup>38</sup> L. Uvarov,<sup>36</sup> G. Vankova-Kirilova,<sup>1</sup> F. Vannucci,<sup>5</sup>  
 V. Venturi,<sup>44</sup> S. Vilchinski,<sup>55</sup> Heinz Vincke,<sup>44</sup> Helmut Vincke,<sup>44</sup> C. Visone,<sup>14,59</sup>  
 K. Vlasik,<sup>38</sup> A. Volkov,<sup>32,33</sup> R. Voronkov,<sup>32</sup> S. van Waasen,<sup>9</sup> R. Wanke,<sup>10</sup>  
 P. Wertelaers,<sup>44</sup> O. Williams,<sup>44</sup> J.-K. Woo,<sup>24</sup> M. Wurm,<sup>10</sup> S. Xella,<sup>3</sup> D. Yilmaz,<sup>49</sup>  
 A.U. Yilmazer,<sup>49</sup> C.S. Yoon,<sup>22</sup> Yu. Zaytsev,<sup>30</sup> A. Zelenov<sup>36</sup> and J. Zimmerman<sup>6</sup>

<sup>1</sup>Faculty of Physics, Sofia University, Sofia, Bulgaria

- <sup>2</sup>*Universidad Técnica Federico Santa María and Centro Científico Tecnológico de Valparaíso, Valparaíso, Chile*
- <sup>3</sup>*Niels Bohr Institute, University of Copenhagen, Copenhagen, Denmark*
- <sup>4</sup>*LAL, Univ. Paris-Sud, CNRS/IN2P3, Université Paris-Saclay, Orsay, France*
- <sup>5</sup>*LPNHE, IN2P3/CNRS, Sorbonne Université, Université Paris Diderot, F-75252 Paris, France*
- <sup>6</sup>*Humboldt-Universität zu Berlin, Berlin, Germany*
- <sup>7</sup>*Physikalisches Institut, Universität Bonn, Bonn, Germany*
- <sup>8</sup>*Universität Hamburg, Hamburg, Germany*
- <sup>9</sup>*Forschungszentrum Jülich GmbH (KFA), Jülich, Germany*
- <sup>10</sup>*Institut für Physik and PRISMA Cluster of Excellence, Johannes Gutenberg Universität Mainz, Mainz, Germany*
- <sup>11</sup>*Sezione INFN di Bari, Bari, Italy*
- <sup>12</sup>*Sezione INFN di Bologna, Bologna, Italy*
- <sup>13</sup>*Sezione INFN di Cagliari, Cagliari, Italy*
- <sup>14</sup>*Sezione INFN di Napoli, Napoli, Italy*
- <sup>15</sup>*Laboratori Nazionali dell'INFN di Frascati, Frascati, Italy*
- <sup>16</sup>*Laboratori Nazionali dell'INFN di Gran Sasso, L'Aquila, Italy*
- <sup>17</sup>*Aichi University of Education, Kariya, Japan*
- <sup>18</sup>*Kobe University, Kobe, Japan*
- <sup>19</sup>*Nagoya University, Nagoya, Japan*
- <sup>20</sup>*College of Industrial Technology, Nihon University, Narashino, Japan*
- <sup>21</sup>*Toho University, Funabashi, Chiba, Japan*
- <sup>22</sup>*Physics Education Department & RINS, Gyeongsang National University, Jinju, Korea*
- <sup>23</sup>*Gwangju National University of Education,<sup>a</sup> Gwangju, Korea*
- <sup>24</sup>*Jeju National University,<sup>a</sup> Jeju, Korea*
- <sup>25</sup>*Korea University, Seoul, Korea*
- <sup>26</sup>*Sungkyunkwan University,<sup>a</sup> Suwon-si, Gyeong Gi-do, Korea*
- <sup>27</sup>*University of Leiden, Leiden, The Netherlands*
- <sup>28</sup>*LIP, Laboratory of Instrumentation and Experimental Particle Physics, Portugal*
- <sup>29</sup>*Joint Institute for Nuclear Research (JINR), Dubna, Russia*
- <sup>30</sup>*Institute of Theoretical and Experimental Physics (ITEP) NRC “Kurchatov Institute”, Moscow, Russia*
- <sup>31</sup>*Institute for Nuclear Research of the Russian Academy of Sciences (INR RAS), Moscow, Russia*
- <sup>32</sup>*P.N. Lebedev Physical Institute (LPI RAS), Moscow, Russia*
- <sup>33</sup>*National Research Centre “Kurchatov Institute”, Moscow, Russia*
- <sup>34</sup>*National University of Science and Technology “MISIS”, Moscow, Russia*
- <sup>35</sup>*Institute for High Energy Physics (IHEP) NRC “Kurchatov Institute”, Protvino, Russia*
- <sup>36</sup>*Petersburg Nuclear Physics Institute (PNPI) NRC “Kurchatov Institute”, Gatchina, Russia*
- <sup>37</sup>*St. Petersburg Polytechnic University (SPbPU),<sup>b</sup> St. Petersburg, Russia*
- <sup>38</sup>*National Research Nuclear University (MEPhI), Moscow, Russia*
- <sup>39</sup>*Skobeltsyn Institute of Nuclear Physics of Moscow State University (SINP MSU), Moscow, Russia*
- <sup>40</sup>*Yandex School of Data Analysis, Moscow, Russia*

---

<sup>a</sup>Associated to Gyeongsang National University, Jinju, Korea.

<sup>b</sup>Associated to Petersburg Nuclear Physics Institute (PNPI), Gatchina, Russia.

- <sup>41</sup>*Institute of Physics, University of Belgrade, Serbia*  
<sup>42</sup>*Stockholm University, Stockholm, Sweden*  
<sup>43</sup>*Uppsala University, Uppsala, Sweden*  
<sup>44</sup>*European Organization for Nuclear Research (CERN), Geneva, Switzerland*  
<sup>45</sup>*University of Geneva, Geneva, Switzerland*  
<sup>46</sup>*École Polytechnique Fédérale de Lausanne (EPFL), Lausanne, Switzerland*  
<sup>47</sup>*Physik-Institut, Universität Zürich, Zürich, Switzerland*  
<sup>48</sup>*Middle East Technical University (METU), Ankara, Turkey*  
<sup>49</sup>*Ankara University, Ankara, Turkey*  
<sup>50</sup>*H.H. Wills Physics Laboratory, University of Bristol, Bristol, United Kingdom*  
<sup>51</sup>*STFC Rutherford Appleton Laboratory, Didcot, United Kingdom*  
<sup>52</sup>*Imperial College London, London, United Kingdom*  
<sup>53</sup>*University College London, London, United Kingdom*  
<sup>54</sup>*University of Warwick, Warwick, United Kingdom*  
<sup>55</sup>*Taras Shevchenko National University of Kyiv, Kyiv, Ukraine*  
<sup>56</sup>*Università di Bari, Bari, Italy*  
<sup>57</sup>*Università di Bologna, Bologna, Italy*  
<sup>58</sup>*Università di Cagliari, Cagliari, Italy*  
<sup>59</sup>*Università di Napoli “Federico II”, Napoli, Italy*  
<sup>60</sup>*Also at Moscow Institute of Physics and Technology (MIPT), Moscow Region, Russia*  
<sup>61</sup>*Consorzio CREATE, Napoli, Italy*  
<sup>62</sup>*Università della Basilicata, Potenza, Italy*  
<sup>63</sup>*Università di Napoli Parthenope, Napoli, Italy*  
<sup>64</sup>*Université catholique de Louvain (CP3), Louvain-la-Neuve, Belgium*  
<sup>65</sup>*Sezione INFN di Milano, Milano, Italy*

*E-mail:* [luca.buonocore@physik.uzh.ch](mailto:luca.buonocore@physik.uzh.ch), [martina.ferrillo@cern.ch](mailto:martina.ferrillo@cern.ch)

ABSTRACT: Dark matter is a well-established theoretical addition to the Standard Model supported by many observations in modern astrophysics and cosmology. In this context, the existence of weakly interacting massive particles represents an appealing solution to the observed thermal relic in the Universe. Indeed, a large experimental campaign is ongoing for the detection of such particles in the sub-GeV mass range. Adopting the benchmark scenario for light dark matter particles produced in the decay of a dark photon, with  $\alpha_D = 0.1$  and  $m_{A'} = 3m_\chi$ , we study the potential of the SHiP experiment to detect such elusive particles through its Scattering and Neutrino detector (SND). In its 5-years run, corresponding to  $2 \cdot 10^{20}$  protons on target from the CERN SPS, we find that SHiP will improve the current limits in the mass range for the dark matter from about 1 MeV to 300 MeV. In particular, we show that SHiP will probe the thermal target for Majorana candidates in most of this mass window and even reach the Pseudo-Dirac thermal relic.

KEYWORDS: Beyond Standard Model, Dark matter, Fixed target experiments

ARXIV EPRINT: [2010.11057](https://arxiv.org/abs/2010.11057)

---

## Contents

<b>1</b>	<b>Introduction</b>	<b>1</b>
<b>2</b>	<b>Vector portal</b>	<b>3</b>
<b>3</b>	<b>The SHiP experiment</b>	<b>3</b>
<b>4</b>	<b>Light dark matter production and detection</b>	<b>5</b>
4.1	Meson decay	8
4.2	Proton Bremsstrahlung	12
4.3	QCD prompt production	13
<b>5</b>	<b>Background estimate</b>	<b>14</b>
<b>6</b>	<b>Sensitivity</b>	<b>19</b>
<b>7</b>	<b>Conclusions</b>	<b>21</b>

---

## 1 Introduction

One of the main challenges in particle physics today is figuring out the microscopic identity and the cosmological origin of dark matter (DM). The theoretical landscape is broad and it spans over many orders of magnitude in the mass/coupling parameter space. A compelling idea to explore is DM as a thermal relic of the early universe. The canonical example of this scenario is the Weakly Interacting Massive Particle (WIMP), a particle in the GeV-TeV mass range interacting with the visible sector via weak-sized interactions. Searches for WIMPs are in full swing [1, 2]. However, the interesting parameter space goes beyond what has been explored in the past decade: thermal DM can be as heavy as 100 TeV or as light as a few keV. Recently, a lot of attention has been directed towards light DM (LDM) in the keV-GeV mass range [3].

Direct detection has traditionally employed the Migdal Effect [4] using liquid Argon [5, 6] or liquid Xenon [7–10], while a novel strategy based on silicon devices has allowed to design new experiments optimised for sub-GeV DM, as SENSEI [11]. Since current DM direct detection experiments searching for elastic nuclear recoils rapidly lose sensitivity once the candidate mass drops below a few GeV [1, 12], experiments at the intensity frontier represent an alternative yet appealing route and play an important role in this quest [3]. Fixed target experiments represent the prototype for such searches, although other collider experiments might be relevant in the same parameter space, as showed by the mono-photon searches at BaBar [13] and Belle II [14].

In particular, neutrino fixed target experiments could efficiently search for LDM via signatures of DM scattering with electrons and/or nuclei in their near detectors [15–26].

Here we present the sensitivity of the SHiP scattering and neutrino detector (SND), to LDM. We focus on the hypothesis that the DM couples to the SM through the exchange of a massive vector mediator, dubbed in the literature dark photon, and we have considered the cleanest signature given by the LDM-electron scattering. The scattering with nuclei, both coherent and deep inelastic scattering, although plagued by a larger neutrino background, might be an alternative detection strategy and will be the subject of a forthcoming dedicated analysis.

In a proton beam dump experiment signal yields are largely reduced as the interaction with the dark photon  $A'$  is probed twice, if compared to electron fixed target experiments which make use of search strategies based on missing energy, such as NA64 [27], or missing momentum, such as the LDMX proposal [28]. Indeed, the LDM detection is achieved through its scattering within the downstream detector. Hence, the expected LDM yield scales as  $\epsilon^4 \alpha_D$  ( $\epsilon$  being the interaction strength of the dark photon to SM particles and  $\alpha_D$  the LDM- $A'$  coupling), where a factor  $\epsilon^2$  comes from production and another  $\epsilon^2 \alpha_D$  is due to detection. This has to be compared to the  $\epsilon^2$  scaling of typical missing energy/momentum experiments, which prove however to be not sensitive to LDM coupling constant  $\alpha_D$ . Due to their higher penetrating power and enhancements from meson decay reactions and/or strong interactions, proton beams are characterised by dark photon production rates larger than the ones achievable in electron beams of comparable intensity, which in part compensate for the detection suppression factor.

The potential to directly probe the dark sector mediator coupling  $\alpha_D$ , together with a wider sensitivity which encompasses other viable dark matter models, shows to a large extent the complementarity between the two approaches. This is even a more pressing aspect in the light of a possible discovery, as in general the observation of an excess alone is not sufficient to claim a discovery of a Dark matter particle. Indeed, intensity frontier probes do not depend on whether the particle  $\chi$  produced through prompt DP decay is DM or not, as the only necessary ingredient is its stability concerning the target-detector distance. The observed excess might have an instrumental origin rather than a genuine New Physics (NP) effect. This applies also to the constraints that the SHiP experiment can place. With this regard, invaluable contribution could come from complementary DM observations from a cosmic source to unequivocally probe its thermal origin. In addition, since the SHiP experiment has a direct sensitivity to LDM interactions, we anticipate the possibility to use the time of flight measurement to uncontroversially discriminate massive NP particles from the SM neutrino background.

The paper is organised as follows: in section 2 we give a brief presentation of the model focusing on the main motivations. After introducing the SHiP experiment in section 3, we discuss the relevant production and detection mechanisms, in section 4. The detailed analysis of the neutrino background is the topic of section 5. We then pass to the discussion of the signal reviewing the main processes taken into account in our simulation. Finally, we show the main results on the sensitivity reach of the SHiP experiment in section 6 and we give our conclusions in section 7.

## 2 Vector portal

Thermal freeze-out can naturally explain the origin of the DM relic density for a sub-GeV particle provided the interaction with the visible sector is mediated by a new light force carrier [2, 29]. Here, we will consider as benchmark model the dark photon (DP) [30] vector portal where the DP  $A'_\mu$  is the gauge boson of a new dark gauge group  $U(1)_D$  kinetically mixed with the photon, and a scalar  $\chi$  charged under  $U(1)_D$  that serves as a DM candidate. Then, the low-energy effective Lagrangian describing the DM reads

$$\mathcal{L}_{\text{DM}} = \mathcal{L}_{A'} + \mathcal{L}_\chi \tag{2.1}$$

where:

$$\mathcal{L}_{A'} = -\frac{1}{4}F'_{\mu\nu}F'^{\mu\nu} + \frac{m_{A'}^2}{2}A'^\mu A'_\mu - \frac{1}{2}\epsilon F'_{\mu\nu}F^{\mu\nu}, \tag{2.2}$$

where  $\epsilon$  is the DP-photon kinetic mixing parameter and  $m_{A'}$  is the mass of the DP, while:

$$\mathcal{L}_\chi = \frac{ig_D}{2}A'^\mu J_\mu^\chi + \frac{1}{2}\partial_\mu\chi^\dagger\partial^\mu\chi - m_\chi^2\chi^\dagger\chi, \tag{2.3}$$

where  $J_\mu^\chi = [(\partial_\mu\chi^\dagger)\chi - \chi^\dagger\partial_\mu\chi]$ ,  $g_D$  is the  $U(1)_D$  gauge coupling and  $m_\chi$  is the mass of the dark matter particle. The region of the parameter space relevant for  $\chi$  searches at beam-dump facilities corresponds to  $m_{A'} > 2m_\chi$  and  $g_D \gg \epsilon e$  which implies  $BR(A' \rightarrow \chi\chi^\dagger) \sim 1$ .

In case  $\chi$  is DM, precise measurements of the temperature anisotropies of the cosmic microwave background (CMB) radiation significantly constrain the parameter space. In particular, they rule out Dirac fermions with mass below 10 GeV as a thermal DM candidate and more in general every DM candidate that acquires its relic abundance via  $s$ -wave annihilation into SM particles [31, 32]. Hence, a complex scalar dark matter candidate  $\chi$  is safe from such constraints as well as a Majorana or Pseudo-Dirac fermion. Tighter bounds come instead from the Planck measurement of the effective number of neutrino species  $N_{\text{eff}}$  [32] and rule out the minimal DP model considered here if the complex scalar is lighter than 9 MeV [33].

In order to show the region of parameter space relevant for thermal freeze-out, we will present the SHiP sensitivity in the  $(m_\chi, Y)$  plane where  $Y$  is defined as:

$$Y \equiv \epsilon^2 \alpha_D \left(\frac{m_\chi}{m_{A'}}\right)^4, \quad \alpha_D = \frac{g_D^2}{4\pi}. \tag{2.4}$$

In the assumption  $m_{A'} > 2m_\chi$ , the parameter  $Y$  is linked to the DM annihilation cross section via the formula [34]:

$$\sigma(\chi\bar{\chi} \rightarrow f\bar{f})v \propto \frac{8\pi v^2 Y}{m_\chi^2}, \tag{2.5}$$

where  $v$  is the relative velocity between the colliding DM particles.

## 3 The SHiP experiment

The Search for Hidden Particles (SHiP) experiment has been proposed as a general-purpose experiment [35] at the CERN Super-Proton-Synchrotron (SPS), addressed to explore the

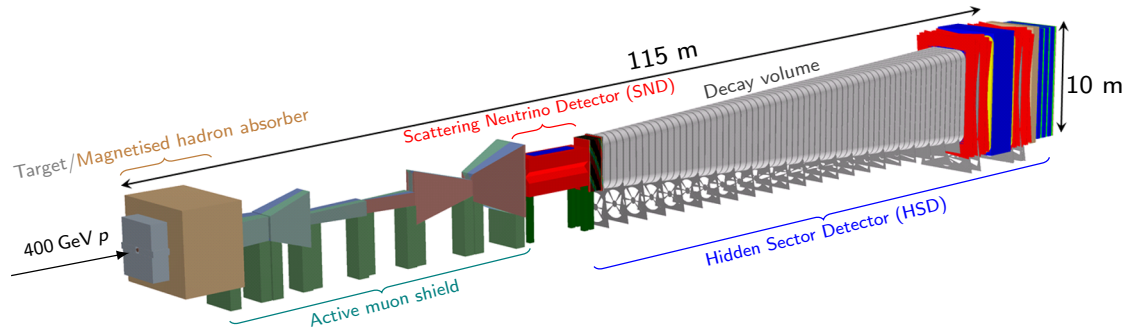


**Figure 1.** Overview of the SHiP experimental layout.

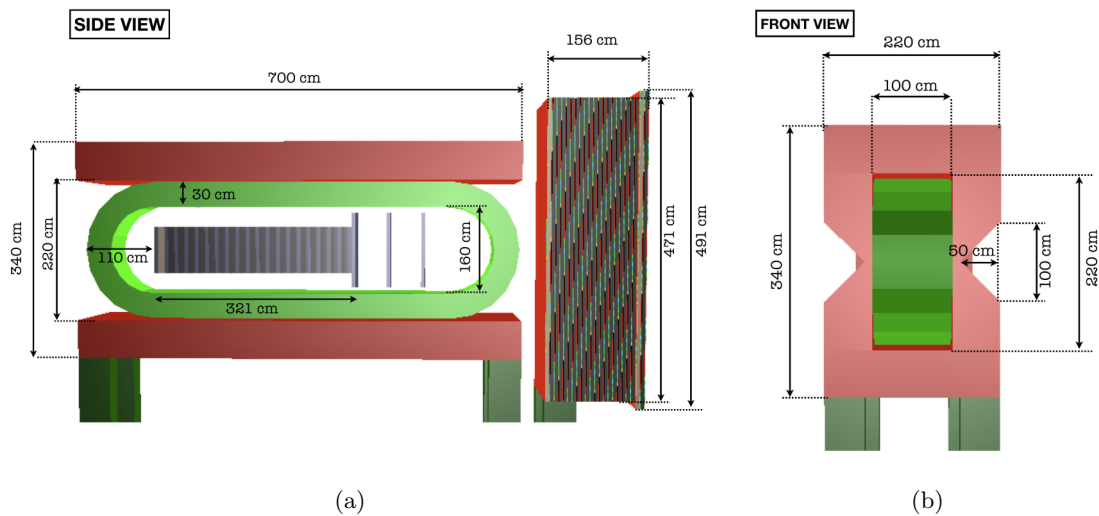


**Figure 2.** Side (a) and front (b) views of the Scattering Neutrino Detector layout adopted for this study, with a detail of the magnet (red) and of the coil (green).

high-intensity frontier for NP searches, thus complementing the LHC research program [35]. It is particularly targeted at the observation of long-lived weakly interacting particles of mass below  $10 \text{ GeV}/c^2$ , foreseen in many Standard Model (SM) extensions. The use of a beam-dump facility [36] will result in a copious flux of charmed hadrons, from which not only hidden sector particles originate [37], but also tau neutrinos and their corresponding anti-particles. Therefore, being also a neutrino factory, SHiP will perform a wide neutrino physics program, as well as a first direct observation of the tau anti-neutrino, which represents the last particle to be directly observed to complete the SM framework. The SHiP Scattering Neutrino Detector (SND) is an apparatus designed for LDM particles searches, since it exploits an optimised combination of a dense target and high-granularity scattering detector, being it based on nuclear emulsion technology. In figure 1 a sketch of the experimental facility as currently implemented in the official simulation framework of the experiment FairShip [38] is shown. A brief overview of the simulated processes within FairShip and corresponding simulation software is reported in table 1.

A 400 GeV/c proton beam will be delivered onto a thick heavy-metal hybrid target, specifically designed to maximise the charm production yield and thus hidden sector particles and tau neutrino yields. Over five years of SPS operations, a total of  $2 \times 10^{20}$  protons on target (*p.o.t.*) collisions will be delivered, where each proton spill will have nominally  $4 \times 10^{13}$  *p.o.t.*. A hadron stopper follows the beam-dump target, with the goal to absorb the SM particles produced in the beam interaction. In addition, a series of sweeping magnets, referred to as Muon Shield [39], act as a deflecting device for the residual muons, further cleaning the flux of particles from leftover backgrounds to hidden sector particles and neutrino searches.

The SND, shown in figure 2 in the setup adopted for this study, is located downstream of the muon sweeper. Placed in a magnetised region of 1.2 Tesla in the horizontal direction and perpendicular to the beam axis [40], it consists of a  $(90 \times 75 \times 321)$  cm<sup>3</sup> high-granularity tracking device which exploits the Emulsion Cloud Chamber (ECC) technique developed by the OPERA experiment [41], which was successfully used for tau neutrino detection [42, 43]. Each elementary unit of the modular detector, called brick (figure 3), consists of alternating 56 lead plates of 1 mm thickness, passive material to increase the interaction probability, and 57 nuclear emulsion films of 0.3 mm thickness, acting as tracking detector with micrometric accuracy. It is worth noting that the brick also functions as a high-granularity sampling calorimeter with more than five active layers for every radiation length  $X_0$  over a total thickness of  $10 X_0$  [44]. The ECC technology is also particularly efficient in the  $e/\pi^0$  separation. The Compact Emulsion Spectrometer (CES), made up of a sequence of emulsion films and air gaps, is attached immediately downstream of the brick for electric charge measurement for particles not reaching the spectrometer. Despite the magnetic field, electron charge measurement is not possible due to early showering happening within the brick and the consequent information loss. The resulting weight of each ECC brick is approximately 8.3 kg, adding up to  $\sim 8$  tons for the whole SND. The bricks are then assembled to shape 19 walls of  $\sim 50$  units each, alternated with planes of electronic detector, called Target Tracker (TT), planes. For the time being, we consider the SciFi detector [45] as a feasible TT technological option. The TT additionally provide the time stamp of the event and help in linking the emulsion tracks to those reconstructed in the spectrometer and the muon system downstream of the SND. These features make the SND perfectly tailored for neutrino physics using all three flavours, as well as detection of light dark matter particles scattering off of electrons and nuclei of the SND.

An approximately 50 m long vacuum decay vessel is positioned downstream of the SND. The proposed facility is completed with a Hidden Sector Detector (HSD), equipped with calorimeters and muon detectors for the identification of long-lived Beyond Standard Model (BSM) particles.

#### 4 Light dark matter production and detection

At a proton beam dump, DP can be abundantly produced in several channels:

1. *Light meson decay*: proton collisions on a heavy target result in a copious flux of outgoing mesons. Hence, DP may be produced in radiative decays of neutral mesons,



Simulation	Software
SHiP detector: geometry and transport	GEANT4 [46]
Proton on target collisions	PYTHIA v8.2 [47]
Heavy flavour cascade production	PYTHIA v6.4 [48]
Neutrino interactions	GENIE [49]

**Table 1.** Details of the different steps of the simulation process within the FairShip framework and corresponding employed software.

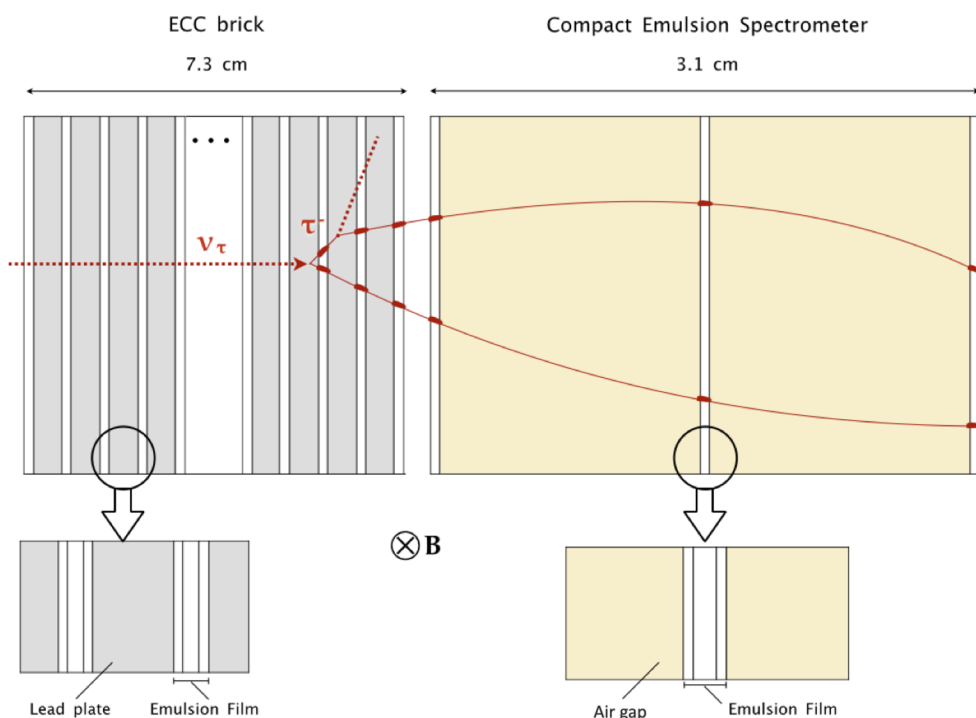


**Figure 3.** Schematic illustration of the basic unit of the Scattering Neutrino Detector and the ECC brick: on the left, emulsion films interleaved with lead plates; on the right, the Compact Emulsion Spectrometer.

whereas a final state photon converts into a DP. The production cross-section is proportional to  $\epsilon^2$  and the relevant contributions come from the lightest mesons, because of decay modes with photons with relatively high branching ratio:  $\pi^0, \eta, \omega$  [15].

2. *Proton bremsstrahlung*: being a charged particle surrounded by its own electromagnetic field, the proton radiates low-frequency and/or quasi-collinear photons with high probability when it undergoes a scattering process. Vector states like DP mediators can then be generated via radiative process  $p A \rightarrow p A A'$  [50] in proton interactions with the target nuclei.

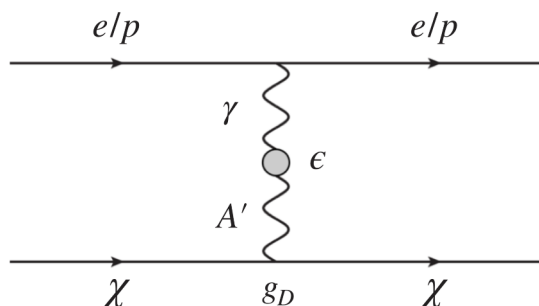


**Figure 4.** Light dark matter interaction processes which can be probed by the SHiP experiment within the Scattering Neutrino Detector, i.e. elastic scattering off electrons ( $\chi e^- \rightarrow \chi e^-$ ) and off protons ( $\chi p \rightarrow \chi p$ ).

3. *Direct perturbative QCD production:* it corresponds to the dominant production mechanism for higher masses ( $m_{A'} \gtrsim 1 \text{ GeV}$ ). At the lowest order in the strong interaction, DP are produced through the quark-antiquark annihilation process  $q\bar{q} \rightarrow A'$  [15]. At higher orders, one can also have the associated production with a jet, according to the quark-gluon scattering process  $qg \rightarrow qA'$ , and with multiple jets.

In addition, secondary leptons produced in the dump can contribute to the flux of photons, and thereby of DPs, by different re-scattering processes occurring within the target. Such lepton-induced processes are usually sub-dominant at a proton beam dump. However, they are not completely negligible, as nicely shown in a the dedicated analysis [51], and might be relevant in scenarios in which the New Physics does not couple with coloured particles. We do not include them in this work. Therefore, our estimates should be considered conservative in this regard. The minimal DP model can be probed by the SHiP experiment through the direct detection of LDM elastic scattering process off of the electrons and nuclei of the SND (figure 4) For the majority of the events  $\chi e^- \rightarrow \chi e^-$ , the scattered electron is sufficiently energetic to generate an electromagnetic shower within the brick. Given that the ECC device acts as a high-granularity sampling calorimeter, it is thus possible to reconstruct the electron and measure its energy. Furthermore any activity in the proximity of the primary vertex can be spotted down to 100 MeV or below, thanks to the micrometrical position resolution of the nuclear emulsion device and the high sampling rate. These features translate into capability to accurately identify and tackle background events to LDM searches, as further described in section 5. As a consequence, LDM scattering events can be distinguished from a large neutrino-induced background.

An estimate of the order of magnitude of the expected yield of LDM interactions at SHiP can be determined as follows. The number of LDM-electron scattering events in the SND detector is given by the standard formula

$$\mathcal{N}_{\text{LDM}} = \sigma(\chi e^- \rightarrow \chi e^-) \cdot \frac{\phi}{A_{\text{SND}}} \cdot N_{e^-}, \quad (4.1)$$

where  $N_{e^-}$  is the numbers of scattering centres, i.e. the electrons in the detector,  $\phi$  is the flux of incident LDM particles and  $A_{\text{SND}}$  represents the transverse area in  $(x, y)$  of the

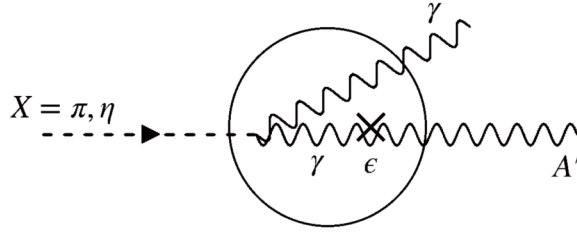


**Figure 5.** Effective vertex for the decay process  $X \rightarrow \gamma A'$ ,  $X = \pi^0, \eta$ .

SND. The elastic LDM-electron scattering cross section is roughly given by

$$\sigma(\chi e^- \rightarrow \chi e^-) \simeq \frac{4\pi\alpha\alpha_D\epsilon^2}{m_{A'}^2}. \quad (4.2)$$

The flux  $\phi$  mainly depends on the specific value of the DP mass which in turn determines the relative importance of the different production mechanisms. For example, for  $m_{A'} \ll m_\pi$ , LDM production in the beam dump is dominated by pion decays. In this case and under the assumption that all the primary proton impinging on the target will eventually interact in the beam dump,  $\phi$  can be written as

$$\phi \simeq 2 \cdot N_{p.o.t.} \cdot \lambda_{\pi^0} \cdot \epsilon^2 \cdot \mathcal{A}_{geo}. \quad (4.3)$$

In eq. (4.3),  $N_{p.o.t.}$  is the total number of *p.o.t.* delivered in the five years of data-taking;  $\lambda_{\pi^0}$  denotes the multiplicity of  $\pi^0$ s per *p.o.t.*;  $\mathcal{A}_{geo}$  embeds the geometrical acceptance of the SND to LDM interaction vertices, corresponding to an angular coverage  $|(\theta_x, \theta_y)| \leq (12, 10)$  mrad from the proton beam dump. If considering an average value of  $\lambda_{\pi^0} \sim 6$  as provided by the simulation of prompt proton-nucleon collisions with `Pythia`<sup>1</sup> [47], a geometrical acceptance  $\mathcal{A}_{geo} \sim 30\%$  and if assuming a coupling close to the current experimental constraints  $\epsilon \sim 5 \times 10^{-5}$  for a 10 MeV-DP and  $\alpha_D \sim 0.1$ , the expected number of LDM candidates foreseen in SHiP is  $\sim 1.3 \times 10^4$ .

We used `MadDump` [52] as the principal tool for the simulation of signal events. Its general philosophy and all the technical details are outlined in ref. [52]. We generate the event samples at the particle level and apply the selection criteria on the recoil electrons without taking into account other detector effects besides the geometrical acceptance. This is consistent with what has been done in the estimate of the background event rate. Since the target length is way larger than the proton interaction length in the material, we assume all of them to interact within the beam dump. In the following, we give further details for each production mechanism.

#### 4.1 Meson decay

The relevant parameter space within the reach of the SHiP SND corresponds to  $m_{A'} > 2m_\chi$  and  $g_D \gg \epsilon e$ . Indeed, in this scenario, the DP decays almost entirely into DM after travelling a very short distance, maximising the DM flux reaching the SHiP SND. The

<sup>1</sup>We use `Pythia(v8.230)` and simulate events under the flag `SoftQCD:Inelastic`.

decay rate for light mesons decaying into dark photons is then dominated by the formation of an on-shell dark photon which decays promptly into dark matter,  $BR(A' \rightarrow \chi\bar{\chi}) \simeq 1$ . The production process is then well described by an effective Lagrangian with mesons as dynamical degrees of freedom leading to interaction vertices like  $X\gamma A'$  ( $X = \pi^0, \eta$ , see figure 5) and  $\omega\pi^0 A'$ . The corresponding branching ratios scale with  $\epsilon^2$  and are given by:

$$\frac{BR(\pi^0, \eta, \eta' \rightarrow \gamma A')}{BR(\pi^0, \eta, \eta' \rightarrow \gamma\gamma)} \simeq 2\epsilon^2 \left(1 - \frac{m_{A'}^2}{m_{\pi^0, \eta, \eta'}^2}\right)^3 \quad (4.4)$$

$$\frac{BR(\omega \rightarrow \pi^0 A')}{BR(\omega \rightarrow \pi^0 \gamma)} \simeq \epsilon^2 (m_\omega^2 - m_\pi^2)^{-3} \left[ (m_{A'}^2 - (m_\pi + m_\omega)^2)(m_{A'}^2 - (m_\pi - m_\omega)^2) \right]^{3/2}. \quad (4.5)$$

An interested reader can find useful insights about the formulas above in [16, 53, 54]. The full simulation process is performed in three steps:

- i. production of the input meson fluxes originating from the incoming protons impinging and interacting within the target (beam dump);
- ii. generation of DM fluxes from the BSM meson decays in the relevant DM mass range;
- iii. generation of the corresponding DM –  $e^-$  scattering events within the detector acceptance and the selection criteria.

MadDump provides a unified framework to handle the last two steps, in which all the new physics content is involved. The main source of uncertainties comes from the meson fluxes. Indeed, the description of the proton-nucleus interactions is highly non-trivial and experimental data are available only for a limited collection of energies and nuclear targets. Phenomenological and data-driven parametrisations for the distributions of the light mesons have been proposed in the literature [55]. An alternative strategy is provided by Monte Carlo programs like `Pythia` [47]. Recently, `Pythia(8)` results have been compared with existing experimental data for the inclusive production of  $\pi^0$  and  $\eta$  mesons in  $pp$  collisions [56]. A fairly good agreement has been found for mesons with high momentum and within middle-high rapidity range (where the Feynman variable  $0.025 < x_F < 0.3$ ), which represent the bulk of our events in acceptance.

Furthermore, secondary interactions of hadrons in the beam-dump target may affect the particle multiplicities, which in turn may increase the LDM yields and impact the sensitivity reach of the experiment. It is thus important to estimate the so-called cascade effects [57]. As the main input for the lightest mesons ( $\pi^0, \eta$ ) we use the fluxes generated with `GEANT4(v10.3.2)` within the `FairShip` software framework, which takes into account the secondary interactions adapting what has been used in ref. [58]. We also consider samples of mesons from primary proton-nucleon interactions generated with `Pythia`, as a reference to assess the impact of the cascade. For the  $\omega$ , we rely on the `Pythia` samples only.

In tables 2, 3 and 4, we report a selection of results for  $\pi^0$  and  $\eta$ , comparing the `FairShip` and `Pythia` samples. An important parameter in the `FairShip` simulation is the energy cut-off  $E_{\text{cut}}$  applied to the particles produced at each interaction vertex: particles with energy less than  $E_{\text{cut}}$  are removed from the list of those considered for new interactions within the

meson	$N_{\pi^0}/p.o.t.$	$N_{\pi^0}/p.o.t.$
	FairShip	Pythia
$\pi^0$	42	6
$\eta$	5.5	0.8

**Table 2.** Average particle multiplicities per *p.o.t.* in 400 GeV proton collisions as estimated with FairShip, applying a cut-off  $E_{\text{cut}} > 500$  MeV on secondary particles, and with Pythia, for primary interactions only.

target. We report the result for  $E_{\text{cut}} > 500$  MeV. Primary proton-proton interactions, as generated with Pythia, give an average particle multiplicity per *p.o.t.* of  $N_{\pi^0}/p.o.t. = 6$  and  $N_{\eta}/p.o.t. = 0.8$ , for  $\pi^0$  and  $\eta$  respectively. From the samples of mesons generated with FairShip, we get  $N_{\pi^0}/p.o.t. = 42$  and  $N_{\eta}/p.o.t. = 5.5$ . Therefore, we observe that secondary interactions occurring within the beam-dump target greatly increase the particle multiplicities and, in turn, lead to a rise of the DM yield by the same amount. However, this does not translate directly into an enhancement of the signal yield in the SND. Indeed, in order to produce a detectable scattering event one should take into account

- the geometrical acceptance,
- the path travelled within the detector,
- the cross section for the scattering process.

We consider separately the effect due to the geometrical acceptance, defining an effective number of mesons per *p.o.t.*  $N_X^{\text{eff}}/p.o.t.$  as the average number of mesons of species  $X$  per *p.o.t.* which produce a DM particle impinging on the detector surface. For different  $m_{A'}$  values, we report in tables 3 and 4 our estimate of  $N_{\pi^0}^{\text{eff}}/p.o.t.$  and  $N_{\eta}^{\text{eff}}/p.o.t.$  as estimated with Pythia and FairShip. The comparison shows that the increase due to the cascade is around 50 – 70%. The explanation is that the secondary particles mainly populate the soft part of the spectrum, as it is clearly shown in the left panels of figure 6 and figure 7 which have to be compared with the corresponding right panels describing the spectrum from prompt yields. Moreover, the cross section for the elastic LDM- $e^-$  scattering grows with the energy of the incoming dark-matter particle before saturating to a constant behaviour [59]. Hence, we expect that scattering events initiated by LDM particles produced in secondary interactions, being softer, will be less probable. This is clearly demonstrated by the last two columns in tables 3 and 4 in which we report the final signal yields  $N_s$  (corresponding to the benchmark point  $\alpha_D = 0.1$  and  $m_{A'} = 3m_\chi$  and  $\epsilon = 10^{-4}$ ) due to FairShip and Pythia samples respectively. From the comparison, we see that the impact of the secondary interactions is reduced to that given by the geometrical acceptance only. In conclusion, our finding is that for  $\pi^0$ , the cascade modestly affects ( $\sim 15 - 40\%$ ) the signal event yields within the detector volume, while for  $\eta$  it is negligible.

$m_{A'}$ (MeV)	$N_{\pi^0}^{\text{eff}}/p.o.t.$ (FairShip)	$N_{\pi^0}^{\text{eff}}/p.o.t.$ (Pythia)	$N_s$ (FairShip)	$N_s$ (Pythia)
10	1.2	0.80	$1.7 \cdot 10^4$	$1.3 \cdot 10^4$
30	1.1	0.72	$8.6 \cdot 10^3$	$7.3 \cdot 10^3$
60	0.70	0.46	$2.0 \cdot 10^3$	$1.8 \cdot 10^3$
90	0.24	0.15	$3.1 \cdot 10^2$	$2.5 \cdot 10^2$
120	0.013	0.0083	7.4	6.7

**Table 3.** Comparison between  $\pi^0$  samples generated using FairShip (with an energy cut of  $E_{\text{cut}} > 500$  MeV in secondary vertices) and Pythia.  $N_{\pi^0}^{\text{eff}}/p.o.t.$  is the effective number of  $\pi^0$ s per p.o.t. producing LDM particles within the geometrical acceptance.  $N_s$  is the signal yield for the benchmark point  $\alpha_D = 0.1$  and  $m_{A'} = 3m_\chi$  and  $\epsilon = 10^{-4}$  corresponding to  $2 \cdot 10^{20} p.o.t.$

$m_{A'}$ (MeV)	$N_\eta^{\text{eff}}/p.o.t.$ (FairShip)	$N_\eta^{\text{eff}}/p.o.t.$ (Pythia)	$N_s$ (FairShip)	$N_s$ (Pythia)
10	0.15	0.10	$1.1 \cdot 10^3$	$8.1 \cdot 10^2$
130	0.13	0.092	25	24
250	0.099	0.059	1.6	1.5
370	0.033	0.020	$1.16 \cdot 10^{-1}$	$1.15 \cdot 10^{-1}$
520	0.00020	0.00012	$1.9 \cdot 10^{-4}$	$1.8 \cdot 10^{-4}$

**Table 4.** Comparison between  $\eta$  samples generated using FairShip (with an energy cut of  $E_{\text{cut}} > 500$  MeV in secondary vertices) and Pythia.  $N_\eta^{\text{eff}}/p.o.t.$  is the effective number of  $\eta$ s per p.o.t. which give raise to LDM particles within the geometrical acceptance.  $N_s$  is the LDM yield for the benchmark point  $\alpha_D = 0.1$  and  $m_{A'} = 3m_\chi$  and  $\epsilon = 10^{-4}$  corresponding to  $2 \cdot 10^{20} p.o.t.$

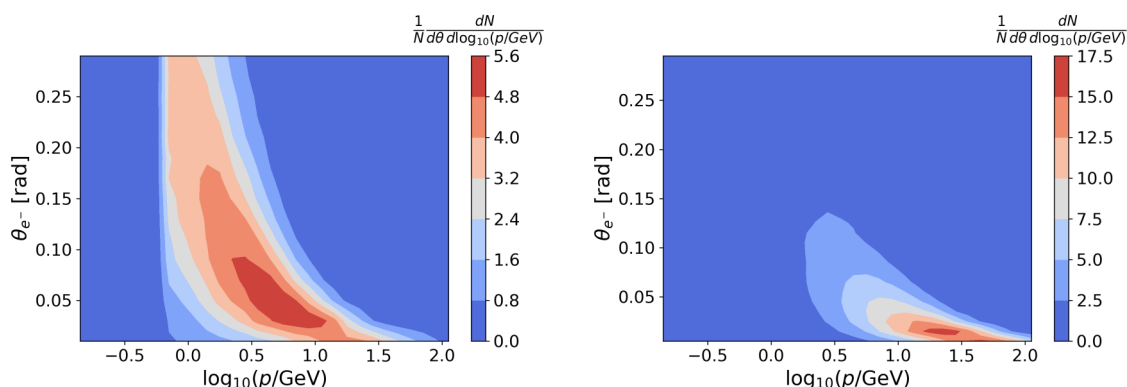


**Figure 6.** 2D contour plot of the momentum ( $p$ ) and the production angle ( $\theta$ ) correlation for  $\pi^0$ s produced in the collisions of 400 GeV protons hitting the SHiP beam-dump target. Left: simulation with FairShip including  $\pi^0$  production in the interactions of secondary hadrons with the target nuclei. Right: simulation of the prompt proton-nucleon  $\pi^0$  production with Pythia.

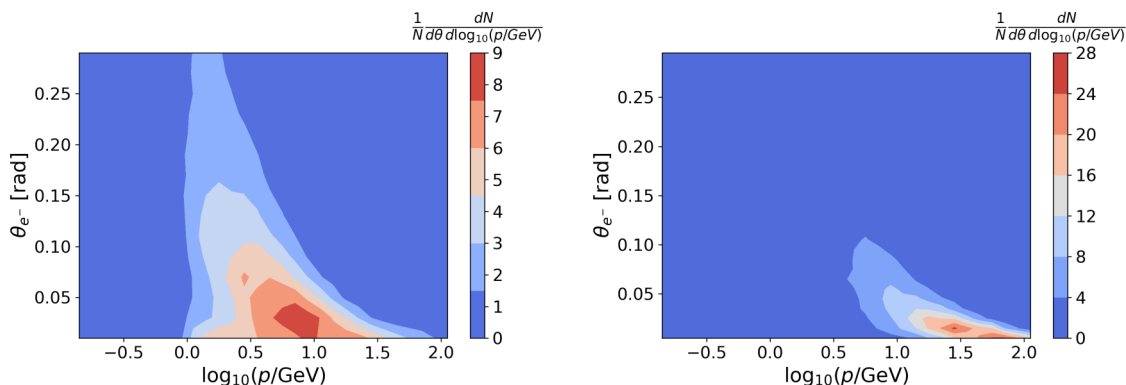


**Figure 7.** 2D contour plot of the momentum ( $p$ ) and the production angle ( $\theta$ ) correlation for the  $\eta$ s produced in the collisions of 400 GeV protons hitting the SHiP beam-dump target. Left: simulation with FairShip including  $\eta$  production in the interactions of secondary hadrons with the target nuclei. Right: simulation of the prompt proton-nucleon  $\eta$  production with Pythia.

## 4.2 Proton Bremsstrahlung

In the mass range  $500 \text{ MeV} \lesssim m_{A'} \lesssim 1 \text{ GeV}$ , the production of  $A'$  is dominated by the proton bremsstrahlung mechanism. The photon emission cross section is indeed enlarged in the collinear direction so that a sizeable fraction of  $A'$  is produced within the geometrical acceptance for an on-axis detector as the SND ( $\sim 20\%$ ). In this limit, the process can be described by a generalisation of the Fermi-Williams-Weizsäcker method [60–62], based on the assumption that the  $p - N$  scattering is dominated by the exchange in the  $1^{--}$  channel. We extend MadDump include the bremsstrahlung from the primary protons. Following refs. [50, 63], we parametrise the four-momentum vector of the emitted  $A'$  as  $p_{A'} = (E_{A'}, p_T \cos(\phi), p_T \sin(\phi), zP)$ , with  $E_{A'} = zP + (p_T^2 + m_{A'}^2)/(2zP)$ , where  $P$  is the momentum of the incident proton,  $z$  is the fraction of the proton momentum carried by the outgoing  $A'$ ,  $p_T$  is the momentum perpendicular to the beam momentum and  $\phi$  is the azimuthal angle. We generate unweighted  $A'$  events according to the differential production rate

$$\frac{d^2 N_{A'}}{dz dp_T^2} = \frac{\sigma_{pA}(s')}{\sigma_{pA}(s)} F_{1,p}^2(m_{A'}^2) w_{ba}(z, p_T^2), \quad (4.6)$$

where  $s' = 2m_p(E_p - E_{A'})$ ,  $s = 2m_p E_p$  and the photon splitting function is

$$w_{ba}(z, p_T^2) = \frac{\epsilon^2 \alpha}{2\pi H} \left[ \frac{1 + (1-z)^2}{z} - 2z(1-z) \left( \frac{2m_p^2 + m_{A'}^2}{H} - z^2 \frac{2m_p^4}{H^2} \right) + 2z(1-z)(1 + (1-z)^2) \frac{m_p^2 m_{A'}^2}{H^2} + 2z(1-z)^2 \frac{m_{A'}^4}{H^2} \right],$$

with  $H = p_T^2 + (1-z)m_{A'}^2 + z^2 m_p^2$ . In the above formula,  $F_{1,p}$  is the time-like proton form-factor, as provided by the parameterisation in ref. [64]. It effectively incorporates off-shell mixing with vector mesons such as  $\rho$  and  $\omega$ , corresponding to a resonance effect around  $m_{A'} \sim 770 \text{ MeV}$  [65]. In ref. [63], the authors compare the description of the peak region

by adopting the time-like proton form factors and by adding by hand the vector mixing within an on-shell computation, finding small deviations in the peak region. Assessing the size of this uncertainty is beyond the scope of this work.

The next steps of the simulation, namely the decay  $A' \rightarrow \chi\bar{\chi}$  and the  $\chi - e^-$  scattering in the SND, are handled by standard MadDump functions. The whole process has been integrated into the new MadDump mode `bremsstrahlung-interaction`.

The normalisation of the flux of the original  $A'$  is given by the integral of the differential production rate eq. (4.6) in the validity range of the equivalent photon approximation, given by the kinematical conditions

$$E_p, E_{A'}, E_p - E_{A'} \gg m_p, m_{A'}, |p_T|. \quad (4.7)$$

Following refs. [50, 63, 66], we adopt  $z \in [0.1, 0.9]$ . For a relatively high energy experiment such as SHiP, the minimum DP energy  $E_P$  corresponds then to  $\sim 40$  GeV and we can set its maximum transverse momentum  $p_T$  to 4 GeV, i.e. an order of magnitude less. We expect electron bremsstrahlung to be sub-dominant as discussed for example in [66, 67]. As for the cascade effects, extra dark photons may arise from the bremsstrahlung of secondary charged hadrons. Similarly to what happens in the case of mesons, the picture is complicated by the impact of the geometrical acceptance and the convolution with the scattering cross section. For the case the proton undergoes a chain of elastic proton-nucleon collisions, so that it retains all of its initial energy, we can make a rough estimate by means of the following simplified calculation. Let  $p_{\text{el}}$  be the probability that the incoming proton undergoes an elastic scattering interaction with a nucleon in the target and  $p_{\text{brem}}$  the probability of a dark photon produced in the proton bremsstrahlung. Under the assumption that  $p_{\text{brem}}$  does not depend much on the number of previous elastic collisions, the probability that a dark photon is produced in this chain is

$$p = p_{\text{brem}} (1 + p_{\text{el}} \times p_{\text{el}} + p_{\text{el}} \times p_{\text{el}} \times p_{\text{el}} + \dots) = p_{\text{brem}} \sum_{n=0}^{\infty} p_{\text{el}}^n = p_{\text{brem}} \frac{1}{1 - p_{\text{el}}}. \quad (4.8)$$

At the energy of SHiP,  $p_{\text{el}} \simeq 0.25$  so that we estimate a mild increment of  $\sim 30\%$ . In the following, we keep the conservative estimate based only upon the bremsstrahlung of the primary protons.

### 4.3 QCD prompt production

QCD parton processes become relevant for  $m_{A'} \gtrsim 1$  GeV, at the edge where perturbation theory starts to become reliable. Indeed, at scales  $\lesssim 1$  GeV the strong coupling  $\alpha_s$  is  $O(1)$  and the description of the hadrons in terms of constituent partons is spoiled by the confinement. In the attempt of estimating the relative importance of this production mechanism, we have tried to push the perturbative computation down to  $m_{A'} \sim 300$  MeV. The main tree-level diagrams correspond to the Drell-Yan-like production and the associated production with QCD radiation, figure 8. The latter allows for smaller  $m_{A'}$  values since the characteristic scale of the process, given by the transverse momentum of the emitted parton, can be kept to be higher than the  $\Lambda_{\text{QCD}}$  scale. A minimum cut on the



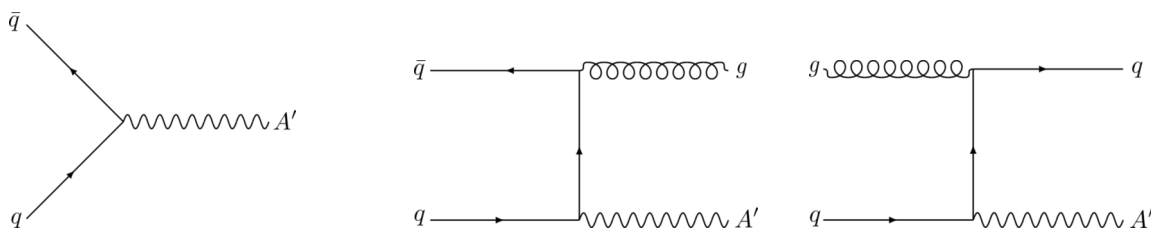


**Figure 8.** Main tree-level partonic QCD contributions: Drell-Yan-like production (left panel), associated production with the emission of extra QCD radiation (right panel).

$p_T$  of the QCD radiation is physically required to tame infrared singularities. The cross section diverges logarithmically up to scales of order  $O(\Lambda_{\text{QCD}})$ , when perturbation theory eventually breaks down. The transverse momentum cut-off is a severe requirement for an on-axis set-up as SHiP, due to its small angular acceptance. We find that even for relatively small values of the cut-off,  $p_T \sim 800$  MeV, the production rate is not sufficient to produce a significant yield of LDM within the geometrical acceptance. Therefore, we focus only on Drell-Yan-like production. We rely on `MadGraph5(v.2.66)` [68], which is integrated in `MadDump` as it is based on the former package, for the generation of the events, and we use the `NNPDF2.3LO` [69, 70] set as our choice of the proton parton distribution function (PDF). In the normalisation of the number of produced LDM particles, we effectively take into account nuclear effects in the following way

$$N_{\text{LDM}} = 2 \times \frac{\sigma_{pA \rightarrow \chi\bar{\chi}}}{\sigma_{pA \rightarrow \text{all}}} \times N_{p.o.t.} = 2 \times \frac{A \sigma_{pp \rightarrow \chi\bar{\chi}}}{A^{0.71} \sigma_{pp \rightarrow \text{all}}} \times N_{p.o.t.} = 2 \times A^{0.29} \times \frac{\sigma_{pp \rightarrow \chi\bar{\chi}}}{\sigma_{pp \rightarrow \text{all}}} \times N_{p.o.t.},$$

where  $A = A_{\text{Molybdenum}} = 96$ ; the nuclear rescaling as  $A^{0.71}$  is taken from ref. [71] and  $\sigma_{pp \rightarrow \text{all}} = 40$  mb [72].

In this case, the characteristic scale of the process coincides with  $m_{A'}$ . As mentioned before, we cannot use scales  $\lesssim 1$  GeV, where both the strong coupling and PDF are ill-defined from the perturbative point of view. To push our projection into the sub-GeV range, we adopt the following prescription: we set both the re-normalisation scale  $\mu_R$  (at which the strong coupling constant is evaluated) and the factorisation scale  $\mu_F$  (at which the PDF is evaluated) to a fixed value chosen to be  $\mu_R = \mu_F = 1.5$  GeV, the lowest scale variation point associated to open charm production.

## 5 Background estimate

Neutrinos emerging from the beam-dump target and interacting in the SND are the relevant background source to the detection of LDM elastic scattering, whenever the topology at the primary vertex consists of a single outgoing charged track, an electron. The expected background yield for five years of data-taking has been estimated by means of the `GENIE` [49] Monte Carlo software, supplied with the spectrum of neutrinos produced at the beam dump as simulated with `Pythia v6.4.28` within `FairShip` and including secondary production, for the generation of the following neutrino interactions in the whole kinematic phase space:

- *Elastic scattering* (EL) of  $\nu_e(\bar{\nu}_e)$ ,  $\nu_\mu(\bar{\nu}_\mu)$  off the electrons of the SND, which is a source of irreducible background as it shares the same topology of LDM elastic interactions:

$$\nu_\ell + e^- \rightarrow \nu_\ell + e^- .$$

- *Resonant scattering* (RES) of  $\nu_e(\bar{\nu}_e)$  off nucleons  $A(n, p)$ :

$$\begin{aligned} \nu_e(\bar{\nu}_e) + A &\rightarrow e^-(e^+) + \Delta^{+/++} , \\ \nu_e(\bar{\nu}_e) + A &\rightarrow e^-(e^+) + (N^* \rightarrow \text{inv}) . \end{aligned}$$

- *Deep Inelastic scattering* (DIS) of  $\nu_e(\bar{\nu}_e)$  off nucleons  $A$ , representing background when only the electron track at the primary vertex is reconstructed because of unidentified hadrons:

$$\nu_e(\bar{\nu}_e) + A \rightarrow e^-(e^+) + X .$$

- *Quasi-elastic scattering* (QE) of  $\nu_e(\bar{\nu}_e)$ , with the primary proton undetected because it is below the energy threshold:

$$\begin{aligned} \nu_e + n &\rightarrow e^- + p , \\ \bar{\nu}_e + p &\rightarrow e^+ + n . \end{aligned}$$

Charged current interactions of  $\nu_\ell(\bar{\nu}_\ell)$  with  $\ell = \mu, \tau$  do not represent a concern because they are easily discernible from LDM events by reconstructing the charged lepton produced in the final state. Electron decay modes of the  $\tau$  lepton are a negligible background source, since an early decay of the parent track ( $\sim 1\%$  occurrence) leading to an undetected  $\tau$  would occur with less than a per-mill probability. In addition, we do not consider  $\nu_\tau(\bar{\nu}_\tau)$  elastic scattering processes as background, due to the suppression resulting from the combination of smaller flux  $\phi_{\nu_\tau}$  ( $\sim 1$  order of magnitude smaller than  $\phi_{\nu_e}$  and  $\sim 2$  orders of magnitude smaller than  $\phi_{\nu_\mu}$ ) and cross section.

The whole  $\nu$  spectrum is made to interact within the SND and the surrounding materials. Moreover, for this study we assume the detection efficiency to be unitary [73].

The simulated sample of neutrinos undergoes a two-steps selection procedure, in order to be tagged as residual background.

First, only interactions occurring within geometrical acceptance and associated with a single charged final state track, an electron, are selected:  $\nu$  vertices are further considered in the analysis only if located inside the SND volume, whereas all the out-coming charged tracks are inspected in order to assess their visibility in the nuclear emulsion medium. The visibility threshold depends crucially on the exploited tracking device technology; for this study we assume 170 MeV/c for the protons, 100 MeV/c for the other charged particles including the electrons. These are derived as benchmark values from the OPERA experiment, where charged-particle reconstruction is possible only if two consecutive straight track segments, before and after a lead plate, are found to be in agreement [74]. A further handle considered here for signal against background discrimination is the presence of neutral particles, e.g. photons or  $\pi^0$ s, nearby the interaction vertex, since it is not foreseen in any LDM elastic scattering event.

The second step of the event identification procedure consists of a kinematic selection in the energy  $E_e$  and polar angle with respect to the incoming neutrino/LDM direction  $\theta_e$  of the scattered electron. For the elastic case, these quantities are constrained by the kinematic relation  $E_e \theta_e^2 \leq 2 m_e$ , valid in the regime  $E_{in} \gg m_e, m_\chi$ , where  $E_{in}$  is the energy of the incident neutrino/LDM particle. In order to choose the energy and angle ranges for the selection, an optimisation procedure is performed, aiming at maximising the following significance:

$$\Sigma = \frac{S}{\sqrt{\sigma_{\text{stat}}^2 + \sigma_{\text{sys}}^2}} = \frac{S}{\sqrt{B + \sum_{\substack{i \in [\text{EL}, \text{QE}, \text{RES}, \text{DIS}] \\ \ell \in [\nu_e, \nu_\mu, \bar{\nu}_e, \bar{\nu}_\mu]}} (\kappa_{i\ell} B_{i\ell})^2}}, \quad (5.1)$$

where  $S$  denotes the signal yield, while  $B_{i\ell}$  are the individual contributions to the background yield  $B$  per interaction category and neutrino flavour, each of them weighted by a factor  $\kappa_{i\ell}$  accounting for the systematic uncertainty. We have focused on the relevant systematics, arising from the uncertainty on the neutrino cross sections (assumed flavour-independent,  $\kappa_i$ ) and on the incoming neutrino flux produced at the beam dump (interaction-independent,  $\tilde{\kappa}_\ell$ ), so that we have assumed  $\kappa_{i\ell} = \sqrt{\kappa_i^2 + \tilde{\kappa}_\ell^2}$ . As for the former, we assume the following: 5% for DIS [75], 18% for RES [76], 8% for QE [77], while we neglect the uncertainty on the EL cross section that is well known within the SM [78]. As for the uncertainty on the incoming neutrino flux, this will be well constrained by an independent measurement of the abundant CC-DIS interactions occurring within the SHiP detector (expected  $\sim 10^6$  for  $\nu_{e,\mu}$ ). Since the corresponding cross section is lepton-universal and known within  $\sim 5\%$  accuracy down to  $E_\nu$  of 2.5 GeV [75], we assume it to be the driving systematic uncertainty on the neutrino flux. While SHiP is capable of disentangling  $\nu_\mu$  from  $\bar{\nu}_\mu$  interactions by measuring the charge of the primary muon, thus providing a different estimate for  $\nu_\mu$  and  $\bar{\nu}_\mu$  fluxes, with regard to electron species it will measure a combination of the lepton and anti-lepton initiated events. As the relative abundance of  $\nu_e$  and  $\bar{\nu}_e$  produced at the beam dump can be assessed, the individual fluxes can be estimated accordingly. For neutrino energies below 2.5 GeV we double the uncertainty on the flux assuming them to be at 10%.

Since the signal yield  $S$  depends on the mass hypothesis placed on the LDM candidate and thus on the DP, we adopt the most-general assumption of maximising the experimental sensitivity with respect to the broadest possible range of masses. Therefore,  $S$  is given as the average of the signal yields for three DP mass hypotheses: 50 MeV, 250 MeV and 500 MeV.

The selection optimisation strategy is based on a grid-search method and proceeds as follows:

- an energy window  $[E_{\text{min}}, E_{\text{max}}]$  is identified, according to the signal events distributions;
- in the given energy range, the significance  $\Sigma$  values are determined in uniform angular intervals of 5 mrad spread;
- the selection ranges, corresponding to the maximum  $\Sigma$ , are chosen for the analysis.

	$\nu_e$	$\bar{\nu}_e$	$\nu_\mu$	$\bar{\nu}_\mu$	all
Elastic scattering on $e^-$	68	41	60	38	207
Quasi-elastic scattering	9	9			18
Resonant scattering	—	5			5
Deep inelastic scattering	—	—			—
Total	77	55	60	38	230

**Table 5.** Expected neutrino background yield to light dark matter elastic scattering search in the SHiP experiment, corresponding to  $2 \times 10^{20}$  delivered *p.o.t.* The current estimate is the result of a combined geometrical, topological and kinematical selection, aimed at identifying only interactions occurring within the Scattering Neutrino Detector with one visible track in the final state being an electron. Tracks under a defined visibility threshold are discarded ( $p < 100$  MeV/c for charged,  $p < 170$  MeV/c for protons). A kinematic cut in  $E_e \in [1, 5]$  GeV and  $\theta_e \in [10, 30]$  mrad of the scattered electron is chosen as result of the signal significance optimisation procedure and determines the final number of background events. We refer to the section 5 for further details on the analysis and the associated uncertainties.

As shown in figure 9, signal events are mostly concentrated at energies below 10 GeV. Two energy windows have thus been considered:  $[1, 5]$  GeV and  $[1, 10]$  GeV, where the lower cut is placed as a minimum requirement for the recoil electron to produce a detectable electromagnetic shower within the ECC brick. The motivation to consider an additional tighter energy range resides in the opportunity to further suppress the high energetic components of the neutrino background, as illustrated in figure 10 which shows the relevant EL and QE contributions. DIS and RES processes are not shown since they exhibit signatures with higher multiplicities of charged tracks at the primary vertex.

The results of the optimisation are reported in figure 11, showing indeed a preference for the tighter energy window  $E_e \in [1, 5]$  GeV and an angular range  $\theta_e \in [10, 30]$  mrad.

The corresponding background yield estimate is reported in table 5.

Neutrino elastic scattering processes, involving either electronic and muonic species, represent the dominant background source and are to some degree irreducible, since they share the same topology as the signal.

With regard to quasi-elastic  $\nu_e$  and  $\bar{\nu}_e$  interactions, a small but non-negligible contribution is observed. The process  $\nu_e n \rightarrow e^- p$  mimics the signal when the proton at the primary vertex is not identified, because of the 170 MeV/c threshold. Improvements in the proton identification efficiency with dedicated techniques, including Machine Learning clustering algorithms, will be the subject of future studies. When considering anti-neutrinos, events as  $\bar{\nu}_e p \rightarrow e^+ n$  are topologically irreducible since we assume for the present study the neutron to be undetectable within the SND. This effect compensates the larger (by a factor of  $\sim 3$ ) neutrino flux, thus making the two contributions comparable.

In the case of resonant neutrino scattering, the outgoing electron is often accompanied by a further charged track, which helps discriminating between background and signal.

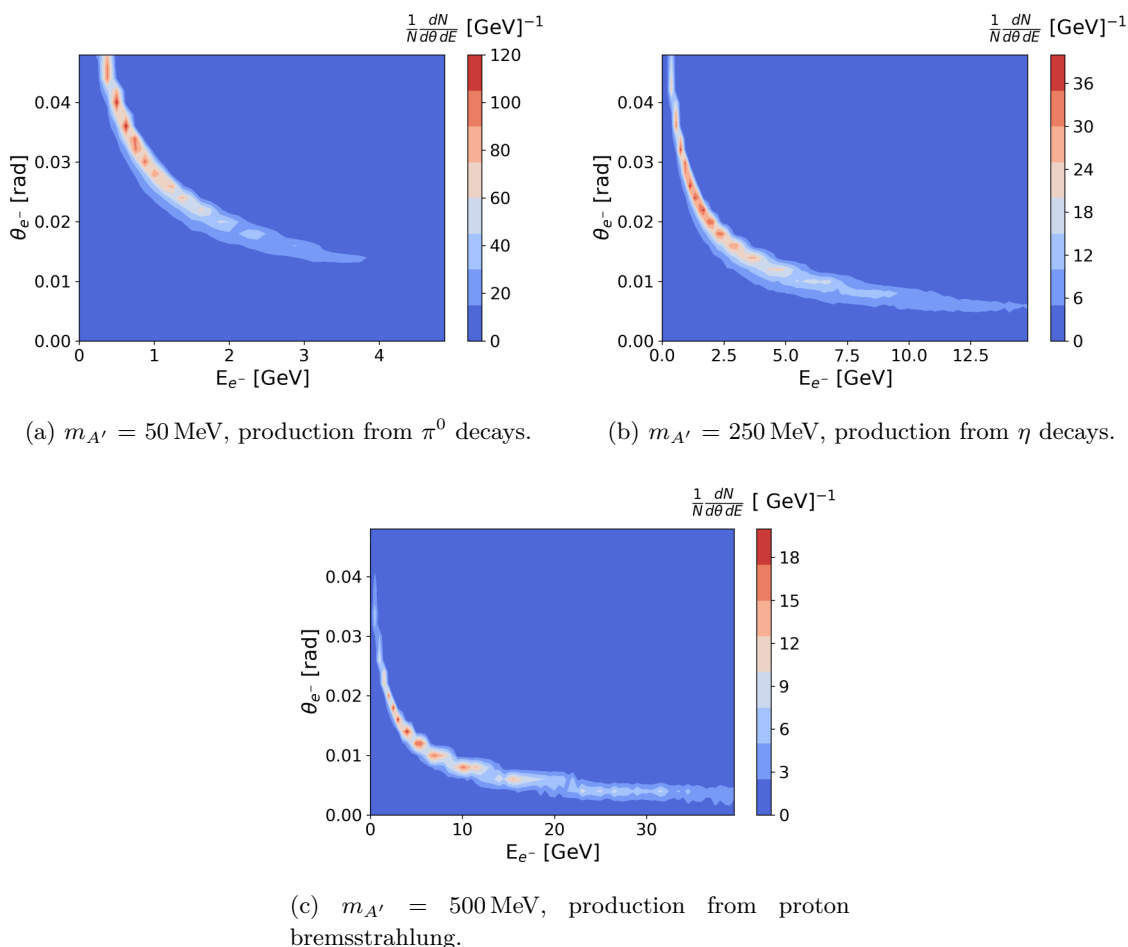


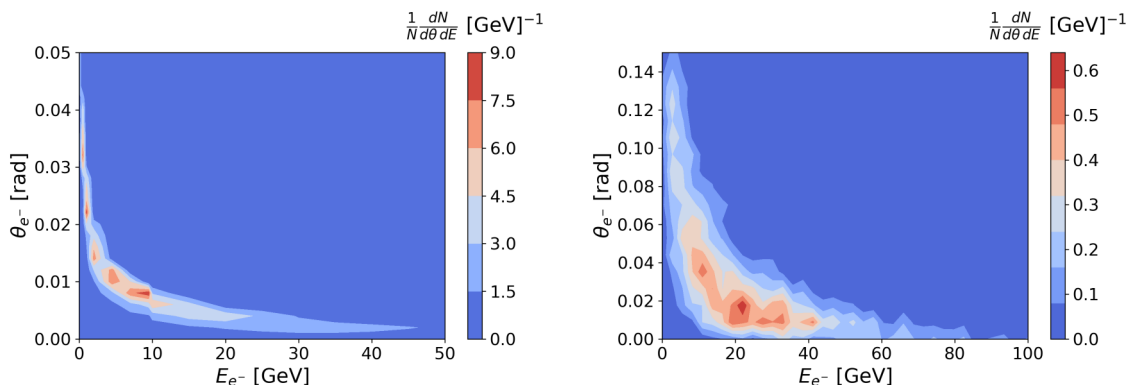
**Figure 9.** 2D-contour plot in the energy-polar angle plane of the recoil electron in LDM- $e^-$  scattering for three different mass DP candidates: (a) 50 MeV, (b) 250 MeV, (c) 500 MeV. The colour range is expressed in arbitrary units. A clear correlation is observed between the mass of the DP candidate and the electron energy-angle spectrum: the higher is the mass the smaller the recoil angle and the higher the associated energy. In the mass range we are interested in, most of the signal lies in the energy region below 10 GeV.

Nevertheless, some topologically irreducible interactions are present as well:

$$\bar{\nu}_e p \rightarrow e^+ N^*, \quad N^* \rightarrow \Lambda^0 K_{L/S}^0,$$

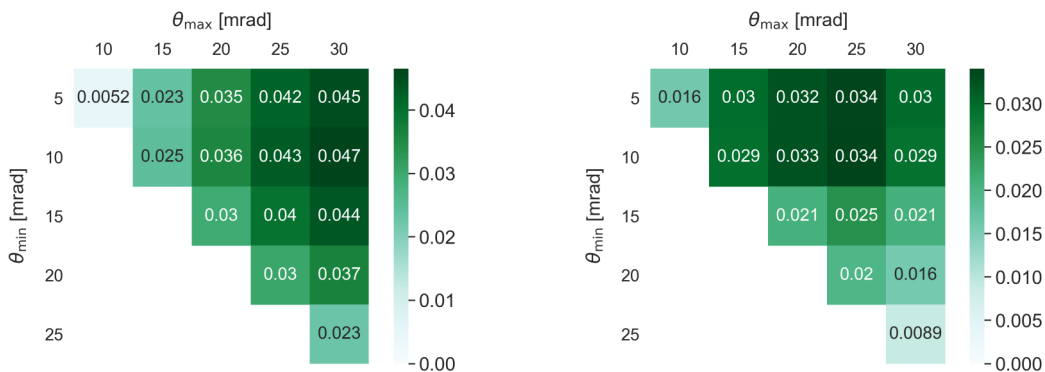
where the  $K_{L/S}^0$  is considered undetectable within the SND for this study. Future improvements lie in the employment of combined information of ECC and TT, coming from the linking of the emulsion tracks with those reconstructed in the electronic tracking system. Moreover, some final states with the pattern  $e^+(n)\gamma$  contribute, when the emitted photon is too soft to be identified via the reconstruction of the electron-positron pairs from its conversion.

The contribution from neutrino deep inelastic scattering processes is, on the contrary, negligible, as a consequence of the high rejection power observed on these event categories, which exhibit a topology with a high multiplicity of charged tracks.



(a) Sum of the EL  $\nu_\ell (\bar{\nu}_\ell)$  scattering contributions ( $\ell = e, \mu$ ). (b) Sum of the QE  $\nu_e (\bar{\nu}_e)$  scattering contributions.

**Figure 10.** 2D plot of the scattered electron energy  $E_{e^-}$  Vs. angle  $\theta_{e^-}$  for the relevant background sources from neutrino and anti-neutrino species: (a) EL scattering from  $\nu_\ell (\bar{\nu}_\ell)$  being  $\ell = e, \mu$ ; (b) QE scattering from  $\nu_e (\bar{\nu}_e)$ .



(a) Grid values for  $E_e \in [1, 5]$  GeV.

(b) Grid values for  $E_e \in [1, 10]$  GeV.

**Figure 11.** Grid-search optimisation of the significance  $\Sigma$  as a function of the angular cut for a fixed energy window. The left axis represents the lower cut value for  $\theta_e$  whereas the upper axis is the higher one. The plots in the two panels share the same normalisation. The best selection corresponds to the tighter energy window (a) and the angular range  $[10, 30]$  mrad.

In the eventuality of an observed excess in the number of events, SHiP may collect data in a bunched beam mode, exploiting the time of flight measurement to separate massive particles like LDM from neutrinos.

## 6 Sensitivity

Once the significance of eq. (5.1) is maximised, the optimal energy and angle ranges are employed to determine the yields of signal and background, following a cut-and-count procedure, per each fixed value of the mediator mass  $m_{A'}$ . The 90% confidence level (C.L.) exclusion limits on the  $\epsilon$  coupling at fixed mass  $m_{A'}$  are then retrieved by adopting

a single-tail Poissonian statistics. Statistical and systematic uncertainties are combined as reported after eq. (5.1).

In figure 12, we report our projection for the SHiP SND exclusion limit at 90% C.L. in the  $m_\chi - Y$  plane of the dark-photon model. As stated above, we consider the benchmark scenario  $\alpha_D = 0.1$  and  $m_\chi = m_{A'}/3$ . In figure 13, we separate the contributions given by the different production mechanisms. In the low mass range  $m_\chi \lesssim 150$  MeV, the main contribution comes from the decay of the lightest mesons.  $\pi$  decays dominate the  $A'$  yield up to masses close to the  $m_\pi \rightarrow \gamma A'$  kinematic threshold. When approaching this threshold, the decay rate rapidly closes due to the steep suppression given by the phase space factor and with further increasing  $m_\chi$  mass the  $\eta \rightarrow \gamma A'$  starts to dominate. The contribution of the  $\omega$  is subdominant in the whole available mass range, which justifies *a posteriori* the fact that we do not include in our analysis  $A'$  production from decays of heavier meson like the  $\eta'$ .

We find that the contribution due to pQCD is very small in the mass region explored. By varying the factorisation scale in the range  $800 \text{ MeV} < \mu_F < 3 \text{ GeV}$ , we estimate the uncertainty associated with missing higher orders to be about 15% on the signal yield within acceptance. We believe that this is an underestimation of the uncertainty as at next-to-leading order the process starts to receive radiative corrections proportional to the strong coupling constant at a scale close to  $\Lambda_{\text{QCD}}$ , and new production channels open. While we do not expect that this will lead to a sizeable impact on the sensitivity, neglecting it leads anyway to a conservative estimate of the signal; hence, we have not considered the contribution of pQCD in our final result.

In the mass range  $1 \text{ MeV} < m_\chi < 300 \text{ MeV}$ , the SHiP upper limit fairly improves the current strongest experimental limits (BaBar [13], Na64 [27]), even by more than an order of magnitude in the central region ( $5 \text{ MeV} < m_\chi < 100 \text{ MeV}$ ). In this range and for the benchmark point under investigation, SHiP will cover the still unexplored parameter space corresponding to the solution of the relic density given by a scalar LDM. In the range  $3 \text{ MeV} < m_\chi < 300 \text{ MeV}$ , SHiP will reach the thermal target for a Majorana candidate. Furthermore, it will exceed the thermal target for a Pseudo-Dirac candidate for masses around  $10 \text{ MeV} < m_\chi < 40 \text{ MeV}$ .

We notice that for  $m_\chi \lesssim 5 \text{ MeV}$  the SHiP line saturates. In this region, the dark matter mass starts to become negligible and the selection requirements affect similarly the signal and the background. The rise in the signal production rate due to a lower mass is then balanced by a smaller fraction of events passing the kinematics selection, leading to the observed flat sensitivity in the small mass range. The distinctive peak at  $m_\chi \simeq 257 \text{ GeV}$  corresponds to the  $\rho - \omega$  resonant region, which is effectively taken into account by the time-like proton form factors used in the modelling of the proton bremsstrahlung mechanism.

In figure 14, the comparison between the SHiP sensitivity reach and that of other concurrent experiments clearly shows strengths and the complementarity offered by the proposed experimental scenario. Indeed the SHiP experiment will place constraints in unexplored regions of parameters space by exploiting a high intensity proton beam dump at 400 GeV and a micrometrical resolution tracking capability with the ECC. Thus, it offers a diverse approach to this NP search with respect to other experimental scenarios including direct searches and electron beam-line technologies.

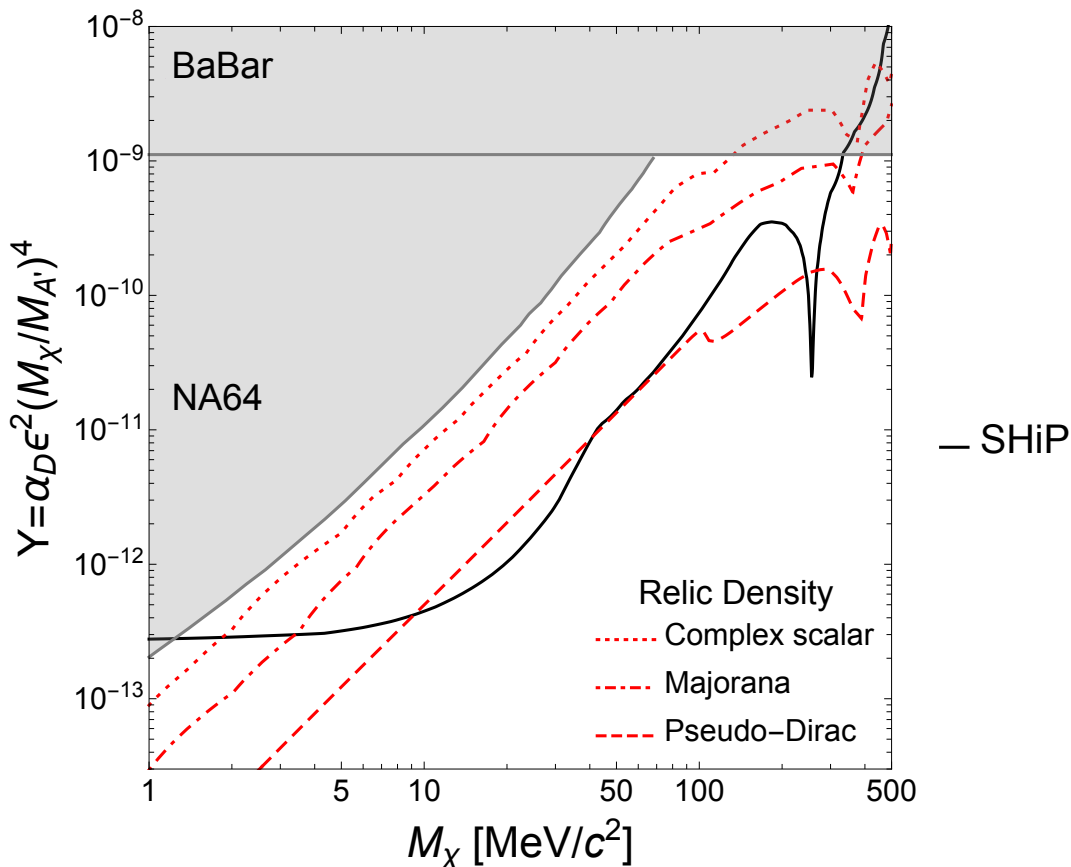


**Figure 12.** SHiP SND exclusion limit at 90%  $CL$  relative to a  $A'$  decaying into  $\chi\bar{\chi}$  pairs for the benchmark point  $\alpha_D = 0.1$  and  $m_{A'} = 3m_\chi$ . The current strongest experimental limits are also shown (BaBar [13], NA64 [27]), together with the three thermal relic lines corresponding to the scalar and the Majorana [3], and the Pseudo-Dirac DM [79] hypothesis.

## 7 Conclusions

Light dark matter particles  $\chi$  with masses in the sub-GeV region represent an appealing scenario for the explanation of the observed thermal relic density in the Universe. In this work, we have studied the potential offered by the SHiP SND to reveal LDM which couple to SM particles via a new gauge force mediated by a vector boson,  $A'$ . We have assumed the simplest DP model, with coupling  $g_D$  to  $\chi$  and  $A'$  kinetically mixed with the SM photon with mixing parameter  $\epsilon$ . We have focused on the relevant scenario for the SHiP SND:  $m_{A'} > 2m_\chi$  and  $g_D \gg \epsilon e$ . Our main result is that for DM masses in  $[1, 300]$  MeV the SHiP experiment will reach an unexplored region of the parameter space. For the benchmark point considered, the sensitivity of the SHiP SND is even below the thermal relic line corresponding to a Majorana DM candidate in the mass window  $[3, 300]$  MeV and it will reach the target for a Pseudo-Dirac candidate within  $[15, 30]$  MeV. Our analysis is based on a robust simulation framework for both the signal and the background which includes the relevant physical processes propagated within the detector. In particular, interactions of



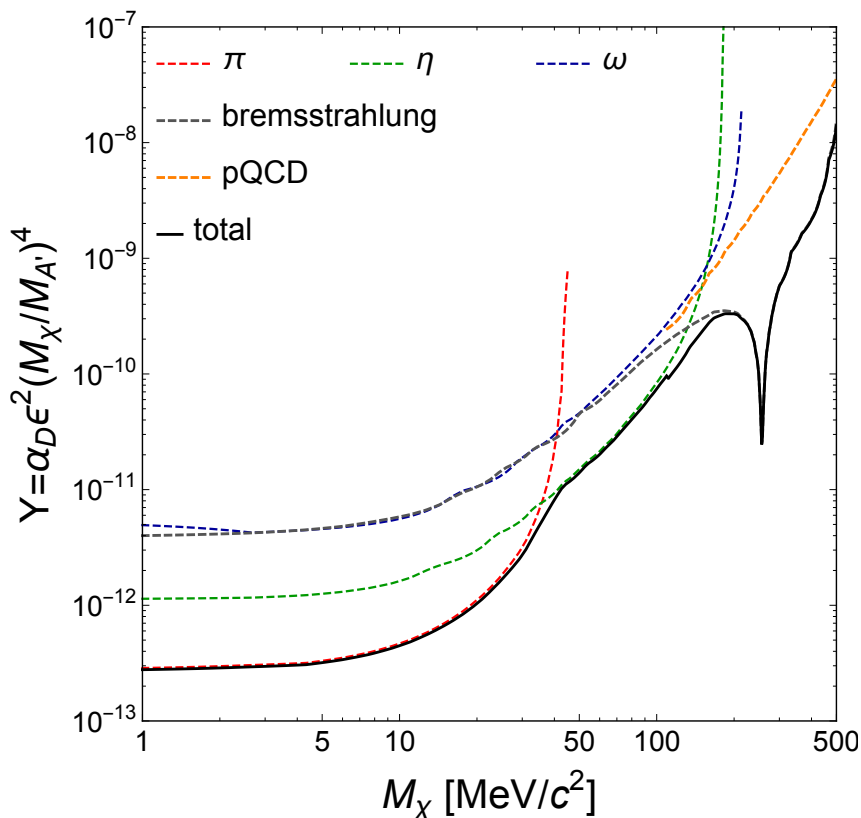


**Figure 13.** SHiP SND exclusion limit at 90%  $CL$  relative to a  $A'$  decaying into  $\chi\bar{\chi}$  pairs for the benchmark point  $\alpha_D = 0.1$  and  $m_{A'} = 3m_\chi$ . The contributions from the different production mechanisms are reported separately.

secondary particles in the beam-dump target have been taken into account in the neutrino background modelling, assuming unitary detection efficiency. As for the signal, we have consistently adopted 100% detection efficiency within the selection requirements and we have studied the impact of the cascade effect on meson multiplicities and the resulting dark matter production yield. We have observed that the impact of the cascade is quite modest and affects mainly the low masses.

In this work, we have focused on the elastic  $\chi e \rightarrow \chi e$  signature detectable within the SHiP Scattering and Neutrino Detector. Other signatures, as the elastic scattering with nuclei, may lead to an improvement of the sensitivity. We leave their study to forthcoming works. In our case, the main background sources arise from elastic  $\nu_\ell/\bar{\nu}_\ell$ -electron and quasi-elastic  $\nu_e/\bar{\nu}_e$  scattering. We have considered the region  $E_e \in [1, 5]$  GeV and  $\theta_e \in [10, 30]$  mrad, where  $e$  is the recoil electron. We have found that about 230 neutrino events survive the selection requirements, for  $2 \times 10^{20}$  *p.o.t.* corresponding to 5 years of data-taking.

We conclude by mentioning that, should an excess of events be observed, a time of flight measurement of particles scattering within the SND might represent a smoking gun to discriminate LDM from neutrino events, thus leading to an inarguable discovery.

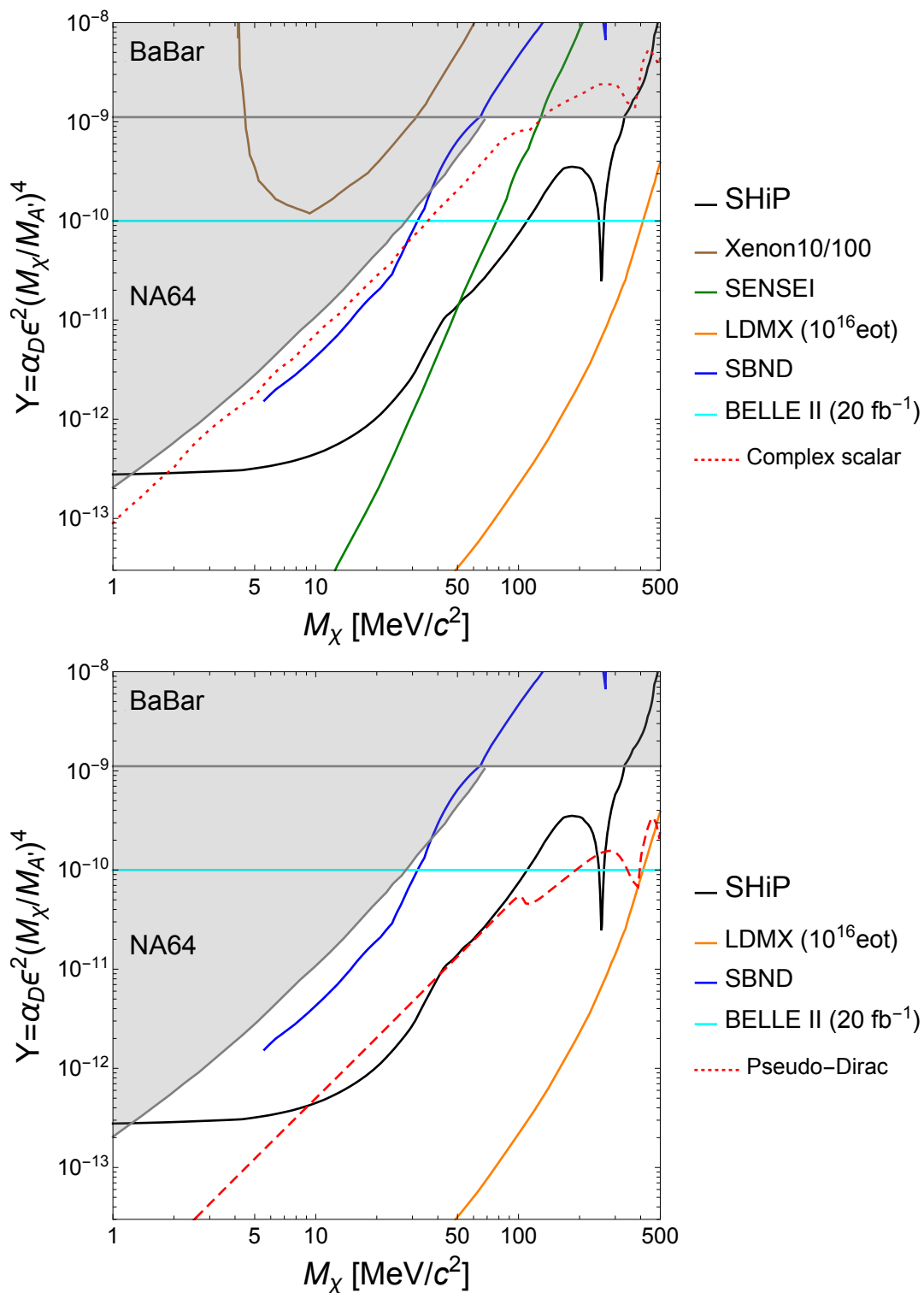


**Figure 14.** Comparison of existing and projected limits among the SHiP and other experiments as taken from ref. [80] for scalar (top panel) and Pseudo-Dirac dark matter (bottom panel).

## Acknowledgments

The support from the Swiss National Science Foundation (SNF) under Contract No. BSSGI0\_155990, 200020\_188464 and IZSAZ2\_173357 is acknowledged.

The SHiP Collaboration wishes to thank the Castaldo company (Naples, Italy) for their contribution to the development studies of the decay vessel. The support from the National Research Foundation of Korea with grant numbers of 2018R1A2B2007757, 2018R1D1A3B07050649, 2018R1D1A1B07050701, 2017R1D1A1B03036042, 2017R1A6A3A01075752, 2016R1A2B4012302, and 2016R1A6A3A11930680 is acknowledged. The support from the FCT — Fundação para a Ciência e a Tecnologia of Portugal with grant number CERN/FIS-PAR/0030/2017 is acknowledged. The support from the Russian Foundation for Basic Research (RFBR), grant 17-02-00607, and the support from the TAEK of Turkey are acknowledged.

**Open Access.** This article is distributed under the terms of the Creative Commons Attribution License ([CC-BY 4.0](https://creativecommons.org/licenses/by/4.0/)), which permits any use, distribution and reproduction in any medium, provided the original author(s) and source are credited.

## References

- [1] M. Schumann, *Direct detection of WIMP dark matter: concepts and status*, *J. Phys. G* **46** (2019) 103003 [[arXiv:1903.03026](https://arxiv.org/abs/1903.03026)] [[INSPIRE](#)].
- [2] P.J. Fox, *TASI lectures on WIMPs and supersymmetry*, *PoS(TASI2018)005* (2019) [[INSPIRE](#)].
- [3] M. Battaglieri et al., *U.S. cosmic visions: new ideas in dark matter 2017. Community report*, in *U.S. cosmic visions: new ideas in dark matter*, (2017) [[arXiv:1707.04591](https://arxiv.org/abs/1707.04591)] [[INSPIRE](#)].
- [4] M. Ibe, W. Nakano, Y. Shoji and K. Suzuki, *Migdal effect in dark matter direct detection experiments*, *JHEP* **03** (2018) 194 [[arXiv:1707.07258](https://arxiv.org/abs/1707.07258)] [[INSPIRE](#)].
- [5] DARKSIDE collaboration, *Low-mass dark matter search with the DarkSide-50 experiment*, *Phys. Rev. Lett.* **121** (2018) 081307 [[arXiv:1802.06994](https://arxiv.org/abs/1802.06994)] [[INSPIRE](#)].
- [6] G. Angloher et al., *Results from 730 kg days of the CRESST-II dark matter search*, *Eur. Phys. J. C* **72** (2012) 1971 [[arXiv:1109.0702](https://arxiv.org/abs/1109.0702)] [[INSPIRE](#)].
- [7] R. Essig, A. Manalaysay, J. Mardon, P. Sorensen and T. Volansky, *First direct detection limits on sub-GeV dark matter from XENON10*, *Phys. Rev. Lett.* **109** (2012) 021301 [[arXiv:1206.2644](https://arxiv.org/abs/1206.2644)] [[INSPIRE](#)].
- [8] XENON collaboration, *Dark matter search results from a one ton-year exposure of XENON1T*, *Phys. Rev. Lett.* **121** (2018) 111302 [[arXiv:1805.12562](https://arxiv.org/abs/1805.12562)] [[INSPIRE](#)].
- [9] DARWIN collaboration, *DARWIN: direct dark matter search with the ultimate detector*, *J. Phys. Conf. Ser.* **1468** (2020) 012068 [[INSPIRE](#)].
- [10] PANDAX-II collaboration, *Dark matter results from 54-ton-day exposure of PandaX-II experiment*, *Phys. Rev. Lett.* **119** (2017) 181302 [[arXiv:1708.06917](https://arxiv.org/abs/1708.06917)] [[INSPIRE](#)].
- [11] SENSEI collaboration, *SENSEI: first direct-detection constraints on sub-GeV dark matter from a surface run*, *Phys. Rev. Lett.* **121** (2018) 061803 [[arXiv:1804.00088](https://arxiv.org/abs/1804.00088)] [[INSPIRE](#)].

- [12] L. Roszkowski, E.M. Sessolo and S. Trojanowski, *WIMP dark matter candidates and searches — current status and future prospects*, *Rept. Prog. Phys.* **81** (2018) 066201 [[arXiv:1707.06277](#)] [[INSPIRE](#)].
- [13] BABAR collaboration, *Search for invisible decays of a dark photon produced in  $e^+e^-$  collisions at BaBar*, *Phys. Rev. Lett.* **119** (2017) 131804 [[arXiv:1702.03327](#)] [[INSPIRE](#)].
- [14] BELLE-II collaboration, *The Belle II physics book*, *PTEP* **2019** (2019) 123C01 [Erratum *ibid.* **2020** (2020) 029201] [[arXiv:1808.10567](#)] [[INSPIRE](#)].
- [15] B. Batell, M. Pospelov and A. Ritz, *Exploring portals to a hidden sector through fixed targets*, *Phys. Rev. D* **80** (2009) 095024 [[arXiv:0906.5614](#)] [[INSPIRE](#)].
- [16] P. deNiverville, M. Pospelov and A. Ritz, *Observing a light dark matter beam with neutrino experiments*, *Phys. Rev. D* **84** (2011) 075020 [[arXiv:1107.4580](#)] [[INSPIRE](#)].
- [17] P. deNiverville, D. McKeen and A. Ritz, *Signatures of sub-GeV dark matter beams at neutrino experiments*, *Phys. Rev. D* **86** (2012) 035022 [[arXiv:1205.3499](#)] [[INSPIRE](#)].
- [18] MINIBOONE collaboration, *Low mass WIMP searches with a neutrino experiment: a proposal for further MiniBooNE running*, [arXiv:1211.2258](#) [[INSPIRE](#)].
- [19] B. Batell, P. deNiverville, D. McKeen, M. Pospelov and A. Ritz, *Leptophobic dark matter at neutrino factories*, *Phys. Rev. D* **90** (2014) 115014 [[arXiv:1405.7049](#)] [[INSPIRE](#)].
- [20] D.E. Soper, M. Spannowsky, C.J. Wallace and T.M.P. Tait, *Scattering of dark particles with light mediators*, *Phys. Rev. D* **90** (2014) 115005 [[arXiv:1407.2623](#)] [[INSPIRE](#)].
- [21] B.A. Dobrescu and C. Frugiuele, *GeV-scale dark matter: production at the main injector*, *JHEP* **02** (2015) 019 [[arXiv:1410.1566](#)] [[INSPIRE](#)].
- [22] P. Coloma, B.A. Dobrescu, C. Frugiuele and R. Harnik, *Dark matter beams at LBNF*, *JHEP* **04** (2016) 047 [[arXiv:1512.03852](#)] [[INSPIRE](#)].
- [23] C. Frugiuele, *Probing sub-GeV dark sectors via high energy proton beams at LBNF/DUNE and MiniBooNE*, *Phys. Rev. D* **96** (2017) 015029 [[arXiv:1701.05464](#)] [[INSPIRE](#)].
- [24] P. deNiverville and C. Frugiuele, *Hunting sub-GeV dark matter with the NOvA near detector*, *Phys. Rev. D* **99** (2019) 051701 [[arXiv:1807.06501](#)] [[INSPIRE](#)].
- [25] G. Magill, R. Plestid, M. Pospelov and Y.-D. Tsai, *Millicharged particles in neutrino experiments*, *Phys. Rev. Lett.* **122** (2019) 071801 [[arXiv:1806.03310](#)] [[INSPIRE](#)].
- [26] MINIBOONE DM collaboration, *Dark matter search in nucleon, pion, and electron channels from a proton beam dump with MiniBooNE*, *Phys. Rev. D* **98** (2018) 112004 [[arXiv:1807.06137](#)] [[INSPIRE](#)].
- [27] D. Banerjee et al., *Dark matter search in missing energy events with NA64*, *Phys. Rev. Lett.* **123** (2019) 121801 [[arXiv:1906.00176](#)] [[INSPIRE](#)].
- [28] LDMX collaboration, *Light Dark Matter eXperiment (LDMX)*, [arXiv:1808.05219](#) [[INSPIRE](#)].
- [29] B. Batell, A. Freitas, A. Ismail and D. McKeen, *Flavor-specific scalar mediators*, *Phys. Rev. D* **98** (2018) 055026 [[arXiv:1712.10022](#)] [[INSPIRE](#)].
- [30] B. Holdom, *Two U(1)'s and  $\epsilon$  charge shifts*, *Phys. Lett. B* **166** (1986) 196 [[INSPIRE](#)].
- [31] T. Lin, H.-B. Yu and K.M. Zurek, *On symmetric and asymmetric light dark matter*, *Phys. Rev. D* **85** (2012) 063503 [[arXiv:1111.0293](#)] [[INSPIRE](#)].

- [32] PLANCK collaboration, *Planck 2015 results. XIII. Cosmological parameters*, *Astron. Astrophys.* **594** (2016) A13 [[arXiv:1502.01589](#)] [[INSPIRE](#)].
- [33] P.F. Depta, M. Hufnagel, K. Schmidt-Hoberg and S. Wild, *BBN constraints on the annihilation of MeV-scale dark matter*, *JCAP* **04** (2019) 029 [[arXiv:1901.06944](#)] [[INSPIRE](#)].
- [34] E. Izaguirre, G. Krnjaic, P. Schuster and N. Toro, *Analyzing the discovery potential for light dark matter*, *Phys. Rev. Lett.* **115** (2015) 251301 [[arXiv:1505.00011](#)] [[INSPIRE](#)].
- [35] SHiP collaboration, *A facility to Search for Hidden Particles (SHiP) at the CERN SPS*, [arXiv:1504.04956](#) [[INSPIRE](#)].
- [36] SHiP collaboration, *The experimental facility for the Search for Hidden Particles at the CERN SPS*, 2019 *JINST* **14** P03025 [[arXiv:1810.06880](#)] [[INSPIRE](#)].
- [37] SHiP collaboration, *Sensitivity of the SHiP experiment to heavy neutral leptons*, *JHEP* **04** (2019) 077 [[arXiv:1811.00930](#)] [[INSPIRE](#)].
- [38] SHiP collaboration, *Fairship*, <https://github.com/ShipSoft/FairShip>.
- [39] SHiP collaboration, *The active muon shield in the SHiP experiment*, 2017 *JINST* **12** P05011 [[arXiv:1703.03612](#)] [[INSPIRE](#)].
- [40] SHiP collaboration, *The magnet of the scattering and neutrino detector for the SHiP experiment at CERN*, 2020 *JINST* **15** P01027 [[arXiv:1910.02952](#)] [[INSPIRE](#)].
- [41] R. Acquafredda et al., *The OPERA experiment in the CERN to Gran Sasso neutrino beam*, 2009 *JINST* **4** P04018 [[INSPIRE](#)].
- [42] OPERA collaboration, *Discovery of  $\tau$  neutrino appearance in the CNGS neutrino beam with the OPERA experiment*, *Phys. Rev. Lett.* **115** (2015) 121802 [[arXiv:1507.01417](#)] [[INSPIRE](#)].
- [43] OPERA collaboration, *Final results of the OPERA experiment on  $\nu_\tau$  appearance in the CNGS neutrino beam*, *Phys. Rev. Lett.* **120** (2018) 211801 [Erratum *ibid.* **121** (2018) 139901] [[arXiv:1804.04912](#)] [[INSPIRE](#)].
- [44] OPERA collaboration, *Final results of the search for  $\nu_\mu \rightarrow \nu_e$  oscillations with the OPERA detector in the CNGS beam*, *JHEP* **06** (2018) 151 [[arXiv:1803.11400](#)] [[INSPIRE](#)].
- [45] LHCb collaboration, *SciFi — a large scintillating fibre tracker for LHCb*, *Nucl. Instrum. Meth. A* **845** (2017) 481 [[INSPIRE](#)].
- [46] GEANT4 collaboration, *GEANT4 — a simulation toolkit*, *Nucl. Instrum. Meth. A* **506** (2003) 250 [[INSPIRE](#)].
- [47] T. Sjöstrand et al., *An introduction to PYTHIA 8.2*, *Comput. Phys. Commun.* **191** (2015) 159 [[arXiv:1410.3012](#)] [[INSPIRE](#)].
- [48] T. Sjöstrand, S. Mrenna and P.Z. Skands, *PYTHIA 6.4 physics and manual*, *JHEP* **05** (2006) 026 [[hep-ph/0603175](#)] [[INSPIRE](#)].
- [49] C. Andreopoulos et al., *The GENIE neutrino Monte Carlo generator*, *Nucl. Instrum. Meth. A* **614** (2010) 87 [[arXiv:0905.2517](#)] [[INSPIRE](#)].
- [50] J. Blümlein and J. Brunner, *New exclusion limits on dark gauge forces from proton Bremsstrahlung in beam-dump data*, *Phys. Lett. B* **731** (2014) 320 [[arXiv:1311.3870](#)] [[INSPIRE](#)].
- [51] A. Celentano, L. Darmé, L. Marsicano and E. Nardi, *New production channels for light dark matter in hadronic showers*, *Phys. Rev. D* **102** (2020) 075026 [[arXiv:2006.09419](#)] [[INSPIRE](#)].

- [52] L. Buonocore, C. Frugiuele, F. Maltoni, O. Mattelaer and F. Tramontano, *Event generation for beam dump experiments*, *JHEP* **05** (2019) 028 [[arXiv:1812.06771](#)] [[INSPIRE](#)].
- [53] Y. Kahn, G. Krnjaic, J. Thaler and M. Toups, *DAE $\delta$ ALUS and dark matter detection*, *Phys. Rev. D* **91** (2015) 055006 [[arXiv:1411.1055](#)] [[INSPIRE](#)].
- [54] S. Gardner, R.J. Holt and A.S. Tadepalli, *New prospects in fixed target searches for dark forces with the SeaQuest experiment at Fermilab*, *Phys. Rev. D* **93** (2016) 115015 [[arXiv:1509.00050](#)] [[INSPIRE](#)].
- [55] M. Bonesini, A. Marchionni, F. Pietropaolo and T. Tabarelli de Fatis, *On particle production for high-energy neutrino beams*, *Eur. Phys. J. C* **20** (2001) 13 [[hep-ph/0101163](#)] [[INSPIRE](#)].
- [56] B. Döbrich, J. Jaeckel and T. Spadaro, *Light in the beam dump — ALP production from decay photons in proton beam-dumps*, *JHEP* **05** (2019) 213 [*Erratum ibid.* **10** (2020) 046] [[arXiv:1904.02091](#)] [[INSPIRE](#)].
- [57] SHiP collaboration, *Heavy flavour cascade production in a beam dump*, CERN-SHiP-NOTE-2015-009, (2015).
- [58] SHiP collaboration, *Measurement of the muon flux for the SHiP experiment*, [arXiv:2001.04784](#) [[INSPIRE](#)].
- [59] L. Buonocore, C. Frugiuele and P. deNiverville, *Hunt for sub-GeV dark matter at neutrino facilities: a survey of past and present experiments*, *Phys. Rev. D* **102** (2020) 035006 [[arXiv:1912.09346](#)] [[INSPIRE](#)].
- [60] E. Fermi, *On the theory of the impact between atoms and electrically charged particles*, *Z. Phys.* **29** (1924) 315 [[INSPIRE](#)].
- [61] E.J. Williams, *Nature of the high-energy particles of penetrating radiation and status of ionization and radiation formulae*, *Phys. Rev.* **45** (1934) 729 [[INSPIRE](#)].
- [62] C.F. von Weizsäcker, *Radiation emitted in collisions of very fast electrons*, *Z. Phys.* **88** (1934) 612 [[INSPIRE](#)].
- [63] P. deNiverville, C.-Y. Chen, M. Pospelov and A. Ritz, *Light dark matter in neutrino beams: production modelling and scattering signatures at MiniBooNE, T2K and SHiP*, *Phys. Rev. D* **95** (2017) 035006 [[arXiv:1609.01770](#)] [[INSPIRE](#)].
- [64] A. Faessler, M.I. Krivoruchenko and B.V. Martemyanov, *Once more on electromagnetic form factors of nucleons in extended vector meson dominance model*, *Phys. Rev. C* **82** (2010) 038201 [[arXiv:0910.5589](#)] [[INSPIRE](#)].
- [65] D.E. Morrissey and A.P. Spray, *New limits on light hidden sectors from fixed-target experiments*, *JHEP* **06** (2014) 083 [[arXiv:1402.4817](#)] [[INSPIRE](#)].
- [66] D. Gorbunov, A. Makarov and I. Timiryasov, *Decaying light particles in the SHiP experiment: signal rate estimates for hidden photons*, *Phys. Rev. D* **91** (2015) 035027 [[arXiv:1411.4007](#)] [[INSPIRE](#)].
- [67] A. Berlin, S. Gori, P. Schuster and N. Toro, *Dark sectors at the Fermilab SeaQuest experiment*, *Phys. Rev. D* **98** (2018) 035011 [[arXiv:1804.00661](#)] [[INSPIRE](#)].
- [68] J. Alwall, M. Herquet, F. Maltoni, O. Mattelaer and T. Stelzer, *MadGraph 5: going beyond*, *JHEP* **06** (2011) 128 [[arXiv:1106.0522](#)] [[INSPIRE](#)].
- [69] R.D. Ball et al., *Parton distributions with LHC data*, *Nucl. Phys. B* **867** (2013) 244 [[arXiv:1207.1303](#)] [[INSPIRE](#)].

- [70] NNPDF collaboration, *Parton distributions with QED corrections*, *Nucl. Phys. B* **877** (2013) 290 [[arXiv:1308.0598](#)] [[INSPIRE](#)].
- [71] S. Alekhin et al., *A facility to Search for Hidden Particles at the CERN SPS: the SHiP physics case*, *Rept. Prog. Phys.* **79** (2016) 124201 [[arXiv:1504.04855](#)] [[INSPIRE](#)].
- [72] PARTICLE DATA GROUP collaboration, *Review of particle physics*, *Phys. Rev. D* **98** (2018) 030001 [[INSPIRE](#)].
- [73] A. Alexandrov et al., *Improving the detection efficiency in nuclear emulsion trackers*, *Nucl. Instrum. Meth. A* **776** (2015) 45 [[INSPIRE](#)].
- [74] OPERA collaboration, *New results on  $\nu_\mu \rightarrow \nu_\tau$  appearance with the OPERA experiment in the CNGS beam*, *JHEP* **11** (2013) 036 [Erratum *ibid.* **04** (2014) 014] [[arXiv:1308.2553](#)] [[INSPIRE](#)].
- [75] NOMAD collaboration, *A precise measurement of the muon neutrino-nucleon inclusive charged current cross-section off an isoscalar target in the energy range  $2.5 < E_\nu < 40$  GeV by NOMAD*, *Phys. Lett. B* **660** (2008) 19 [[arXiv:0711.1183](#)] [[INSPIRE](#)].
- [76] MINIBOONE collaboration, *Measurement of neutrino-induced charged-current charged pion production cross sections on mineral oil at  $E_\nu \sim 1$  GeV*, *Phys. Rev. D* **83** (2011) 052007 [[arXiv:1011.3572](#)] [[INSPIRE](#)].
- [77] NOMAD collaboration, *A study of quasi-elastic muon neutrino and antineutrino scattering in the NOMAD experiment*, *Eur. Phys. J. C* **63** (2009) 355 [[arXiv:0812.4543](#)] [[INSPIRE](#)].
- [78] J.A. Formaggio and G.P. Zeller, *From eV to EeV: neutrino cross sections across energy scales*, *Rev. Mod. Phys.* **84** (2012) 1307 [[arXiv:1305.7513](#)] [[INSPIRE](#)].
- [79] M. Duerr, T. Ferber, C. Hearty, F. Kahlhoefer, K. Schmidt-Hoberg and P. Tunney, *Invisible and displaced dark matter signatures at Belle II*, *JHEP* **02** (2020) 039 [[arXiv:1911.03176](#)] [[INSPIRE](#)].
- [80] R. Alemany et al., *Summary report of physics beyond colliders at CERN*, [arXiv:1902.00260](#) [[INSPIRE](#)].



# Sensitivity of the SHiP experiment to dark photons decaying to a pair of charged particles

SHiP Collaboration\*

Received: 11 November 2020 / Accepted: 10 May 2021 / Published online: 25 May 2021  
© The Author(s) 2021

**Abstract** Dark photons are hypothetical massive vector particles that could mix with ordinary photons. The simplest theoretical model is fully characterised by only two parameters: the mass of the dark photon  $m_{\gamma_D}$  and its mixing parameter with the photon,  $\varepsilon$ . The sensitivity of the SHiP detector is reviewed for dark photons in the mass range between 0.002 and 10 GeV. Different production mechanisms are simulated, with the dark photons decaying to pairs of visible fermions, including both leptons and quarks. Exclusion contours are presented and compared with those of past experiments. The SHiP detector is expected to have a unique sensitivity for  $m_{\gamma_D}$  ranging between 0.8 and  $3.3^{+0.2}_{-0.5}$  GeV, and  $\varepsilon^2$  ranging between  $10^{-11}$  and  $10^{-17}$ .

## 1 Introduction

The CERN beam facility located near Geneva, Switzerland, comprises several particle accelerators among which the Super Proton Synchrotron (SPS) and the Large Hadron Collider (LHC) [1]. The SPS is an essential part of the accelerator chain delivering 400 GeV proton beams to the LHC but also to fixed-target experiments. The LHC is planned to be upgraded into a high-luminosity machine starting operation around 2026 with the HL-LHC program [2]. In parallel to the high-energy frontier probed by the LHC, a complementary way of exploring the parameter space of potential new physics is through the “intensity frontier”. The SPS physics programme is hence proposed to be further extended via the construction of a beam dump facility (BDF) [3]. The BDF foresees the full exploitation of the SPS accelerator, which with its present performance could allow the delivery of up to  $4 \times 10^{19}$  protons on target per year, while respecting the beam requirements of the HL-LHC and maintaining the operation of the existing SPS beam facilities.

By probing lower-energy scenarios with high-intensity beams, the aim is to identify whether new physics could be

hidden from sight due to weak connections through portals instead of direct interactions with the known particles, with the new particles belonging to a hidden sector. The simplest renormalisable extensions of the standard model (SM) are possible through three types of portals [4, 5], involving either a scalar (e.g. dark Higgs boson [6, 7]), a vector (e.g. dark photon [8, 9]) or fermions (e.g. heavy neutral leptons [10]). The LHC experiments have already derived strong constraints on short-lived high-mass mediators [11–14]. Scenarios with long-lived mediators with relatively low masses however remain largely unexplored. The SHiP (Search for Hidden Particles) experiment [15] has been proposed in 2013 [16] and is designed to look for particles which would decay in the range 50–120 m from their production vertices. The sensitivity of the SHiP detector to heavy neutral leptons has been investigated in Ref. [17]. This article is dedicated to studying the sensitivity of the SHiP detector to dark photons.

After describing briefly the SHiP detector and its simulation in Sect. 2, the model considered for the dark photon production and decay is reviewed in Sect. 3. The sensitivity of the SHiP detector in the minimal dark photon model with decays to charged particles is given in Sect. 4 for the three production modes studied. Finally Sect. 5 provides a conclusion.

## 2 The SHiP detector and simulation

SHiP [15] is a new general purpose fixed-target experiment intended to exploit the proposed BDF to search for particles present in hidden portal models. The 400 GeV proton beam extracted from the SPS will be dumped on a high density target with the aim of accumulating  $2 \times 10^{20}$  protons on target during 5 years of operation. A dedicated detector, based on a long vacuum tank followed by a spectrometer and particle identification detectors, will allow probing a variety of models with light long-lived exotic particles and masses below  $\mathcal{O}(10)$  GeV. A critical component of SHiP is the muon shield, which deflects the high flux of muons

\* e-mail: [a.magnan@imperial.ac.uk](mailto:a.magnan@imperial.ac.uk)



**Fig. 1** Positions of the vessel and tracking stations along the beam axis ( $z$ ). The vessel dimensions  $\delta x_{\text{phys}}$  and  $\delta y_{\text{phys}}$  represent the upstream and downstream physics acceptance in the plane transverse to the beam axis

*SHiP Spectrometer Tracker*

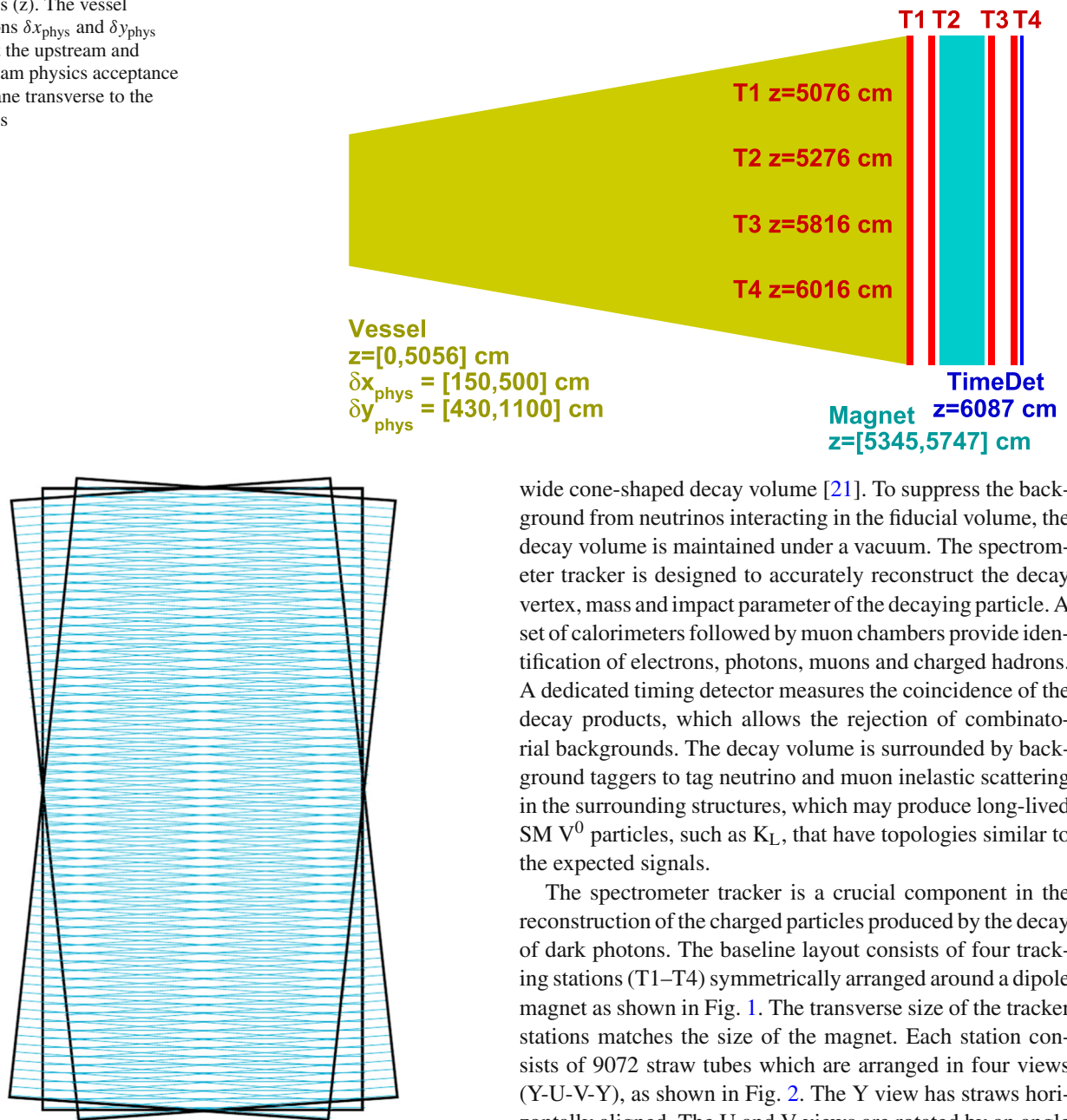


**Fig. 2** Schematic drawing of the three “views” that compose each straw chamber

produced in the target [18, 19], that would represent a serious background in the search for hidden-sector particles. The detector is designed to fully reconstruct the exclusive decays of hidden particles and to reject the background down to below 0.1 events in the sample of  $2 \times 10^{20}$  protons on target [20].

The detector consists of a large magnetic spectrometer located downstream of a 50 m-long and up to  $5 \times 11$  m-

wide cone-shaped decay volume [21]. To suppress the background from neutrinos interacting in the fiducial volume, the decay volume is maintained under a vacuum. The spectrometer tracker is designed to accurately reconstruct the decay vertex, mass and impact parameter of the decaying particle. A set of calorimeters followed by muon chambers provide identification of electrons, photons, muons and charged hadrons. A dedicated timing detector measures the coincidence of the decay products, which allows the rejection of combinatorial backgrounds. The decay volume is surrounded by background taggers to tag neutrino and muon inelastic scattering in the surrounding structures, which may produce long-lived SM  $V^0$  particles, such as  $K_L$ , that have topologies similar to the expected signals.

The spectrometer tracker is a crucial component in the reconstruction of the charged particles produced by the decay of dark photons. The baseline layout consists of four tracking stations (T1–T4) symmetrically arranged around a dipole magnet as shown in Fig. 1. The transverse size of the tracker stations matches the size of the magnet. Each station consists of 9072 straw tubes which are arranged in four views (Y-U-V-Y), as shown in Fig. 2. The Y view has straws horizontally aligned. The U and V views are rotated by an angle of  $\theta_{\text{stereo}} = \pm 5^\circ$ . The x coordinate is hence measured with an accuracy of  $1/\sin(\theta_{\text{stereo}})$ , directly impacting the measurement of the decay vertex, of the opening angle of the daughter particles (which enters the invariant mass), and of the impact parameter at the production target. In order to provide good spatial resolution and minimise the contribution from multiple scattering, the straw tubes are made of thin polyethylene terephthalate (PET). More detail about the initial design of the straw detector can be found in Refs. [20, 22]. The pattern recognition algorithms applied to the hits on the straw spec-

trometer are described in Ref. [23], and the algorithms for particle identification are presented in Ref. [24].

In the simulation, proton fixed-target collisions are generated by PYTHIA 8.2 [25], inelastic neutrino interactions by GENIE [26] and inelastic muon interactions by PYTHIA 6 [27]. The heavy-flavour cascade production is also taken into account [28]. The SHiP detector response is simulated in the GEANT4 [29] framework. The simulation is done within FairShip, which is based on the FairRoot framework [30].

### 3 Dark photon production and decay

The minimal dark photon model contains an additional  $\mathcal{U}(1)$  gauge group to the SM,  $A'_{\mu}$ , whose vector gauge boson is called the dark photon  $\gamma^D$ . A kinetic mixing term between the dark photon with field strength  $F'_{\mu\nu}$  and the SM  $\mathcal{U}(1)$  gauge bosons with field strength  $F_Y^{\mu\nu}$  is allowed [8], with a reduced strength parameterised by a coupling  $\varepsilon$ , also called the kinetic mixing parameter. The corresponding terms in the Lagrangian can hence be written as:

$$\mathcal{L} = \mathcal{L}_{\text{SM}} - \frac{1}{4}(F'_{\mu\nu})^2 - \frac{\varepsilon}{2}F'_{\mu\nu}F_Y^{\mu\nu} + \frac{1}{2}m_{\gamma^D}^2(A'_{\mu})^2. \quad (1)$$

In its simplest form, the knowledge of the mass of the dark photon  $m_{\gamma^D}$  and the kinetic mixing parameter  $\varepsilon$  is enough to characterise the model and calculate production cross section and decay properties.

Three different mechanisms are possible for the production of such new particles at a fixed-target experiment. All of them are studied in this paper.

The initial 400 GeV proton beam interacts with the nucleons from the target material, producing mesons. For meson decay channels involving photons, the photon can mix with the dark photon, as described in Sect. 3.1. This mode is opened only for dark photon masses below 0.9 GeV, as for mesons with masses above this threshold the main decay channels do not involve photons anymore.

The proton–nucleon interaction could also lead to the radiation of a dark photon via a bremsstrahlung process, as described in Sect. 3.2. This mode is heavily suppressed when the dark photon mass exceeds that of the proton, and remains relevant only for masses below  $\simeq 2$  GeV.

The third production mode is via a Drell–Yan like process in Quantum Chromodynamic (QCD), i.e. quark–antiquark annihilation into the dark photon, as described in Sect. 3.3. This process is relevant for dark photon masses in the range  $\mathcal{O}(1\text{--}10)$  GeV. Using the parton model with a factorisation scale below the GeV scale cannot give sensible results, as expected from the range of validity of parton distribution functions, and hence this region of the parameter space has not been considered for this production mechanism.

**Table 1** Meson decay channels considered for the  $\gamma^D$  production. The last column shows the average number of mesons expected per proton–proton interaction

$m_{\gamma^D}$ (GeV)	Meson	$\text{Br}(\gamma + X)$ [25]	$n_{\text{meson}} / \text{pp}$
0–0.135	$\pi^0 \rightarrow \gamma^D \gamma$	0.98799	$6.147 \pm 0.003$
0–0.548	$\eta \rightarrow \gamma^D \gamma$	0.3931181	$0.703 \pm 0.008$
0–0.648	$\omega \rightarrow \gamma^D \pi^0$	0.0834941	$0.825 \pm 0.009$
0–0.958	$\eta' \rightarrow \gamma^D \gamma$	0.0219297	$0.079 \pm 0.003$

In this paper, the assumption is made that only the initial proton interacts. In reality, similar interactions could also happen with protons or mesons coming from cascade decays happening in the target material. For electromagnetic processes (electron bremsstrahlung of photons mixing with the dark photon), it has been shown in Ref. [31] that their contribution is negligible compared to the main production mechanisms described above. The study however remains to be done for hadronic interactions in the cascade decays, and will be the subject of future work. Hence the expectations presented here are conservative and the sensitivity could be improved in the future when this contribution is added.

As a final state, the dark photon decay to pairs of leptons or quarks as described in Sect. 3.4 is considered.

#### 3.1 Production in meson decay

The PYTHIA 8.2 [25] Monte Carlo (MC) generator is used to produce inclusive QCD events in proton–proton (p–p) collisions, through all available non-diffractive processes. Diffractive processes are less important in meson production, expected to decrease the number of mesons produced by about 15% according to PYTHIA simulation. Because the diffractive processes also suffer from larger theoretical uncertainties, they have not been considered. The leading-order (LO) NNPDF2.3 PDF set [32] has been used with the default Monash 2013 tune [33], and the strong coupling constant set to  $\alpha_s = 0.13$ . One proton beam momentum is set to 400 GeV and the other to 0 (protons or neutrons from the fixed-target material). The mesons that are produced are then used as sources of dark photons, if they have decay channels to photons and their decay to a dark photon of mass  $m_{\gamma^D}$  is kinematically allowed. Four processes are found dominant (with other contributions neglected) and shown in Table 1. The decay tables of these four mesons are reset to having only one decay channel allowed with 100% branching ratio ( $\pi^0 \rightarrow \gamma \gamma$ ,  $\eta \rightarrow \gamma \gamma$ ,  $\omega \rightarrow \pi^0 \gamma$ ,  $\eta' \rightarrow \gamma \gamma$ ). All relevant processes are then added together.

The branching ratios of the mesons to these new decay channels are functions of the  $m_{\gamma^D}$ , the kinetic mixing parameter  $\varepsilon$ , the meson type, pseudo-scalar or vector, and the meson mass [4, 31, 34]. For pseudo-scalar mesons  $\mathcal{P}$  ( $\pi^0$ ,  $\eta^0$  and  $\eta'$ ),

the branching ratio to  $\gamma^D \gamma$  is given by:

$$\text{Br}(\mathcal{P} \rightarrow \gamma^D \gamma) \simeq 2\varepsilon^2 \left(1 - \frac{m_{\gamma^D}^2}{m_{\mathcal{P}}^2}\right)^3 \text{Br}(\mathcal{P} \rightarrow \gamma \gamma). \quad (2)$$

For vector mesons  $\mathcal{V}(\omega)$ , the branching ratio to a  $\gamma^D$  and a pseudo-scalar meson  $\mathcal{P}$  is given by:

$$\text{Br}(\mathcal{V} \rightarrow \mathcal{P} \gamma^D) \simeq \varepsilon^2 \times \text{Br}(\mathcal{V} \rightarrow \mathcal{P} \gamma) \times \frac{[(m_{\gamma^D}^2 - (m_{\mathcal{V}} + m_{\mathcal{P}})^2)(m_{\gamma^D}^2 - (m_{\mathcal{V}} - m_{\mathcal{P}})^2)]^{3/2}}{(m_{\mathcal{V}}^2 - m_{\mathcal{P}}^2)^3}. \quad (3)$$

For the branching ratios of the mesons to  $\gamma \gamma$  or  $\gamma \pi^0$ , the same values as implemented in PYTHIA 8.2 are used. The average number of mesons produced per pp interaction is shown for each meson type in the last column of Table 1, from non-diffractive pp collisions simulated with PYTHIA 8.2 [25], with its associated statistical uncertainty. For inclusive pp collisions (adding also elastic and diffractive processes), the average meson multiplicities predicted by Pythia are found to be in good agreement with existing measurements [35].

The cross section for the production of dark photons via meson decays produced in non-diffractive primary interactions of the proton beam is then computed as:

$$\sigma_{\text{meson}} = \sigma_{\text{SHiP}}^{\text{inel}} \times \sum_{\text{mesons}} \Theta(m_{\text{meson}} - m_{\gamma^D}) \times n_{\text{meson}}/\text{pp} \times \text{Br}(\text{meson} \rightarrow \gamma^D + X), \quad (4)$$

using Eqs. (2) and (3) and values reported in Table 1. The  $\Theta(m_{\text{meson}} - m_{\gamma^D})$  factor is a step function ensuring that only the mesons in the accessible mass range are considered. To take into account the fact that the nucleon is bound in the target, and not free as assumed by PYTHIA in our simulation of this process, the total normalisation is taken using the inelastic proton–nucleon cross section corresponding to the SHiP target,  $\sigma_{\text{SHiP}}^{\text{inel}}$  (see Sect. 4). In terms of the approximate scaling for hadron-nucleus interactions of  $\sigma_{pA}/\sigma_{pp} \simeq A^\alpha$ , this corresponds to  $\alpha \simeq 0.71$ . The cross section is proportional to  $\varepsilon^2$ , from the dependency of  $\text{Br}(\text{meson} \rightarrow \gamma^D + X)$  in Eqs. (2) and (3).

### 3.2 Production in proton bremsstrahlung

In analogy with ordinary photon bremsstrahlung of scattering protons, the same process is used for dark photon production by scattering of the incoming 400 GeV proton beam on the target protons. Following Refs. [31,36], the differential  $\gamma^D$  production rate can be expressed as:

$$\frac{d^2 N}{dz dp_{\perp}^2} = \frac{\sigma_{pp}(s')}{\sigma_{pp}(s)} w_{ba}(z, p_{\perp}^2), \quad (5)$$

$$w_{ba}(z, p_{\perp}^2) = \frac{\varepsilon^2 \alpha_{\text{QED}}}{2\pi H} \left[ \frac{1 + (1 - z)^2}{z} \right]$$

$$-2z(1 - z) \left( \frac{2m_p^2 + m_{\gamma^D}^2}{H} - z^2 \frac{2m_p^4}{H^2} \right) + 2z(1 - z) (1 + (1 - z)^2) \frac{m_p^2 m_{\gamma^D}^2}{H^2} + 2z(1 - z)^2 \frac{m_{\gamma^D}^4}{H^2} \Big],$$

where  $\sigma_{pp}(s/s')$  are the total proton–proton cross sections evaluated for the incoming/outgoing proton energy scales,  $m_p$  is the proton mass (set to  $m_p = 0.938272$  GeV [37]),  $P$  and  $E_p$  are the proton beam initial momentum and energy respectively,  $p$  and  $E_{\gamma^D}$  are the momentum and energy of the generated dark photon respectively,  $p_{\perp}$  and  $p_{\parallel}$  are the components of the  $\gamma^D$  momentum orthogonal and parallel to the direction of the incoming proton respectively,  $z$  is the fraction of the proton momentum carried away by the dark photon in the beam direction,  $\alpha_{\text{QED}}$  is the fine structure constant of Quantum Electro Dynamic (QED), set to  $1/137$ ,  $s' = 2m_p(E_p - E_{\gamma^D})$ ,  $s = 2m_p E_p$  and  $H(p_{\perp}^2, z) = p_{\perp}^2 + (1 - z)m_{\gamma^D}^2 + z^2 m_p^2$ .

In this formulation, the nuclear effects from having bound rather than free protons in the target material cancel in the ratio  $\frac{\sigma_{pp}(s')}{\sigma_{pp}(s)}$ .

However, the above formula does not take into account possible QCD contributions when the mass of the emitted  $\gamma^D$  exceeds that of the proton, and the bremsstrahlung process starts to depend on the internal partons. It does not take into account the possibility of enhancement in the cross section due to nuclear resonances in the so-called vector meson dominance (VMD) model either. In consequence, two independent approaches are followed, leading to two different estimates of the final cross section.

In the first approach, when the mass of the dark photon is larger than 1 GeV, the standard dipole form factor [38] is included in the proton- $\gamma^D$  vertex, leading to a penalty factor that models the strong suppression of the bremsstrahlung production:

$$\text{penalty}(m_{\gamma^D}) = \left( \frac{m_{\gamma^D}^2}{0.71 \text{ GeV}^2} \right)^{-4} \quad \text{for } m_{\gamma^D}^2 > 0.71 \text{ GeV}^2. \quad (6)$$

According to Ref. [31], this form factor is conservative and probably underestimates the rates. The direct parton–parton QCD production will dominate above 1.5 GeV and is described in Sect. 3.3.

In the second approach, the VMD form factor taken from Refs. [39,40] is used, leading to an enhancement of the cross section by a factor  $10^4$  around the  $\rho$  and  $\omega$  meson mass of 0.8 GeV, and still up to a factor 10 in the tail due to also con-

sidering resonances of masses 1.25 and 1.45 GeV following the description in Ref. [40].

The total p-p cross section  $\sigma_{pp}(s)$  is taken from experimental data:

$$\sigma_{pp}(s) = Z + B \log^2\left(\frac{s}{s_0}\right) + Y_1 \left(\frac{s_1}{s}\right)^{\eta_1} - Y_2 \left(\frac{s_1}{s}\right)^{\eta_2}, \quad (7)$$

where  $Z = 35.45$  mb,  $B = 0.308$  mb,  $Y_1 = 42.53$  mb,  $Y_2 = 33.34$  mb,  $\sqrt{s_0} = 5.38$  GeV,  $\sqrt{s_1} = 1$  GeV,  $\eta_1 = 0.458$  and  $\eta_2 = 0.545$  [41]. This formulation has been compared to the latest parameterisation from Ref. [37], and found to be almost identical for the momentum range of interest here.

Reformulating Eq. (5) as a function of the  $\gamma^D$  angle  $\theta$  to the beam line and its total momentum  $p$ , a two-dimensional normalised probability density function (PDF)  $f(p, \theta)$  is extracted, and shown in Fig. 3 for two representative choices of  $m_{\gamma^D}$ . Note that due to the simple dependency of the production rate scaling as  $\varepsilon^2$ , the normalised PDF is independent of  $\varepsilon$ . The dark photons are generated with maximum probability on each side of the beam axis ( $\theta$  close to 0) with a factor of 5 more chance to have  $p < 100$  GeV compared to  $p > 200$  GeV, for the low masses, and increased probability to have high momentum as the mass increases.

Events are generated using a PYTHIA 8 particle gun with the  $\gamma^D$  as particle, randomly choosing the  $\gamma^D(p, \theta)$  values according to the normalised 2D PDF  $f(p, \theta)$ , extracted for each  $m_{\gamma^D}$  point studied.

The integral of  $\frac{d^2N}{dpd\theta} \times \text{FF}$ , with FF the penalty dipole form factor or the VMD form factor, in the range of momenta and solid angle kinematically allowed, provides an estimate of the dark photon production rate per pp interaction through proton bremsstrahlung, scaling as  $\varepsilon^2$ . The production cross sections using the dipole form factor and VMD form factor methods are expressed by:

$$\sigma_{\text{pbrem}} = \sigma_{\text{SHiP}}^{\text{inel}} \times \int_{p_{\text{min}}}^{p_{\text{max}}} \int_{\theta=-\theta_{\text{max}}}^{\theta_{\text{max}}} \text{FF} \times \frac{d^2N}{dpd\theta} d\theta dp, \quad (8)$$

and shown in Fig. 4. The conditions of validity of the approximation used to derive Eq. (5) [42, 43] require a lower momentum bound for the  $\gamma^D$  at  $p_{\text{min}} = 0.1P_p$  [36], and an upper bound at  $p_{\text{max}} = 0.9P_p$ , as well as an upper bound on  $p_{\perp} < 4$  GeV, giving  $\theta_{\text{max}} \simeq 0.1$  rad.

### 3.3 Drell–Yan production

For production of the dark photon in parton–parton scattering, the generic implementation of a resonance that couples both to SM fermion pairs and hidden particles is used, as implemented in PYTHIA 8.2 under the ‘‘HiddenValley’’ Z’ model [44]. A cross-check has been done that similar kinematic distributions for the dark photons are found using

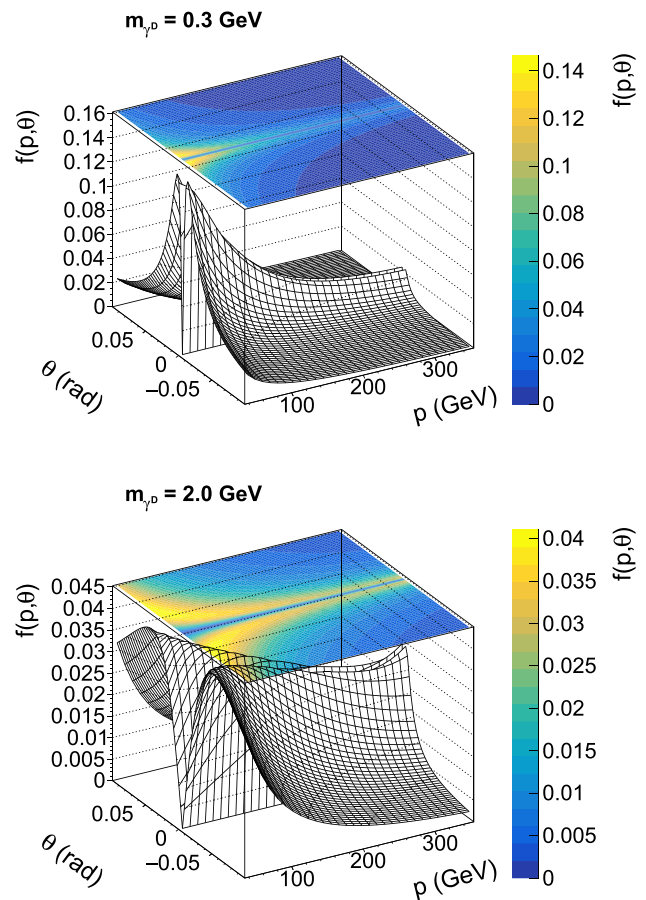


**Fig. 3** Normalised probability density function of producing a dark photon with angle  $\theta$  and momentum  $p$  through proton bremsstrahlung, for two representative examples of  $m_{\gamma^D}$ : 0.3 GeV (top) and 2 GeV (bottom)

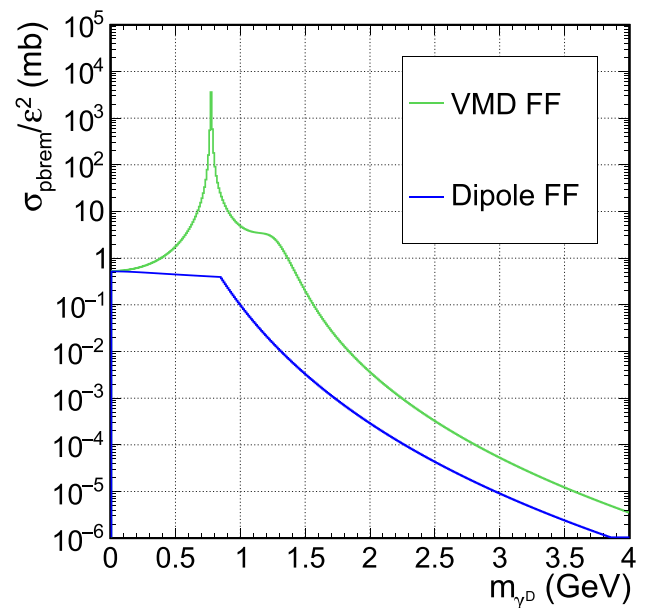


**Fig. 4** Proton bremsstrahlung production cross section as a function of  $m_{\gamma^D}$

another  $Z'$  implementation in PYTHIA from the “New Gauge Bosons” class of processes [45].

The dark photons are generated in the mass range  $1.4 < m_{\gamma^D} < 10$  GeV. Below 1.4 GeV one leaves the domain of perturbative QCD and the parton model cannot be used anymore.

The LO cross section given by PYTHIA when the new particle has the properties of the dark photon is shown in Fig. 5. The nuclear effects are neglected and the parton–parton cross section from PYTHIA is used without modification. Like for the meson and proton bremsstrahlung processes, it is found to scale as  $\varepsilon^2$ . The LO NNPDF2.3 PDF set [32] has been used with the default Monash 2013 tune [33], and the strong coupling constant set to  $\alpha_s = 0.13$ . An empirical function is extracted to parameterise the cross section (in mb) as a function of the  $\gamma^D$  mass (in GeV) in a continuous way, described in Eq. (9). The impact of several sources of theoretical uncertainties (PDF choice [46], QCD scales,  $\alpha_s$ ) are studied and shown in Fig. 5 (see also Sect. 4.4). The impact of nuclear effects is checked using the nuclear modification factors available in PYTHIA, with the most recent nuclear PDF set EPPS16 [47], using the two atomic masses ( $A = 84$  and 117) available around the SHiP target material one ( $A = 96$ ). Both give very similar results, with a cross section varying within  $\pm 6\%$  from the NNPDF2.3 proton PDF one, depending on the  $\gamma^D$  mass. The alternative generator Madgraph5\_aMC@NLO v2.7.2 [48] is also used to cross check the cross section calculation. The parameterisation of the width of the resonance, dependent on the branching ratios to fermion pairs, is a little different and explains the difference seen.

$$1.4 < m_{\gamma^D} \leq 3 \text{ GeV} : \sigma_{\text{QCD}} = \varepsilon^2 \times e^{-2.05488 - 1.96804 \times m_{\gamma^D}}, \tag{9}$$

$$m_{\gamma^D} > 3 \text{ GeV} : \sigma_{\text{QCD}} = \varepsilon^2 \times e^{-5.51532 - 0.830917 \times m_{\gamma^D}}.$$

Higher-order contributions to the process could lead to a sizable increase of the cross section at such low masses. Using the MATRIX v1.0.5 program [49–54], the ratio of next-to-next-to-leading-order (NNLO) over LO differential cross sections for standard Drell–Yan production at  $\sqrt{s} = 27.43$  GeV as a function of the dilepton invariant mass  $M_{\ell\ell}$  is found to be rather flat at  $1.7 \pm 0.17$  (stat) for  $M_{\ell\ell}$  between 1.4 and 5 GeV, increasing up to 2.2 at  $M_{\ell\ell} = 10$  GeV. The QCD scale uncertainties on the ratio are found to be  $^{+20\%}_{-11\%}$  in the range  $2 < M_{\ell\ell} < 5$  GeV increasing above  $\pm 30\%$  for  $M_{\ell\ell}$  above 10 GeV or below 2 GeV. The MSTW 2008 NNLO PDF set [55] has been used for all calculations. These calculations are also found to be in fair agreement (within 10%) with a study performed more specifically in proton-antiproton collisions, with a special interest for low dilepton masses and in particular for  $\sqrt{s} = 30$  GeV, from Ref. [56], and consider-

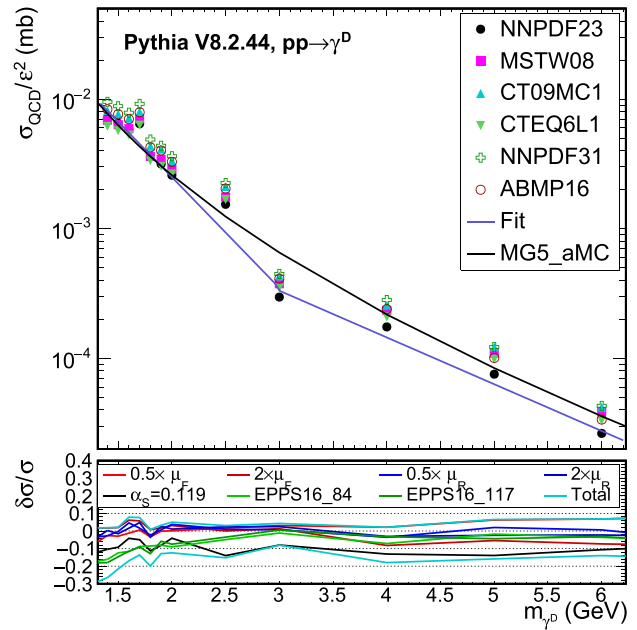


**Fig. 5** QCD production cross section at LO as a function of  $m_{\gamma^D}$ . The fit function is described in Eq. (9). The upper pad shows the impact of different PDF sets [55, 57–60]. The lower pad shows the relative uncertainties from several theoretical uncertainty sources on the cross section calculated by PYTHIA, and their sum in quadrature under “Total”

ing soft-gluon resummations at all orders. Given the lack of experimental data at these low masses and low  $\sqrt{s}$  to confirm the size of the expected correction and the impact from PDF and non-perturbative effects on the actual dark photon production, a final k-factor of  $1.7 \pm 0.7$  is applied to the LO PYTHIA cross section from Eq. (9).

The relative contribution from each process is shown in Fig. 6, as a function of  $m_{\gamma^D}$ , for the three production modes, in the two scenarios considered for the proton bremsstrahlung mode.

### 3.4 Dark photon decays

Except for the meson production mode, in which the new particle couples to the parent meson via mixing with the photon and hence cannot be a resonance from PYTHIA’s point-of-view, in QCD and proton bremsstrahlung the  $\gamma^D$  is implemented as a resonance. In all cases, the decay channels are implemented as follows.

The partial decay width of the dark photon into a lepton pair is given by [36]:

$$\Gamma(\gamma^D \rightarrow \ell^+ \ell^-) = \frac{1}{3} \alpha_{QED} m_{\gamma^D} \varepsilon^2 \sqrt{1 - \frac{4m_\ell^2}{m_{\gamma^D}^2}} \times \left( 1 + \frac{2m_\ell^2}{m_{\gamma^D}^2} \right), \tag{10}$$

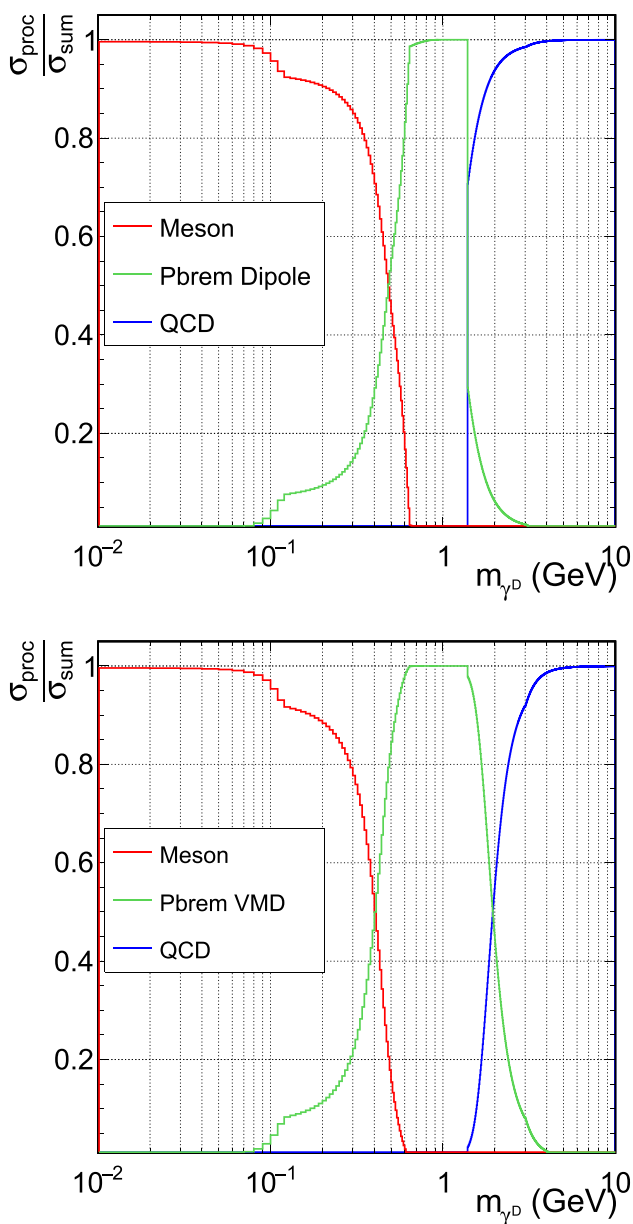


**Fig. 6** Relative contributions to the cross section as a function of  $m_{\gamma^D}$  for the three production modes studied, using the dipole form factor for proton bremsstrahlung (top) or the VMD form factor (bottom)

where  $m_\ell$  is the lepton mass, for electron, muon or tau leptons, if kinematically allowed. Following the approach used by the authors of Ref. [61], the partial decay width into quark pairs is computed as:

$$\Gamma(\gamma^D \rightarrow \text{hadrons}) = \Gamma(\gamma^D \rightarrow \mu^+\mu^-)R(m_{\gamma^D}), \quad (11)$$

where

$$R(\sqrt{s}) = \frac{\sigma(e^+e^- \rightarrow \text{hadrons})}{\sigma(e^+e^- \rightarrow \mu^+\mu^-)}, \quad (12)$$

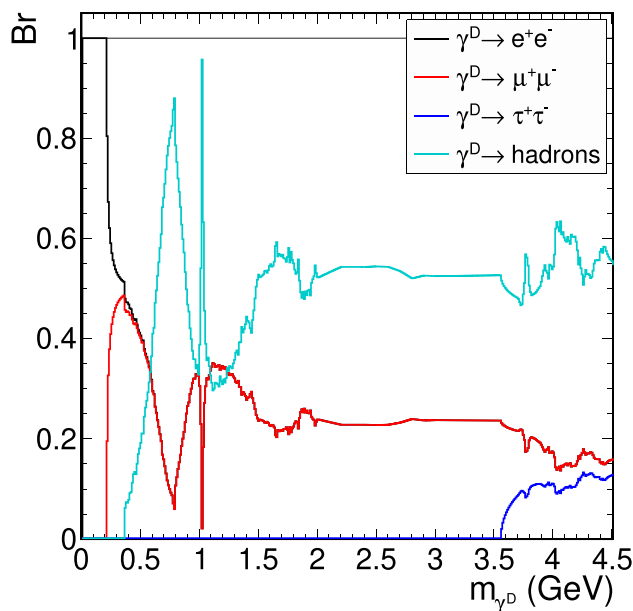


**Fig. 7** Branching ratio of the  $\gamma^D$  into pairs of leptons or quarks as a function of its mass

is the energy-dependent R-ratio quantifying the hadronic annihilation in  $e^+e^-$  collisions [62], tabulated from 0.3 to 10.29 GeV.

The lifetime of the  $\gamma^D$  is then naturally set to the inverse of its total width, summing all the kinematically-allowed channels for calculating the total width. It is proportional to  $1/\varepsilon^2$ . The branching ratios to individual channels are set to the ratio of the partial over total width, and are hence independent of  $\varepsilon$ . For separating the hadronic channels into the different quark-flavoured pairs allowed kinematically, the coupling is assumed to be proportional to the quark charge  $q$  as  $n_C \times q^2$  [63], with  $n_C = 3$  the number of coloured charges. When the  $\gamma^D$  is implemented as a resonance in PYTHIA, the decay goes explicitly through the pair of quarks, before hadronisation. Otherwise the hadrons are found as direct decay products of the  $\gamma^D$ .

The branching ratio of the  $\gamma^D$  into pairs of leptons or quarks is shown in Fig. 7 as a function of  $m_{\gamma^D}$ . The hadronic decays become available above the pion mass threshold. The expected lifetime of the  $\gamma^D$  as a function of its mass and  $\varepsilon$  mixing parameter is shown in Fig. 8.

### 4 SHiP sensitivity

In order to maximise the statistical power of the limited number of events produced with PYTHIA in the different production modes, the  $\gamma^D$  decay vertex position is randomly assigned to be inside the decay vessel of length  $L_{\text{Vessel}} = 50.760$  m, and the associated probability of this happening is given as a function of the  $\gamma^D$  four-momentum ( $p, E_{\gamma^D}$ ) and

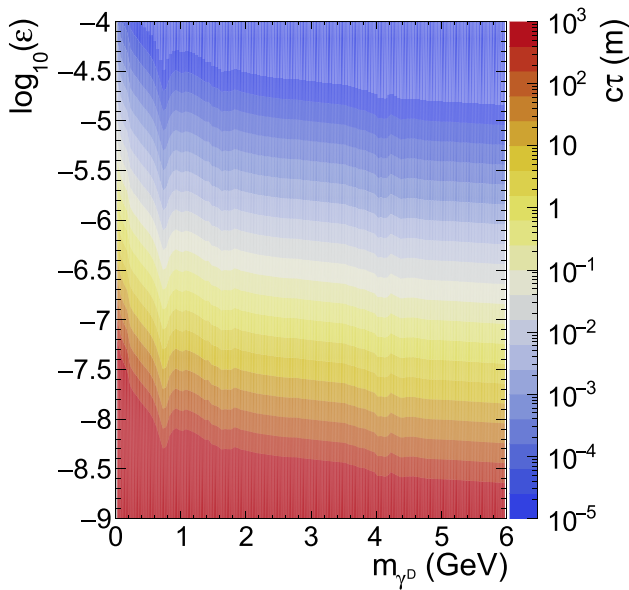


**Fig. 8** Expected lifetime of the dark photon as a function of its mass and of the kinetic mixing parameter  $\epsilon$

lifetime  $c\tau$ :

$$w_{\text{vtx}}(\ell) = e^{-\frac{\ell+L_0}{\beta \times \gamma \times c\tau}} \times \frac{L_{\text{Vessel}}}{\beta \times \gamma \times c\tau}, \quad (13)$$

with  $\gamma = E_{\gamma^D}/\sqrt{E_{\gamma^D}^2 - p^2}$ ,  $\beta = p/E_{\gamma^D}$ ,  $L_0$  is the distance from the target to the entrance of the decay vessel, and  $\ell$  is randomly distributed between 0 and  $L_{\text{Vessel}}$  with a flat prior.

The total event rate expected is then extracted from the cross sections  $\sigma_{\text{prod}}$  defined in Sect. 3, i.e. Eqs. (4), (8) and (9) for the meson, proton bremsstrahlung and QCD productions, respectively, normalising to the luminosity expected from the  $N = 2 \times 10^{20}$  proton-on-target events that will be collected by the end of the SHiP physics program. The expected rate is taking into account the detector acceptance and the efficiency to reconstruct the decay products in the SHiP detector,  $\mathcal{P}_{\text{vessel}}$  and  $\mathcal{P}_{\text{reco}}$  described in detail in Sects. 4.2 and 4.3, respectively, and following Eq. (14):

$$\mathcal{N}_{\gamma^D} = \sigma_{\text{prod}} \times \mathcal{L}_{\text{SHiP}} \times \text{Br}(\gamma^D \rightarrow \text{ch} + \text{ch}) \times \mathcal{P}_{\text{vessel}} \times \mathcal{P}_{\text{reco}}. \quad (14)$$

The SHiP luminosity is defined as:  $\mathcal{L}_{\text{SHiP}} = \frac{N}{\sigma_{\text{SHiP}}^{\text{inel}}}$ , using an inelastic proton–nucleon cross section of  $\sigma_{\text{SHiP}}^{\text{inel}} = 10.7 \text{ mb}$  [15], which directly corresponds to the SHiP target material (Molybdenum) nuclear interaction length and density.

The strategy of the analysis relies on identifying the decays of the  $\gamma^D$  into at least two charged particles,  $\gamma^D \rightarrow \text{ch} + \text{ch}$ . The reconstructed charged tracks must originate from a common vertex. These requirements are enough to ensure that almost no background event will survive the selection,

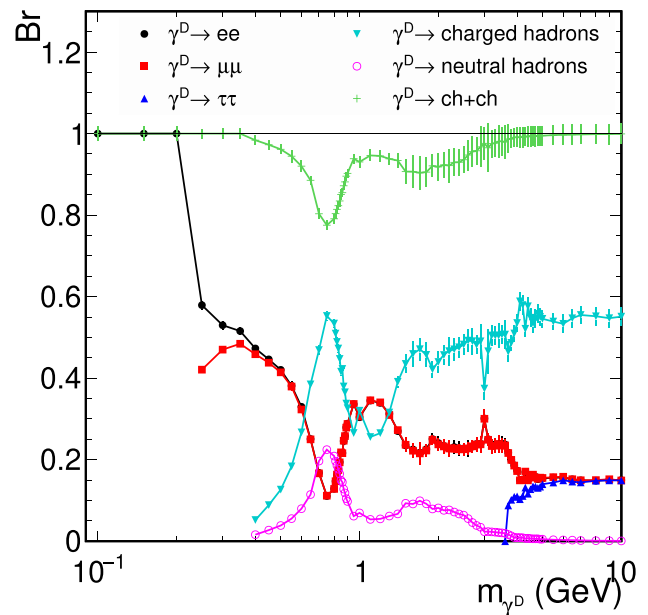


**Fig. 9** Branching ratio to the visible decay channels, as a function of  $m_{\gamma^D}$ .  $\text{Br}(\gamma^D \rightarrow \text{ch} + \text{ch})$  is equal to  $1 - \text{Br}(\gamma^D \rightarrow \text{neutral hadrons})$

as demonstrated in Refs. [5, 15]. The 90% confidence level (CL) limits on the existence of a  $\gamma^D$  with given  $(m_{\gamma^D}, \epsilon)$  are hence set by excluding regions where more than  $\mathcal{N}_{\gamma^D} = 2.3$  events are expected.

### 4.1 Decay channels

The following final states are considered, whenever available for a given  $m_{\gamma^D}$ :  $e^+e^-$ ,  $\mu^+\mu^-$ ,  $\tau^+\tau^-$ , and any hadronic decay channels leading to charged particles (e.g.  $\pi^+\pi^- + X$ ,  $K^+K^- + X$ ). The branching ratio to the different final states is shown in Fig. 9 for all the simulated  $(m_{\gamma^D}, \epsilon)$  points in the three different production modes, as a function of  $m_{\gamma^D}$ , calculating the mean value over the different  $\epsilon$  samples. All events classified under “ $e^+e^-$ ”, “ $\mu^+\mu^-$ ”, “ $\tau^+\tau^-$ ” and “charged hadrons” have at least two charged particles, their sum is represented as “ch + ch”. Only the events classified under “neutral hadrons” are lost due to the analysis selection described in Sect. 4.3. Compared to Fig. 7, Fig. 9 highlights the mass scan actually simulated, and the separation of the hadronic final states into the charged and neutral ones.

### 4.2 Vessel acceptance

For events which have two charged particles, the  $\gamma^D$  decay vertex is further required to be within the vessel volume. The efficiency of this selection,  $\mathcal{P}_{\text{vessel}}$  is defined as the ratio of the sum of the weights  $w_{\text{vtx}}(\ell)$  of events passing the vertex selection described in Table 2 over the total number of events with a dark photon decaying to at least two charged particles.

This efficiency is shown in Fig. 10 as a function of  $(m_{\gamma^D}, \varepsilon)$ , for the three production modes. It is mostly driven by the lifetime of the  $\gamma^D$ , and the kinematics of the  $\gamma^D$  produced in the target. Its maximum is around 5% for the production via meson decay, 10% for the proton bremsstrahlung production, and for higher masses in QCD production.

### 4.3 Reconstruction of the decay products

The strategy employed in this analysis relies uniquely on the reconstruction of charged particles by the SHiP straw tracker. Future extensions of this work could consider also calorimeter deposits (with the possibility to fully reconstruct  $\pi^0$  decays to two photons) and muon detectors. Events are retained if two tracks are found passing the criteria summarised in Table 2, namely that the two tracks are within the fiducial area of the detector up to the fourth layer after the magnet, the fit converged with good quality requirements ( $\chi^2/\text{NDF} < 5$  with NDF the number of degrees of freedom of the fit). The tracks are required to have an impact parameter (IP) less than 0.1 m in the  $(x, y)$  plane, a momentum  $p$  above 1 GeV, and a distance of closest approach (DOCA) below 1 cm. Criteria on the number of hits (NDF > 25) or presence of hits before/after the magnet are meant to reduce backgrounds which could come from particles re-entering the detector volume due to the magnetic field. At the moment, the resolution of the timing detector is neglected, and MC truth information is used instead.

The efficiency of having two good tracks passing the selection for events which had two charged particles and  $\gamma^D$  vertex in the decay volume,  $\mathcal{P}_{\text{reco}}$  is shown in Fig. 11. Once the  $\gamma^D$  decays in the vessel volume, the reconstruction efficiency is above 80% in most of the parameter space. For production via meson decay, a dependency on  $\varepsilon$  is observed, with the efficiency dropping to below 50% as  $\varepsilon$  decreases. This is found to be related to the wider angular distribution of dark photons produced in meson decays, introducing a dependency on the position of the decay vertex.

### 4.4 Systematic uncertainties

The following sources of systematic uncertainties from theory are investigated, for the three production modes. The missing contributions from cascade decays will be the subject of future work and is not considered.

For the meson production, the overall rate is affected by the following uncertainties:

- Branching ratios of the mesons to decay channels with photons from Table 1: from Ref. [37], the uncertainties on the measurement of these branching ratios are 0.03, 0.5, 3.4 and 3.6% for  $\pi^0 \rightarrow \gamma\gamma$ ,  $\eta^0 \rightarrow \gamma\gamma$ ,  $\omega \rightarrow \pi^0\gamma$

and  $\eta' \rightarrow \gamma\gamma$  respectively, translating directly to the final rate.

- Uncertainty on the meson multiplicities and shape of their kinematics properties: PYTHIA 8.2 has been compared with data in several existing publications. A comparison to NA27 and NA56 data is made in Ref. [64] for the inclusive production of  $\pi^0$  mesons, and reasonable agreement is found, within 30% in the kinematic regions targeted by our measurement. In this comparison, the Pythia p-p cross section is scaled by a factor  $A^{2/3}$  to be compared to the p-Be collisions from the data. The scaled Pythia cross section is also found to be in good agreement with the full parametrisation of the pion invariant cross section taken from Ref. [65]. PHENIX and ALICE also measured inclusive  $\pi^0$ ,  $\eta$  and  $\omega$  production and ratios [66–68], and showed global agreement within about 20% with the PYTHIA 8 (Monash 2013 Tune) simulation.

Adding the different sources in quadrature, this results in a total systematic uncertainty of  $\pm 30\%$ .

For the proton bremsstrahlung, the theory systematic uncertainties concern:

- uncertainties on the inelastic p-p cross section  $\sigma_{pp}(s)$ , which will mostly cancel in the ratio  $\frac{\sigma_{pp}(s')}{\sigma_{pp}(s)}$ , are neglected.
- Dipole form factor versus VMD form factor: the two scenarios are presented separately in the final exclusion limits.
- Contribution from protons undergoing elastic scattering before radiating the  $\gamma^D$ : an upper bound is derived using a factor  $\frac{1}{1-P_{\text{el}}} = 1.34$  [69], with  $P_{\text{el}}$  the probability for an incoming proton to generate an elastic scattering,  $P_{\text{el}} = \frac{\sigma_{pp}^{\text{elastic}}}{\sigma_{pp}^{\text{tot}}}$  and  $\sigma_{pp}^{\text{elastic}} = 10.35$  mb from PYTHIA, summing elastic and single-diffractive contributions.
- Boundary conditions used in the integration of Eq. (8): by varying the upper bound on  $p_{\perp}$  by  $\pm 2$  GeV, the total rate is changed by  $^{+15\%}_{-30\%}$ . Varying the lower and upper bounds  $p_{\text{min}}$  ( $p_{\text{max}}$ ) by  $\pm 0.04$  ( $\pm 0.04$ ), the total rate is changed by  $^{+40\%}_{-25\%}$ .

A total systematic uncertainty of  $^{+50\%}_{-40\%}$  is assumed to cover these sources.

For the QCD production, the theory systematic uncertainties concern the parameterisation of the LO cross section, the choice of NNLO k-factor and the impact from QCD scales and PDFs. Figure 5 shows the relative contributions from QCD scales and PDF on PYTHIA's LO cross section. The choice of PDF set is giving large variations in normalisation, but not affecting the overall shape of the cross section versus mass. The PDF set chosen is conservatively the one giving the lowest cross section. As discussed in Sect. 3.3, in the end the uncertainty is dominated by the NNLO k-factor of



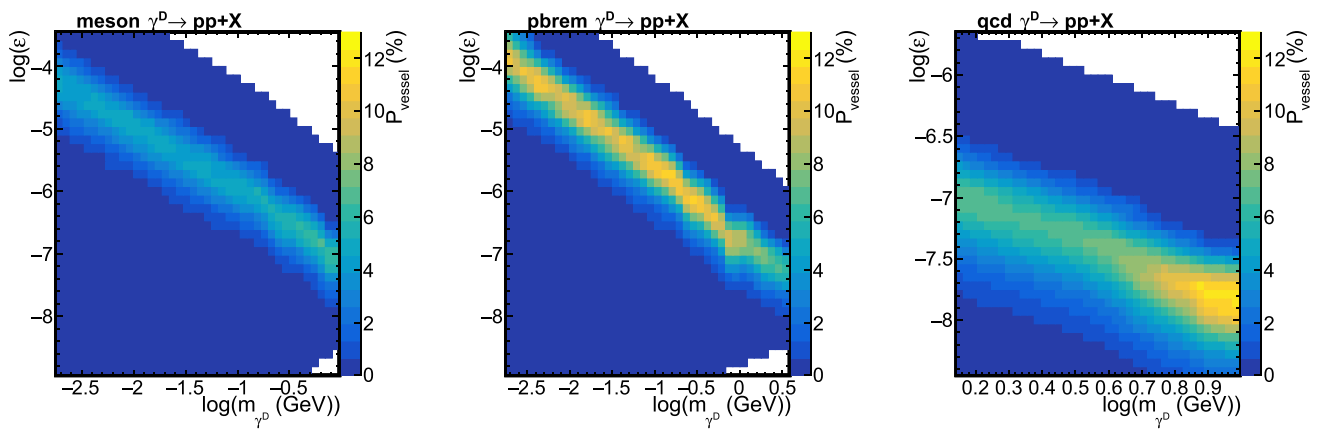


**Fig. 10** Efficiency of requiring the  $\gamma^D$  decay vertex to be inside the decay vessel volume, for the three production modes studied. An interpolation between the simulated  $(m_{\gamma^D}, \epsilon)$  values is performed using a linear interpolation via Delaunay triangulation

**Table 2** Selection criteria applied on the reconstructed events. See Fig. 1 for the layout simulated

Decay vertex	z position within the range [610, 5076] cm x–y within vessel volume and at least 5 cm away from its inner walls
Straw tracker hits	In each layer – before and after magnet – up to tracking station 4
Tracks	$\geq 2$ tracks NDF > 25, $\chi^2/\text{NDF} < 5$ , DOCA < 1 cm, $p > 1$ GeV, IP < 0.1 m

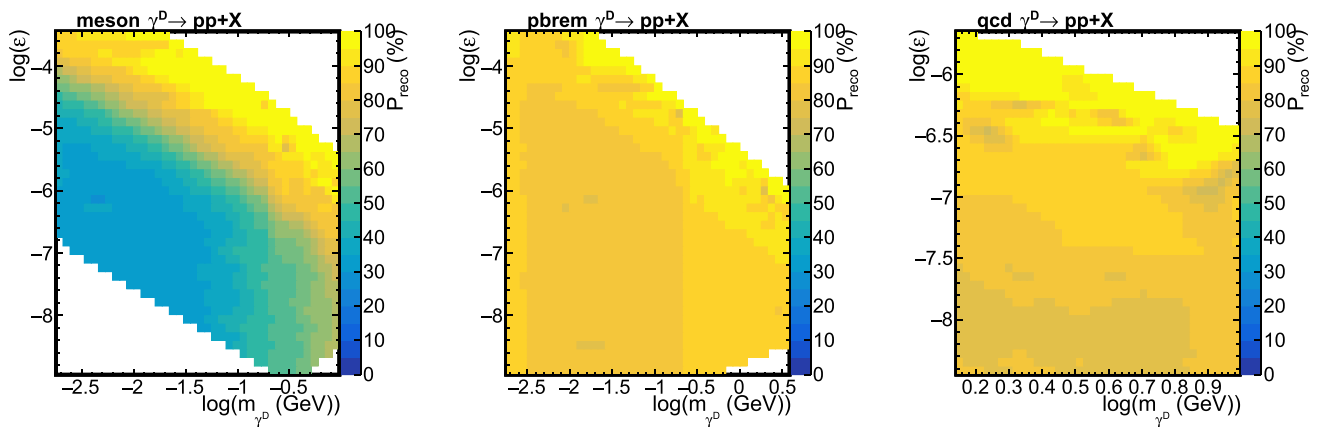


**Fig. 11** Efficiency of requiring two good tracks, for events with two charged particles and  $\gamma^D$  vertex inside the vessel volume, for the three production modes studied. An interpolation between the simulated  $(m_{\gamma^D}, \epsilon)$  values is performed using a linear interpolation via Delaunay triangulation

$1.7 \pm 0.7$ . The total systematic uncertainty is hence taken as  $\pm 40\%$ .

Experimental systematic uncertainties concern the measurement of the luminosity, the modeling of the tracking efficiency and the assumptions entering the 0-background estimate. They have been neglected in this study, as they are expected to be small compared to the theoretical uncertainties.

#### 4.5 Extraction of the limit

Events are generated following a discrete grid in  $(m_{\gamma^D}, \epsilon)$  values, and passed through the full simulation of the SHiP detector and reconstruction algorithms. The  $\gamma^D$  mass is varied between the electron-pair production threshold and 10 GeV, in 0.001 to 1 GeV steps. The kinetic mixing parameter  $\epsilon$  is varied between  $10^{-4}$  and  $10^{-9}$  in varying-size steps in  $\log(\epsilon)$ .

To find the  $\epsilon$  values that allow to reach 2.3 expected events, the expected rate is studied as a function of  $\epsilon$  for the discrete mass points, with a linear interpolation between fully-simulated values. Between mass points, a linear interpola-

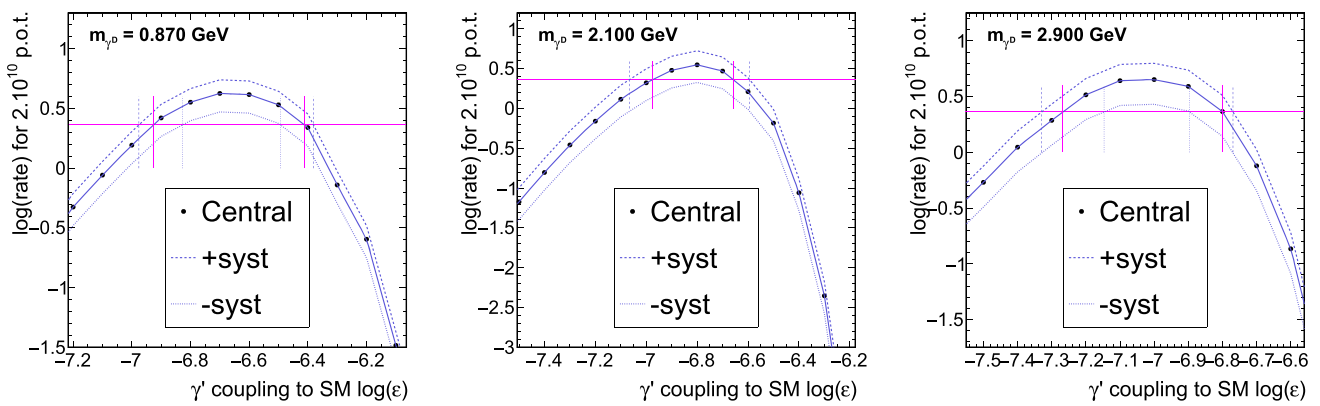
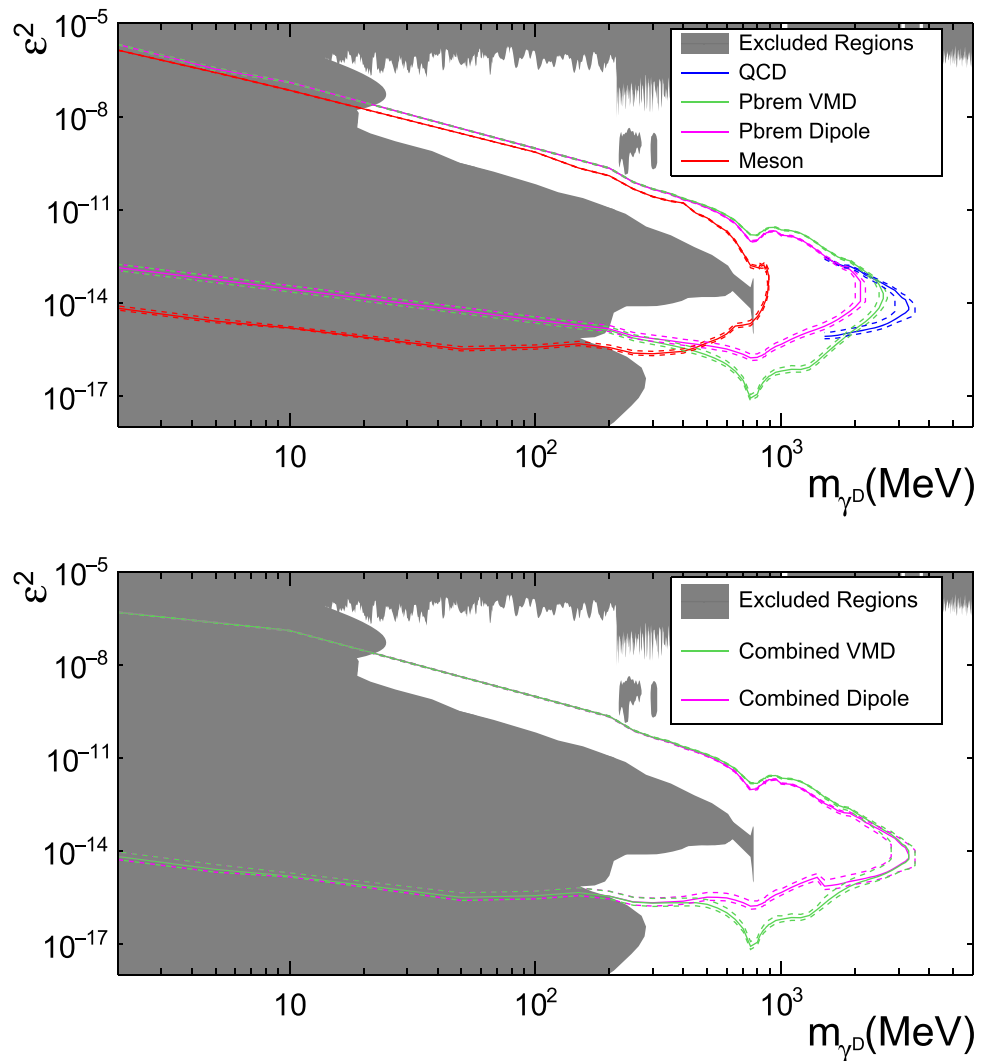


**Fig. 12** Expected rate as a function of  $\epsilon$ , for  $m_{\gamma_D} = 0.87$  (left), 2.1 (middle) or 2.9 (right) GeV and meson, proton bremsstrahlung with dipole form factor or QCD production, respectively. The horizontal pink line shows the 2.3 events threshold used to set the limit. Vertical pink (dashed blue) lines show the result of the interpolation (varying the yields up and down according to the total systematic uncertainties detailed in Sect. 4.4)

**Fig. 13** Expected 90% exclusion region as a function of the dark photon mass and of the kinetic mixing parameter  $\epsilon^2$ , for the three production modes studied (top), and their combinations for the two proton bremsstrahlung scenarios (bottom). The dashed lines highlight the  $1-\sigma$  uncertainty band using the systematics described in Sect. 4.4. The excluded region in grey is from Ref. [70]



tion is also performed. The rate of events is driven by two aspects. For large  $\varepsilon$  values, larger cross sections are expected but the detection efficiency decreases rapidly due to small lifetimes and decays happening before the decay vessel. As  $\varepsilon$  decreases, the cross section decreases as  $\varepsilon^2$  but the events have more and more probability to reach the vessel and the rate increases, up to a turning point where the decay vertex happens after the decay vessel and/or the cross section becomes too small. Hence the 90% CL exclusion region is contained inside a lower and upper limits on  $\varepsilon^2$  for each mass point. The dependency of the excluded region on the mass is driven by the kinematic properties of the  $\gamma^D$  and its decay products, affecting the detector acceptance and selection efficiency.

As shown in Fig. 12 for representative mass points, for all processes, the upper bounds have little dependency on the absolute normalisation of the rate (so in particular systematic uncertainties on the cross sections and other quantities affecting the overall rate), due to the very steep dependency of the rate as a function of  $\varepsilon$ . The lower bounds are however more sensitive.

The 90% CL exclusion contour is shown in Fig. 13 for the three production modes studied, and their combinations, in the  $(m_{\gamma^D}, \varepsilon^2)$  plane. The excluded region shown in grey is from past experiments sensitive to this process [70]. For  $\varepsilon^2 > 10^{-6}$ , in the full mass range studied, the current sensitivity is coming from searches for dilepton resonances (e.g. Refs [71–78]). These results are complemented for low masses at lower  $\varepsilon^2$  values by those from the reinterpretation of data from fixed-target experiments (e.g. [79–83]), and by recent dedicated searches for long-lived  $\gamma^D$  decaying to leptons [84, 85]. The very-low coupling exclusions are from cosmological constraints, in particular bounds from Supernova 1987A data [86–88].

The SHiP experiment is expected to have a unique sensitivity in the mass region  $m_{\gamma^D}$  ranging between 0.8 and  $3.3_{-0.5}^{+0.2}$  GeV, and  $\varepsilon^2$  ranging between  $10^{-11}$  and  $10^{-17}$ .

## 5 Conclusion

The sensitivity of the SHiP detector has been investigated for the simplest vector portal model, in which the only hidden-sector particle connecting to SM particles is a dark photon. The model is fully parameterised by only two parameters, the mass of the dark photon  $m_{\gamma^D}$  and the kinetic mixing parameter  $\varepsilon$ . Three different production mechanisms have been investigated, namely the production via meson decays from non-diffractive proton–nucleon interactions, by proton bremsstrahlung and by QCD parton–parton interaction.

Different sources of systematic uncertainties have been considered, dominated by theory predictions on the cross

section times branching ratios (meson decays), two scenarios of nuclear form factor (proton bremsstrahlung) and higher-order corrections (QCD scattering). Only the primary proton–nucleon interaction is taken into account, secondaries from hadronic interactions in cascade decays could lead to an improvement in the sensitivity and will be the object of future work. The dark photon is assumed to decay to pairs of leptons or quarks, and only decay channels producing at least two charged particles coming from a common vertex are used.

With the selection applied, backgrounds are neglected and 90% CL exclusion contours are extracted and compared with those from past experiments. The SHiP detector is expected to have a unique sensitivity for  $m_{\gamma^D}$  ranging between 0.8 and  $3.3_{-0.5}^{+0.2}$  GeV, and  $\varepsilon^2$  ranging between  $10^{-11}$  and  $10^{-17}$ .

**Acknowledgements** The SHiP Collaboration wishes to thank the Castaldo company (Naples, Italy) for their contribution to the development studies of the decay vessel. The SHiP Collaboration acknowledges support from the following funding agencies: the TAEK of Turkey with Grant number 2018TAEK(CERN)-A5.H6.F2-17; the National Research Foundation of Korea with grant numbers 2018R1A2B2007757, 2018R1D1A3B07050649, 2018R1D1A1B07050701, 2017R1D1A1B03036042, 2017R1A6A3A01075752, 2016R1A2B4012302, and 2016R1A6A3A11930680; the Fundação para a Ciência e a Tecnologia of Portugal with grant number CERN/FIS-PAR/0030/2017; the Russian Foundation for Basic Research (RFBR), with Grant number 17-02-00607.

**Data Availability Statement** This manuscript has associated data in a data repository. [Authors' comment: Data available within the DarkCast repository [89].]

**Open Access** This article is licensed under a Creative Commons Attribution 4.0 International License, which permits use, sharing, adaptation, distribution and reproduction in any medium or format, as long as you give appropriate credit to the original author(s) and the source, provide a link to the Creative Commons licence, and indicate if changes were made. The images or other third party material in this article are included in the article's Creative Commons licence, unless indicated otherwise in a credit line to the material. If material is not included in the article's Creative Commons licence and your intended use is not permitted by statutory regulation or exceeds the permitted use, you will need to obtain permission directly from the copyright holder. To view a copy of this licence, visit <http://creativecommons.org/licenses/by/4.0/>.  
Funded by SCOAP<sup>3</sup>.

## References

1. L. Evans, P. Bryant, JINST **3**, S08001 (2008). <https://doi.org/10.1088/1748-0221/3/08/S08001>
2. G. Apollinari, I. Béjar Alonso, O. Brüning, M. Lamont, L. Rossi, High-luminosity large hadron collider (HL-LHC): preliminary design report. Technical Report. CERN-2015-005, FERMLAB-DESIGN-2015-02, CERN, Geneva (2015)
3. C. Ahdida et al., A beam dump facility (BDF) at CERN—the concept and a first radiological assessment. Technical Report. CERN-PBC-CONF-2019-001, CERN, Geneva (2019). <https://cds.cern.ch/record/2655435>. Accessed 21 May 2021

4. B. Batell, M. Pospelov, A. Ritz, *Phys. Rev. D* **80**, 095024 (2009). <https://doi.org/10.1103/PhysRevD.80.095024>
5. S. Alekhin et al., *Rep. Prog. Phys.* **79**(12), 124201 (2016). <https://doi.org/10.1088/0034-4885/79/12/124201>
6. B. Patt, F. Wilczek, Higgs-field portal into hidden sectors. Technical Report. MIT-CTP-3745 (2006). <https://arxiv.org/abs/hep-ph/0605188>
7. D. O'Connell, M.J. Ramsey-Musolf, M.B. Wise, *Phys. Rev. D* **75**, 037701 (2007). <https://doi.org/10.1103/PhysRevD.75.037701>
8. B. Holdom, *Phys. Lett.* **166B**, 196 (1986). [https://doi.org/10.1016/0370-2693\(86\)91377-8](https://doi.org/10.1016/0370-2693(86)91377-8)
9. M. Bauer, P. Foldenauer, J. Jaeckel, *JHEP* **18**, 094 (2020). [https://doi.org/10.1007/JHEP07\(2018\)094](https://doi.org/10.1007/JHEP07(2018)094)
10. D. Gorbunov, M. Shaposhnikov, *J. High Energy Phys.* **2007**(10), 015 (2007). <https://doi.org/10.1088/1126-6708/2007/10/015>
11. M. Aaboud et al., *JHEP* **06**, 166 (2018). [https://doi.org/10.1007/JHEP06\(2018\)166](https://doi.org/10.1007/JHEP06(2018)166)
12. M. Aaboud et al., *JHEP* **10**, 182 (2017). [https://doi.org/10.1007/JHEP10\(2017\)182](https://doi.org/10.1007/JHEP10(2017)182)
13. A.M. Sirunyan et al., *Phys. Lett. B* **796**, 131 (2019). <https://doi.org/10.1016/j.physletb.2019.07.013>
14. V. Khachatryan et al., *Phys. Lett. B* **768**, 57 (2017). <https://doi.org/10.1016/j.physletb.2017.02.010>
15. M. Anelli et al., A facility to search for hidden particles (SHiP) at the CERN SPS. Technical Report. CERN-SPSC-2015-016. SPSC-P-350, CERN, Geneva (2015). Technical Proposal. [arXiv:1504.04956](https://arxiv.org/abs/1504.04956). <https://cds.cern.ch/record/2007512>. Accessed 21 May 2021
16. W. Bonivento et al., Proposal to search for heavy neutral leptons at the SPS. Technical Report. CERN-SPSC-2013-024. SPSC-EOI-010, CERN, Geneva (2013). <http://cds.cern.ch/record/1606085>. Accessed 21 May 2021
17. C. Ahdida et al., *JHEP* **04**, 077 (2019). [https://doi.org/10.1007/JHEP04\(2019\)077](https://doi.org/10.1007/JHEP04(2019)077)
18. C. Ahdida et al., Measurement of the muon flux for the SHiP experiment. Technical Report. CERN-EP-2020-006, CERN, Geneva (2020). <https://arxiv.org/abs/2001.04784>
19. A. Akmete et al., *JINST* **12**(05), P05011 (2017). <https://doi.org/10.1088/1748-0221/12/05/P05011>
20. C. Ahdida et al., SHiP experiment—comprehensive design study report. Technical Report. CERN-SPSC-2019-049. SPSC-SR-263, CERN, Geneva (2019). <https://cds.cern.ch/record/2704147>. Accessed 21 May 2021
21. A. Miano, A. Fiorillo, A. Salzano, A. Prota, R. Jacobsson, *Arch. Civ. Mech. Eng.* **21**, 3 (2020). <https://doi.org/10.1007/s43452-020-00152-9>
22. I. Bereziuk, O. Bezshyyko, M. Ferro-Luzzi, Initial design studies of the SHiP straw detector. Technical Report. CERN-SHIP-NOTE-2015-001, CERN, Geneva (2015). <https://cds.cern.ch/record/2005286>. Accessed 21 May 2021
23. E. Van Herwijnen, H. Dijkstra, M. Ferro-Luzzi, T. Ruf, Simulation and pattern recognition for the SHiP Spectrometer Tracker. Technical Report. CERN-SHIP-NOTE-2015-002, CERN, Geneva (2015). <https://cds.cern.ch/record/2005715>. Accessed 21 May 2021
24. B. Hosseini, W.M. Bonivento, Particle identification tools and performance in the SHiP experiment. Technical Report. CERN-SHIP-NOTE-2017-002, CERN, Geneva (2017). <https://cds.cern.ch/record/2282039>. Accessed 21 May 2021
25. T. Sjöstrand, S. Ask, J.R. Christiansen, R. Corke, N. Desai, P. Ilten, S. Mrenna, S. Prestel, C.O. Rasmussen, P.Z. Skands, *Comput. Phys. Commun.* **191**, 159 (2015). <https://doi.org/10.1016/j.cpc.2015.01.024>
26. C. Andreopoulos et al., *Nucl. Instrum. Methods* **A614**, 87 (2010). <https://doi.org/10.1016/j.nima.2009.12.009>
27. T. Sjöstrand, S. Mrenna, P. Skands, *JHEP* **5**, 26. <https://doi.org/10.1088/1126-6708/2006/05/026>
28. H. Dijkstra, T. Ruf, Heavy flavour cascade production in a beam dump. Technical Report. CERN-SHIP-NOTE-2015-009, CERN, Geneva (2015). <https://cds.cern.ch/record/2115534>. Accessed 21 May 2021
29. S. Agostinelli et al., *Nucl. Instrum. Methods* **A506**, 250 (2003). [https://doi.org/10.1016/S0168-9002\(03\)01368-8](https://doi.org/10.1016/S0168-9002(03)01368-8)
30. M. Al-Turany, D. Bertini, R. Karabowicz, D. Kresan, P. Malzacher, T. Stockmanns, F. Uhlig, *J. Phys.: Conf. Ser.* **396**(2), 022001 (2012). <https://doi.org/10.1088/1742-9596/396/2/022001>
31. D. Gorbunov, A. Makarov, I. Timiryasov, *Phys. Rev. D* **91**(3), 035027 (2015). <https://doi.org/10.1103/PhysRevD.91.035027>
32. R.D. Ball et al., *Nucl. Phys. B* **867**, 244 (2013). <https://doi.org/10.1016/j.nuclphysb.2012.10.003>
33. P. Skands, S. Carrazza, J. Rojo, *Eur. Phys. J. C* **74**(8), 3024 (2014). <https://doi.org/10.1140/epjc/s10052-014-3024-y>
34. A. Berlin, S. Gori, P. Schuster, N. Toro, *Phys. Rev. D* **98**(3), 035011 (2018). <https://doi.org/10.1103/PhysRevD.98.035011>
35. M. Aguilar-Benitez et al., *Z. Phys. C* **50**, 405 (1991). <https://doi.org/10.1007/BF01551452>
36. J. Blümlein, J. Brunner, *Phys. Lett. B* **731**, 320 (2014). <https://doi.org/10.1016/j.physletb.2014.02.029>
37. C. Patrignani et al., *Chin. Phys. C* **40**(10), 100001 (2016). <https://doi.org/10.1088/1674-1137/40/10/100001>
38. L.N. Hand, D.G. Miller, R. Wilson, *Rev. Mod. Phys.* **35**, 335 (1963). <https://doi.org/10.1103/RevModPhys.35.335>
39. P. deNiverville, C.Y. Chen, M. Pospelov, A. Ritz, *Phys. Rev. D* **95**(3), 035006 (2017). <https://doi.org/10.1103/PhysRevD.95.035006>
40. A. Faessler, M.I. Krivoruchenko, B.V. Martemyanov, *Phys. Rev. C* **82**, 038201 (2010). <https://doi.org/10.1103/PhysRevC.82.038201>
41. K. Nakamura et al., *J. Phys. G: Nucl. Part. Phys.* **37**(7A), 075021 (2010). <https://doi.org/10.1088/0954-3899/37/7a/075021>
42. K. Kim, Y. Tsai, *Phys. Rev. D* **8**(9), 3109 (1973)
43. K. Kim, Y. Tsai, *Phys. Lett. B* **40**(6), 665 (1972). [https://doi.org/10.1016/0370-2693\(72\)90622-3](https://doi.org/10.1016/0370-2693(72)90622-3)
44. L. Carloni, J. Rathsmann, T. Sjöstrand, *JHEP* **04**, 091 (2011). [https://doi.org/10.1007/JHEP04\(2011\)091](https://doi.org/10.1007/JHEP04(2011)091)
45. C. Ciobanu, T. Junk, G. Veramendi, J. Lee, G. De Lentdecker, K.S. McFarland, K. Maeshima, Z' generation with PYTHIA. Technical Report. FERMILAB-FN-0773-E, FERMILAB, Batavia (2005). <https://doi.org/10.2172/15020136>
46. A. Buckley, J. Ferrando, S. Lloyd, K. Nordström, B. Page, M. Rüfenacht, M. Schönherr, G. Watt, *Eur. Phys. J. C* **75**, 132 (2015). <https://doi.org/10.1140/epjc/s10052-015-3318-8>
47. K.J. Eskola, P. Paakkinen, H. Paukkunen, C.A. Salgado, *Eur. Phys. J. C* **77**(3), 163 (2017). <https://doi.org/10.1140/epjc/s10052-017-4725-9>
48. J. Alwall, R. Frederix, S. Frixione, V. Hirschi, F. Maltoni, O. Mattelaer, H.S. Shao, T. Stelzer, P. Torrielli, M. Zaro, *JHEP* **07**, 079 (2014). [https://doi.org/10.1007/JHEP07\(2014\)079](https://doi.org/10.1007/JHEP07(2014)079)
49. M. Grazzini, S. Kallweit, M. Wiesemann, *Eur. Phys. J. C* **78**(7), 537 (2018). <https://doi.org/10.1140/epjc/s10052-018-5771-7>
50. S. Catani, L. Cieri, G. Ferrera, D. de Florian, M. Grazzini, *Phys. Rev. Lett.* **103**, 082001 (2009). <https://doi.org/10.1103/PhysRevLett.103.082001>
51. F. Cascioli, P. Maierhöfer, S. Pozzorini, *Phys. Rev. Lett.* **108**, 111601 (2012). <https://doi.org/10.1103/PhysRevLett.108.111601>
52. A. Denner, S. Dittmaier, L. Hofer, *Comput. Phys. Commun.* **212**, 220 (2017). <https://doi.org/10.1016/j.cpc.2016.10.013>
53. S. Catani, L. Cieri, D. de Florian, G. Ferrera, M. Grazzini, *Eur. Phys. J. C* **72**, 2195 (2012). <https://doi.org/10.1140/epjc/s10052-012-2195-7>
54. S. Catani, M. Grazzini, *Phys. Rev. Lett.* **98**, 222002 (2007). <https://doi.org/10.1103/PhysRevLett.98.222002>
55. A.D. Martin, W.J. Stirling, R.S. Thorne, G. Watt, *Eur. Phys. J. C* **63**, 189 (2009). <https://doi.org/10.1140/epjc/s10052-009-1072-5>

56. H. Shimizu, G.F. Sterman, W. Vogelsang, H. Yokoya, *Phys. Rev. D* **71**, 114007 (2005). <https://doi.org/10.1103/PhysRevD.71.114007>
57. R.D. Ball et al., *Eur. Phys. J. C* **77**(10), 663 (2017). <https://doi.org/10.1140/epjc/s10052-017-5199-5>
58. H.L. Lai, J. Huston, S. Mrenna, P. Nadolsky, D. Stump, W.K. Tung, C.P. Yuan, *JHEP* **04**, 035 (2010). [https://doi.org/10.1007/JHEP04\(2010\)035](https://doi.org/10.1007/JHEP04(2010)035)
59. J. Pumplin, D.R. Stump, J. Huston, H.L. Lai, P.M. Nadolsky, W.K. Tung, *JHEP* **07**, 012 (2002). <https://doi.org/10.1088/1126-6708/2002/07/012>
60. S. Alekhin, J. Blümlein, S. Moch, R. Placakyte, *Phys. Rev. D* **96**(1), 014011 (2017). <https://doi.org/10.1103/PhysRevD.96.014011>
61. J.D. Bjorken, R. Essig, P. Schuster, N. Toro, *Phys. Rev. D* **80**, 075018 (2009). <https://doi.org/10.1103/PhysRevD.80.075018>
62. K.A. Olive et al., *Chin. Phys. C* **38**, 090001 (2014). <https://doi.org/10.1088/1674-1137/38/9/090001>
63. M.X. Liu, *Mod. Phys. Lett. A* **32**(10), 1730008 (2017). <https://doi.org/10.1142/S0217732317300087>
64. B. Döbrich, J. Jaeckel, T. Spadaro, *JHEP* **05**, 213 (2019). [https://doi.org/10.1007/JHEP05\(2019\)213](https://doi.org/10.1007/JHEP05(2019)213)
65. M. Bonesini, A. Marchionni, F. Pietropaolo, T. Tabarelli de Fatis, *Eur. Phys. J. C* **20**, 13 (2001). <https://doi.org/10.1007/s100520100656>
66. S. Acharya et al., *Eur. Phys. J. C* **78**(3), 263 (2018). <https://doi.org/10.1140/epjc/s10052-018-5612-8>
67. S. Acharya et al., Production of  $\omega(782)$  in pp collisions at  $\sqrt{s} = 7$  TeV. Technical Report. ALICE-PUBLIC-2018-004, CERN, Geneva (2018). <http://cds.cern.ch/record/2316785>. Accessed 21 May 2021
68. A. Adare et al., *Phys. Rev. C* **84**, 044902 (2011). <https://doi.org/10.1103/PhysRevC.84.044902>
69. C. Ahdida et al., *JHEP* **4**, 199 (2021). [https://doi.org/10.1007/JHEP04\(2021\)199](https://doi.org/10.1007/JHEP04(2021)199)
70. J. Beacham, C. Burrage, D. Curtin, A. De Roeck, J. Evans, J.L. Feng, C. Gatto, S. Gninenko, A. Hartin, I. Irastorza et al., *J. Phys. G: Nucl. Part. Phys.* **47**(1), 010501 (2019). <https://doi.org/10.1088/1361-6471/ab4cd2>
71. J.P. Lees et al., *Phys. Rev. Lett.* **113**, 201801 (2014). <https://doi.org/10.1103/PhysRevLett.113.201801>
72. J. Batley et al., *Phys. Lett. B* **746**, 178 (2015). <https://doi.org/10.1016/j.physletb.2015.04.068>
73. H. Merkel et al., *Phys. Rev. Lett.* **112**, 221802 (2014). <https://doi.org/10.1103/PhysRevLett.112.221802>
74. F. Archilli et al., *Phys. Lett. B* **706**(4), 251 (2012). <https://doi.org/10.1016/j.physletb.2011.11.033>
75. D. Babusci et al., *Phys. Lett. B* **720**(1), 111 (2013). <https://doi.org/10.1016/j.physletb.2013.01.067>
76. D. Babusci et al., *Phys. Lett. B* **736**, 459 (2014). <https://doi.org/10.1016/j.physletb.2014.08.005>
77. A. Anastasi et al., *Phys. Lett. B* **757**, 356 (2016). <https://doi.org/10.1016/j.physletb.2016.04.019>
78. R. Aaij et al., *Phys. Rev. Lett.* **120**, 061801 (2018). <https://doi.org/10.1103/PhysRevLett.120.061801>
79. J.D. Bjorken, S. Ecklund, W.R. Nelson, A. Abashian, C. Church, B. Lu, L.W. Mo, T.A. Nunamaker, P. Rassmann, *Phys. Rev. D* **38**, 3375 (1988). <https://doi.org/10.1103/PhysRevD.38.3375>
80. B. Batell, R. Essig, Z. Surujon, *Phys. Rev. Lett.* **113**, 171802 (2014). <https://doi.org/10.1103/PhysRevLett.113.171802>
81. F. Bergsma et al., *Phys. Lett. B* **157**(5), 458 (1985). [https://doi.org/10.1016/0370-2693\(85\)90400-9](https://doi.org/10.1016/0370-2693(85)90400-9)
82. E.M. Riordan et al., *Phys. Rev. Lett.* **59**, 755 (1987). <https://doi.org/10.1103/PhysRevLett.59.755>
83. A. Bross, M. Crisler, S. Pordes, J. Volk, S. Errede, J. Wrbanek, *Phys. Rev. Lett.* **67**, 2942 (1991). <https://doi.org/10.1103/PhysRevLett.67.2942>
84. R. Aaij et al., *Phys. Rev. Lett.* **124**(4), 041801 (2020). <https://doi.org/10.1103/PhysRevLett.124.041801>
85. D. Banerjee et al., *Phys. Rev. D* **101**(7), 071101 (2020). <https://doi.org/10.1103/PhysRevD.101.071101>
86. A. Fradette, M. Pospelov, J. Pradler, A. Ritz, *Phys. Rev. D* **90**(3), 035022 (2014). <https://doi.org/10.1103/PhysRevD.90.035022>
87. D. Kazanas, R.N. Mohapatra, S. Nussinov, V.L. Teplitz, Y. Zhang, *Nucl. Phys. B* **890**, 17 (2014). <https://doi.org/10.1016/j.nuclphysb.2014.11.009>
88. J.H. Chang, R. Essig, S.D. McDermott, *JHEP* **01**, 107 (2017). [https://doi.org/10.1007/JHEP01\(2017\)107](https://doi.org/10.1007/JHEP01(2017)107)
89. P. Ilten, Y. Soreq, M. Williams, W. Xue, Serendipity in dark photon searches. *JHEP* **6**, 4 (2018). [https://doi.org/10.1007/JHEP06\(2018\)004](https://doi.org/10.1007/JHEP06(2018)004)

## SHiP Collaboration

C. Ahdida<sup>44</sup>, A. Akmete<sup>48</sup>, R. Albanese<sup>14,d,h</sup>, A. Alexandrov<sup>14,32,34,d</sup>, A. Anokhina<sup>39,k</sup>, S. Aoki<sup>18</sup>, G. Arduini<sup>44</sup>, E. Atkin<sup>38</sup>, N. Azorskiy<sup>29</sup>, J. J. Back<sup>54</sup>, A. Bagulya<sup>32</sup>, F. Baaltasar Dos Santos<sup>44</sup>, A. Baranov<sup>40</sup>, F. Bardou<sup>44</sup>, G. J. Barker<sup>54</sup>, M. Battistin<sup>44</sup>, J. Bauche<sup>44</sup>, A. Bay<sup>46</sup>, V. Bayliss<sup>51</sup>, G. Bencivenni<sup>15</sup>, A. Y. Berdnikov<sup>37</sup>, Y. A. Berdnikov<sup>37</sup>, M. Bertani<sup>15</sup>, C. Betancourt<sup>47</sup>, I. Bezshyiko<sup>47</sup>, O. Bezshyyko<sup>55</sup>, D. Bick<sup>8</sup>, S. Bieschke<sup>8</sup>, A. Blanco<sup>28</sup>, J. Boehm<sup>51</sup>, M. Bogomilov<sup>1</sup>, I. Boiarska<sup>3</sup>, K. Bondarenko<sup>27,57</sup>, W. M. Bonivento<sup>13</sup>, J. Borburgh<sup>44</sup>, A. Boyarsky<sup>27,55</sup>, R. Brenner<sup>43</sup>, D. Breton<sup>4</sup>, V. Büscher<sup>10</sup>, A. Buonaura<sup>47</sup>, S. Buontempo<sup>14</sup>, S. Cadeddu<sup>13</sup>, A. Calcaterra<sup>15</sup>, M. Calviani<sup>44</sup>, M. Campanelli<sup>53</sup>, M. Casolino<sup>44</sup>, N. Charitonidis<sup>44</sup>, P. Chau<sup>10</sup>, J. Chauveau<sup>5</sup>, A. Chepurinov<sup>39</sup>, M. Chernyavskiy<sup>32</sup>, K.-Y. Choi<sup>26</sup>, A. Chumakov<sup>2</sup>, P. Ciambone<sup>15</sup>, V. Cicero<sup>12</sup>, L. Congedo<sup>11,a</sup>, K. Cornelis<sup>44</sup>, M. Cristinziani<sup>7</sup>, A. Crupano<sup>14,d</sup>, G. M. Dallavalle<sup>12</sup>, A. Datwyler<sup>47</sup>, N. D'Ambrosio<sup>16</sup>, G. D'Appollonio<sup>13,c</sup>, R. de Asmundis<sup>14</sup>, J. De Carvalho Saraiva<sup>28</sup>, G. De Lellis<sup>14,34,44,d</sup>, M. de Magistris<sup>14,j</sup>, A. De Roeck<sup>44</sup>, M. De Serio<sup>11,a</sup>, D. De Simone<sup>47</sup>, L. Dedenko<sup>39</sup>, P. Dergachev<sup>34</sup>, A. Di Crescenzo<sup>14,d</sup>, L. Di Giulio<sup>44</sup>, N. Di Marco<sup>16</sup>, C. Dib<sup>2</sup>, H. Dijkstra<sup>44</sup>, V. Dmitrenko<sup>38</sup>, L. A. Dougherty<sup>44</sup>, A. Dolmatov<sup>33</sup>, D. Domenici<sup>15</sup>, S. Donskov<sup>35</sup>, V. Drohan<sup>55</sup>, A. Dubreuil<sup>45</sup>, O. Durhan<sup>48</sup>, M. Ehlert<sup>6</sup>, E. Elikkaya<sup>48</sup>, T. Enik<sup>29</sup>, A. Etenko<sup>33,38</sup>, F. Fabbri<sup>12</sup>, O. Fedin<sup>36</sup>, F. Fedotovs<sup>52</sup>, G. Felici<sup>15</sup>, M. Ferrillo<sup>47</sup>, M. Ferro-Luzzi<sup>44</sup>, K. Filippov<sup>38</sup>, R. A. Fini<sup>11</sup>, P. Fonte<sup>28</sup>, C. Franco<sup>28</sup>, M. Fraser<sup>44</sup>, R. Fresa<sup>14,i,h</sup>, R. Froeschl<sup>44</sup>, T. Fukuda<sup>19</sup>, G. Galati<sup>14,d</sup>, J. Gall<sup>44</sup>, L. Gatignon<sup>44</sup>, G. Gavrilo<sup>36</sup>, V. Gentile<sup>14,d</sup>, B. Goddard<sup>44</sup>, L. Golinka-Bezshyyko<sup>55</sup>, A. Golovatiuk<sup>14,d</sup>, V. Golovtsov<sup>36</sup>, D. Golubkov<sup>30</sup>, A. Golutvin<sup>34,52</sup>, P. Gorbounov<sup>44</sup>, D. Gorbunov<sup>31</sup>, S. Gorbunov<sup>32</sup>, V. Gorkavenko<sup>55</sup>, M. Gorshenkov<sup>34</sup>, V. Grachev<sup>38</sup>, A. L. Grandchamp<sup>46</sup>, E. Graverini<sup>46</sup>, J.-L. Grenard<sup>44</sup>, D. Grenier<sup>44</sup>, V. Grichine<sup>32</sup>, N. Gruzinskii<sup>36</sup>, A. M. Guler<sup>48</sup>, Yu. Guz<sup>35</sup>, G. J. Haefeli<sup>46</sup>, C. Hagner<sup>8</sup>, H. Hakobyan<sup>2</sup>, I. W. Harris<sup>46</sup>, E. van Herwijnen<sup>34</sup>, C. Hessler<sup>44</sup>, A. Hollnagel<sup>10</sup>, B. Hosseini<sup>52</sup>, M. Hushchyn<sup>40</sup>, G. Iaselli<sup>11,a</sup>, A. Iuliano<sup>14,d</sup>, R. Jacobsson<sup>44</sup>, D. Joković<sup>41</sup>, M. Jonker<sup>44</sup>, I. Kadenko<sup>55</sup>, V. Kain<sup>44</sup>, B. Kaiser<sup>8</sup>, C. Kamiscioglu<sup>49</sup>, D. Karpenkov<sup>34</sup>, K. Kershaw<sup>44</sup>, M. Khabibullin<sup>31</sup>, E. Khalikov<sup>39</sup>, G. Khaustov<sup>35</sup>, G. Khorauli<sup>10</sup>, A. Khotyantsev<sup>31</sup>, Y. G. Kim<sup>23</sup>, V. Kim<sup>36,37</sup>, N. Kitagawa<sup>19</sup>, J.-W. Ko<sup>22</sup>, K. Kodama<sup>17</sup>, A. Kolesnikov<sup>29</sup>, D. I. Kolev<sup>1</sup>, V. Kolosov<sup>35</sup>, M. Komatsu<sup>19</sup>, A. Kono<sup>21</sup>, N. Konovalova<sup>32,34</sup>, S. Kormannshaus<sup>10</sup>, I. Korol<sup>6</sup>, I. Korol'ko<sup>30</sup>, A. Korzenev<sup>45</sup>, V. Kostyukhin<sup>7</sup>, E. Koukovini Platia<sup>44</sup>, S. Kovalenko<sup>2</sup>, I. Krasilnikova<sup>34</sup>, Y. Kudenko<sup>31,38,g</sup>, E. Kurbatov<sup>40</sup>, P. Kurbatov<sup>34</sup>, V. Kurochka<sup>31</sup>, E. Kuznetsova<sup>36</sup>, H. M. Lacker<sup>6</sup>, M. Lamont<sup>44</sup>, G. Lanfranchi<sup>15</sup>, O. Lantwin<sup>34,47</sup>, A. Lauria<sup>14,d</sup>, K. S. Lee<sup>25</sup>, K. Y. Lee<sup>22</sup>, N. Leonardo<sup>28</sup>, J.-M. Lévy<sup>5</sup>, V. P. Loschiavo<sup>14,h</sup>, L. Lopes<sup>28</sup>, E. Lopez Sola<sup>44</sup>, V. Lyubovitskij<sup>2</sup>, J. Maalmi<sup>4</sup>, A.-M. Magnan<sup>52</sup>, V. Maleev<sup>36</sup>, A. Malinin<sup>33</sup>, Y. Manabe<sup>19</sup>, A. K. Managadze<sup>39</sup>, M. Manfredi<sup>44</sup>, S. Marsh<sup>44</sup>, A. M. Marshall<sup>50</sup>, A. Mefodev<sup>31</sup>, P. Mermod<sup>45</sup>, A. Miano<sup>14,d</sup>, S. Mikado<sup>20</sup>, Yu. Mikhaylov<sup>35</sup>, D. A. Milstead<sup>42</sup>, O. Mineev<sup>31</sup>, A. Montanari<sup>12</sup>, M. C. Montesi<sup>14,d</sup>, K. Morishima<sup>19</sup>, S. Movchan<sup>29</sup>, Y. Muttoni<sup>44</sup>, N. Naganawa<sup>19</sup>, M. Nakamura<sup>19</sup>, T. Nakano<sup>19</sup>, S. Nasybulin<sup>36</sup>, P. Ninin<sup>44</sup>, A. Nishio<sup>19</sup>, B. Obinyakov<sup>33</sup>, S. Ogawa<sup>21</sup>, N. Okateva<sup>32,34</sup>, B. Opitz<sup>8</sup>, J. Osborne<sup>44</sup>, M. Ovchynnikov<sup>27,55</sup>, N. Owtscharenko<sup>7</sup>, P. H. Owen<sup>47</sup>, P. Pacholek<sup>44</sup>, A. Paoloni<sup>15</sup>, B. D. Park<sup>22</sup>, A. Pastore<sup>11</sup>, M. Patel<sup>34,52</sup>, D. Pereyma<sup>30</sup>, A. Perillo-Marcone<sup>44</sup>, G. L. Petkov<sup>1</sup>, K. Petridis<sup>50</sup>, A. Petrov<sup>33</sup>, D. Podgrudkov<sup>39,k</sup>, V. Poliakov<sup>35</sup>, N. Polukhina<sup>32,34,38</sup>, J. Prieto Prieto<sup>44</sup>, M. Prokudin<sup>30</sup>, A. Prota<sup>14,d</sup>, A. Quercia<sup>14,d</sup>, A. Rademakers<sup>44</sup>, A. Rakai<sup>44</sup>, F. Ratnikov<sup>40</sup>, T. Rawlings<sup>51</sup>, F. Redi<sup>46</sup>, S. Ricciardi<sup>51</sup>, M. Rinaldesi<sup>44</sup>, Volodymyr Rodin<sup>55</sup>, Viktor Rodin<sup>55</sup>, P. Robbe<sup>4</sup>, A. B. Rodrigues Cavalcante<sup>46</sup>, T. Roganova<sup>39</sup>, H. Rokujo<sup>19</sup>, G. Rosa<sup>14,d</sup>, T. Rovelli<sup>12,b</sup>, O. Ruchayskiy<sup>3</sup>, T. Ruf<sup>44</sup>, V. Samoylenko<sup>35</sup>, V. Samsonov<sup>38</sup>, F. Sanchez Galan<sup>44</sup>, P. Santos Diaz<sup>44</sup>, A. Sanz Ull<sup>44</sup>, A. Saputi<sup>15</sup>, O. Sato<sup>19</sup>, E. S. Savchenko<sup>34</sup>, J. S. Schliwinski<sup>6</sup>, W. Schmidt-Parzefall<sup>8</sup>, N. Serra<sup>34,47</sup>, S. Sgobba<sup>44</sup>, O. Shadura<sup>55</sup>, A. Shakin<sup>34</sup>, M. Shaposhnikov<sup>46</sup>, P. Shatalov<sup>30,34</sup>, T. Shchedrina<sup>32,34</sup>, L. Shchutka<sup>46</sup>, V. Shevchenko<sup>33,34</sup>, H. Shibuya<sup>21</sup>, S. Shirobokov<sup>52</sup>, A. Shustov<sup>38</sup>, S. B. Silverstein<sup>42</sup>, S. Simone<sup>11,a</sup>, R. Simoniello<sup>10</sup>, M. Skorokhvatov<sup>33,38</sup>, S. Smirnov<sup>38</sup>, G. Soares<sup>28</sup>, J. Y. Sohn<sup>22</sup>, A. Sokolenko<sup>55</sup>, E. Solodko<sup>44</sup>, N. Starkov<sup>32,34</sup>, L. Stoel<sup>44</sup>, M. E. Stramaglia<sup>46</sup>, D. Sukhonos<sup>44</sup>, Y. Suzuki<sup>19</sup>, S. Takahashi<sup>18</sup>, J. L. Tastet<sup>3</sup>, P. Teterin<sup>38</sup>, S. Than Naing<sup>32</sup>, I. Timiryasov<sup>46</sup>, V. Tioukov<sup>14</sup>, D. Tommasini<sup>44</sup>, M. Torii<sup>19</sup>, N. Tosi<sup>12</sup>, D. Treille<sup>44</sup>, R. Tsenov<sup>1,29</sup>, S. Ulin<sup>38</sup>, E. Ursov<sup>39,k</sup>, A. Ustyuzhanin<sup>40,34</sup>, Z. Uteshev<sup>38</sup>, L. Uvarov<sup>36</sup>, G. Vankova-Kirilova<sup>1</sup>, F. Vannucci<sup>5</sup>, V. Venturi<sup>44</sup>, I. Vidulin<sup>39,k</sup>, S. Vilchinski<sup>55</sup>, Heinz Vincke<sup>44</sup>, Helmut Vincke<sup>44</sup>, C. Visone<sup>14,d</sup>, K. Vlasik<sup>38</sup>, A. Volkov<sup>32,33</sup>, R. Voronkov<sup>32</sup>, S. van Waasen<sup>9</sup>, R. Wanke<sup>10</sup>, P. Wertelaers<sup>44</sup>, O. Williams<sup>44</sup>, J.-K. Woo<sup>24</sup>, M. Wurm<sup>10</sup>, S. Xella<sup>3</sup>, D. Yilmaz<sup>49</sup>, A. U. Yilmazer<sup>49</sup>, C. S. Yoon<sup>22</sup>, Yu. Zaytsev<sup>30</sup>, A. Zelenov<sup>36</sup>, J. Zimmerman<sup>6</sup>

<sup>1</sup> Faculty of Physics, Sofia University, Sofia, Bulgaria<sup>2</sup> Universidad Técnica Federico Santa María and Centro Científico Tecnológico de Valparaíso, Valparaíso, Chile<sup>3</sup> Niels Bohr Institute, University of Copenhagen, Copenhagen, Denmark<sup>4</sup> LAL, Univ. Paris-Sud, CNRS/IN2P3, Université Paris-Saclay, Orsay, France<sup>5</sup> LPNHE, IN2P3/CNRS, Sorbonne Université, Université Paris Diderot, 75252 Paris, France

- 6 Humboldt-Universität zu Berlin, Berlin, Germany
- 7 Physikalisches Institut, Universität Bonn, Bonn, Germany
- 8 Universität Hamburg, Hamburg, Germany
- 9 Forschungszentrum Jülich GmbH (KFA), Jülich, Germany
- 10 Institut für Physik and PRISMA Cluster of Excellence, Johannes Gutenberg Universität Mainz, Mainz, Germany
- 11 Sezione INFN di Bari, Bari, Italy
- 12 Sezione INFN di Bologna, Bologna, Italy
- 13 Sezione INFN di Cagliari, Cagliari, Italy
- 14 Sezione INFN di Napoli, Naples, Italy
- 15 Laboratori Nazionali dell'INFN di Frascati, Frascati, Italy
- 16 Laboratori Nazionali dell'INFN di Gran Sasso, L'Aquila, Italy
- 17 Aichi University of Education, Kariya, Japan
- 18 Kobe University, Kobe, Japan
- 19 Nagoya University, Nagoya, Japan
- 20 College of Industrial Technology, Nihon University, Narashino, Japan
- 21 Toho University, Funabashi, Chiba, Japan
- 22 Physics Education Department and RINS, Gyeongsang National University, Jinju, Korea
- 23 Gwangju National University of Education<sup>e</sup>, Gwangju, Korea
- 24 Jeju National University<sup>e</sup>, Jeju, Korea
- 25 Korea University, Seoul, Korea
- 26 Sungkyunkwan University<sup>e</sup>, Suwon-si, Gyeong Gi-do, Korea
- 27 University of Leiden, Leiden, The Netherlands
- 28 LIP, Laboratory of Instrumentation and Experimental Particle Physics, Lisbon, Portugal
- 29 Joint Institute for Nuclear Research (JINR), Dubna, Russia
- 30 Institute of Theoretical and Experimental Physics (ITEP) NRC “Kurchatov Institute”, Moscow, Russia
- 31 Institute for Nuclear Research of the Russian Academy of Sciences (INR RAS), Moscow, Russia
- 32 P.N. Lebedev Physical Institute (LPI RAS), Moscow, Russia
- 33 National Research Centre “Kurchatov Institute”, Moscow, Russia
- 34 National University of Science and Technology “MISiS”, Moscow, Russia
- 35 Institute for High Energy Physics (IHEP) NRC “Kurchatov Institute”, Protvino, Russia
- 36 Petersburg Nuclear Physics Institute (PNPI) NRC “Kurchatov Institute”, Gatchina, Russia
- 37 St. Petersburg Polytechnic University (SPbPU)<sup>f</sup>, St. Petersburg, Russia
- 38 National Research Nuclear University (MEPhI), Moscow, Russia
- 39 Skobeltsyn Institute of Nuclear Physics of Moscow State University (SINP MSU), Moscow, Russia
- 40 Yandex School of Data Analysis, Moscow, Russia
- 41 Institute of Physics, University of Belgrade, Belgrade, Serbia
- 42 Stockholm University, Stockholm, Sweden
- 43 Uppsala University, Uppsala, Sweden
- 44 European Organization for Nuclear Research (CERN), Geneva, Switzerland
- 45 University of Geneva, Geneva, Switzerland
- 46 École Polytechnique Fédérale de Lausanne (EPFL), Lausanne, Switzerland
- 47 Physik-Institut, Universität Zürich, Zurich, Switzerland
- 48 Middle East Technical University (METU), Ankara, Turkey
- 49 Ankara University, Ankara, Turkey
- 50 H.H. Wills Physics Laboratory, University of Bristol, Bristol, UK
- 51 STFC Rutherford Appleton Laboratory, Didcot, UK
- 52 Imperial College London, London, UK
- 53 University College London, London, UK
- 54 University of Warwick, Warwick, UK
- 55 Taras Shevchenko National University of Kyiv, Kiev, Ukraine

<sup>a</sup> Università di Bari, Bari, Italy

<sup>b</sup> Università di Bologna, Bologna, Italy

<sup>c</sup> Università di Cagliari, Cagliari, Italy

<sup>d</sup> Università di Napoli “Federico II”, Naples, Italy

<sup>e</sup> Associated to Gyeongsang National University, Jinju, Korea

<sup>f</sup> Associated to Petersburg Nuclear Physics Institute (PNPI), Gatchina, Russia

<sup>g</sup> Also at Moscow Institute of Physics and Technology (MIPT), Moscow Region, Russia

<sup>h</sup> Consorzio CREATE, Naples, Italy

<sup>i</sup> Università della Basilicata, Potenza, Italy

<sup>j</sup> Università di Napoli Parthenope, Naples, Italy

<sup>k</sup> Also at Faculty of Physics M.V. Lomonosov Moscow State University, Moscow, Russia





# Measurement of the muon flux from 400 GeV/c protons interacting in a thick molybdenum/tungsten target

SHiP Collaboration\*

Received: 27 January 2020 / Accepted: 27 February 2020 / Published online: 29 March 2020  
© CERN for the benefit of the SHiP collaboration 2020

**Abstract** The SHiP experiment is proposed to search for very weakly interacting particles beyond the Standard Model which are produced in a 400 GeV/c proton beam dump at the CERN SPS. About  $10^{11}$  muons per spill will be produced in the dump. To design the experiment such that the muon-induced background is minimized, a precise knowledge of the muon spectrum is required. To validate the muon flux generated by our Pythia and GEANT4 based Monte Carlo simulation (FairShip), we have measured the muon flux emanating from a SHiP-like target at the SPS. This target, consisting of 13 interaction lengths of slabs of molybdenum and tungsten, followed by a 2.4 m iron hadron absorber was placed in the H4 400 GeV/c proton beam line. To identify muons and to measure the momentum spectrum, a spectrometer instrumented with drift tubes and a muon tagger were used. During a 3-week period a dataset for analysis corresponding to  $(3.27 \pm 0.07) \times 10^{11}$  protons on target was recorded. This amounts to approximatively 1% of a SHiP spill.

## 1 Introduction

The aim of the SHiP experiment [1] is to search for very weakly interacting particles beyond the Standard Model which are produced by the interaction of 400 GeV/c protons from the CERN SPS with a beam dump. The SPS will deliver  $4 \times 10^{13}$  protons on target (POT) per spill, with the aim of accumulating  $2 \times 10^{20}$  POT during five years of operation. The target is composed of a mixture of TZM (Titanium-Zirconium doped Molybdenum,  $3.6\lambda^1$ ), W ( $9.2\lambda$ ) and Ta ( $0.5\lambda$ ) to increase the charm cross-section relative to the total cross-section and to reduce the probability that long-lived hadrons decay.

An essential task for the experiment is to keep the Standard Model background level to less than 0.1 event after

$2 \times 10^{20}$  POT. About  $10^{11}$  muons per spill will be produced in the dump, mainly from the decay of  $\pi$ ,  $K$ ,  $\rho$ ,  $\omega$  and charmed mesons. These muons would give rise to a serious background for many hidden particle searches, and hence their flux has to be reduced as much as possible. To achieve this, SHiP will employ a novel magnetic shielding concept [2] that will suppress the background by five orders of magnitude. The design of this shield relies on the precise knowledge of the kinematics of the produced muons, in particular the muons with a large momentum ( $>100$  GeV/c) and a large transverse momentum ( $>3$  GeV/c) as they can escape the shield and end up in the detector acceptance.

To validate the muon spectrum as predicted by our simulation, and hence the design of the shield, the SHiP Collaboration measured the muon flux in the experiment in the 400 GeV/c proton beam at the H4 beam line of the SPS at CERN in July 2018 [3].

## 2 Experimental setup and data

### 2.1 Spectrometer

The experimental setup, as implemented in FairShip (the SHiP software framework), is shown in Fig. 1. A cylindrical SHiP-like<sup>2</sup> target (10 cm diameter and 154.3 cm length) was followed by a hadron absorber made of iron blocks ( $240 \times 240 \times 240$  cm<sup>3</sup>) and surrounded by iron and concrete shielding blocks. The dimensions of the hadron absorber were optimised to stop pions and kaons while keeping a good  $p_T$  acceptance of traversing muons. The SPS beam counters (XSCI.022.480/481, S0 in Fig. 1) and beam counter S1 were used to count the number of POT seen by the experiment.

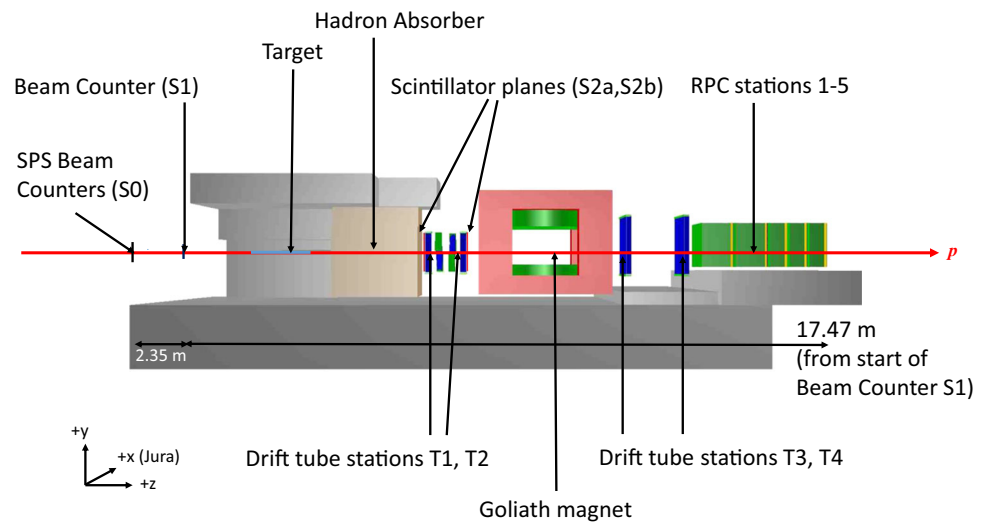
A spectrometer was placed downstream of the hadron absorber. It consisted of four drift-tube stations (T1–T4, modified from the OPERA experiment [4]) with two stations

<sup>1</sup>  $\lambda$  is the interaction length.

\* e-mail: [eric.van.herwijnen@cern.ch](mailto:eric.van.herwijnen@cern.ch) (corresponding author)

<sup>2</sup> Without Ta cladding, but with thicker Mo and W slabs to preserve the same number of interaction lengths.

**Fig. 1** Layout of the experimental setup to measure the  $\mu$ -flux. The FairShip (the SHiP software framework) coordinate system is also shown



upstream and two stations downstream of the Goliath magnet [5]. The drift-tubes were arranged in modules of 48 tubes, staggered in four layers of twelve tubes with a total width of approximately 50 cm. The four modules of height 110 cm making up stations T1 and T2 were arranged in a stereo setup ( $x - u$  views for T1 and  $v - x$  views for T2), with a stereo angle of  $60^\circ$ . T3 and T4 had only  $x$  views and were made of four modules of 160 cm height.

The drift-tube trigger (S2) consisted of two scintillator planes, placed before (S2a) and behind (S2b) the first two tracking stations.

A muon tagger was placed behind the two downstream drift-tube stations. It consisted of five planes of single-gap resistive plate chambers (RPCs), operated in avalanche mode, interleaved with  $1 \times 80$  cm and  $3 \times 40$  cm thick iron slabs. In addition to this, a 80 cm thick iron slab was positioned immediately upstream of the first chamber. The active area of the RPCs was  $190 \text{ cm} \times 120 \text{ cm}$  and each chamber was read out by two panels of  $x/y$  strips with a 1 cm pitch.

The two upstream tracking stations were centered on the beam line, whereas the two downstream stations and the RPCs were centered on the Goliath magnet<sup>3</sup> opening to maximize the acceptance.

The data acquisition was triggered by the coincidence of S1 and S2. For more details on the DAQ framework, see [6], and for a description of the trigger and the DAQ conditions during data taking, see [7].

The protons were delivered in 4.8 s duration spills (slow extraction). There were either one or two spills per SPS super-cycle, with intensities  $\sim 3 \times 10^6$  protons per second. The 1-sigma width of the beam spot was 2 mm. For physics analysis, 20128 useful spills were recorded with the full magnetic field of 1.5 T, with  $2.81 \times 10^{11}$  raw S1 counts. After normalization

(see Sect. 3.1) this corresponds to  $(3.25 \pm 0.07) \times 10^{11}$  POT. Additional data were taken with the magnetic field switched off for detector alignment and tracking efficiency measurement.

### 3 Data analysis

#### 3.1 Normalization

The calculation of the number of POT delivered to the experiment must take the different signal widths and dead times of the various scintillators into account. Moreover, some protons from the so-called halo, might fall outside the acceptance of S1 and will only be registered by S0.

In low-intensity runs these effects are small. We select some spills of these runs and split them into 50 slices of 0.1 s. We then determine the number of POT per slice and count the number of reconstructed muons in each slice, which should be independent of the intensity. By leaving the dead times as free parameters in a straight line fit, we find [8] that the number of POT required to have an event with at least one reconstructed muon is  $710 \pm 15$ . The systematic error of 15 POT accounts for the variation between the runs used for the normalization. The statistical error is negligible.

The efficiency of the trigger relies on the efficiency of detecting a muon signal in two scintillator planes S2a and S2b (see Fig. 1 and [8]). Each plane is equipped with two photo-multipliers (PMs), and the signal of each of the PMs is recorded for each event. The calculated trigger inefficiency is less than 1‰ and is hence neglected. Multiplying the number of reconstructed muons found in the 20128 spills by 710 we calculated that this data set corresponds to  $(3.25 \pm 0.07) \times 10^{11}$  POT.

<sup>3</sup> The centre of the Goliath magnet is 17.86 cm above the beam line.

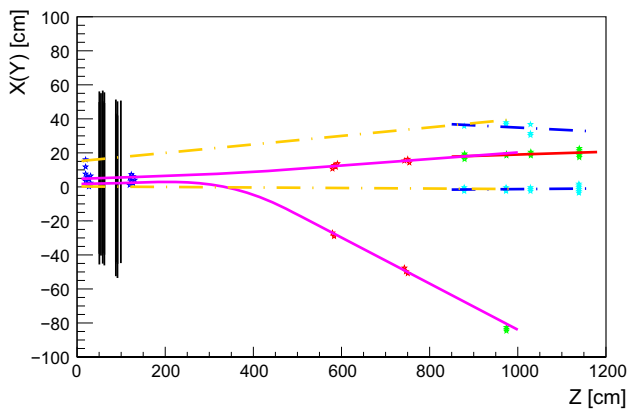


**Fig. 2** A two-muon event (most events are single-muon events) in the event display. The blue crosses are hits in Drift-tube stations T1 and T2, the red crosses are hits in T3 and T4. The green and light blue are hits in the RPC stations. The orange (blue) dotted lines are drift tube (RPC) track segments in the y projection; the pink (red) curves are track segments in the x projection

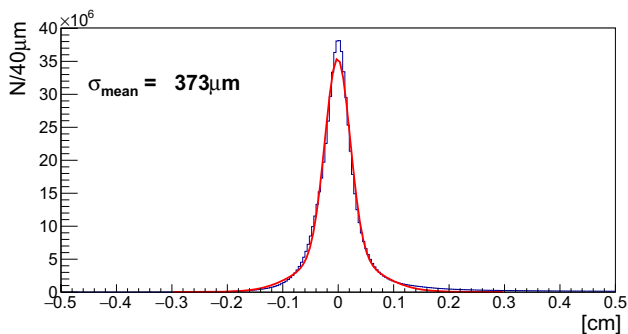
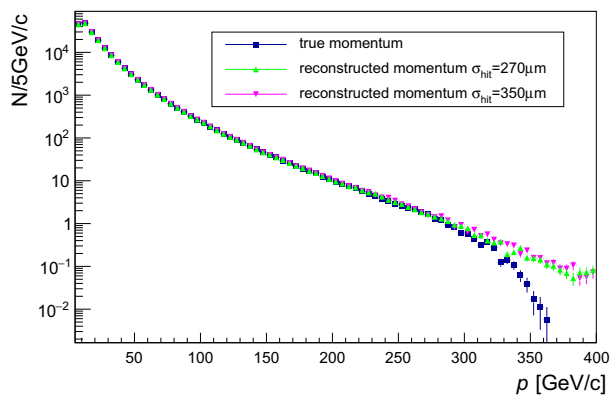


**Fig. 3** Average of all drift-tube residuals. The fit is a double Gaussian and the resulting hit resolution ( $\sigma_{\text{mean}}$ ) is the average of the two sigma's



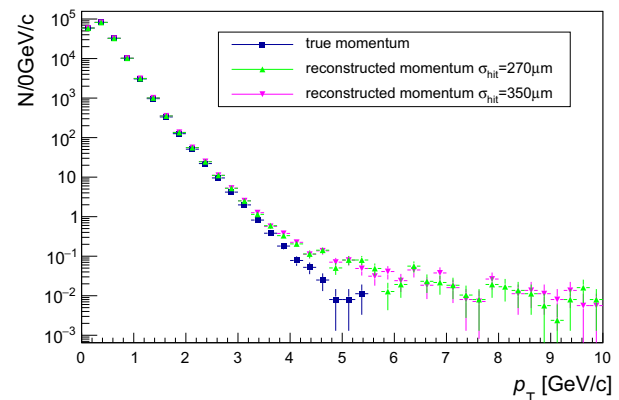
### 3.2 Tracking

For the drift-tubes, the relation between the measured drift-time and the distance of the track to the wire (the “ $r-t$ ” relation) is obtained from the Time to Digital Converter (TDC) distribution by assuming a uniformly illuminated tube. When reconstructing the data, the  $r-t$  relations are established first by looking the TDC distributions of simple events (i.e. events with at least 2 and a maximum of 6 hits per tracking station). In the simulation, the true drift radius is smeared with the expected resolution. The pattern recognition subsequently selects hits and clusters to form track candidates and provides the starting values for the track fit. The RPC pattern recognition proceeds similarly. Drift-tube tracks are then extrapolated to RPC tracks and tagged as muons if they have hits in at least three RPC stations. Figure 2 shows a two-muon event in the event display.

### 3.3 Momentum resolution

The expected drift-tube hit resolution based on the OPERA results is  $270 \mu\text{m}$  [4]. However, due to residual misalignment and imperfect  $r-t$  relations, the measured hit resolution was slightly worse,  $373 \mu\text{m}$ , as shown in Fig. 3. To study the impact of degraded spatial drift-tube resolution the momentum distribution from the simulation was folded with additional smearing as shown in Fig. 4. The tails towards large momentum  $p$  and  $p_T$  are caused mainly by tracks fitted with wrong drift times due to background hits.

From Fig. 4 we conclude that the momentum resolution is not strongly affected by the degraded resolution of the drift-tubes that is observed. The effect of the degraded drift-tube resolution is therefore negligible for our studies of the momentum spectrum. To account for residual effects in the track reconstruction, the resolution in the simulation was set to  $350 \mu\text{m}$ .

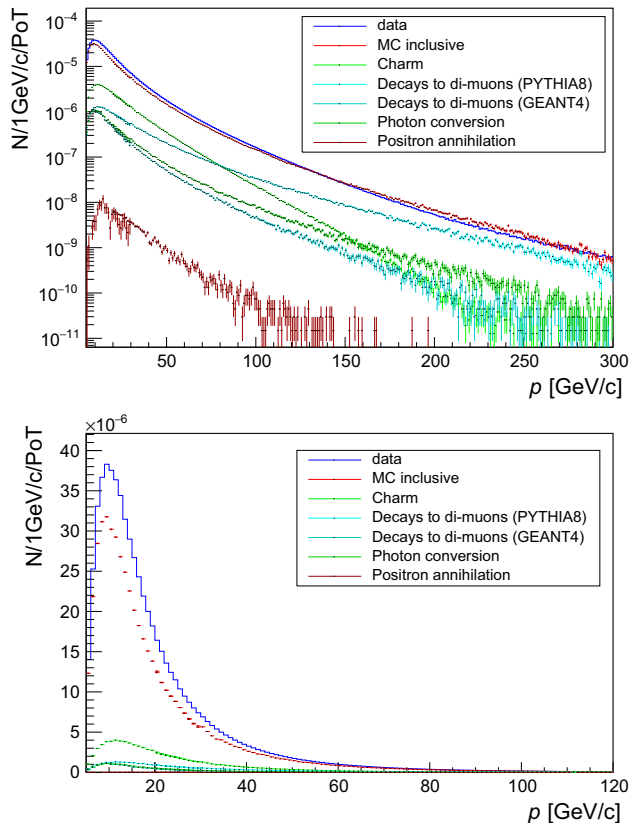


**Fig. 4** Effect of additional Gaussian smearing on the momentum distribution in the simulation, left  $p$ , right  $p_T$ . The distributions correspond to the simulation truth before reconstruction (navy blue), the nominal res-

olution  $\sigma_{\text{hit}} = 270 \mu\text{m}$  (green) and a degraded resolution  $\sigma_{\text{hit}} = 350 \mu\text{m}$  (pink)

**Table 1** Simulation samples made for SHiP background studies.  $\chi$  is the fraction of protons that produce heavy flavour

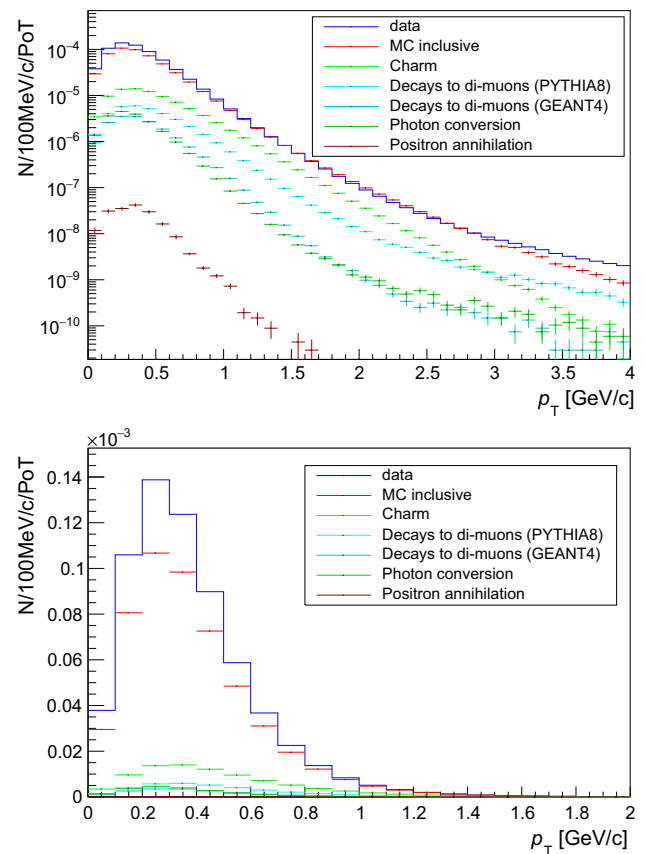
$E_{\text{kin}} > E_{\text{min}}$ (GeV)	mbias/cascade	POT
1	mbias	$1.8 \times 10^9$
1	charm ( $\chi_{c\bar{c}} = 1.7 \times 10^{-3}$ )	$10.2 \times 10^9$
10	mbias	$65.0 \times 10^9$
10	charm ( $\chi_{c\bar{c}} = 1.7 \times 10^{-3}$ )	$153.3 \times 10^9$
10	beauty ( $\chi_{b\bar{b}} = 1.3 \times 10^{-7}$ )	$5336.0 \times 10^9$

**Fig. 5** Measured muon momentum distributions from data and simulation, top full range in log scale, bottom detail of the low momentum range with a linear scale. The distributions are normalized to the number of POT. For simulated data, some individual sources are highlighted, muons from charm (green), from dimuon decays of low-mass resonances in Pythia8 (cyan), in Geant4 (turquoise), photon conversion (dark green) and positron annihilation (brown)

### 3.4 Tracking efficiencies

The tracking efficiency in the simulation depends on the station occupancy, and in data and simulation the occupancies are different (apparently caused by different amounts of delta rays). By taking this into account, the efficiency in the simulation is reduced from 96.6 to 94.8%.

To determine the tracking efficiency in data, we use the RPCs to identify muon tracks in the data with the magnetic

**Fig. 6** Transverse momentum distributions from data and simulation, top full range in log scale, bottom detail of lower transverse momentum with a linear scale. The distributions are normalized to the number of POT. For the simulation, some individual sources are highlighted, muons from charm (green), from dimuon decays of low-mass resonances in Pythia8 (cyan), in Geant4 (turquoise), photon conversion (dark green) and positron annihilation (brown)

field turned off. We then take the difference between the tracking efficiency in the simulation with magnetic field off (96.9%) and the measured efficiency (93.6%) as the systematic error: 3.3%. For more details on the analysis and reconstruction, see [9].

## 4 Comparison with the simulation

A large sample of muons was generated (with Pythia6, Pythia8 [10] and GEANT4 [11] in FairShip) for the background studies of SHiP, corresponding to the number of POT as shown in Table 1. The energy cuts ( $E_{\text{min}}$ ) of 1 GeV and 10 GeV were imposed to save computing time. The primary proton nucleon interactions are simulated by Pythia8 (using the default tune). The emerging particles are transported by GEANT4 through the target and hadron absorber producing a dataset of also referred to as “mbias” events. A special setting of GEANT4 was used to switch on muon interactions to produce rare dimuon decays of low-

**Fig. 7**  $p_T$  distributions in slices of  $p$  for data and simulation. The units on the vertical axes are the number of tracks per bin, with the simulation normalised to the data

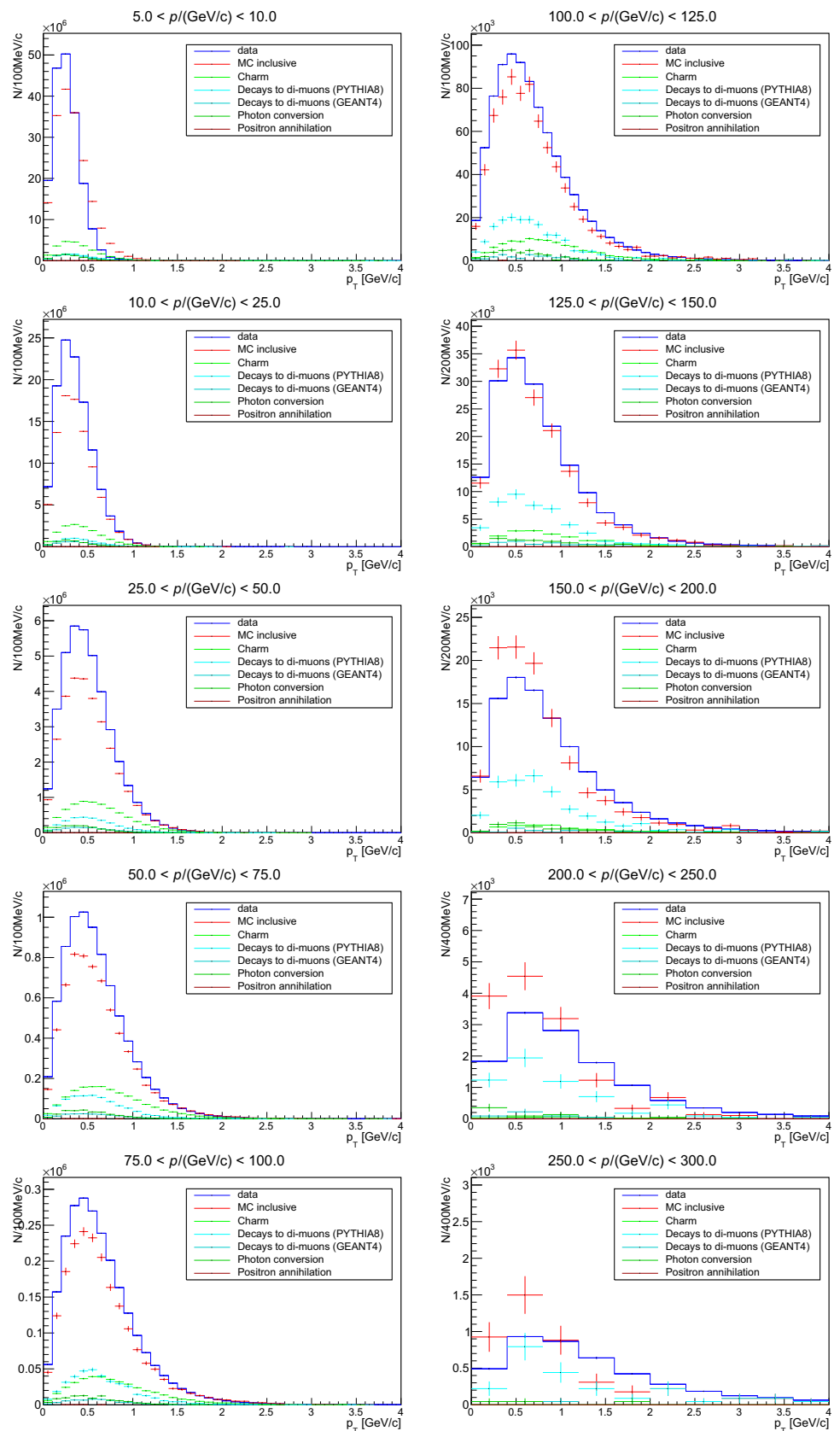


**Table 2** Number of reconstructed tracks in different momentum bins per  $10^9$  POT per GeV/c for data and simulation. The statistical errors for data are negligible. For data, the uncertainties are dominated by the uncertainty in the POT normalization, 2.1%. For the simulation, the main uncertainty is due to a different reconstruction efficiency in the simulation compared to data, 3.3%

Interval (GeV/c)	Data	Simulation	Ratio
5–10	$(1.13 \pm 0.02) \times 10^5$	$(1.12 \pm 0.03) \times 10^5$	$1.01 \pm 0.04$
10–25	$(2.40 \pm 0.05) \times 10^4$	$(1.85 \pm 0.06) \times 10^4$	$1.29 \pm 0.05$
25–50	$(4.80 \pm 0.10) \times 10^3$	$(3.76 \pm 0.11) \times 10^3$	$1.28 \pm 0.05$
50–75	$(9.83 \pm 0.2) \times 10^2$	$(8.0 \pm 0.2) \times 10^2$	$1.23 \pm 0.05$
75–100	$(2.95 \pm 0.06) \times 10^2$	$(2.5 \pm 0.08) \times 10^2$	$1.20 \pm 0.05$
100–125	$(1.1 \pm 0.02) \times 10^2$	$(0.9 \pm 0.03) \times 10^2$	$1.14 \pm 0.05$
125–150	$21.0 \pm 0.4$	$20.1 \pm 7.5$	$1.04 \pm 0.04$
150–200	$6.4 \pm 0.1$	$6.6 \pm 0.3$	$0.96 \pm 0.04$
200–250	$0.76 \pm 0.02$	$0.88 \pm 0.06$	$0.86 \pm 0.06$
250–300	$0.26 \pm 0.01$	$0.26 \pm 0.03$	$0.97 \pm 0.11$

mass resonances. Since GEANT4 does not have production of heavy flavour in particle interactions, an extra procedure was devised to simulate heavy-flavour production not only in the primary  $pN$  collision but also in collisions of secondary particles with the target nucleons. For performance reasons, this was done with Pythia6. The mbias and charm/beauty datasets were combined by removing the heavy-flavour contribution from the mbias and inserting the cascade data with appropriate weights. The details of the full heavy-flavour production for both the primary and cascade interactions are described in [12].

## 5 Results

The main objective of this study is to validate our simulations for the muon background estimation for the SHiP experiment. For this purpose, we compare the reconstructed momentum distributions ( $p$  and  $p_T$ ) from data and simulation.

As discussed in the previous section (see also Fig. 4), the events outside the limits ( $p > 350$  GeV/c or  $p_T > 5$  GeV/c) are dominated by wrongly reconstructed trajectories due to background hits and the limited precision of the tracking detector. In SHiP, where the hadron absorber is 5 m long, only muons with momentum  $p > 5$  GeV/c have sufficient energy to traverse the entire absorber. We therefore restrict our comparison to  $5$  GeV/c  $< p < 300$  GeV/c and  $p_T < 4$  GeV/c. For momenta below 10 GeV/c, we only rely on the reconstruction with the tracking detector, since they do not reach the RPC stations. Above 10 GeV/c we require the matching between drift-tube and RPC tracks.

Figures 5 and 6 show the  $p$  and  $p_T$  distributions of muon tracks. The distributions are normalized to the number of POT for data (see Sect. 3.1) and simulation respectively. For the simulated sample, muons from some individual sources are also shown in addition to their sum.

In Fig. 7, we show the  $p_T$  distributions in slices of  $p$ . Table 2 shows a numerical comparison of the number of tracks in the different momentum bins.

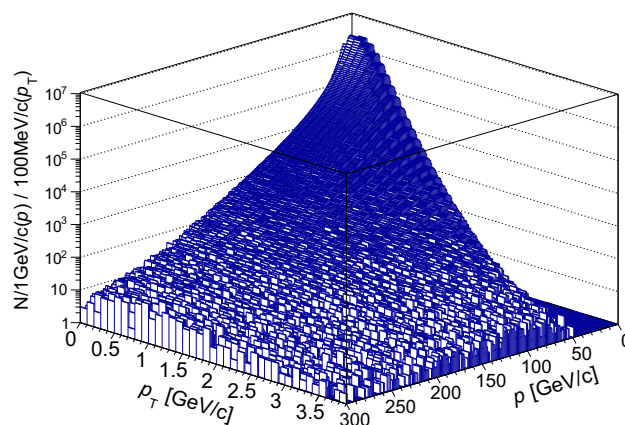


**Fig. 8**  $p_T$  vs  $p$  for data. The units on the vertical axis are the number of tracks per  $p$ ,  $p_T$  bin in the entire data set

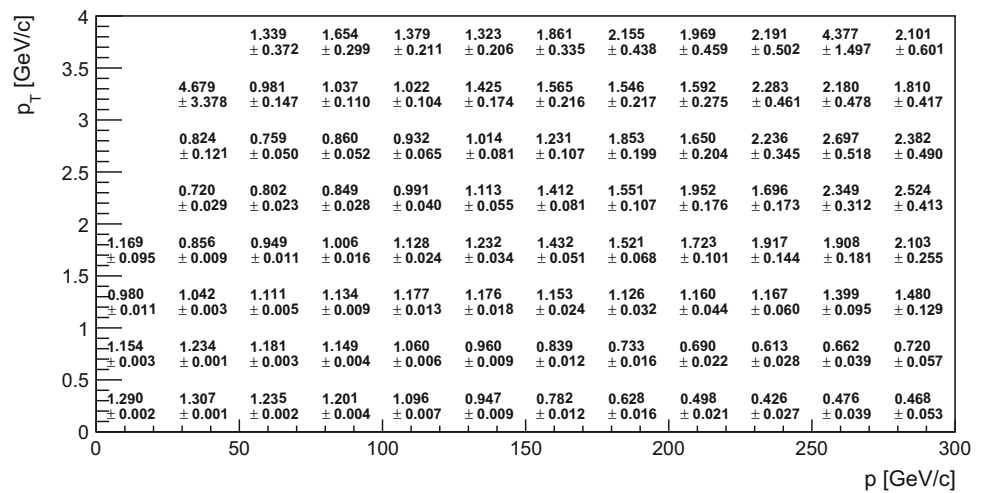
Figure 8 shows the muon  $p - p_T$  distribution in data.

Figure 9 gives a view of the differences between data and simulation in the  $p - p_T$  plane. Plotted is the difference between number of data and simulated tracks divided by the sum of the tracks in data and simulation in bins of  $p$  and  $p_T$ .

For momenta above 150 GeV/c, the simulation underestimates tracks with larger  $p_T$ , while the total number of tracks predicted are in agreement within 20%. The difference between data and simulation is probably caused by a different amount of muons from pion and kaon decays. It was seen that by increasing the contribution of muons from pion and kaon decays in the simulation the difference between data and simulation was reduced.

The FLUKA [13, 14] generator is used to determine the radiation levels in the SHiP environment. To benchmark FLUKA with typical settings used for radiological estimates related to muons in the SHiP environment, the muon flux setup was implemented in FLUKA and the simulation with this setup was compared to that made with Pythia/GEANT4. The results of this comparison are given in Annex 1. This independent prediction provides additional support for the validity of the SHiP background simulation.

**Fig. 9** Ratio of data and MC tracks,  $R = \frac{N_{Data}}{N_{MC}}$  in bins of  $p$  and  $p_T$



### 6 Conclusions

We have measured the muon flux from 400 GeV/c protons impinging on a heavy tungsten/molybdenum target. The physics processes underlying this are a combination of the production of muons through decays of non-interacting pions and kaons, the production and decays of charm particles and low-mass resonances, and the transportation of the muons through 2.4 m iron. Some 20–30% differences in the absolute rates are observed. The simulation underestimates contributions to larger transverse momentum for higher muon momenta. Given the complexity of the underlying processes, the agreement between the prediction by the simulation and the measured rate is remarkable.

Systematic errors for the track reconstruction (3%) and POT normalization (15 POT)/ $\mu$ -event have been studied and estimated.

A further understanding of the simulation and the data will be obtained with an analysis of di-muon events, the results of which will be the subject of a future publication.

**Acknowledgements** The SHiP Collaboration acknowledges support from the following Funding Agencies: the National Research Foundation of Korea (with Grant numbers of 2018R1A2B2007757, 2018R1D1A3B07050649, 2018R1D1A1B07050701, 2017R1D1A1B03036042, 2017R1A6A3A01075752, 2016R1A2B4012302, and 2016R1A6A3A11930680); the Russian Foundation for Basic Research (RFBR, Grant 17-02-00607) and the TAEK of Turkey. This work is supported by a Marie Skłodowska-Curie Innovative Training Network Fellowship of the European Commissions Horizon 2020 Programme under contract number 765710 INSIGHTS. We thank M. Al-Turany, F. Uhlig, S. Neubert and A. Gheata their assistance with FairRoot. We acknowledge G. Eulisse and P.A. Munkes for help with Alibuild. The measurements reported in this paper would not have been possible without a significant financial contribution from CERN. In addition, several member institutes made large financial and in-kind contributions to the construction of the target and the spectrometer sub detectors, as well as providing expert manpower for commissioning, data taking and analysis. This help is gratefully acknowledged.

**Data Availability Statement** This manuscript has no associated data or the data will not be deposited. [Authors’ comment: The raw datasets analysed during the current study are available from the corresponding author on reasonable request.]

**Open Access** This article is licensed under a Creative Commons Attribution 4.0 International License, which permits use, sharing, adaptation, distribution and reproduction in any medium or format, as long as you give appropriate credit to the original author(s) and the source, provide a link to the Creative Commons licence, and indicate if changes were made. The images or other third party material in this article are included in the article’s Creative Commons licence, unless indicated otherwise in a credit line to the material. If material is not included in the article’s Creative Commons licence and your intended use is not permitted by statutory regulation or exceeds the permitted use, you will need to obtain permission directly from the copyright holder. To view a copy of this licence, visit <http://creativecommons.org/licenses/by/4.0/>.

Funded by SCOAP<sup>3</sup>.

### Appendix A: FLUKA-GEANT4 comparison

#### Appendix A.1: Simulation samples

The geometry of the muon flux spectrometer was reproduced in FLUKA with a few approximations [15]. A large sample of muons was generated with FLUKA for simulating primary proton nucleon interactions as well as the transport of the emerging particles. This sample was used for the comparison with GEANT4. For performance reasons three samples were made with different momentum thresholds (set for all particles). This increased the statistics in the corresponding momentum bins. The number of POT for the three samples is shown in Table 3.

To be consistent with the GEANT4 simulations done for SHiP, the comparison is limited to  $5 \text{ GeV}/c < p < 300 \text{ GeV}/c$  and  $p_T < 4 \text{ GeV}/c$ . The primary proton-nuclei interactions are simulated and transported through the target and hadron absorber by FLUKA. Special settings of FLUKA were used to include:

**Table 3** FLUKA samples produced for Muon Flux comparison with GEANT4

Momentum threshold for transport of all particles (GeV/c)	POT	Muon momentum range (GeV/c)
5	$1.37 \times 10^8$	$5 < p < 30$
27	$5.43 \times 10^8$	$30 < p < 100$
97	$5.03 \times 10^8$	$p > 100$

- full simulation of muon nuclear interactions and production of secondary hadrons;
- delta ray production from muons ( $> 10$  MeV);
- pair production and bremsstrahlung by high-energy muons;
- full transport and decay of charmed hadrons and tau leptons;
- decays of pions, kaons and muons described with maximum accuracy and polarisation.

The physics settings utilised in the FLUKA simulations were chosen such as to activate all relevant processes like charm decays and most accurate pion and kaon decay descriptions, and to be as close as possible to the physics lists employed in the GEANT4 simulations.

### 6.1 Appendix A.2: Results

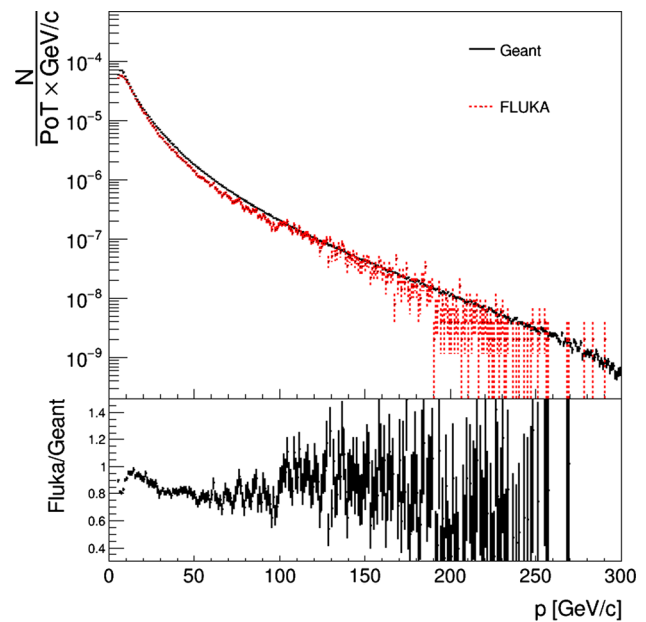
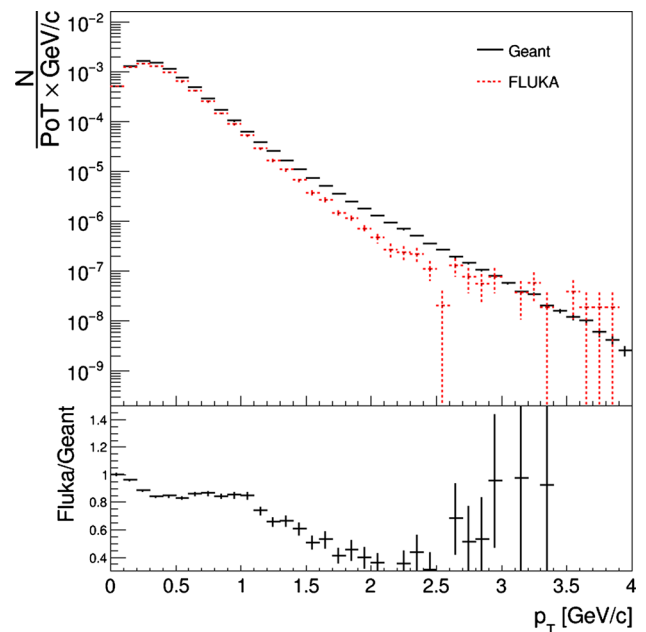
In this section, we compare the reconstructed momentum distributions,  $p$  and  $p_T$ , between FLUKA and GEANT4.

Tracks are considered to be muons if they have hits in the T1, T2, T3 and T4 stations. The distributions are taken at the T1 station and normalized to the number of POT.

As shown in Fig. 5, FLUKA predicts a lower rate compared to GEANT4. In the momentum range  $5 \text{ GeV}/c < p < 200 \text{ GeV}/c$ , the agreement between the two simulations is at the level of  $\sim 20\%$ , above  $200 \text{ GeV}/c$  there is a discrepancy of a factor  $\sim 3$ .

As shown in Fig. 6, FLUKA predicts a lower rate compared to GEANT4. In the transverse momentum range  $0 < p_T < 1 \text{ GeV}/c$  the agreement between the two simulations is at the level of  $\sim 20\%$ , while above  $1 \text{ GeV}/c$ , there is a discrepancy of a factor  $\sim 3$  (Figs. 10, 11).

It should be noted that FLUKA does not allow users to change the underlying physics models or cross sections themselves. The uncertainties shown are therefore purely statistical. Given the complexity of the processes underlying the production of muons and the approximations included in the geometry implementations, the agreement between the FLUKA and GEANT4 simulations is reasonable. The differences between FLUKA and GEANT4 over the full muon momentum and transverse momentum spectra are within a factor 3. The large discrepancies of up to a factor 2–3 are

**Fig. 10** Momentum distributions from FLUKA and GEANT4. The distributions are normalized to the number of POT**Fig. 11** Transverse momentum distributions from FLUKA and GEANT4. The distributions are normalized to the number of POT

mostly in the tails documenting the systematic differences between the FLUKA and GEANT4 models in these regions. Therefore a safety factor of 3 is recommended for future radiological estimates related to muons in the SHiP environment.

### References

1. The SHiP Collaboration, *A facility to Search for Hidden Particles (SHIP) at the CERN SPS*. 2015. [arXiv:1504.04956v1](https://arxiv.org/abs/1504.04956v1)



2. The SHiP Collaboration, The active muon shield in the SHiP experiment. *JINST* **12**(05), P05011 (2017)
3. The SHiP Collaboration, *Muon flux measurements for SHiP at H4*. CERN-SPSC-2017-020 (2017)
4. R. Zimmermann, J. Ebert, C. Hagner, B. Koppitz, V. Savelev, W. Schmidt-Parzefall, J. Sewing, Y. Zaitsev, The precision tracker of the OPERA detector. *Nucl. Instrum. Meth. A* **555**, 435–450 (2005)
5. M. Rosenthal et al., *Magnetic field measurements of the GOLIATH magnet in EHN1*. CERN-ACC-NOTE-2018-0028 (2018)
6. P. Gorbunov, *DAQ Framework for the 2018 combined beam tests*. CERN-SHiP-INT-2017-004 (2017)
7. M. Jonker et al. *Data acquisition and trigger for the 2018 SHiP test beam measurements*. CERN-SHiP-INT-2019-004 (2019)
8. H. Dijkstra, *Normalization of proton flux during muon flux beam test*. CERN-SHiP-INT-2019-001 (2019)
9. C. Ahdida et al., *Measurement of the muon flux for the SHiP experiment*. CERN-SHiP-NOTE-2019-003 (2019)
10. T. Sjöstrand, S. Mrenna, P. Skands, A brief introduction to Pythia 8.1. *Comput. Phys. Commun.* **178**(11), 852–867 (2008)
11. S. Agostinelli et al., GEANT4: a simulation toolkit. *Nucl. Instrum. Meth. A* **506**, 250–303 (2003)
12. H. Dijkstra, T. Ruf, *Heavy Flavour cascade production in a beam dump*. CERN-SHiP-NOTE-2015-009 (2015)
13. T.T. Bohlen et al., The FLUKA code: developments and challenges for high energy and medical applications. *Nuclear Data Sheets* **120** (2014)
14. A. Fassò, A. Ferrari, J. Ranft, P.R. Sala, *FLUKA: a multi-particle transport code*. CERN-2005-10 (2005), INFN/TC-05/11, SLAC-R-773
15. C. Ahdida et al., *FLUKA-Geant comparison for the muon flux experiment*. CERN-SHiP-NOTE-2019-005 (2019)

## SHiP Collaboration

C. Ahdida<sup>44</sup>, A. Akmete<sup>48</sup>, R. Albanese<sup>14,d,h</sup>, A. Alexandrov<sup>14,32,34,d</sup>, A. Anokhina<sup>39</sup>, S. Aoki<sup>18</sup>, G. Arduini<sup>44</sup>, E. Atkin<sup>38</sup>, N. Azorskiy<sup>29</sup>, J. J. Back<sup>54</sup>, A. Bagulya<sup>32</sup>, F. Baaltasar Dos Santos<sup>44</sup>, A. Baranov<sup>40</sup>, F. Bardou<sup>44</sup>, G. J. Barker<sup>54</sup>, M. Battistin<sup>44</sup>, J. Bauche<sup>44</sup>, A. Bay<sup>46</sup>, V. Bayliss<sup>51</sup>, G. Bencivenni<sup>15</sup>, A. Y. Berdnikov<sup>37</sup>, Y. A. Berdnikov<sup>37</sup>, M. Bertani<sup>15</sup>, C. Betancourt<sup>47</sup>, I. Bezshyiko<sup>47</sup>, O. Bezshyyko<sup>55</sup>, D. Bick<sup>8</sup>, S. Bieschke<sup>8</sup>, A. Blanco<sup>28</sup>, J. Boehm<sup>51</sup>, M. Bogomilov<sup>1</sup>, I. Boiarska<sup>3</sup>, K. Bondarenko<sup>27,44</sup>, W. M. Bonivento<sup>13</sup>, J. Borburgh<sup>44</sup>, A. Boyarsky<sup>27,55</sup>, R. Brenner<sup>43</sup>, D. Breton<sup>4</sup>, V. Büscher<sup>10</sup>, A. Buonauro<sup>47</sup>, S. Buontempo<sup>14</sup>, S. Cadeddu<sup>13</sup>, A. Calcaterra<sup>15</sup>, M. Calviani<sup>44</sup>, M. Campanelli<sup>53</sup>, M. Casolino<sup>44</sup>, N. Charitonidis<sup>44</sup>, P. Chau<sup>10</sup>, J. Chauveau<sup>5</sup>, A. Chepurinov<sup>39</sup>, M. Chernyavskiy<sup>32</sup>, K.-Y. Choi<sup>26</sup>, A. Chumakov<sup>2</sup>, P. Ciambone<sup>15</sup>, V. Cicero<sup>12</sup>, L. Congedo<sup>11,a</sup>, K. Cornelis<sup>44</sup>, M. Cristinziani<sup>7</sup>, A. Crupano<sup>14,d</sup>, G. M. Dallavalle<sup>12</sup>, A. Datwyler<sup>47</sup>, N. D'Ambrosio<sup>16</sup>, G. D'Appollonio<sup>13,c</sup>, R. de Asmundis<sup>14</sup>, J. De Carvalho Saraiva<sup>28</sup>, G. De Lellis<sup>14,34,44,d</sup>, M. de Magistris<sup>14,d</sup>, A. De Roeck<sup>44</sup>, M. De Serio<sup>11,a</sup>, D. De Simone<sup>47</sup>, L. Dedenko<sup>39</sup>, P. Dergachev<sup>34</sup>, A. Di Crescenzo<sup>14,d</sup>, L. Di Giulio<sup>44</sup>, N. Di Marco<sup>16</sup>, C. Dib<sup>2</sup>, H. Dijkstra<sup>44</sup>, V. Dmitrenko<sup>38</sup>, S. Dmitrievskiy<sup>29</sup>, L. A. Dougherty<sup>44</sup>, A. Dolmatov<sup>30</sup>, D. Domenici<sup>15</sup>, S. Donskov<sup>35</sup>, V. Drohan<sup>55</sup>, A. Dubreuil<sup>45</sup>, O. Durhan<sup>48</sup>, M. Ehlert<sup>6</sup>, E. Elikkaya<sup>48</sup>, T. Enik<sup>29</sup>, A. Etenko<sup>33,38</sup>, F. Fabbri<sup>12</sup>, O. Fedin<sup>36</sup>, F. Fedotovs<sup>52</sup>, G. Felici<sup>15</sup>, M. Ferrillo<sup>47</sup>, M. Ferro-Luzzi<sup>44</sup>, K. Filippov<sup>38</sup>, R. A. Fini<sup>11</sup>, P. Fonte<sup>28</sup>, C. Franco<sup>28</sup>, M. Fraser<sup>44</sup>, R. Fresa<sup>14,i</sup>, R. Froeschl<sup>44</sup>, T. Fukuda<sup>19</sup>, G. Galati<sup>14,d</sup>, J. Gall<sup>44</sup>, L. Gatignon<sup>44</sup>, G. Gavrilo<sup>38</sup>, V. Gentile<sup>14,d</sup>, B. Goddard<sup>44</sup>, L. Golinka-Bezshyyko<sup>55</sup>, A. Golovatiuk<sup>14,d</sup>, D. Golubkov<sup>30</sup>, A. Golutvin<sup>34,52</sup>, P. Gorbounov<sup>44</sup>, D. Gorbunov<sup>31</sup>, S. Gorbunov<sup>32</sup>, V. Gorkavenko<sup>55</sup>, M. Gorshenkov<sup>34</sup>, V. Grachev<sup>38</sup>, A. L. Grandchamp<sup>46</sup>, E. Graverini<sup>46</sup>, J.-L. Grenard<sup>44</sup>, D. Grenier<sup>44</sup>, V. Grichine<sup>32</sup>, N. Gruzinskii<sup>36</sup>, A. M. Guler<sup>48</sup>, Yu. Guz<sup>35</sup>, G. J. Haefeli<sup>46</sup>, C. Hagner<sup>8</sup>, H. Hakobyan<sup>2</sup>, I. W. Harris<sup>46</sup>, E. van Herwijnen<sup>44</sup>, C. Hessler<sup>44</sup>, A. Hollnagel<sup>10</sup>, B. Hosseini<sup>52</sup>, M. Hushchyn<sup>40</sup>, G. Iaselli<sup>11,a</sup>, A. Iuliano<sup>14,d</sup>, R. Jacobsson<sup>44</sup>, D. Joković<sup>41</sup>, M. Jonker<sup>44</sup>, I. Kadenko<sup>55</sup>, V. Kain<sup>44</sup>, B. Kaiser<sup>8</sup>, C. Kamiscioglu<sup>49</sup>, D. Karpenkov<sup>34</sup>, K. Kershaw<sup>44</sup>, M. Khabibullin<sup>31</sup>, E. Khalikov<sup>39</sup>, G. Khaustov<sup>35</sup>, G. Khoriauli<sup>10</sup>, A. Khotyantsev<sup>31</sup>, Y. G. Kim<sup>23</sup>, V. Kim<sup>36,37</sup>, N. Kitagawa<sup>19</sup>, J.-W. Ko<sup>22</sup>, K. Kodama<sup>17</sup>, A. Kolesnikov<sup>29</sup>, D. I. Kolev<sup>1</sup>, V. Kolosov<sup>35</sup>, M. Komatsu<sup>19</sup>, A. Kono<sup>21</sup>, N. Konovalova<sup>32,34</sup>, S. Kormannshaus<sup>10</sup>, I. Korol<sup>16</sup>, I. Korol'ko<sup>30</sup>, A. Korzenev<sup>45</sup>, V. Kostyukhin<sup>7</sup>, E. Koukovini Platia<sup>44</sup>, S. Kovalenko<sup>2</sup>, I. Krasilnikova<sup>34</sup>, Y. Kudenko<sup>31,38,g</sup>, E. Kurbatov<sup>40</sup>, P. Kurbatov<sup>34</sup>, V. Kurochka<sup>31</sup>, E. Kuznetsova<sup>36</sup>, H. M. Lacker<sup>6</sup>, M. Lamont<sup>44</sup>, G. Lanfranchi<sup>15</sup>, O. Lantwin<sup>47</sup>, A. Lauria<sup>14,d</sup>, K. S. Lee<sup>25</sup>, K. Y. Lee<sup>22</sup>, J.-M. Lévy<sup>5</sup>, V. P. Loschiavo<sup>14,h</sup>, L. Lopes<sup>28</sup>, E. Lopez Sola<sup>44</sup>, V. Lyubovitskij<sup>2</sup>, J. Maalmi<sup>4</sup>, A. Magnan<sup>52</sup>, V. Maleev<sup>36</sup>, A. Malinin<sup>33</sup>, Y. Manabe<sup>19</sup>, A. K. Managadze<sup>39</sup>, M. Manfredi<sup>44</sup>, S. Marsh<sup>44</sup>, A. M. Marshall<sup>50</sup>, A. Mefodev<sup>31</sup>, P. Mermod<sup>45</sup>, A. Miano<sup>14,d</sup>, S. Mikado<sup>20</sup>, Yu. Mikhaylov<sup>35</sup>, D. A. Milstead<sup>42</sup>, O. Mineev<sup>31</sup>, A. Montanari<sup>12</sup>, M. C. Montesi<sup>14,d</sup>, K. Morishima<sup>19</sup>, S. Movchan<sup>29</sup>, Y. Muttoni<sup>44</sup>, N. Naganawa<sup>19</sup>, M. Nakamura<sup>19</sup>, T. Nakano<sup>19</sup>, S. Nasybulin<sup>36</sup>, P. Ninin<sup>44</sup>, A. Nishio<sup>19</sup>, A. Novikov<sup>38</sup>, B. Obinyakov<sup>33</sup>, S. Ogawa<sup>21</sup>, N. Okateva<sup>32,34</sup>, B. Opitz<sup>8</sup>, J. Osborne<sup>44</sup>, M. Ovchynnikov<sup>27,55</sup>, N. Owtscharenko<sup>7</sup>, P. H. Owen<sup>47</sup>, P. Pacholek<sup>44</sup>, A. Paoloni<sup>15</sup>, B. D. Park<sup>22</sup>, A. Pastore<sup>11</sup>, M. Patel<sup>34,52</sup>, D. Pereyma<sup>30</sup>, A. Perillo-Marccone<sup>44</sup>, G. L. Petkov<sup>1</sup>, K. Petridis<sup>50</sup>, A. Petrov<sup>33</sup>, D. Podgrudkov<sup>39</sup>, V. Poliakov<sup>35</sup>, N. Polukhina<sup>32,34,38</sup>, J. Prieto Prieto<sup>44</sup>, M. Prokudin<sup>30</sup>, A. Prota<sup>14,d</sup>, A. Quercia<sup>14,d</sup>, A. Rademakers<sup>44</sup>, A. Rakai<sup>44</sup>, F. Ratnikov<sup>40</sup>, T. Rawlings<sup>51</sup>, F. Redi<sup>46</sup>, S. Ricciardi<sup>51</sup>, M. Rinaldesi<sup>44</sup>, Volodymyr Rodin<sup>55</sup>, Viktor Rodin<sup>55</sup>, P. Robbe<sup>4</sup>, A. B. Rodrigues Cavalcante<sup>46</sup>, T. Roganova<sup>39</sup>, H. Rokujo<sup>19</sup>, G. Rosa<sup>14,d</sup>, T. Rovelli<sup>12,b</sup>, O. Ruchayskiy<sup>3</sup>, T. Ruf<sup>44</sup>, V. Samoylenko<sup>35</sup>, V. Samsonov<sup>38</sup>, F. Sanchez Galan<sup>44</sup>, P. Santos Diaz<sup>44</sup>, A. Sanz Ull<sup>44</sup>, A. Saputi<sup>15</sup>, O. Sato<sup>19</sup>, E. S. Savchenko<sup>34</sup>, J. S. Schliwinski<sup>6</sup>, W. Schmidt-Parzefall<sup>8</sup>, N. Serra<sup>34,47</sup>,

S. Sgobba<sup>44</sup>, O. Shadura<sup>55</sup>, A. Shakin<sup>34</sup>, M. Shaposhnikov<sup>46</sup>, P. Shatalov<sup>30,34</sup>, T. Shchedrina<sup>32,34</sup>, L. Shchutska<sup>46</sup>, V. Shevchenko<sup>33,34</sup>, H. Shibuya<sup>21</sup>, L. Shihora<sup>6</sup>, S. Shirobokov<sup>52</sup>, A. Shustov<sup>38</sup>, S. B. Silverstein<sup>42</sup>, S. Simone<sup>11,a</sup>, R. Simoniello<sup>10</sup>, M. Skorokhvatov<sup>33,38</sup>, S. Smirnov<sup>38</sup>, J. Y. Sohn<sup>22</sup>, A. Sokolenko<sup>55</sup>, E. Solodko<sup>44</sup>, N. Starkov<sup>32,34</sup>, L. Stoel<sup>44</sup>, M. E. Stramaglia<sup>46</sup>, D. Sukhonos<sup>44</sup>, Y. Suzuki<sup>19</sup>, S. Takahashi<sup>18</sup>, J. L. Tastet<sup>3</sup>, P. Teterin<sup>38</sup>, S. Than Naing<sup>32</sup>, I. Timiryasov<sup>46</sup>, V. Tioukov<sup>14</sup>, D. Tommasini<sup>44</sup>, M. Torii<sup>19</sup>, N. Tosi<sup>12</sup>, D. Treille<sup>44</sup>, R. Tsenov<sup>1,29</sup>, S. Ulin<sup>38</sup>, E. Ursov<sup>39</sup>, A. Ustyuzhanin<sup>34,40</sup>, Z. Uteshev<sup>38</sup>, G. Vankova-Kirilova<sup>1</sup>, F. Vannucci<sup>5</sup>, V. Venturi<sup>44</sup>, S. Vilchinski<sup>55</sup>, Heinz Vincke<sup>44</sup>, Helmut Vincke<sup>44</sup>, C. Visone<sup>14,d</sup>, K. Vlasik<sup>38</sup>, A. Volkov<sup>32,33</sup>, R. Voronov<sup>32</sup>, S. van Waasen<sup>9</sup>, R. Wanke<sup>10</sup>, P. Wertelaers<sup>44</sup>, O. Williams<sup>44</sup>, J.-K. Woo<sup>24</sup>, M. Wurm<sup>10</sup>, S. Xella<sup>3</sup>, D. Yilmaz<sup>49</sup>, A. U. Yilmazer<sup>49</sup>, C. S. Yoon<sup>22</sup>, Yu. Zaytsev<sup>30</sup>, J. Zimmerman<sup>6</sup>

- <sup>1</sup> Faculty of Physics, Sofia University, Sofia, Bulgaria
- <sup>2</sup> Universidad Técnica Federico Santa María and Centro Científico Tecnológico de Valparaíso, Valparaíso, Chile
- <sup>3</sup> Niels Bohr Institute, University of Copenhagen, Copenhagen, Denmark
- <sup>4</sup> LAL, Univ. Paris-Sud, CNRS/IN2P3, Université Paris-Saclay, Orsay, France
- <sup>5</sup> LPNHE, IN2P3/CNRS, Sorbonne Université, Université Paris Diderot, 75252 Paris, France
- <sup>6</sup> Humboldt-Universität zu Berlin, Berlin, Germany
- <sup>7</sup> Physikalisches Institut, Universität Bonn, Bonn, Germany
- <sup>8</sup> Universität Hamburg, Hamburg, Germany
- <sup>9</sup> Forschungszentrum Jülich GmbH (KFA), Jülich, Germany
- <sup>10</sup> Institut für Physik and PRISMA Cluster of Excellence, Johannes Gutenberg Universität Mainz, Mainz, Germany
- <sup>11</sup> Sezione INFN di Bari, Bari, Italy
- <sup>12</sup> Sezione INFN di Bologna, Bologna, Italy
- <sup>13</sup> Sezione INFN di Cagliari, Cagliari, Italy
- <sup>14</sup> Sezione INFN di Napoli, Naples, Italy
- <sup>15</sup> Laboratori Nazionali dell'INFN di Frascati, Frascati, Italy
- <sup>16</sup> Laboratori Nazionali dell'INFN di Gran Sasso, L'Aquila, Italy
- <sup>17</sup> Aichi University of Education, Kariya, Japan
- <sup>18</sup> Kobe University, Kobe, Japan
- <sup>19</sup> Nagoya University, Nagoya, Japan
- <sup>20</sup> College of Industrial Technology, Nihon University, Narashino, Japan
- <sup>21</sup> Toho University, Funabashi, Chiba, Japan
- <sup>22</sup> Physics Education Department & RINS, Gyeongsang National University, Jinju, Korea
- <sup>23</sup> Gwangju National University of Education, Gwangju, Korea
- <sup>24</sup> Jeju National University, Jeju, Korea
- <sup>25</sup> Korea University, Seoul, Korea
- <sup>26</sup> Sungkyunkwan University, Suwon-si, Gyeong Gi-do, Korea
- <sup>27</sup> University of Leiden, Leiden, The Netherlands
- <sup>28</sup> LIP-Laboratory of Instrumentation and Experimental Particle Physics, Lisbon, Portugal
- <sup>29</sup> Joint Institute for Nuclear Research (JINR), Dubna, Russia
- <sup>30</sup> Institute of Theoretical and Experimental Physics (ITEP) NRC 'Kurchatov Institute', Moscow, Russia
- <sup>31</sup> Institute for Nuclear Research of the Russian Academy of Sciences (INR RAS), Moscow, Russia
- <sup>32</sup> P.N. Lebedev Physical Institute (LPI RAS), Moscow, Russia
- <sup>33</sup> National Research Centre 'Kurchatov Institute', Moscow, Russia
- <sup>34</sup> National University of Science and Technology "MISIS", Moscow, Russia
- <sup>35</sup> Institute for High Energy Physics (IHEP) NRC 'Kurchatov Institute', Protvino, Russia
- <sup>36</sup> Petersburg Nuclear Physics Institute (PNPI) NRC 'Kurchatov Institute', Gatchina, Russia
- <sup>37</sup> St. Petersburg Polytechnic University (SPbPU), Saint Petersburg, Russia
- <sup>38</sup> National Research Nuclear University (MEPhI), Moscow, Russia
- <sup>39</sup> Skobeltsyn Institute of Nuclear Physics of Moscow State University (SINP MSU), Moscow, Russia
- <sup>40</sup> Yandex School of Data Analysis, Moscow, Russia
- <sup>41</sup> Institute of Physics, University of Belgrade, Serbia
- <sup>42</sup> Stockholm University, Stockholm, Sweden
- <sup>43</sup> Uppsala University, Uppsala, Sweden

- <sup>44</sup> European Organization for Nuclear Research (CERN), Geneva, Switzerland
- <sup>45</sup> University of Geneva, Geneva, Switzerland
- <sup>46</sup> École Polytechnique Fédérale de Lausanne (EPFL), Lausanne, Switzerland
- <sup>47</sup> Physik-Institut, Universität Zürich, Zürich, Switzerland
- <sup>48</sup> Middle East Technical University (METU), Ankara, Turkey
- <sup>49</sup> Ankara University, Ankara, Turkey
- <sup>50</sup> H.H. Wills Physics Laboratory, University of Bristol, Bristol, UK
- <sup>51</sup> STFC Rutherford Appleton Laboratory, Didcot, UK
- <sup>52</sup> Imperial College London, London, UK
- <sup>53</sup> University College London, London, UK
- <sup>54</sup> University of Warwick, Warwick, UK
- <sup>55</sup> Taras Shevchenko National University of Kyiv, Kyiv, Ukraine
- <sup>a</sup> Università di Bari, Bari, Italy
- <sup>b</sup> Università di Bologna, Bologna, Italy
- <sup>c</sup> Università di Cagliari, Cagliari, Italy
- <sup>d</sup> Università di Napoli “Federico II”, Napoli, Italy
- <sup>e</sup> Associated to Gyeongsang National University, Jinju, Korea
- <sup>f</sup> Associated to Petersburg Nuclear Physics Institute (PNPI), Gatchina, Russia
- <sup>g</sup> Also at Moscow Institute of Physics and Technology (MIPT), Moscow Region, Russia
- <sup>h</sup> Consorzio CREATE, Naples, Italy
- <sup>i</sup> Università della Basilicata, Potenza, Italy

# Sensitivity of the SHiP experiment to Heavy Neutral Leptons



## The SHiP collaboration

**C. Ahdida,<sup>1</sup> R. Albanese,<sup>2,a</sup> A. Alexandrov,<sup>2</sup> A. Anokhina,<sup>3</sup> S. Aoki,<sup>4</sup> G. Arduini,<sup>1</sup>  
 E. Atkin,<sup>5</sup> N. Azorskiy,<sup>6</sup> F. Baaltasar Dos Santos,<sup>1</sup> J.J. Back,<sup>7</sup> A. Bagulya,<sup>8</sup>  
 A. Baranov,<sup>9</sup> F. Bardou,<sup>1</sup> G.J. Barker,<sup>7</sup> M. Battistin,<sup>1</sup> J. Bauche,<sup>1</sup> A. Bay,<sup>10</sup>  
 V. Bayliss,<sup>11</sup> G. Bencivenni,<sup>12</sup> Y.A. Berdnikov,<sup>13</sup> A.Y. Berdnikov,<sup>13</sup> I. Berezkina,<sup>8</sup>  
 M. Bertani,<sup>12</sup> C. Betancourt,<sup>14</sup> I. Bezshyiko,<sup>14</sup> O. Bezshyyko,<sup>15</sup> D. Bick,<sup>16</sup>  
 S. Bieschke,<sup>16</sup> A. Blanco,<sup>17</sup> J. Boehm,<sup>11</sup> M. Bogomilov,<sup>18</sup> K. Bondarenko,<sup>19,15</sup>  
 W.M. Bonivento,<sup>20</sup> J. Borburgh,<sup>1</sup> A. Boyarsky,<sup>19,15</sup> R. Brenner,<sup>21</sup> D. Breton,<sup>22</sup>  
 R. Brundler,<sup>14</sup> M. Bruschi,<sup>23</sup> V. Büscher,<sup>25</sup> A. Buonauro,<sup>14</sup> S. Buontempo,<sup>2</sup>  
 S. Cadeddu,<sup>20</sup> A. Calcaterra,<sup>12</sup> M. Calviani,<sup>1</sup> M. Campanelli,<sup>24</sup> M. Casolino,<sup>1</sup>  
 N. Charitonidis,<sup>1</sup> P. Chau,<sup>25</sup> J. Chauveau,<sup>26</sup> A. Chepurnov,<sup>3</sup> M. Chernyavskiy,<sup>8</sup>  
 K.-Y. Choi,<sup>55</sup> A. Chumakov,<sup>27</sup> P. Ciambone,<sup>12</sup> K. Cornelis,<sup>1</sup> M. Cristinziani,<sup>28</sup>  
 A. Crupano,<sup>2,d</sup> G.M. Dallavalle,<sup>23</sup> A. Datwyler,<sup>14</sup> N. D'Ambrosio,<sup>16</sup>  
 G. D'Appollonio,<sup>20,c</sup> L. Dedenko,<sup>3</sup> P. Dergachev,<sup>29</sup> J. De Carvalho Saraiva,<sup>17</sup>  
 G. De Lellis,<sup>2,d</sup> M. de Magistris,<sup>2,d</sup> A. De Roeck,<sup>1</sup> M. De Serio,<sup>30,a</sup> D. De Simone,<sup>2,d</sup>  
 C. Dib,<sup>27</sup> H. Dijkstra,<sup>1</sup> P. Dipinto,<sup>30,a</sup> A. Di Crescenzo,<sup>2,d</sup> N. Di Marco,<sup>31</sup>  
 V. Dmitrenko,<sup>5</sup> S. Dmitrievskiy,<sup>6</sup> A. Dolmatov,<sup>32</sup> D. Domenici,<sup>12</sup> S. Donskov,<sup>33</sup>  
 L.A. Dougherty,<sup>1</sup> V. Drohan,<sup>15</sup> A. Dubreuil,<sup>34</sup> J. Ebert,<sup>16</sup> T. Enik,<sup>6</sup> A. Etenko,<sup>35,5</sup>  
 F. Fabbri,<sup>23</sup> L. Fabbri,<sup>23,b</sup> A. Fabich,<sup>1</sup> O. Fedin,<sup>36</sup> F. Fedotovs,<sup>37</sup> M. Ferro-Luzzi,<sup>1</sup>  
 G. Felici,<sup>12</sup> K. Filippov,<sup>5</sup> R.A. Fini,<sup>30</sup> P. Fonte,<sup>17</sup> C. Franco,<sup>17</sup> M. Fraser,<sup>1</sup> R. Fresa,<sup>2,i</sup>**

<sup>a</sup>Università di Bari, Bari, Italy

<sup>d</sup>Università di Napoli "Federico II", Napoli, Italy

<sup>c</sup>Università di Cagliari, Cagliari, Italy

<sup>b</sup>Università di Bologna, Bologna, Italy

<sup>i</sup>Università della Basilicata, Potenza, Italy

R. Froeschl,<sup>1</sup> T. Fukuda,<sup>38</sup> G. Galati,<sup>2,d</sup> J. Gall,<sup>1</sup> L. Gatignon,<sup>1</sup> G. Gavrilov,<sup>5</sup>  
 V. Gentile,<sup>2,d</sup> B. Goddard,<sup>1</sup> L. Golinka-Bezshyyko,<sup>15</sup> A. Golovatiuk,<sup>15</sup> D. Golubkov,<sup>32</sup>  
 A. Golutvin,<sup>37</sup> P. Gorbounov,<sup>1</sup> S. Gorbunov,<sup>8</sup> D. Gorbunov,<sup>39</sup> V. Gorkavenko,<sup>15</sup>  
 Y. Gornushkin,<sup>6</sup> M. Gorshenkov,<sup>29</sup> V. Grachev,<sup>5</sup> A.L. Grandchamp,<sup>10</sup> G. Granich,<sup>8</sup>  
 E. Graverini,<sup>14</sup> J.-L. Grenard,<sup>1</sup> D. Grenier,<sup>1</sup> V. Grichine,<sup>8</sup> N. Gruzinskii,<sup>36</sup> Yu. Guz,<sup>33</sup>  
 G.J. Haefeli,<sup>10</sup> C. Hagner,<sup>16</sup> H. Hakobyan,<sup>27</sup> I.W. Harris,<sup>10</sup> C. Hessler,<sup>1</sup>  
 A. Hollnagel,<sup>25</sup> B. Hosseini,<sup>37</sup> M. Hushchyn,<sup>9</sup> G. Iaselli,<sup>30,a</sup> A. Iuliano,<sup>2,d</sup>  
 V. Ivantchenko,<sup>8</sup> R. Jacobsson,<sup>1</sup> D. Joković,<sup>54</sup> M. Jonker,<sup>1</sup> I. Kadenko,<sup>15</sup> V. Kain,<sup>1</sup>  
 C. Kamiscioglu,<sup>40</sup> K. Kershaw,<sup>1</sup> M. Khabibullin,<sup>39</sup> E. Khalikov,<sup>3</sup> G. Khaustov,<sup>33</sup>  
 G. Khorauli,<sup>25</sup> A. Khotyantsev,<sup>39</sup> Y.G. Kim,<sup>41</sup> V. Kim,<sup>36,13</sup> S.H. Kim,<sup>42</sup>  
 N. Kitagawa,<sup>38</sup> J.-W. Ko,<sup>42</sup> K. Kodama,<sup>43</sup> A. Kolesnikov,<sup>6</sup> D.I. Kolev,<sup>18</sup> V. Kolosov,<sup>33</sup>  
 M. Komatsu,<sup>38</sup> N. Kondrateva,<sup>8</sup> A. Kono,<sup>44</sup> N. Konovalova,<sup>8,29</sup> S. Kormannshaus,<sup>25</sup>  
 I. Korol,<sup>45</sup> I. Korol'ko,<sup>32</sup> A. Korzenev,<sup>34</sup> V. Kostyukhin,<sup>28</sup> E. Koukovini Platia,<sup>1</sup>  
 S. Kovalenko,<sup>27</sup> I. Krasilnikova,<sup>29</sup> Y. Kudenko,<sup>5,39,g</sup> E. Kurbatov,<sup>9</sup> P. Kurbatov,<sup>29</sup>  
 V. Kurochka,<sup>39</sup> E. Kuznetsova,<sup>36</sup> H.M. Lacker,<sup>45</sup> M. Lamont,<sup>1</sup> G. Lanfranchi,<sup>12</sup>  
 O. Lantwin,<sup>37</sup> A. Lauria,<sup>2,d</sup> K.S. Lee,<sup>46</sup> K.Y. Lee,<sup>42</sup> J.-M. Lévy,<sup>26</sup> L. Lopes,<sup>17</sup>  
 E. Lopez Sola,<sup>1</sup> V.P. Loschiavo,<sup>2,h</sup> V. Lyubovitskij,<sup>27</sup> A. M. Guler,<sup>47</sup> J. Maalmi,<sup>22</sup>  
 A. Magnan,<sup>37</sup> V. Maleev,<sup>36</sup> A. Malinin,<sup>35</sup> Y. Manabe,<sup>38</sup> A.K. Managadze,<sup>3</sup>  
 M. Manfredi,<sup>1</sup> S. Marsh,<sup>1</sup> A.M. Marshall,<sup>48</sup> A. Mefodev,<sup>39</sup> P. Mermod,<sup>34</sup> A. Miano,<sup>2,d</sup>  
 S. Mikado,<sup>49</sup> Yu. Mikhaylov,<sup>33</sup> D.A. Milstead,<sup>50</sup> O. Mineev,<sup>39</sup> A. Montanari,<sup>23</sup>  
 M.C. Montesi,<sup>2,d</sup> K. Morishima,<sup>38</sup> S. Movchan,<sup>6</sup> Y. Muttoni,<sup>1</sup> N. Naganawa,<sup>38</sup>  
 M. Nakamura,<sup>38</sup> T. Nakano,<sup>38</sup> S. Nasybulin,<sup>36</sup> P. Ninin,<sup>1</sup> A. Nishio,<sup>38</sup> A. Novikov,<sup>5</sup>  
 B. Obinyakov,<sup>35</sup> S. Ogawa,<sup>44</sup> N. Okateva,<sup>8,29</sup> B. Opitz,<sup>16</sup> J. Osborne,<sup>1</sup>  
 M. Ovchynnikov,<sup>19,15</sup> P.H. Owen,<sup>14</sup> N. Owtscharenko,<sup>28</sup> P. Pacholek,<sup>1</sup> A. Paoloni,<sup>12</sup>  
 R. Paparella,<sup>30</sup> B.D. Park,<sup>42</sup> S.K. Park,<sup>46</sup> A. Pastore,<sup>23</sup> M. Patel,<sup>37</sup> D. Pereyma,<sup>32</sup>  
 A. Perillo-Marcone,<sup>1</sup> G.L. Petkov,<sup>18</sup> K. Petridis,<sup>48</sup> A. Petrov,<sup>35</sup> D. Podgrudkov,<sup>3</sup>  
 V. Poliakov,<sup>33</sup> N. Polukhina,<sup>8,29,5</sup> J. Prieto Prieto,<sup>1</sup> M. Prokudin,<sup>32</sup> A. Prota,<sup>2,d</sup>  
 A. Quercia,<sup>2,d</sup> A. Rademakers,<sup>1</sup> A. Rakai,<sup>1</sup> F. Ratnikov,<sup>9</sup> T. Rawlings,<sup>11</sup> F. Redi,<sup>10</sup>  
 S. Ricciardi,<sup>11</sup> M. Rinaldesi,<sup>1</sup> P. Robbe,<sup>22</sup> Viktor Rodin,<sup>15</sup> Volodymyr Rodin,<sup>15</sup>  
 A.B. Rodrigues Cavalcante,<sup>10</sup> T. Roganova,<sup>3</sup> H. Rokujo,<sup>38</sup> G. Rosa,<sup>2,d</sup> T. Rovelli,<sup>23,b</sup>  
 O. Ruchayskiy,<sup>51</sup> T. Ruf,<sup>1</sup> V. Samoylenko,<sup>33</sup> V. Samsonov,<sup>5</sup> F. Sanchez Galan,<sup>1</sup>  
 P. Santos Diaz,<sup>1</sup> A. Sanz Ull,<sup>1</sup> A. Saputi,<sup>12</sup> O. Sato,<sup>38</sup> E.S. Savchenko,<sup>29</sup>  
 W. Schmidt-Parzefall,<sup>16</sup> N. Serra,<sup>14</sup> S. Sgobba,<sup>1</sup> O. Shadura,<sup>15</sup> A. Shakin,<sup>29</sup>  
 M. Shaposhnikov,<sup>10</sup> P. Shatalov,<sup>32</sup> T. Shchedrina,<sup>8,29</sup> L. Shchutska,<sup>15</sup>  
 V. Shevchenko,<sup>35</sup> H. Shibuya,<sup>44</sup> S. Shirobokov,<sup>37</sup> A. Shustov,<sup>5</sup> S.B. Silverstein,<sup>50</sup>  
 S. Simone,<sup>30,a</sup> R. Simoniello,<sup>25</sup> M. Skorokhvatov,<sup>5,35</sup> S. Smirnov,<sup>5</sup> J.Y. Sohn,<sup>42</sup>  
 A. Sokolenko,<sup>15</sup> E. Solodko,<sup>1</sup> N. Starkov,<sup>8,35</sup> L. Stoel,<sup>1</sup> B. Storaci,<sup>14</sup>  
 M.E. Stramaglia,<sup>10</sup> D. Sukhonos,<sup>1</sup> Y. Suzuki,<sup>38</sup> S. Takahashi,<sup>4</sup> J.L. Tastet,<sup>51</sup>  
 P. Teterin,<sup>5</sup> S. Than Naing,<sup>8</sup> I. Timiryasov,<sup>10</sup> V. Tioukov,<sup>2</sup> D. Tommasini,<sup>1</sup> M. Torii,<sup>38</sup>  
 N. Tosi,<sup>23</sup> D. Treille,<sup>1</sup> R. Tsenov,<sup>18,6</sup> S. Ulin,<sup>5</sup> A. Ustyuzhanin,<sup>9</sup> Z. Uteshev,<sup>5</sup>

<sup>g</sup>Also at Moscow Institute of Physics and Technology (MIPT), Moscow Region, Russia

<sup>h</sup>Consorzio CREATE, Napoli, Italy

**G. Vankova-Kirilova,<sup>18</sup> F. Vannucci,<sup>26</sup> E. van Herwijnen,<sup>1</sup> S. van Waasen,<sup>52</sup>  
 P. Venkova,<sup>45</sup> V. Venturi,<sup>1</sup> S. Vilchinski,<sup>15</sup> M. Villa,<sup>23,b</sup> Heinz Vincke,<sup>1</sup>  
 Helmut Vincke,<sup>1</sup> C. Visone,<sup>2,j</sup> K. Vlasik,<sup>5</sup> A. Volkov,<sup>8,35</sup> R. Voronkov,<sup>8</sup> R. Wanke,<sup>25</sup>  
 P. Wertelaers,<sup>1</sup> J.-K. Woo,<sup>53</sup> M. Wurm,<sup>25</sup> S. Xella,<sup>51</sup> D. Yilmaz,<sup>40</sup> A.U. Yilmazer,<sup>40</sup>  
 C.S. Yoon,<sup>42</sup> P. Zarubin,<sup>6</sup> I. Zarubina<sup>6</sup> and Yu. Zaytsev<sup>32</sup>**

<sup>1</sup>*European Organization for Nuclear Research (CERN), Geneva, Switzerland*

<sup>2</sup>*Sezione INFN di Napoli, Napoli, Italy*

<sup>3</sup>*Skobeltsyn Institute of Nuclear Physics of Moscow State University (SINP MSU), Moscow, Russia*

<sup>4</sup>*Kobe University, Kobe, Japan*

<sup>5</sup>*National Research Nuclear University (MEPhI), Moscow, Russia*

<sup>6</sup>*Joint Institute for Nuclear Research (JINR), Dubna, Russia*

<sup>7</sup>*University of Warwick, Warwick, United Kingdom*

<sup>8</sup>*P.N. Lebedev Physical Institute (LPI), Moscow, Russia*

<sup>9</sup>*Yandex School of Data Analysis, Moscow, Russia*

<sup>10</sup>*École Polytechnique Fédérale de Lausanne (EPFL), Lausanne, Switzerland*

<sup>11</sup>*STFC Rutherford Appleton Laboratory, Didcot, United Kingdom*

<sup>12</sup>*Laboratori Nazionali dell'INFN di Frascati, Frascati, Italy*

<sup>13</sup>*St. Petersburg Polytechnic University (SPbPU),<sup>f</sup> St. Petersburg, Russia*

<sup>14</sup>*Physik-Institut, Universität Zürich, Zürich, Switzerland*

<sup>15</sup>*Taras Shevchenko National University of Kyiv, Kyiv, Ukraine*

<sup>16</sup>*Universität Hamburg, Hamburg, Germany*

<sup>17</sup>*LIP, Laboratory of Instrumentation and Experimental Particle Physics, Portugal*

<sup>18</sup>*Faculty of Physics, Sofia University, Sofia, Bulgaria*

<sup>19</sup>*University of Leiden, Leiden, The Netherlands*

<sup>20</sup>*Sezione INFN di Cagliari, Cagliari, Italy*

<sup>21</sup>*Uppsala University, Uppsala, Sweden*

<sup>22</sup>*LAL, Univ. Paris-Sud, CNRS/IN2P3, Université Paris-Saclay, Orsay, France*

<sup>23</sup>*Sezione INFN di Bologna, Bologna, Italy*

<sup>24</sup>*University College London, London, United Kingdom*

<sup>25</sup>*Institut für Physik and PRISMA Cluster of Excellence, Johannes Gutenberg Universität Mainz, Mainz, Germany*

<sup>26</sup>*LPNHE, IN2P3/CNRS, Sorbonne Université, Université Paris Diderot, F-75252 Paris, France*

<sup>27</sup>*Universidad Técnica Federico Santa María and Centro Científico Tecnológico de Valparaíso, Valparaíso, Chile*

<sup>28</sup>*Physikalisches Institut, Universität Bonn, Bonn, Germany*

<sup>29</sup>*National University of Science and Technology "MISiS", Moscow, Russia*

<sup>30</sup>*Sezione INFN di Bari, Bari, Italy*

<sup>31</sup>*Laboratori Nazionali dell'INFN di Gran Sasso, L'Aquila, Italy*

<sup>32</sup>*Institute of Theoretical and Experimental Physics (ITEP) NRC 'Kurchatov Institute', Moscow, Russia*

<sup>33</sup>*Institute for High Energy Physics (IHEP) NRC 'Kurchatov Institute', Protvino, Russia*

<sup>j</sup>Università del Sannio, Benevento, Italy

<sup>f</sup>Associated to Petersburg Nuclear Physics Institute (PNPI), Gatchina, Russia

- <sup>34</sup> *University of Geneva, Geneva, Switzerland*  
<sup>35</sup> *National Research Centre ‘Kurchatov Institute’, Moscow, Russia*  
<sup>36</sup> *Petersburg Nuclear Physics Institute (PNPI) NRC ‘Kurchatov Institute’, Gatchina, Russia*  
<sup>37</sup> *Imperial College London, London, United Kingdom*  
<sup>38</sup> *Nagoya University, Nagoya, Japan*  
<sup>39</sup> *Institute for Nuclear Research of the Russian Academy of Sciences (INR RAS), Moscow, Russia*  
<sup>40</sup> *Ankara University, Ankara, Turkey*  
<sup>41</sup> *Gwangju National University of Education,<sup>e</sup> Gwangju, Korea*  
<sup>42</sup> *Physics Education Department & RINS, Gyeongsang National University, Jinju, Korea*  
<sup>43</sup> *Aichi University of Education, Kariya, Japan*  
<sup>44</sup> *Toho University, Funabashi, Chiba, Japan*  
<sup>45</sup> *Humboldt-Universität zu Berlin, Berlin, Germany*  
<sup>46</sup> *Korea University, Seoul, Korea*  
<sup>47</sup> *Middle East Technical University (METU), Ankara, Turkey*  
<sup>48</sup> *H.H. Wills Physics Laboratory, University of Bristol, Bristol, United Kingdom*  
<sup>49</sup> *College of Industrial Technology, Nihon University, Narashino, Japan*  
<sup>50</sup> *Stockholm University, Stockholm, Sweden*  
<sup>51</sup> *Niels Bohr Institute, University of Copenhagen, Copenhagen, Denmark*  
<sup>52</sup> *Forschungszentrum Jülich GmbH (KFA), Jülich, Germany*  
<sup>53</sup> *Jeju National University,<sup>e</sup> Jeju, Korea*  
<sup>54</sup> *Institute of Physics, University of Belgrade, Serbia*  
<sup>55</sup> *Sungkyunkwan University,<sup>e</sup> Suwon-si, Gyeong Gi-do, Korea*

*E-mail:* [kyrylo.bondarenko@gmail.com](mailto:kyrylo.bondarenko@gmail.com)

**ABSTRACT:** Heavy Neutral Leptons (HNLs) are hypothetical particles predicted by many extensions of the Standard Model. These particles can, among other things, explain the origin of neutrino masses, generate the observed matter-antimatter asymmetry in the Universe and provide a dark matter candidate.

The SHiP experiment will be able to search for HNLs produced in decays of heavy mesons and travelling distances ranging between  $\mathcal{O}(50\text{ m})$  and tens of kilometers before decaying. We present the sensitivity of the SHiP experiment to a number of HNL’s benchmark models and provide a way to calculate the SHiP’s sensitivity to HNLs for arbitrary patterns of flavour mixings. The corresponding tools and data files are also made publicly available.

**KEYWORDS:** Beyond Standard Model, Fixed target experiments

**ARXIV EPRINT:** [1811.00930](https://arxiv.org/abs/1811.00930)

---

<sup>e</sup>Associated to Gyeongsang National University, Jinju, Korea

---

**Contents**

<b>1</b>	<b>The SHiP experiment and Heavy Neutral Leptons</b>	<b>1</b>
<b>2</b>	<b>Monte Carlo simulation of heavy neutral leptons at SHiP</b>	<b>3</b>
<b>3</b>	<b>SHiP sensitivity for benchmark HNL models</b>	<b>6</b>
<b>4</b>	<b>Model independent SHiP sensitivity</b>	<b>7</b>
<b>5</b>	<b>Conclusion</b>	<b>9</b>
<b>A</b>	<b>HNL decays</b>	<b>11</b>

---

**1 The SHiP experiment and Heavy Neutral Leptons**

**The SHiP experiment.** The Search for Hidden Particles (SHiP) experiment [1–4] is a new general purpose fixed target facility proposed at the CERN Super Proton Synchrotron (SPS) accelerator to search for long-lived exotic particles with masses between few hundred MeV and few GeV. These particles are expected to be predominantly produced in the decays of heavy hadrons. The facility is therefore designed to maximise the production and detector acceptance of charm and beauty mesons, while providing the cleanest possible environment. The 400 GeV proton beam extracted from the SPS will be dumped on a high density target with the aim of accumulating  $2 \times 10^{20}$  protons on target during 5 years of operation. The charm production at SHiP exceeds that of any existing and planned facility.

A dedicated detector, based on a long vacuum tank followed by a spectrometer and by particle identification detectors, will allow probing a variety of models with light long-lived exotic particles. Since particles originating in charm and beauty meson decays are produced with a significant transverse momentum with respect to the beam axis, the detector should be placed as close as possible to the target. A critical component of SHiP is therefore the muon shield [5], which deflects away from the detector the high flux of muons produced in the target, that would otherwise represent a very serious background for hidden particle searches. To suppress the background from neutrinos interacting in the fiducial volume, the decay volume is maintained under vacuum [3]. The detector is designed to reconstruct the exclusive decays of hidden particles and to reduce the background to less than 0.1 events in the sample of  $2 \times 10^{20}$  protons on target [4]. The detector consists of a large magnetic spectrometer located downstream of a 50 m long and  $5 \times 10$  m wide decay volume. The spectrometer is designed to accurately reconstruct the decay vertex, mass and impact parameter of the decaying particle with respect to the target. A set of calorimeters followed by muon chambers provide identification of electrons, photons, muons



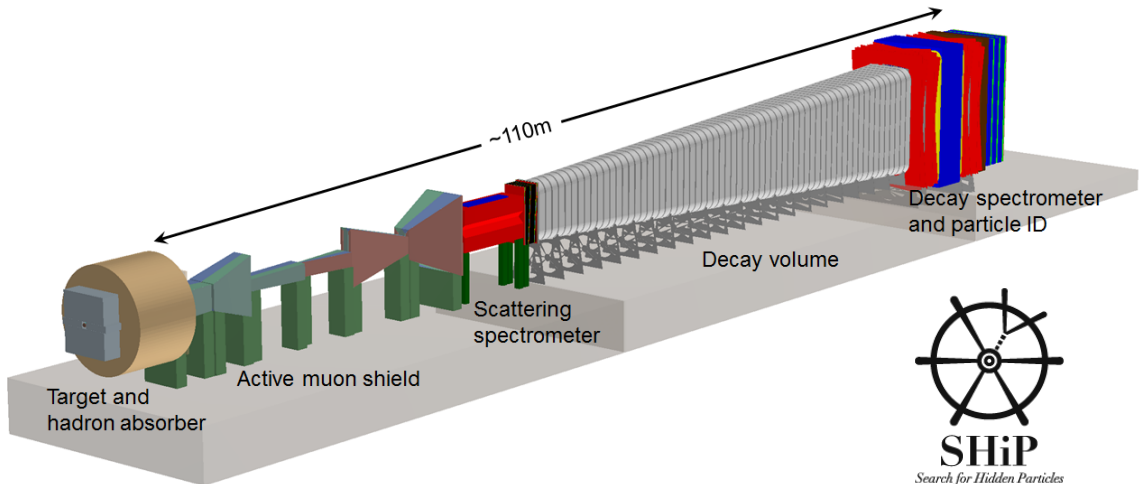


**Figure 1.** Overview of the SHiP experimental facility.

and charged hadrons. A dedicated timing detector measures the coincidence of the decay products, which allows the rejection of combinatorial background.

The decay volume is surrounded by background taggers to tag neutrino and muon inelastic scattering in the surrounding structures, which may produce long-lived neutral Standard Model particles, such as  $K_L$ , that have similar topologies to the expected signal.

The experimental facility is also ideally suited for studying the interactions of tau neutrinos. It will therefore host an emulsion cloud chamber based on the Opera concept, upstream of the hidden particle decay volume, followed by a muon spectrometer. The SHiP facility layout is shown in figure 1. Recent progress report [4] outlines the up-to-date experimental design as well as describes changes since the initial technical proposal [2].

**Heavy Neutral Leptons.** Among hypothetical long-lived particles that can be probed by the SHiP experiment are Heavy Neutral Leptons (or HNLs) [6]. The idea that HNLs — also known as right-handed, Majorana or sterile neutrinos — can be responsible for the smallness of neutrino masses goes back to the 1970s [7–12]. It has subsequently been understood that the same particles could be responsible for the generation of the matter-antimatter asymmetry of the Universe [13]. The idea of this scenario, called leptogenesis, was developed since the 1980s (see reviews [14–19] and references therein). In particular, it was found that the Majorana mass scale of right-handed neutrinos can be as low as  $\mathcal{O}(\text{GeV})$  [20–22], thus providing a possibility for a leptogenesis scenario to be probed at a particle physics laboratory in the near future.

It was demonstrated in 2005 that by adding just three HNLs to the Standard Model one could not only explain neutrino oscillations and the origin of the baryon asymmetry of the Universe, but also provide a dark matter candidate [21, 23]. Two of the HNLs should have masses in the GeV range, see [24] for a review. This model, dubbed Neutrino Minimal Standard Model (or  $\nu\text{MSM}$ ), is compatible with all the measurements so far performed by accelerator experiments and at the same time provides a solution for the puzzles of modern

physics [24, 25]. This made models with GeV scale HNLs a subject of intensive theoretical studies in the recent years [19, 26–45].

HNLs are massive Majorana particles that possess neutrino-like interactions with  $W$  and  $Z$  bosons (the interaction with the Higgs boson does not play a role in our analysis and will be ignored). The interaction strength is suppressed compared to that of ordinary neutrinos by flavour dependent mixing angles  $U_\alpha \ll 1$  ( $\alpha = \{e, \mu, \tau\}$ ). Thus, even the simplest HNL model contains 4 parameters: the HNL mass  $M_N$  and 3 mixing angles  $U_\alpha^2$ .<sup>1</sup> The idea of experimental searches for such particles goes back to the 1980s (see e.g. [46–50]) and a large number of experiments have searched for them in the past (see review of the past searches in [51–53]). HNLs are being searched at currently running experiments, including LHCb, CMS, ATLAS, T2K, Belle and NA62 [54–61].

The sensitivity of the SHiP experiment to HNLs was previously explored for several benchmark models [2, 65, 66] assuming particular ratios between the three HNL mixing angles [51]. This paper updates the previous results in a number of important ways. A recent work [67] revised the branching ratios of HNL production and decay channels. In addition, the estimates of the numbers of  $D$ - and  $B$ -mesons now include cascade production [64]. We update the lower limit of the SHiP sensitivity region and also evaluate the upper bound for the first time. We discuss potential impact of HNL production from  $B_c$  mesons. Moreover, our current sensitivity estimates are not limited to a set of benchmark models. Rather, we compute a *sensitivity matrix* — a model-independent tool to calculate the SHiP sensitivity for any model of HNL flavour mixings.

The paper is organised as follows. Section 2 describes the simulation of HNL events. The resulting sensitivity curves for mixing with each individual flavour, for the benchmark models of ref. [2] as well as the sensitivity matrix — are discussed in section 3. We present our method to evaluate the SHiP sensitivity to HNLs in a model-independent way in section 4 and conclude in section 5.

## 2 Monte Carlo simulation of heavy neutral leptons at SHiP

A detailed Monte Carlo simulation suite for the SHiP experiment, `FairShip`, was developed based on the `FairRoot` software framework [69]. In `FairShip` simulations primary collisions of protons are generated with `Pythia 8` [70] and the subsequent propagation and interactions of particles simulated with `GEANT4` [71]. Neutrino interactions are simulated with `GENIE` [72]; heavy flavour production and inelastic muon interactions with `Pythia 6` [73] and `GEANT4`. Secondary heavy flavour production in cascade interactions of hadrons originated by the initial proton collision [64] is also taken into account, which leads to an increase of the overall HNL production fraction (see table 1). The SHiP detector response is simulated using `GEANT4`. The pattern recognition algorithms applied to the hits on the straw spectrometer are described in [74], and the algorithms for particle identification are presented in [75].

---

<sup>1</sup>The mixing angles  $U_\alpha$  are in general complex numbers. However, the properties of HNLs that are important for us depend only on  $|U_\alpha|$ . Throughout this work we will write  $U_\alpha^2$  instead of  $|U_\alpha|^2$  for compactness.

$pN$ cross-section	$\bar{c}c$ fraction	$\bar{b}b$ fraction	Cascade enhancement $f_{\text{cascade}}$	
			charm [64]	beauty [64]
$\sigma_{pN}$ [2]	$X_{\bar{c}c}$ [62]	$X_{\bar{b}b}$ [63]		
10.7 mb	$1.7 \times 10^{-3}$	$1.6 \times 10^{-7}$	2.3	1.7

**Table 1.** Charm and beauty production fractions and cascade enhancement factors for the SHiP experiment. Cross-section  $\sigma_{pN}$  is an average proton-nucleon inelastic cross-section for the molybdenum target [2].

The simulation takes the HNL mass  $M_N$  and its three flavour mixings  $U_e^2, U_\mu^2, U_\tau^2$  as input parameters. For the pure HNLs mixing to a single SM flavour, the number of detected HNL events  $N_{\text{events}}$  is estimated as<sup>2</sup>

$$N_{\text{events}} = N_{\text{prod}} \times P_{\text{det}} \tag{2.1}$$

where  $N_{\text{prod}}$  is the number of produced HNLs that fly in the direction of the fiducial volume and  $P_{\text{det}}$  is the probability of HNL detection in the Hidden Sector detector. The number of produced HNLs is

$$N_{\text{prod}} = \sum_{q \in (c,b)} N_q \times \sum_h f(q \rightarrow h) \times \text{BR}(h \rightarrow N + X) \times \epsilon_{\text{decay}}, \tag{2.2}$$

where  $f(q \rightarrow h)$  is the  $h$  meson production fraction<sup>3</sup> at SHiP (see table 2),  $\text{BR}(h \rightarrow N + X)$  is the mass dependent inclusive branching ratios for  $h$  mesons decays with HNL in the final state and  $\epsilon_{\text{decay}}$  is the *geometrical acceptance* — the fraction of produced HNLs that fly into direction of the fiducial volume. Figure 2 shows the product between the meson production fraction and its inclusive decay branching fraction into sterile neutrinos. Finally,  $N_q$  is the total number of produced quarks and antiquarks of the given flavour  $q$  taking into account the quark-antiquark production fraction  $X_{\bar{q}q}$  and the cascade enhancement factor  $f_{\text{cascade}}$  given in table 1,

$$N_q = 2 \times X_{\bar{q}q} \times f_{\text{cascade}} \times N_{\text{POT}}. \tag{2.3}$$

The HNL *detection probability* is given by

$$P_{\text{det}} = P_{\text{decay}} \times \text{BR}(N \rightarrow \text{visible}) \times \epsilon_{\text{det}}, \tag{2.4}$$

where  $\text{BR}(N \rightarrow \text{visible})$  is the total HNL decay branching ratio into visible channels (see HNL decay channels in appendix A),  $P_{\text{decay}}$  is the probability that the HNL decays inside the fiducial volume,

$$P_{\text{decay}} = \exp\left(-\frac{l_{\text{ini}}}{l_{\text{decay}}}\right) - \exp\left(-\frac{l_{\text{fin}}}{l_{\text{decay}}}\right), \tag{2.5}$$

<sup>2</sup>The case of the general mixing ratio is discussed in section 4.

<sup>3</sup>The meson production fraction is the probability that a quark of a given flavour hadronizes into the given meson. In the sum over hadrons we consider only lightest hadrons of a given flavour that have only weak decays. Higher resonances have negligible branching to HNLs as they mostly decay via strong interactions.

meson	$f(q \rightarrow \text{meson})$	meson	$f(q \rightarrow \text{meson})$
$D^+$	0.207	$B^+$	0.417
$D^0$	0.632	$B^0$	0.418
$D_s$	0.088	$B_s$	0.113
$J/\psi$	0.01	$B_c$	$\leq 2.6 \times 10^{-3}$

**Table 2.** Production fraction and expected number of different mesons in SHiP taking into account cascade production [68]. For  $f(b \rightarrow B_c)$  see text for details.

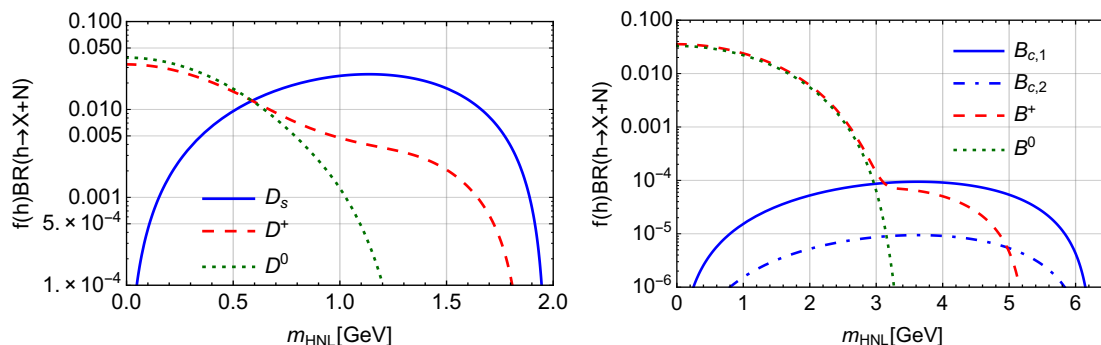


**Figure 2.** HNL production branching ratios multiplied with the production fraction of the meson decaying into HNL, for charm (left) and beauty (right) mesons [67]. The mixing angles have been set to  $U_e^2 = 1$ ,  $U_\mu^2 = U_\tau^2 = 0$ . The production from  $D^+$  and  $B^+$  remains relevant for higher masses for  $D^0$  and  $B^0$  because of the fully leptonic decays  $h^+ \rightarrow N + \ell^+$ . The  $B_c$  production fraction is unknown (see text for details) and we show two examples:  $f(b \rightarrow B_c) = 2 \times 10^{-3}$  ( $B_{c,1}$  line) and  $f(b \rightarrow B_c) = 2 \times 10^{-4}$  ( $B_{c,2}$  line).

where  $l_{ini}$  is the distance travelled by HNL before it entered the decay vessel;  $l_{fin}$  is the distance to the end of the decay vessel along the HNL trajectory;  $l_{decay} = c\gamma\tau_N$  is the HNL decay length ( $\gamma$  and  $\tau_N$  being HNL gamma factor and proper lifetime). Finally,  $\epsilon_{det}$  is the efficiency of detecting the charged daughters of the decaying HNL. It takes into account the track reconstruction efficiency and the selection efficiency, further described in [2, 65, 75]. In order to distinguish the signal candidates from possible SM background, we put a criteria that at least two charged tracks reconstructed to the decay point are present. The reconstruction efficiencies for the decay channels  $N \rightarrow \mu\mu\nu$  and  $N \rightarrow \mu\pi$  are given in e.g. [2, section 5.2.2.2]. Using FairShip, a scan was done over the HNL parameter space. For each set of HNL parameters we ran a simulation with 300 HNL events, produced randomly from decay of mesons. We determined  $P_{decay}$ ,  $\epsilon_{decay}$  and  $\epsilon_{det}$  in each of them and average over simulations to find the expected number of detected events,  $\bar{N}_{events}$ .

For HNLs with masses  $M_N \lesssim 500$  MeV kaon decays are the dominant production channel. While  $\mathcal{O}(10^{20})$  kaons are expected at SHiP, most of them are stopped in the target or hadron stopper before decaying. As a consequence, only HNLs originating from charm and beauty mesons are included in the estimation of the sensitivity. SHiP can however explore the  $\nu$ MSM parameter space down to the constraints given by Big Bang

nucleosynthesis observations [76, 77], even with this conservative assumption. It is expected that the NA62 experiment will also probe the region below the kaon mass [78].

For HNL masses  $M_N \gtrsim 3 \text{ GeV}$  the contribution of  $B_c$  mesons to the HNL production can be relevant because the  $B_c^+ \rightarrow N + \ell^+$  decay width is proportional to the CKM matrix element  $|V_{cb}|^2$ , while the decays of  $B^+$  are proportional to  $|V_{ub}|^2$  [51, 67]. The ratio  $|V_{cb}|^2/|V_{ub}|^2 \sim 10^2$ , which explains the relative importance of  $B_c$  channels even for small production fraction  $f(b \rightarrow B_c)$ . This production fraction has not been measured at the SHiP center of mass energy. If the  $B_c$  production fraction at SHiP is at the LHC level, its contribution will be dominant. However, at some unknown energy close to the  $B_c$  mass this production fraction becomes negligible. The existing Tevatron measurement place  $f(b \rightarrow B_c) = 2.08_{-0.95}^{+1.06} \times 10^{-3}$  at  $\sqrt{s} = 1.8 \text{ TeV}$  [79]. More recent LHCb measurement at  $\sqrt{s} = 7$  and  $8 \text{ TeV}$  gave  $f(b \rightarrow B_c)/f(b \rightarrow B^+) = 0.008 \pm 0.004$  [80]. Using  $f(b \rightarrow B^+) = 0.33$  from the LHCb measurement performed at  $\sqrt{s} = 7 \text{ TeV}$  [81], one obtains  $f(b \rightarrow B_c) = 2.6 \times 10^{-3}$ . Theoretical evaluations have mostly been performed for TeV energies (see e.g. [82–85]) with the exception of the works [86, 87] that computed the production fraction down to energies of tens of GeV (where they found the fraction to be negligible). However, by comparing predictions of [87] with LHCb or Tevatron measurements, we see that (i) it underpredicts the value of  $f(b \rightarrow B_c)$  by about an order of magnitude at these energies and (ii) it predicts stronger than observed change of the production fraction between LHC and Tevatron energies. Therefore we have to treat  $f(b \rightarrow B_c)$  as an unknown parameter somewhere between its LHC value and zero and provide two estimates: an optimistic estimate for which  $f(b \rightarrow B_c)$  is at the LHC level and a pessimistic estimate where we do not include  $B_c$  mesons at all. In the simulation we take the angular distribution of  $B_c$  mesons to be the same as that of  $B^+$  mesons, based on comparisons performed with the BCVEGPY [88] and FONLL [89, 90] packages, while we rescale the energy distribution according to the meson mass.

Detailed background studies have proven that the yield of background events passing the online and offline event selections is negligible [2]. Therefore, the 90% confidence region is defined as the region of the parameter space where one expects on average  $\bar{N}_{\text{events}} \geq 2.3$  reconstructed HNL events, corresponding to the discovery threshold with an expected background yield of 0.1 events.

### 3 SHiP sensitivity for benchmark HNL models

Figure 3 presents the 90% C.L. sensitivity curves for HNLs mixing to only one SM flavour. The sensitivity curves have a characteristic “cigar-like shape” for masses  $M_N > 2 \text{ GeV}$ . The *upper boundary* is determined by the condition that the decay length of a produced particle becomes comparable with the distance between the target and the decay volume, and therefore the HNLs produced at the target may not reach the decay volume, see eq. (2.5). For masses  $M_N < 2 \text{ GeV}$  such an upper boundary also exists, but it is outside the plot range, owing to a much larger number of parent  $D$  mesons. The *lower boundary* of the sensitivity region is determined by the parameters at which decays become too rare

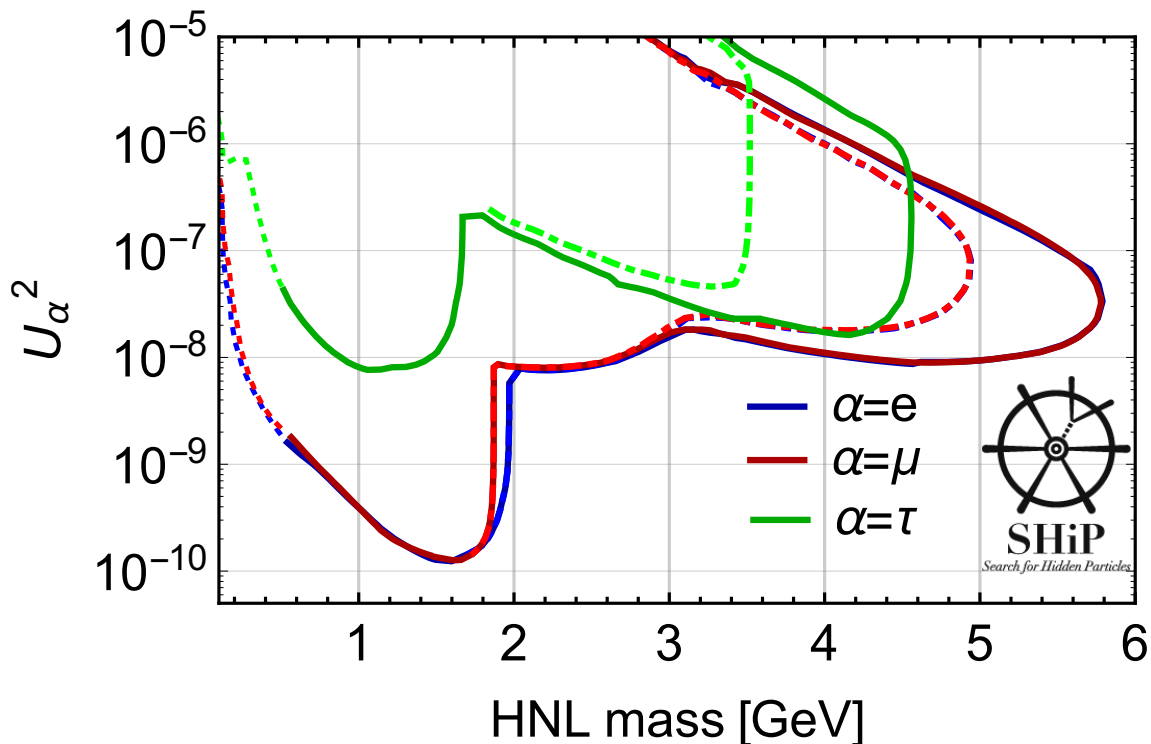


**Figure 3.** SHiP sensitivity curves (90% CL) for HNLs mixing to a single SM flavour: electron (blue), muon (red) and tau (green). To indicate the uncertainty related to the unknown production fraction of  $B_c$  meson (see text for details), we show two types of curve for each flavour. Solid curves show the sensitivity contours when the production fraction of  $B_c$  mesons equals to that at LHC energies:  $f(b \rightarrow B_c) = 2.6 \times 10^{-3}$ . Dashed-dotted lines do not include contributions from  $B_c$ . Below 0.5 GeV only production from  $D$  and  $B$  mesons is included (dotted lines).

(decay length much larger than the detector size). The intersection of the upper and lower boundaries defines the *maximal mass* which can be probed at the experiment.

We also provide updated sensitivity estimates for the three benchmark models I–III presented in the Technical Proposal [2, 65]. These models allow to explain neutrino flavour oscillations while at the same time maximizing the mixing to one particular flavour, and are defined by the following ratios of flavour couplings [51]:

$$\text{I. } U_e^2 : U_\mu^2 : U_\tau^2 = 52 : 1 : 1$$

$$\text{II. } U_e^2 : U_\mu^2 : U_\tau^2 = 1 : 16 : 3.8$$

$$\text{III. } U_e^2 : U_\mu^2 : U_\tau^2 = 0.061 : 1 : 4.3$$

The sensitivity curves for these models are shown in figure 4.

#### 4 Model independent SHiP sensitivity

In this section we provide an efficient way to estimate the SHiP sensitivity to an HNL model with an arbitrary ratio  $U_e^2 : U_\mu^2 : U_\tau^2$ . It is based on the observation that the dependence

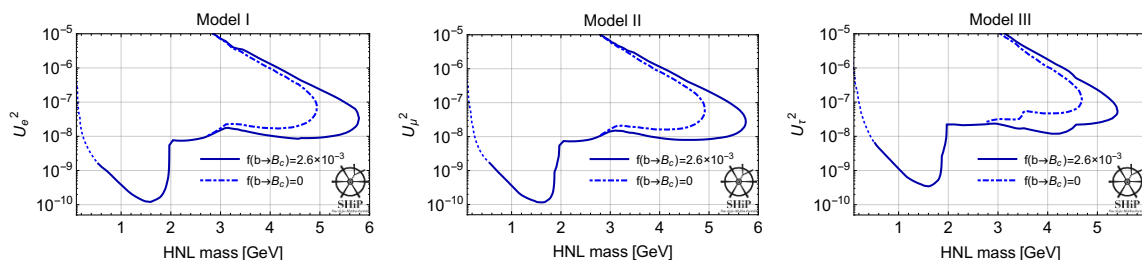


**Figure 4.** Sensitivity curves for 3 benchmark models I–III (90%CL). Individual curves are explained in figure 3.

of the number of events,  $N_{\text{events}}$ , on the mass and mixing angles of HNL factorizes, and therefore all relevant information can be extracted from a handful of simulations, rather than from a scan over an entire 4-dimensional HNL parameter space ( $M_N, U_e^2, U_\mu^2, U_\tau^2$ ).

All information about the HNL production in a particular experiment is contained in  $N_\alpha(M_N)$  — the number of HNLs that would be produced through all possible channels with the mixings  $U_\alpha^2 = 1$  and  $U_{\beta \neq \alpha}^2 = 0$ :

$$N_\alpha \equiv \sum_{\text{hadrons } h} N_h \sum_{\text{channels}} \text{BR}(h \rightarrow N + X_\alpha) \epsilon_{\text{decay}, \alpha} \Big|_{U_\alpha^2=1; U_{\beta \neq \alpha}^2=0} \quad (4.1)$$

Here  $N_h$  is the number of hadrons of a given type  $h$ ,  $\text{BR}(h \rightarrow N + X_\alpha)$  is the branching ratio for their decay into an HNL plus any number of other particles  $X_\alpha$  with total lepton flavour number  $L_\alpha = 1$  and  $\epsilon_{\text{decay}, \alpha}$  is the geometrical acceptance of HNL that in general depends not only on the mass but also on the flavour. The overall number of HNLs (given by eq. (2.2)) produced via the mixing with the flavour  $\alpha$  and flying in the direction of the decay vessel is given by

$$N_{\text{prod}, \alpha}(M_N | \vec{U}^2) = U_\alpha^2 N_\alpha(M_N). \quad (4.2)$$

The decay probability  $P_{\text{decay}}$  should be treated differently, depending on the ratio of the decay length and the distance from the target to the decay vessel. It also depends on the production channel through the mean gamma factor  $\gamma_\alpha$  entering the decay length.

In the limit when the decay length much larger than the distance between the beam target and the exit lid of the SHiP decay volume, the  $U_\beta^2$  dependence of the decay probability can be accounted for similarly to eq. (4.2):

$$P_{\text{decay}, \alpha}^{\text{linear}}(M_N | \vec{U}^2) = \frac{l_{\text{fin}} - l_{\text{ini}}}{\gamma_\alpha c \hbar} \sum_{\beta} U_\beta^2 \Gamma_\beta(M_N), \quad (4.3)$$

where  $\Gamma_\beta$  is a decay width of the HNL of mass  $M_N$  that has mixing angles  $U_\beta^2 = 1$ ,  $U_{\alpha \neq \beta}^2 = 0$ , the definitions of lengths  $l_{\text{ini}}, l_{\text{fin}}$  are given after eq. (2.5). The index  $\alpha$  in eq. (4.3) indicates that the HNL was produced via mixing  $U_\alpha^2$  (although can decay through the mixing with any flavour), so  $\gamma_\alpha$  is the mean gamma factor of HNLs produced through the mixing with the flavour  $\alpha$ .

In the general case, when the decay length  $l_{\text{decay}}$  is not necessarily larger than  $l_{\text{fin}}$ , the analogous decay probability  $P_{\text{decay},\alpha}$  can be expressed via (4.3) as follows:

$$P_{\text{decay},\alpha}(M_N|\vec{U}^2) = \left[ \exp\left(-\frac{l_{\text{ini}}}{l_{\text{fin}} - l_{\text{ini}}} P_{\text{decay},\alpha}^{\text{linear}}(M_N|\vec{U}^2)\right) - \exp\left(-\frac{l_{\text{fin}}}{l_{\text{fin}} - l_{\text{ini}}} P_{\text{decay},\alpha}^{\text{linear}}(M_N|\vec{U}^2)\right) \right] \times \text{BR}(N \rightarrow \text{visible}), \quad (4.4)$$

where  $\text{BR}(N \rightarrow \text{visible})$  is the probability that the HNL decays into the final states detectable by SHiP.

Finally, we define the HNL detection efficiency as

$$\epsilon_{\text{det}}(M_N|\vec{U}^2) = \sum_{\beta} \text{BR}(N \rightarrow X_{\beta}) \times \epsilon_{\text{det},\beta}, \quad (4.5)$$

where  $\text{BR}(N \rightarrow X_{\beta})$  is the branching ratio of a decay through the mixing angle  $\beta$  and  $\epsilon_{\text{det},\beta}$  is the probability that the HNL decay products are successfully detected.

As a result, the number of detected events is given by

$$N_{\text{decay}}(M_N|\vec{U}^2) = \sum_{\alpha} N_{\text{prod},\alpha}(M_N|\vec{U}^2) P_{\text{decay},\alpha}(M_N|\vec{U}^2) \epsilon_{\text{det}}(M_N|\vec{U}^2). \quad (4.6)$$

*We see that it is sufficient to know 9 functions of the HNL mass —  $N_{\alpha}(M_N)$ ,  $P_{\text{decay},\alpha}^{\text{linear}}(M_N)$  and  $\epsilon_{\text{det},\alpha}(M_N)$  — to determine the number of detected events for any combination of the mixing angles.*

To determine these numbers we ran 9 Monte Carlo simulations for each mass. We first ran 3 simulations with vectors  $\vec{U}^2 = (x, 0, 0)$ ,  $\vec{U}^2 = (0, x, 0)$ ,  $\vec{U}^2 = (0, 0, x)$ , where  $x$  is any sufficiently small number such that  $l_{\text{decay}} \gg l_{\text{det}}$ . We then ran a set of 6 non-physical simulations, where a particle is produced solely via channel  $\alpha$  and decays solely through the channel  $\beta \neq \alpha$ . Using results of these simulations we extract  $N_{\alpha}$ ,  $P_{\alpha}$  and  $\epsilon_{\text{det},\alpha}$  values that allow us to generate the expected number of detected events for any values of masses and couplings.

The results are available at Zenodo platform [91] with instructions for reading the file and generating sensitivity curves at different confidence levels.

## 5 Conclusion

Using a detailed Monte Carlo simulation of HNL production in decays of charm and beauty mesons, and of the detector response to the signal generated by a decaying HNL, we calculated the sensitivity of the SHiP experiment to HNLs, updating the results presented in the Technical Proposal [2]. In particular, we assess the potential impact of HNL production from  $B_c$  mesons decay, showing its influence on the extent of the probed HNL mass range. We take into account cascade production of  $B$  and  $D$  mesons as well as revised estimates of branching ratios of HNL production and decay, and we extend our calculation to masses below  $\sim 500$  MeV, where SHiP has a potential to fully explore the allowed region. Finally, we present our results as a publicly available dataset, providing a model-independent way to calculate the SHiP sensitivity for any pattern of HNL flavour mixings.



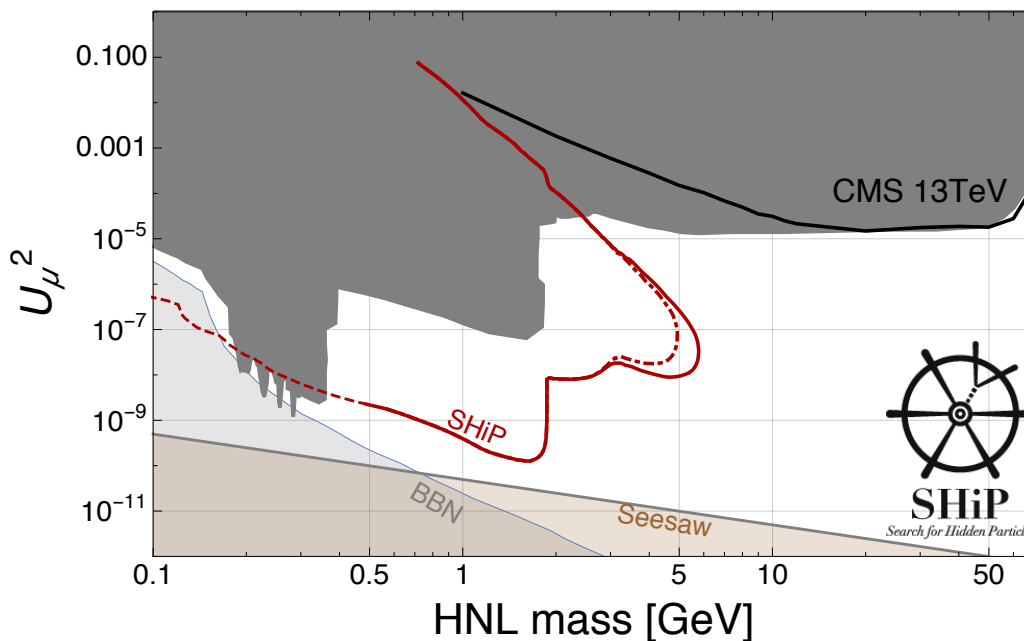


**Figure 5.** Parameter space of HNLs and potential reach of the SHiP experiment for the mixing with muon flavour. Dark gray area is excluded from previous experiments, see e.g. [6]. Black solid line is the recent bound from the CMS 13 TeV run [57]. Solid and dashed-dotted red lines indicate the uncertainty, related to the production fraction of  $B_c$  mesons at SHiP energies that has not been measured experimentally or reliably calculated (see section 2 for details). The sensitivity of SHiP below kaon mass (dashed line) is based on the number of HNLs produced in the decay of  $D$ -mesons only and does not take into account HNL production from kaon decays. The primordial nucleosynthesis bounds on HNL lifetime are from [76]. The seesaw line indicates the parameters obeying the seesaw relation  $|U_\mu|^2 \sim m_\nu/M_N$ , where for active neutrino mass we substitute  $m_\nu = \sqrt{\Delta m_{\text{atm}}^2} \approx 0.05$  eV [6].

The SHiP experiment offers an increase of up to 3 orders of magnitude in the sensitivity to heavy neutral leptons, figure 5. It is capable of probing cosmologically interesting region of the HNL parameter space, and of potentially discovering the origin of neutrino masses and of the matter-antimatter asymmetry of the Universe.

### Acknowledgments

The SHiP Collaboration wishes to thank the Castaldo company (Naples, Italy) for their contribution to the development studies of the decay vessel. The support from the National Research Foundation of Korea with grant numbers of 2018R1A2B2007757, 2018R1D1A3B07050649, 2018R1D1A1B07050701, 2017R1D1A1B03036042, 2017R1A6A3A01075752, 2016R1A2B4012302, and 2016R1A6A3A11930680 is acknowledged. The support from the European Research Council (ERC) under the European Union’s Horizon 2020 research and innovation programme (GA No 694896) is acknowledged. The support from the Russian Foundation for Basic Research (RFBR) and the support from the TAEK of Turkey are acknowledged.

## A HNL decays

For completeness we list the relevant HNL decay channels in table 3 (reproduced from [67]).

Channel	Opens at [MeV]	Relevant from [MeV]	Relevant up to [MeV]	Max BR [%]	Reference in [67]
$N \rightarrow \nu_\alpha \nu_\beta \bar{\nu}_\beta$	$\sum m_\nu \approx 0$	$\sum m_\nu \approx 0$	—	100	(3.5)
$N \rightarrow \nu_\alpha e^+ e^-$	1.02	1.29	—	21.8	(3.4)
$N \rightarrow \nu_\alpha \pi^0$	135	136	3630	57.3	(3.7)
$N \rightarrow e^- \pi^+$	140	141	3000	33.5	(3.6)
$N \rightarrow \mu^- \pi^+$	245	246	3000	19.7	(3.6)
$N \rightarrow e^- \nu_\mu \mu^+$	106	315	—	5.15	(3.1)
$N \rightarrow \mu^- \nu_e e^+$	106	315	—	5.15	(3.1)
$N \rightarrow \nu_\alpha \mu^+ \mu^-$	211	441	—	4.21	(3.4)
$N \rightarrow \nu_\alpha \eta$	548	641	2330	3.50	(3.7)
$N \rightarrow e^- \rho^+$	770	780	4550	10.4	(3.8)
$N \rightarrow \nu_\alpha \rho^0$	770	780	3300	4.81	(3.9)
$N \rightarrow \mu^- \rho^+$	875	885	4600	10.2	(3.8)
$N \rightarrow \nu_\alpha \omega$	783	997	1730	1.40	(3.9)
$N \rightarrow \nu_\alpha \eta'$	958	1290	2400	1.86	(3.7)
$N \rightarrow \nu_\alpha \phi$	1019	1100	4270	5.90	(3.9)
$N \rightarrow e^- D_s^{*+}$	2110	2350	—	3.05	(3.8)
$N \rightarrow \mu^- D_s^{*+}$	2220	2370	—	3.03	(3.8)
$N \rightarrow e^- D_s^+$	1970	2660	4180	1.23	(3.6)
$N \rightarrow \mu^- D_s^+$	2070	2680	4170	1.22	(3.6)
$N \rightarrow \nu_\alpha \eta_c$	2980	3940	—	1.26	(3.7)
$N \rightarrow \tau^- \nu_e e^+$	1780	3980	—	1.52	(3.1)
$N \rightarrow e^- \nu_\tau \tau^+$	1780	3980	—	1.52	(3.1)
$N \rightarrow \tau^- \nu_\mu \mu^+$	1880	4000	—	1.51	(3.1)
$N \rightarrow \mu^- \nu_\tau \tau^+$	1880	4000	—	1.51	(3.1)

**Table 3.** List of the relevant HNL decay channels with branching ratio above 1% covering the HNL mass range up to 5 GeV implemented in **FairShip**. The numbers are provided for  $|U_e|^2 = |U_\mu|^2 = |U_\tau|^2$ . For neutral current channels (with neutrinos in the final state) the sum over neutrino flavours is taken, otherwise the lepton flavour is shown explicitly. Columns: (1) the HNL decay channel. (2) The HNL mass at which the channel opens. (3) The HNL mass starting from which the channel becomes relevant (branching ratio of this channel exceeds 1%). For multi-meson final states we provide our best-guess estimates. (4) HNL mass above which the channel contributes less than 1%, with “—” indicating that the channel is still relevant at  $M_N = 5$  GeV. (5) The maximum branching ratio of the channel for  $M_N < 5$  GeV. (6) Reference to the appropriate formula for decay width in ref. [67].

**Open Access.** This article is distributed under the terms of the Creative Commons Attribution License ([CC-BY 4.0](https://creativecommons.org/licenses/by/4.0/)), which permits any use, distribution and reproduction in any medium, provided the original author(s) and source are credited.

## References

- [1] W. Bonivento et al., *Proposal to Search for Heavy Neutral Leptons at the SPS*, [arXiv:1310.1762](https://arxiv.org/abs/1310.1762) [[INSPIRE](#)].
- [2] SHiP collaboration, *A facility to Search for Hidden Particles (SHiP) at the CERN SPS*, [arXiv:1504.04956](https://arxiv.org/abs/1504.04956) [[INSPIRE](#)].
- [3] SHiP collaboration, *The experimental facility for the Search for Hidden Particles at the CERN SPS*, 2019 *JINST* **14** P03025 [[arXiv:1810.06880](https://arxiv.org/abs/1810.06880)] [[INSPIRE](#)].
- [4] SHiP collaboration, *SHiP Experiment — Progress Report*, CERN-SPSC-2019-010.
- [5] SHiP collaboration, *The active muon shield in the SHiP experiment*, 2017 *JINST* **12** P05011 [[arXiv:1703.03612](https://arxiv.org/abs/1703.03612)] [[INSPIRE](#)].
- [6] S. Alekhin et al., *A facility to Search for Hidden Particles at the CERN SPS: the SHiP physics case*, *Rept. Prog. Phys.* **79** (2016) 124201 [[arXiv:1504.04855](https://arxiv.org/abs/1504.04855)] [[INSPIRE](#)].
- [7] P. Minkowski,  $\mu \rightarrow e\gamma$  at a Rate of One Out of  $10^9$  Muon Decays?, *Phys. Lett.* **67B** (1977) 421 [[INSPIRE](#)].
- [8] T. Yanagida, *Horizontal gauge symmetry and masses of neutrinos*, *Conf. Proc.* **C 7902131** (1979) 95 [[INSPIRE](#)].
- [9] S.L. Glashow, *The Future of Elementary Particle Physics*, *NATO Sci. Ser.* **B 61** (1980) 687 [[INSPIRE](#)].
- [10] M. Gell-Mann, P. Ramond and R. Slansky, *Complex Spinors and Unified Theories*, *Conf. Proc.* **C 790927** (1979) 315 [[arXiv:1306.4669](https://arxiv.org/abs/1306.4669)] [[INSPIRE](#)].
- [11] R.N. Mohapatra and G. Senjanović, *Neutrino Mass and Spontaneous Parity Nonconservation*, *Phys. Rev. Lett.* **44** (1980) 912 [[INSPIRE](#)].
- [12] R.N. Mohapatra and G. Senjanović, *Neutrino Masses and Mixings in Gauge Models with Spontaneous Parity Violation*, *Phys. Rev. D* **23** (1981) 165 [[INSPIRE](#)].
- [13] M. Fukugita and T. Yanagida, *Resurrection of grand unified theory baryogenesis*, *Phys. Rev. Lett.* **89** (2002) 131602 [[hep-ph/0203194](https://arxiv.org/abs/hep-ph/0203194)] [[INSPIRE](#)].
- [14] W. Buchmüller, P. Di Bari and M. Plümacher, *Leptogenesis for pedestrians*, *Annals Phys.* **315** (2005) 305 [[hep-ph/0401240](https://arxiv.org/abs/hep-ph/0401240)] [[INSPIRE](#)].
- [15] S. Davidson, E. Nardi and Y. Nir, *Leptogenesis*, *Phys. Rept.* **466** (2008) 105 [[arXiv:0802.2962](https://arxiv.org/abs/0802.2962)] [[INSPIRE](#)].
- [16] M. Shaposhnikov, *Baryogenesis*, *J. Phys. Conf. Ser.* **171** (2009) 012005 [[INSPIRE](#)].
- [17] A. Pilaftsis, *The Little Review on Leptogenesis*, *J. Phys. Conf. Ser.* **171** (2009) 012017 [[arXiv:0904.1182](https://arxiv.org/abs/0904.1182)] [[INSPIRE](#)].
- [18] M. Drewes et al., *ARS Leptogenesis*, *Int. J. Mod. Phys. A* **33** (2018) 1842002 [[arXiv:1711.02862](https://arxiv.org/abs/1711.02862)] [[INSPIRE](#)].

- [19] E.J. Chun et al., *Probing Leptogenesis*, *Int. J. Mod. Phys. A* **33** (2018) 1842005 [[arXiv:1711.02865](#)] [[INSPIRE](#)].
- [20] E.K. Akhmedov, V.A. Rubakov and A. Yu. Smirnov, *Baryogenesis via neutrino oscillations*, *Phys. Rev. Lett.* **81** (1998) 1359 [[hep-ph/9803255](#)] [[INSPIRE](#)].
- [21] T. Asaka and M. Shaposhnikov, *The nuMSM, dark matter and baryon asymmetry of the universe*, *Phys. Lett. B* **620** (2005) 17 [[hep-ph/0505013](#)] [[INSPIRE](#)].
- [22] M. Shaposhnikov, *The nuMSM, leptonic asymmetries and properties of singlet fermions*, *JHEP* **08** (2008) 008 [[arXiv:0804.4542](#)] [[INSPIRE](#)].
- [23] T. Asaka, S. Blanchet and M. Shaposhnikov, *The nuMSM, dark matter and neutrino masses*, *Phys. Lett. B* **631** (2005) 151 [[hep-ph/0503065](#)] [[INSPIRE](#)].
- [24] A. Boyarsky, O. Ruchayskiy and M. Shaposhnikov, *The Role of sterile neutrinos in cosmology and astrophysics*, *Ann. Rev. Nucl. Part. Sci.* **59** (2009) 191 [[arXiv:0901.0011](#)] [[INSPIRE](#)].
- [25] M. Shaposhnikov, *Is there a new physics between electroweak and Planck scales?*, in *Astroparticle Physics: Current Issues, 2007 (APCI07)*, Budapest, Hungary, June 21–23, 2007 (2007) [[arXiv:0708.3550](#)] [[INSPIRE](#)].
- [26] L. Canetti, M. Drewes and M. Shaposhnikov, *Matter and Antimatter in the Universe*, *New J. Phys.* **14** (2012) 095012 [[arXiv:1204.4186](#)] [[INSPIRE](#)].
- [27] M. Drewes and B. Garbrecht, *Leptogenesis from a GeV Seesaw without Mass Degeneracy*, *JHEP* **03** (2013) 096 [[arXiv:1206.5537](#)] [[INSPIRE](#)].
- [28] L. Canetti, M. Drewes, T. Frossard and M. Shaposhnikov, *Dark Matter, Baryogenesis and Neutrino Oscillations from Right Handed Neutrinos*, *Phys. Rev. D* **87** (2013) 093006 [[arXiv:1208.4607](#)] [[INSPIRE](#)].
- [29] L. Canetti, M. Drewes and M. Shaposhnikov, *Sterile Neutrinos as the Origin of Dark and Baryonic Matter*, *Phys. Rev. Lett.* **110** (2013) 061801 [[arXiv:1204.3902](#)] [[INSPIRE](#)].
- [30] B. Garbrecht, F. Gautier and J. Klaric, *Strong Washout Approximation to Resonant Leptogenesis*, *JCAP* **09** (2014) 033 [[arXiv:1406.4190](#)] [[INSPIRE](#)].
- [31] B. Shuve and I. Yavin, *Baryogenesis through Neutrino Oscillations: A Unified Perspective*, *Phys. Rev. D* **89** (2014) 075014 [[arXiv:1401.2459](#)] [[INSPIRE](#)].
- [32] L. Canetti, M. Drewes and B. Garbrecht, *Probing leptogenesis with GeV-scale sterile neutrinos at LHCb and Belle II*, *Phys. Rev. D* **90** (2014) 125005 [[arXiv:1404.7114](#)] [[INSPIRE](#)].
- [33] A.M. Gago, P. Hernández, J. Jones-Pérez, M. Losada and A. Moreno Briceño, *Probing the Type I Seesaw Mechanism with Displaced Vertices at the LHC*, *Eur. Phys. J. C* **75** (2015) 470 [[arXiv:1505.05880](#)] [[INSPIRE](#)].
- [34] T. Hambye and D. Teresi, *Higgs doublet decay as the origin of the baryon asymmetry*, *Phys. Rev. Lett.* **117** (2016) 091801 [[arXiv:1606.00017](#)] [[INSPIRE](#)].
- [35] P. Hernández, M. Kekic, J. López-Pavón, J. Racker and J. Salvado, *Testable Baryogenesis in Seesaw Models*, *JHEP* **08** (2016) 157 [[arXiv:1606.06719](#)] [[INSPIRE](#)].
- [36] A. Caputo, P. Hernández, M. Kekic, J. López-Pavón and J. Salvado, *The seesaw path to leptonic CP-violation*, *Eur. Phys. J. C* **77** (2017) 258 [[arXiv:1611.05000](#)] [[INSPIRE](#)].
- [37] J. Ghiglieri and M. Laine, *Neutrino dynamics below the electroweak crossover*, *JCAP* **07** (2016) 015 [[arXiv:1605.07720](#)] [[INSPIRE](#)].

- [38] M. Drewes, B. Garbrecht, D. Gueter and J. Klaric, *Leptogenesis from Oscillations of Heavy Neutrinos with Large Mixing Angles*, *JHEP* **12** (2016) 150 [[arXiv:1606.06690](#)] [[INSPIRE](#)].
- [39] J. Ghiglieri and M. Laine, *GeV-scale hot sterile neutrino oscillations: a derivation of evolution equations*, *JHEP* **05** (2017) 132 [[arXiv:1703.06087](#)] [[INSPIRE](#)].
- [40] A. Caputo, P. Hernández, J. Lopez-Pavon and J. Salvado, *The seesaw portal in testable models of neutrino masses*, *JHEP* **06** (2017) 112 [[arXiv:1704.08721](#)] [[INSPIRE](#)].
- [41] S. Eijima and M. Shaposhnikov, *Fermion number violating effects in low scale leptogenesis*, *Phys. Lett. B* **771** (2017) 288 [[arXiv:1703.06085](#)] [[INSPIRE](#)].
- [42] T. Asaka, S. Eijima, H. Ishida, K. Minogawa and T. Yoshii, *Initial condition for baryogenesis via neutrino oscillation*, *Phys. Rev. D* **96** (2017) 083010 [[arXiv:1704.02692](#)] [[INSPIRE](#)].
- [43] S. Eijima, M. Shaposhnikov and I. Timiryasov, *Freeze-out of baryon number in low-scale leptogenesis*, *JCAP* **11** (2017) 030 [[arXiv:1709.07834](#)] [[INSPIRE](#)].
- [44] S. Antusch et al., *Probing Leptogenesis at Future Colliders*, *JHEP* **09** (2018) 124 [[arXiv:1710.03744](#)] [[INSPIRE](#)].
- [45] S. Eijima, M. Shaposhnikov and I. Timiryasov, *Parameter space of baryogenesis in the  $\nu$ MSM*, [arXiv:1808.10833](#) [[INSPIRE](#)].
- [46] R.E. Shrock, *Pure Leptonic Decays With Massive Neutrinos and Arbitrary Lorentz Structure*, *Phys. Lett.* **112B** (1982) 382 [[INSPIRE](#)].
- [47] R.E. Shrock, *Electromagnetic Properties and Decays of Dirac and Majorana Neutrinos in a General Class of Gauge Theories*, *Nucl. Phys. B* **206** (1982) 359 [[INSPIRE](#)].
- [48] R.E. Shrock, *General Theory of Weak Leptonic and Semileptonic Decays. 1. Leptonic Pseudoscalar Meson Decays, with Associated Tests For and Bounds on, Neutrino Masses and Lepton Mixing*, *Phys. Rev. D* **24** (1981) 1232 [[INSPIRE](#)].
- [49] R.E. Shrock, *General Theory of Weak Processes Involving Neutrinos. 2. Pure Leptonic Decays*, *Phys. Rev. D* **24** (1981) 1275 [[INSPIRE](#)].
- [50] M. Gronau, C.N. Leung and J.L. Rosner, *Extending Limits on Neutral Heavy Leptons*, *Phys. Rev. D* **29** (1984) 2539 [[INSPIRE](#)].
- [51] D. Gorbunov and M. Shaposhnikov, *How to find neutral leptons of the  $\nu$ MSM?*, *JHEP* **10** (2007) 015 [*Erratum ibid.* **11** (2013) 101] [[arXiv:0705.1729](#)] [[INSPIRE](#)].
- [52] A. Atre, T. Han, S. Pascoli and B. Zhang, *The Search for Heavy Majorana Neutrinos*, *JHEP* **05** (2009) 030 [[arXiv:0901.3589](#)] [[INSPIRE](#)].
- [53] F.F. Deppisch, P.S. Bhupal Dev and A. Pilaftsis, *Neutrinos and Collider Physics*, *New J. Phys.* **17** (2015) 075019 [[arXiv:1502.06541](#)] [[INSPIRE](#)].
- [54] LHCb collaboration, *Search for Majorana neutrinos in  $B^- \rightarrow \pi^+ \mu^- \mu^-$  decays*, *Phys. Rev. Lett.* **112** (2014) 131802 [[arXiv:1401.5361](#)] [[INSPIRE](#)].
- [55] CMS collaboration, *Search for heavy Majorana neutrinos in  $\mu^\pm \mu^\pm + jets$  events in proton-proton collisions at  $\sqrt{s} = 8$  TeV*, *Phys. Lett. B* **748** (2015) 144 [[arXiv:1501.05566](#)] [[INSPIRE](#)].
- [56] ATLAS collaboration, *Search for heavy Majorana neutrinos with the ATLAS detector in pp collisions at  $\sqrt{s} = 8$  TeV*, *JHEP* **07** (2015) 162 [[arXiv:1506.06020](#)] [[INSPIRE](#)].

- [57] CMS collaboration, *Search for heavy neutral leptons in events with three charged leptons in proton-proton collisions at  $\sqrt{s} = 13$  TeV*, *Phys. Rev. Lett.* **120** (2018) 221801 [[arXiv:1802.02965](#)] [[INSPIRE](#)].
- [58] A. Izmaylov and S. Suvorov, *Search for heavy neutrinos in the ND280 near detector of the T2K experiment*, *Phys. Part. Nucl.* **48** (2017) 984 [[INSPIRE](#)].
- [59] SHiP collaboration, *Prospects of the SHiP and NA62 experiments at CERN for hidden sector searches*, *PoS(NuFact2017)* **139** (2017) [[arXiv:1712.01768](#)] [[INSPIRE](#)].
- [60] NA62 collaboration, *Search for heavy neutral lepton production in  $K^+$  decays*, *Phys. Lett. B* **778** (2018) 137 [[arXiv:1712.00297](#)] [[INSPIRE](#)].
- [61] BELLE collaboration, *Search for heavy neutrinos at Belle*, *Phys. Rev. D* **87** (2013) 071102 [*Erratum ibid.* **D 95** (2017) 099903] [[arXiv:1301.1105](#)] [[INSPIRE](#)].
- [62] HERA-B collaboration, *Measurement of  $D^0$ ,  $D^+$ ,  $D_s^+$  and  $D^{*+}$  Production in Fixed Target 920 GeV Proton-Nucleus Collisions*, *Eur. Phys. J. C* **52** (2007) 531 [[arXiv:0708.1443](#)] [[INSPIRE](#)].
- [63] C. Lourenco and H.K. Wohri, *Heavy flavour hadro-production from fixed-target to collider energies*, *Phys. Rept.* **433** (2006) 127 [[hep-ph/0609101](#)] [[INSPIRE](#)].
- [64] SHiP collaboration, *Heavy Flavour Cascade Production in a Beam Dump*, [CERN-SHiP-NOTE-2015-009](#).
- [65] SHiP collaboration, *SHiP sensitivity to Heavy Neutral Leptons*, [CERN-SHiP-NOTE-2016-003](#).
- [66] S.N. Gninenko, D.S. Gorbunov and M.E. Shaposhnikov, *Search for GeV-scale sterile neutrinos responsible for active neutrino oscillations and baryon asymmetry of the Universe*, *Adv. High Energy Phys.* **2012** (2012) 718259 [[arXiv:1301.5516](#)] [[INSPIRE](#)].
- [67] K. Bondarenko, A. Boyarsky, D. Gorbunov and O. Ruchayskiy, *Phenomenology of GeV-scale Heavy Neutral Leptons*, *JHEP* **11** (2018) 032 [[arXiv:1805.08567](#)] [[INSPIRE](#)].
- [68] SHiP collaboration, *Mass dependence of branching ratios into HNL for FairShip*, [CERN-SHiP-NOTE-2016-001](#).
- [69] M. Al-Turany et al., *The FairRoot framework*, *J. Phys. Conf. Ser.* **396** (2012) 022001 [[INSPIRE](#)].
- [70] T. Sjöstrand, S. Mrenna and P.Z. Skands, *A Brief Introduction to PYTHIA 8.1*, *Comput. Phys. Commun.* **178** (2008) 852 [[arXiv:0710.3820](#)] [[INSPIRE](#)].
- [71] GEANT4 collaboration, *GEANT4: A Simulation toolkit*, *Nucl. Instrum. Meth. A* **506** (2003) 250 [[INSPIRE](#)].
- [72] C. Andreopoulos et al., *The GENIE Neutrino Monte Carlo Generator*, *Nucl. Instrum. Meth. A* **614** (2010) 87 [[arXiv:0905.2517](#)] [[INSPIRE](#)].
- [73] T. Sjöstrand, S. Mrenna and P.Z. Skands, *PYTHIA 6.4 Physics and Manual*, *JHEP* **05** (2006) 026 [[hep-ph/0603175](#)] [[INSPIRE](#)].
- [74] SHiP collaboration, *Simulation and pattern recognition for the SHiP Spectrometer Tracker*, [CERN-SHiP-NOTE-2015-002](#).
- [75] SHiP collaboration, *Particle Identification tools and performance in the SHiP Experiment*, [CERN-SHiP-NOTE-2017-002](#).

- [76] A.D. Dolgov, S.H. Hansen, G. Raffelt and D.V. Semikoz, *Heavy sterile neutrinos: Bounds from big bang nucleosynthesis and SN1987A*, *Nucl. Phys. B* **590** (2000) 562 [[hep-ph/0008138](#)] [[INSPIRE](#)].
- [77] O. Ruchayskiy and A. Ivashko, *Restrictions on the lifetime of sterile neutrinos from primordial nucleosynthesis*, *JCAP* **10** (2012) 014 [[arXiv:1202.2841](#)] [[INSPIRE](#)].
- [78] NA62 collaboration, *Searches for very weakly-coupled particles beyond the Standard Model with NA62*, in *Proceedings, 13th Patras Workshop on Axions, WIMPs and WISPs, (PATRAS 2017)*, Thessaloniki, Greece, 15–19 May 2017, pp. 145–148 (2018) [[DOI:10.3204/DESY-PROC-2017-02/dobrich\\_babette](#)] [[arXiv:1711.08967](#)] [[INSPIRE](#)].
- [79] K.-m. Cheung,  *$B_c$  meson production at the Tevatron revisited*, *Phys. Lett. B* **472** (2000) 408 [[hep-ph/9908405](#)] [[INSPIRE](#)].
- [80] LHCb collaboration, *Observation of  $B_c^+ \rightarrow D^0 K^+$  decays*, *Phys. Rev. Lett.* **118** (2017) 111803 [[arXiv:1701.01856](#)] [[INSPIRE](#)].
- [81] LHCb collaboration, *Measurement of  $b$ -hadron production fractions in 7 TeV  $pp$  collisions*, *Phys. Rev. D* **85** (2012) 032008 [[arXiv:1111.2357](#)] [[INSPIRE](#)].
- [82] A.V. Berezhnoy, A.K. Likhoded and O.P. Yushchenko, *Some features of the hadronic  $B_c^{(*)}$  meson production at large  $p_T$* , *Phys. Atom. Nucl.* **59** (1996) 709 [[hep-ph/9504302](#)] [[INSPIRE](#)].
- [83] A.V. Berezhnoy, *Color flows for the process  $gg \rightarrow B_c + c + \bar{b}$* , *Phys. Atom. Nucl.* **68** (2005) 1866 [[hep-ph/0407315](#)] [[INSPIRE](#)].
- [84] C.-H. Chang, C.-F. Qiao, J.-X. Wang and X.-G. Wu, *The Color-octet contributions to  $P$ -wave  $B_c$  meson hadroproduction*, *Phys. Rev. D* **71** (2005) 074012 [[hep-ph/0502155](#)] [[INSPIRE](#)].
- [85] A.V. Berezhnoy, A.K. Likhoded and A.A. Martynov, *Associative Production of  $B_c$  and  $D$  Mesons at LHC*, *Phys. Rev. D* **83** (2011) 094012 [[arXiv:1011.1555](#)] [[INSPIRE](#)].
- [86] K. Kolodziej, A. Leike and R. Ruckl, *Production of  $B_c$  mesons in hadronic collisions*, *Phys. Lett. B* **355** (1995) 337 [[hep-ph/9505298](#)] [[INSPIRE](#)].
- [87] K. Kolodziej and R. Ruckl, *On the energy dependence of hadronic  $B_c$  production*, *Nucl. Instrum. Meth. A* **408** (1998) 33 [[hep-ph/9803327](#)] [[INSPIRE](#)].
- [88] C.-H. Chang, C. Driouiichi, P. Eerola and X.G. Wu, *BCVEGPY: An Event generator for hadronic production of the  $B_c$  meson*, *Comput. Phys. Commun.* **159** (2004) 192 [[hep-ph/0309120](#)] [[INSPIRE](#)].
- [89] M. Cacciari, M. Greco and P. Nason, *The  $p_T$  spectrum in heavy flavor hadroproduction*, *JHEP* **05** (1998) 007 [[hep-ph/9803400](#)] [[INSPIRE](#)].
- [90] M. Cacciari, S. Frixione and P. Nason, *The  $p_T$  spectrum in heavy flavor photoproduction*, *JHEP* **03** (2001) 006 [[hep-ph/0102134](#)] [[INSPIRE](#)].
- [91] SHiP collaboration, *HNL sensitivity of SHiP experiment*, <https://zenodo.org/record/1472071>.



# First particle-by-particle measurement of emittance in the Muon Ionization Cooling Experiment

MICE Collaboration

D. Adams<sup>15</sup>, D. Adey<sup>25,34</sup>, R. Asfandiyarov<sup>13</sup>, G. Barber<sup>18</sup>, A. de Bari<sup>6</sup>, R. Bayes<sup>16</sup>, V. Bayliss<sup>15</sup>, R. Bertoni<sup>4</sup>, V. Blackmore<sup>18,a</sup>, A. Blondel<sup>13</sup>, J. Boehm<sup>15</sup>, M. Bogomilov<sup>1</sup>, M. Bonesini<sup>4</sup>, C. N. Booth<sup>20</sup>, D. Bowring<sup>25</sup>, S. Boyd<sup>22</sup>, T. W. Bradshaw<sup>15</sup>, A. D. Bross<sup>25</sup>, C. Brown<sup>15,23</sup>, G. Charnley<sup>14</sup>, G. T. Chatzitheodoridis<sup>16,21</sup>, F. Chignoli<sup>4</sup>, M. Chung<sup>10</sup>, D. Cline<sup>30</sup>, J. H. Cobb<sup>19</sup>, D. Colling<sup>18</sup>, N. Collomb<sup>14</sup>, P. Cooke<sup>17</sup>, M. Courthold<sup>15</sup>, L. M. Cremaldi<sup>28</sup>, A. DeMello<sup>26</sup>, A. J. Dick<sup>21</sup>, A. Dobbs<sup>18</sup>, P. Dornan<sup>18</sup>, F. Drielsma<sup>13</sup>, K. Dumbell<sup>14</sup>, M. Ellis<sup>23</sup>, F. Filthaut<sup>11,32</sup>, P. Franchini<sup>22</sup>, B. Freemire<sup>27</sup>, A. Gallagher<sup>14</sup>, R. Gamet<sup>17</sup>, R. B. S. Gardener<sup>23</sup>, S. Gourlay<sup>26</sup>, A. Grant<sup>14</sup>, J. R. Greis<sup>22</sup>, S. Griffiths<sup>14</sup>, P. Hanlet<sup>27</sup>, G. G. Hanson<sup>29</sup>, T. Hartnett<sup>14</sup>, C. Heidt<sup>29</sup>, P. Hodgson<sup>20</sup>, C. Hunt<sup>18</sup>, S. Ishimoto<sup>9</sup>, D. Jokovic<sup>12</sup>, P. B. Jurj<sup>18</sup>, D. M. Kaplan<sup>27</sup>, Y. Karadzhev<sup>13</sup>, A. Klier<sup>29</sup>, Y. Kuno<sup>8</sup>, A. Kurup<sup>18</sup>, P. Kyberd<sup>23</sup>, J.-B. Lagrange<sup>18</sup>, J. Langlands<sup>20</sup>, W. Lau<sup>19</sup>, D. Li<sup>26</sup>, Z. Li<sup>3</sup>, A. Liu<sup>25</sup>, K. Long<sup>18</sup>, T. Lord<sup>22</sup>, C. Macwaters<sup>15</sup>, D. Maletic<sup>12</sup>, B. Martlew<sup>14</sup>, J. Martyniak<sup>18</sup>, R. Mazza<sup>4</sup>, S. Middleton<sup>18</sup>, T. A. Mohayai<sup>27</sup>, A. Moss<sup>14</sup>, A. Muir<sup>14</sup>, I. Mullacrane<sup>14</sup>, J. J. Nebrensky<sup>23</sup>, D. Neuffer<sup>25</sup>, A. Nichols<sup>15</sup>, J. C. Nugent<sup>16</sup>, A. Oates<sup>14</sup>, D. Orestano<sup>7</sup>, E. Overton<sup>20</sup>, P. Owens<sup>14</sup>, V. Palladino<sup>5</sup>, M. Palmer<sup>24</sup>, J. Pasternak<sup>18</sup>, V. Pec<sup>20</sup>, C. Pidcott<sup>22,33</sup>, M. Popovic<sup>25</sup>, R. Preece<sup>15</sup>, S. Prestemon<sup>26</sup>, D. Rajaram<sup>27</sup>, S. Ricciardi<sup>15</sup>, M. Robinson<sup>20</sup>, C. Rogers<sup>15</sup>, K. Ronald<sup>21</sup>, P. Rubinov<sup>25</sup>, H. Sakamoto<sup>8,31</sup>, D. A. Sanders<sup>28</sup>, A. Sato<sup>8</sup>, M. Savic<sup>12</sup>, P. Snopok<sup>27</sup>, P. J. Smith<sup>20</sup>, F. J. P. Soler<sup>16</sup>, Y. Song<sup>2</sup>, T. Stanley<sup>15</sup>, G. Stokes<sup>14</sup>, V. Suezaki<sup>27</sup>, D. J. Summers<sup>28</sup>, C. K. Sung<sup>10</sup>, J. Tang<sup>2</sup>, J. Tarrant<sup>15</sup>, I. Taylor<sup>22</sup>, L. Tortora<sup>7</sup>, Y. Torun<sup>27</sup>, R. Tsenov<sup>1</sup>, M. Tucker<sup>14</sup>, M. A. Uchida<sup>18</sup>, S. Virostek<sup>26</sup>, G. Vankova-Kirilova<sup>1</sup>, P. Warburton<sup>14</sup>, S. Wilbur<sup>20</sup>, A. Wilson<sup>15</sup>, H. Witte<sup>24</sup>, C. White<sup>14</sup>, C. G. Whyte<sup>21</sup>, X. Yang<sup>30</sup>, A. R. Young<sup>21</sup>, M. Zisman<sup>26</sup>

<sup>1</sup> Department of Atomic Physics, St. Kliment Ohridski University of Sofia, Sofia, Bulgaria

<sup>2</sup> Institute of High Energy Physics, Chinese Academy of Sciences, Beijing, China

<sup>3</sup> Sichuan University, Chengdu, China

<sup>4</sup> Dipartimento di Fisica G. Occhialini, Sezione INFN Milano Bicocca, Milan, Italy

<sup>5</sup> Sezione INFN Napoli and Dipartimento di Fisica, Università Federico II, Complesso Universitario di Monte S. Angelo, Naples, Italy

<sup>6</sup> Sezione INFN Pavia and Dipartimento di Fisica, Pavia, Italy

<sup>7</sup> INFN Sezione di Roma Tre and Dipartimento di Matematica e Fisica, Università Roma Tre, Rome, Italy

<sup>8</sup> Department of Physics, Graduate School of Science, Osaka University, Toyonaka, Osaka, Japan

<sup>9</sup> High Energy Accelerator Research Organization (KEK), Institute of Particle and Nuclear Studies, Tsukuba, Ibaraki, Japan

<sup>10</sup> UNIST, Ulsan, Korea

<sup>11</sup> Nikhef, Amsterdam, The Netherlands

<sup>12</sup> Institute of Physics, University of Belgrade, Belgrade, Serbia

<sup>13</sup> DPNC, Section de Physique, Université de Genève, Geneva, Switzerland

<sup>14</sup> STFC Daresbury Laboratory, Daresbury, Cheshire, UK

<sup>15</sup> STFC Rutherford Appleton Laboratory, Harwell Oxford, Didcot, UK

<sup>16</sup> School of Physics and Astronomy, The University of Glasgow, Kelvin Building, Glasgow, UK

<sup>17</sup> Department of Physics, University of Liverpool, Liverpool, UK

<sup>18</sup> Blackett Laboratory, Department of Physics, Imperial College London, London, UK

<sup>19</sup> Department of Physics, University of Oxford, Denys Wilkinson Building, Oxford, UK

<sup>20</sup> Department of Physics and Astronomy, University of Sheffield, Sheffield, UK

<sup>21</sup> SUPA and the Department of Physics, University of Strathclyde, Glasgow, UK

<sup>22</sup> Department of Physics, University of Warwick, Coventry, UK

<sup>23</sup> Brunel University, Uxbridge, UK

<sup>24</sup> Brookhaven National Laboratory, Upton, NY, USA

<sup>25</sup> Fermilab, Batavia, IL, USA

<sup>26</sup> Lawrence Berkeley National Laboratory, Berkeley, CA, USA

<sup>27</sup> Illinois Institute of Technology, Chicago, IL, USA

<sup>28</sup> University of Mississippi, Oxford, MS, USA

<sup>29</sup> University of California, Riverside, CA, USA



<sup>30</sup> University of California, Los Angeles, CA, USA

<sup>31</sup> Current address: RIKEN, Wako, Japan

<sup>32</sup> Also at Radboud University, Nijmegen, The Netherlands

<sup>33</sup> Current address: Department of Physics and Astronomy, University of Sheffield, Sheffield, UK

<sup>34</sup> Current address: Institute of High Energy Physics, Chinese Academy of Sciences, Beijing, China

Received: 31 October 2018 / Accepted: 11 February 2019

© The Author(s) 2019

**Abstract** The Muon Ionization Cooling Experiment (MICE) collaboration seeks to demonstrate the feasibility of ionization cooling, the technique by which it is proposed to cool the muon beam at a future neutrino factory or muon collider. The emittance is measured from an ensemble of muons assembled from those that pass through the experiment. A pure muon ensemble is selected using a particle-identification system that can reject efficiently both pions and electrons. The position and momentum of each muon are measured using a high-precision scintillating-fibre tracker in a 4 T solenoidal magnetic field. This paper presents the techniques used to reconstruct the phase-space distributions in the upstream tracking detector and reports the first particle-by-particle measurement of the emittance of the MICE Muon Beam as a function of muon-beam momentum.

## 1 Introduction

Stored muon beams have been proposed as the source of neutrinos at a neutrino factory [1,2] and as the means to deliver multi-TeV lepton-antilepton collisions at a muon collider [3,4]. In such facilities the muon beam is produced from the decay of pions generated by a high-power proton beam striking a target. The tertiary muon beam occupies a large volume in phase space. To optimise the muon yield for a neutrino factory, and luminosity for a muon collider, while maintaining a suitably small aperture in the muon-acceleration system requires that the muon beam be ‘cooled’ (i.e., its phase-space volume reduced) prior to acceleration. An alternative approach to the production of low-emittance muon beams through the capture of  $\mu^+\mu^-$  pairs close to threshold in electron-positron annihilation has recently been proposed [5]. To realise the luminosity required for a muon collider using this scheme requires the substantial challenges presented by the accumulation and acceleration of the intense positron beam, the high-power muon-production target, and the muon-capture system to be addressed.

A muon is short-lived, with a lifetime of  $2.2\mu\text{s}$  in its rest frame. Beam manipulation at low energy ( $\leq 1\text{ GeV}$ ) must be carried out rapidly. Four cooling techniques are in use at particle accelerators: synchrotron-radiation cooling [6]; laser cooling [7–9]; stochastic cooling [10]; and electron cooling [11]. In each case, the time taken to cool the beam is long compared to the muon lifetime. In contrast, ionization cooling is a process that occurs on a short timescale. A muon beam passes through a material (the absorber), loses energy, and is then re-accelerated. This cools the beam efficiently with modest decay losses. Ionization cooling is therefore the technique by which it is proposed to increase the number of particles within the downstream acceptance for a neutrino factory, and the phase-space density for a muon collider [12–14]. This technique has never been demonstrated experimentally and such a demonstration is essential for the development of future high-brightness muon accelerators or intense muon facilities.

The international Muon Ionization Cooling Experiment (MICE) has been designed [15] to perform a full demonstration of transverse ionization cooling. Intensity effects are negligible for most of the cooling channels conceived for the neutrino factory or muon collider [16]. This allows the MICE experiment to record muon trajectories one particle at a time. The MICE collaboration has constructed two solenoidal spectrometers, one placed upstream, the other downstream, of the cooling cell. An ensemble of muon trajectories is assembled offline, selecting an initial distribution based on quantities measured in the upstream particle-identification detectors and upstream spectrometer. This paper describes the techniques used to reconstruct the phase-space distributions in the spectrometers. It presents the first measurement of the emittance of momentum-selected muon ensembles in the upstream spectrometer.

## 2 Calculation of emittance

Emittance is a key parameter in assessing the overall performance of an accelerator [17]. The luminosity achieved by a collider is inversely proportional to the emittance of the colliding beams, and therefore beams with small emittance are required.

D. Cline, M. Zisman: Deceased.

<sup>a</sup> e-mail: [v.blackmore@imperial.ac.uk](mailto:v.blackmore@imperial.ac.uk)

A beam travelling through a portion of an accelerator may be described as an ensemble of particles. Consider a beam that propagates in the positive  $z$  direction of a right-handed Cartesian coordinate system,  $(x, y, z)$ . The position of the  $i^{\text{th}}$  particle in the ensemble is  $\mathbf{r}_i = (x_i, y_i)$  and its transverse momentum is  $\mathbf{p}_{Ti} = (p_{xi}, p_{yi})$ ;  $\mathbf{r}_i$  and  $\mathbf{p}_{Ti}$  define the coordinates of the particle in transverse phase space. The normalised transverse emittance,  $\varepsilon_N$ , of the ensemble approximates the volume occupied by the particles in four-dimensional phase space and is given by

$$\varepsilon_N = \frac{1}{m_\mu} \sqrt[4]{\det \mathcal{C}}, \tag{1}$$

where  $m_\mu$  is the rest mass of the muon,  $\mathcal{C}$  is the four-dimensional covariance matrix,

$$\mathcal{C} = \begin{pmatrix} \sigma_{xx} & \sigma_{xp_x} & \sigma_{xy} & \sigma_{xp_y} \\ \sigma_{xp_x} & \sigma_{p_x p_x} & \sigma_{yp_x} & \sigma_{p_x p_y} \\ \sigma_{xy} & \sigma_{yp_x} & \sigma_{yy} & \sigma_{yp_y} \\ \sigma_{xp_y} & \sigma_{p_x p_y} & \sigma_{yp_y} & \sigma_{p_y p_y} \end{pmatrix}, \tag{2}$$

and  $\sigma_{\alpha\beta}$ , where  $\alpha, \beta = x, y, p_x, p_y$ , is given by

$$\sigma_{\alpha\beta} = \frac{1}{N-1} \left( \sum_i^N \alpha_i \beta_i - \frac{(\sum_i^N \alpha_i)(\sum_i^N \beta_i)}{N} \right), \tag{3}$$

and  $N$  is the number of muons in the ensemble.

The MICE experiment was operated such that muons passed through the experiment one at a time. The phase-space coordinates of each muon were measured. An ensemble of muons that was representative of the muon beam was assembled using the measured coordinates. The normalised transverse emittance of the ensemble was then calculated by evaluating the sums necessary to construct the covariance matrix,  $\mathcal{C}$ , and using Eq. 1.

### 3 The Muon Ionization Cooling Experiment

The muons for MICE came from the decay of pions produced by an internal target dipping directly into the circulating proton beam of the ISIS synchrotron at the Rutherford Appleton Laboratory (RAL) [18, 19]. The burst of particles resulting from one target dip is referred to as a ‘spill’. A transfer line of nine quadrupoles, two dipoles and a superconducting ‘decay solenoid’ selected a momentum bite and transported the beam into the experiment [20]. The small fraction of pions that remained in the beam were rejected during analysis using the time-of-flight hodoscopes, TOF0 and TOF1, and Cherenkov counters that were installed in the MICE Muon Beam line upstream of the cooling experiment [21, 22]. A ‘diffuser’ was installed at the upstream end of the experiment to vary the initial emittance of the beam by introducing a changeable amount of tungsten and brass, which are high- $Z$  materials, into the beam path [20].

A schematic diagram of the experiment is shown in Fig. 1. It contained an absorber/focus-coil module sandwiched between two spectrometer-solenoid modules that provided a uniform magnetic field for momentum measurement. The focus-coil module had two separate windings that were operated with the same, or opposed, polarities. A lithium-hydride or liquid-hydrogen absorber was placed at the centre of the focus-coil module. An iron Partial Return Yoke (PRY) was installed around the experiment to contain the field produced by the solenoidal spectrometers (not shown in Fig. 1). The PRY was installed at a distance from the beam axis such that its effect on the trajectories of particles travelling through the experiment was negligible.

The emittance was measured upstream and downstream of the absorber and focus-coil module using scintillating-fibre tracking detectors [26] immersed in the solenoidal field provided by three superconducting coils E1, C, and E2. The

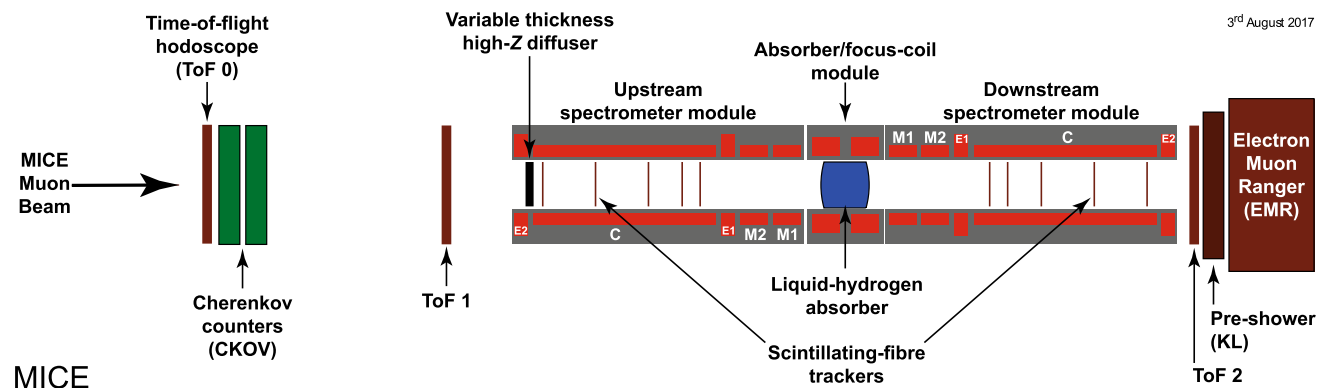


**Fig. 1** Schematic diagram of the MICE experiment. The red rectangles represent the coils of the spectrometer solenoids and focus-coil module. The individual coils of the spectrometer solenoids are labelled E1, C, E2, M1 and M2. The various detectors (time-of-flight hodoscopes

(TOF0, TOF1) [23, 24], Cherenkov counters [25], scintillating-fibre trackers [26], KLOE-Light (KL) calorimeter [20, 27], and Electron Muon Ranger (EMR) [28, 29]) are also represented. The Partial Return Yoke (PRY) is not shown

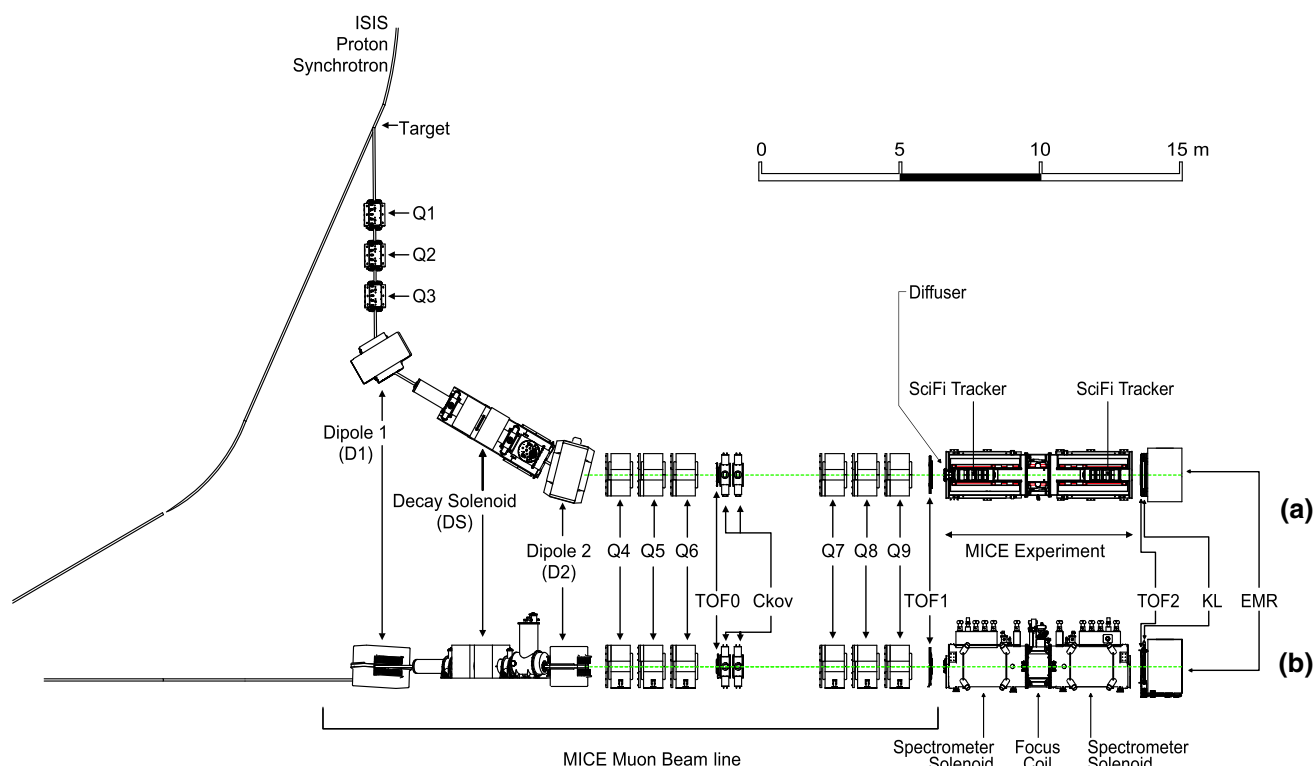


**Fig. 2** **a** Top and **b** side views of the MICE Muon Beam line, its instrumentation, and the experimental configuration. A titanium target dipped into the ISIS proton synchrotron and the resultant spill of particles was captured with a quadrupole triplet (Q1–3) and transported

trackers were used to reconstruct the trajectories of individual muons at the entrance and exit of the absorber. The trackers were each constructed from five planar stations of scintillating fibres, each with an active radius of 150 mm. The track parameters were reported at the nominal reference plane: the surface of the scintillating-fibre plane closest to the absorber [30]. Hall probes were installed on the tracker to measure the magnetic-field strength in situ. The instrumentation up- and downstream of the spectrometer modules was used to select a pure sample of muons. The reconstructed tracks of the selected muons were then used to measure the muon-beam emittance at the upstream and downstream tracker reference planes. The spectrometer-solenoid modules also contained two superconducting ‘matching’ coils (M1, M2) that were used to match the optics between the uniform-field region and the neighbouring focus-coil module. The MICE coordinate system is such that the  $z$  axis is coincident with the beam direction, the  $y$  axis points vertically upward, and the  $x$  axis completes a right-handed co-ordinate system. This paper discusses the measurement of emittance using only the tracker and beam-line instrumentation upstream of the absorber. The diffuser was fully retracted for the data presented here, i.e. no extra material was introduced into the centre of the beam line, so that the incident particle distribution could be assessed.

through momentum-selecting dipoles (D1, D2). The quadrupole triplets (Q4–6, Q7–9) transported particles to the upstream spectrometer module. The time-of-flight of particles, measured between TOF0 and TOF1, was used for particle identification

#### 4 MICE Muon beam line

The MICE Muon Beam line is shown schematically in Fig. 2. It was capable of delivering beams with normalised transverse emittance in the range  $3 \lesssim \varepsilon_N \lesssim 10$  mm and mean momentum in the range  $140 \lesssim p_\mu \lesssim 240$  MeV/ $c$  with a root-mean-squared (RMS) momentum spread of  $\sim 20$  MeV/ $c$  [20] after the diffuser (Fig. 1).

Pions produced by the momentary insertion of a titanium target [18, 19] into the ISIS proton beam were captured using a quadrupole triplet (Q1–3) and transported to a first dipole magnet (D1), which selected particles of a desired momentum bite into the 5 T decay solenoid (DS). Muons produced in pion decay in the DS were momentum-selected using a second dipole magnet (D2) and focused onto the diffuser by a quadrupole channel (Q4–6 and Q7–9). In positive-beam running, a borated polyethylene absorber of variable thickness was inserted into the beam just downstream of the decay solenoid to suppress the high rate of protons that were produced at the target [31].

The composition and momentum spectra of the beams delivered to MICE were determined by the interplay between the two bending magnets D1 and D2. In ‘muon mode’, D2 was set to half the current of D1, selecting backward-going

muons in the pion rest frame. This produced an almost pure muon beam.

Data were taken in October 2015 in muon mode at a nominal momentum of 200 MeV/c, with ISIS in operation at 700 MeV. These data [32] are used here to characterise the properties of the beam accepted by the upstream solenoid with all diffuser irises withdrawn from the beam. The upstream E1-C-E2 coils in the spectrometer module were energised and produced a field of 4 T, effectively uniform across the tracking region, while all other coils were unpowered. Positively charged particles were selected due to their higher production rate in 700 MeV proton-nucleus collisions.

## 5 Simulation

Monte Carlo simulations were used to determine the accuracy of the kinematic reconstruction, to evaluate the efficiency of the response of the scintillating-fibre tracker, and to study systematic uncertainties. A sufficient number of events were generated to ensure that statistical uncertainties from the simulations were negligible in comparison to those of the data.

The beam impinging on TOF0 was modelled using G4beamline [33]. Particles were produced at the target using a parameterised particle-production model. These particles were tracked through the MICE Muon Beam line taking into account all material in and surrounding the beam line and using realistic models of the fields and apertures of the various magnets. The G4beamline simulation was tuned to reproduce the observed particle distributions at TOF0.

The MICE Analysis User Software (MAUS) [34] package was used to simulate the passage of particles from TOF0 through the remainder of the MICE Muon Beam line and through the solenoidal lattice. This simulation includes the response of the instrumentation and used the input distribution produced using G4beamline. MAUS was also used for offline reconstruction and to provide fast real-time detector reconstruction and data visualisation during MICE running. MAUS uses GEANT4 [35, 36] for beam propagation and the simulation of detector response. ROOT [37] was used for data visualisation and for data storage. The particles generated were subjected to the same trigger requirements as the data and processed by the same reconstruction programs.

## 6 Beam selection

Data were buffered in the front-end electronics and read out at the end of each spill [20]. For the reconstructed data presented here, the digitisation of analogue signals received from the detectors was triggered by a coincidence of signals in the PMTs serving a single scintillator slab in TOF1. Any slab in TOF1 could generate a trigger.

The following cuts were used to select muons passing through the upstream tracker:

- *One reconstructed space-point in TOF0 and TOF1* Each TOF hodoscope was composed of two perpendicular planes of scintillator slabs arranged to measure the  $x$  and  $y$  coordinates. A space-point was formed from the intersection of hits in the  $x$  and  $y$  projections. Figure 3a, b show the hit multiplicity in TOF0 plotted against the hit multiplicity in TOF1 for reconstructed data and reconstructed Monte Carlo respectively. The sample is dominated by events with one space-point in both TOF0 and TOF1. This cut removes events in which two particles enter the experiment within the trigger window.
- *Relative time-of-flight between TOF0 and TOF1,  $t_{\text{rel}}$ , in the range  $1 \leq t_{\text{rel}} \leq 6 \text{ ns}$*  The time of flight between TOF0 and TOF1,  $t_{01}$ , was measured relative to the mean positron time of flight,  $t_e$ . Figure 3c shows the relative time-of-flight distribution in data (black, circles) and simulation (filled histogram). All cuts other than the relative time-of-flight cut have been applied in this figure. The time-of-flight of particles relative to the mean positron time-of-flight is calculated as

$$t_{\text{rel}} = t_{01} - (t_e + \delta t_e),$$

where  $\delta t_e$  accounts for the difference in transit time, or path length travelled, between electrons and muons in the field of the quadrupole triplets [21]. This cut removes electrons from the selected ensemble as well as a small number of pions. The data has a longer tail compared to the simulation, which is related to the imperfect simulation of the longitudinal momentum of particles in the beam (see Sect. 7.1).

- *A single track reconstructed in the upstream tracker with a track-fit  $\chi^2$  satisfying  $\frac{\chi^2}{N_{\text{DOF}}} \leq 4$*   $N_{\text{DOF}}$  is the number of degrees of freedom. The distribution of  $\frac{\chi^2}{N_{\text{DOF}}}$  is shown in Fig. 3d. This cut removes events with poorly reconstructed tracks. Multi-track events, in which more than one particle passes through the same pixel in TOF0 and TOF1 during the trigger window, are rare and are also removed by this cut. The distribution of  $\frac{\chi^2}{N_{\text{DOF}}}$  is broader and peaked at slightly larger values in the data than in the simulation.
- *Track contained within the fiducial volume of the tracker* The radius of the track measured by the tracker,  $R_{\text{track}}$ , is required to satisfy  $R_{\text{track}} < 150 \text{ mm}$  to ensure the track does not leave and then re-enter the fiducial volume. The track radius is evaluated at 1 mm intervals between the stations. If the track radius exceeds 150 mm at any of these positions, the event is rejected.

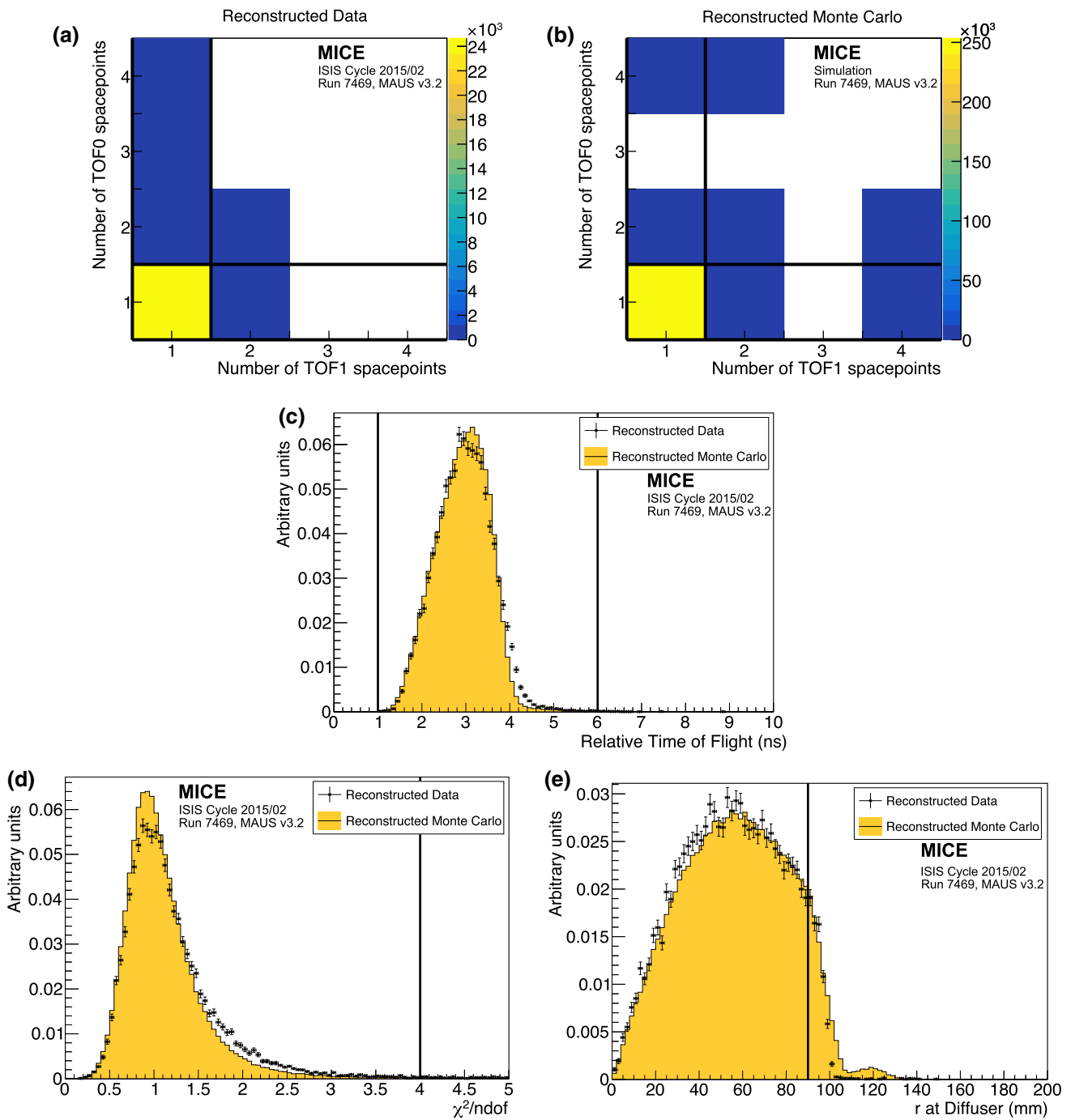


**Fig. 3** Distribution of the quantities that were used to select the sample used to reconstruct the emittance of the beam: **a** the number of space-points in TOF0 plotted against the number of space-points in TOF1 for reconstructed data, and **b** reconstructed simulation; **c** distribution of the relative time-of-flight,  $t_{rel}$ ; **d** distribution of  $\frac{\chi^2}{N_{DOF}}$ ; and **e** distribution

of  $R_{diff}$ . The 1D distributions show reconstructed data as solid (black) circles and reconstructed MAUS simulation as the solid (yellow) histogram. The solid (black) lines indicate the position of the cuts made on these quantities. Events enter these plots if all cuts other than the cut under examination are passed

– *Extrapolated track radius at the diffuser,  $R_{diff} \leq 90$  mm*  
 Muons that pass through the annulus of the diffuser, which includes the retracted irises, lose a substantial amount of energy. Such muons may re-enter the track-

ing volume and be reconstructed but have properties that are no longer characteristic of the incident muon beam. The aperture radius of the diffuser mechanism (100 mm) defines the transverse acceptance of the beam injected

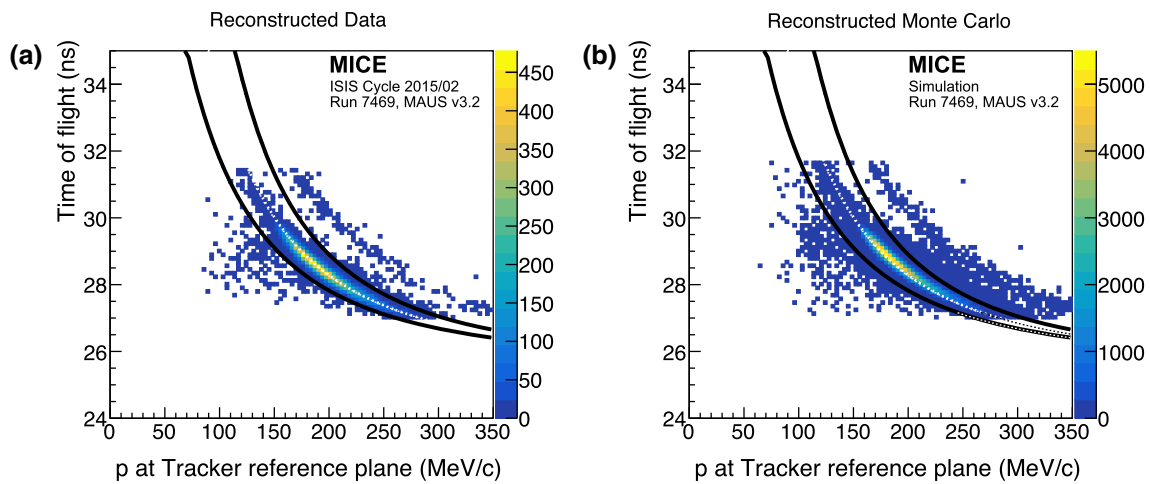


**Fig. 4** Time of flight between TOF0 and TOF1 ( $t_{01}$ ) plotted as a function of the muon momentum,  $p$ , measured in the upstream tracker. All cuts other than the muon hypothesis have been applied. Particles within the black lines are selected. The white dotted line is the trajectory of

a muon that loses the most probable momentum (20 MeV/c) between TOF1 and the tracker in **a** reconstructed data, and **b** reconstructed Monte Carlo

**Table 1** The number of particles that pass each selection criterion. A total of 24,660 particles pass all of the cuts

Cut	No. surviving particles	Cumulative surviving particles
None	53 276	53 276
One space-point in TOF0 and TOF1	37 619	37 619
Relative time of flight in range 1–6 ns	37 093	36 658
Single reconstructed track with $\frac{\chi^2}{\text{N}_{\text{DOF}}} \leq 4$	40 110	30 132
Track within fiducial volume of tracker	52 039	29 714
Extrapolated track radius at diffuser $\leq 90$ mm	42 592	25 310
Muon hypothesis	34 121	24 660
All	24 660	24 660

into the experiment. Back-extrapolation of tracks to the exit of the diffuser yields a measurement of  $R_{\text{diff}}$  with a resolution of  $\sigma_{R_{\text{diff}}} = 1.7$  mm. Figure 3e shows the distribution of  $R_{\text{diff}}$ , where the difference between data and simulation lies above the accepted radius. These differences are due to approximations in modelling the outer material of the diffuser. The cut on  $R_{\text{diff}}$  accepts particles that passed at least  $5.9\sigma_{R_{\text{diff}}}$  inside the aperture limit of the diffuser.

– *Particle consistent with muon hypothesis* Figure 4 shows  $t_{01}$ , the time-of-flight between TOF0 and TOF1, plotted as a function of  $p$ , the momentum reconstructed by the upstream tracking detector. Momentum is lost between TOF1 and the reference plane of the tracker in the material of the detectors. A muon that loses the most probable momentum,  $\Delta p \simeq 20$  MeV/c, is shown as the dotted (white) line. Particles that are poorly reconstructed, or have passed through support material upstream of the tracker and have lost significant momentum, are excluded

by the lower bound. The population of events above the upper bound are ascribed to the passage of pions, or mis-reconstructed muons, and are also removed from the analysis.

A total of 24,660 events pass the cuts listed above. Table 1 shows the number of particles that survive each individual cut. Data distributions are compared to the distributions obtained using the MAUS simulation in Figs. 3 and 4. Despite minor disagreements, the agreement between the simulation and data is sufficiently good to give confidence that a clean sample of muons has been selected.

The expected pion contamination of the unselected ensemble of particles has been measured to be  $\leq 0.4\%$  [22]. Table 2 shows the number of positrons, muons, and pions in the MAUS simulation that pass all selection criteria. The criteria used to select the muon sample for the analysis presented here efficiently reject electrons and pions from the Monte Carlo sample.

**Table 2** The number of reconstructed electrons, muons, and pions at the upstream tracker that survive each cut in the Monte Carlo simulation. Application of all cuts removes almost all positrons and pions in the reconstructed Monte Carlo sample. In the Monte Carlo simulation, a total of 253,504 particles pass all of the cuts described in the text

Cut	$e$	$\mu$	$\pi$	Total
None	14,912	432,294	1610	463,451
One space-point in TOF0 and TOF1	11,222	353,613	1213	376,528
Relative Time of flight in range 1–6 ns	757	369,337	1217	379,761
Single reconstructed track with $\frac{\chi^2}{\text{NDOF}} \leq 4$	10,519	407,276	1380	419,208
Track within fiducial volume of tracker	14,527	412,857	1427	443,431
Tracked radius at diffuser $\leq 90$ mm	11,753	311,076	856	334,216
Muon hypothesis (above lower limit)	3225	362,606	411	367,340
Muon hypothesis (below upper limit)	12,464	411,283	379	424,203
Muon hypothesis (overall)	2724	358,427	371	361,576
All	22	253,475	5	253,504

## 7 Results

### 7.1 Phase-space projections

The distributions of  $x$ ,  $y$ ,  $p_x$ ,  $p_y$ ,  $p_z$ , and  $p = \sqrt{p_x^2 + p_y^2 + p_z^2}$  are shown in Fig. 5. The total momentum of the muons that make up the beam lie within the range  $140 \lesssim |p| \lesssim 260 \text{ MeV}/c$ . The results of the MAUS simulation, which are also shown in Fig. 5, give a reasonable description of the data. In the case of the longitudinal component of momentum,  $p_z$ , the data are peaked to slightly larger values than the simulation. The difference is small and is reflected in the distribution of the total momentum,  $p$ . As the simulation began with particle production from the titanium target, any difference between the simulated and observed particle distributions would be apparent in the measured longitudinal and total momentum distributions. The scale of the observed disagreement is small, and as such the simulation adequately describes the experiment. The distributions of the components of the transverse phase space ( $x$ ,  $p_x$ ,  $y$ ,  $p_y$ ) are well described by the simulation. Normalised transverse emittance is calculated with respect to the means of the distributions (Eq. 2), and so is unaffected by this discrepancy.

The phase space occupied by the selected beam is shown in Fig. 6. The distributions are plotted at the reference surface of the upstream tracker. The beam is moderately well centred in the  $(x, y)$  plane. Correlations are apparent that couple the position and momentum components in the transverse plane. The transverse position and momentum coordinates are also seen to be correlated with total momentum. The correlation in the  $(x, p_y)$  and  $(y, p_x)$  plane is due to the solenoidal field, and is of the expected order. The dispersion and chromaticity of the beam are discussed further in Sect. 7.2.

### 7.2 Effect of dispersion, chromaticity, and binning in longitudinal momentum

Momentum selection at D2 introduces a correlation, dispersion, between the position and momentum of particles. Figure 7 shows the transverse position and momentum with respect to the total momentum,  $p$ , as measured at the upstream-tracker reference plane. Correlations exist between all four transverse phase-space co-ordinates and the total momentum.

Emittance is calculated in 10 MeV/ $c$  bins of total momentum in the range  $185 \leq p \leq 255 \text{ MeV}/c$ . This bin size was chosen as it is commensurate with the detector resolution. Calculating the emittance in momentum increments makes the effect of the optical mismatch, or chromaticity, small compared to the statistical uncertainty. The range of  $185 \leq p \leq 255 \text{ MeV}/c$  was chosen to maximise the number of particles in each bin that are not scraped by the aperture of the diffuser.

### 7.3 Uncertainties on emittance measurement

#### 7.3.1 Statistical uncertainties

The statistical uncertainty on the emittance in each momentum bin is calculated as  $\sigma_\varepsilon = \frac{\varepsilon}{\sqrt{2N}}$  [38–40], where  $\varepsilon$  is the emittance of the ensemble of muons in the specified momentum range and  $N$  is the number of muons in that ensemble. The number of events per bin varies from  $\sim 4000$  for  $p \sim 190 \text{ MeV}/c$  to  $\sim 700$  for  $p \sim 250 \text{ MeV}/c$ .

### 7.4 Systematic uncertainties

#### 7.4.1 Uncorrelated systematic uncertainties

Systematic uncertainties related to the beam selection were estimated by varying the cut values by an amount correspond-

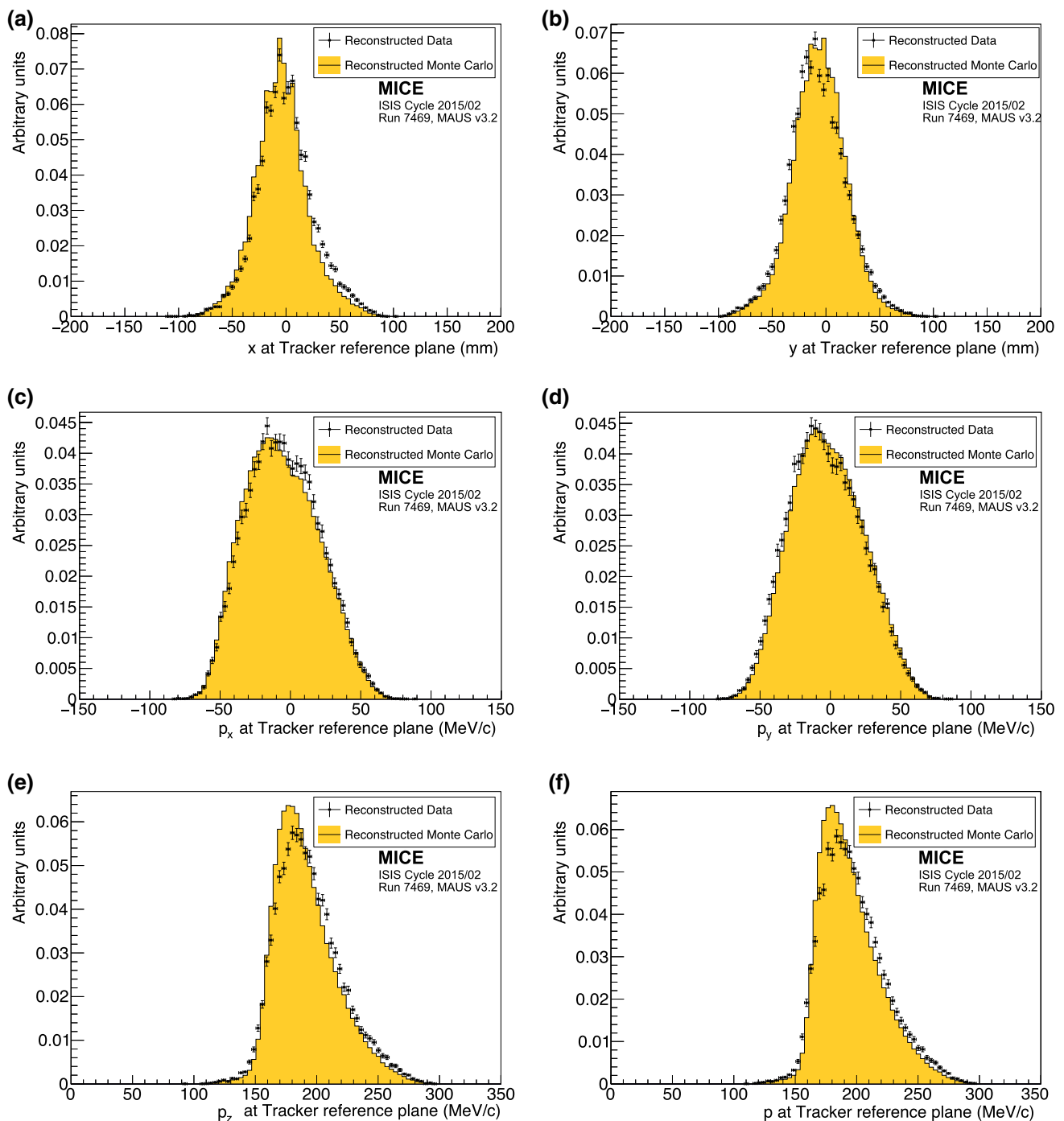


**Fig. 5** Position and momentum distributions of muons reconstructed at the reference surface of the upstream tracker: **a**  $x$ , **b**  $y$ , **c**  $p_x$ , **d**  $p_y$ , **e**  $p_z$ , and **f**  $p$ , the total momentum. The data are shown as the solid circles while the results of the MAUS simulation are shown as the yellow histogram

ing to the RMS resolution of the quantity in question. The emittance of the ensembles selected with the changed cut values were calculated and compared to the emittance calculated using the nominal cut values and the difference taken as the uncertainty due to changing the cut boundaries. The overall uncertainty due to beam selection is summarised in Table 3. The dominant beam-selection uncertainty is in the

selection of particles that successfully pass within the inner 90 mm of the diffuser aperture.

Systematic uncertainties related to possible biases in calibration constants were evaluated by varying each calibration constant by its resolution. Systematic uncertainties related to the reconstruction algorithms were evaluated using the MAUS simulation. The positive and negative deviations



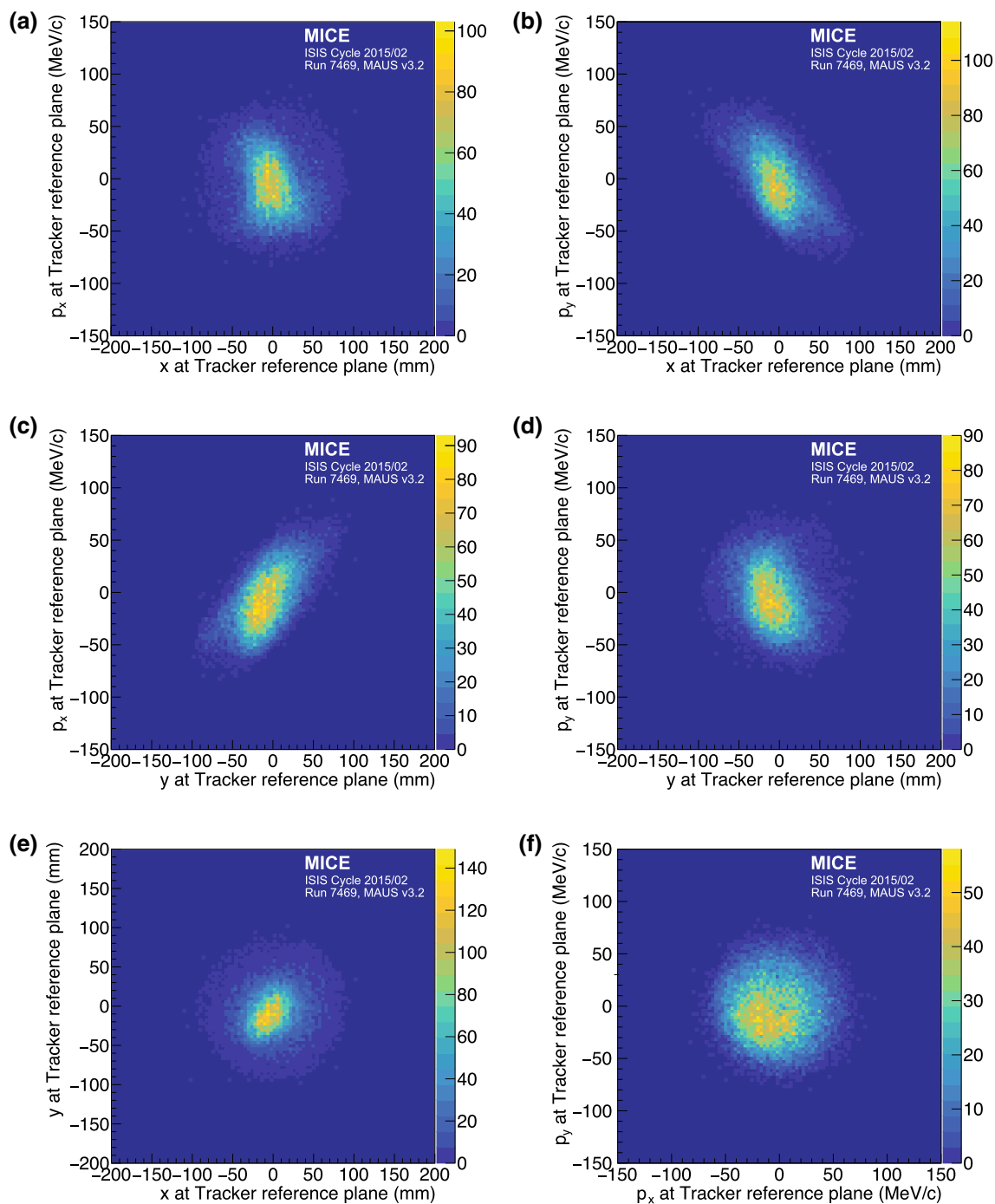


**Fig. 6** Transverse phase space occupied by selected muons transported through the MICE Muon Beam line to the reference plane of the upstream tracker. **a** ( $x, p_x$ ), **b** ( $x, p_y$ ), **c** ( $y, p_x$ ), **d** ( $y, p_y$ ), **e** ( $x, y$ ), and **f** ( $p_x, p_y$ )

from the nominal emittance were added in quadrature separately to obtain the total positive and negative systematic uncertainty. Sources of correlated uncertainties are discussed below.

#### 7.4.2 Correlated systematic uncertainties

Some systematic uncertainties are correlated with the total momentum,  $p$ . For example, the measured value of  $p$  dictates the momentum bin to which a muon is assigned for the emittance calculation. The uncertainty on the emittance reconstructed in each bin has been evaluated by allowing the

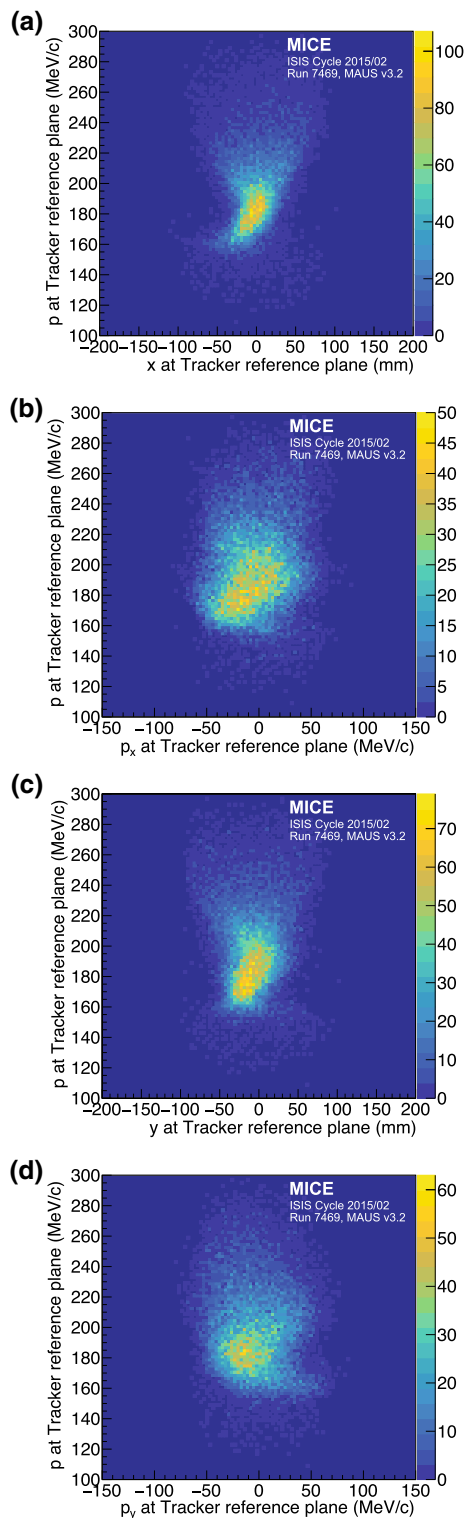


**Fig. 7** The effect of dispersion, the dependence of the components of transverse phase space on the momentum,  $p$ , is shown at the reference surface of the upstream tracker: **a**) ( $x, p$ ); **b**) ( $p_x, p$ ); **c**) ( $y, p$ ); **d**) ( $p_y, p$ )

momentum of each muon to fluctuate around its measured value according to a Gaussian distribution of width equal to

the measurement uncertainty on  $p$ . In Table 3 this uncertainty is listed as ‘Binning in  $p$ ’.

A second uncertainty that is correlated with total momentum is the uncertainty on the reconstructed  $x$ ,  $p_x$ ,  $y$ , and  $p_y$ . The effect on the emittance was evaluated with the same procedure used to evaluate the uncertainty due to binning in total momentum. This is listed as ‘Tracker resolution’ in Table 3.

Systematic uncertainties correlated with  $p$  are primarily due to the differences between the model of the apparatus used in the reconstruction and the hardware actually used in the experiment. The most significant contribution arises from the magnetic field within the tracking volume. Particle tracks are reconstructed assuming a uniform solenoidal field, with no fringe-field effects. Small non-uniformities in the magnetic field in the tracking volume will result in a disagreement between the true parameters and the reconstructed values. To quantify this effect, six field models (one optimal and five additional models) were used to estimate the deviation in reconstructed emittance from the true value under realistic conditions. Three families of field model were investigated, corresponding to the three key field descriptors: field scale, field alignment, and field uniformity. The values of these descriptors that best describe the Hall-probe measurements were used to define the optimal model and the uncertainty in the descriptor values were used to determine the  $1\sigma$  variations.

#### 7.4.3 Field scale

Hall-probes located on the tracker provided measurements of the magnetic field strength within the tracking volume at known positions. An optimal field model was produced with a scale factor of 0.49% that reproduced the Hall-probe measurements. Two additional field models were produced which used scale factors that were one standard deviation,  $\pm 0.03\%$ , above and below the nominal value.

#### 7.4.4 Field alignment

A field-alignment algorithm was developed based on the determination of the orientation of the field with respect to the mechanical axis of the tracker using coaxial tracks with  $p_T \approx 0$  [41]. The field was rotated with respect to the tracker by  $1.4 \pm 0.1$  mrad about the  $x$  axis and  $0.3 \pm 0.1$  mrad about the  $y$  axis. The optimal field model was created such that the simulated alignment is in agreement with the measurements. Two additional models that vary the alignment by one standard deviation were also produced.

#### 7.4.5 Field uniformity

A COMSOL [42] model of the field was used to generate the optimal model which includes the field generated by each coil

**Table 3** Emittance together with the statistical and systematic uncertainties and biases as a function of mean total momentum, ( $p$ )

Source	( $p$ ) (MeV/c)	190	200	210	220	230	240	250
Measured emittance (mm rad)		3.40	3.65	3.69	3.65	3.69	3.62	3.31
Statistical uncertainty		$\pm 3.8 \times 10^{-2}$	$\pm 4.4 \times 10^{-2}$	$\pm 5.0 \times 10^{-2}$	$\pm 5.8 \times 10^{-2}$	$\pm 7.0 \times 10^{-2}$	$\pm 8.4 \times 10^{-2}$	$\pm 9.2 \times 10^{-2}$
Beam selection:								
Diffuser aperture		$4.9 \times 10^{-2}$	$5.3 \times 10^{-2}$	$4.9 \times 10^{-2}$	$4.7 \times 10^{-2}$	$4.2 \times 10^{-2}$	$11.0 \times 10^{-2}$	$4.4 \times 10^{-2}$
$\chi^2_{\text{DOF}} \leq 4$		$-3.5 \times 10^{-2}$	$-5.1 \times 10^{-2}$	$-5.7 \times 10^{-2}$	$-5.0 \times 10^{-2}$	$-3.5 \times 10^{-2}$	$-5.0 \times 10^{-2}$	$-9.6 \times 10^{-2}$
Muon hypothesis		$5.1 \times 10^{-3}$	$2.0 \times 10^{-3}$	$1.0 \times 10^{-2}$	$4.1 \times 10^{-3}$	$1.2 \times 10^{-3}$	$5.5 \times 10^{-3}$	$7.9 \times 10^{-3}$
		$-4.8 \times 10^{-3}$	$-1.3 \times 10^{-3}$	$-1.8 \times 10^{-3}$	$-3.3 \times 10^{-3}$	$-2.8 \times 10^{-4}$	$-6.5 \times 10^{-3}$	$-4.7 \times 10^{-4}$
		$4.5 \times 10^{-3}$	$2.2 \times 10^{-4}$	$6.4 \times 10^{-3}$	$3.1 \times 10^{-3}$	$1.4 \times 10^{-3}$	$2.6 \times 10^{-3}$	$1.3 \times 10^{-3}$
Beam selection (Overall)		$-3.2 \times 10^{-3}$	$-6.8 \times 10^{-3}$	$-8.8 \times 10^{-4}$	$-4.7 \times 10^{-3}$	$-1.1 \times 10^{-2}$	$-6.7 \times 10^{-2}$	$-4.1 \times 10^{-3}$
		$4.9 \times 10^{-2}$	$5.3 \times 10^{-2}$	$5.0 \times 10^{-2}$	$4.7 \times 10^{-2}$	$4.2 \times 10^{-2}$	$1.1 \times 10^{-1}$	$4.5 \times 10^{-2}$
		$-3.6 \times 10^{-2}$	$-5.2 \times 10^{-2}$	$-5.8 \times 10^{-2}$	$-5.0 \times 10^{-2}$	$-3.9 \times 10^{-2}$	$-8.4 \times 10^{-2}$	$-9.6 \times 10^{-2}$
Binning in $p$		$\pm 1.8 \times 10^{-2}$	$\pm 2.1 \times 10^{-2}$	$\pm 2.3 \times 10^{-2}$	$\pm 2.9 \times 10^{-2}$	$\pm 3.5 \times 10^{-2}$	$\pm 4.3 \times 10^{-2}$	$\pm 5.2 \times 10^{-2}$
Magnetic field misalignment and scale:								
Bias		$-1.3 \times 10^{-2}$	$-1.4 \times 10^{-2}$	$-1.5 \times 10^{-2}$	$-1.6 \times 10^{-2}$	$-1.6 \times 10^{-2}$	$-1.7 \times 10^{-2}$	$-1.6 \times 10^{-2}$
Uncertainty		$\pm 2.0 \times 10^{-4}$	$\pm 2.9 \times 10^{-4}$	$\pm 8.0 \times 10^{-4}$	$\pm 4.8 \times 10^{-4}$	$\pm 5.5 \times 10^{-4}$	$\pm 4.8 \times 10^{-4}$	$\pm 4.9 \times 10^{-4}$
Tracker resolution		$\pm 1.6 \times 10^{-3}$	$\pm 2.1 \times 10^{-3}$	$\pm 2.8 \times 10^{-3}$	$\pm 3.8 \times 10^{-3}$	$\pm 5.3 \times 10^{-3}$	$\pm 7.0 \times 10^{-3}$	$\pm 9.5 \times 10^{-3}$
Total systematic uncertainty		$5.2 \times 10^{-2}$	$5.7 \times 10^{-2}$	$5.5 \times 10^{-2}$	$5.6 \times 10^{-2}$	$5.5 \times 10^{-2}$	$11.7 \times 10^{-2}$	$6.9 \times 10^{-2}$
		$-4.0 \times 10^{-2}$	$-5.6 \times 10^{-2}$	$-6.2 \times 10^{-2}$	$-5.8 \times 10^{-2}$	$-5.2 \times 10^{-2}$	$-9.5 \times 10^{-2}$	$-11.0 \times 10^{-2}$
Corrected emittance (mm rad)		3.41	3.66	3.71	3.67	3.71	3.65	3.34
Total uncertainty		$\pm 0.06$	$\pm 0.07$	$+0.07$	$\pm 0.08$	$\pm 0.09$	$+0.14$	$+0.12$
			$-0.08$	$-0.08$			$-0.13$	$-0.14$
Total uncertainty (%)		$+1.90$	$+1.96$	$+2.01$	$+2.19$	$+2.40$	$+3.97$	$+3.47$
		$-1.63$	$-1.94$	$-2.15$	$-2.34$	$-2.37$	$-3.49$	$-4.30$

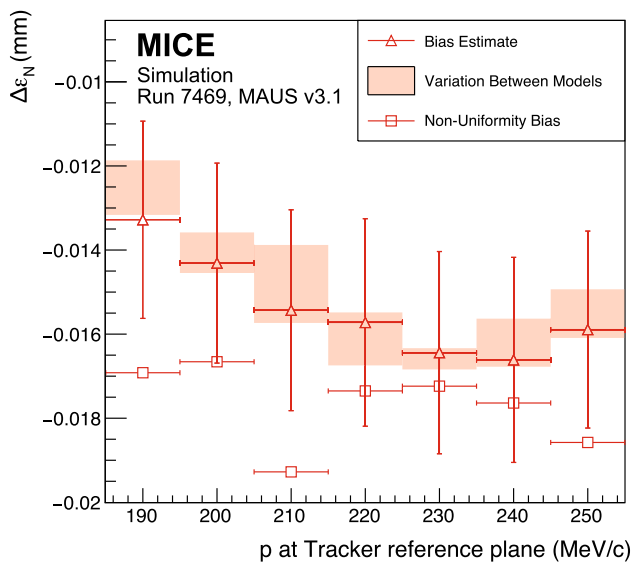


**Fig. 8** The systematic bias and uncertainty on the reconstructed emittance under different magnetic field model assumptions. The bias estimate (open triangles) includes the non-uniformity bias (open squares). The variation between the models (see text) is indicated by the shaded bands

using the ‘as-built’ parameters and the partial return yoke. A simple field model was created using only the individual coil geometries to provide additional information on the effect of field uniformity on the reconstruction. The values for the simple field model were normalised to the Hall-probe measurements as for the other field models. This represents a significant deviation from the COMSOL model, but demonstrates the stability of the reconstruction with respect to changes in field uniformity, as the variation in emittance between all field models is small (less than 0.002 mm).

For each of the 5 field models, multiple 2000-muon ensembles were generated for each momentum bin. The deviation of the calculated emittance from the true emittance was found for each ensemble. The distribution of the difference between the ensemble emittance and the true emittance was assumed to be Gaussian with mean  $\varepsilon$  and variance  $s^2 = \sigma^2 + \theta^2$ , where  $\sigma$  is the statistical uncertainty and  $\theta$  is an additional systematic uncertainty. The systematic bias for each momentum bin was then calculated as [43]

$$\Delta\varepsilon_N = \langle\varepsilon\rangle - \varepsilon_{\text{true}}, \tag{4}$$

where  $\varepsilon_{\text{true}}$  is the true beam emittance in that momentum bin and  $\langle\varepsilon\rangle$  is the mean emittance from the  $N$  ensembles. The systematic uncertainty was calculated assuming that the distribution of residuals of  $\varepsilon_i$  from the mean,  $\langle\varepsilon\rangle$ , satisfies a  $\chi^2$  distribution with  $N - 1$  degrees of freedom,

$$\chi^2_{N-1} = \sum_i^N \frac{(\varepsilon_i - \langle\varepsilon\rangle)^2}{\sigma^2 + \theta^2}, \tag{5}$$

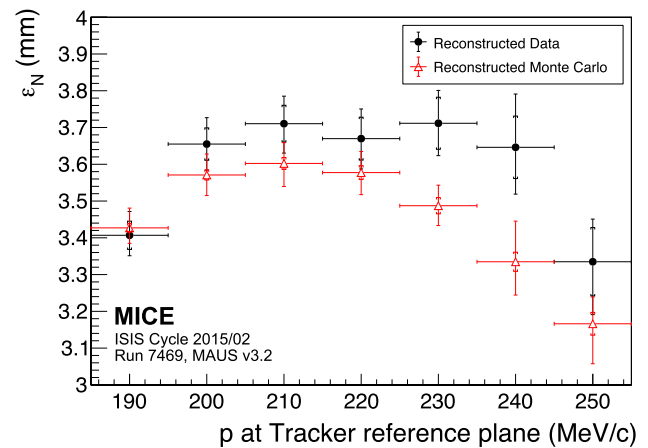


**Fig. 9** Normalised transverse emittance as a function of total momentum,  $p$ , for data (black, filled circle) and reconstructed Monte Carlo (red, open triangle). The inner error bars show the statistical uncertainty. The outer error bars show the quadratic sum of the statistical and systematic uncertainties

and  $\theta$  was estimated by minimising the expression  $(\chi^2_{N-1} - (N - 1))^2$  [43].

The uncertainty,  $\theta$ , was consistent with zero in all momentum bins, whereas the bias,  $\Delta\varepsilon_N$ , was found to be momentum dependent as shown in Fig. 8. The bias was estimated from the mean difference between the reconstructed and true emittance values using the optimal field model. The variation in the bias was calculated from the range of values reconstructed for each of the additional field models. The model representing the effects of non-uniformities in the field was considered separately due to the significance of the deviation from the optimal model.

The results show a consistent systematic bias in the reconstructed emittance of  $\approx -0.015$  mm that is a function of momentum (see Table 3). The absolute variation in the mean values between the models that were used was smaller than the expected statistical fluctuations, demonstrating the stability of the reconstruction across the expected variations in field alignment and scale. The effect of the non-uniformity model was larger but still demonstrates consistent reconstruction. The biases calculated from the optimal field model were used to correct the emittance values in the final calculation (Sect. 7.5).

### 7.5 Emittance

The normalised transverse emittance as a function of  $p$  is shown in Fig. 9. The emittance has been corrected for the systematic bias shown in Table 3. The uncertainties plotted are those summarised in Table 3, where the inner bars represent the statistical uncertainty and outer bars the total uncertainty. The emittance of the measured muon ensembles (black, filled circle) is approximately flat in the range

$195 \leq p \leq 245 \text{ MeV}/c$ , corresponding to the design momentum of the experiment. The mean emittance in this region is  $\approx 3.7 \text{ mm}$ . The emittance of the reconstructed Monte Carlo is consistently lower than that of the data, and therefore gives only an approximate simulation of the beam.

## 8 Conclusions

A first particle-by-particle measurement of the emittance of the MICE Muon Beam was made using the upstream scintillating-fibre tracking detector in a 4 T solenoidal field. A total of 24,660 muons survive the selection criteria. The position and momentum of these muons were measured at the reference plane of the upstream tracking detector. The muon sample was divided into 10 MeV/c bins of total momentum,  $p$ , from 185–255 MeV/c to account for dispersion, chromaticity, and scraping in apertures upstream of the tracking detector. The emittance of the measured muon ensembles is approximately flat from  $195 \leq p \leq 245 \text{ MeV}/c$  with a mean value of  $\approx 3.7 \text{ mm}$  across this region.

The total uncertainty on this measurement ranged from  $+1.9\%$  to  $+3.5\%$ , increasing with total momentum,  $p$ . As  $p$  increases, the number of muons in the reported ensemble decreases, increasing the statistical uncertainty. At the extremes of the momentum range, a larger proportion of the input beam distribution is scraped on the aperture of the diffuser. This contributes to an increase in systematic uncertainty at the limits of the reported momentum range. The systematic uncertainty introduced by the diffuser aperture highlights the need to study ensembles where the total momentum,  $p$ , is close to the design momentum of the beam line. The total systematic uncertainty on the measured emittance is larger than that on a future measurement of the ratio of emittance before and after an absorber. The measurement is sufficiently precise to demonstrate muon ionization cooling.

The technique presented here represents the first precise measurement of normalised transverse emittance on a particle-by-particle basis. This technique will be applied to muon ensembles up- and downstream of a low- $Z$  absorber, such as liquid hydrogen or lithium hydride, to measure emittance change across the absorber and thereby to study ionization cooling.

**Acknowledgements** The work described here was made possible by grants from Department of Energy and National Science Foundation (USA), the Istituto Nazionale di Fisica Nucleare (Italy), the Science and Technology Facilities Council (UK), the European Community under the European Commission Framework Programme 7 (AIDA project, grant agreement no. 262025, TIARA project, grant agreement no. 261905, and EuCARD), the Japan Society for the Promotion of Science, the National Research Foundation of Korea (No. NRF-2016R1A5A1013277), and the Swiss National Science Foundation, in the framework of the SCOPES programme. We gratefully acknowledge all sources of support. We are grateful for the support given to us by the

staff of the STFC Rutherford Appleton and Daresbury Laboratories. We acknowledge the use of Grid computing resources deployed and operated by GridPP in the UK, <http://www.gridpp.ac.uk/>.

**Data Availability Statement** This manuscript has associated data in a data repository. [Authors' comment: The data that support the findings of this study are publicly available on the GridPP computing Grid via the data DOIs (the MICE unprocessed data: 10.17633/rd.brunel.3179644; the MICE reconstructed data: 10.17633/rd.brunel.5955850). Publications using the MICE data must contain the following statement: "We gratefully acknowledge the MICE collaboration for allowing us access to their data. Third-party results are not endorsed by the MICE collaboration and the MICE collaboration does not accept responsibility for any errors in the third-party's understanding of the MICE data."]

**Open Access** This article is distributed under the terms of the Creative Commons Attribution 4.0 International License (<http://creativecommons.org/licenses/by/4.0/>), which permits unrestricted use, distribution, and reproduction in any medium, provided you give appropriate credit to the original author(s) and the source, provide a link to the Creative Commons license, and indicate if changes were made. Funded by SCOAP<sup>3</sup>.

## References

1. S. Geer, Phys. Rev. D **57**, 6989 (1998). <https://doi.org/10.1103/PhysRevD.57.6989>
2. M. Apollonio, et al., Oscillation physics with a neutrino factory (2002). [arXiv:hep-ph/0210192](https://arxiv.org/abs/hep-ph/0210192)
3. D.V. Neuffer, R.B. Palmer, Conf. Proc. C **940627**, 52 (1995)
4. R.B. Palmer, Rev. Accel. Sci. Tech. **7**, 137 (2014). <https://doi.org/10.1142/S1793626814300072>
5. M. Boscolo, M. Antonelli, O.R. Blanco-Garcia, S. Guiducci, S. Liuzzo, P. Raimondi, F. Collamati, Low emittance muon accelerator studies with production from positrons on target (2018). <https://doi.org/10.1103/PhysRevAccelBeams.21.061005>. [arXiv:1803.06696](https://arxiv.org/abs/1803.06696) [physics.acc-ph]
6. S.Y. Lee, *Accelerator Physics*, 3rd edn. (World Scientific Publishing Co, Singapore, 2012). <https://doi.org/10.1142/8335>
7. S. Schröder, R. Klein, N. Boos, M. Gerhard, R. Grieser, G. Huber, A. Karafillidis, M. Krieg, N. Schmidt, T. Kühl, R. Neumann, V. Balykin, M. Grieser, D. Habs, E. Jaeschke, D. Krämer, M. Kristensen, M. Music, W. Petrich, D. Schwalm, P. Sigray, M. Steck, B. Wanner, A. Wolf, Phys. Rev. Lett. **64**, 2901 (1990). <https://doi.org/10.1103/PhysRevLett.64.2901>
8. J.S. Hangst, M. Kristensen, J.S. Nielsen, O. Poulsen, J.P. Schiffer, P. Shi, Phys. Rev. Lett. **67**, 1238 (1991). <https://doi.org/10.1103/PhysRevLett.67.1238>
9. P.J. Channell, J. Appl. Phys. **52**(6), 3791 (1981). <https://doi.org/10.1063/1.329218>
10. J. Marriner, Nucl. Instrum. Methods A **532**, 11 (2004). <https://doi.org/10.1016/j.nima.2004.06.025>
11. V.V. Parkhomchuk, A.N. Skrinsky, Physics-Uspekhi **43**(5), 433 (2000)
12. A.N. Skrinsky, V.V. Parkhomchuk, Sov. J. Part. Nucl. **12**, 223 (1981) [**Fiz. Elem. Chast. Atom. Yadra** **12,557 (1981)**]
13. D. Neuffer, Conf. Proc. C **830811**, 481 (1983)
14. D. Neuffer, Part. Accel. **14**, 75 (1983)
15. The MICE collaboration, International MUON Ionization Cooling Experiment. <http://mice.iit.edu>. Accessed 4 Mar 2019
16. M. Apollonio et al., JINST **4**, P07001 (2009). <https://doi.org/10.1088/1748-0221/4/07/P07001>
17. J.B. Rosenzweig, *Fundamentals of Beam Physics* (Oxford University Press, Oxford, 2003)

18. C.N. Booth et al., JINST **8**, P03006 (2013). <https://doi.org/10.1088/1748-0221/8/03/P03006>
19. C.N. Booth et al., JINST **11**(05), P05006 (2016). <https://doi.org/10.1088/1748-0221/11/05/P05006>
20. M. Bogomilov et al., JINST **7**, P05009 (2012). <https://doi.org/10.1088/1748-0221/7/05/P05009>
21. D. Adams et al., Eur. Phys. J. C **73**(10), 2582 (2013). <https://doi.org/10.1140/epjc/s10052-013-2582-8>
22. M. Bogomilov et al., JINST **11**(03), P03001 (2016). <https://doi.org/10.1088/1748-0221/11/03/P03001>
23. R. Bertoni, Nucl. Instrum. Methods A **615**, 14 (2010). <https://doi.org/10.1016/j.nima.2009.12.065>
24. R. Bertoni, M. Bonesini, A. de Bari, G. Cecchet, Y. Karadzhov, R. Mazza, The construction of the MICE TOF2 detector (2010). <http://mice.iit.edu/micenotes/public/pdf/MICE0286/MICE0286.pdf>. Accessed 4 Mar 2019
25. L. Cremaldi, D.A. Sanders, P. Sonnek, D.J. Summers, J. Reidy Jr., I.E.E.E. Trans. Nucl. Sci. **56**, 1475 (2009). <https://doi.org/10.1109/TNS.2009.2021266>
26. M. Ellis, Nucl. Instrum. Methods A **659**, 136 (2011). <https://doi.org/10.1016/j.nima.2011.04.041>
27. F. Ambrosino, Nucl. Instrum. Methods A **598**, 239 (2009). <https://doi.org/10.1016/j.nima.2008.08.097>
28. R. Asfandiyarov et al., JINST **11**(10), T10007 (2016). <https://doi.org/10.1088/1748-0221/11/10/T10007>
29. D. Adams et al., JINST **10**(12), P12012 (2015). <https://doi.org/10.1088/1748-0221/10/12/P12012>
30. A. Dobbs, C. Hunt, K. Long, E. Santos, M.A. Uchida, P. Kyberd, C. Heidt, S. Blot, E. Overton, JINST **11**(12), T12001 (2016). <https://doi.org/10.1088/1748-0221/11/12/T12001>
31. S. Blot, *Proceedings 2nd International Particle Accelerator Conference (IPAC 11) 4–9 September 2011* (San Sebastian, 2011) <https://accelconf.web.cern.ch/accelconf/IPAC2011/papers/mopz034.pdf>. Accessed 4 Mar 2019
32. The MICE Collaboration, The MICE RAW Data. <https://doi.org/10.17633/rd.brunel.3179644> (MICE/Step4/07000/07469.tar)
33. T. Roberts, et al., G4beamline; a “Swiss Army Knife” for Geant4, optimized for simulating beamlines. <http://public.muonsinc.com/Projects/G4beamline.aspx>. Accessed 17 Sept 2018
34. D. Rajaram, C. Rogers, The mice offline computing capabilities (2014). <http://mice.iit.edu/micenotes/public/pdf/MICE0439/MICE0439.pdf> (MICE Note 439)
35. S. Agostinelli, Nucl. Instrum. Methods Phys. Res. A **506**, 250 (2003)
36. J. Allison et al., IEEE Trans. Nucl. Sci. **53**, 270 (2006). <https://doi.org/10.1109/TNS.2006.869826>
37. R. Brun, F. Rademakers, Nucl. Instrum. Methods A **389**, 81 (1997). [https://doi.org/10.1016/S0168-9002\(97\)00048-X](https://doi.org/10.1016/S0168-9002(97)00048-X)
38. J. Cobb, Statistical errors on emittance measurements (2009). <http://mice.iit.edu/micenotes/public/pdf/MICE341/MICE268.pdf>. Accessed 4 Mar 2019
39. J. Cobb, Statistical errors on emittance and optical functions (2011). <http://mice.iit.edu/micenotes/public/pdf/MICE341/MICE341.pdf>. Accessed 4 Mar 2019
40. J.H. Cobb, Statistical Errors on Emittance (2015, Private communication)
41. C. Hunt, Private communication Publication-in-progress
42. COMSOL Multiphysics software Webpage: <https://www.comsol.com>. Accessed 4 Mar 2019
43. L. Lyons, J. Phys. A Math. Gen. **25**(7), 1967 (1992). <http://stacks.iop.org/0305-4470/25/i=7/a=035>



# Rigidity dependence of Forbush decreases in the energy region exceeding the sensitivity of neutron monitors

M. Savić, N. Veselinović\*, A. Dragić, D. Maletić, D. Joković, R. Banjanac, V. Udovičić

*Institute of Physics, University of Belgrade, Pregrevica 118, 11080 Zemun, Serbia*

Received 2 May 2018; received in revised form 14 September 2018; accepted 24 September 2018

Available online 28 September 2018

## Abstract

Applicability of our present setup for solar modulation studies in a shallow underground laboratory is tested on four prominent examples of Forbush decrease during solar cycle 24. Forbush decreases are of interest in space weather application and study of energy-dependent solar modulation, and they have been studied extensively. The characteristics of these events, as recorded by various neutron monitors and our detectors, were compared, and rigidity spectrum was found. Linear regression was performed to find power indices that correspond to each event. As expected, a steeper spectrum during more intense extreme solar events with strong X-flares shows a greater modulation of galactic cosmic rays. Presented comparative analysis illustrates the applicability of our setup for studies of solar modulation in the energy region exceeding the sensitivity of neutron monitors.

© 2018 COSPAR. Published by Elsevier Ltd. All rights reserved.

**Keywords:** Forbush decrease; Muon CR station; Median rigidity

## 1. Introduction

Galactic cosmic rays (GCRs) traverse the heliosphere; this leads to variation in the cosmic ray (CR) flux due to solar activity. The influence of solar and heliospheric modulation is pronounced for primary CR particles with low rigidity or momentum over unit charge. CRs interact, upon arrival, with Earth's atmosphere causing electromagnetic and hadronic showers. A network of ground-based CR detectors, neutron monitors (NMs), and muon detectors, located at various locations around the globe, as well as airborne balloons and satellites, provide valuable data to study the effect of these modulations on the integrated CR flux with time. Energies of the primary particles in NMs are sensitive to the state of solar activity and reach up to 40 GeV. Muon detectors have a significant response from 10 GeV up to several hundred GeV for surface, and

one order of magnitude greater for underground detectors, depending on the depth (Duldig, 2000). This energy interval allows muon detectors to monitor not only modulation effects on lower-energy CRs but also galactic effects on primary CRs with high energies where solar modulation is negligible. Because of the sensitivity to different energies of the primary particle flux, observations of muon detectors complement those of NMs in studies of long-term CR variations, CR anisotropy, and gradients or rigidity spectrum of Forbush decreases (FDs).

FDs (Forbush, 1954) represent decreases of the observed GCR intensity under the influence of coronal mass ejections (CMEs) and interplanetary counterparts of coronal mass ejections (ICMEs) and/or high-speed streams of solar wind (HSS) from the coronal holes (Belov, 2008). FDs belong to two types depending on the drivers: non-recurrent and recurrent decreases. This work addresses several non-recurrent FDs.

These sporadic FDs are caused by ICMEs. As the matter with its magnetic field moves through the solar system,

\* Corresponding author.

E-mail address: [veselinovic@ipb.ac.rs](mailto:veselinovic@ipb.ac.rs) (N. Veselinović).

it suppresses the CR intensity. FDs of this kind have an asymmetric profile, and the intensity of GCRs has a sudden onset and recovers gradually. Sometimes an early phase of FD prior to the dip (precursor of FD) shows an increase in CR intensity. These precursors of FDs are caused by GCR acceleration at the front of the advancing disturbance on the outer boundary of the ICME, as the primary CR particles are being reflected from the approaching shock (Papailiou et al., 2013). The FD profile depends on the area, velocity, and intensity of CME magnetic field produced in extreme events that originate at the Sun (Chauhan et al., 2008).

Data from observed modulation of GCR intensity contain information regarding the transport of GCRs through the interplanetary environment. GCR transport parameters are connected with the interplanetary magnetic field (IMF) in the heliosphere. It is empirically established that the radial diffusion coefficient is proportional to the rigidity of CR (Ahluwalia, 2005). In this article, we present an analysis of the amplitude of FD during four events, which were recorded by plastic scintillator muon detectors, located at the Belgrade muon station, as well as by a network of NMs.

## 2. Belgrade CR station

The Low-Background Laboratory for Nuclear Physics (LBNLP) is a part of the Institute of Physics, University of Belgrade. It is composed of two separate laboratory facilities, ground-level laboratory (GLL) and underground laboratory (UL), dug into a cliff. The overburden of the UL is approximately 12 m of loess soil, which is equivalent to 25 m of water (m.w.e). Laboratory is dedicated to measurements of low radiation activities and studies of muon and electromagnetic components of CRs at ground and shallow underground levels. The geographic position of the laboratory is at 75 m a.s.l., at 44°51'N latitude and 20°23'E longitude; geomagnetic vertical rigidity cutoff is 5.3 GV at the surface. The equipment was upgraded in 2008, and now, it consists of two identical sets of detectors and accompanying data processing electronics: one is situated in GLL and the other in UL. Detectors are a pair of plastic scintillator detectors, with dimensions of 100 cm × 100 cm × 5 cm and four PMTs that are directly coupled to the corners. Signals from two opposite PMTs on a single detector are summed, and the coincidence of the two diagonals is found. Fig. 1 presents the coincident sum spectra of two diagonals of large scintillator detectors.

Summing over diagonals suppresses the acquisition of electromagnetic component of the secondary CR shower and collects mainly the muon component of secondary CRs. A well-defined peak in the energy spectra corresponds to a muon energy loss of ~11 MeV. The average muon flux measured in the laboratory is 137(6) muons/m<sup>2</sup>s for GLL and 45(2) muons/m<sup>2</sup>s for UL. For more detailed description, see Dragić et al. (2011). Integral of this distribution, without low energy part, is used to form time series of this

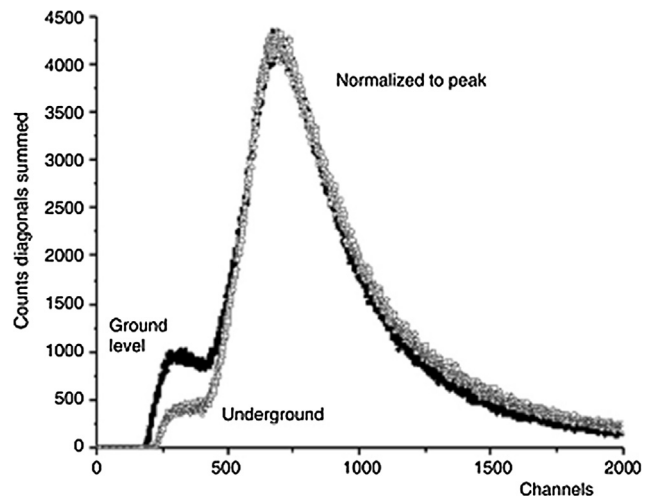


Fig. 1. The coincident spectra of two diagonals of large plastic detectors in UL and GLL normalized for comparison.

CR muons spectrum integrated over different time intervals. This time series is then corrected for efficiency, atmospheric pressure, and temperature (Savić et al., 2015).

The CR flux measured at the ground level varies because of changes in atmospheric conditions. Effects of the atmospheric pressure can be easily accounted for, similar like for NMs, but the temperature effect is somewhat more difficult to treat. The difficulties arise from the interplay of positive and negative temperature effects. With temperature increase, the atmospheric density decreases; hence, less pions interact and more muons are created from decay. The result is a positive effect of more muons at the ground level. On the other hand, the altitude of muon production level is high due to the expansion of the atmosphere when the temperature is high, muon path length is long, and decay probability of muons is high before they reach the ground level. Negative effect is dominant for low-energy muons (mostly detected in GLL) and positive for high-energy muons. A proper treatment of the temperature effect requires knowledge of the entire temperature profile of the atmosphere. This meteorological variation must be corrected to study CR variations originating outside the atmosphere.

For ground (and underground)-based CR detectors, the response function, i.e., the relation between particles of GCR spectra at the top of the atmosphere and recorded secondary particles at the surface level, should be accurately known. The total detector count rate can be expressed as follows (Caballero-Lopez and Moraal, 2012):

$$\begin{aligned} N(R_0, h, t) &= \sum_i \int_{R_0}^{\infty} (S_i(R, h) j_i(R, t)) dR \\ &= \int_{R_0}^{\infty} W(R, h, t) dR \end{aligned} \quad (1)$$

where  $N(R_0, h, t)$  is the detector counting rate,  $R_0$  is the geomagnetic cutoff rigidity,  $h$  is the atmospheric depth, and  $t$  represents time.  $S_i(R, h)$  represents the detector yield



function for primary particles of type  $i$  and  $j_i(R, t)$  represents the primary particle rigidity spectrum of type  $i$  at time  $t$ . The total response function  $W(R, h, t)$  is the sum of  $S_i(R, h)$  and  $j_i(R, t)$ . The maximum value of this function is in the range of 4–7 GV at sea level, depending on the solar modulation epoch at time  $t$  (Clem and Dorman, 2000). One of the methods to find this response function is to use the numerical simulation of propagation of CRs through the atmosphere. CORSIKA simulation package (Heck et al., 1998) was to simulate CR transport through the atmosphere and GEANT4 (Agostinelli et al., 2003) to simulate the propagation of secondary CRs through overburden and response of the detectors to find the relationship between the count rate at our site and the flux of primary particles on top of the atmosphere.

The excellent agreement of the simulated and measured flux (Fig. 2) allows us to establish that the cutoff energy for primary CR protons for showers detected in GLL is caused by its geomagnetic rigidity, and the median energy is  $\sim 60$  GeV. For UL, the cutoff energy due to earth overburden is 12 GeV, and the median energy is  $\sim 120$  GeV. These values give us opportunity to study solar modulation at energies exceeding energies detected with a NM. Observation of the solar activity and related magnetic disturbances in the heliosphere that create transient CR intensity variation at several different energies can provide an energy-dependent description of these phenomena.

### 3. Data analysis

The new setup in the LBLNP, presented by Dragić et al. (2011) coincides with the start of the 24th solar cycle, thus allowing us to observe the increase and decrease in solar activity and the effect of solar modulation at energies higher than ones studied using NMs.

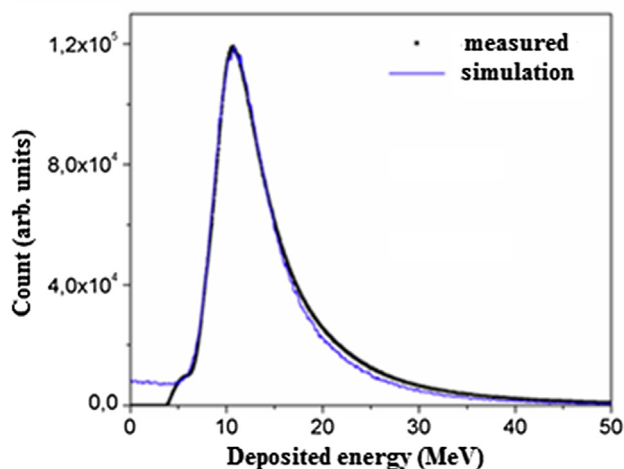


Fig. 2. Simulated (blue line) and measured spectra (black line) for muon detectors in UL. (For interpretation of the references to colour in this figure legend, the reader is referred to the web version of this article.)

Muon time series was searched for days where the average muon flux was significantly lower than the background level. The background level is determined from the moving averages of hourly count rates 10 days before the event. These decreases in the count rate, in GLL and UL, are then compared with space weather events of solar cycle 24. Data collected in UG and GLL are compared with four NM stations from the neutron monitor database [<http://www.nmdb.eu/>]. Three of these NMs (Athens, Rome, and Jungfraujoch) have cutoff rigidity and geographic proximity similar to the Belgrade CR station.

A high correlation is found between the count rates measured by the NMs in the LBLNP in March 2012 (Table 1), but for GLL and UL, as the cutoff energy of the primary flux increases, the correlation slightly decreases.

#### 3.1. Selected Forbush decreases

The Belgrade CR station has detected, both in GLL and UL, several significant structures connected to some extreme solar effects. Several, more prominent, Forbush decreases occurred in March 2012, September 2014, June 2015, and most recently in September 2017.

The FD that occurred on March 8, 2012 was recorded at the Belgrade CR station as well as at other stations (Fig. 3). This FD was separated into two following two CMEs. These CMEs produced an intense disturbance in the interplanetary space and caused a severe geomagnetic storm when the shockwave reached Earth on March 8, 2012. During this event, a very complex combination of modulation occurs (Lingri et al., 2016). Two CMEs from the same active region as the September 10 (X1.6) flare produced FD on September 12, 2014. There was a relatively fast partial halo CME and a larger and rapidly moving halo CME trailing behind the first one on September 10. These two gave rise to the FD that was first detected by NMs on September 12, 2014. This FD was not a classical two-step FD as expected, probably due to the interaction of slower and faster CMEs. The FD profile (Fig. 3) showed a small second step several hours after the first, similar to the FD that occurred in February 2011 (Papaioannou et al., 2013). In June 2015, a large activity occurred in the Sun from powerful AR 2371 that produced several CMEs from the Sun. These CMEs induced a complex modulation of GCRs that led to an FD occurrence on June 22, 2015 with an unusual structure (Samara et al., 2018).

A sudden burst of activity from the Sun early in September 2017, after a prolonged period of low solar activity, produced several flares, including the largest solar flare seen from Earth since 2006, an X9.3 flare. This activity produced several Earth-directed CMEs. Throughout this time, Earth experienced a series of geomagnetic storms, which started promptly after the first CME. This unusual activity produced an FD, which was recorded with detectors in terms of ground level enhancement (GLE) on Earth and Mars (Guo et al., 2018).

Table 1

Correlation matrix of the linear correlation coefficient (in%) for recorded hourly flux at the Belgrade CR station with its temperature- and pressure-corrected underground and ground-level detectors (UL\_tpc and GLL\_tpc), only pressure-corrected detectors (UL\_pc, GLL\_pc), and raw data detectors (UL\_raw and GLL\_raw) and recordings at Rome, Oulu, Jungfraujoch (Jung.) and Athens NMs for March 2012.

UL_tpc	75	81	80	81	76	73	78	86	97	100
UL_pc	77	83	83	83	73	78	72	84	100	97
UL_raw	57	71	70	74	94	49	51	100	84	86
GLL_tpc	86	86	84	83	59	90	100	51	72	78
GLL_pc	90	92	90	89	56	100	90	49	78	73
GLL_raw	63	79	78	81	100	56	59	94	73	76
Oulu	90	98	98	100	81	89	83	74	83	81
Jung.	91	98	100	98	78	92	84	70	83	80
Rome	91	100	98	98	79	92	86	71	83	81
Athens	100	91	91	90	63	90	86	57	77	75
	Athens	Rome	Jung.	Oulu	GLL_raw	GLL_pc	GLL_tpc	UL_raw	UL_pc	UL_tpc

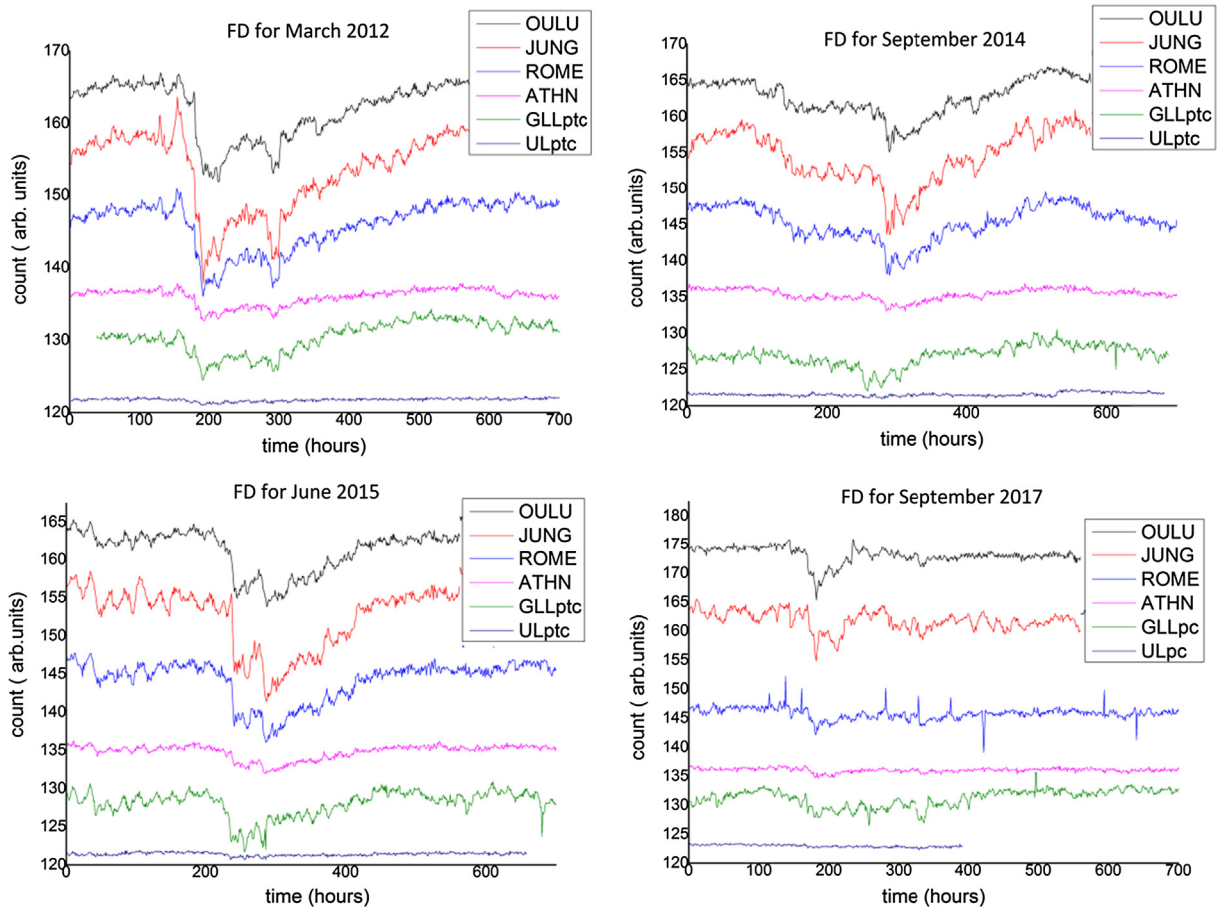


Fig. 3. Comparison of hourly time series over a one month period for pressure- and temperature-corrected count rates of the Belgrade muon monitor station (GLL<sub>ptc</sub> and UL<sub>ptc</sub>) and NMs at Athens (ATHN), Rome (ROME), Jungfraujoch (JUNG), and Oulu (OULU) for extreme solar events in March 2012, September 2014, and June 2015. Count rates are shifted for comparison. For extreme solar event in September 2017, for GLL and UL, the count rate is pressure-corrected only.

#### 4. FD and median rigidity

For each event, we study the energy dependence of FD amplitude. The energy dependence of FD amplitude is

expected to follow the power law:  $\Delta N/N \sim R^{-\gamma}$  (Cane, 2000). To obtain reliable values of amplitudes, we defined amplitude as a relative decrease in the hourly count rate of the minimum compared with the average of seven days'

Table 2  
Median and cutoff rigidity for several stations.

Stations	Median rigidity $R_m$ (GV)	Min. rigidity $R_0$ (GV)
Athens	25.1	8.53
Mexico	25.1	8.28
Almaty	15.8	6.69
Lomnický štít	12.6	3.84
Moscow	15.8	2.43
Kiel	15.8	2.36
Yakutsk	12.6	1.65
Apatity	12.6	0.65
Inuvik	12.6	0.3
Mc Murdo	12.6	0.3
Thule	12.6	0,3
South Pole	10	0.1
UL	122	12.3
GLL	63	5.3

count rate before FDs (not including possible precursory increases). Such a long base period was used because of the higher activity of the Sun prior to registered FDs and sensitivity of the muon detectors.

Amplitudes are determined for two of our detectors and for 12 NMs. To investigate the rigidity spectrum of

Table 3

Power indices of the median rigidity dependence of the dip of the FD. Power indices are obtained for NMs only, NMs and the Belgrade muon station, and Belgrade station only.

$\gamma$	NM only	NM + Belgrade	Belgrade station only
March 2012	$0.82 \pm 0.08$	$0.78 \pm 0.03$	0.715
Sept. 2014	$0.79 \pm 0.16$	$0.67 \pm 0.06$	0.744
June 2015	$0.57 \pm 0.05$	$0.58 \pm 0.02$	0.764
Sept. 2017	$1.27 \pm 0.16$	$0.86 \pm 0.07$	0.739

mentioned FDs, the median rigidity  $R_m$  is defined.  $R_m$  is the rigidity of the response of the detector to GCR spectrum where 50% of the detector counting rate lies below  $R_m$  (Ahluwalia and Fikani, 2007). For this study, we used a list of  $R_m$  for 12 NM stations given by Minamino et al. (2014). For an NM, the median rigidity can be computed from the detector response function derived from surveys for particulate station, usually around the minima of solar activity; this is because the intensity of lowest rigidity GCRs is maximum at that time.

For the Belgrade muon station,  $R_m$  was found using the response function acquired by the Monte Carlo method of

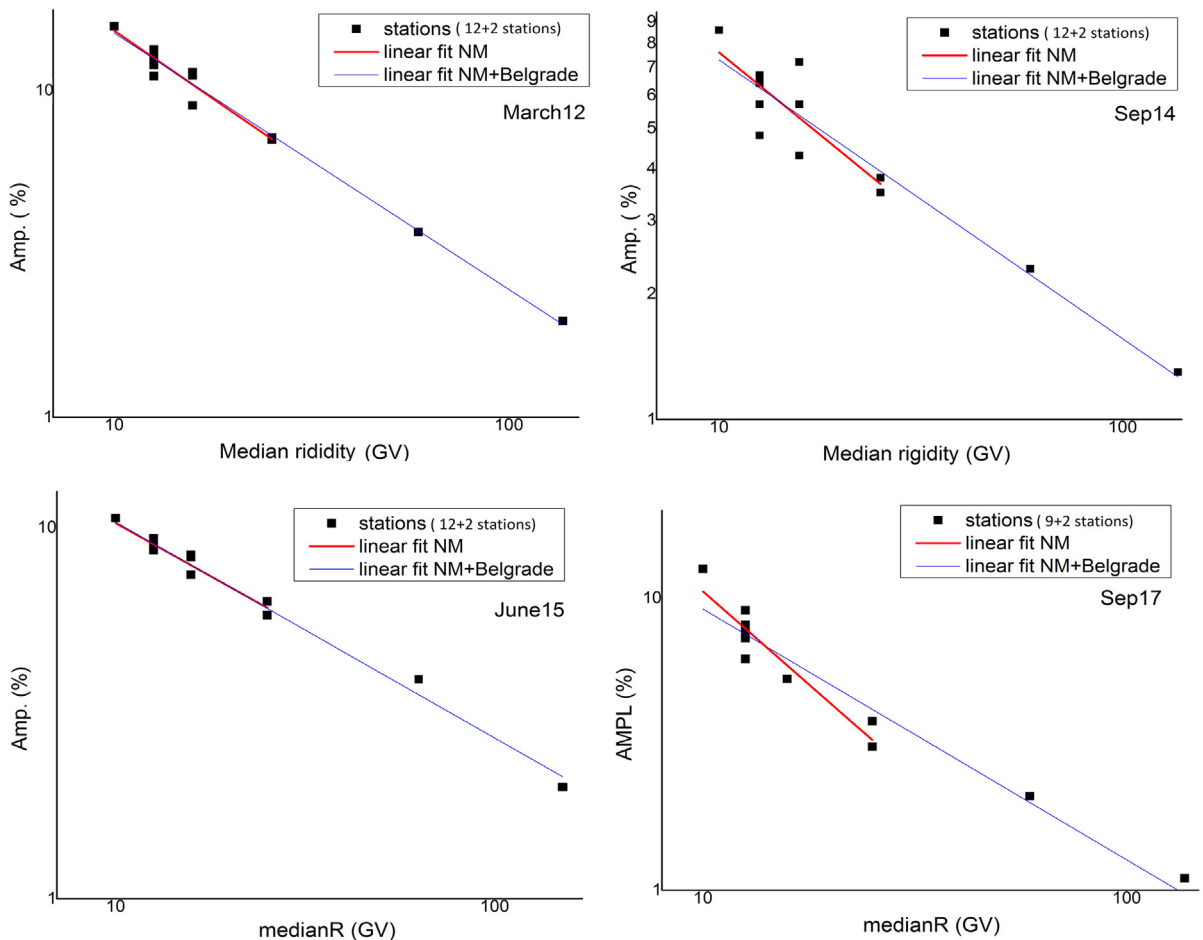


Fig. 4. Rigidity spectrum of FD from March 8, 2012, September 12, 2014, June 22, 2015, and September 8, 2017. Points represent the amplitude of the event as seen by NMs and the Belgrade CR station.

CR transport. Approximate values of  $R_m$  for the detectors used in this study are provided in Table 2.

For every selected event, a scatter plot is drawn (Fig. 4). All plots show, plotted in log-log scale, a clear median rigidity dependence of the amplitude of FD decrease.

Linear regression was performed to find power indices corresponding to each event. Power indices are given in Table 3.

Higher power indices can be due to more complex variations in GCRs. This more complex variation is a result of a series of CMEs during this event that leads to large compound ICME structure with multiple shocks and transient flow (Zhao and Zhang, 2016). Results obtained from the power law are generally consistent with those obtained in previous studies (Ahluwalia and Fikani, 2007, Lingri et al., 2016, Klyueva et al., 2017) conducted for NMs only.

A more significant difference observed for indices during the 2017 event was because we used only pressure-corrected data for the muon flux recorded at the Belgrade station. For all other events and data, we performed both pressure and temperature correction. Without temperature corrections, variation in the count rate in muon detectors is higher and it can affect the results.

We expect that when the newly improved, internally developed technique for temperature correction of the CR flux is implemented, the amplitude of the FD measured at the Belgrade muon station will be more consistent with other events and measurements. More data points on the graphs are needed to understand indices better, particularly in an energy region between NM and our laboratory. Similar work (Braun et al., 2009) discussed the extension up to 15 and 33 GeV, but there are no data available for FDs during cycle 24 and cannot be incorporated into this work. As for other operating muon telescopes, there is an agreement between the data obtained at our stations data and the URAGAN data for FD in June 2015 (Barbashina et al., 2016), but we have no data on other FDs and/or median energies of other stations. Our new experimental setup described elsewhere (Veselinović et al. 2017) will provide two additional median energies (121 and 157 GeV) to monitor variations in the CR flux.

## 5. Conclusion

The Belgrade CR station, with both ground level and underground setups, monitors the effect of solar modulation on the CR flux since 2008. Extreme solar events, like Forbush decreases, were detected during solar cycle 24 at the site, suggesting that these phenomena can be studied at energies higher than typical ones detected with NMs. GLL and UL data, as well as data from several NM stations, were used to analyze four intense FDs. The magnitude of FDs is energy (rigidity) dependent and follows the power law. Data used to find the rigidity dependence of these transient solar modulation of GCR were obtained over much higher range of rigidities than region NMs are

sensitive in, thus allowing more extensive studies of CR solar modulation processes.

## Acknowledgements

We acknowledge the NMDB ([www.nmdb.eu](http://www.nmdb.eu)), founded under the European Union's FP7 programme (contract no. 213007), for providing data. We acknowledge individual monitors for following the information given on the respective station information page. *Athens NM data were kindly provided by the Physics Department of the National and Kapodistrian University of Athens. Jungfrauoch NM data were kindly provided by the Physikalisches Institut, University of Bern, Switzerland. Oulu NM data were kindly provided by <http://cosmicrays oulu.fi> and Sodankylä Geophysical Observatory. Rome NM data were kindly provided by SVIRCO NM, supported by INAF/IAPS-UNIRoma3 COLLABORATION.* We thank the anonymous referees for useful advices.

The present work was funded by the Ministry of Education, Science and Technological Development of the Republic of Serbia, under Project No. 171002.

## References

- Agostinelli, S., et al., GEANT4—A Simulation Toolkit, 2003. Nuclear Instruments and Methods in Physics Research Section A 506, pp. 250–303. [https://doi.org/10.1016/S0168-9002\(03\)01368-8](https://doi.org/10.1016/S0168-9002(03)01368-8).
- Ahluwalia, H.S., 2005. Cycle 20 solar wind modulation of galactic cosmic rays: understanding the challenge. *J. Geophys. Res.* 110, A10106. <https://doi.org/10.1029/2005JA011106>.
- Ahluwalia, H.S., Fikani, M.M., 2007. Cosmic ray detector response to transient solar modulation: Forbush decreases. *J. Geophys. Res.* 112 (A8), A08105. <https://doi.org/10.1029/2006JA011958>.
- Barbashina, N.S., Ampilogov, N.V., Astapov, I.I., Borog, V.V., Dmitrieva, A.N., Petrukhin, A.A., Sitko, O.A., Shutenko, V.V., Yakovleva, E.I., 2016. Characteristics of the Forbush decrease of 22 June 2015 measured by means of the muon hodoscope URAGAN. *J. Phys.: Conf. Ser.* 675 (3). <https://doi.org/10.1088/1742-6596/675/3/032038>, article id. 032038.
- Belov, A.V., 2008. Forbush effects and their connection with solar, interplanetary and geomagnetic phenomena. In: *Proceedings of the International Astronomical Union 4.S257*, pp. 439–450. <https://doi.org/10.1017/S1743921309029676>.
- Braun, I., Engler, J., Hörandela, J.R., Milke, J., 2009. Forbush decreases and solar events seen in the 10–20 GeV energy range by the Karlsruhe Muon Telescope. *Adv. Space Res.* 43 (4), 480–488. <https://doi.org/10.1016/j.asr.2008.07.012>.
- Caballero-Lopez, R.A., Moraal, H., 2012. Cosmic-ray yield and response functions in the atmosphere. *J. Geophys. Res. Space Phys.* 117 (A12), 7461–7469. <https://doi.org/10.1029/2012JA017794>.
- Cane, H.V., 2000. Coronal mass ejections and Forbush decreases. *Space Sci. Rev.* 93 (1–2), 55–77. <https://doi.org/10.1023/1026532125747>.
- Chauhan, M.L., Jain Manjula, S.K., Shrivastava, S.K., 2008. Study of two major Forbush decrease events of 2005. In: *Proceedings of the 30th International Cosmic Ray Conference*, Mexico City, vol. 1 (SH), pp. 307–310. <https://doi.org/10.7529/ICRC2011/V10/0097>.
- Clem, J.M., Dorman, L.I., 2000. Neutron monitor response functions, cosmic rays and earth. *Space Sci. Rev.* 93 (1/2), 335–359. <https://doi.org/10.1023/A:1026515722112>.
- Dragić, A., Udovičić, V., Banjanac, R., Joković, D., Maletić, D., Veselinović, N., Savić, M., Puzović, J., Aničin, I.V., 2011. The new setup in the Belgrade low-level and cosmic-ray laboratory. *Nucl.*

- Technol. Radiat. Protect. 26 (3), 181–192. <https://doi.org/10.2298/NTRP1101064N>.
- Duldig, M.L., 2000. Muon observations. In: Bieber, J.W., Eroshenko, E., Evenson, P., Flückiger, E.O., Kallenbach, R. (Eds.), *Cosmic Rays and Earth*. Space Sciences Series of ISSI. Springer, Dordrecht, pp. 207–226. [https://doi.org/10.1007/978-94-017-1187-6\\_1](https://doi.org/10.1007/978-94-017-1187-6_1).
- Forbush, S.E., 1954. World-wide cosmic ray variations, 1937–1952. *J. Geophys. Res.* 59 (4), 525–542. <https://doi.org/10.1029/JZ059i004p00525>.
- Guo, J., Dumbović, M., Wimmer-Schweingruber, R.F., Temmer, M., Lohf, H., Wang, Y., Veronig, A., Hassler, D.M., Leila, M., Mays, L. M., Zeitlin, C., Ehresmann, B., Witasse, O., Freiherr von Forstner, J. L., Heber, B., Holmström, M., Posner, A., 2018. Modeling the evolution and propagation of the 2017 September 9th and 10th CMEs and SEPs arriving at Mars constrained by remote-sensing and in-situ measurement. Also Available at: arXiv preprint arXiv:1803.00461.
- Heck, D., Knapp, J., Capdevielle, J.N., Schatz, G., Thouw, T., 1998. *CORSIKA: a Monte Carlo code to simulate extensive air showers*. Forschungszentrum Karlsruhe GmbH, p. V +90, TIB Hannover, D-30167 Hannover.
- Klyueva, A.I., Belov, A.V., Eroshenko, E.A., 2017. Specific features of the rigidity spectrum of Forbush effects. *Geomag. Aeron.* 57 (2), 177–189. <https://doi.org/10.1134/S0016793217020050>.
- Lingri, D., Mavromichalaki, H., Belov, A., Eroshenko, E., Yanke, V., Abunin, A., Abunina, M., 2016. Solar activity parameters and associated Forbush decreases during the minimum between cycles 23 and 24 and the ascending phase of cycle 24. *Sol. Phys.* 291 (3), 1025–1041. <https://doi.org/10.1007/s11207-016-0863-8>.
- Minamino, Mohanty, Morishita, et al. for the GRAPES-3 Collaboration, 2014. Rigidity Dependence of Forbush Decreases, Poster #654. In: *Proceedings of the 33rd International Cosmic Ray Conference*, Rio de Janeiro, Brazil, pp. 3612–3615.
- Papailiou, M., Mavromichalaki, H., Abunina, M., Belov, A., Eroshenko, E., Yanke, V., Kryakunova, O., 2013. Forbush decreases associated with western solar sources and geomagnetic storms: a study on precursors. *Sol. Phys.* 283 (2), 557–563. <https://doi.org/10.1007/s11207-013-0231-x>.
- Papaioannou, A., Belov, A.A., Mavromichalaki, H., Eroshenko, E., Yanke, V., Asvestari, E., Abunin, A., Abunina, M., 2013. The first Forbush decrease of solar cycle 24. *J. Phys. Conf. Ser.* 409 (1). <https://doi.org/10.1088/1742-6596/409/1/012202>.
- Samara, E., Smpontias, I.A., Lytrosyngounis, I., Lingri, D., Mavromichalaki, H., Sgouropoulos, C., 2018. Unusual cosmic ray variations during the Forbush decreases of June 2015. *Sol. Phys.* 293 (67). <https://doi.org/10.1007/S11207-018-1290-9>.
- Savić, M., Maletić, D., Joković, D., Veselinović, N., Banjanac, R., Udovičić, V., Dragić, V., 2015. Pressure and temperature effect corrections of atmospheric muon data in the Belgrade cosmic-ray station. *J. Phys. Conf. Ser.* 632 (1). <https://doi.org/10.1088/1742-6596/632/1/012059>, article id. 012059.
- Veselinović, N., Dragić, A., Savić, M., Maletić, D., Joković, D., Banjanac, R., Udovičić, V., 2017. An underground laboratory as a facility for studies of cosmic-ray solar modulation. *Nucl. Instrum. Meth.* A875, 10–15. <https://doi.org/10.1016/j.nima.2017.09.008>.
- Zhao, L.-L., Zhang, H., 2016. Transient galactic cosmic-ray modulation during solar cycle 24: a comparative study of two prominent forbush decrease events. *Astrophys. J.* 827 (1). <https://doi.org/10.3847/0004-637X>.



# An underground laboratory as a facility for studies of cosmic-ray solar modulation



N. Veselinović, A. Dragić\*, M. Savić, D. Maletić, D. Joković, R. Banjanac, V. Udovičić

*Institute of Physics, University of Belgrade, Pregrevica 118, 11080 Zemun, Serbia*

## ARTICLE INFO

### Keywords:

Cosmic ray muons  
Forbush decrease  
Response function

## ABSTRACT

The possibility of utilizing a shallow underground laboratory for the study of energy dependent solar modulation process is investigated. The laboratory is equipped with muon detectors at ground level and underground (25mwe), and with an underground asymmetric muon telescope to have a single site detection system sensitive to different median energies of primary cosmic-ray particles. The detector response functions to galactic cosmic rays are determined from Monte Carlo simulation of muon generation and propagation through the atmosphere and soil, based on CORSIKA and GEANT4 simulation packages. The present setup is suitable for studies of energy dependence of Forbush decreases and other transient or quasi-periodic cosmic-ray variations.

© 2017 Elsevier B.V. All rights reserved.

## 1. Introduction

Galactic cosmic rays (GCR) arriving at Earth after propagating through the heliosphere interact with nuclei in the atmosphere. These interactions of primary CRs lead to production of a cascade (shower) of secondary particles: hadrons, electrons, photons, muons, neutrinos. Ground based CR detectors are designed to detect some species of secondary cosmic radiation. Widely in use are neutron monitors [1,2], muon telescopes [3,4], various types of air shower arrays [5],  $\gamma$ -ray air Cherenkov detectors [6], air fluorescence detectors [7] etc.

The flux and energy spectra of GCR are modulated by the solar magnetic field, convected by the solar wind. Particularly affected are GCR at the low energy side of the spectrum (up to  $\sim 100$  GeV). Therefore, secondary CRs generated in the atmosphere can be used for studying solar and heliospheric processes. Among the best known effects of the solar modulation are CR flux variations with 11 year period of the solar cycle, 22 year magnetic cycle, diurnal variation and Forbush decrease. The so called corotation with the solar magnetic field results in the flux variation with the 27-day period of solar rotation.

Modulation effects have been studied extensively by neutron monitors (NM) [8,9], sensitive up to several tens of GeV, depending on their geomagnetic location and atmospheric depth. Muon detectors at ground level are sensitive to primary particles of higher energies than NMs. Underground muon detectors correspond to even higher energy primaries. For this reason muon observations complement NM observations in studies of long-term CR variations, CR anisotropy and gradients

or rigidity spectrum of Forbush decreases. However, muon observations suffer from difficulties to disentangle variations of atmospheric origin. While the effect of atmospheric pressure is similar to NMs and easy to account for, the temperature effect is more complicated. The entire temperature profile of the atmosphere is contributing, with different net temperature effect on muon flux at different atmospheric layers, as a result of interplay of positive and negative temperature effects. The positive temperature effect is a consequence of reduced atmospheric density with the temperature increase, resulting in less pion interactions and more decays into muons [10]. The negative temperature effect comes from the increased altitude of muon production at the periods of high temperature, with the longer muon path length and the higher decay probability before reaching the ground level [11]. Both effects are accounted for by the integral method of Dorman [12]. The negative temperature effect is dominant for low energy muons (detected at ground level) and the positive for high energy muons (detected deep underground). At shallow depth of several tens of meters of water equivalent both temperature effects contribute to the overall temperature effect. Several detector systems with different sensitivity to primaries at the same location have the advantage of sharing common atmospheric and geomagnetic conditions.

Belgrade CR station is equipped with muon detectors at ground level and at the depth of 25 m.w.e. Underground laboratory is reached only by muons exceeding energy threshold of 12 GeV. The existing detectors are recently amended by additional setup in an attempt to fully exploit laboratory's possibilities to study solar modulation at different

\* Corresponding author.

E-mail address: [dragic@ipb.ac.rs](mailto:dragic@ipb.ac.rs) (A. Dragić).

median rigidities. In the present paper the detector systems at the Belgrade CR station are described. Response functions of muon detectors to galactic cosmic rays are calculated. The detector system represents useful extension of modulation studies with neutron monitors to higher energies, as it is demonstrated in the case of a recent Forbush event.

## 2. Description of Belgrade CR station

The Belgrade cosmic-ray station, situated at the Low Background Laboratory for Nuclear Physics at Institute of Physics, is located at near-sea level at the altitude of 78 m a.s.l. Its geographic position is: latitude 44°51'N and longitude 20°23'E, with vertical cut-off rigidity 5.3 GV. It consists of the ground level lab (GLL) and the underground lab (UL) which has useful area of 45 m<sup>2</sup>, dug at a depth of 12 m. The soil overburden consists of loess with an average density  $2.0 \pm 0.1$  g/cm<sup>3</sup>. Together with the 30 cm layer of reinforced concrete the laboratory depth is equivalent to 25 m.w.e. At this depth, practically only the muonic component of the atmospheric shower is present [13].

### 2.1. Old setup

The experimental setup [14] consists of two identical sets of detectors and read out electronics, one situated in the GLL and the other in the UL. Each setup utilizes a plastic scintillation detector with dimensions 100 cm × 100 cm × 5 cm equipped with 4 PMTs optically attached to beveled corners of a detector. Preamplifier output of two diagonally opposing PMTs are summed and fed to a digitizer input (CAEN FADC, type N1728B). FADC operates at 100 MHz frequency with 14 bit resolution. The events generating enough scintillation light to produce simultaneous signals in both inputs exceeding the given threshold are identified as muon events. The simulated total energy deposit spectrum is presented on the left panel of Fig. 1. After the appropriate threshold conditions are imposed on the signals from two diagonals, the spectrum is reduced to the one represented on the right panel of the same figure. Contribution from different CR components are indicated on both graphs and experimentally recorded spectrum is plotted as well.

Particle identification is verified by a two-step Monte Carlo simulation. In the first step development of CR showers in the atmosphere is traced, starting from the primary particles at the top of the atmosphere by CORSIKA simulation package. CORSIKA output contains information on generated particles (muons, electrons, photons, etc.) and their momenta at given observation level. More details on CORSIKA simulation will be given in Section 3. This output serves as an input for the second step in simulation, based on GEANT4. In the later step energy deposit by CR particles in the plastic scintillator detector are determined, together with the light collection at PMTs. Contributions from different CR components to recorded spectrum are also shown in Fig. 1.

According to the simulation, 87.5% of events in the coincident spectrum originate from muons. To account for the contribution from other particles to the experimental spectrum not all the events in the spectrum are counted when muon time series are constructed. Muon events are defined by setting the threshold corresponding to muon fraction of recorded spectrum. Threshold is set in terms of “constant fraction” of the spectrum maximum, which also reduces count rate fluctuations due to inevitable shifts of the spectrum during long-term measurements.

### 2.2. Upgrade of the detector system

Existing detectors enable monitoring of CR variations at two different median energies. An update is contemplated that would provide more differentiated response. Two ideas are considered. First one was to extend the sensitivity to higher energies with detection of multi-muon events underground. An array of horizontally oriented muon detectors ought to be placed in the UL. Simultaneous triggering of more than

one detector is an indication of a multi-muon event. The idea was exploited in the EMMA underground array [15], located at the deeper underground laboratory in Pyhasalmi mine, Finland, with the intention to reach energies in the so called knee region. For a shallow underground laboratory, exceeding the energy region of solar modulation would open the possibility to study CR flux variations originating outside the heliosphere. Second idea is an asymmetric muon telescope separating muons with respect to zenith angle. Later idea is much less expensive to be put into practice.

Both ideas will be explained in detail and response function to GCR for existing and contemplated detectors calculated in the next section.

## 3. Calculation of response functions

Nature of variations of primary cosmic radiation can be deduced from the record of ground based cosmic ray detectors provided relation between the spectra of primary and secondary particles at surface level are known with sufficient accuracy. Relation can be expressed in terms of rigidity or kinetic energy.

Total detector count rate can be expressed as:

$$N(E_{th}, h, t) = \sum_i \int_{E_{th}}^{\infty} Y_i(E, h) \cdot J_i(E, t) dE \quad (1)$$

where  $E$  is primary particle energy,  $i$  is type of primary particle (we take into account protons and  $\alpha$  particles),  $J_i(E, t)$  is energy spectrum of primary particles,  $h$  is atmospheric depth and  $Y_i(E, h)$  is the so called yield function.  $E_{th}$  is the threshold energy of primary particles. It depends on location (geomagnetic latitude and atmospheric altitude) and detector construction details. At a given location on Earth, only particles with rigidity above vertical rigidity cut-off contribute to the count rate. Also, detector construction often prevents detection of low energy particles. For instance, muon detectors are sometimes covered with a layer of lead. In present configuration our detectors are lead free.

Historically, yield functions were calculated empirically, often exploiting the latitude variations of neutron and muonic CR component [16–18]. With the advancement of computing power and modern transport simulation codes it became possible to calculate yield functions from the interaction processes in the atmosphere [19,20]. The yield function for muons is calculated as:

$$Y_i(E, h) = \int_{E_{th}}^{\infty} \int S(\theta, \phi) \cdot \Phi_{i,\mu}(E_i, h, E, \theta, \phi) dE d\Omega \quad (2)$$

where  $S(\theta, \phi)$  is the effective detector area and integration is performed over upper hemisphere.  $\Phi_{i,\mu}(E_i, h, E, \theta, \phi)$  is the differential muon flux per primary particle of the type  $i$  with the energy  $E_i$ .

Total differential response function:

$$W(E, h, t) = \sum_i Y_i(E, h) \cdot J_i(E, t) \quad (3)$$

when normalized to the total count rate gives the fraction of count rate originating from the primary particles with the energy in the infinitesimal interval around  $E$ . Integration of differential response function gives the cumulative response function.

The response functions of our CR detectors are calculated using Monte Carlo simulation of CR transport through the atmosphere with CORSIKA simulation package. Simulation was performed with protons and  $\alpha$ -particles as primary particles. They make ~94% (79% + 14.7%) of all primaries [21]. Implemented hadron interaction models were FLUKA for energies below 80 GeV, and QGSJET II-04 for higher energies. If the old version of QGSJET is used, a small discontinuity in response function is noticed at the boundary energy between two models. Geomagnetic field corresponds to the location of Belgrade  $B_x = 22.61$   $\mu$ T,  $B_z = 42.27$   $\mu$ T. Power law form of differential energy spectrum of galactic cosmic rays  $J_p(E) \sim E^{-2.7}$  is assumed. Energy range of primary particles is between 1 GeV and  $2 \cdot 10^7$  GeV. Interval of zenith angles is  $0^\circ < \theta < 70^\circ$ . Low energy thresholds for secondary particles are: 150 MeV for hadrons and muons and 15 MeV for electrons

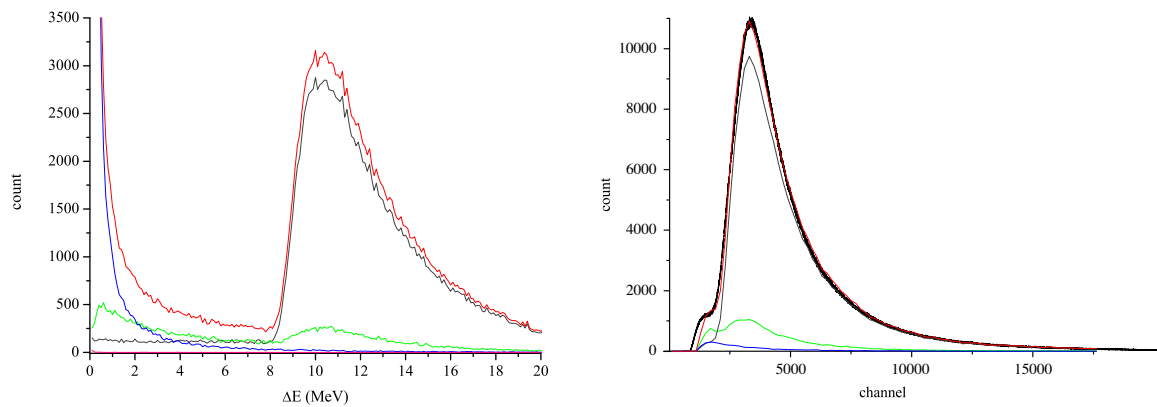


**Fig. 1.** Left —  $\Delta E$  spectrum in the plastic scintillator detector, derived from GEANT simulation; right — the same, but for the events exceeding threshold on both diagonals. Contribution of different CR components to the total energy deposit in the detector: muons—gray line, photons—blue line, electrons—green line and sum of all contributions — red line. The black curve on the right panel is the experimental spectrum. (For interpretation of the references to color in this figure legend, the reader is referred to the web version of this article.)

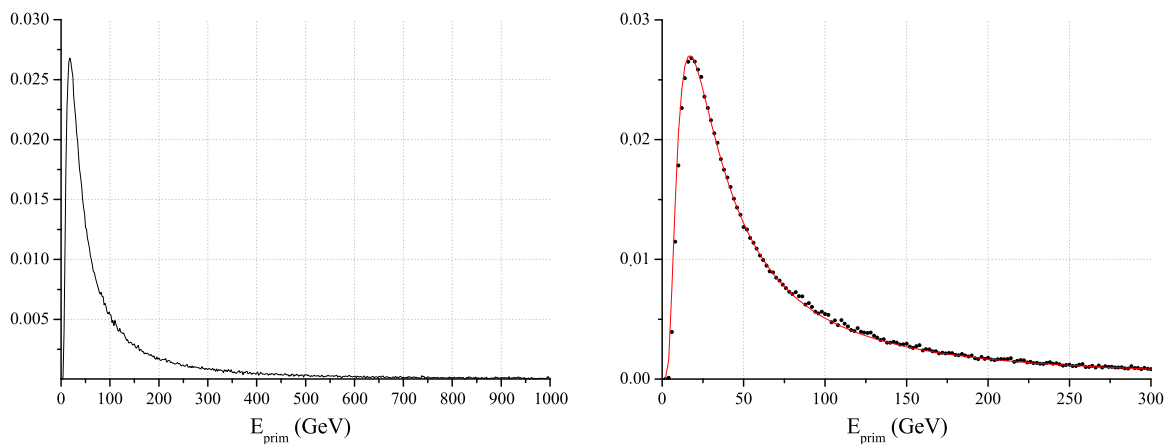


**Fig. 2.** Left: normalized total response function of ground level muon detector to galactic cosmic rays; right: same as left, fitted with Dorman function (red line). (For interpretation of the references to color in this figure legend, the reader is referred to the web version of this article.)

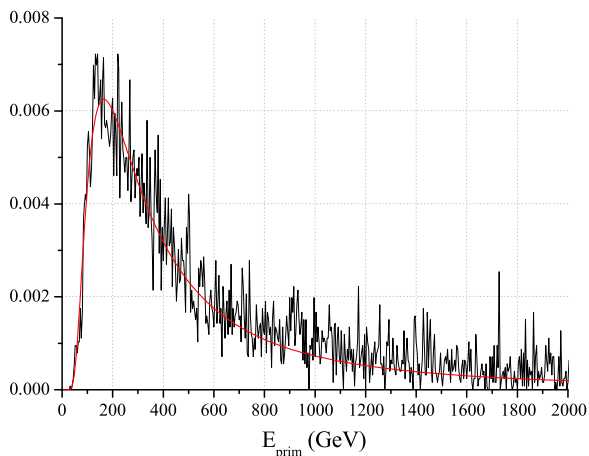


**Fig. 3.** Response function for multi-muon events in UL to galactic cosmic rays.

and photons. Selected atmospheric model is AT511 (Central European atmosphere for May 11 1993). Observational level is at 78m a.s.l.

For calculation of response functions for underground detectors, simulation of particle propagation through the soil overburden is performed using the code based on GEANT4 package. For precise calculation of energy loss, chemical composition of the soil needs to be known. The

composition used in our work is taken from a geochemical study of neighboring loess sections of Batajnica and Stari Slankamen [22]. Most abundant constituents are quartz ( $\text{SiO}_2$ ) 70%, alumina ( $\text{Al}_2\text{O}_3$ ) 15% and quicklime ( $\text{CaO}$ ) 10%, while others include  $\text{Fe}_2\text{O}_3$ ,  $\text{MgO}$ ,  $\text{TiO}_2$ ,  $\text{K}_2\text{O}$ ,... Inaccuracy of our knowledge of the soil chemical composition should not strongly affect our results since, at relevant energies, dominant energy loss mechanism for muons is ionization which, according to Bethe–Bloch formula depends mostly on  $\langle Z \rangle / \langle A \rangle$ . Soil density profile is probed during laboratory construction. It varies slowly with depth and average density is found to be  $(2.0 \pm 0.1) \text{ g/cm}^3$ .

In the simulation, the effective area and angular acceptance of different modes of asymmetric muon telescope (single, coincident and anticoincident) are taken into account.

According to Dorman [12], response function can be parametrized as:

$$W(E) = \begin{cases} 0, & \text{if } E < E_{th}; \\ a \cdot k \cdot \exp(-aE^{-k}), & \text{otherwise;} \\ \frac{a \cdot k \cdot \exp(-aE^{-k})}{E^{(k+1)}(1 - aE_{th}^{-k})}, & \end{cases} \quad (4)$$

with the high energy asymptotics:  $W(E) \approx a \cdot k \cdot E^{-(k+1)}$ .

### 3.1. Ground level

Calculated response function for ground level muon detector is presented on Fig. 2, together with fitted Dorman function (4).



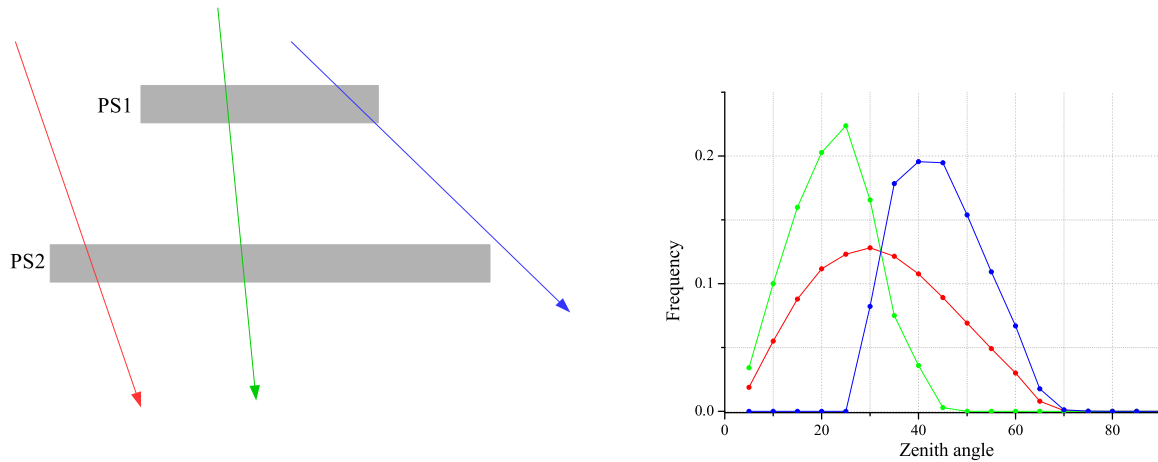


Fig. 4. Left: Schematic view of the asymmetric muon telescope; PS1 — plastic scintillator detector 1, PS2 — plastic scintillator detector 2. Right: angular distribution of detected muons in single mode (red), coincident mode (green) and anticoincident mode (blue), normalized to number of counts in each mode. (For interpretation of the references to color in this figure legend, the reader is referred to the web version of this article.)

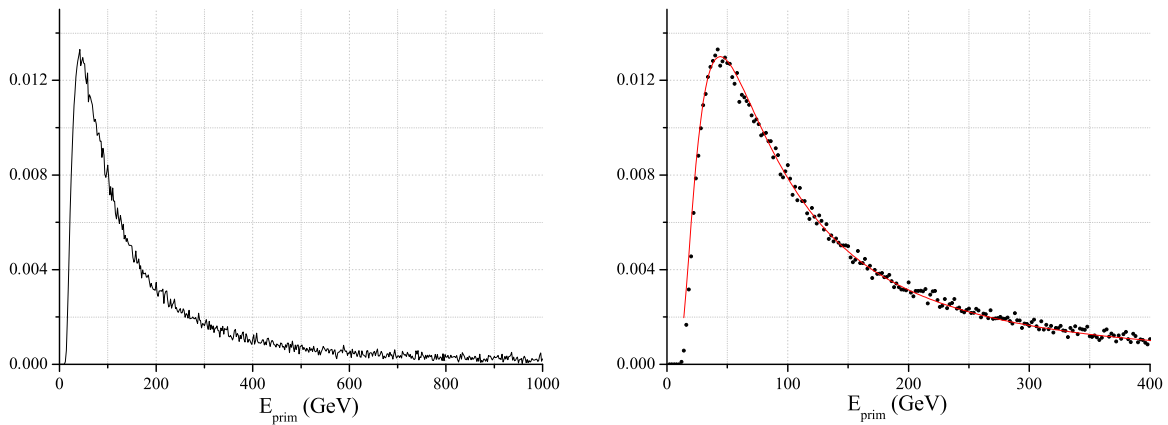


Fig. 5. Response function of single mode of ASYMUT in the UL to galactic cosmic rays. On the right panel the energy interval of interest is enlarged and Dorman function fit is plotted (red line). (For interpretation of the references to color in this figure legend, the reader is referred to the web version of this article.)

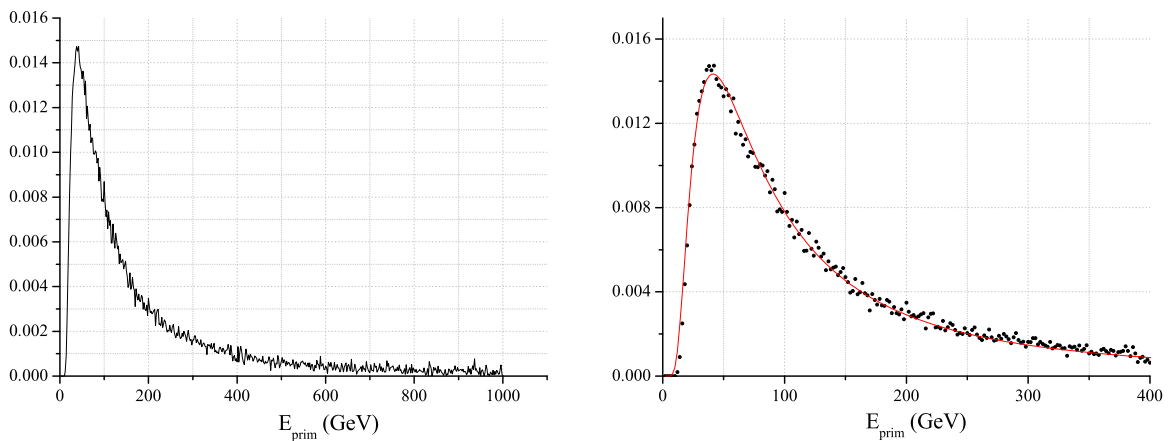


Fig. 6. Response function of coincident mode of asymmetric muon telescope in the UL to galactic cosmic rays. On the right panel the interesting energy interval is enlarged and Dorman function fit is plotted (red line). (For interpretation of the references to color in this figure legend, the reader is referred to the web version of this article.)

### 3.2. Underground

#### 3.2.1. Multi-muon events

Count rate of multi-muon events underground turned out to be too low for the above mentioned array detector experiment to be feasible in our laboratory. To collect enough events for construction of the response function (Fig. 3), allowed muon separation is 200 m, fairly

exceeding laboratory dimensions. Under these conditions calculated median energy is 270 GeV.

#### 3.2.2. ASYmmetric MUon Telescope (ASYMUT)

Asymmetric muon telescope is an inexpensive detector, constructed from components already available in the laboratory. It consists of two plastic scintillators of unequal dimensions. The lower is identical to the

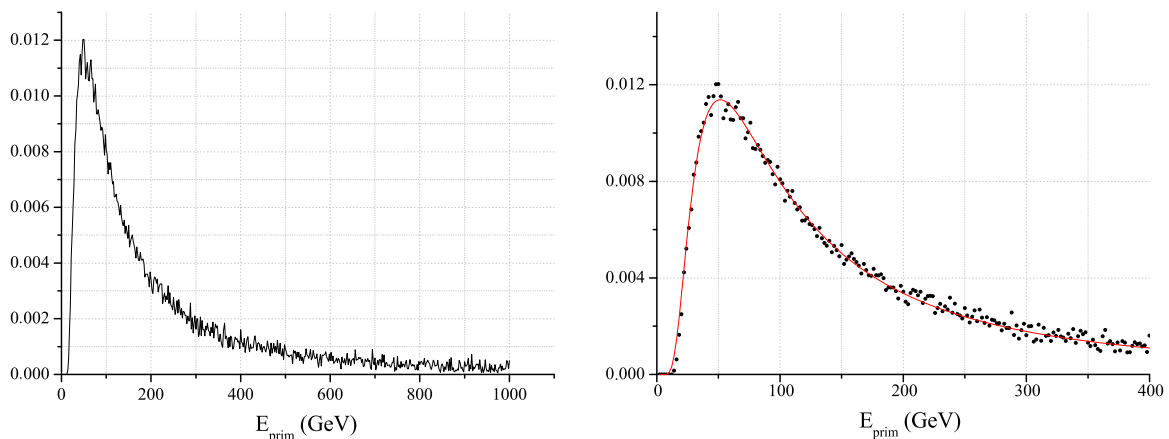


**Fig. 7.** Response function of anticoincident mode of asymmetric muon telescope in the UL to galactic cosmic rays. On the right panel the interesting energy interval is enlarged and Dorman function fit is plotted (red line). (For interpretation of the references to color in this figure legend, the reader is referred to the web version of this article.)

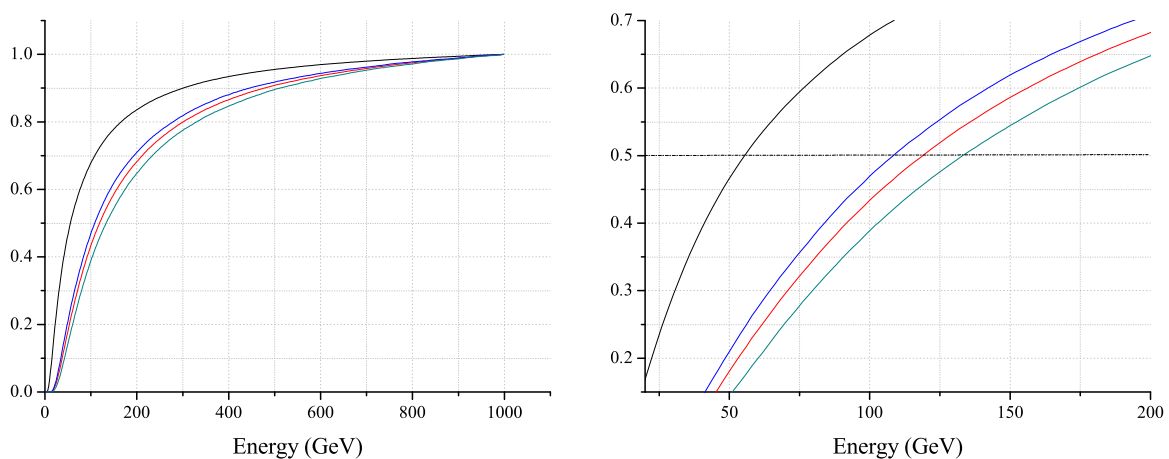


**Fig. 8.** Cumulative response function to galactic cosmic rays of different muon detectors in the Belgrade CR station: black curve — GLL; red curve — single UL; green curve — CC mode and blue curve — ANTI CC mode of asymmetric muon telescope. The 0.5 level corresponds to median energy. Cumulative response function with enlarged region around this level is shown in the right picture. (For interpretation of the references to color in this figure legend, the reader is referred to the web version of this article.)

one located in the GLL ( $100 \times 100 \times 5$  cm) and upper one is  $50 \times 46 \times 5$  cm. Detectors are separated vertically by 78 cm, as depicted in Fig. 4, to have roughly the same count rate in the coincident and anticoincident mode. Lower detector in single mode operates in the same manner as the one in the GLL, with wide angular acceptance. The coincident mode is composed of the events registered in both upper and lower detector. In the anticoincident mode, muons passing through the upper but not the lower detector are counted. Therefore, the later mode favors inclined muon paths. Different angular distribution means different path length of muons registered in three modes of ASYMUT (right part of Fig. 4) and also different energy distribution of parental primary particles.

The response functions to GCR of three modes of ASYMUT are shown on Figs. 5–7 and respective cumulative response functions are shown on Fig. 8.

Important parameters describing shapes of response functions are summarized in Table 1. The most often used characteristics of a detector system is its median energy  $E_{med}$ . Primary particles with the energy below  $E_{med}$  give 50% contribution to detector count rate. The energy interval  $(E_{0.05}, E_{0.95})$  is responsible for 90% of registered events. Fitted value of the parameter  $k$  from Dorman function (Eq. (4)) is also presented. The parameters  $E_{0.05}$  and  $E_{med}$  are determined with 1 GeV accuracy, while the uncertainty of  $E_{0.95}$  is much higher due to small number of very high energy events and is conservatively estimated as 10%.

**Table 1**

Sensitivity of Belgrade CR detectors (GLL — ground level; UL — underground based ASYMUT single mode; CC — ASYMUT coincident mode; ANTI — ASYMUT anticoincident mode) to GCR primary particles. Primaries with the energy below  $E_{0.05}$  (and above  $E_{0.95}$ ) contribute with 5% to the count rate of a corresponding detector.  $E_{med}$  is median energy,  $E_{th}$  threshold energy and  $k$  is Dorman parameter.

det	$E_{th}$ (GeV)	$E_{0.05}$ (GeV)	$E_{med}$ (GeV)	$E_{0.95}$ (GeV)	$k$
GLL	5	11	59	915	0.894(1)
UL	12	31	137	1811	0.971(4)
CC	12	27	121	1585	1.015(3)
ANTI	14	35	157	2031	0.992(4)

### 3.3. Conclusions

Usefulness of our setup for solar modulation studies is tested on the example of investigation of a Forbush decrease of 8 March 2012. In the first half of March 2012 several M and X class solar flares erupted from the active region 1429 on the Sun. The strongest were two X class flares that bursted on March 7. The first one is the X5.4 class flare (peaked at 00:24 UT) and the second one is the X1.3 class flare (peaked at 01:14 UT). The two flares were accompanied by two fast CMEs, one of which was Earth-directed [23]. Several magnetic storms were also registered on Earth, and a series of Forbush decreases is registered. The most pronounced one was registered on March 8. Characteristics of this event as recorded by various neutron monitors and our detectors are compared.

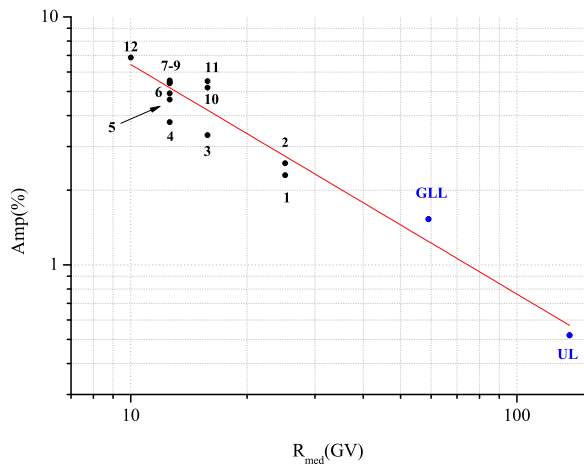


Fig. 9. Rigidity spectrum of FD from 12 March 2012. Black points represent the amplitude of the event as seen by twelve NMs: 1 — Athens, 2 — Mexico City; 3 — Almaty, 4 — Lomnický štít; 5 — Moscow; 6 — Kiel; 7 — Yakutsk; 8 — Apatity; 9 — Inuvik; 10 — McMurdo; 11 — Thule; 12 — South Pole. Blue points are from Belgrade CR station: GLL — ground level and UL — underground. (For interpretation of the references to color in this figure legend, the reader is referred to the web version of this article.)

Amplitude of a Forbush decrease is one of its main characteristics. Dependence of FD amplitude on median rigidity (or energy) is expected to follow the power law:  $\Delta N/N \sim R^{-\gamma}$  [12].

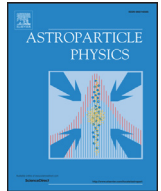
For investigation of rigidity spectrum of mentioned FD data from 12 NMs are combined with the data from our two detectors (GLL and UL) that were operational at the time of the event. Neutron monitor data in the period between 1 March 2012 and 1 April 2012 are taken from the NMDB database ([www.nmdb.eu](http://www.nmdb.eu)) [24]. The exponent of the rigidity spectrum of this FD  $\gamma$  is obtained by the least-square fitting of the data with the power function (Fig. 9) and found to be  $\gamma = 0.92 \pm 0.18$ . Presented analysis illustrates applicability of our setup for studies of consequences of CR solar modulation process in the energy region exceeding sensitivity of neutron monitors.

## Acknowledgments

We are very grateful to late Prof. Ivan Aničin for his enthusiastic contributions, deep insights and valuable advice not just regarding work presented in this paper but also for being a real spiritus agens of our lab. We acknowledge the NMDB database ([www.nmdb.eu](http://www.nmdb.eu)), founded under the European Union's FP7 programme (contract no. 213007) for providing NM data. The present work was funded by the Ministry of Education, Science and Technological Development of the Republic of Serbia, under the Project No. 171002.

## References

- [1] J.A. Simpson, The cosmic ray nucleonic component: The invention and scientific uses of the neutron monitor, *Cosmic Rays Earth* (2000) 11–32.
- [2] J.W. Bieber, Neutron monitoring: Past, present, future, in: Jonathan F.O. (Ed.) AIP Conference Proceedings, vol. 1516, No. 1, 2013.
- [3] M.L. Duldig, Muon observations, in: *Cosmic Rays and Earth*, Springer, Netherlands, 2000, pp. 207–226.
- [4] S. Cecchini, M. Spurio, Atmospheric muons: experimental aspects, *Geosci. Instrum. Methods Data Syst. Discuss.* 2 (2012) 603–641.
- [5] K.-H. Kampert, A.A. Watson, Extensive air showers and ultra high-energy cosmic rays: a historical review, *Eur. Phys. J. H* 37 (3) (2012) 359–412.
- [6] A. de Angelis, O. Mansutti, M. Persic, Very-high energy gamma astrophysics, *Riv. Nuovo Cimento* 31 (4) (2008) 187–246. <http://dx.doi.org/10.1393/ncr/i2008-10032-2>.
- [7] F. Arqueros, J.R. Hörandel, B. Keilhauer, Air fluorescence relevant for cosmic-ray detection — review of pioneering measurements, *Nucl. Instrum. Methods A* 597 (2008) 23–31. <http://dx.doi.org/10.1016/j.nima.2008.08.055>.
- [8] J.A. Lockwood, W.R. Webber, The 11 year solar modulation of cosmic rays as deduced from neutron monitor variations and direct measurements at low energies, *J. Geophys. Res.* 72 (23) (1967) 5977–5989.
- [9] I.G. Usoskin, G.A. Bazilevskaya, G.A. Kovaltsov, Solar modulation parameter for cosmic rays since 1936 reconstructed from ground-based neutron monitors and ionization chambers, *J. Geophys. Res.* 116 (2011) A02104. <http://dx.doi.org/10.1029/2010JA016105>.
- [10] A. Duperier, The meson intensity at the surface of the earth and the temperature at the production level, *Proc. Phys. Soc. A* 62 (11) (1949) 684.
- [11] P.M. Blackett, On the instability of the barytron and the temperature effect of cosmic rays, *Phys. Rev.* 54 (11) (1938) 973.
- [12] L. Dorman, *Cosmic Rays in the Earth's Atmosphere and Underground*, Springer Science + Business Media, LLC., New York, 2004.
- [13] G. Hausser, Cosmic ray-induced background in ge-spectrometry, *Nucl. Instrum. Methods B* 83 (1–2) (1993) 223–228.
- [14] A. Dragić, V. Udovičić, R. Banjanac, D. Joković, D. Maletić, N. Veselinović, M. Savić, J. Puzović, I.V. Aničin, The new setup in the Belgrade low-level and cosmic-ray laboratory, *Nucl. Technol. Radiat. Prot.* 26 (3) (2011) 181–192. <http://dx.doi.org/10.2298/NTRP1101064N>.
- [15] T. Kalliokoski, L. Bezrukov, T. Enqvist, H. Fynbo, L. Inzhechik, P. Jones, J. Joutsenvaara, J. Karjalainen, P. Kuusiniemi, K. Loo, B. Lubsandorzhiev, V. Petkov, T. Rih, J. Sarkamo, M. Slupecki, W. Trzaska, A. Virkajrvi, Can EMMA solve the puzzle of the knee? *Prog. Part. Nucl. Phys.* 66 (2011) 468–472.
- [16] W.H. Fonger, Cosmic radiation intensity-time variations and their origin. II. Energy dependence of 27-day variations, *Phys. Rev.* 91 (2) (1953) 351.
- [17] E.E. Brown, Neutron yield functions for the nucleonic component of cosmic radiation, *Il Nuovo Cimento* (1955–1965) 6 (4) (1957) 956–962.
- [18] L. Dorman, *Cosmic Ray Variations*, State Publishing House for Technical and Theoretical Literature, 1957.
- [19] E.O. Fluckiger, et al., A parameterized neutron monitor yield function for space weather applications, in: *Proceedings of the 30th International Cosmic Ray Conference*, Mexico City, Mexico, vol. 1 (SH), 2008, pp. 289–292.
- [20] M. Zazyan, A. Chilingarian, Calculations of the sensitivity of the particle detectors of ASEC and SEVAN networks to galactic and solar cosmic rays, *Astropart. Phys.* 32 (2009) 185–192.
- [21] K. Nakamura, et al., 24. Cosmic rays, *J. Phys. G* 37 (2010) 075021.
- [22] B. Bugle, B. Glaser, L. Zoller, U. Hambach, S. Markovic, I. Glaser, N. Gerasimenko, Geochemical characterization and origin of Southeastern and Eastern European loesses (Serbia, Romania, Ukraine), *Quat. Sci. Rev.* 27 (2008) 1058–1075.
- [23] NASA Goddard Space Weather Research Center, Summary of the space weather event associated with the X5.4 and X1.3 flare on March 7.
- [24] H. Mavromichalaki, et al., Applications and usage of the real-time Neutron Monitor Database, *Adv. Space Res.* 47 (12) (2011) 2210–2222.



# A novel method for atmospheric correction of cosmic-ray data based on principal component analysis

M. Savić, A. Dragić\*, D. Maletić, N. Veselinović, R. Banjanac, D. Joković, V. Udovičić

Institute of Physics, University of Belgrade, Pregrevice 118, Zemun 11080, Serbia



## ARTICLE INFO

### Article history:

Received 23 August 2018  
 Revised 8 December 2018  
 Accepted 29 January 2019  
 Available online 29 January 2019

### Keywords:

Cosmic rays  
 Muons  
 Atmospheric corrections  
 Principal component analysis

## ABSTRACT

A new method for atmospheric correction of cosmic ray data is designed. It's fully empirical, based on the principal component analysis. The method requires knowledge of the pressure and the temperature profile of the atmosphere. It's applicable to all muon detectors. The method is tested on muon data from two detectors in Belgrade cosmic ray station, one located on the ground level and the other at the depth of 25 mwe. Correction reduces variance by 64.5% in ground level detector data and 38.1% in underground data. At the same time, the amplitude of the annual variation is reduced by 86.0% at ground level and 54.9% underground. With the same data sets the presented method performs better than the integral correction method.

© 2019 Elsevier B.V. All rights reserved.

## 1. Introduction

Count rates of ground based or underground cosmic-ray (CR) muon detectors are affected by atmospheric parameters (air pressure and temperature at different heights). The proper description of atmospheric effects is necessary for understanding primary CR variations, originating outside of the atmosphere.

Early studies in CR temporal variations [1,2] revealed the existence of a variation caused by the change of air pressure, the so called "barometric effect". With the increase in pressure the atmosphere represents thicker absorber, resulting in reduced number of muons reaching the ground level. Therefore, muon flux is expected to be anti-correlated with atmospheric pressure.

Observed negative correlation between muon flux and atmospheric temperature, the so called "negative temperature effect", has been explained by Blackett [3] to be a consequence of muon decay. During warm periods the atmosphere is expanded and the main layer of muon production (~100 mb) is higher, resulting in longer muon path and lower surviving probability to the ground level. Low energy muons are more affected, while the flux of high energy muons, capable of penetrating great depth, does not suffer. At deep underground experiments another type of temperature effect, "positive temperature effect" is pronounced [4]. Development of nuclear emulsions capable of detecting energetic charged particles lead to discovery of charged pions in CRs and  $\pi - \mu$  decay [5–7]. The positive temperature effect is interpreted as a conse-

quence of latter process [8,9]. Pions created in the interactions of primary CR particles with the atmospheric nuclei can decay into muons or interact with air nuclei. Higher temperature in the production layer means lower air density and consequently, lower interaction probability and higher muon production.

In most cases linear regression is sufficient to account for the barometric effect. The temperature effects are treated by empirical and theoretical methods. In addition to the barometric coefficient  $\beta$ , **the method of effective level of generation** [8] introduces two empirical parameters:  $\alpha_H$  to encounter for muon intensity variations  $\delta I_\mu$  correlated with the change of the height of generation level  $\delta H$  (negative effect) and  $\alpha_T$  for the changes of the temperature of this level (positive temperature effect).

$$\delta I_\mu = \beta \delta p + \alpha_H \delta H + \alpha_T \delta T \quad (1)$$

Duperier method has been successfully used in many studies for the atmospheric corrections of muon data ([10–15] etc.).

It's been argued [16,17] that for correct temperature correction of muon detectors count rate the vertical temperature profile of the entire atmosphere needs to be known. In the so called **integral method** the muon intensity variations caused by the temperature are described by the equation:

$$\frac{\delta I_\mu}{I_\mu} = \int_0^{h_0} W_T(h) \delta T(h) dh \quad (2)$$

where  $\delta T(h)$  is the variation of temperature at isobaric level  $h$  with respect to the referent value and  $W_T(h)$  is the temperature coefficient density. The coefficients are calculated theoretically and the best known calculations are given in references [18,19].

\* Corresponding author.

E-mail address: [dragic@ipb.ac.rs](mailto:dragic@ipb.ac.rs) (A. Dragić).

The **mass-average temperature method** [20] is a variant of the integral method, based on the assumption of small changes of the temperature coefficient density  $W_T(h)$  with the atmospheric depth  $h$  allowing its average value  $\overline{W}_T$  to be put in front of the integral in the Eq. (2) and on determination of the mass-averaged temperature  $T_m$ :

$$\frac{\delta I_\mu}{I_\mu} = \overline{W}_T(h) \int_0^{h_0} \delta T(h) dh = \overline{W}_T(h) \cdot \delta T_m \quad (3)$$

The method was used in numerous studies ([21–23] to name a few).

Another form of the integral method is **the effective temperature method** [24]. By introducing the temperature coefficient  $\alpha_T$ :

$$\alpha_T = \int_0^{h_0} W_T(h) dh$$

the Eq. (2) can be normalized as:

$$\frac{\delta I_\mu}{I_\mu} = \int_0^{h_0} W_T(h) dh \cdot \frac{\int_0^{h_0} W_T(h) \delta T(h) dh}{\int_0^{h_0} W_T(h) dh} = \alpha_T \cdot \delta T_{eff} \quad (4)$$

where the effective temperature  $T_{eff}$  is defined as:

$$T_{eff} = \frac{\int_0^{h_0} W_T(h) T(h) dh}{\int_0^{h_0} W_T(h) dh}$$

The latter method is popular with the underground muon telescopes [25,26].

Different methods of atmospheric correction might be compared on the basis of several criteria. One is requirement of the lowest variance of corrected data. Since the most prominent temperature effect on CR time series is seasonal variation, another criterion is the smallest residual amplitude of seasonal variation after correction is applied. The latter does not take into account possible genuine seasonal variation of non-atmospheric origin.

Early studies comparing Duprier's empirical and Dorman's theoretical methods ([27] and references therein) found similar accuracy of two methods, with essentially the same corrections at sea level, but with the integral method overestimating the temperature effect.

A more recent study [28] compared different methods of atmospheric correction for data from Nagoya and Tibet supertelescopes, as well as Yakutsk, Moscow and Novosibirsk telescopes. They found the mass-averaged temperature method to practically coincide with the integral method. On the other hand, the effective level of generation method for Nagoya shows discrepancy from the integral method in winter time, being able to eliminate only 50% of the temperature effect. Even with the integral method in the case of Tibet muon telescope the removal of temperature effect is achieved with the density of temperature coefficients 3 times higher than calculated ones. The precise origin of disagreement is unknown.

The method of the effective level of generation takes care of key physical causes of the temperature effect. However, it does not make optimal use of the temperature data. Also, the assumption of a single level of main muon production is a simplification. Detailed CORSIKA simulation of the shower development in the atmosphere reveals the actual distribution of the muon generation heights (see Fig. 1).

Different implementations of the integral method exist, employing different approximations, choice of parameters, models of the atmosphere, whether kaon contribution is taken into account, leading to differences in calculated density temperature coefficients (see for instance discussion in [29]). As already mentioned, on the case of Tibet telescope [28] theoretical calculations do not fully correspond to the local experimental conditions and the origin of disagreement is difficult to trace.

The effective temperature method lacks universality, since it works best with the data from deep underground detectors.

Here we propose a new method for atmospheric corrections. It's fully empirical, makes use of the available temperature data through entire atmosphere and it's applicable to arbitrary detector irrespective to energy sensitivity and is simple to implement. The method is based on the principal component analysis, thus reducing dimensionality of the problem, exploiting correlations between atmospheric variables and ensuring mutual independence of correction parameters. The price is loss of clear physical interpretation of these parameters, since the pressure and the temperature at different levels are treated on equal footing.

## 2. Method description

### 2.1. Meteorological data

Set of variables that enter principal component decomposition consists of atmospheric temperature profile for the given location as well as locally measured atmospheric pressure. Meteorological balloon soundings for Belgrade are not done frequently enough to be used for suggested analysis. As a consequence, modeled temperatures were used instead. However, there were enough balloon sounding data for testing consistency of the modeled temperatures.

There are several weather and global climate numerical models available today. Here, Global Forecast System [30] data was used. GFS is a weather forecast model, developed by National Centers for Environmental Prediction [31], which is able to predict large number of atmospheric and land-soil parameters. Apart from forecast data, GFS also provides retrospective data produced taking into account most recent measurements by a world wide array of meteorological stations. Retrospective data are produced four times a day at 00:00, 06:00, 12:00 and 18:00 UTC. Data with finer temporal resolution are obtained by cubic spline interpolation. Temperatures for the following 25 isobaric levels (in mb) were used for initial analysis: 10, 20, 30, 50, 70, 100, 150, 200, 250, 300, 350, 400, 450, 500, 550, 600, 650, 700, 750, 800, 850, 900, 925, 975, 1000. Horizontal spatial resolution for modeled data is 0.5 degrees, so coordinates closest to the experiment location (latitude 44.86, longitude 20.39), were selected with this precision. Before any further analysis was done, GFS modeled temperature profiles were compared to local meteorological balloon soundings for Belgrade, where balloon data was available. Fig. 2 shows profile of differences between modeled and measured values for different isobaric levels. Disagreement was found between measured and modeled temperature at the lowest level. As a result, it was decided not to use temperature data for isobaric level of 1000 mb in further analysis. Ground temperature data measured by local meteorological stations was used for lowest layer instead. Similar problem with the GFS data was reported before by [28] who found 5°C deviation in the summer time near ground level at Yakutsk location.

Atmospheric pressure and ground level temperature from the Republic Hydro-meteorological Service of Serbia was used to compose unique local pressure and temperature time series.

### 2.2. Cosmic-ray data

The analysis is performed on data from Belgrade muon detectors. The Belgrade cosmic-ray station, together with the present detector arrangement is described in details elsewhere [32]. Two muon detectors are located in the laboratory, one at the ground level and the other at the depth of 25 mwe. Data are recorded on the event-by event basis and can be integrated into the time series with the arbitrary time resolution. For most purposes hourly data are used. Muon detectors are sensitive to primary cosmic rays

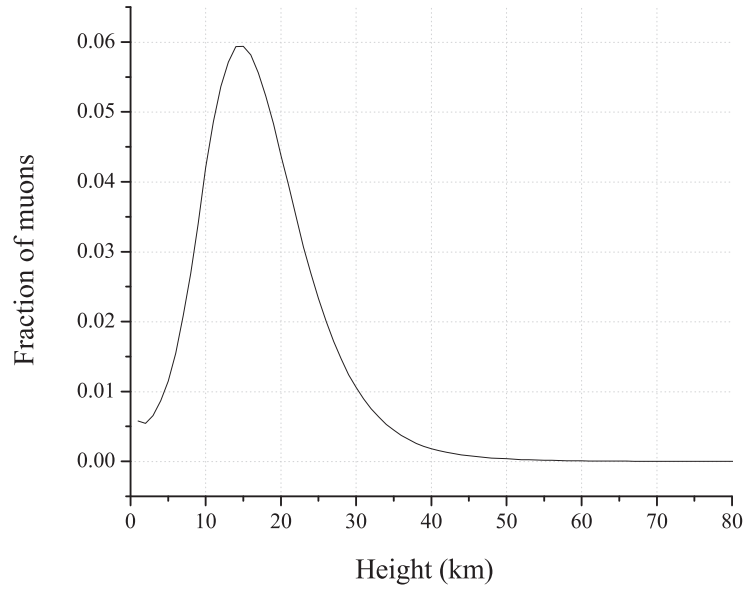


Fig. 1. Distribution of muon generation at different heights in the atmosphere, according to CORSIKA simulation.

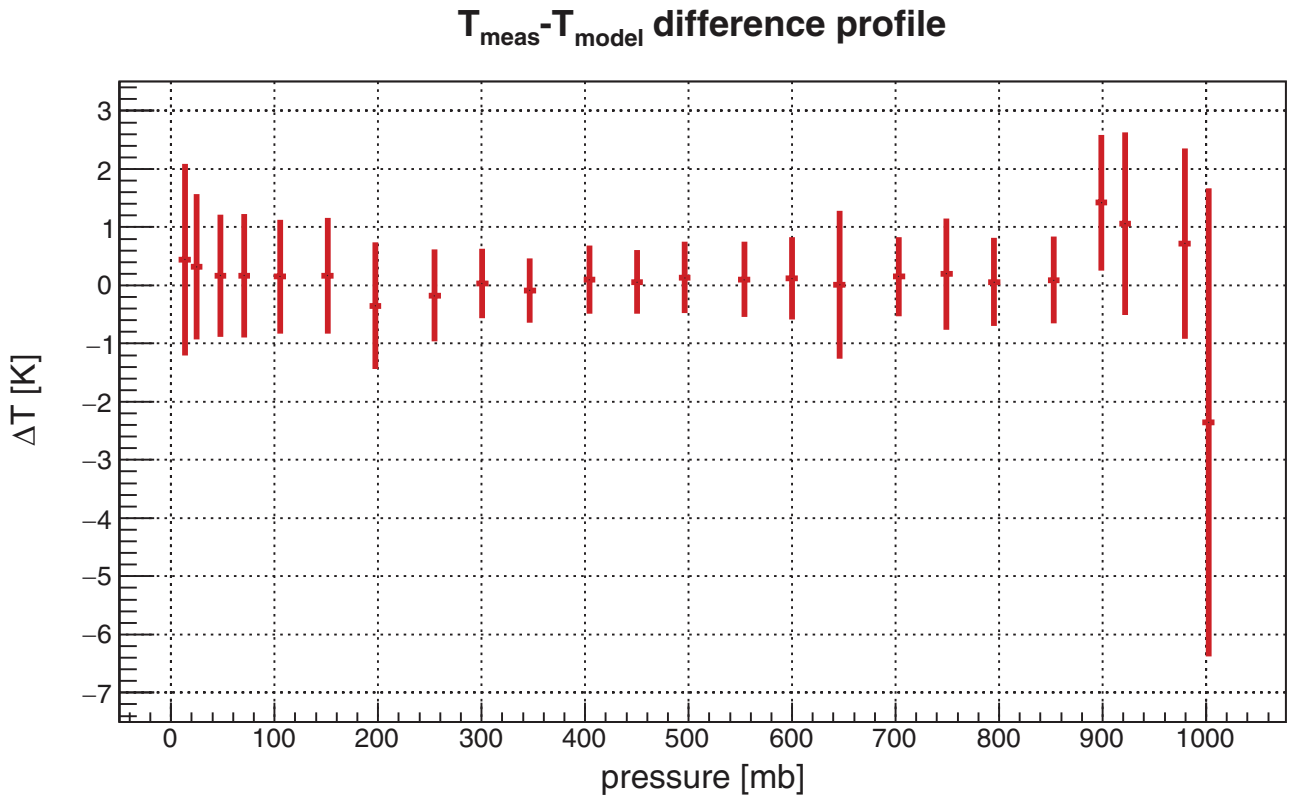


Fig. 2. Distribution of differences between measured temperatures and modeled by GFS.

of 59 GeV median energy in the case of ground level detector and 137 GeV for underground detector.

### 2.3. Principal component decomposition

Principal component analysis is a convenient and widely used data reduction method when dealing with strongly correlated

data. It transforms the original set of variables into a set of uncorrelated variables (called principal components (PC)). The principal components are ordered according to decreasing variance. In our case, there are 26 input variables: 24 modeled temperatures (isobaric level 1000 mb temperature excluded), locally measured ground level temperature and local atmospheric pressure. Initial variables were centered and normalized before

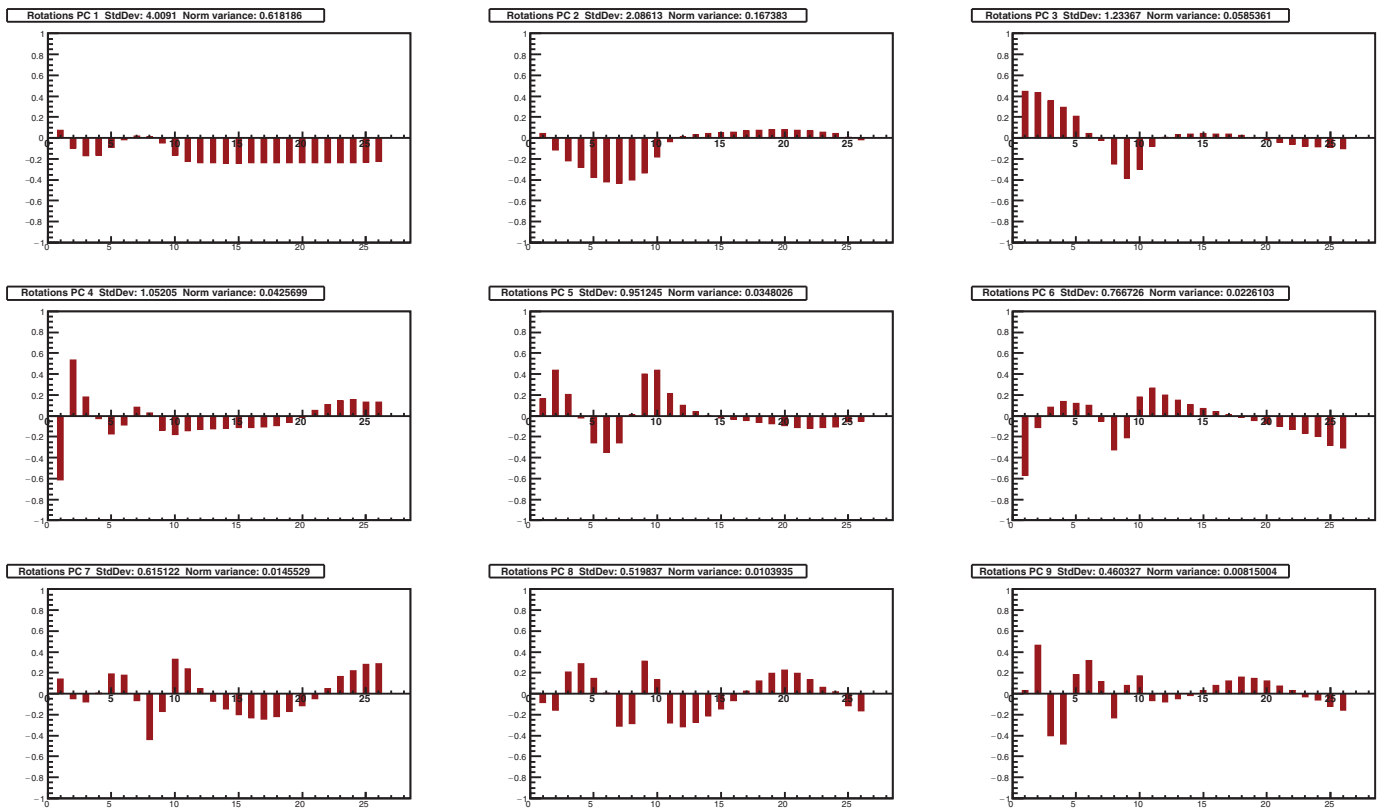


**Fig. 3.** Composition of nine principal components with largest variance (in decreasing order). Input variables are displayed on X-axis: 1 being pressure, 2 temperature of 10 mb isobaric level, 26 being local ground level temperature. Y-axis represents rotations.

decomposition. After decomposition, a new set of 26 principal components was obtained. Decomposition should not be regarded as universal, but it should be redone for every location and period under study.

One year was selected as a suitable time period for the analysis, in order to reduce possible seasonal bias, due to atmospheric temperature annual variation. Additional criteria were quality and consistency of muon data. Taking this into account, final time interval selected for analysis was from 01.06.2010 to 31.05.2011.

**Fig. 3** shows composition plots for the first nine principal components, that account for 98% of total variance. X-axis represents input atmospheric variables, first being atmospheric pressure, followed by 10 mb layer temperature, last being ground level local temperature. Y-axis represents decomposition rotations for a given principal component. Interesting features observed on these plots are that first two principal components depend almost exclusively on temperature. The first one is mostly combination of temperatures in the troposphere (isobaric levels 250–1000 mb) with almost equal weights. The second eigenvector accounts for significant variance of temperatures in higher atmospheric levels (10–250 mb), with the strongest contribution centered in the tropopause. Components 3 to 6 have mixed p-T composition. The correlation of atmospheric pressure and temperature at different heights is not surprising. The diurnal and semi-diurnal oscillations of pressure are attributed to the warming of the upper atmosphere by the Sun [33]. This correlation makes it impossible to define a single barometric parameter in PCA based method of atmospheric corrections. It's worth mentioning that Dorman [34] recognizes three different barometric effects: absorption, decay and genera-

tion effect. It also indicates that empirical methods with separated pressure and temperature corrections might lead to overcorrection.

The values of the eigenvectors for these first nine components are also given in [Table 1](#).

**Fig. 4** shows plot of proportion of variance as well as plot of cumulative variance for obtained principal components. Corresponding numerical values are given in [Table 2](#).

Usually, only a first few principal components (containing high fraction of total variance) are of practical interest. There are various different methods and rules for choosing how many PCs to retain in the analysis, none completely free of subjectivity (see for example a thorough discussion in [35]). A rule based on cumulative percentage of total variation usually recommends to retain PCs responsible for 70–90% of total variation. When one or two components are dominant, higher value (95%) is appropriate. In our case it would mean keeping first 6 PCs. According to Kaiser's rule only PCs with the eigenvalue  $\lambda > 1$  should be retained. Jolliffe [35] suggested 0.7 as correct level, exceeded by six of our PCs. Another rule proposes to retain components with the eigenvalue above mean, a condition satisfied by first seven of our PCs. Another popular model is broken stick, but in application to our problem is too restrictive, leading to only two relevant PCs. The scree graph or log-eigenvalue diagram don't provide clean cut with our set of PCs.

To test the meaningfulness of potentially relevant PCs, the time series from PC data are constructed and tested whether they are distinguishable from white noise. The procedure is often done when principal component analysis is applied to atmospheric physics problems [36]. The time series with hourly resolution for the first three PCs are plotted on [Fig. 5](#).

**Table 1**  
Definition of first nine principal components.

Variables	Principal components								
	PC1	PC2	PC3	PC4	PC5	PC6	PC7	PC8	PC9
<i>p</i>	0.07699	0.04117	0.44694	-0.61285	0.16301	-0.57121	0.14028	-0.08106	0.03443
<i>T</i> (10)	-0.0947	-0.11603	0.43488	0.5344	0.43741	-0.11036	-0.04499	-0.15825	0.46469
<i>T</i> (20)	-0.16947	-0.21766	0.35754	0.18029	0.20527	0.08546	-0.07719	0.20635	-0.40309
<i>T</i> (30)	-0.16476	-0.27825	0.29593	-0.02505	-0.02204	0.14134	0.00634	0.28574	-0.47812
<i>T</i> (50)	-0.09124	-0.37682	0.20969	-0.17322	-0.25798	0.12084	0.19349	0.14645	0.18493
<i>T</i> (70)	-0.01483	-0.42304	0.04507	-0.08651	-0.3472	0.09965	0.18155	0.01024	0.31886
<i>T</i> (100)	0.02192	-0.43132	-0.02451	0.08228	-0.25692	-0.04937	-0.06464	-0.3103	0.1183
<i>T</i> (150)	0.01487	-0.40127	-0.24673	0.03037	0.012	-0.32566	-0.43658	-0.28393	-0.23316
<i>T</i> (200)	-0.04737	-0.33404	-0.38636	-0.13563	0.40141	-0.2069	-0.16852	0.31181	0.07995
<i>T</i> (250)	-0.16218	-0.17984	-0.29739	-0.18123	0.43708	0.18013	0.32866	0.13662	0.17389
<i>T</i> (300)	-0.22473	-0.03266	-0.07561	-0.14073	0.21179	0.26504	0.23807	-0.27931	-0.06785
<i>T</i> (350)	-0.2369	0.01439	0.00488	-0.12991	0.0998	0.1988	0.05306	-0.31612	-0.0771
<i>T</i> (400)	-0.23956	0.03362	0.02958	-0.12159	0.04075	0.14932	-0.06959	-0.27189	-0.04852
<i>T</i> (450)	-0.24028	0.04271	0.0402	-0.11503	0.00384	0.10744	-0.14772	-0.21165	-0.01823
<i>T</i> (500)	-0.24005	0.04935	0.0428	-0.11304	-0.02187	0.07218	-0.19893	-0.14512	0.03068
<i>T</i> (550)	-0.23958	0.05695	0.03965	-0.11295	-0.03254	0.0388	-0.23263	-0.06843	0.08056
<i>T</i> (600)	-0.23881	0.06549	0.03681	-0.10649	-0.04369	0.01102	-0.24562	0.02401	0.12499
<i>T</i> (650)	-0.23854	0.07279	0.0236	-0.09184	-0.06132	-0.01542	-0.21788	0.12597	0.15977
<i>T</i> (700)	-0.23835	0.0801	0.00429	-0.06052	-0.07601	-0.04668	-0.16785	0.19559	0.14932
<i>T</i> (750)	-0.23842	0.08071	-0.01837	-0.01332	-0.09245	-0.07308	-0.11295	0.22563	0.12401
<i>T</i> (800)	-0.23814	0.07557	-0.03907	0.05036	-0.10989	-0.09943	-0.04696	0.19596	0.07735
<i>T</i> (850)	-0.23701	0.0675	-0.06202	0.1081	-0.11988	-0.12745	0.04989	0.13672	0.0304
<i>T</i> (900)	-0.23535	0.05462	-0.07977	0.14776	-0.11454	-0.16955	0.16551	0.06204	-0.02952
<i>T</i> (925)	-0.23414	0.04606	-0.08313	0.15641	-0.10257	-0.19925	0.21877	0.01715	-0.05804
<i>T</i> (975)	-0.23108	0.00789	-0.08827	0.13022	-0.05888	-0.28046	0.284	-0.11523	-0.12249
<i>T</i> (1000)	-0.22494	-0.01582	-0.10092	0.13401	-0.04977	-0.30749	0.28553	-0.16516	-0.15908

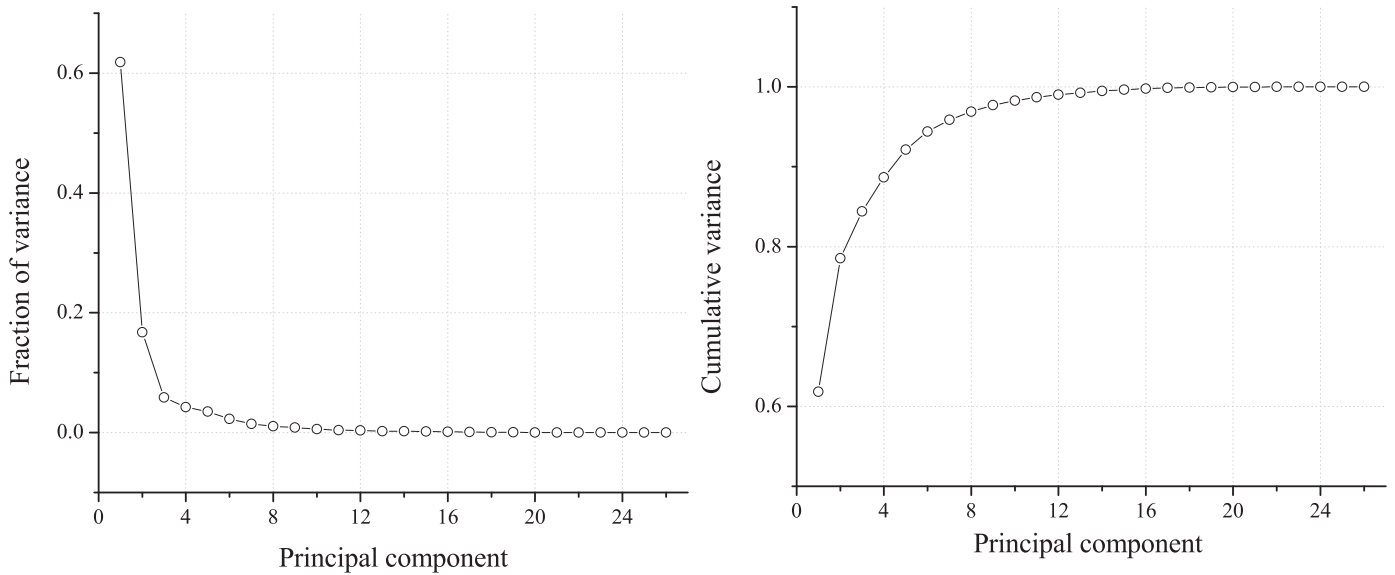


**Fig. 4.** Proportion of variance (left) and cumulative proportion of variance (right) for all 26 principal components.

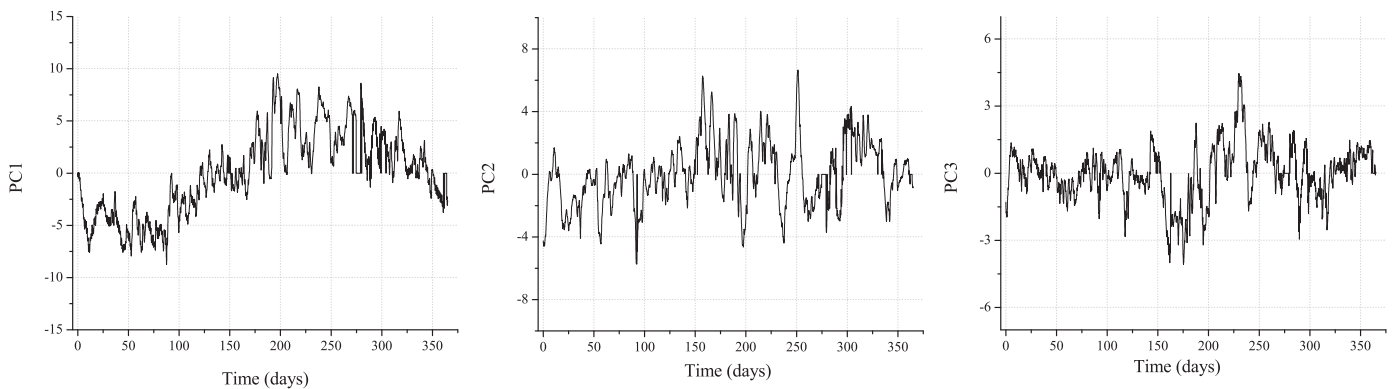


**Fig. 5.** Time series of the first 3 PCs.



**Table 2**  
Variance (individual and cumulative) for all 26 PCs.

Principal component	Eigenvalue	Percentage of variance	Cumulative variance (%)
1	4.0091	0.618186	0.618186
2	2.08613	0.167383	0.785569
3	1.23367	0.0585361	0.844105
4	1.05205	0.0425699	0.886675
5	0.951245	0.0348026	0.921478
6	0.766726	0.0226103	0.944088
7	0.615122	0.0145529	0.958641
8	0.519837	0.0103935	0.969034
9	0.460327	0.00815004	0.977184
10	0.382006	0.00561263	0.982797
11	0.32832	0.00414592	0.986943
12	0.294489	0.00333553	0.990278
13	0.247876	0.00236317	0.992642
14	0.239462	0.00220546	0.994847
15	0.206157	0.00163465	0.996482
16	0.184453	0.00130857	0.99779
17	0.144657	8.04834E-4	0.998595
18	0.119676	5.5086E-4	0.999146
19	0.0938189	3.38538E-4	0.999485
20	0.0739496	2.10328E-4	0.999695
21	0.0586253	1.32189E-4	0.999827
22	0.0414996	6.62391E-5	0.999893
23	0.0338811	4.41511E-5	0.999937
24	0.0281359	3.04472E-5	0.999968
25	0.0219102	1.84637E-5	0.999986
26	0.0188263	1.36319E-5	1

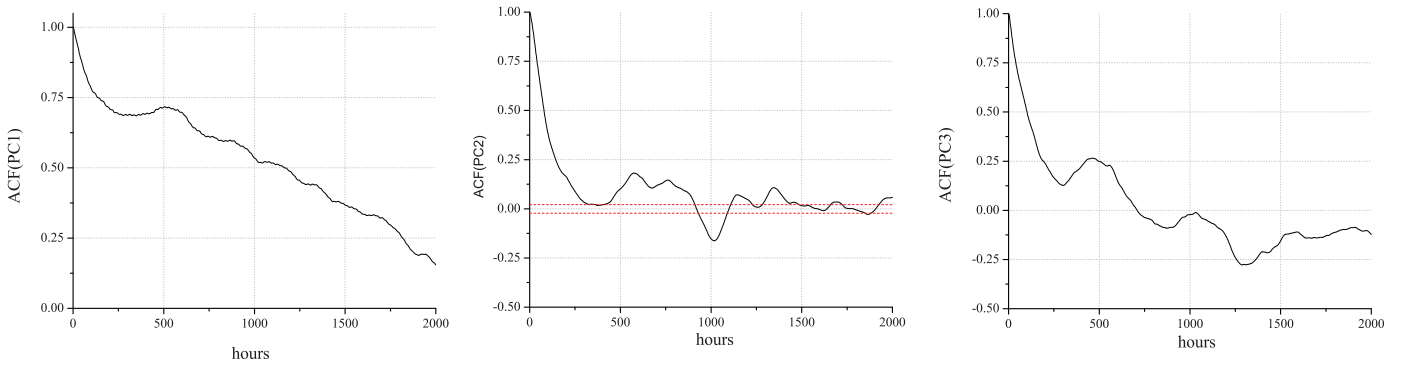


**Fig. 6.** Autocorrelation function of the first 3 PCs. Time lag is given in hours. In the case of PC2, 95% significance level is indicated by dashed red line. (For interpretation of the references to color in this figure legend, the reader is referred to the web version of this article.)

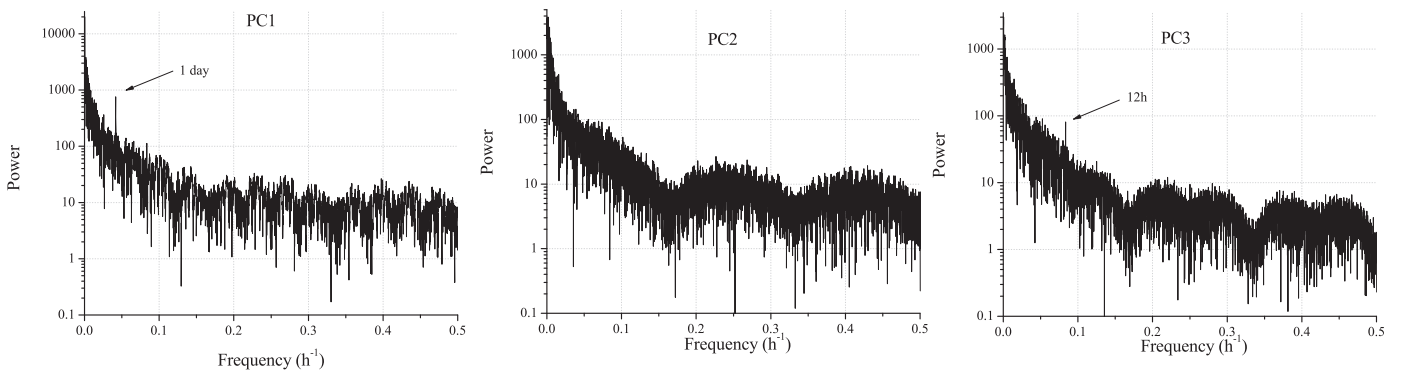


**Fig. 7.** Spectral analysis of time series of the first 3 PCs.

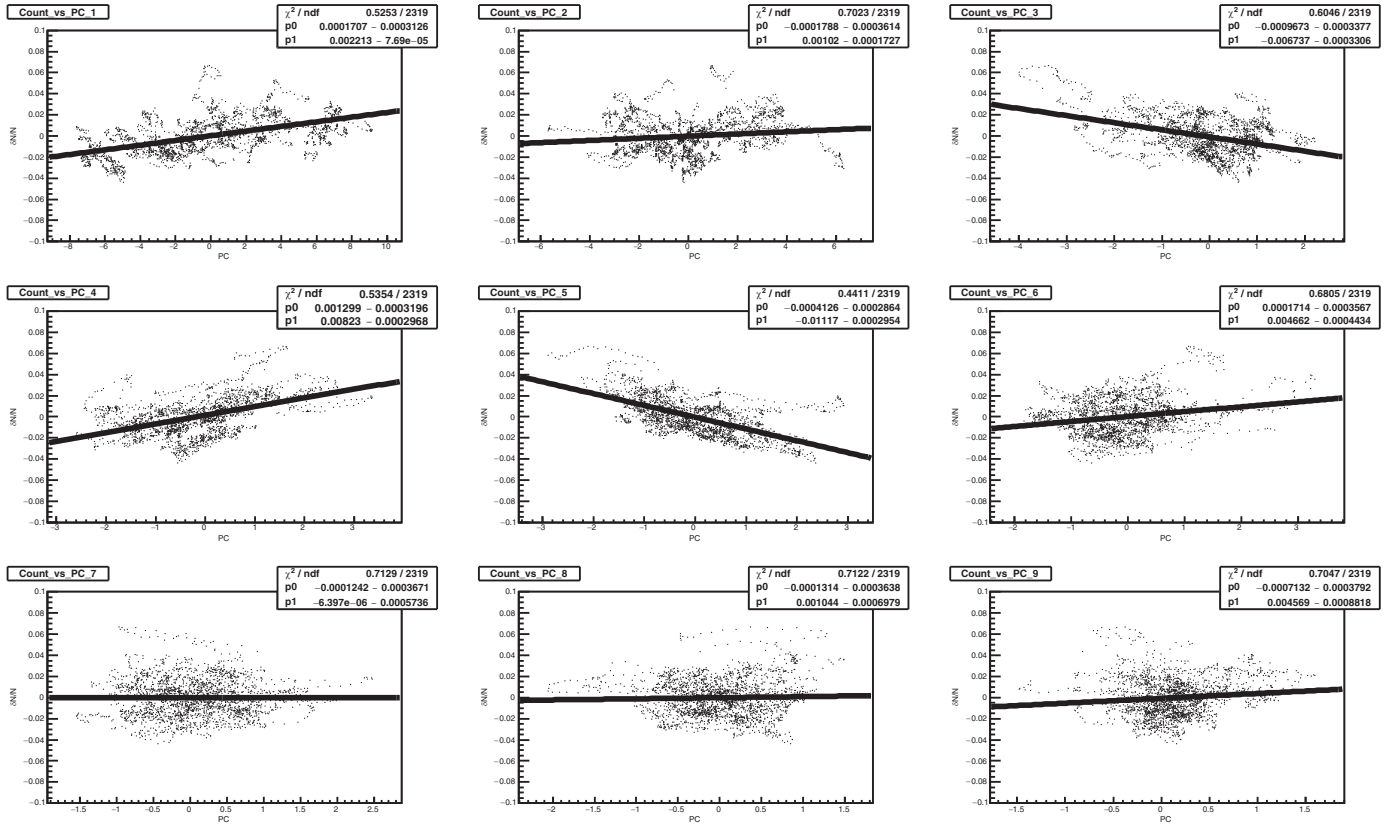


Fig. 8. Muon count dependence on principal components for the first nine principal components (GLL).

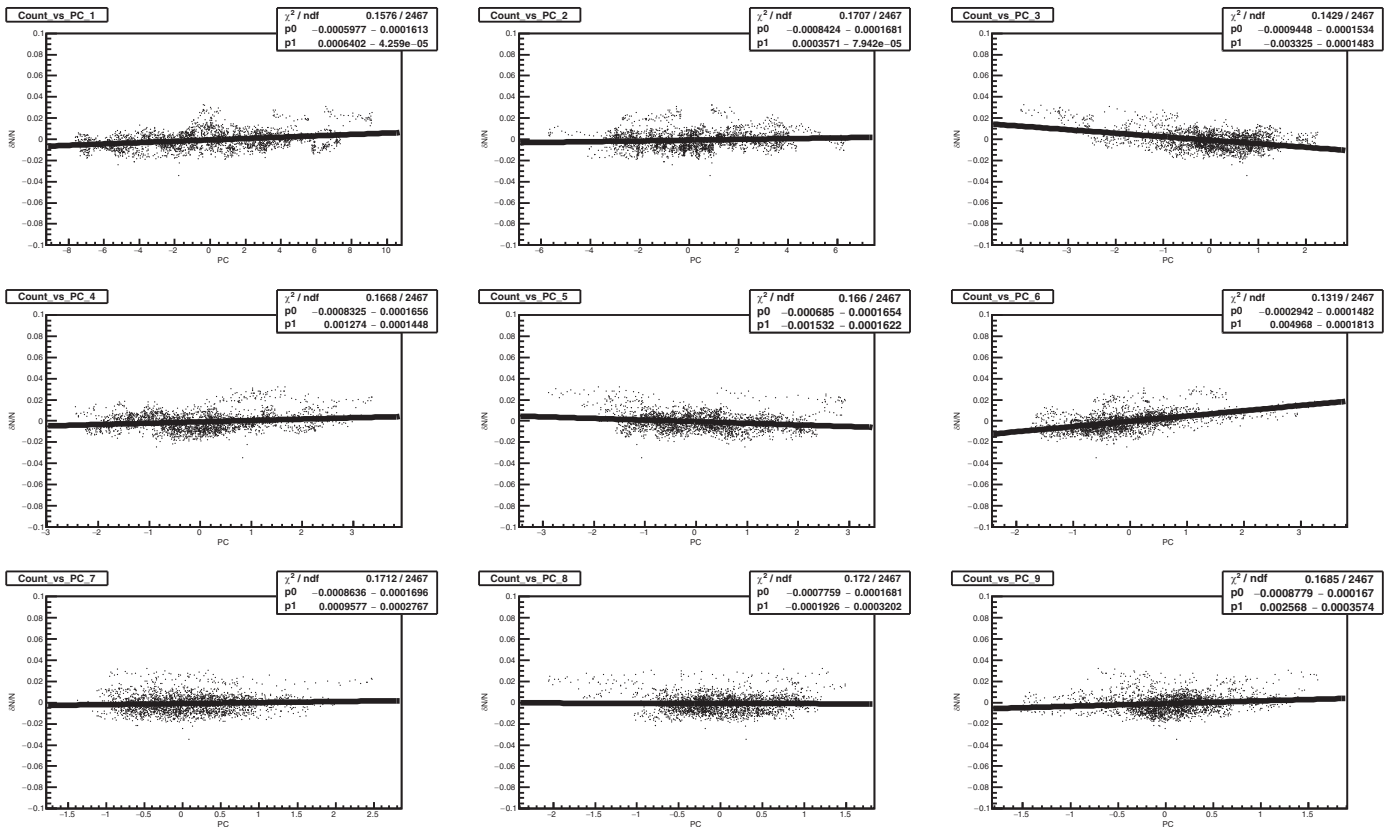


Fig. 9. Muon count dependence on principal components for the first nine principal components (UL).

The subsequent temperature and pressure measurements are highly correlated, as evident from autocorrelation function plot for selected PCs (Fig. 6).

The spectral analysis of the PC time series reveals, for PCs with the strong pressure component, semi-diurnal periodicity in addition to diurnal (Fig. 7).

Since our purpose is the regression of muon data with principal components, selecting the components with significantly high variance is not the main issue. It is more important to identify PCs with high correlation with CR data. Components with relatively low variance, can have high predictive power.

#### 2.4. Correlation of principal components with CR muon count rate and correction of muon data

Scatter plot of muon count rate vs. PCs, together with the linear fit for the first nine principal components are shown on Fig. 8 (GLL) and Fig. 9 (UL). In the analysis hourly summed muon counts and principal component values for the respective hour were used. To minimize the effect of geomagnetic disturbances, only data for International Quiet Days were taken into account. The International Quiet Days are the days with minimum geomagnetic activity for each month. The selection of quiet days is deduced from  $K_p$  index. In our analysis 5 quietest days for each month are considered. The values of correlation coefficients are listed in Table 3.

Principal components PC1, PC3, PC4, PC5 and PC6 have been identified as ones with significant contribution to the muon flux variation. Interestingly enough, the PC2, responsible for 16.7% variance of the meteorological data has very little effect on muon flux, at neither ground nor underground level. Ground level muon flux variation is more affected by the first principal component, depending chiefly on the temperature in the troposphere. The finding agrees with usual negative temperature effect. The other PCs are difficult to compare with traditional correction parameters. Yet, the effect of PC3, that is composed more from upper atmosphere temperatures and hence could be loosely associated with positive temperature effect, is more pronounced for the underground muon flux. Fourth and fifth principal components with strong pressure contribution affect more ground level muon flux. On the other hand, PC6, also the one with high pressure component, has more pronounced influence on underground muon flux.

Gradients obtained from the fits for the significant principal components 1, 3, 4, 5 and 6 were then used to calculate the PCA corrected muon count according to the formula:

$$N_{\mu}^{(corr)} = N_{\mu} - \langle N_{\mu} \rangle \sum_i k_i PC_i, \quad i = 1, 3, 4, 5, 6 \quad (5)$$

where  $N_{\mu}^{(corr)}$  corr is the corrected muon count,  $N_{\mu}$  is the raw muon count,  $\langle N_{\mu} \rangle$  is the mean count for the whole period,  $k_i$  are the gradients and  $PC_i$  are the corresponding principal components. Resulting corrected muon count time series are plotted on Figs. 10 (GLL) and 11 (UL) along with raw and pressure only corrected time series. Pressure corrected time series are produced for reference. Barometric coefficient was determined by applying linear regression to the same data set used for PCA. Data was previously corrected for temperature effect using integral method, as in Ref. [37]. Pressure corrected and PCA corrected time series are fitted with sine function with annual period in order to illustrate how PCA correction affects yearly variation induced by temperature effect.

PCA based atmospheric corrections remove 64.5% of total variance in GLL time series and 38.1% in UL time series. Pressure corrected CR time series exhibit annual variation, a consequence of

**Table 3**  
Correlation coefficients between principal components and muon count rate in the ground level laboratory (GLL) and underground laboratory (UL).

PC	1	2	3	4	5	6	7	8	9	10	11	12	13	14	15	16	17	18	19	20	21	22	23	24	25	26
GLL	0.43	0.01	-0.37	0.48	-0.55	0.30	-0.01	0.03	-0.01	0.06	0.00	-0.04	0.00	0.01	0.02	-0.01	0.00	-0.01	-0.01	0.03	-0.03	0.00	0.02	-0.01	0.04	0.02
UL	0.26	0.02	-0.48	0.21	-0.19	0.52	0.02	0.04	0.07	0.04	0.01	-0.04	-0.07	0.06	-0.02	-0.05	0.04	0.04	-0.02	-0.02	0.00	0.01	0.00	-0.03	0.01	0.01

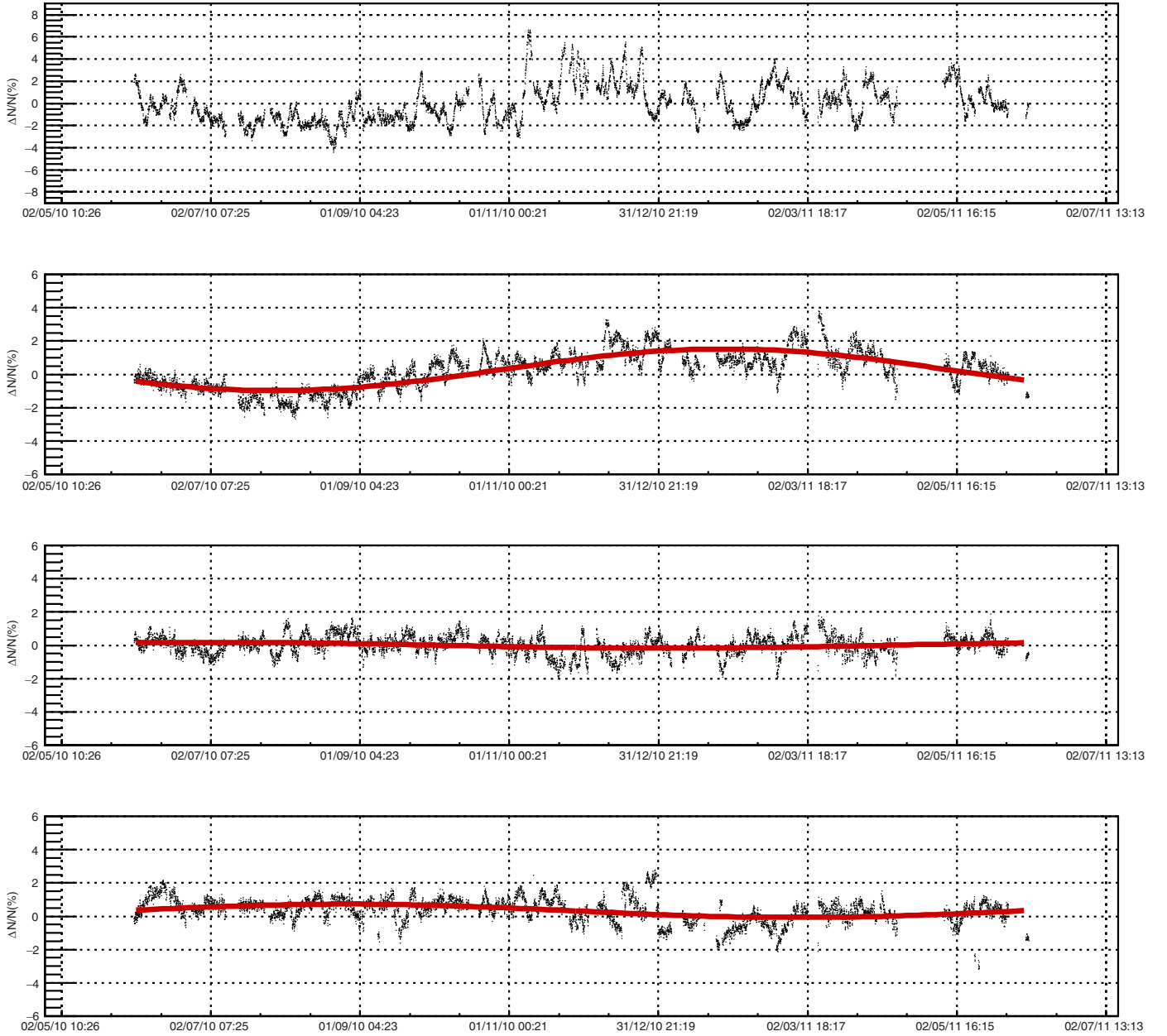


**Fig. 10.** Raw (upper panel), pressure corrected (middle panel), pressure+temperature corrected with PCA method (3rd panel from the top) and pressure+temperature corrected with integral method (lower panel) normalized muon count rate for GLL. The sine function with one year period is fitted to the data.

the temperature effect. The performance of the temperature correction may be tested by comparing the amplitude of the annual variation before and after correction. With presented method the amplitude of the annual variation is reduced by 86% (54.9%) in the case of GLL (UL) with respect to the pressure only corrected time series.

To further test the new method, the atmospheric correction of GLL data are performed by the integral method. The correction resulted in 56.25% of variance reduction and 68.1% of reduction of the amplitude of the annual wave. At least in the case of our CR data set the new method performs somewhat better than the integral method.

### 3. Conclusion

The principal component analysis is successfully used to construct a new empirical method for the atmospheric corrections of CR muon data. The method is equally applicable to all muon detectors, irrespective to location: ground level, shallow or deep underground. It requires knowledge of the atmospheric pressure and temperatures along the entire atmosphere, which is nowadays available in databases such as GFS. The method is suitable for the near real-time correction, with the delay defined by the availability of the atmospheric data (one day in the case of present GFS data). When applied to Belgrade muon data from two detectors

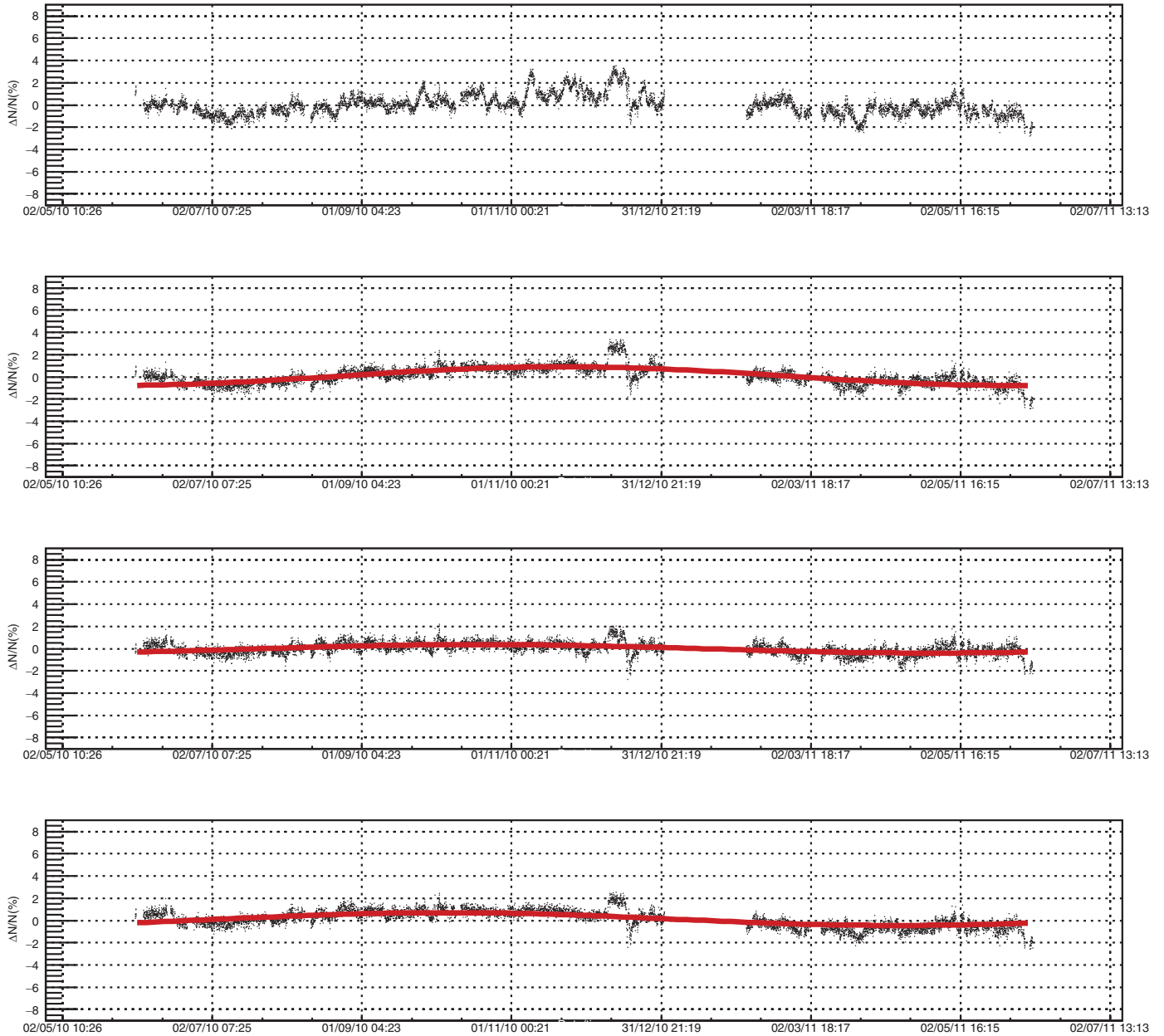


**Fig. 11.** Raw (upper panel), pressure corrected (middle panel), pressure+temperature corrected with PCA method (3rd panel from the top) and pressure+temperature corrected with integral method (lower panel) normalized muon count rate for UL. The sine function with one year period is fitted to the data.

(ground level and at 25 mwe), the method requires correction to five parameters, determined from linear regression. With the same CR dataset, the present method yields results superior to the integral method in terms of variance reduction and reduction of the annual variation. The new method is also suitable for temperature corrections of the neutron monitor data, which is seldom done in practice.

### Acknowledgments

The authors are deeply grateful to Dr. Viktor Yanke for the encouragement and useful advice. The present work was funded by the Ministry of Education, Science and Technological Development of the Republic of Serbia, under the Project no. 171002.

### References

- [1] L. Myssowsky, L. Tuwim, Unregelmäßige intensitätsschwankungen der höhenstrahlung in geringer seehöhe, *Zeitsch. Phys.* 39 (2–3) (1926) 146–150.
- [2] E. Steinke, Über schwankungen und barometereffekt der kosmischen ultrastrahlung im meeresniveau, *Zeitsch. Phys.* 64 (1–2) (1930) 48–63.
- [3] P.M. Blackett, On the instability of the barytron and the temperature effect of cosmic rays, *Phys. Rev.* 54 (11) (1938) 973.
- [4] M. Forro, Temperature effect of cosmic radiation at 1000-m water equivalent depth, *Phys. Rev.* 72 (9) (1947) 868.
- [5] C.M.G. Lattes, G.P. Occhialini, C.F. Powell, Observations on the tracks of slow mesons in photographic emulsions, *Nature* 160 (4067) (1947) 486.
- [6] C.M.G. Lattes, H. Muirhead, G.P. Occhialini, C.F. Powell, Processes involving charged mesons, *Nature* 159 (4047) (1947) 694.
- [7] G. Occhialini, C. Powell, Nuclear disintegrations produced by slow charged particles of small mass, *Nature* 159 (4032) (1947) 186.
- [8] A. Duperier, The meson intensity at the surface of the earth and the temperature at the production level, *Proc. Phys. Soc. Lond. Sect. A* 62 (11) (1949) 684.
- [9] A. Duperier, Temperature of the upper atmosphere and meson production, *Nature* 167 (4243) (1951) 312.

- [10] C. Baker, D. Hall, J. Humble, M. Duldig, Atmospheric correction analysis for the Mawson muon telescopes, in: International Cosmic Ray Conference, 3, 1993, p. 753.
- [11] A. Maghrabi, M. Almutayri, Atmospheric effect on cosmic ray muons at high cut-off rigidity station, *Adv. Astron.* 2016 (2016).
- [12] C.R. Braga, A. Dal Lago, T. Kuwabara, N.J. Schuch, K. Munakata, Temperature effect correction for the cosmic ray muon data observed at the Brazilian Southern Space Observatory in São Martinho da Serra, *J. Phys.* 409 (2013) 012138 IOP Publishing..
- [13] G.C. Castagnoli, M. Dodero, Temperature effect of the muon component underground and pion attenuation length, *Il Nuovo Cimento B* (1965–1970) 51 (2) (1967) 525–534.
- [14] A. Fenton, R. Jacklyn, R. Taylor, Cosmic ray observations at 42 m we underground at hobart, tasmania, *Il Nuovo Cimento* (1955–1965) 22 (2) (1961) 285–295.
- [15] M. Zazyan, M. Ganeva, M. Berkova, V. Yanke, R. Hippler, Atmospheric effect corrections of mustang data, *J. Space Weather Space Clim.* 5 (2015) A6.
- [16] L. Dorman, The temperature effect of the hard component of cosmic rays, *Doklady Akad. Nauk SSSR* 95 (1954).
- [17] E. Feinberg, On the nature of cosmic ray barometric and temperature effects, *DAN SSSR* 53 (5) (1946) 421–424.
- [18] L.I. Dorman, Cosmic ray variations, Technical Report, Foreign Technology Div Wright-Patterson AFB OHIO, 1957.
- [19] K. Maeda, M. Wada, Atmospheric temperature effect upon the cosmic-ray intensity at sea level, *J. Sci. Res. Inst.* 48 (1954).
- [20] V. Dvornikov, Y.Y. Krest'yannikov, A. Sergeev, Determination of the variation of average-mass temperature of the atmosphere by data of cosmic ray intensity, *Geomag. Aeron.* 16 (1976) 923–925.
- [21] V. Yanchukovsky, G.Y. Filimonov, R. Hisamov, Atmospheric variations in muon intensity for different zenith angles, *Bull. Russ. Acad. Sci.* 71 (7) (2007) 1038–1040.
- [22] R. De Mendonça, C. Braga, E. Echer, A. Dal Lago, K. Munakata, T. Kuwabara, M. Kozai, C. Kato, M. Rockenbach, N. Schuch, et al., The temperature effect in secondary cosmic rays (muons) observed at the ground: analysis of the Global MUON Detector Network data, *Astrophys. J.* 830 (2) (2016) 88.
- [23] A. Dmitrieva, I. Astapov, A. Kovylyaeva, D. Pankova, Temperature effect correction for muon flux at the earth surface: estimation of the accuracy of different methods, *J. Phys.* 409 (2013) 012130. IOP Publishing.
- [24] P.H. Barrett, L.M. Bollinger, G. Cocconi, Y. Eisenberg, K. Greisen, Interpretation of cosmic-ray measurements far underground, *Rev. Mod. Phys.* 24 (3) (1952) 133.
- [25] S. Tilav, P. Desiati, T. Kuwabara, D. Rocco, F. Rothmaier, M. Simmons, H. Wising, et al., Atmospheric variations as observed by IceCube, arXiv:1001.0776 (2010).
- [26] P. Adamson, C. Andreopoulos, K. Arms, R. Armstrong, D. Auty, D. Ayres, C. Backhouse, J. Barnett, G. Barr, W. Barrett, et al., Observation of muon intensity variations by season with the Minos far detector, *Phys. Rev. D* 81 (1) (2010) 012001.
- [27] H. Carmichael, M. Bercovitch, J.F. Steljes, Introduction of meteorological corrections into meson monitor data, *Tellus* 19 (1) (1967) 143–160, doi:10.1111/j.2153-3490.1967.tb01468.x.
- [28] M.D. Berkova, A.V. Belov, E.A. Eroshenko, V.G. Yanke, Temperature effect of the muon component and practical questions for considering it in real time, *Bull. Russ. Acad. Sci.* 75 (6) (2011) 820–824, doi:10.3103/S1062873811060086.
- [29] A. Dmitrieva, R. Kokoulin, A. Petrukhin, D. Timashkov, Corrections for temperature effect for ground-based muon hodoscopes, *Astropart. Phys.* 34 (6) (2011) 401–411, doi:10.1016/j.astropartphys.2010.10.013.
- [30] Global forecast system (GFS), <https://www.ncdc.noaa.gov/data-access/modeldata/model-datasets/global-forecast-system-gfs>.
- [31] National centers for environmental prediction (NCEP), <http://www.ncep.noaa.gov/>.
- [32] A. Dragić, V. Udovičić, R. Banjanac, D. Joković, D. Maletić, N. Veselinović, M. Savić, J. Puzović, I.V. Aničin, The new setup in the Belgrade low-level and cosmic-ray laboratory, *Nucl. Technol. Radiat. Protect.* 26 (3) (2011) 181–192.
- [33] B. Haurwitz, The diurnal surface-pressure oscillation, *Arch. Meteorol. Geophys. Bioklimatol. Ser. A* 14 (4) (1965) 361–379, doi:10.1007/BF02253483.
- [34] L.I. Dorman, *Cosmic Rays in the Earth's Atmosphere and Underground*, Springer Netherlands, 2004, doi:10.1007/978-1-4020-2113-8.
- [35] I. Jolliffe, *Principal Component Analysis*, Springer-Verlag, 2002, doi:10.1007/b98835.
- [36] R.W. Preisendorfer, D.M. Curtis, *Principal component analysis in meteorology and oceanography*, Elsevier, Amsterdam, 1988.
- [37] M. Savić, D. Maletić, D. Joković, N. Veselinović, R. Banjanac, V. Udovičić, A. Dragić, Pressure and temperature effect corrections of atmospheric muon data in the belgrade cosmic-ray station, *J. Phys. Conf. Ser.* 632 (1) (2015) 012059.



# Study of gamma ray transitions and level scheme of $^{56}_{25}\text{Mn}$ using the $^{55}_{25}\text{Mn}(n_{th}, 2\gamma)$ reaction

David Knezevic<sup>a,b,\*</sup>, Nikola Jovancevic<sup>b</sup>, Anatoly M. Sukhovoj<sup>c</sup>,  
Aleksandar Dragic<sup>a</sup>, Liudmila V. Mitsyna<sup>c</sup>, Zsolt Revay<sup>d</sup>,  
Christian Stieghorst<sup>d</sup>, Stephan Oberstedt<sup>e</sup>, Miodrag Krmar<sup>b</sup>,  
Ilija Arsenic<sup>f</sup>, Dimitrije Maletic<sup>a</sup>, Dejan Jokovic<sup>a</sup>

<sup>a</sup> University of Belgrade, Institute of Physics Belgrade, Pregrevica 118, 11080 Zemun, Serbia

<sup>b</sup> University of Novi Sad, Faculty of Science, Department of Physics, Trg Dositeja Obradovica 3, 21000 Novi Sad, Serbia

<sup>c</sup> Joint Institute for Nuclear Research, 141980 Moscow region, Dubna, Russia

<sup>d</sup> Technische Universität München, Heinz Maier-Leibnitz Zentrum (MLZ), Lichtenbergstr. 1, D-85747 Garching, Germany

<sup>e</sup> European Commission, Joint Research Centre, Directorate G – Nuclear Safety and Security, Unit G.2, Retieseweg 111, B-2440 Geel, Belgium

<sup>f</sup> University of Novi Sad, Faculty of Agriculture, Trg Dositeja Obradovica 8, 21000 Novi Sad, Serbia

Received 20 May 2019; received in revised form 9 September 2019; accepted 12 September 2019  
Available online 18 September 2019

## Abstract

This work provides new data about the level scheme of  $^{56}_{25}\text{Mn}$  studied by the  $^{55}_{25}\text{Mn}(n_{th}, 2\gamma)$  reaction. The spectroscopic information were collected using the gamma-gamma coincidence spectrometer at the Technische Universität München, Heinz Maier-Leibnitz Zentrum (MLZ), Garching, Germany. The intensities, energies of primary and secondary transitions of 71 energy-resolved cascades, as well as intermediate cascade levels were determined. The updated level scheme of  $^{56}_{25}\text{Mn}$  was obtained from analyzing the intensity spectra of the strongest cascades. The comparison with the existing data in the ENSDF database shows that 23 primary transitions, 24 intermediate cascades levels as well as 32 secondary transitions determined in this work can be recommended as new nuclear data.

© 2019 Published by Elsevier B.V.

\* Corresponding author at: University of Belgrade, Institute of Physics Belgrade, Pregrevica 118, 11080 Zemun, Serbia.  
E-mail addresses: [davidk@ipb.ac.rs](mailto:davidk@ipb.ac.rs) (D. Knezevic), [nikola.jovancevic@df.uns.ac.rs](mailto:nikola.jovancevic@df.uns.ac.rs) (N. Jovancevic).

*Keywords:* Gamma ray spectrometry; Thermal neutron capture; Level scheme; Gamma ray cascades

---

## 1. Introduction

Accurate data about the nuclear level scheme play an important role in the understanding of the nuclear properties. They are necessary for studying nuclear reactions as well as for determining nuclear structure parameters. In this work we chose to study the level scheme of the  $^{56}\text{Mn}$ . For that purpose, we used the two-step gamma-cascade method based on measurements of coincident prompt gamma rays following thermal neutron capture [1–4]. An advantage of this technique is a low Compton background in collected spectra owing to the use of the background-subtraction algorithm [1].

The properties of  $^{56}\text{Mn}$  nucleus have been studied by means of thermal and resonance neutron capture [5–24] but also by other methods, such as the  $^{56}\text{Cr}$   $\beta^-$  decay [25],  $^{48}\text{Ca}(^{11}\text{B}, 3n\gamma)$  [26],  $^{54}\text{Cr}(^3\text{He}, p)$  [27],  $^{54}\text{Cr}(\alpha, d)$  [28],  $^{55}\text{Mn}(d, p)$  [29–32],  $^{56}\text{Fe}(\mu^-, \nu\gamma)$  [33],  $^{56}\text{Fe}(t, ^3\text{He})$  [34],  $^{56}\text{Fe}(^{12}\text{C}, ^{12}\text{N})$  [35,36],  $^{58}\text{Fe}(d, \alpha)$  [37]. The overview of excitation data shows the need for collecting new accurate spectroscopic data on  $^{56}\text{Mn}$ .

In this work, we present new information on the  $^{56}\text{Mn}$  nucleus (levels, gamma ray transition energies and their intensities per capture). The obtained results were compared with the existing ENSDF data [38]. As it is an odd-odd nucleus, the  $^{56}\text{Mn}$  can also be interesting from a theoretical point of view, such as studying the level density and the radiative strength function. Since the two-step gamma ray-cascades method provides the possibility to estimate simultaneously the level density and radiative strength functions, in a future work, these nuclear parameters may be obtained for this nuclei as well, as it was done in [39–44] for other investigated nuclei.

## 2. Experimental setup and measurement

The objective of this experiment was the detection of two-step gamma ray cascades in  $^{56}\text{Mn}$  following thermal neutron capture on  $^{55}\text{Mn}$ ,  $^{55}\text{Mn}(n_{th}, 2\gamma)^{56}\text{Mn}$ . The measurement was carried out at the PGAA station of Technische Universität München, Heinz Maier-Leibnitz Zentrum (MLZ), Garching, Germany [45,46].

The experimental setup consisted of two HPGe detectors with relative efficiencies of 60% and 30%. The distance between detectors was 22.5 cm (this distance is the distance between the detector cap of the 60% detector and the point on the axis of the 30% detector that lies on the line determined by the detector cap of the 60% detector and the position of the sample). Target was placed at 9 cm from the detector with a 30% efficiency (distance measured on the above mentioned line) as shown in Fig. 1. The other detector was surrounded by an active anti-Compton suppression made of bismuth germanate (BGO). The shielding against scattered neutrons consisted of a 1 mm thick boron-containing plastic tube that was built around the detectors. The detector was also surrounded by 10 cm of lead shielding to reduce background gamma ray radiation. The necessary experimental data for the analysis (energy of both detected coincident photons and time difference between their detection) were collected by a N1728B CAEN ADC digitizer. For the mono-isotopic manganese ( $^{55}\text{Mn}$ ) the preparation of a high-purity target for the experiment is considerably easier compared to nuclei of more complex isotopic composition. The target was high-purity (99.9%) natural manganese powder with the mass of 50 mg. The relative efficiency of the detectors was determined from single gamma ray spectra accumulated using a PVC tar-



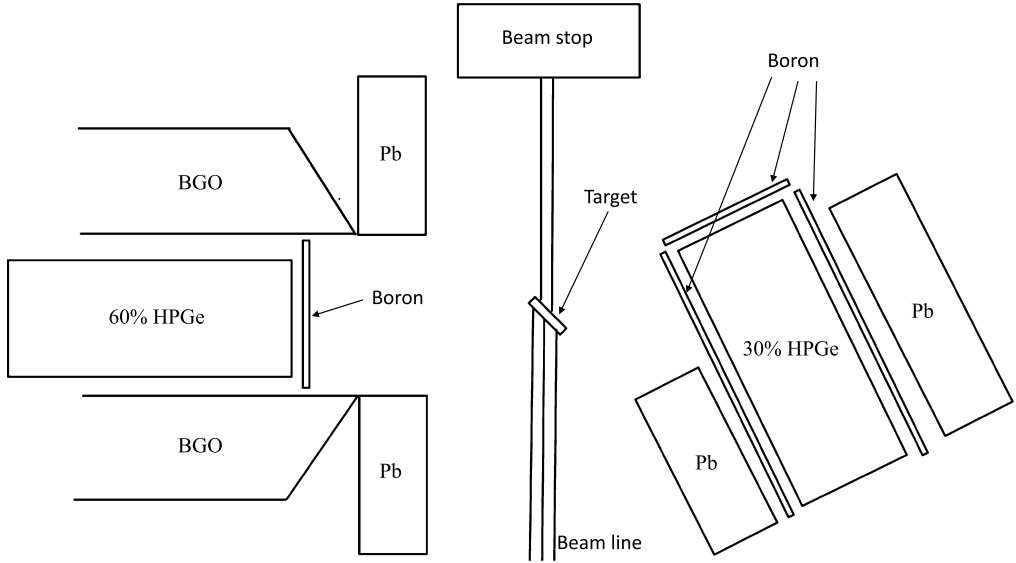


Fig. 1. Sketch of the experimental setup.

get (the  $^{35}\text{Cl}(n,\gamma)^{36}\text{Cl}$  reaction) [47]. For the 30% detector the efficiency curve was  $\ln(\epsilon) = -1.124210 \cdot \ln(E_\gamma) - 2.01161 \cdot \ln(E_\gamma/1022) + 0.453523 \cdot \ln^2(E_\gamma/1022)$ , and for the 60% detector it was  $\ln(\epsilon) = -0.751695 \cdot \ln(E_\gamma) + 0.150324 \cdot \ln(E_\gamma/1022) - 0.177287 \cdot \ln^2(E_\gamma/1022)$ . Manganese two gamma ray events were recorded for 105.6 h.

### 3. Result and discussion

Only a short description of the applied procedure to extract the cascade events and intensities is presented here. The detailed description can be found in Ref. [1].

The most important part of the collected spectrum of sums of amplitudes for coincident pulses (SACP) is shown in Fig. 2. The five marked peaks in Fig. 2 present the two-step cascade peaks of  $^{56}_{25}\text{Mn}$  for transitions from the neutron binding energy (7270.0(5) keV) to the ground state and to the first four excited states with the energies of 26.5, 110.4, 212.0 and 341.0 keV. In Table 1, the core information about these five cascade peaks is presented. The remaining unmarked peaks in the SACP spectrum correspond to background events (Fig. 2). They may come from recording of coincidences of the first with the third or fourth quantum of the multiple-step gamma ray cascades or from neutron interaction with surrounding materials. In Table 1, there is also information about part of the resolved intensity, that represents the fraction of the total intensity (% per decay) observed in the spectra  $E_{\gamma,1} + E_{\gamma,2} = \text{const}$  in the form of pairs of intense energy-resolved peaks in Fig. 3 and Fig. 4. These cascades are observed in the form of pairs of standard peaks. Their intensity is given in column 4 of Table 2 in the form of  $I_{\gamma\gamma}$ . The concept of “part of resolved cascade intensity” is used in further analysis to determine the ratio of the sum of the intensity of only resolved peaks to the total sum of the intensities of all resolved and unresolved cascades. The total sum includes all cascades without exception, primary and secondary transitions that satisfy the rules of selection by multiplicity. The cascades to other spins and multipolarities are impossible to determine in this type of experiment.

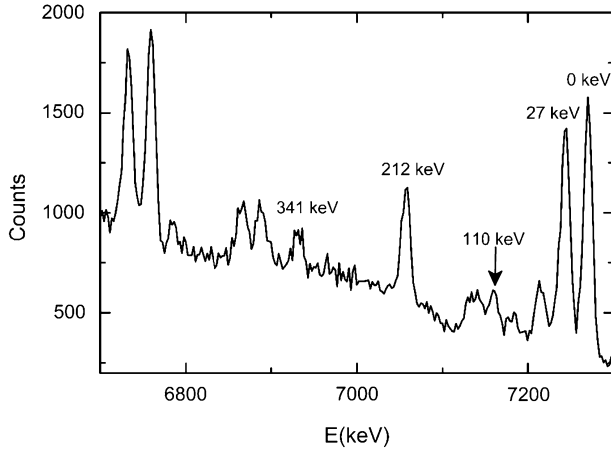


Fig. 2. Spectrum of sums of amplitudes for coincident pulses (SACP) at the radiative capture of thermal neutrons in  $^{55}\text{Mn}$  nucleus. Peaks of the full capture of two quanta are labeled by energy of the final level of the resolved cascades.

Table 1

Information about the two-step cascades to the ground state and the first four excited states collected in the experiment. The spin values of the final levels were taken from [38].

Gamma ray cascade total energy (keV)	Final level ( $E_f$ ) of the cascade (keV)	Spin of level $E_f$	Part of resolved cascade intensity	Full intensities % per decay
7270	0	3+	70(5)	17(3)
7243	26.5	2+	70(7)	13(3)
7160	110.4	1+	51(9)	5.0(10)
7058	212.0	4+	49(5)	16.0(20)
6929	341.0	3+	40(6)	6.0(10)
Sum of total			56(3)	57(5)

From collected SACP spectra the two-step-cascade (TSC) spectra were obtained. This was done for five energy-resolved amplitude peaks. The obtained TSC spectra represent the cascades from the initial state to the defined low-lying final levels of the  $^{56}_{25}\text{Mn}$  nucleus. The elimination of Compton background and random coincidences was done by gating on the region nearby the peaks of interest in Fig. 2. Figs. 3 and 4 show examples of the obtained TSC spectra for cascade total energies of 6929 and 7058 keV. The background in the two-step-cascade (TSC) spectra of mono-isotopic manganese is practically absent.

The mirror-symmetrical peaks [2] in the TSC spectra represent primary and secondary transitions of the investigated two-step gamma ray cascade. The peaks' positions correspond to the energies,  $E_{\gamma,1}$  and  $E_{\gamma,2}$ , of primary and secondary quanta of the cascades. The relative intensity of each peak is proportional to its area. The criteria for selecting if the structure in the TSC spectrum is a peak is based on searching for the peak structures with non zero count across multiple channels, and then verifying the existence of the peak using the fitting procedure. All energy-resolved peaks are approximated by the Gauss function, and the background is approximated by a constant or a weakly varying linear function. The ratio of the area of all peaks to the sum of the spectrum gives the value of the proportion of resolved peaks detected in the experiment. The remainder is a continuum of the unresolved cascades.

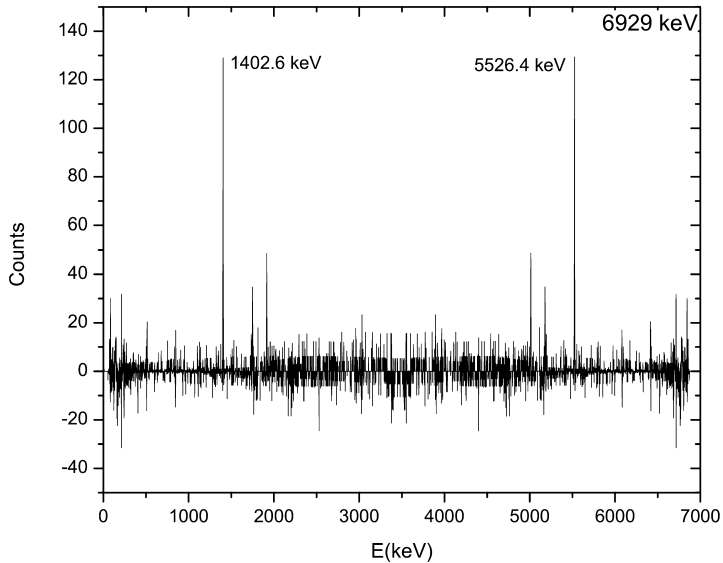


Fig. 3. Two step cascade (TSC) spectrum with the total energy of 6930 keV. The final level of the cascade is 340.957(6) keV (value taken from [38]). This spectrum represents the TSC spectrum with low number of cascades (8 pairs of gamma rays). The energies of the most intense pair of gamma rays are labeled.

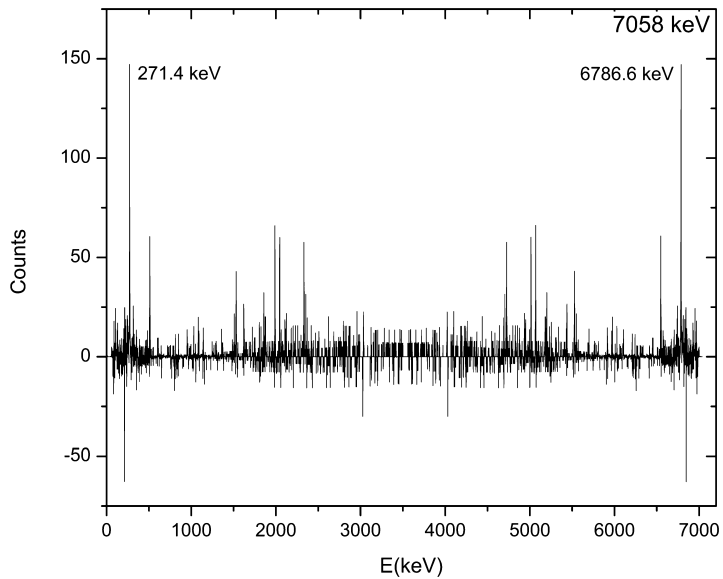


Fig. 4. Two step cascade (TSC) spectrum with the total energy of 7058 keV. The final level of the cascade is 212.004(5) keV (value taken from [38]). This spectrum represents the TSC spectrum with high number of cascades (22 pairs of gamma rays). The energies of the most intense pair of gamma rays are labeled.

Details of the method and the maximum likelihood function used to determine the energies of primary and secondary cascade transitions were presented in [1,4]. The intensities of 71 resolved cascades are determined from five TSC distributions. In all investigated cascades, primary tran-

sitions (except for 7 of them) have the higher energy in comparison with the energy of secondary quanta. All detected primary and secondary gamma ray transitions and their intensities as well as the energies of intermediate levels are presented in Table 2.

In order to compare the data of the cascade spectra (Figs. 3 and 4) with the experimental data for strongest primary transitions with  $E_{\gamma,1}$ =7058, 7160, 6929, 6784, 5527 and 5181 keV, the branching coefficients ( $Br$ ) of their secondary transitions were obtained independently (using existing ENSDF data), which gave data of absolute intensity of the cascades for normalization of the data from Table 2.

The intensities of primary gamma transitions to individual low-lying levels  $i_1$  are generally known. The product  $i_1 \cdot Br$  is the absolute intensity of one of these cascades to the intermediate level. Then, from the proportion with three known values  $i_1$ ,  $i_2$ ,  $i_1 \cdot Br$  and the total sum of the intensity of all transitions of the given stages  $i_{\gamma\gamma} = 100\%$ , we obtain the ratio  $I_{\gamma\gamma} = i_1 \cdot Br \cdot i_1 i_2 / 100$ . It is equal to the sum of  $I_{\gamma\gamma}$  of all two-quantum cascades (resolved and unresolved energetically for the cascade with the corresponding finite level). The values of the total intensity  $I_{\gamma\gamma}$  obtained in such a way (Table 1), which include both the resolved cascades and unresolved cascade continuum with sub-threshold intensity, show that, for the investigated nucleus, we have obtained in this experiment 57% of total intensity of all two-step cascades. At that, 56% of this intensity  $I_{\gamma\gamma}$  falls to the share of the energy-resolved cascades (Table 2).

The data were compared with the existing ones in the ENSDF database [38]. From this comparison, 22 primary transitions that existed in the ENSDF data set were determined. 23 primary transitions, which are not included in the ENSDF library, can be therefore recommended as new data. 21 intermediate levels are identified in our experiment and already listed in the ENSDF database. However, for 24 levels observed in this study, there are no data in the ENSDF library yet. The difference between number of primary gamma rays and levels comes from the fact that in some cases, as is the case of gamma ray with energy (database value [38]) 5432.9 keV, that is identified as primary gamma-ray corresponding to experimental value of 5431.5 keV, gamma-rays exist in the database, but do not have a scheme position assigned to them, so the authors tentatively assigned the scheme position for a number of gamma rays as the primary gamma rays of the cascades. Same is the case for gamma ray with energies (database values [38]) 6019.2, 4324.1 and 3034.1 keV. In this work, we observed 32 secondary gamma ray transitions for which there is no information in the ENSDF database. 14 of these new observed secondary transitions come from the levels already in the ENSDF library, and 18 from levels determined for the first time in this work. Also, 11 secondary gamma rays observed in this study are listed in the ENSDF database, but do not have an assigned position in the decay scheme. In this paper we assigned the decay scheme positions for gamma rays with energies (database values [38]) of 1140.4, 2147.3, 2437.8, 2582.0, 2864.4, 2832.9, 2740.3, 2937.6, 3135.6, 4127.7 and 4024.5 keV.

The comparison of determined energies of levels and gamma rays with the ones from the ENSDF database shows an average deviation of about 1.5 keV. For levels and gamma rays where the deviation was larger than 2 keV, ENSDF values were in some cases assigned tentatively by the authors. This relatively large discrepancy can be explained by insufficient statistics in the present TSC spectra, as well as by the keV/Ch difference between the two detectors during measurement, which can cause uncertainty in the determination of the energy.

The level scheme of  $^{56}_{25}\text{Mn}$  obtained in this work is presented in Figs. 5 and 6.

Spin of the neutron capture level is determined by the ground state spin of the capturing nuclei  $\pm$  the 1/2 spin of the neutron. This state decays primarily via dipole transition, predominantly of electric multipolarity. As the compound-state of  $^{55}_{25}\text{Mn}$  is  $5/2^-$ , after a capture of a thermal neutron primary gamma ray transitions can be emitted from the decay of levels with spins  $2^-$  or

Table 2

Comparison of the experimental data with the ENSDF database.  $E_{\gamma,1}$  and  $E_{\gamma,2}$  are the energies of the first and second quanta of the cascade, respectively,  $E_i$  is the energy of the intermediate level and  $E_f$  are the final levels of the two step gamma ray cascade.  $I_{\gamma\gamma}$  is the intensity of the cascade (per 100 decays) observed in the experiment. The experimental uncertainty of  $E_{\gamma,2}$  has the same absolute values as for  $E_{\gamma,1}$  (listed in the table). Values in bold are values for which there is no data in the ENSDF library.

Present work				ENSDF			
$E_{\gamma,1}$ (keV)	$E_{\gamma,2}$ (keV)	$E_i$ (keV)	$I_{\gamma\gamma}$	$E_f$ (keV)	$E_{\gamma,1}$ (keV)	$E_{\gamma,2}$ (keV)	$E_i$ (keV)
7160.6(3)	82.9	109.0(6)	4.8(6)	26.516(3)	7159.7(2)	83.8990(15)	110.428(3)
7058.80(21)	211.20	211.2(5)	9.2(8)	g.s.	7057.8(2)	212.017(6)	212.004(5)
<b>7053.1(13)</b>	106.5	216.9(14)	0.9(4)	110.428(3)	–	104.6234(20)	215.057(3)
6925.1(12)	344.9	344.9(13)	0.10(5)	g.s.	6928.7(2)	340.990(25)	340.957(6)
6929.9(6)	313.6	340.1(8)	1.3(4)	26.516(3)	6928.7(2)	314.395(10)	340.957(6)
6786.6(7)	271.4	483.4(9)	1.3(4)	212.004(5)	6783.3(2)	271.175(9)	486.251(8)
6786.6(17)	142.4	483.4(18)	0.22(15)	340.957(6)	6783.3(2)	145.320(20)	486.251(8)
<b>6733.0(8)</b>	<b>510.5</b>	<b>537.0(9)</b>	0.55(17)	26.516(3)	–	–	–
<b>6699.7(27)</b>	229.3	<b>570.3(27)</b>	0.15(17)	340.957(6)	–	229.867(7)	–
6101.8(12)	1141.7	1168.2(13)	0.25(16)	26.516(3)	6103.9(2)	1140.4(10)	1166.54(21)
6101.8(9)	<b>1057.8</b>	1168.2(10)	0.16(5)	110.428(3)	6103.9(2)	–	1166.54(21)
6101.8(14)	<b>956.2</b>	1168.2(15)	0.09(4)	212.004(5)	6103.9(2)	–	1166.54(21)
6021.8(20)	<b>1221.7</b>	<b>1248.2(21)</b>	0.08(6)	26.516(3)	6019.2(8)	–	–
5919.4(15)	<b>1324.1</b>	1350.6(16)	0.18(11)	26.516(3)	5920.5(2)	–	1349.95(21)
<b>5916.7(13)</b>	<b>1141.3</b>	<b>1353.3(14)</b>	0.08(4)	212.004(5)	–	–	–
<b>5789.8(27)</b>	<b>1453.7</b>	<b>1480.2(27)</b>	0.09(8)	26.516(3)	–	–	–
5759.7(4)	<b>1510.3</b>	1510.3(6)	0.79(14)	g.s.	5760.9(2)	–	1509.55(21)
5759.7(13)	<b>1298.3</b>	1510.3(14)	0.07(3)	212.004(5)	5760.9(2)	–	1509.55(21)
5759.7(17)	1169.3	1510.3(18)	0.034(24)	340.957(6)	5760.9(2)	1169.71(13)	1509.55(21)
<b>5547.5(10)</b>	<b>1510.5</b>	<b>1722.5(11)</b>	0.10(4)	212.004(5)	–	–	–
5526.4(13)	1717.1	1743.6(14)	0.12(8)	26.516(3)	5527.4(2)	1716.63(14)	1744.3(10)
5526.4(5)	<b>1531.6</b>	1743.6(7)	0.46(8)	212.004(5)	5527.4(2)	–	1744.3(10)
5526.4(6)	1402.6	1743.6(8)	0.82(24)	340.957(6)	5527.4(2)	1401.7(10)	1744.3(10)
5438.7(12)	<b>1720.9</b>	1831.3(13)	0.07(3)	110.428(3)	5437.0(2)	–	1833.67(21)
5438.7(16)	<b>1619.3</b>	1831.3(17)	0.08(5)	212.004(5)	5437.0(2)	–	1833.67(21)
5431.5(24)	<b>1626.5</b>	<b>1838.5(25)</b>	0.10(7)	212.004(5)	5432.9(2)	–	–
<b>5313.6(16)</b>	<b>1956.4</b>	<b>1956.4(17)</b>	0.07(5)	g.s.	–	–	–
<b>5270.3(11)</b>	<b>1889.3</b>	<b>1999.7(12)</b>	0.17(7)	110.428(3)	–	–	–
<b>5250.8(16)</b>	2019.2	2019.2(17)	0.13(8)	g.s.	–	2016.5(2)	2016.39(15)
<b>5201(3)</b>	2042.5	<b>2069(3)</b>	0.12(11)	26.516(3)	–	2044.7(2)	–
5197.8(14)	<b>1961.8</b>	2072.2(15)	0.08(4)	110.428(3)	5199.1(2)	–	2071.39(15)
5197.8(11)	<b>1860.2</b>	2072.2(12)	0.17(9)	212.004(5)	5199.1(2)	–	2071.39(15)
<b>5182.7(11)</b>	2060.8	<b>2087.3(12)</b>	0.46(23)	26.516(3)	–	2063.2(2)	–
5180.6(7)	2089.7	2089.7(9)	0.54(10)	g.s.	5181.6(2)	2090.4(2)	2089.38(15)
5180.6(17)	1877.7	2089.7(18)	0.18(9)	212.004(5)	5181.6(2)	1876.2(10)	2089.38(15)
5180.6(7)	1748.7	2089.7(9)	0.49(14)	340.957(6)	5181.6(2)	1747.0(10)	2089.38(15)
<b>5064.4(13)</b>	2179.1	2205.6(14)	0.40(20)	26.516(3)	–	2176.6(2)	2202.73(15)
<b>5064.4(16)</b>	<b>1993.6</b>	2205.6(17)	0.22(12)	212.004(5)	–	–	2202.73(15)
<b>5030.8(23)</b>	<b>2128.8</b>	2239.2(24)	0.07(5)	110.428(3)	–	–	2235.14(21)
5013.5(9)	2044.5	2256.5(10)	0.26(13)	212.004(5)	5015.0(2)	2044.7(2)	2255.24(15)
5013.5(5)	1915.5	2256.5(7)	0.5(11)	340.957(6)	5015.0(2)	1915.2(10)	2255.24(15)
4950.9(12)	2292.6	2319.1(13)	0.31(14)	26.516(3)	4949.4(2)	2294.8(2)	2321.15(10)
4950.9(14)	2208.7	2319.1(15)	0.12(7)	110.428(3)	4949.4(2)	2211.3(2)	2321.15(10)
4907.4(11)	2252.2	2362.6(12)	0.12(7)	110.428(3)	4907.9(2)	2254.8(2)	2362.62(21)
4907.4(11)	2150.6	2362.6(12)	0.054(22)	212.004(5)	4907.9(2)	2147.3(2)	2362.62(21)

(continued on next page)

Table 2 (continued)

Present work				ENDSDF			
$E_{\gamma,1}$ (keV)	$E_{\gamma,2}$ (keV)	$E_i$ (keV)	$I_{\gamma\gamma}$	$E_f$ (keV)	$E_{\gamma,1}$ (keV)	$E_{\gamma,2}$ (keV)	$E_i$ (keV)
4831.9(13)	2438.1	2438.1(14)	0.23(11)	g.s.	4829.7(2)	2437.8(2)	2441.27(15)
4831.9(25)	2327.7	2438.1(25)	0.10(7)	110.428(3)	4829.7(2)	2331.2(2)	2441.27(15)
<b>4730.2(14)</b>	<b>2539.8</b>	<b>2539.0(15)</b>	0.14(10)	g.s.	–	–	–
4726.3(5)	2331.7	2543.7(7)	0.64(12)	212.004(5)	4725.0(2)	2331.2(2)	2545.65(20)
<b>4659(3)</b>	2584	<b>2611(3)</b>	0.17(26)	26.516(3)	–	2582.0(2)	–
4551.1(19)	<b>2506.9</b>	2718.9(20)	0.07(5)	212.004(5)	4550.6(2)	–	2719.96(21)
4379.0(14)	2864.5	2891.0(15)	0.15(11)	26.516(3)	4381.0(2)	2864.4(2)	2889.57(21)
<b>4341.3(16)</b>	<b>2716.7</b>	<b>2928.7(17)</b>	0.09(5)	212.004(5)	–	–	–
4325.1(22)	2834.5	<b>2944.9(23)</b>	0.05(4)	110.428(3)	4324.1(2)	2832.9(2)	–
4317.7(20)	2740.3	2952.3(21)	0.06(5)	212.004(5)	4319.5(2)	2740.3(8)	2951.07(21)
<b>4263.3(16)</b>	3006.9	<b>3006.9(17)</b>	0.17(10)	g.s.	–	3003.4(2)	–
<b>4263.3(23)</b>	<b>2794.9</b>	<b>3006.9(24)</b>	0.06(4)	212.004(5)	–	–	–
4224.5(16)	3045.5	3045.5(17)	0.19(10)	g.s.	4223.5(2)	3047.5(2)	3047.34(15)
4224.5(14)	2935.1	3045.5(15)	0.09(5)	110.428(3)	4223.5(2)	2937.6(8)	3047.34(15)
<b>4134.8(22)</b>	3135.2	<b>3135.2(23)</b>	0.16(10)	g.s.	–	3135.6(2)	–
<b>3879(4)</b>	<b>3391</b>	<b>3391(4)</b>	0.07(9)	g.s.	–	–	–
3871.6(14)	3057.4	3398.4(15)	0.09(5)	340.957(6)	3873.0(2)	3058.2(2)	3397.61
3751.1(13)	<b>3408.5</b>	3518.9(14)	0.22(10)	110.428(3)	3752.3(2)	–	3518.32(21)
<b>3592.8(14)</b>	<b>3465.2</b>	<b>3677.2(15)</b>	0.12(6)	212.004(5)	–	–	–
3035.0(11)	4124.6	<b>4235.0(12)</b>	0.20(7)	110.428(3)	3034.1(2)	4127.7(8)	–
3035.0(20)	4023.0	<b>4235.0(21)</b>	0.13(9)	212.004(5)	3034.1(2)	4024.5(10)	–
3035.0(17)	<b>3894.0</b>	<b>4235.0(18)</b>	0.13(7)	340.957(6)	3034.1(2)	–	–
<b>2959.5(14)</b>	<b>4200.1</b>	<b>4310.5(15)</b>	0.06(3)	110.428(3)	–	–	–
<b>2959(5)</b>	<b>4098</b>	<b>4311(5)</b>	0.05(6)	212.004(5)	–	–	–
<b>2588(3)</b>	<b>4571</b>	<b>4682(3)</b>	0.08(10)	110.428(3)	–	–	–
<b>2179.7(9)</b>	<b>4878.3</b>	<b>5090.3(10)</b>	0.12(4)	212.004(5)	–	–	–

$3^-$ , exciting the levels with spins from  $J=1$  to  $J=4$ . Cross section for the neutron resonance with a spin of  $2^-$  is 8.36 b, for spin  $3^-$  this cross section is 3.57 b, and for boundary resonance with cross section of 1.39 b, the spin is unknown [22]. Spin interval for the nuclear levels that are excited by secondary transitions of the cascade is from  $J=0$  to  $J=5$ . Such limitation on the possible values of spins is due to decay of excited nucleus by mainly dipole E1- and M1-transitions, at least, if cascade energy is larger than 6930 MeV. Cascades of less total energy with  $\Delta J=3$  were not observed in our experiment. A contribution of quadrupole gamma ray transitions to the total gamma ray spectrum is negligible.

Insufficient resolution of HPGe-detectors did not allow to uncouple the two-step cascades to doublets of final levels 212.026/215.128 keV and 335.529/340.989 keV. But small shift of average of total-energy sum of these doublets (7058 and 6934 keV) give us the reason to think that cascades to the final levels with the energies of 212 and 340 keV and corresponded to them spins  $4^+$  and  $3^+$  are dominated in the decay scheme.

#### 4. Conclusion

In this paper, new spectroscopic information was obtained for  $^{56}_{25}\text{Mn}$  by investigating two-step gamma ray cascades following thermal-neutron capture on  $^{55}_{25}\text{Mn}$ . The level scheme and gamma ray transitions for the  $^{56}_{25}\text{Mn}$  nucleus were obtained. The data show good agreement with the ones from the ENSDF library. 24 new levels were observed with 23 new primary and 32 secondary

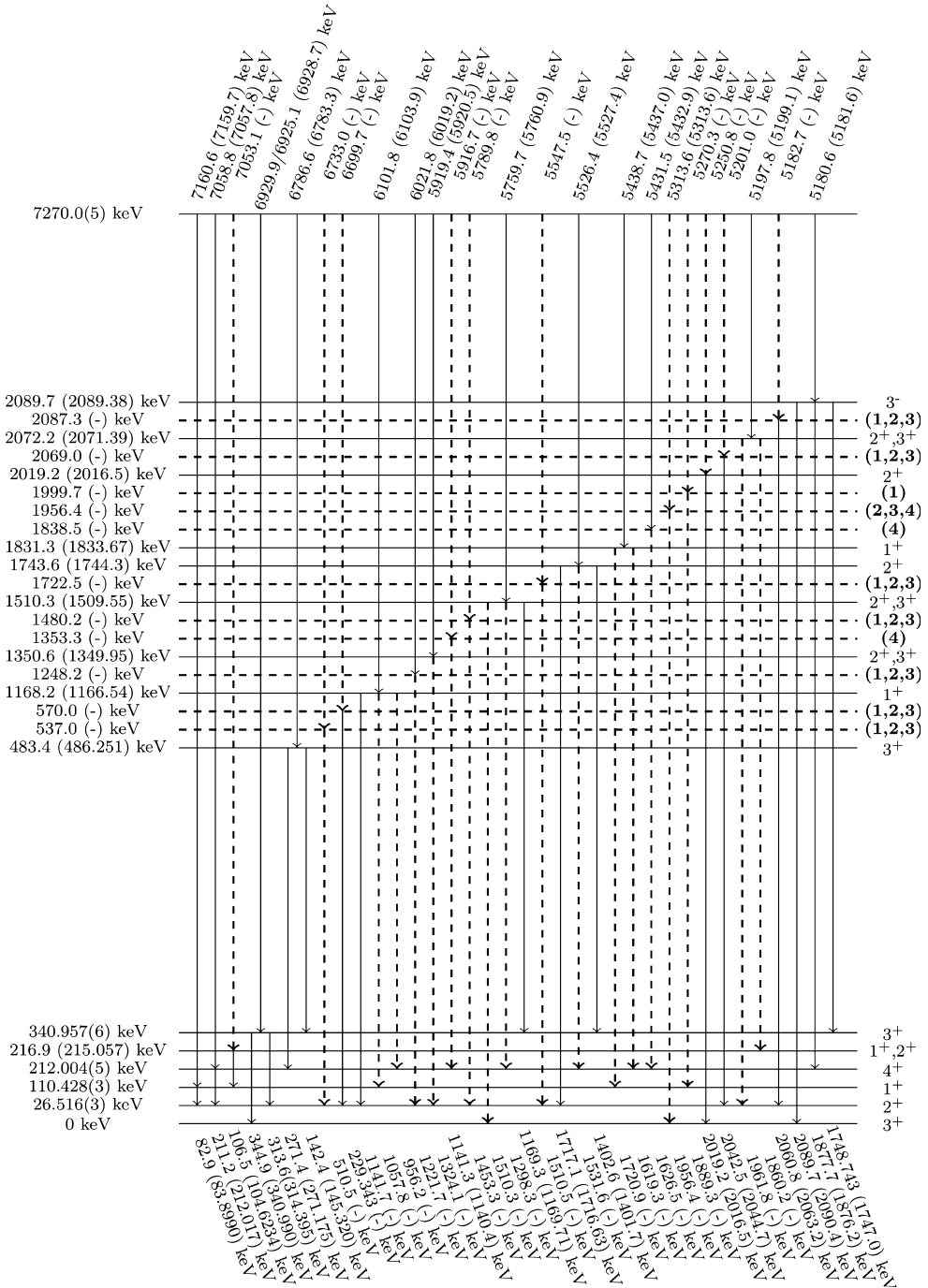


Fig. 5. Experimental level scheme of  $^{56}_{25}\text{Mn}$  with intermediate level energies up to 2100 keV. Dashed lines – levels and gamma rays not found in the ENSDF library; bold spin values – values suggested by the authors for the levels without spin information in the ENSDF library. All energy values, except the energy values for the first 4 low-lying levels are given in the form: Experimental value(ENSDF value).

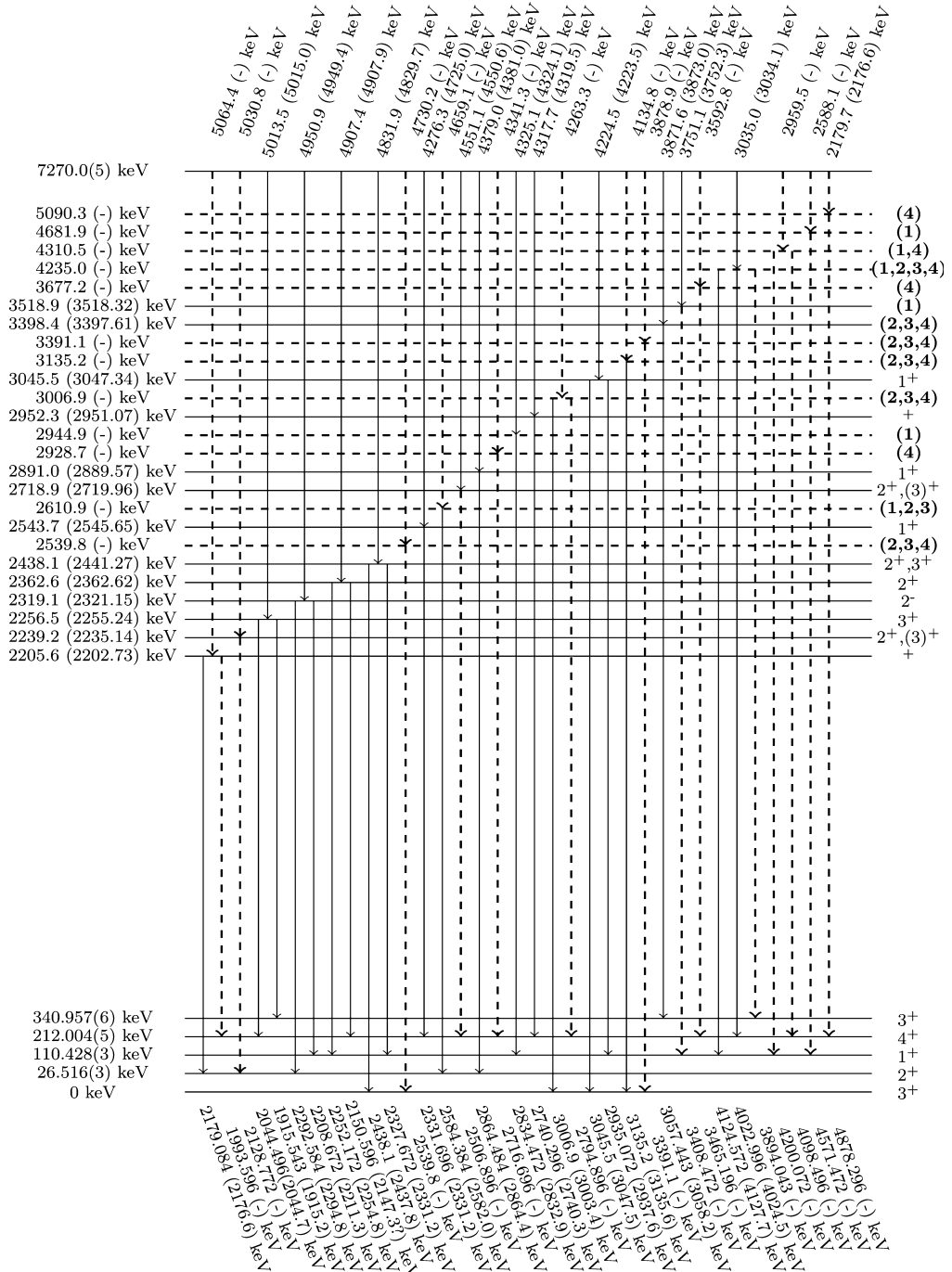


Fig. 6. Experimental level scheme of  $^{56}_{25}\text{Mn}$  with intermediate level energies from 2200 to 5100 keV. Dashed lines – levels and gamma rays not found in the ENSDF library; bold spin values – values suggested by the authors for the levels without spin information in the ENSDF library. All energy values, except the energy values for the first 4 low-lying levels are given in the form: Experimental value(ENSDF value).



gamma ray transitions in the energy range between 0.3 MeV and 7.1 MeV. These new results can be useful for future investigations of nuclear structure parameters such as the nuclear level density and radiative strength function.

## Acknowledgement

The authors gratefully acknowledge the financial support provided by the FRM II to perform the experiment at the Heinz Maier-Leibnitz Zentrum (MLZ), Garching, Germany.

## References

- [1] S. Boneva, E. Vasil'eva, Y.P. Popov, A. Sukhovoï, V. Khitrov, Two-quantum cascades of radiative neutron capture I. Spectroscopy of excited states of complex nuclei in the neutron binding energy region, *Sov. J. Part. Nucl.* 22 (2) (1991) 232–248 (English Translation).
- [2] Y.P. Popov, A. Sukhovoï, V. Khitrov, Y.S. Yazvitskij, Study on the  $\gamma$  decay of  $^{165}\text{Dy}$  with the help of the  $(n, 2\gamma)$  reaction, *Izv. Akad. Nauk SSSR, Ser. Fiz.* 48 (5) (1984) 891–900.
- [3] A. Sukhovoï, V. Khitrov, Method of improving the amplitude resolution of the spectra of gamma-transition cascades in the computer processing of encoded coincidence data, *Instrum. Exp. Tech.* 27 (5) (1985) 1071–1074.
- [4] E. Vasilieva, A. Sukhovoï, V. Khitrov, Direct experimental estimate of parameters that determine the cascade gamma decay of compound states of heavy nuclei, *Phys. At. Nucl.* 64 (2) (2001) 153–168.
- [5] R.W. Bauer, M. Deutsch, Nuclear orientation of Mn-56, *Phys. Rev.* 117 (2) (1960) 519.
- [6] S. Du Toit, L. Bollinger, Lifetimes of energy levels in Al-28, Mn-56, Cu-64, Rh-104, and I-128 excited by slow neutron capture, *Phys. Rev.* 123 (2) (1961) 629.
- [7] I. Estulin, A. Melioransky, L. Kalinkin, Transitions between low-lying excited states of Mn-54 and Ho-166, *Nucl. Phys.* 24 (1) (1961) 118–125.
- [8] P. Carlos, H. Nifenecker, J. Fagot, J. Matuszek, Étude de cascades  $\gamma$ — $\gamma$  dans la capture thermique de neutrons par les isotopes  $^{55}\text{Mn}$ ,  $^{56}\text{Fe}$ ,  $^{59}\text{Co}$ ,  $^{199}\text{Hg}$ , *J. Phys.* 25 (11) (1964) 957–960.
- [9] L. Hughes, T. Kennett, W. Prestwich, A study of the  $^{55}\text{Mn}(n, \gamma)^{56}\text{Mn}$  reaction, *Nucl. Phys.* 80 (1) (1966) 131–144.
- [10] D. Dorioman, M. Popa, M. Cristu, Gamma Rays from Thermal Neutron Capture in Manganese, Germanium, and Iridium Nuclei, *Tech. Rep., Inst. of Atomic Physics, Bucharest*, 1967.
- [11] R. Alves, J. Kuchly, J. Julien, C. Samour, J. Morgenstern, Capture radiative partielle des neutrons de résonance dans le chlore, le manganèse, le fer, le cuivre, le thulium et le mercure, *Nucl. Phys. A* 135 (2) (1969) 241–280.
- [12] J. Kopecký, E. Warming, Circular polarization measurements with a Ge (Li) detector, *Nucl. Phys. A* 127 (2) (1969) 385–398.
- [13] J. Mellema, H. Postma, Investigation of nuclear level spins of  $^{56}\text{Mn}$  by means of nuclear orientation, *Nucl. Phys. A* 154 (2) (1970) 385–406.
- [14] V. Orphan, N.C. Rasmussen, T. Harper, Line and Continuum Gamma-Ray Yields from Thermal-Neutron Capture in 75 Elements, *Tech. Rep., Gulf Energy And Environmental Systems INC San Diego CA*, 1970.
- [15] J. Boulter, W. Prestwich, Lifetimes of the 26 and 110 keV levels in  $^{56}\text{Mn}$ , *Can. J. Phys.* 49 (23) (1971) 2911–2916.
- [16] P. Van Assche, H. Baader, H. Koch, B. Maier, U. Gruber, O. Schult, J. McGrory, J. Comfort, R. Rimawi, R. Chrien, et al., Energy levels of  $^{56}\text{Mn}$ , *Nucl. Phys. A* 160 (2) (1971) 367–384.
- [17] F. Stecher-Rasmussen, K. Abrahams, J. Kopecky, W. Ratynski, Circular polarization of neutron-capture gamma-rays from Mn, Ni, Ga and W, *Nucl. Phys. A* 1 (1972) 250.
- [18] H. Börner, O. Schult, Resonance neutron capture in  $^{55}\text{Mn}$  and levels in  $^{56}\text{Mn}$ , *Z. Naturforsch. A* 29 (3) (1974) 385–388.
- [19] A. Colenbrander, T. Kennett, An investigation of the reaction  $^{55}\text{Mn}(n, \gamma)^{56}\text{Mn}$ , *Can. J. Phys.* 53 (3) (1975) 236–250.
- [20] P. Delheij, K. Abrahams, W. Huiskamp, H. Postma, The  $^{55}\text{Mn}(n, \gamma)^{56}\text{Mn}$  reaction studied with polarized neutrons and polarized manganese nuclei, *Nucl. Phys. A* 341 (1) (1980) 45–55.
- [21] M. Islam, T. Kennett, S. Kerr, W. Prestwich, A self-consistent set of neutron separation energies, *Can. J. Phys.* 58 (2) (1980) 168–173.
- [22] S. Mughabghab, *Neutron Cross Sections: Neutron Resonance Parameters and Thermal Cross Sections, Part A: Z=1-60, vol. 1*, Elsevier, 2012.
- [23] R. Macklin, Resonance neutron capture by manganese below 2.5 keV, *Nucl. Sci. Eng.* 89 (4) (1985) 362–365.

- [24] A. Wapstra, G. Audi, The 1983 atomic mass evaluation: (i). atomic mass table, Nucl. Phys. A 432 (1) (1985) 1–54.
- [25] B. Dropesky, A. Schardt, T. Shull, Note on the decay of the new nuclide Cr-56, Nucl. Phys. 16 (2) (1960) 357–359.
- [26] A.M. Nathan, J.W. Olness, E.K. Warburton, J.B. McGrory, Yrast decay schemes from heavy ion +  $^{48}\text{Ca}$  fusion-evaporation reactions. i.  $^{54-56}\text{Mn}$ ,  $^{56}\text{Cr}$ , and  $^{52-53}\text{V}$ , Phys. Rev. C 16 (1977) 192–214, <https://doi.org/10.1103/PhysRevC.16.192>.
- [27] T. Caldwell, D. Pullen, T. Mulligan, O. Hansen, ( $\tau$ , p) reactions on Cr. ii.  $^{54}\text{Cr}$  ( $\tau$ , p),  $^{56}\text{Mn}$ , Tech. Rep., Univ. of Pennsylvania, Philadelphia, 1971.
- [28] U. Fister, R. Jahn, P. von Neumann-Cosel, P. Schenk, T. Trelle, D. Wenzel, U. Wienands, Stretched proton-neutron configurations in fp-shell nuclei:(i). experimental results of the ( $\alpha$ , d) reaction, Nucl. Phys. A 569 (3) (1994) 421–440.
- [29] J. Green, A. Smith, W. Buechner, M. Mazari, Excited states in Mn 56, Phys. Rev. 108 (3) (1957) 841.
- [30] J. Bjerregaard, P. Dahl, O. Hansen, G. Sidenius, Energy levels from (p, p'), (d, p) and (d,  $\alpha$ ) reactions on the stable isotopes between Sc-45 and Ni-58, Nucl. Phys. 51 (1964) 641–666.
- [31] J.R. Comfort, Nuclear structure of manganese-56, Phys. Rev. 177 (4) (1969) 1573.
- [32] A. Garcia, A. Lopez, F. Senent, The  $^{55}\text{Mn}$  (d, p)  $^{56}\text{Mn}$  reaction, An. Fis. 67 (1971) 181.
- [33] D.F. Measday, T.J. Stocki,  $\gamma$  rays from muon capture in natural Ca, Fe, and Ni, Phys. Rev. C 73 (4) (2006) 045501.
- [34] F. Ajzenberg-Selove, R.E. Brown, E.R. Flynn, J.W. Sunier, ( $t$ ,  $^3\text{He}$ ) reactions on  $^{56}\text{Fe}$ ,  $^{58}\text{Fe}$ , and  $^{58}\text{Ni}$ , Phys. Rev. C 31 (1985) 777–786, <https://doi.org/10.1103/PhysRevC.31.777>.
- [35] N. Anantaraman, S.M. Austin, J. Winfield, Heavy ion reactions as probes for spin strength, Nucl. Phys. A 482 (1–2) (1988) 331–342.
- [36] S. Albergo, S. Costa, R. Potenza, J. Romanski, C. Tuvé, L. Jarczyk, B. Kamys, A. Magiera, A. Strzalkowski, R. Barna, V. D'Amico, D. De Pasquale, G. Mannino, Elastic transfer in the  $^{11}\text{B}+^{12}\text{C}$  system in the c.m. energy range 5–40 MeV, Phys. Rev. C 43 (1991) 2704–2710, <https://doi.org/10.1103/PhysRevC.43.2704>.
- [37] H. Kelleter, D. Bachner, B. Schmidt, W. Seliger, Level investigation by means of the (d,  $\alpha$ ) reaction (ii).  $^{52}\text{Mn}$  and  $^{56}\text{Mn}$ , Nucl. Phys. A 183 (3) (1972) 509–522.
- [38] H. Junde, H. Su, Y. Dong, Nuclear data sheets for A=56, Nucl. Data Sheets 112 (6) (2011) 1513–1645.
- [39] V. Khitrov, A. Sukhovoij, New technique for a simultaneous estimation of the level density and radiative strength functions of dipole transitions at  $E_{ex} < B_n - 0.5$  MeV, arXiv preprint, arXiv:nucl-ex/0110017.
- [40] A. Sukhovoij, L. Mitsyna, N. Jovancevic, Overall picture of the cascade gamma decay of neutron resonances within a modified practical model, Phys. At. Nucl. 79 (3) (2016) 313–325.
- [41] D. Vu, A. Sukhovoij, L. Mitsyna, S. Zeinalov, N. Jovancevic, D. Knezevic, M. Krmar, A. Dragic, Representation of radiative strength functions within a practical model of cascade gamma decay, Phys. At. Nucl. 80 (2) (2017) 237–250.
- [42] A. Sukhovoij, New model of the cascade gamma decay of neutron resonances for practitioners: basic concepts and attainable precision, Phys. At. Nucl. 78 (2) (2015) 230–245.
- [43] A.M. Sukhovoij, L.V. Mitsyna, The next-generation practical model of the cascade gamma-decay of neutron resonance and expected parameters for an arbitrary nucleus, in: Proceedings, 22nd International Seminar on Interaction of Neutrons with Nuclei: Fundamental Interactions and Neutrons, Nuclear Structure, Ultracold Neutrons, Related Topics (ISINN 22), Dubna, Russia, May 27–30, 2014, 2015.
- [44] S. Boneva, V. Khitrov, A. Sukhovoij, A. Vojnov, Excitation study of high-lying states of differently shaped heavy nuclei by the method of two-step cascades, Nucl. Phys. A 589 (2) (1995) 293–306.
- [45] Z. Revay, PGAA: Prompt gamma and in-beam neutron activation analysis facility, J. Large-Scale Res. Fac. JLSRF 1 (2015) 20.
- [46] Z. Révay, P. Kudějová, K. Kleszcz, S. Söllradl, C. Genreith, In-beam activation analysis facility at MLZ, Garching, Nucl. Instrum. Methods Phys. Res., Sect. A, Accel. Spectrom. Detect. Assoc. Equip. 799 (2015) 114–123.
- [47] B. Krusche, K. Lieb, H. Daniel, T. Von Egidy, G. Barreau, H. Börner, R. Brissot, C. Hofmeyr, R. Rascher, Gamma ray energies and  $^{36}\text{Cl}$  level scheme from the reaction  $^{35}\text{Cl}(n, \gamma)$ , Nucl. Phys. A 386 (2) (1982) 245–268.

PAPER • OPEN ACCESS

# Track reconstruction and matching between emulsion and silicon pixel detectors for the SHiP-charm experiment

To cite this article: The SHiP Collaboration *et al* 2022 *JINST* 17 P03013

View the [article online](#) for updates and enhancements.

You may also like

- [A new calibration method for charm jet identification validated with proton-proton collision events at  \$s = 13\$  TeV](#)  
The CMS collaboration, Armen Tumasyan, Wolfgang Adam et al.
- [Identification of hadronic tau lepton decays using a deep neural network](#)  
A. Tumasyan, W. Adam, J.W. Andrejkovic et al.
- [The ATLAS Fast Tracker system](#)  
The ATLAS collaboration, G. Aad, B. Abbott et al.



The Electrochemical Society  
Advancing solid state & electrochemical science & technology

## 242nd ECS Meeting

Oct 9 – 13, 2022 • Atlanta, GA, US

Presenting more than 2,400  
technical abstracts in 50 symposia



ECS Plenary Lecture  
featuring  
**M. Stanley Whittingham**,  
Binghamton University  
Nobel Laureate –  
2019 Nobel Prize in Chemistry



Register now!



# Track reconstruction and matching between emulsion and silicon pixel detectors for the SHiP-charm experiment



## The SHiP Collaboration

C. Ahdida,<sup>45</sup> A. Akmete,<sup>49</sup> R. Albanese,<sup>15,d,h</sup> J. Alt,<sup>7</sup> A. Alexandrov,<sup>15,33,35,d</sup> A. Anokhina,<sup>40</sup>  
 S. Aoki,<sup>19</sup> G. Arduini,<sup>45</sup> E. Atkin,<sup>39</sup> N. Azorskiy,<sup>30</sup> J.J. Back,<sup>55</sup> A. Bagulya,<sup>33</sup>  
 F. Baaltasar Dos Santos,<sup>45</sup> A. Baranov,<sup>41</sup> F. Bardou,<sup>45</sup> G.J. Barker,<sup>55</sup> M. Battistin,<sup>45</sup>  
 J. Bauche,<sup>45</sup> A. Bay,<sup>47</sup> V. Bayliss,<sup>52</sup> G. Bencivenni,<sup>16</sup> A.Y. Berdnikov,<sup>38</sup> Y.A. Berdnikov,<sup>38</sup>  
 M. Bertani,<sup>16</sup> C. Betancourt,<sup>48</sup> I. Bezshyiko,<sup>48</sup> O. Bezshyyko,<sup>56</sup> D. Bick,<sup>8</sup> S. Bieschke,<sup>8</sup>  
 A. Blanco,<sup>29</sup> J. Boehm,<sup>52</sup> M. Bogomilov,<sup>1</sup> I. Boiarska,<sup>3</sup> K. Bondarenko,<sup>28,58</sup> W.M. Bonivento,<sup>14</sup>  
 J. Borburgh,<sup>45</sup> A. Boyarsky,<sup>28,56</sup> R. Brenner,<sup>44</sup> D. Breton,<sup>4</sup> A. Brignoli,<sup>6</sup> V. Büscher,<sup>10</sup>  
 A. Buonaura,<sup>48</sup> S. Buontempo,<sup>15</sup> S. Cadeddu,<sup>14</sup> A. Calcaterra,<sup>16</sup> M. Calviani,<sup>45</sup>  
 M. Campanelli,<sup>54</sup> M. Casolino,<sup>45</sup> N. Charitonidis,<sup>45</sup> P. Chau,<sup>10</sup> J. Chauveau,<sup>5</sup> A. Chepurinov,<sup>40</sup>  
 M. Chernyavskiy,<sup>33</sup> K.-Y. Choi,<sup>27</sup> A. Chumakov,<sup>2</sup> P. Ciambone,<sup>16</sup> V. Cicero,<sup>13</sup> M. Climescu,<sup>10</sup>  
 A. Conaboy,<sup>6</sup> L. Congedo,<sup>12,a</sup> K. Cornelis,<sup>45</sup> M. Cristinziani,<sup>11,\*</sup> A. Crupano,<sup>15,d</sup>  
 G.M. Dallavalle,<sup>13</sup> A. Datwyler,<sup>48</sup> N. D'Ambrosio,<sup>17</sup> G. D'Appollonio,<sup>14,c</sup> R. de Asmundis,<sup>15</sup>  
 J. De Carvalho Saraiva,<sup>29</sup> G. De Lellis,<sup>15,35,45,d</sup> M. de Magistris,<sup>15,j</sup> A. De Roeck,<sup>45</sup>  
 M. De Serio,<sup>12,a</sup> D. De Simone,<sup>48</sup> L. Dedenko,<sup>40</sup> P. Dergachev,<sup>35</sup> A. Di Crescenzo,<sup>15,d</sup>  
 L. Di Giulio,<sup>45</sup> N. Di Marco,<sup>17</sup> C. Dib,<sup>2</sup> H. Dijkstra,<sup>45</sup> V. Dmitrenko,<sup>39</sup> L.A. Dougherty,<sup>45</sup>  
 A. Dolmatov,<sup>34</sup> D. Domenici,<sup>16</sup> S. Donskov,<sup>36</sup> V. Drohan,<sup>56</sup> A. Dubreuil,<sup>46</sup> O. Durhan,<sup>49</sup>  
 M. Ehler,<sup>6</sup> E. Elikkaya,<sup>49</sup> T. Enik,<sup>30</sup> A. Etenko,<sup>34,39</sup> F. Fabbri,<sup>13</sup> O. Fedin,<sup>37</sup> F. Fedotovs,<sup>53</sup>  
 G. Felici,<sup>16</sup> M. Ferrillo,<sup>48</sup> M. Ferro-Luzzi,<sup>45</sup> K. Filippov,<sup>39</sup> R.A. Fini,<sup>12</sup> H. Fischer,<sup>7</sup> P. Fonte,<sup>29</sup>  
 C. Franco,<sup>29</sup> M. Fraser,<sup>45</sup> R. Fresa,<sup>15,i,h</sup> R. Froeschl,<sup>45</sup> T. Fukuda,<sup>20</sup> G. Galati,<sup>15,d</sup> J. Gall,<sup>45</sup>  
 L. Gatignon,<sup>45</sup> G. Gavrilo,<sup>37</sup> V. Gentile,<sup>15,d</sup> B. Goddard,<sup>45</sup> L. Golinka-Bezshyyko,<sup>56</sup>  
 A. Golovatiuk,<sup>15,d</sup> V. Golovtsov,<sup>37</sup> D. Golubkov,<sup>31</sup> A. Golutvin,<sup>53,35</sup> P. Gorbounov,<sup>45</sup>  
 D. Gorbunov,<sup>32</sup> S. Gorbunov,<sup>33</sup> V. Gorkavenko,<sup>56</sup> M. Gorshenkov,<sup>35</sup> V. Grachev,<sup>39</sup>  
 A.L. Grandchamp,<sup>47</sup> E. Graverini,<sup>47</sup> J.-L. Grenard,<sup>45</sup> D. Grenier,<sup>45</sup> V. Grichine,<sup>33</sup>

N. Gruzinskii,<sup>37</sup> A.M. Guler,<sup>49</sup> Yu Guz,<sup>36</sup> G.J. Haefeli,<sup>47</sup> C. Hagner,<sup>8</sup> H. Hakobyan,<sup>2</sup> I.W. Harris,<sup>47</sup> E. van Herwijnen,<sup>35</sup> C. Hessler,<sup>45</sup> A. Hollnagel,<sup>10</sup> B. Hosseini,<sup>53</sup> M. Hushchyn,<sup>41</sup> G. Iaselli,<sup>12,a</sup> A. Iuliano,<sup>15,d</sup> R. Jacobsson,<sup>45</sup> D. Joković,<sup>42</sup> M. Jonker,<sup>45</sup> I. Kadenko,<sup>56</sup> V. Kain,<sup>45</sup> B. Kaiser,<sup>8</sup> C. Kamiscioglu,<sup>50</sup> D. Karpenkov,<sup>35</sup> K. Kershaw,<sup>45</sup> M. Khabibullin,<sup>32</sup> E. Khalikov,<sup>40</sup> G. Khaustov,<sup>36</sup> G. Khoriauli,<sup>10</sup> A. Khotyantsev,<sup>32</sup> Y.G. Kim,<sup>24</sup> V. Kim,<sup>37,38</sup> N. Kitagawa,<sup>20</sup> J.-W. Ko,<sup>23</sup> K. Kodama,<sup>18</sup> A. Kolesnikov,<sup>30</sup> D.I. Kolev,<sup>1</sup> V. Kolosov,<sup>36</sup> M. Komatsu,<sup>20</sup> A. Kono,<sup>22</sup> N. Konovalova,<sup>33,35</sup> S. Kormannshaus,<sup>10</sup> I. Korol,<sup>6</sup> I. Korol'ko,<sup>31</sup> A. Korzenev,<sup>46</sup> V. Kostyukhin,<sup>11</sup> E. Koukovini Platia,<sup>45</sup> S. Kovalenko,<sup>2</sup> I. Krasilnikova,<sup>35</sup> Y. Kudenko,<sup>32,39,g</sup> E. Kurbatov,<sup>41</sup> P. Kurbatov,<sup>35</sup> V. Kurochka,<sup>32</sup> E. Kuznetsova,<sup>37</sup> H.M. Lacker,<sup>6</sup> M. Lamont,<sup>45</sup> G. Lanfranchi,<sup>16</sup> O. Lantwin,<sup>48,35</sup> A. Lauria,<sup>15,d</sup> K.S. Lee,<sup>26</sup> K.Y. Lee,<sup>23</sup> N. Leonardo,<sup>29</sup> J.-M. Lévy,<sup>5</sup> V.P. Loschiavo,<sup>15,h</sup> L. Lopes,<sup>29</sup> E. Lopez Sola,<sup>45</sup> F. Lyons,<sup>7</sup> V. Lyubovitskij,<sup>2</sup> J. Maalmi,<sup>4</sup> A.-M. Magnan,<sup>53</sup> V. Maleev,<sup>37</sup> A. Malinin,<sup>34</sup> Y. Manabe,<sup>20</sup> A.K. Managadze,<sup>40</sup> M. Manfredi,<sup>45</sup> S. Marsh,<sup>45</sup> A.M. Marshall,<sup>51</sup> A. Mefodev,<sup>32</sup> P. Mermod,<sup>46</sup> A. Miano,<sup>15,d</sup> S. Mikado,<sup>21</sup> Yu. Mikhaylov,<sup>36</sup> A. Mikulenko,<sup>28</sup> D.A. Milstead,<sup>43</sup> O. Mineev,<sup>32</sup> A. Montanari,<sup>13</sup> M.C. Montesi,<sup>15,d</sup> K. Morishima,<sup>20</sup> S. Movchan,<sup>30</sup> Y. Muttoni,<sup>45</sup> N. Naganawa,<sup>20</sup> M. Nakamura,<sup>20</sup> T. Nakano,<sup>20</sup> S. Nasybulin,<sup>37</sup> P. Ninin,<sup>45</sup> A. Nishio,<sup>20</sup> B. Obinyakov,<sup>34</sup> S. Ogawa,<sup>22</sup> N. Okateva,<sup>33,35</sup> J. Osborne,<sup>45</sup> M. Ovchynnikov,<sup>28,56</sup> N. Owscharenko,<sup>11,\*</sup> P.H. Owen,<sup>48</sup> P. Pacholek,<sup>45</sup> A. Paoloni,<sup>16</sup> B.D. Park,<sup>23</sup> A. Pastore,<sup>12</sup> M. Patel,<sup>53,35</sup> D. Pereyma,<sup>31</sup> A. Perillo-Marccone,<sup>45</sup> G.L. Petkov,<sup>1</sup> K. Petridis,<sup>51</sup> A. Petrov,<sup>34</sup> D. Podgrudkov,<sup>40</sup> V. Poliakov,<sup>36</sup> N. Polukhina,<sup>33,35,39</sup> J. Prieto Prieto,<sup>45</sup> M. Prokudin,<sup>31</sup> A. Prota,<sup>15,d</sup> A. Quercia,<sup>15,d</sup> A. Rademakers,<sup>45</sup> A. Rakai,<sup>45</sup> F. Ratnikov,<sup>41</sup> T. Rawlings,<sup>52</sup> F. Redi,<sup>47</sup> A. Reghunath,<sup>6</sup> S. Ricciardi,<sup>52</sup> M. Rinaldesi,<sup>45</sup> Volodymyr Rodin,<sup>56</sup> Viktor Rodin,<sup>56</sup> P. Robbe,<sup>4</sup> A.B. Rodrigues Cavalcante,<sup>47</sup> T. Roganova,<sup>40</sup> H. Rokujo,<sup>20</sup> G. Rosa,<sup>15,d</sup> T. Rovelli,<sup>13,b</sup> O. Ruchayskiy,<sup>3</sup> T. Ruf,<sup>45</sup> V. Samoylenko,<sup>36</sup> V. Samsonov,<sup>39</sup> F. Sanchez Galan,<sup>45</sup> P. Santos Diaz,<sup>45</sup> A. Sanz Ull,<sup>45</sup> A. Saputi,<sup>16</sup> O. Sato,<sup>20</sup> E.S. Savchenko,<sup>35</sup> J.S. Schliwinski,<sup>6</sup> W. Schmidt-Parzefall,<sup>8</sup> M. Schumann,<sup>7</sup> N. Serra,<sup>48,35</sup> S. Sgobba,<sup>45</sup> O. Shadura,<sup>56</sup> A. Shakin,<sup>35</sup> M. Shaposhnikov,<sup>47</sup> P. Shatalov,<sup>31,35</sup> T. Shchedrina,<sup>33,35</sup> L. Shchutska,<sup>47</sup> V. Shevchenko,<sup>34,35</sup> H. Shibuya,<sup>22</sup> L. Shihora,<sup>6</sup> S. Shirobokov,<sup>53</sup> A. Shustov,<sup>39</sup> S.B. Silverstein,<sup>43</sup> S. Simone,<sup>12,a</sup> R. Simoniello,<sup>10</sup> M. Skorokhvatov,<sup>39,34</sup> S. Smirnov,<sup>39</sup> G. Soares,<sup>29</sup> J.Y. Sohn,<sup>23</sup> A. Sokolenko,<sup>56</sup> E. Solodko,<sup>45</sup> N. Starkov,<sup>33,35</sup> L. Stoel,<sup>45</sup> M.E. Stramaglia,<sup>47</sup> D. Sukhonos,<sup>45</sup> Y. Suzuki,<sup>20</sup> S. Takahashi,<sup>19</sup> J.L. Tastet,<sup>3</sup> P. Teterin,<sup>39</sup> S. Than Naing,<sup>33</sup> I. Timiryasov,<sup>47</sup> V. Tioukov,<sup>15</sup> D. Tommasini,<sup>45</sup> M. Torii,<sup>20</sup> N. Tosi,<sup>13</sup> D. Treille,<sup>45</sup> R. Tsenov,<sup>1,30</sup> S. Ulin,<sup>39</sup> E. Ursov,<sup>40</sup> A. Ustyuzhanin,<sup>41,35</sup> Z. Uteshev,<sup>39</sup> L. Uvarov,<sup>37</sup> G. Vankova-Kirilova,<sup>1</sup> F. Vannucci,<sup>5</sup> P. Venkova,<sup>6</sup> V. Venturi,<sup>45</sup> I. Vidulin,<sup>40</sup> S. Vilchinski,<sup>56</sup> Heinz Vincke,<sup>45</sup> Helmut Vincke,<sup>45</sup> C. Visone,<sup>15,d</sup> K. Vlasik,<sup>39</sup> A. Volkov,<sup>33,34</sup> R. Voronkov,<sup>33</sup> S. van Waasen,<sup>9</sup> R. Wanke,<sup>10</sup> P. Wertelaers,<sup>45</sup> O. Williams,<sup>45</sup> J.-K. Woo,<sup>25</sup> M. Wurm,<sup>10</sup> S. Xella,<sup>3</sup> D. Yilmaz,<sup>50</sup> A.U. Yilmazer,<sup>50</sup> C.S. Yoon,<sup>23</sup> Yu. Zaytsev,<sup>31</sup> A. Zelenov<sup>37</sup> and J. Zimmerman<sup>6</sup>

<sup>1</sup>Faculty of Physics, Sofia University, Sofia, Bulgaria

<sup>2</sup>Universidad Técnica Federico Santa María and Centro Científico Tecnológico de Valparaíso, Valparaíso, Chile

<sup>3</sup>Niels Bohr Institute, University of Copenhagen, Copenhagen, Denmark

\*Corresponding author.

- <sup>4</sup>LAL, Univ. Paris-Sud, CNRS/IN2P3, Université Paris-Saclay, Orsay, France
- <sup>5</sup>LPNHE, IN2P3/CNRS, Sorbonne Université, Université Paris Diderot, F-75252 Paris, France
- <sup>6</sup>Humboldt-Universität zu Berlin, Berlin, Germany
- <sup>7</sup>Physikalisches Institut, University of Freiburg, Freiburg, Germany
- <sup>8</sup>Universität Hamburg, Hamburg, Germany
- <sup>9</sup>Forschungszentrum Jülich GmbH (KFA), Jülich, Germany
- <sup>10</sup>Institut für Physik and PRISMA Cluster of Excellence, Johannes Gutenberg Universität Mainz, Mainz, Germany
- <sup>11</sup>Universität Siegen, Siegen, Germany
- <sup>12</sup>Sezione INFN di Bari, Bari, Italy
- <sup>13</sup>Sezione INFN di Bologna, Bologna, Italy
- <sup>14</sup>Sezione INFN di Cagliari, Cagliari, Italy
- <sup>15</sup>Sezione INFN di Napoli, Napoli, Italy
- <sup>16</sup>Laboratori Nazionali dell'INFN di Frascati, Frascati, Italy
- <sup>17</sup>Laboratori Nazionali dell'INFN di Gran Sasso, L'Aquila, Italy
- <sup>18</sup>Aichi University of Education, Kariya, Japan
- <sup>19</sup>Kobe University, Kobe, Japan
- <sup>20</sup>Nagoya University, Nagoya, Japan
- <sup>21</sup>College of Industrial Technology, Nihon University, Narashino, Japan
- <sup>22</sup>Toho University, Funabashi, Chiba, Japan
- <sup>23</sup>Physics Education Department & RINS, Gyeongsang National University, Jinju, Korea
- <sup>24</sup>Gwangju National University of Education,<sup>e</sup> Gwangju, Korea
- <sup>25</sup>Jeju National University,<sup>e</sup> Jeju, Korea
- <sup>26</sup>Korea University, Seoul, Korea
- <sup>27</sup>Sungkyunkwan University,<sup>e</sup> Suwon-si, Gyeong Gi-do, Korea
- <sup>28</sup>University of Leiden, Leiden, The Netherlands
- <sup>29</sup>LIP, Laboratory of Instrumentation and Experimental Particle Physics, Portugal
- <sup>30</sup>Joint Institute for Nuclear Research (JINR), Dubna, Russia
- <sup>31</sup>Institute of Theoretical and Experimental Physics (ITEP) NRC “Kurchatov Institute”, Moscow, Russia
- <sup>32</sup>Institute for Nuclear Research of the Russian Academy of Sciences (INR RAS), Moscow, Russia
- <sup>33</sup>P.N. Lebedev Physical Institute (LPI RAS), Moscow, Russia
- <sup>34</sup>National Research Centre “Kurchatov Institute”, Moscow, Russia
- <sup>35</sup>National University of Science and Technology “MISiS”, Moscow, Russia
- <sup>36</sup>Institute for High Energy Physics (IHEP) NRC “Kurchatov Institute”, Protvino, Russia
- <sup>37</sup>Petersburg Nuclear Physics Institute (PNPI) NRC “Kurchatov Institute”, Gatchina, Russia
- <sup>38</sup>St. Petersburg Polytechnic University (SPbPU),<sup>f</sup> St. Petersburg, Russia
- <sup>39</sup>National Research Nuclear University (MEPhI), Moscow, Russia
- <sup>40</sup>Skobeltsyn Institute of Nuclear Physics of Moscow State University (SINP MSU), Moscow, Russia
- <sup>41</sup>Yandex School of Data Analysis, Moscow, Russia
- <sup>42</sup>Institute of Physics, University of Belgrade, Serbia
- <sup>43</sup>Stockholm University, Stockholm, Sweden
- <sup>44</sup>Uppsala University, Uppsala, Sweden
- <sup>45</sup>European Organization for Nuclear Research (CERN), Geneva, Switzerland
- <sup>46</sup>University of Geneva, Geneva, Switzerland

<sup>47</sup> *École Polytechnique Fédérale de Lausanne (EPFL), Lausanne, Switzerland*

<sup>48</sup> *Physik-Institut, Universität Zürich, Zürich, Switzerland*

<sup>49</sup> *Middle East Technical University (METU), Ankara, Turkey*

<sup>50</sup> *Ankara University, Ankara, Turkey*

<sup>51</sup> *H.H. Wills Physics Laboratory, University of Bristol, Bristol, United Kingdom*

<sup>52</sup> *STFC Rutherford Appleton Laboratory, Didcot, United Kingdom*

<sup>53</sup> *Imperial College London, London, United Kingdom*

<sup>54</sup> *University College London, London, United Kingdom*

<sup>55</sup> *University of Warwick, Warwick, United Kingdom*

<sup>56</sup> *Taras Shevchenko National University of Kyiv, Kyiv, Ukraine*

<sup>a</sup> *Università di Bari, Bari, Italy*

<sup>b</sup> *Università di Bologna, Bologna, Italy*

<sup>c</sup> *Università di Cagliari, Cagliari, Italy*

<sup>d</sup> *Università di Napoli “Federico II”, Napoli, Italy*

<sup>e</sup> *Associated to Gyeongsang National University, Jinju, Korea*

<sup>f</sup> *Associated to Petersburg Nuclear Physics Institute (PNPI), Gatchina, Russia*

<sup>g</sup> *Also at Moscow Institute of Physics and Technology (MIPT), Moscow Region, Russia*

<sup>h</sup> *Consorzio CREATE, Napoli, Italy*

<sup>i</sup> *Università della Basilicata, Potenza, Italy*

<sup>j</sup> *Università di Napoli Parthenope, Napoli, Italy*

E-mail: [markus.cristinziani@uni-siegen.de](mailto:markus.cristinziani@uni-siegen.de),

[nikolaus.owtscharenko@uni-siegen.de](mailto:nikolaus.owtscharenko@uni-siegen.de)

**ABSTRACT:** In July 2018 an optimization run for the proposed charm cross section measurement for SHiP was performed at the CERN SPS. A heavy, moving target instrumented with nuclear emulsion films followed by a silicon pixel tracker was installed in front of the Goliath magnet at the H4 proton beam-line. Behind the magnet, scintillating-fibre, drift-tube and RPC detectors were placed. The purpose of this run was to validate the measurement’s feasibility, to develop the required analysis tools and fine-tune the detector layout. In this paper, we present the track reconstruction in the pixel tracker and the track matching with the moving emulsion detector. The pixel detector performed as expected and it is shown that, after proper alignment, a vertex matching rate of 87% is achieved.

**KEYWORDS:** Particle tracking detectors (Solid-state detectors); Pattern recognition, cluster finding, calibration and fitting methods; Detector alignment and calibration methods (lasers, sources, particle-beams)

ARXIV EPRINT: [2112.11754](https://arxiv.org/abs/2112.11754)

---

## Contents

<b>1</b>	<b>Introduction</b>	<b>1</b>
<b>2</b>	<b>Experimental setup</b>	<b>2</b>
2.1	Beam conditions and data taking	2
2.2	Pixel detector	3
<b>3</b>	<b>Track finding and reconstruction</b>	<b>4</b>
3.1	Emulsion detector	4
3.2	Pixel detector	4
3.3	Alignment and track matching procedure	5
<b>4</b>	<b>Results</b>	<b>6</b>
4.1	Track matching	6
4.2	Physics performance	7
<b>5</b>	<b>Conclusion</b>	<b>8</b>

---

## 1 Introduction

Knowledge of the charm production cross section in a thick target is of key importance for the proposed SHiP [1] experiment. The prediction of charmed-hadron production is essential to establish the sensitivity to detect new particles and to make a precise estimate of the  $\nu_\tau$  flux stemming from charm decays. Current information on charm production at a center-of-mass energy of  $\sqrt{s} = 27$  GeV is limited to measurements with thin targets [2]. For the determination of the flux of charmed hadrons the cascade production is of crucial importance and needs to be verified experimentally. The SHiP-charm project [3] aims at measuring the double-differential cross section,  $d^2\sigma/(dE d\theta)$ , for charm production using the 400 GeV/ $c$  primary proton beam, extracted from SPS to the H4 beam-line of the SPS North Area at CERN. The target consisted of a shorter replica of the SHiP SND detector, and is interleaved with emulsion cloud chambers (ECC) for tracking charm production and decays. This was followed by a magnetized tracking spectrometer and by a muon tagger. In July 2018, an optimization run took place at the H4 beam-line. We address the challenge of reconstructing common tracks (and events) from the information recorded by the fundamentally different ECC and pixel detectors. This is complicated by the fact that the ECC detector carries no timing information and was moving relative to the beam and the pixel detector in order to prevent overexposure during a given spill. In this paper, results of matching ECC tracks and vertices to downstream pixel tracks by means of a  $\chi^2$  minimization of the residuals are presented.



## 2 Experimental setup

The experiment was composed of three major parts: the ECC, the spectrometer and a muon tagger. For the measurement, 400 GeV/ $c$  protons impinging on the ECC, made of tungsten sheets alternated with nuclear emulsion films. A detailed description of the ECC can be found in [4]. The most important properties are a very high spatial resolution and the permanence of each ionization trace. The permanent ionization makes it necessary to limit the occupancy in the emulsion films. The first electronic detector, 1.8 cm downstream of the ECC, was the pixel detector. It was the first of three sub-detectors building the spectrometer together with GOLIATH [5, 6]. Downstream of the magnet, a scintillating-fiber (SciFi) tracker of 40 cm  $\times$  40 cm area per plane was positioned. It was followed by a drift-tube detector [7], covering the outer regions of acceptance. The last detector was the muon tagger, built from resistive-plate chambers (RPCs) and an iron filter. Figure 1 displays the setup along the beam axis. Since the linking of analog ECC information with the pixel-detector tracks is crucial to the overall reconstruction and event selection, this paper focuses on this critical step. For the analysis described below, only the stand-alone data of these two detectors is used. While the ECC is passive, the pixel detector was triggered by the beam counter, a pair of scintillators requiring coincident detection of the primary beam protons.

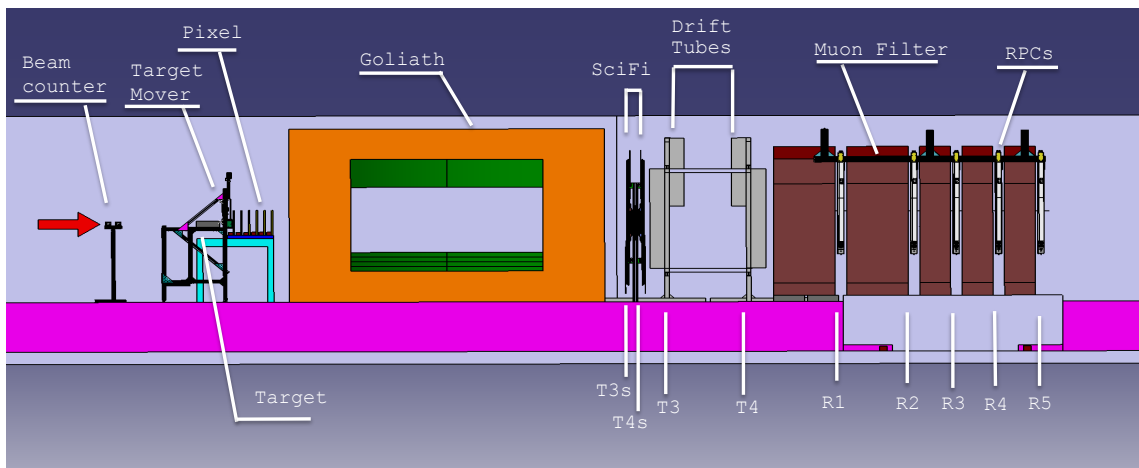


**Figure 1.** Conceptual drawing of the SHiP-charm experiment setup for the 2018 test beam [4]. The ECC is referred to as “target”.

### 2.1 Beam conditions and data taking

The beam in the North Area (and H4 beam-line) is slowly extracted in spills of mostly uniform duration of  $\sim 4.8$  s. The beam was tuned to an elliptical shape with an extent of approximately 2 cm in  $y$  and 0.7 cm in  $x$ .<sup>1</sup> The number of protons per spill ranged from 7700 to 13 800. The occupancy limit on the ECC made it necessary to move the detector through the beam, and the beam shape was chosen to maximize the illuminated active area in this setup. The pixel detector was

<sup>1</sup>The coordinate system is defined such that the  $z$ -axis is parallel to the beam-line, the positive  $y$ -axis points upwards, while positive  $x$  points to the right (direction “Salève”) when looking downstream of the beam. The most downstream emulsion layer is located at  $z = 0$ .

synchronized via the analog start-of-spill signal, which was used to reset trigger counters and/or timestamps before each spill. The trigger counts all incoming protons and every trigger creates a new event. Different target configurations were used for the SHiP-charm test-beam [4]. For this work one dedicated configuration is considered where the target consisted of 29 emulsion films interleaved with 28 tungsten sheets, adding up to a total passive-material budget of 2.5 cm within the 5 cm thick ECC. In this configuration the occupancy on the pixel detector for events with proton interaction was on average 86 cluster per plane per event, creating a high-occupancy environment for track reconstruction. Figure 2 shows the number of cluster per event for the single detector planes. During each of the five spills, the target moved at about  $\pm 2.6$  cm/s along the horizontal axis, inverting the direction with every new spill. In between spills it was shifted upwards by 2 cm, forming a snake-like pattern.

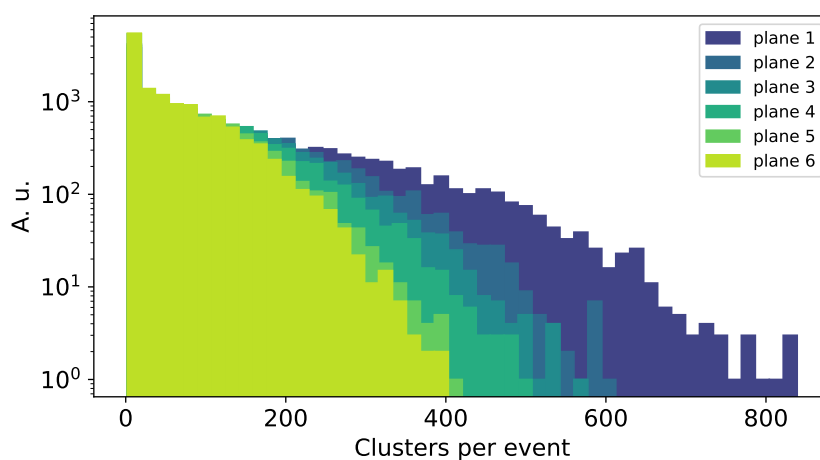


**Figure 2.** Overlay of histograms of the number of clusters per event in events with a proton interaction for all detector planes. The average for the most downstream plane 1 is 134 cluster per event with a maximum of 838.

## 2.2 Pixel detector

As the most upstream element of the spectrometer, the pixel detector connects the analog information of the ECC with data taken by the other electronic sub-detectors: the ionization in the ECC is permanent, without any timing information. Tracks reconstructed in the pixel detector provide the necessary timestamp to fully reconstruct the event.

The pixel tracking detector consisted of six planes, each formed by two ATLAS IBL double-chip modules with hybrid pixels [8]. ATLAS hybrid pixel detectors consist of a pixelated silicon sensor and the FE-I4 read-out chip. The front-end chip offers an analog readout for every sensor pixel. They are electrically connected via solder bumps. Sensor and read-out chip were developed for a high-radiation and high-occupancy environment. The FE-I4 clock runs at 40 MHz which is therefore the maximum timing resolution.

One double-chip module is organized in 160 columns and 336 rows, resulting in 53 760 pixels. The pixel pitch for the rows is 50  $\mu\text{m}$ , and 250  $\mu\text{m}$  for the columns. Pixels in the two central columns are 450  $\mu\text{m}$  wide to compensate for the small but necessary gap between the two independent

front-end chips. To maximize the active area, edge columns are also wider, 500  $\mu\text{m}$ , with partially overlapping guard rings on the sensor. A double-chip sensor measures 4.09 cm  $\times$  1.68 cm, resulting in an active area of about 6.9 cm<sup>2</sup>. The sensors are about 200  $\mu\text{m}$  thick and were biased with  $-80$  V. The sensor's hit detection efficiency is above 99 % [9]. The front-end chips were tuned to a threshold corresponding to about 1600  $e^-$ .

The detector layout was optimized to achieve the best possible pointing resolution towards the ECC. The difference in pixel resolution between the  $x$  and  $y$  dimensions was compensated by rotating every other plane by  $\pi/2$  around the beam axis. This layout allows for three high resolution measurements in each dimension,  $x$  and  $y$ , starting with 50  $\mu\text{m}$  resolution in  $x$  on the first plane. Furthermore, the mounting and position of the planes relative to each other was optimized for maximal acceptance. To create a plane, two modules are placed on opposite sides of a single aluminium frame. This layout allows for a continuous active area. The aluminium frames were cut out to reduce the material budget as much as possible, while retaining the required mechanical stability and thermal contact.

### 3 Track finding and reconstruction

In the following we briefly discuss the independent track reconstruction in the ECC and the pixel detector, the alignment of the two detector systems with respect to each other and finally the matching of common tracks.

#### 3.1 Emulsion detector

Track reconstruction within the ECC is performed in two steps. First the emulsion films are scanned under a microscope to digitize the tracklets, second tracks are reconstructed from the tracklets with the FEDRA software [10]. The intrinsic resolution of the emulsion films is 0.7  $\mu\text{m}$  [11] and the average film-by-film track efficiency was measured to be  $(92 \pm 2)$  % [4]. The reconstructed tracks contain a set of at least two track segments, one for each emulsion plane. For track finding and fitting, a Kalman-Filter algorithm is used, taking into account inefficiencies in the reconstruction of track segments [11]. The track reconstruction purity was measured to be above 95 % [12]. Two-track vertices are identified with a criterion on the distance-of-closest-approach. They are associated to a common vertex based on a vertex probability taking into account the full covariance matrix of all involved tracks. Detailed information regarding the reconstruction is available in reference [4].

#### 3.2 Pixel detector

Tracks in the pixel detector are reconstructed with a local pattern recognition starting from a track seed formed by two hits on the third and last detector plane. Track candidates are validated with a  $\chi^2$  minimization fit. The pattern recognition only considers tracks with opening angles  $\theta_{xz}, \theta_{yz} \leq 150$  mrad, matching the spectrometer acceptance. A detailed description of the reconstruction can be found in [13]. For the investigated run, 36 132 events from 5 spills were recorded. The pixel detector efficiency is between 99.5 and 99.9 %, while the tracking resolution is found to be 15  $\mu\text{m}$  in  $x$  and 26  $\mu\text{m}$  in  $y$  direction [13].

### 3.3 Alignment and track matching procedure

In order to match track candidates between the pixel and the moving emulsion detectors, a set of good track candidates is selected and used for a proper alignment. First, emulsion tracks are selected if they are associated to a vertex with at least six associated tracks. Tracks also have to feature a segment in the most downstream emulsion layer. To minimize the influence of multiple scattering on the track resolution, only the track parameters of that most downstream segment are used in the following. In order to suppress tracks from fully penetrating protons (i.e., the beam), the number of track segments per track must be less than 29 (the total number of segments).

The track parameters of interest for matching are the positions  $x$ ,  $y$  and the track angles  $\theta_x$  and  $\theta_y$  of the furthest downstream track segment. The track angles  $\theta_x$  and  $\theta_y$  are required to be less than 150 mrad each, in order only consider tracks within the spectrometer acceptance. The time information provided with each reconstructed pixel detector track,  $t = \text{timestamp} \times 25 \text{ ns}$ , is used to translate the pixel detector's local coordinate system into the moving emulsion frame and transform the pixel track parameters  $\mathbf{x}^{\text{pix}} = (x, y, z, \theta_x, \theta_y)$ , accordingly. The uncertainty in the time  $t$  is  $\mathcal{O}(\text{ns})$ , which is small compared to the overall uncertainty coming from the spread in  $x$  and the speed of the target mover  $\mathcal{O}(\text{ms})$ , and is thus negligible.

For the alignment, a set of eight parameters is introduced,  $\boldsymbol{\alpha} = (x_0, y_0, z_0, \theta_{xz}, \theta_{yz}, \theta_{xy}, v_x, v_y)$ , where  $x_0, y_0, z_0$  are the offset of the pixel detector with respect to the emulsion reference frame, the two velocities  $v_x$  and  $v_y$  characterize the target mover, and the rotations of the pixel detector about the  $x$ ,  $y$ , and  $z$  axes are denoted by  $\theta_{yz}$ ,  $\theta_{xz}$  and  $\theta_{xy}$ , respectively. The origin is set at the most downstream emulsion layer. We define a track  $\chi_{\text{track}}^2$  of residuals between the emulsion and pixel detectors as

$$\chi_{\text{track}}^2 = \mathbf{r}^T \mathbf{V}^{-1} \mathbf{r}, \quad (3.1)$$

where  $\mathbf{r} = \mathbf{x}^{\text{pix}} - \mathbf{x}^{\text{ECC}} = (\Delta x, \Delta y, \Delta \theta_x, \Delta \theta_y)$  is the vector of residuals and  $\mathbf{V} = \mathbf{V}^{\text{pix}} + \mathbf{V}^{\text{ECC}}$  is the covariance matrix of residuals evaluated at the matching plane of  $z = 0$ . The list of good track matches is constructed by calculating the  $\chi^2$  of every possible pair between emulsion and pixel tracks. Only pairs with a  $\chi^2 < 100$  are considered. Furthermore, there is a requirement on residuals of  $\pm 5 \text{ mm}$  in  $\Delta x$ , and  $\Delta y$  and a  $\pm 15 \text{ mrad}$  cut on the residuals in  $\Delta \theta_x$ , and  $\Delta \theta_y$ . The list is then ordered in increasing values of  $\chi^2$ . A new list is created by starting from the beginning (smallest  $\chi^2$ ) and moving down the list, at each step checking whether either the emulsion or pixel track were already used, in which case the pair would be removed from the list. This creates a set of good track matches with the minimal  $\chi^2$  for a given set of alignment parameters. Whether this is the best possible list (minimal  $\chi^2$ ) will depend on whether the two sub-detectors are properly aligned. The total

$$\chi^2 = \sum_j (\mathbf{r}^T \mathbf{V}^{-1} \mathbf{r})_j, \quad (3.2)$$

is to be minimized, where the sum runs over track pairs  $j$  between the emulsion and pixel tracks [14]. The condition that the sample of tracks is minimal with respect to the alignment parameters can be written as

$$0 \equiv \frac{d\chi^2}{d\boldsymbol{\alpha}} = 2 \sum_j \left( \frac{\partial \mathbf{r}^T}{\partial \boldsymbol{\alpha}} \mathbf{V}^{-1} \mathbf{r} \right)_j. \quad (3.3)$$

The optimal value of  $\alpha$  that satisfies this relation can be determined using the Newton-Raphson method. Given an initial set of alignment parameters  $\alpha_0$ , an updated set  $\alpha_1$  is calculated as

$$\alpha_1 = \alpha_0 - \left( \frac{d^2\chi^2}{d\alpha^2} \right)^{-1} \bigg|_{\alpha_0} \left( \frac{d\chi^2}{d\alpha} \right) \bigg|_{\alpha_0}. \quad (3.4)$$

This step is iterated until a convergence criterion is met, namely a minimal change in  $\chi^2$  with increasing iterations. The alignment procedure can be summarized as follows:

1. Begin with an initial set of alignment parameters  $\alpha_0$ .
2. Calculate the  $\chi^2$  per track pair with eq. (3.1) and find the list of pairs with the minimal  $\chi^2$ .
3. Calculate the total  $\chi^2$  using eq. (3.2).
4. Get a new set of alignment parameters  $\alpha_1$  using eq. (3.4).
5. Go back to Step 2 using  $\alpha_1$  in place of  $\alpha_0$  and repeat until the total  $\chi^2$  converges.

Convergence of the  $\chi^2$  is not necessarily assured. If the misalignment is too large, the optimal set of track pairs could have a  $\chi^2$  so large that it is dominated by combinatorial background, i.e., a pair with a large  $\chi^2$  could take the place of an actual match if they share a track. Therefore, it is important to begin with a set of alignment parameters that are close to the optimal values.

## 4 Results

### 4.1 Track matching

The alignment and matching procedure was performed on the data, where each spill was treated separately. Some alignment parameters are constrained by the initial mechanical alignment in the cavern before data taking, in particular the SHiP-charm setup was surveyed by the CERN EN/SMM group [15]. The distance between the last emulsion layer and the first pixel layer was measured to be  $z_0 = (1.8 \pm 0.1)$  cm while the speed of the target mover in the horizontal direction was measured to be  $v_x = (2.6 \pm 0.1)$  cm/s. The value of  $y_0$  changed depending on the spill and is estimated from the beam profile in  $y$ . The angles  $\theta_{xz}$ ,  $\theta_{yz}$  and  $\theta_{xy}$  and the target mover speed in the vertical direction  $v_y$  are initially set to 0. The alignment parameter  $x_0$  is initially unknown, but can be estimated by setting  $\Delta x = 0$  in the  $\chi^2$  calculation and then looking for a peak in the resulting  $\Delta x$  distribution after alignment.

The evolution of the mean  $\chi^2$  of all tracks is shown in figure 3, illustrating the improvement in the  $\chi^2$  after alignment. The matching resolutions are found to be  $\sigma_x = 44 \mu\text{m}$ ,  $\sigma_y = 80 \mu\text{m}$ ,  $\sigma_{\theta_{xz}} = 4 \text{ mrad}$ , and  $\sigma_{\theta_{yz}} = 3 \text{ mrad}$ .

A shift in  $x_0$  of about 13.7 cm between alternate spills corresponds to the target moving  $v_x \sim 2.6$  cm/s for 5.2 s, closely matching the target moving time, which included 0.4 s before/after the spill. Likewise, an observed shift in  $y_0$  between spills can be explained by a vertical movement of  $v_y \sim 300 \mu\text{m/s}$ . The distance between the last emulsion layer and first pixel layer  $z_0$  is consistent with the survey measurement [15]. The angles  $\theta_{xz}$  and  $\theta_{yz}$  are close to 0, while  $\theta_{xy}$  is about 19 mrad. Since  $v_y$  changes sign between spills, this vertical velocity corresponds to a rotation of the emulsion brick with respect to the beam of about 11 mrad.

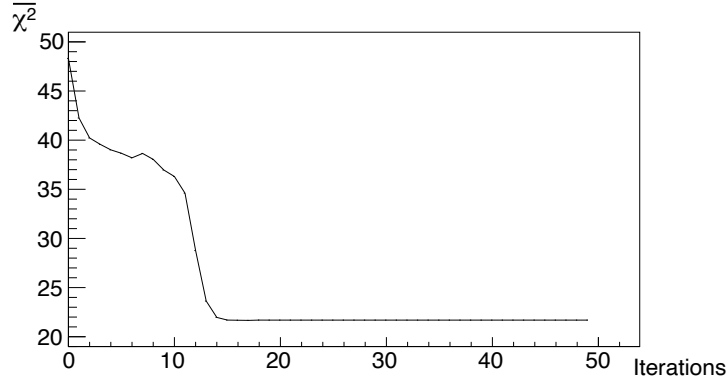


**Figure 3.** The average  $\chi^2$  per track vs. the number of iterations of the alignment procedure.

## 4.2 Physics performance

For the investigation of charmed hadronic interaction in SHiP-charm, a full event reconstruction including particle identification is necessary. This was achieved by measuring track deflection downstream of the magnetic field. Thus, the current analysis is focused on tracks which stay within the experiments acceptance and characteristic events are selected considering two main features.

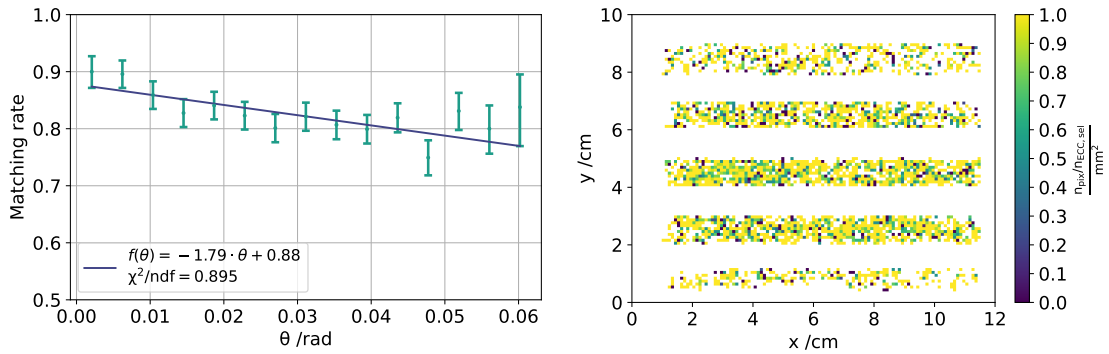


**Figure 4.** Track matching rate in the connected sub-detectors vs. track angle  $\theta$  (left) and vs.  $x$  and  $y$  position of selected tracks (right). The non-uniform distribution of horizontal lines reflects the single spills.

In a first step only tracks from vertices with at least six tracks reconstructed in the ECC are selected. Secondly, the magnetic deflection of tracks beyond the SciFi detectors' acceptance is considered, and only tracks with opening angles smaller than 62 mrad are selected. The detector performance is then quantified in terms of the matching rate  $\epsilon$ . Given a set of  $n$  tracks, the matching rate is defined as the ratio of the number of ECC tracks matched in the pixel detector  $n_{\text{pix}}$  over the number of selected ECC tracks  $n_{\text{ECC,sel}}$ :

$$\epsilon = \frac{n_{\text{pix}}}{n_{\text{ECC,sel}}}.$$

In figure 4 the matching rate distributions for track matching after this selection are shown for the entire run. The average matching rate for selected emulsion tracks is  $(82.6 \pm 0.4)\%$ . With the

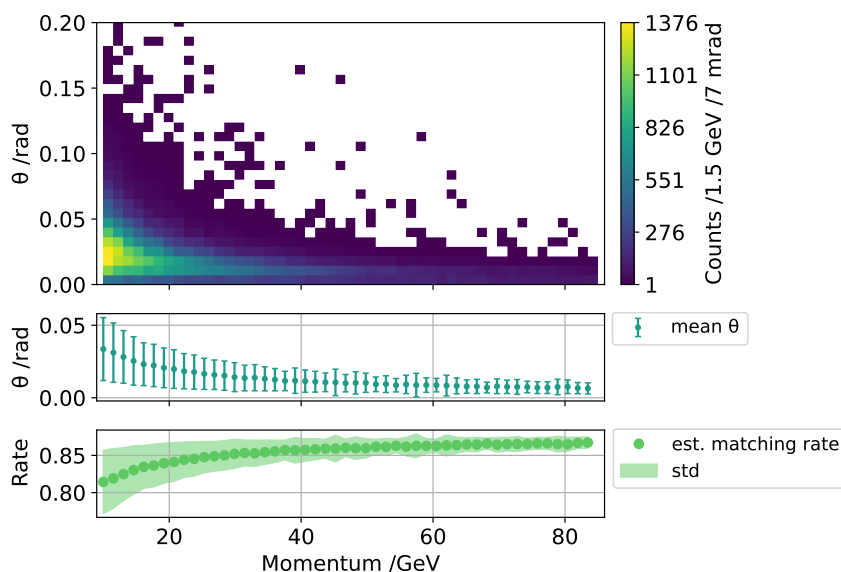


**Figure 5.** Track angle (top), average angle (center) and estimated matching rate (bottom) vs. momentum of Monte Carlo tracks in the emulsion. Only tracks within the experiments acceptance are considered.

successful matching of at least one track a timestamp is assigned not only to the track but to the whole vertex. Thus, after matching, timestamps can be assigned to 87 % of selected vertices. If a vertex is assigned a timestamp, the matching rate for tracks of this vertex is at least 88 % on average, while for 65 % of matched vertices all selected tracks are matched.

The relation between track angle and matching rate can be used to estimate a matching rate with respect to the particles' momentum. In figure 4 (left) the rate is plotted for different track angles and a fit is performed. The uncertainties are computed by quadratic addition of the statistical uncertainty and the estimated systematic uncertainty. The statistical uncertainty is computed as the  $1\text{-}\sigma$  confidence interval of a binomial distribution, according to Bayes' theorem [16, 17]. The systematic uncertainty is determined using the mean difference of the matching rate for varying  $\chi^2$  constraints. The fitted model is applied to the average track angle for given momenta as obtained from a Monte-Carlo simulation of particle interactions in the ECC [4]. Tracks with  $p < 10$  GeV are not considered, as these tracks are leaving the experimental setup after magnetic deflection. The result is plotted in figure 5. For all tracks within the detector acceptance we expect a matching rate of at least 81 %, increasing to 87 % with track momentum.

## 5 Conclusion

In this paper it is demonstrated that a moving emulsion detector without timing information and a stationary high-granularity pixel detector can successfully be used for track reconstruction in a high occupancy environment. The Newton-Raphson method is used to determine a set of eight alignment parameters. Two aspects were crucial for a successful alignment, a small distance between the two detectors and a set of adequate parameters to start the alignment procedure. With the described algorithm, 82.6 % of the emulsion tracks within detector acceptance can be matched, corresponding

to 87 % of characteristic vertices. This proves the combination of ECC and pixel detector as well suited for a charm cross section measurement in the given setup. To evaluate whether the physics program can be met, a second optimization run and a study employing the whole spectrometer would be necessary.

## Acknowledgments

The SHiP Collaboration acknowledges support from the National Research Foundation of Korea, the Fundação para a Ciência e a Tecnologia of Portugal, FCT; the Russian Foundation for Basic Research, RFBR and the TAEK of Turkey. This work is supported by the German Science Foundation (DFG) through a research grant and a Heisenberg professorship under contracts CR-312/4-1 and CR-312/5-1. We thank W. Dietsche, F. Hüggling, J. Janssen and D.L. Pohl of SILAB, Bonn for their assistance with the pixel detector. The measurement reported in this paper would not have been possible without a significant financial contribution from CERN. In addition, several member institutes made large financial and in-kind contributions to the construction of the target and the spectrometer sub-detectors, as well as providing expert manpower for commissioning, data taking and analysis. This help is gratefully acknowledged.

## References

- [1] SHiP collaboration, *A facility to Search for Hidden Particles (SHiP) at the CERN SPS*, Tech. Rep., [CERN-SPSC-2015-016](#), CERN, Geneva (2015) [[arXiv:1504.04956](#)].
- [2] C. Lourenço and H.K. Wöhri, *Heavy flavour hadro-production from fixed-target to collider energies*, *Phys. Rept.* **433** (2006) 127 [[hep-ph/0609101](#)].
- [3] SHiP collaboration, *Measurement of associated charm production induced by 400 GeV/c protons*, Tech. Rep., [CERN-SPSC-2017-033](#), CERN, Geneva (2017).
- [4] SHiP collaboration, *Reconstruction of 400 GeV/c proton interactions with the SHiP-charm project*, Tech. Rep., [CERN-SHiP-NOTE-2020-002](#), CERN, Geneva (2020).
- [5] Y. Gaillard, *Specification technique concernant la refexion de l'electro-aimant Goliath*, Tech. Rep., EDMS 1326984, CERN, Geneva (1969).
- [6] M. Rosenthal et al., *Magnetic Field Measurements of the GOLIATH Magnet in EHN1*, Tech. Rep., [CERN-ACC-NOTE-2018-0028](#), CERN, Geneva (2018).
- [7] R. Zimmermann, J. Ebert, C. Hagner, B. Koppitz, V. Savelev, W. Schmidt-Parzefall et al., *The precision tracker of the OPERA detector*, *Nucl. Instrum. Meth. A* **555** (2005) 435 [*Erratum ibid.* **557** (2006) 690]
- [8] ATLAS IBL collaboration, *Production and Integration of the ATLAS Insertable B-Layer*, *2018 JINST* **13** T05008 [[arXiv:1803.00844](#)].
- [9] ATLAS IBL collaboration, *Prototype ATLAS IBL Modules using the FE-I4A Front-End Readout Chip*, *2012 JINST* **7** P11010 [[arXiv:1209.1906](#)].
- [10] V. Tioukov, I. Kreslo, Y. Petukhov and G. Sirri, *The FEDRA Framework for emulsion data reconstruction and analysis in the OPERA experiment*, *Nucl. Instrum. Meth. A* **559** (2006) 103.
- [11] L. Arrabito et al., *Track reconstruction in the emulsion-lead target of the OPERA experiment using the ESS microscope*, *2007 JINST* **2** P05004 [[arXiv:0705.3102](#)].



- [12] A. Iuliano, *Event reconstruction and data analysis techniques for the SHiP experiment*, Ph.D. Thesis, Università degli Studi di Napoli Federico II, (2021) [<https://cds.cern.ch/record/2776128/files/CERN-THESIS-2021-091.pdf>]
- [13] SHiP collaboration, *Track reconstruction and matching for SHiP-charm*, Tech. Rep., [CERN-SHiP-NOTE-2020-003](#), CERN, Geneva (2020).
- [14] A. Bocci and W. Hulsbergen, *TRT alignment for SRI cosmics and beyond*, Tech. Rep., [ATL-INDET-PUB-2007-009](#), CERN, Geneva (2007).
- [15] B. Cumer and K. Nikolitsas, *H4 test measurement of the charm cross section setup on H4 beam line*, Tech. Rep., [EDMS 2010858](#), CERN, Geneva (2018).
- [16] D. Casadei, *Estimating the selection efficiency*, [2012 JINST 7 P08021](#) [[arXiv:0908.0130](#)].
- [17] M. Paterno, *Calculating Efficiencies and Their Uncertainties*, Tech. Rep., [FERMILAB-TM-2286-CD](#), Fermilab, Batavia, IL, U.S.A. (2004).



# Correlation analysis of solar energetic particles and secondary cosmic ray flux

Nikola Veselinović<sup>a</sup>, Mihailo Savić, Aleksandar Dragić, Dimitrije Maletić, Radomir Banjanac, Dejan Joković, David Knežević, and Vladimir Udovičić

Institute of Physics Belgrade, University of Belgrade, Pregrevica 118, Belgrade 11080, Serbia

Received 31 January 2021 / Accepted 5 May 2021 / Published online 8 June 2021  
© The Author(s), under exclusive licence to EDP Sciences, SIF and Springer-Verlag GmbH Germany, part of Springer Nature 2021

**Abstract.** Galactic cosmic rays entering heliosphere are modulated by interplanetary magnetic field which is carried away from the Sun by the solar wind. Cosmic rays are additionally modulated by coronal mass ejections and shock waves, which can produce Forbush decrease, a transient decrease in the observed galactic cosmic ray intensity. Measurements of magnetic field and plasma parameters in near-Earth space detect regularly coronal mass ejections, so it is important to understand the correlation between near-Earth particles fluxes associated with these coronal mass ejections and Forbush decreases. By combining in situ measurements of solar energetic particles with ground-based observations by the Belgrade muon detector, we analysed the dynamics of the variation of galactic cosmic rays. Correlation between variations of the flux of the cosmic rays and average in situ particle fluxes was investigated during Forbush decreases. Correlation exhibited dependence on the energy of solar wind particles, but also on cut-off rigidities of cosmic rays detected on the ground. The goal of cross-correlation analysis is to help in better understanding of how coronal mass ejections affect space weather as well as the effects they have on primary cosmic ray variations as detected by ground-based cosmic ray detectors.

## 1 Introduction

Space weather has been widely used as a term to define impact of the Sun, heliosphere and geomagnetic field on our biosphere and our technological systems. Understanding space weather is a matter of both scientific interest and practical importance as its impact could potentially be hazardous to our civilisation. Cosmic ray (CR) observations can also be used to study space weather. Primary (or galactic) CRs are high-energy nuclei (mainly protons) that originate from outside of our solar system. Their flux and energy range is covering several tens of orders of magnitude (flux from  $10^{-28}$  up to  $10^4$  ( $\text{m}^2 \text{sr sec eV/nucleon}$ )<sup>-1</sup> and energy range up to  $10^{21}$  eV [10]). As charged particles, CRs are sensitive to magnetic field, so often it is more convenient to use geomagnetic rigidity instead of energy to characterise primary CRs. Geomagnetic rigidity is defined as  $R = B\rho = pq$ , where  $B$  is the magnetic field,  $\rho$  is the gyroradius of the particle due to this field,  $p$  is the particle momentum and  $q$  is its charge [14]. As they traverse interplanetary space, galactic CRs interact with helio-

spheric magnetic field. The heliosphere is the region of space around the Sun dominated by the solar wind and the interplanetary magnetic field (IMF). The solar wind is a stream of supersonic plasma blowing outward from the Sun. IMF represents solar magnetic field carried by highly conducting solar wind plasma. Interaction of CRs with this large-scale field modulates CRs flux intensity measured on Earth, which is nested deep inside the heliosphere. Interaction with the heliosphere causes gradient and curvature drift motion of CRs and scattering by the magnetic irregularities embedded in the solar wind [19]. Variations in the solar magnetic field directly affect the heliosphere, most prominent being the solar cycle variation with a period of about 11 years. Solar cycle affects activity of the Sun which is visible in varying number of sunspots, solar flares (SFs) and coronal mass ejections (CMEs). Coronal mass ejection is an extreme solar activity event, followed by significant release of charged particles and accompanying magnetic field from solar corona. Intensity of measured CRs flux anticorrelates with the activity of the Sun, with lower intensity during maximum of the solar cycle and higher intensity during minimum of solar activity.

One of the transient phenomena of this interaction is the Forbush decrease (FD), which represents a rapid depression in CR flux. It is usually characterised by a sudden decrease reaching minimum within one day, followed by a subsequent gradual recovery phase, which

**Supplementary information** The online version of this article (<https://doi.org/10.1140/epjd/s10053-021-00172-x>) contains supplementary information, which is available to authorized users.

<sup>a</sup> e-mail: [veselinovic@ipb.ac.rs](mailto:veselinovic@ipb.ac.rs) (corresponding author)

can last for several days. Typical causes of FD are transient interplanetary events related to interplanetary coronal mass ejections (ICMEs). If the speed of the ICME is greater than fast magnetosonic wave speed in the solar wind reference frame, ambient solar wind plasma will be compressed. The shock can be formed, which is driven ahead of ICME and can cause enhancement of IMF. FD can also be formed due to corotating interaction regions between different solar wind streams with different speed [2]. In this paper, we will only focus on ICME induced FDs, of which we will study four cases.

Correlation between parameters characterising FDs (like magnitude of the decrease, duration, one-step or two-step FDs, etc.) and solar wind parameters has been studied for some time. There is reasonable evidence for correlation between FD magnitude and amplitude of magnetic field enhancement  $B$ , velocity of CME, maximum solar wind velocities and other parameters as shown in [7, 22]. Also, profile of FDs is modelled and compared with CME magnetic structure, starting from the simple force-free flux rope with circular cross section, but it can deviate from this ideal concept. FD magnitude is explained with cumulative effect of diffusion of CRs through the turbulent sheath region [3, 11]. FD is also energy dependent, where amplitude of decrease is typically around several percent. Higher-rigidity CRs only weakly interact with magnetic disturbances, so no significant change of the flux can be expected for CRs with rigidity of several dozen GV [9]. In order to detect FD at any location, larger statistics are needed for CRs of lower energy. CRs also interact with geomagnetic field which imposes the minimal rigidity CRs must have in order to reach Earth's surface. This geomagnetic cut-off rigidity depends on geomagnetic latitude. It is smaller at the poles and increases with latitude, with some exceptions due to deviation of Earth's magnetic field from the magnetic dipole model (i.e., South Atlantic anomaly [4]).

Primary CRs arriving at Earth interact with atoms and molecules in Earth's atmosphere. CRs with energy above 300–400 MeV/nucleon generate showers of secondary particles. These secondary CRs consist of electrons and photons (electromagnetic component) and harder, in terms of energy, nuclear component of the cascade. Nuclear component, at the bottom of the atmosphere, is composed mainly of muons, protons, neutrons and neutrinos. Secondary CRs can be observed with detectors in the atmosphere (balloon probes), on the ground or even underground. High-energy muons can penetrate deep underground and can be an important component of the background in experiments requiring high sensitivity (dark matter search, proton decay, etc.).

There is a well-known correlation between parameters of solar wind plasma and CR flux, and the goal of this paper is to extend the study of FDs, specifically its magnitude and time evolution, to wider range of parameters of the heliosphere measured routinely with satellites. We concentrate our study on previously scarcely used parameters of the solar wind, particularly flux of

charged particles of different energies. These particles are the source of inhomogeneity in the IMF, so the goal is to try and find distinguishing characteristics of FDs, like magnitude of decrease and FD profile that can be related to the satellite proton flux data, and examine their potential correlation with other space weather parameters. This additional information can be useful in finding explicit connection between parameters of solar wind and CR flux and can lead to better understanding of these complex processes.

## 2 CR data

In order to provide higher count rate, detector on Earth has to be omnidirectional and to detect integral flux over different range of energies. For the last seventy years secondary CRs are measured using standard ground-based neutron monitors (NMs) [6]. There is a worldwide network of NMs (<http://www01.nmdb.eu/>) that measures flux of secondary CRs originated from primary CRs with rigidity range approximately between 1 GV and 20 GV. Every node of the worldwide network of ground stations has its unique cut-off rigidity depending on its geomagnetic coordinates and height. The other type of widely used ground-based CR detectors are muon monitors. Muon monitors are sensitive to primary CRs of higher rigidity and complement NMs measurements [26]. Worldwide network of these muon stations is still rudimentary, but it can provide insight into flux variation of primary CRs with energies higher than CRs detected by NMs. Since both NMs and muon detectors are energy-integrating detectors and use entire atmosphere above it as a moderator, it is not trivial to relate count rate of these detectors to the flux or energy spectrum of primary CRs at the top of the atmosphere. One needs to know the response of a detector to a unit flux of CRs with the given energy, the so-called detector yield function. Yield functions can be calculated either theoretically, using a numerical simulation of the nucleonic cascade caused by energetic cosmic rays in the Earth's atmosphere, e.g., [8], or semi-empirically, for example based on a latitudinal survey [16].

As flux of secondary cosmic rays is also sensitive to varying properties of the atmosphere through which these CRs propagate, it is necessary to conduct flux correction of the measured flux for atmospheric parameters, where atmospheric pressure correction is the most important. In addition to atmospheric pressure, CR muons are sensitive to temperature variations in the atmosphere, starting from the top of the atmosphere all the way to the ground level. There are several procedures for corrections of these effects which are regularly used. Most commonly used are the integral method and the method of effective level of generation, but some novel techniques have also been introduced in recent years [25]. Correction for these atmospheric parameters is necessary in order to increase detector sensitivity to

**Table 1** Properties of primary CR flux related to muons detected at Belgrade CR station

Detector	Muon flux 1/(m <sup>2</sup> s)	$E_{0.05}$ (GeV)	$E_{med}$ (GeV)	$E_{0.95}$ (GeV)	Cut-off rigidity (GV)
GLL	137(6)	11	59(2)	915	5.3
UL	45(2)	31	137(5)	1811	12

variations of primary CRs flux and more precisely study the influence of solar modulation on galactic CRs.

Belgrade CR station started collecting data with the current experimental set-up in 2009. The station consists of two separate detector units: one placed on ground level (GLL) and the other in shallow underground (UL), both utilising the same experimental set-up. Such configuration provides opportunity to monitor muon fluxes in two different energy ranges with all other external parameters (such as atmospheric parameters, geomagnetic location and experimental set-up) being the same. Underground part of the station detects muons originated from primary CRs with higher energy because of the layer of soil overburden (13 m of loess) which absorbs lower-energy muons. Details of the detector systems at the Belgrade CRs station as well as calculated response functions are presented in [29]. The station is situated at the Laboratory for Nuclear Physics at the Institute of Physics Belgrade, Serbia. The altitude of the station is 78 m above sea level. Its geographic coordinates are: 44°51' N and 20°23' E, with geomagnetic latitude of 39°32' N. Sensitivity of Belgrade CR detectors to galactic CRs is given in Table 1, where primary CRs with the energy below  $E_{0.05}$  (and above  $E_{0.95}$ ) contribute with 5% to the count rate of the corresponding detector, and  $E_{med}$  is median energy based on simulation. In preparation for the analysis, detected muon count rates are corrected for efficiency, as well as for barometric and atmospheric temperature effects. Temperature effect correction is done using integral method [24].

### 3 Satellite data

In recent years, satellites provide new direct measurements of primary CRs flux in the heliosphere and the geomagnetic field. Also, detectors mounted on spacecraft allow us to probe even further, as Voyager recently crossed heliospheric boundary and for the first time galactic CRs flux was measured outside the heliosphere. The problem with such measurements is limitation to the size of the detectors, due to constraints of the construction of the satellites. In order to have valid statistics and good resolution, only low-energy particle flux can be measured. These low-energy particles are sensitive to geomagnetic field, which can introduce additional perturbation. Also, measurements of low-energy CRs can be masked by the increased flux of low-energy solar energetic particles (SEPs) in the MeV energy range. FDs detected by ground-based detectors are measured in energy range several orders of

magnitude higher than the energy range available to satellites measurements. (NMs detect flux that originate from  $\sim 10$  GeV, single muon detectors higher than that up to  $\sim 100$  GeV, while solar weather satellite measurements range up to several 100 MeV.) SEP occurrence is sporadic and depends on which part of the solar cycle we are in, so long-term studies with stable data quality are necessary if we are to study solar modulation of CRs. Such long-term measurements have been performed with various spacecrafts during the last four decades. Data measured on different interplanetary locations are then used for modelling of the heliosphere, which is important for understanding and forecasting space weather. This is a relatively new and dynamic field that is still expanding. More in situ measurements that can be catalogued [17] and compared with data from ground based stations will improve our understanding of near space environment.

In this paper, we use proton data from ERNE (Energetic and Relativistic Nuclei and Electron experiment) detector at the SOHO (Solar and Heliospheric Observatory) ([https://omniweb.gsfc.nasa.gov/ftpbrowser/flux\\_spectr\\_m.html](https://omniweb.gsfc.nasa.gov/ftpbrowser/flux_spectr_m.html)), which has been performing measurements in Lagrangian point L1 for the last quarter of a century described in [13] and references therein. Experiments that collect in situ particles data are ERNE and COSTEP (Comprehensive SupraThermal and Energetic Particle analyser), where data are combined to meet requirements of the mission. ERNE detector provides proton flux data in relatively large energy range (1.6 to 131 MeV) separated in several energy channels (1.3–1.6, 1.6–2.0, 2.0–2.5, 2.5–3.2, 3.2–4.0, 4.0–5.0, 5.0–6.4, 6.4–8.0, 8.0–10, 10–13, 13–16, 16–20, 20–25, 25–32, 32–40, 40–50, 50–64, 64–80, 80–100, 100–130 MeV). Measurements are taken with two different detectors: LED (low-energy detector) covers lower-energy and HED (high-energy detector) which covers higher-energy channels [28]. Satellites, including SOHO, also measure in situ parameters of the space environment and gather data about magnetic field, solar wind and concentration and flux of various types of particles on the location. Satellite data relevant to heliospheric studies are, among other places, available at GSFC/Space Physics Data Facility, in the form of low- and high-resolution OMNI data ([https://spdf.gsfc.nasa.gov/pub/data/omni/low\\_res\\_omni/](https://spdf.gsfc.nasa.gov/pub/data/omni/low_res_omni/)). In this study, we used the low-resolution OMNI data that contain hourly data for the solar wind magnetic field and plasma parameters, energetic proton fluxes, and geomagnetic and solar activity indices for different regions in proximity to Earth [12].

## 4 Four prominent FD events during rising phase of solar cycle 24

Previous (24th) solar cycle started in December 2008 and ended in November 2019 (as available from Sunspot Index and Long-term Solar Observations database <http://www.sidc.be/silso/node/167>). It had an unusually weak maximum, with smoothed maximum international sunspot number of 116. For comparison, in cycles 22 and 23 this number was 214 and 180, respectively (as available from Sunspot Index and Long-term Solar Observations database <http://sidc.be/silso/home>). Same period was also characterised by smaller number of FDs, especially ones with larger amplitudes.

There were fifteen strong FDs (with magnitude of decrease larger than 5% for particles with 10 GV rigidity) recorded in the rising phase of solar cycle 24, however in this study we will limit our analysis to four events detected by the Belgrade Cosmic Ray Station (<http://www.cosmic.ipb.ac.rs/>). Other prominent FDs that occurred in this period have not being detected by either GLL or UL detector due to discontinuity of operation, so they have been omitted from this study. All four events followed ejections from an active region on the Sun, accompanied by a solar flare with interplanetary shock wave and sudden storm commencing (SSC), and disturbance in the geomagnetic field. All of these FDs were seen by the NM detector network as well.

First significant FD of solar cycle 24 was recorded on 18 February 2011 and has been caused by a CME heading directly towards Earth [20]. It has been detected by most ground stations around the world. Its morphology is influenced by the interaction of two CMEs, first slower and the second faster (with respective speeds of 390 km/s and 1020 km/s), that occurred a day apart [27]. Geomagnetic activity has been relatively weak due to orientation of the magnetic field of the ejecta [21].

Second event was observed on 7 March 2012. It included an X-class flare (X5.4), that occurred in NOAA AR 11429 with an intense halo CME, followed by several smaller flares and another partial CME. It caused one of the strongest FDs of the last solar cycle. Observed solar activity was also related to the intense geomagnetic storm that followed [15].

A strong SF (X1.6) was detected by several spacecrafts during 10 September 2014, originating from active region NOAA AR 2158. Based on the SOHO coronagraph images, this flare was associated with a CME that was aimed towards Earth, where it arrived on September 12. This activity resulted in a major geomagnetic storm, one of the strongest in 2014.

In the second half of June 2015, solar activity was very intense, since a number of CMEs and flares were produced from the powerful AR 12371, which dominated solar activity during that period [23]. The impact of these CMEs on the Earth's magnetosphere resulted in a moderate to severe G4-class geomagnetic storm that occurred on the summer solstice. The result was a very interesting and unusual modulation galactic CRs flux, which appeared as a series of FDs.

For the study of FD events and their relationship with IMF and geomagnetic disturbances, researchers from IZMIRAN (Pushkov Institute of Terrestrial Magnetism, Ionosphere and Radio Wave Propagation, Russian Academy of Sciences) created an FD database (<http://spaceweather.izmiran.ru/eng/dbs.html>) which contains various FD parameters, as well as their relationship with heliospheric and geomagnetic parameters covering several solar cycles [1]. Properties of the four selected FDs, taken from the IZMIRAN database, are given in Table 2.

## 5 Data analysis

In order to establish the usability of SOHO SEP flux data in the study of CR variations, we will first analyse how muon count rate time series compare with some of the IMF parameters more commonly used in the analysis of solar activity-induced CR variations. To this end, we compare hourly muon count rates (measured by Belgrade muon station and corrected for atmospheric effects) with time series for selected parameters from OMNI database. To give more weight to this qualitative analysis, we concentrate only on periods of extreme solar activity, in particular periods of the occurrence of four FD events described in Sect. 4. We then examine the relationship between measured muon count rates and the SOHO/ERNE SEP flux data and analyse any discerning features in comparison with the ones observed in OMNI data time series. The period selected for this analysis is approximately one solar rotation of 27 days. All probes at L1 are about an hour upstream of the magnetosphere so all their data are interspersed with data from spacecraft close to Earth (e.g., IMP 8). In order to compute hourly averages “at Earth” this time shift has to be taken into account ([https://omniweb.gsfc.nasa.gov/html/ow\\_data.html](https://omniweb.gsfc.nasa.gov/html/ow_data.html)).

Next, we investigate the short-term correlation between SEP flux and muon count rate data during time periods of four selected FDs. Muon time series for this procedure were selected for times where average muon flux was significantly lower than the background level. Background level was determined from moving averages for hourly count rates 10 days before the event. We then perform correlative analysis between SOHO SEP flux data and muon count rates for a period of one year (from 01.06.2010 to 31.05.2011), in order to establish the long-term relationship. For further insight, we also look into the correlation between these variables during the periods of reduced geomagnetic activity (International Quiet Days) and increased geomagnetic activity (International Disturbed Days).

Finally, we look in greater detail into SOHO SEP flux time series. In order to perform more quantitative analysis, time-integrated flux is calculated for SEP data for different SOHO energy bins and for the duration of selected FD events. In order to provide a parameter for characterisation for different FD events, calculated integral flux is plotted as a function of proton energy and

**Table 2** Selected FD and interplanetary disturbance parameters (taken from IZMIRAN database)

Parameter	FD 1	FD 2	FD 3	FD 4	Parameter comment
Date of FD	18.2.2011.	8.3.2012.	12.9.2014.	22.6.2015.	
Date of parent solar event	15.2.2011.	7.3.2012.	10.9.2014.	21.6.2015.	
AR number	1158	11429	2158	12371	NOAA active region
$V_{meanC}$	584	1198	906	1040	The average ICME velocity between the Sun and the Earth, calculated using the time of the beginning of the associated CME observations (in km/s)
$V_{max}$	691	737	730	742	Maximal hourly solar wind speed in the event (in km/s)
$B_{max}$	31	23.1	31.7	37.7	Maximal hourly IMF strength in the event (in nT)
$B_{zmin}$	- 5.5	- 16.1	- 9.5	- 26.3	Minimal hourly Bz component of the IMF in the event (in nT)
$R_{bulk}$	72.25	146.2	131.35	171.25	An estimate of the maximum proton rigidity (in GV) that can be reflected by the total magnetic field, integrated from the event onset to the FD minimum
Magn	5.2	11.7	8.5	8.4	FD magnitude for particles with 10 GV rigidity, calculated as maximal range CRs density variations in the event, obtained by GSM from NM network data ( in %)
MagnM	4.7	13.1	6.9	10.4	FD magnitude for particles with 10 GV rigidity, corrected on magnetospheric effect with Dst-index (in %)
TminM	7	20	9	11	Time from the FD onset to minimum, calculated from the data corrected for magnetospheric effect
$Kp_{max}$	5	8	6.33	8.33	Maximal Kp-index in the event
$Ap_{max}$	48	207	94	236	Maximal 3-hour Ap-index in the event
$Dst_{min}$	- 30	- 143	- 75	- 204	Minimal Dst-index in the event (in nT)
Flare class	X2.2	X5.4	X1.6	M2.6	Associated X-ray flare data
SSN	85	97	126	56	Number of sunspot at the FD onset day

fitted with a power function. Dependence of magnitude for selected FDs on the exponents obtained from fitted distributions is then analysed.

## 6 Results and discussion

Comparison between time series of selected IMF parameters from OMNI database and muon count rate time

series during the periods of four selected FD events is shown in Fig. 1. Observed anticorrelation between muon count rates and proton flux and temperature, as well as with the overall IMF magnetic field and detected plasma speed, is in agreement with previously stated evidence in the literature [30].

Similar comparison between muon count rate time series and selected channels of SOHO/ERNE proton flux data for the same time intervals is shown in Fig.

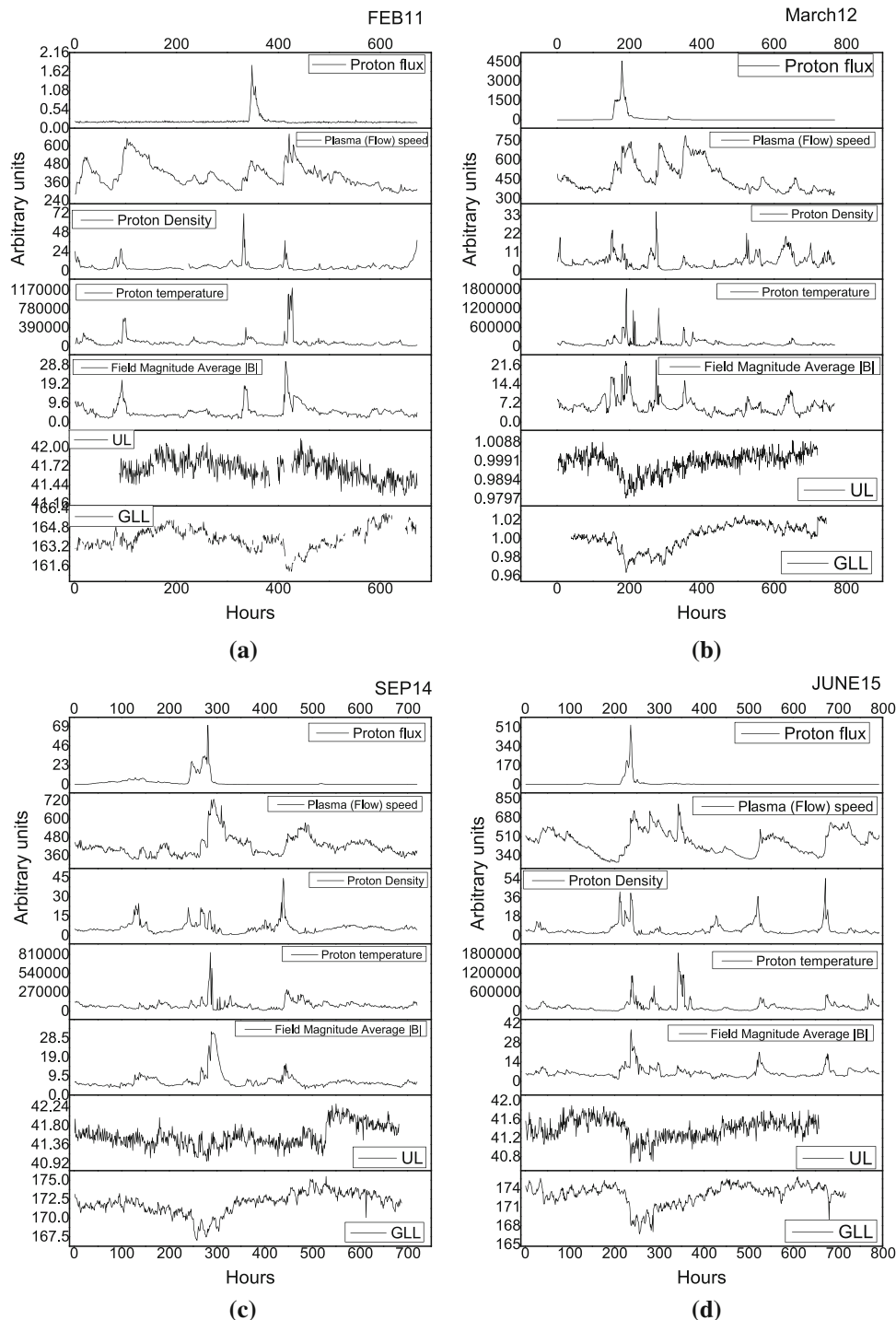


**Fig. 1** Time series for particle and plasma parameters (taken from OMNI database) in the time interval of approximately one month around the occurrence of four selected FD events: **a** February 2011 (start of time interval on 1 February), **b** March 2012 (start of time interval on 1 March), **c** September 2014 (start of time interval on 1 September) and **d** June 2015 (start of time interval on 13 June)

2. For the sake of clarity, we chose three energy channels (1.6–2 MeV, 16–20 MeV, 100–130 MeV), approximately one order of magnitude apart, where first channel is measured with LED and the other two with HED energy channels) and the beginning of FD recorded at ground station. This time lag is also present between

February 2011 event, there is an observable time lag ( $\approx 55$  h) between the increase of measured proton flux at low-energy channels (1.6–2 MeV and 16–20 MeV energy channels) and the beginning of FD recorded at ground station. This time lag is also present between

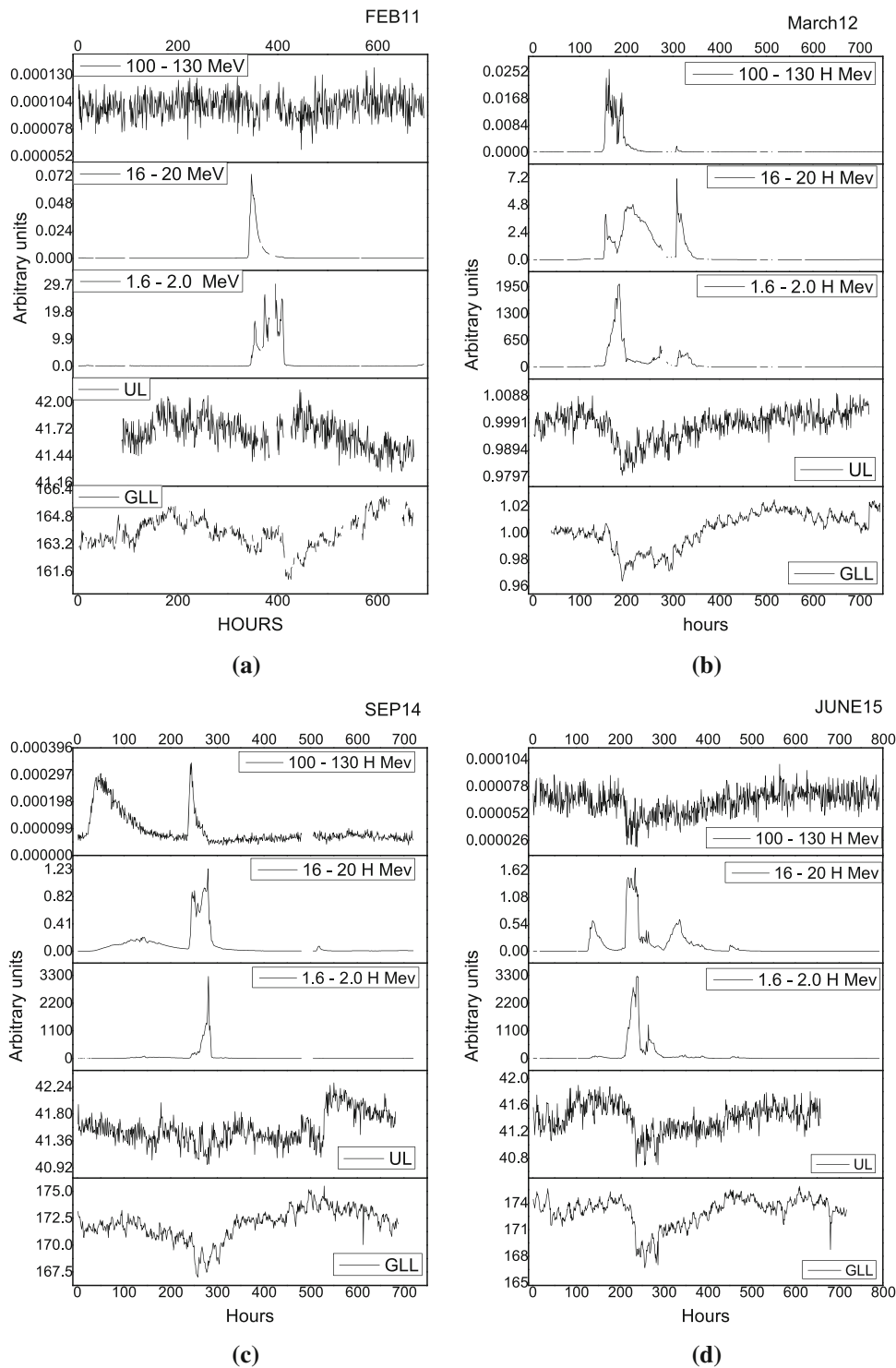


**Fig. 2** Hourly time series for different proton channels from SOHO/ERNE and two muon detectors at Belgrade CR station, in the time interval of approximately one month around the occurrence of four selected FD events: **a**) February (start of time interval on 1 February) 2011, **b** March 2012 (start of time interval on 1 March), **c** September 2014 (start of time interval on 1 September) and **d** June 2015 (start of time interval on 13 June)

OMNI proton flux data and ground station measurements for this FD alone. FD is a complex modulation of CR flux that depends on a lot of parameters, like magnitude of magnetic field and its components,

speed of solar wind and CMEs (with CME average speed  $\approx 490$  km/s), most of which are listed in Table 2. Parameter values for all four ICMEs are mostly comparable, but one difference that stands out is the discrep-



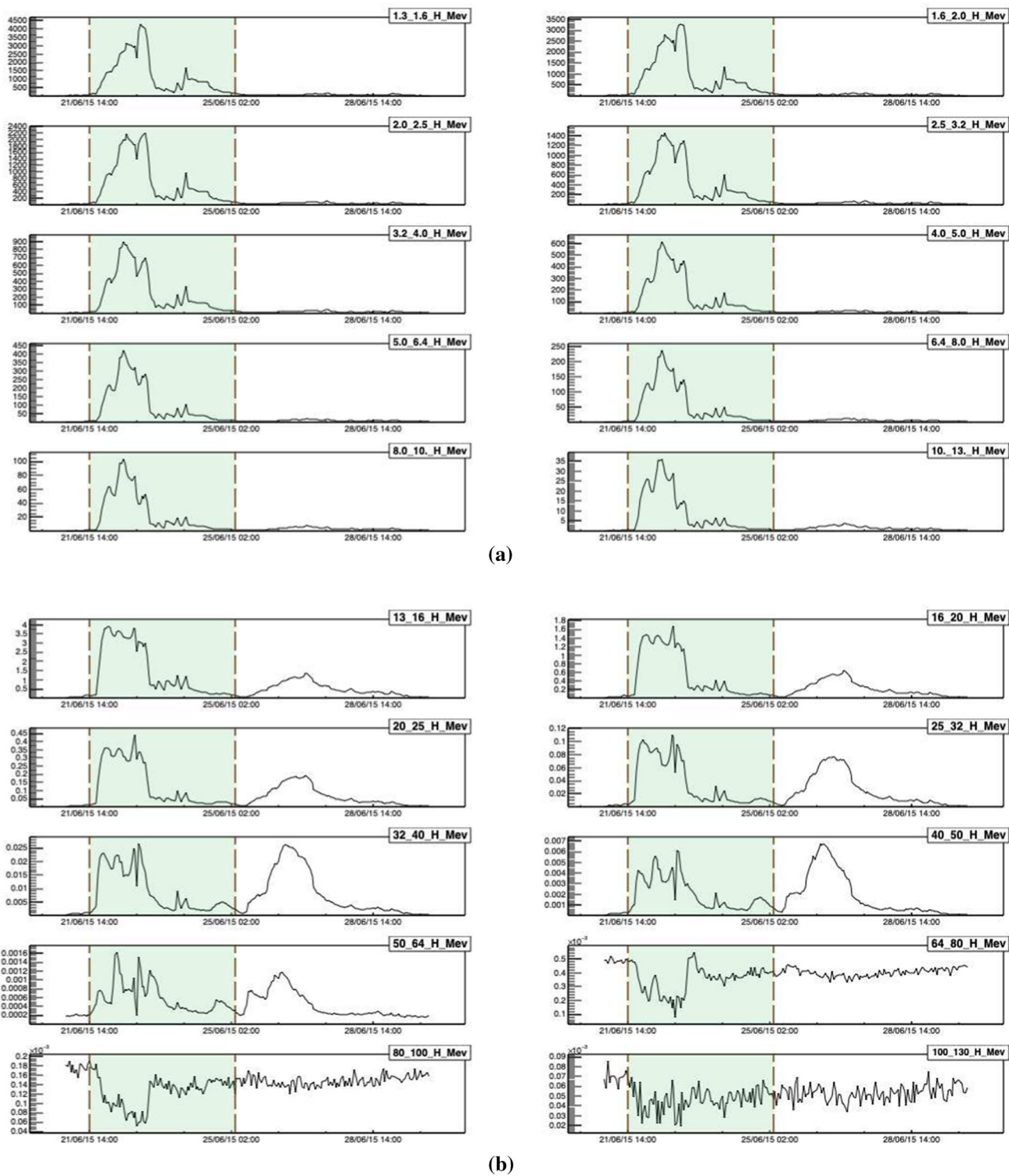


**Fig. 3** Differential SEP fluxes during extreme solar event in June 2015, measured by SOHO/ERNE proton channels. Vertical dashed lines indicate the time for the start and the end of interval used to calculate the integral flux

ancy in average CME velocity (584 km/s from Table 2.) for the FD of February 2011, which can possibly explain the observed time lag for this particular FD.

Based on the observed time lag and other coincident features, we can establish good agreement between

SOHO low-energy channel data and OMNI data time series. As for high-energy channels, SEP time series in 100–130 MeV energy range for February 2011 and June 2015 events appear to correlate with muon count rate measurements on the ground. One possible explanation

**Table 3** Statistical correlation between Belgrade CR station and SOHO/ERNE measurements during the periods of four selected FD events

FD	Energy range (MeV)	GLL		UL	
		Pearson coefficient	<i>P</i> value	Pearson coefficient	<i>P</i> value
FEB 11	1.6–2.0 H	– 0.10877	0.01	– 0.05285	0.2
	16–20 H	– 0.18384	$2 \times 10^{-5}$	– 0.10732	0.01
	100–130 H	0.24204	$< 10^{-6}$	– 0.13212	0.02
MAR 12	1.6–2.0 H	– 0.48477	$< 10^{-6}$	– 0.43994	$< 10^{-6}$
	16–20 H	– 0.72033	$< 10^{-6}$	– 0.68221	$< 10^{-6}$
	100–130 H	– 0.29172	$< 10^{-6}$	– 0.27822	$< 10^{-6}$
SEP 14	1.6–2.0 H	– 0.2839	$< 10^{-6}$	– 0.48052	$< 10^{-6}$
	16–20 H	– 0.37814	$< 10^{-6}$	– 0.63735	$< 10^{-6}$
	100–130 H	– 0.04951	0.007	– 0.10466	0.2
JUN 15	1.6–2.0 H	– 0.3921	$< 10^{-6}$	– 0.27531	$< 10^{-6}$
	16–20 H	– 0.31229	$< 10^{-6}$	– 0.17113	$< 10^{-6}$
	100–130 H	0.48588	$< 10^{-6}$	0.39296	$< 10^{-6}$

could be that in addition to SEP these energy channels are also populated by very low-energy CRs.

We can further investigate this assumption by looking more closely into SOHO SEP flux time series for one of the two weaker FD events. We have selected June 2015 event, as time series for higher-energy channels appear to be slightly more informative. Figure 3 shows proton flux series for all energy channels measured by SOHO/ERNE detector. From these plots, it is apparent that proton fluxes for energies larger than 64 MeV exhibit different dynamic relative to fluxes of lower energies, and seem to be in anticorrelation with them. This indeed supports the assumption these channels are populated by low-energy CR.

Another way we can illustrate this observation more quantitatively is by performing relative analysis. Firstly, we will look into short-term correlations between proton flux and muon count rate time series during four selected FD events. Correlation between respective time series was found using Pearson correlation coefficient. For significance two-tailed test is used. Correlation coefficient and its significance level between ground station and in situ measurement from SOHO/ERNE instrument is given in Table 3.

Due to higher energy of the primary CRs detected in UL, the correlation between SEPs and measured flux in UL is smaller than correlation between SEPs and flux measured in GLL. The greatest anticorrelation (i.e., between GLL and UL data and 16–20 MeV protons  $\approx -0.7$ ) is observed for the strongest ICME (and corresponding FD) of March 2012, and this anticorrelation is observed in all energy channels. However, for lower-intensity events of June 2015 and February 2011, correlations between detected CR flux in GLL and highest energy channel (100–130 MeV) are mostly positive. These observations further confirm the assumption about high-energy channels being populated by low-energy CR, which is especially evident in case of low-intensity FD events.

**Table 4** Pearson correlation coefficient for the correlation between CR flux detected at Belgrade CR station (GLL detector) and flux of protons of different energies detected with SOHO/ERNE detector, for the period of one year (from June 2010 May 2011)

	GLL	
	Pearson coefficient	<i>P</i> value
H 1.3–1.6 MeV	– 0.02	0.13
H 1.6–2.0 MeV	– 0.02	0.16
H 2.0–2.5 MeV	– 0.02	0.20
H 2.5–3.2 MeV	– 0.01	0.27
H 3.2–4.0 MeV	– 0.01	0.36
H 4.0–5.0 MeV	– 0.01	0.57
H 5.0–6.4 MeV	$< 0.01$	0.75
H 6.4–8.0 MeV	$< 0.01$	1.00
H 8.0–10 MeV	$< 0.01$	0.78
H 10–13 MeV	0.01	0.57
H 13–16 MeV	0.01	0.41
H 16–20 MeV	0.01	0.31
H 20–25 MeV	0.01	0.26
H 25–32 MeV	0.01	0.24
H 32–40 MeV	0.01	0.27
H 40–50 MeV	0.01	0.46
H 50–64 MeV	$< 0.01$	0.80
H 64–80 MeV	0.05	$< 0.01$
H 80–100 MeV	0.12	$< 0.01$
H 100–130 MeV	0.07	$< 0.01$

Similar results, with even greater correlation between the entire time profile for flux measured with NMs and solar wind speed and magnetic field during ICME, are reported for stronger FDs during solar cycle 23 [5].

Next, we will analyse long-term correlations between SOHO proton flux and measured muon count rates. Pearson coefficients for this correlation over a period of one year (from June 2010 May 2011), when activity of the Sun was low at the commencement of the 11-years cycle, are presented in Table 4. Here we see very

**Table 5** Pearson correlation coefficient for the correlation between CR flux detected at Belgrade CR station (GLL detector) and flux of protons of different energies detected with SOHO/ERNE detector, during international geomagnetically quiet and disturbed days for the period of one year (from June 2010 May 2011)

	GLL Quiet days		GLL Disturbed days	
	Pearson coefficient	<i>P</i> value	Pearson coefficient	<i>P</i> value
H 1.3–1.6 MeV	0.01	0.61	– 0.05	0.13
H 1.6–2.0 MeV	0.01	0.80	– 0.05	0.14
H 2.0–2.5 MeV	0.02	0.30	– 0.05	0.13
H 2.5–3.2 MeV	0.03	0.11	– 0.05	0.12
H 3.2–4.0 MeV	0.04	0.04	– 0.05	0.10
H 4.0–5.0 MeV	0.05	0.02	– 0.06	0.08
H 5.0–6.4 MeV	0.05	0.01	– 0.06	0.07
H 6.4–8.0 MeV	0.06	0.01	– 0.06	0.06
H 8.0–10 MeV	0.06	0.01	– 0.06	0.06
H 10–13 MeV	0.06	0.01	– 0.06	0.07
H 13–16 MeV	0.06	< 0.01	– 0.06	0.08
H 16–20 MeV	0.06	< 0.01	– 0.05	0.10
H 20–25 MeV	0.06	< 0.01	– 0.05	0.12
H 25–32 MeV	0.06	< 0.01	– 0.05	0.15
H 32–40 MeV	0.06	< 0.01	– 0.04	0.20
H 40–50 MeV	0.06	< 0.01	– 0.02	0.57
H 50–64 MeV	0.07	< 0.01	0.07	0.03
H 64–80 MeV	0.25	< 0.01	0.08	0.02
H 80–100 MeV	0.38	< 0.01	0.11	< 0.01
H 100–130 MeV	0.15	< 0.01	0.09	0.01

little correlation between CR and proton fluxes in all but the highest energy channels (above 64 MeV).

Table 5 shows the same correlation analysis if only data for 10 geomagnetically quietest or 5 geomagnetically most disturbed days of each month ([http://isgi.unistra.fr/events\\_qdays.php](http://isgi.unistra.fr/events_qdays.php)) are used. The fact that we observe a significant increase of positive correlation coefficients in the case of geomagnetically quiet days, further corroborates the assumption about the mixed nature of particles that populate higher-energy channels. Consequentially, care should be taken how data from these channels are treated in analysis.

To provide further quantitative support for the use of SOHO SEP flux measurements in the analysis of FD events, we will calculate integral proton flux in all energy channels for the four selected FDs. Integration intervals are selected to include the period of increased proton flux that corresponds to a particular FD, but not to extend the interval to include potential follow-up structures that cannot be associated with the event. One such selection for all energy channels, for June 2015 event, is indicated by dashed lines in Fig. 3. In Fig. 4, we show thusly calculated integral flux as a function of particle energy (where lower boundary values from SOHO SEP energy bins are taken), using both linear and log scale for clarity.

One feature that can be noticed from plots in Fig. 4 is that integral flux drops off is more steeply in February 2011 than for others studied FDs, where a change in the trend between high-energy and low-energy range can be observed. FD that occurred in March 2012 was the longest and the most intensive of the four. Steepness of

the integral flux for this FD shows relatively more populated proton channels with higher energies compared to weaker FD. This is in agreement with strongest modulation of CRs flux during this FD. There is a discontinuity in the integral flux between proton energy channel 13–16 MeV and 16–20 MeV due to different acquisition method from different instruments, and possibly because of degradation of the detectors on board the spacecraft [13] and saturation of the instrument due to high intensity of solar protons [18].

One simple way to characterise relative abundance of SEP particles of different energies for a given event would be to fit described integral flux distribution with a power function, where (in a simple approximation) larger exponent would indicate greater relative abundance of lower-energy particles, while smaller exponent would point to greater relative abundance of higher-energy particles. Distributions were fitted with a power function given by the formula  $I(E) = a * E^b$  (where  $I$  is the integral flux and  $E$  is particle energy), resulting fits represented by red lines in Fig. 4, while values for the exponents of power function fits are represented in Table 6.

If SOHO protons flux measurements are to be proved useful in the analysis of FD events, SEP flux characteristics should correlate with some of the FD and interplanetary disturbance parameters. To test this, we have analysed dependence of different FD parameters on the exponent of the integral proton flux power distribution (labelled  $b$  in the formula in previous paragraph). We have found some correlation for most tested parameters, most striking being one between the magnitude

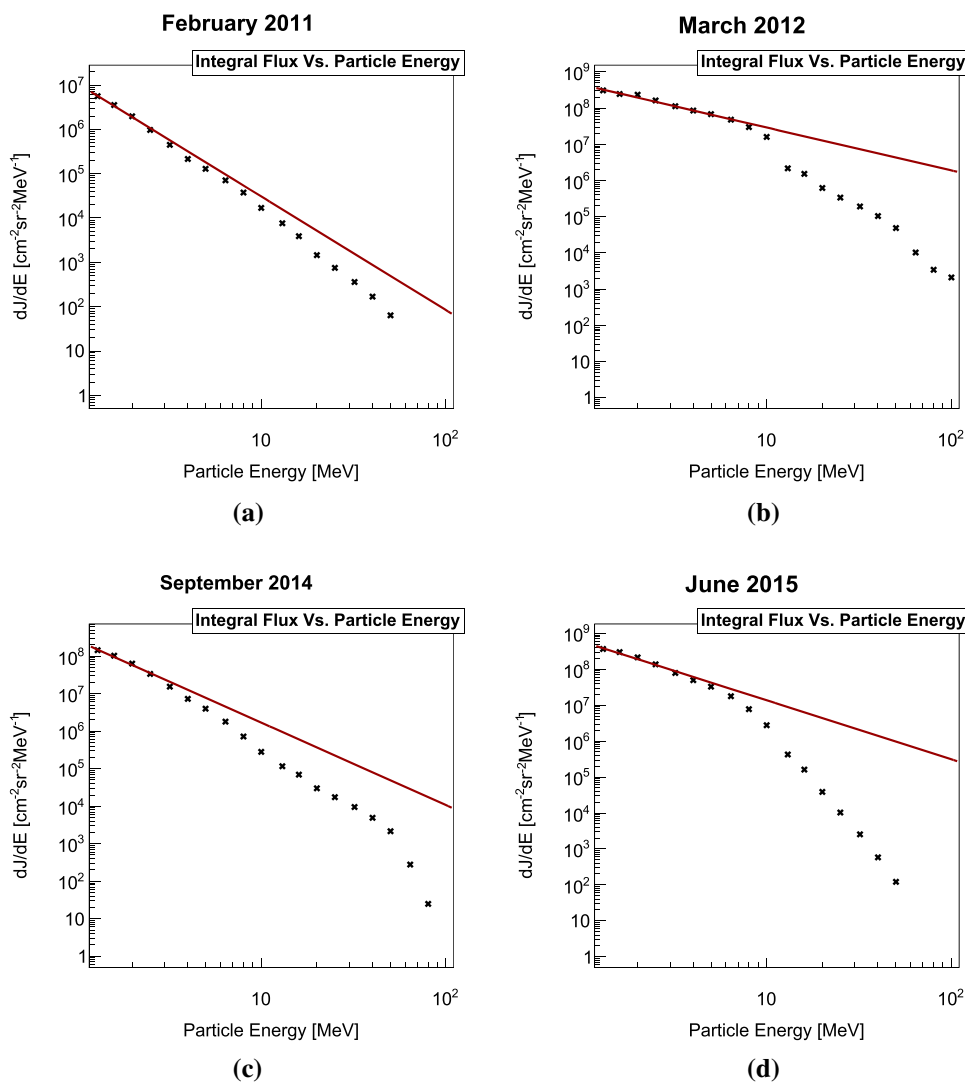


**Fig. 4** Time-integrated flux of differential SEP fluxes during the four selected FD events: **a** February 2011, **b** March 2012, **c** September 2014 and **d** June 2015, in linear and logarithmic scale. Power function fits are represented by red lines

**Table 6** Exponent values of power function fits of integral proton flux distributions

FD	Power function exponent values
FEB 2011	- 2.56
MAR 2012	- 1.18
SEP 2014	- 2.20
JUN 2015	- 1.64

of FD for particles with 10 GV rigidity (corrected for magnetospheric effect) and the exponent of the integral flux. This dependence (strictly for illustrative purposes fitted with linear fit) is shown in Fig. 5.

Observed strong dependence is potentially a very good indicator that SOHO SEP flux measurements can be a valid source of data to be used in the analysis of

interplanetary disturbances and their interaction with cosmic rays.

## 7 Conclusions

Analysing strong aperiodic variations of cosmic ray flux, such as Forbush decreases, allows us to study violent processes that occur on the Sun, and corresponding perturbations in the heliosphere, using Earth-based detectors. In addition to cosmic ray flux and magnetic field data commonly used to study such events, we have extended analysis to include proton flux measurements, obtained using spacecraft mounted detectors. Based on the analysis of four selected Forbush decrease events, we have found SOHO/ERNE proton flux measurements to be consistent with solar plasma parameters, as well as with observations by the ground-based muon detectors.

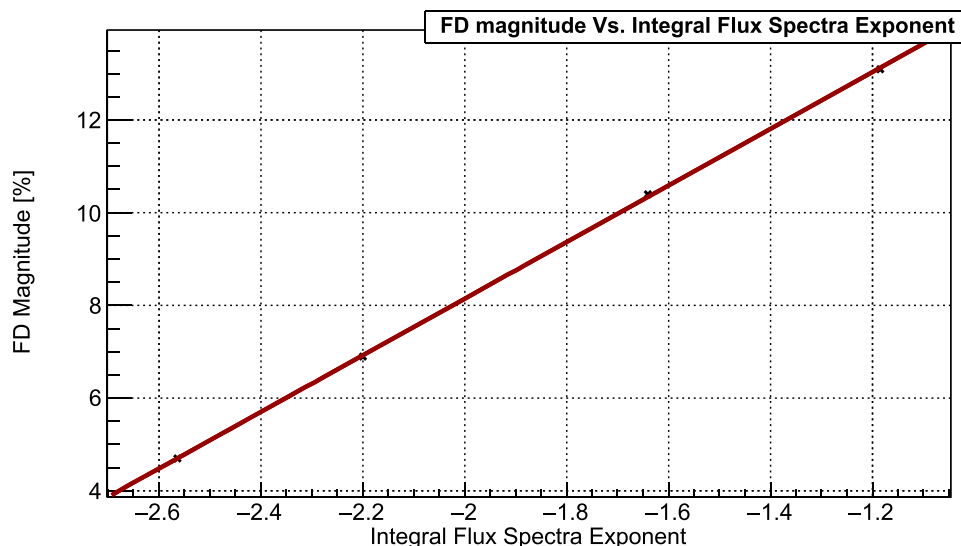


**Fig. 5** Dependence of FD magnitude, corrected for magnetospheric effect with Dst-index for particles with 10 GV rigidity, on the power exponent of the integral SEP flux, four selected FD events: **a** February 2011, **b** March 2012, **c** September 2014 and **d** June 2015. Linear fit (for illustrative purposes) is indicated by the red line

We have concluded that during Forbush decrease events lower-proton-energy channels are dominated by SEP particles, while in higher-energy channels there is a contribution of low-energy cosmic rays, especially apparent during less intense events. We have found a clear correlation between Forbush decrease magnitude (corrected for magnetospheric effect with Dst-index for particles with 10 GV rigidity) and power exponent of the integral flux of SOHO/ERNE measurements. This result gives grounds to further pursue the analysis of heliospheric proton flux data, as it may yield additional valuable information. Such information can potentially help us to classify and study in greater detail the dynamics of interaction of cosmic rays in the heliosphere.

**Acknowledgements** The authors acknowledge funding provided by the Institute of Physics Belgrade, through the grant by the Ministry of Education, Science and Technological Development of the Republic of Serbia. We also acknowledge use of NASA/GSFC's Space Physics Data Facility's OMNIWeb (or CDAWeb or ftp) service and OMNI data as well as team behind SOHO, which is a project of international collaboration between ESA and NASA. We would also like to thank the referees for constructive and useful advice.

**Data Availability Statement** "This manuscript has data included as electronic supplementary material".

## References

1. A.A. Abunin, M.A. Abunina, A.V. Belov, S.P. Gaidash, E.A. Eroshenko, I.I. Pryamushkina, L.A. Trefilova, E.I. Gamza, *J. Phys. Conf. Ser.* **1181**, 012062 (2019). <https://doi.org/10.1088/1742-6596/1181/1/012062>
2. K.P. Arunbabu, H.M. Antia, S.R. Dugad, S.K. Gupta, Y. Hayashi, S. Kawakami, P.K. Mohanty, T. Nonaka, A. Oshima, P. Subramanian, *A and A* **555**, A139 (2013). <https://doi.org/10.1051/0004-6361/201220830>
3. K.P. Arunbabu, H.M. Antia, S.R. Dugad, S.K. Gupta, Y. Hayashi, S. Kawakami, P.K. Mohanty, A. Oshima, P. Subramanian, *A and A* **580**, A41 (2015). <https://doi.org/10.1051/0004-6361/201425115>
4. C.R.A. Augusto, V. Kopenkin, C.E. Navia, K.H. Tsui, H. Shigueoka, A.C. Fauth, E. Kemp, E.J.T. Manganote, M.A. Leigui de Oliveira, P. Miranda, R. Ticona, A. Velarde, *ApJ* **759**, 143 (2012). <https://doi.org/10.1088/0004-637X/759/2/143>
5. A. Bhaskar, G. Vichare, K.P. Arunbabu et al., *Astrophys. Space Sci.* **361**, 242 (2016). <https://doi.org/10.1007/s10509-016-2827-8>
6. V. Belov, *SpaceSci. Rev.* **93**(1), 79–105 (2000). <https://doi.org/10.1023/A:1026584109817>
7. H.V. Cane, *Space Sci. Rev.* **93**, 55–77 (2000). <https://doi.org/10.1023/A:1026532125747>
8. J.M. Clem, L.I. Dorman, *Space Sci. Rev.* **93**, 335–359 (2000). <https://doi.org/10.1023/A:1026508915269>
9. E.S. Comedi, A.S. Elias, B.S. Zossi, S. Bruno, *JASTP* **211**, 105475 (2020). <https://doi.org/10.1016/j.jastp.2020.105475>
10. M. Duldig, *Science* **314**(5798), 429–430 (2006). <https://doi.org/10.1126/science.1134046>
11. M. Dumbović, B. Vršnak, J. Guo et al., *Sol. Phys.* **295**, 104 (2020). <https://doi.org/10.1007/s11207-020-01671-7>
12. J.H. King, N.E. Papitashvili, *J. Geophys. Res.* **110**, A02104 (2005). <https://doi.org/10.1029/2004JA010649>
13. P. Kühl, B. Heber, R. Gómez-Herrero, O. Malandraki, A. Posner, H. Sierks, *J. Space Weather Space Clim.* (2020). <https://doi.org/10.1051/swsc/2020056>
14. S.Y. Lee, *Accelerator Physics*, 2nd edn. (World Scientific, Singapore, 2004)

15. M. Livada, H. Mavromichalaki, C. Plainaki, *Astrophys. Space Sci.* **363**, 8 (2018). <https://doi.org/10.1007/s10509-017-3230-9>
16. R.A. Caballero-Lopez, H. Moraal, *JGR Space Phys.* **117**, A12 (2012). <https://doi.org/10.1029/2012JA017794>
17. R. Miteva, S.W. Samwel, M.V. Costa-Duarte, *JASTP* (2018). <https://doi.org/10.1016/j.jastp.2017.05.003>
18. R. Miteva, D. Danov, in *Proceedings of the tenth Workshop 'Solar Influences on the Magnetosphere, Ionosphere and Atmosphere', Primorsko, Bulgaria*, ed. by K. Georgieva, B. Kirov, D. Danov, 2018. <https://doi.org/10.31401/WS.2018.proc>
19. H. Moraal, *Space Sci. Rev.* **176**, 299–319 (2013). <https://doi.org/10.1007/s11214-011-9819-3>
20. S.Y. Oh, Y. Yi, *A Sol. Phys.* **280**, 197–204 (2012). <https://doi.org/10.1007/s11207-012-0053-2>
21. A. Papaioannou, A. Belov, H. Mavromichalaki et al., *J. Phys. Conf. Ser.* **409**, 012202 (2013). <https://doi.org/10.1088/1742-6596/409/1/012202>
22. A. Papaioannou, M. Belov, E. Abunina, A. Eroshenko, A. Abunin, S. Anastasiadis, Patsourakos, H. Mavromichalaki, *ApJ* **890**, 101 (2020). <https://doi.org/10.3847/1538-4357/ab6bd1>
23. E. Samara, A. Smponias, I. Lytrosyngounis et al., *Sol. Phys.* **293**, 67 (2018). <https://doi.org/10.1007/s11207-018-1290-9>
24. M. Savić, A. Dragić, N. Veselinović et al., *XXV ECRS 2016 Proceedings—eConf C16-09-04.3*, e-Print: 1701.00164 [physics.ins-det], [arXiv:1701.00164v1](https://arxiv.org/abs/1701.00164)
25. M. Savić, A. Dragić, D. Maletić et al., *Astropart. Phys.* (2019). <https://doi.org/10.1016/j.astropartphys.2019.01.006>
26. M. Savić, N. Veselinović, A. Dragić et al., *ASR* **63**, 4 (2019). <https://doi.org/10.1016/j.asr.2018.09.034>. ISSN 0273-1177
27. M. Temmer, A.M. Veronig, V. Peinhardt, B. Vršnak, *ApJ* **785**, 85 (2014). <https://doi.org/10.1088/0004-637X/785/2/85>
28. J. Torsti, E. Valtonen, M. Lumme et al., *Sol. Phys.* **162**, 505–531 (1995). <https://doi.org/10.1007/BF00733438>
29. N. Veselinović, A. Dragić, M. Savić, D. Maletić, D. Joković, R. Banjanac, V. Udovičić, *NIM A* **875**, 1 (2017). <https://doi.org/10.1016/j.nima.2017.09.008>. ISSN 0168-9002
30. L.-L. Zhao, H. Zhang, *ApJ* **827**, 13 (2016). <https://doi.org/10.3847/0004-637X>

PAPER • OPEN ACCESS

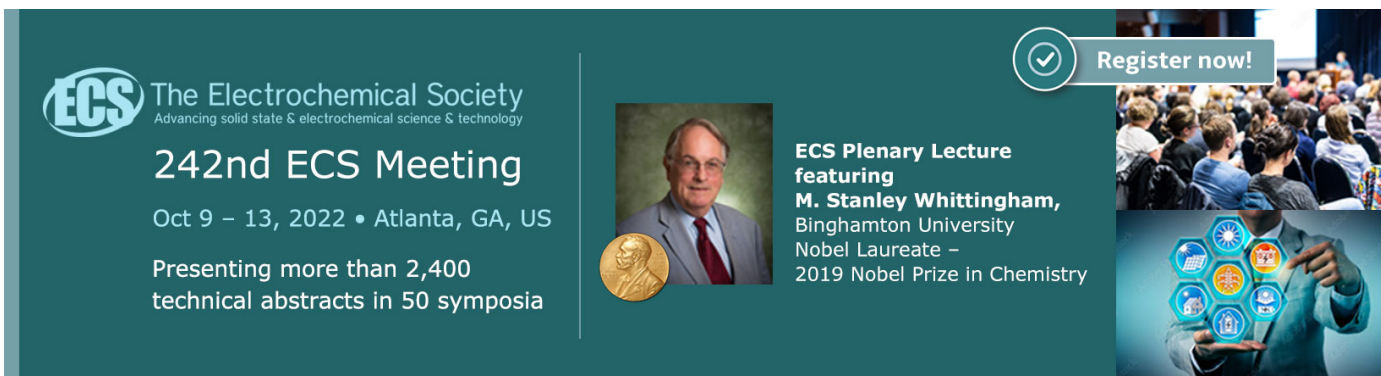
## Performance of the MICE diagnostic system

To cite this article: The MICE collaboration *et al* 2021 *JINST* **16** P08046

View the [article online](#) for updates and enhancements.

### You may also like

- [Search for Gravitational Waves Associated with Gamma-Ray Bursts Detected by Fermi and Swift during the LIGO–Virgo Run O3b](#)  
R. Abbott, T. D. Abbott, F. Acernese et al.
- [Narrowband Searches for Continuous and Long-duration Transient Gravitational Waves from Known Pulsars in the LIGO–Virgo Third Observing Run](#)  
R. Abbott, T. D. Abbott, F. Acernese et al.
- [Identification of hadronic tau lepton decays using a deep neural network](#)  
A. Tumasyan, W. Adam, J.W. Andrejkovic et al.





**ECS** The Electrochemical Society  
Advancing solid state & electrochemical science & technology


## 242nd ECS Meeting

Oct 9 – 13, 2022 • Atlanta, GA, US

Presenting more than 2,400 technical abstracts in 50 symposia

 **ECS Plenary Lecture featuring M. Stanley Whittingham,** Binghamton University Nobel Laureate – 2019 Nobel Prize in Chemistry

 Register now!



## MUON ACCELERATORS FOR PARTICLE PHYSICS — MUON

## Performance of the MICE diagnostic system

## The MICE collaboration

M. Bogomilov,<sup>a</sup> R. Tsenov,<sup>a</sup> G. Vankova-Kirilova,<sup>a</sup> Y.P. Song,<sup>b</sup> J.Y. Tang,<sup>b</sup> Z.H. Li,<sup>c</sup>  
R. Bertoni,<sup>d</sup> M. Bonesini,<sup>d</sup> F. Chignoli,<sup>d</sup> R. Mazza,<sup>d</sup> V. Palladino,<sup>e</sup> A. de Bari,<sup>f</sup> D. Orestano,<sup>g</sup>  
L. Tortora,<sup>g</sup> Y. Kuno,<sup>h</sup> H. Sakamoto,<sup>h,1</sup> A. Sato,<sup>h</sup> S. Ishimoto,<sup>i</sup> M. Chung,<sup>j</sup> C.K. Sung,<sup>j</sup>  
F. Filthaut,<sup>k,2</sup> M. Fedorov,<sup>l</sup> D. Jokovic,<sup>m</sup> D. Maletic,<sup>m</sup> M. Savic,<sup>m</sup> N. Jovancevic,<sup>n</sup> J. Nikolov,<sup>n</sup>  
M. Vretenar,<sup>o</sup> S. Ramberger,<sup>o</sup> R. Asfandiyarov,<sup>p</sup> A. Blondel,<sup>p</sup> F. Drielsma,<sup>p,3</sup> Y. Karadzhov,<sup>p</sup>  
G. Charnley,<sup>q</sup> N. Collomb,<sup>q</sup> K. Dumbell,<sup>q</sup> A. Gallagher,<sup>q</sup> A. Grant,<sup>q</sup> S. Griffiths,<sup>q</sup> T. Hartnett,<sup>q</sup>  
B. Martlew,<sup>q</sup> A. Moss,<sup>q</sup> A. Muir,<sup>q</sup> I. Mullacrane,<sup>q</sup> A. Oates,<sup>q</sup> P. Owens,<sup>q</sup> G. Stokes,<sup>q</sup>  
P. Warburton,<sup>q</sup> C. White,<sup>q</sup> D. Adams,<sup>r</sup> V. Bayliss,<sup>r</sup> J. Boehm,<sup>r</sup> T.W. Bradshaw,<sup>r</sup> C. Brown,<sup>r,4</sup>  
M. Courthold,<sup>r</sup> J. Govans,<sup>r</sup> M. Hills,<sup>r</sup> J.-B. Lagrange,<sup>r</sup> C. Macwaters,<sup>r</sup> A. Nichols,<sup>r</sup>  
R. Preece,<sup>r</sup> S. Ricciardi,<sup>r</sup> C. Rogers,<sup>r</sup> T. Stanley,<sup>r</sup> J. Tarrant,<sup>r</sup> M. Tucker,<sup>r</sup> S. Watson,<sup>r,5</sup>  
A. Wilson,<sup>r</sup> R. Bayes,<sup>s,6</sup> J.C. Nugent,<sup>s</sup> F.J.P. Soler,<sup>s</sup> R. Gamet,<sup>t</sup> P. Cooke,<sup>t</sup> V.J. Blackmore,<sup>u</sup>  
D. Colling,<sup>u</sup> A. Dobbs,<sup>u,7</sup> P. Dornan,<sup>u</sup> P. Franchini,<sup>u,\*</sup> C. Hunt,<sup>u,8</sup> P.B. Jurj,<sup>u</sup> A. Kurup,<sup>u</sup>  
K. Long,<sup>u</sup> J. Martyniak,<sup>u</sup> S. Middleton,<sup>u,9</sup> J. Pasternak,<sup>u</sup> M.A. Uchida,<sup>u,10</sup> J.H. Cobb,<sup>v</sup>  
C.N. Booth,<sup>w</sup> P. Hodgson,<sup>w</sup> J. Langlands,<sup>w</sup> E. Overton,<sup>w,11</sup> V. Pec,<sup>w</sup> P.J. Smith,<sup>w</sup>  
S. Wilbur,<sup>w</sup> G.T. Chatzitheodoridis,<sup>x,12,13</sup> A.J. Dick,<sup>x,13</sup> K. Ronald,<sup>x,13</sup> C.G. Whyte,<sup>x,13</sup>  
A.R. Young,<sup>x,13</sup> S. Boyd,<sup>y</sup> J.R. Greis,<sup>y,14</sup> T. Lord,<sup>y</sup> C. Pidcott,<sup>y,15</sup> I. Taylor,<sup>y,16</sup> M. Ellis,<sup>z,17</sup>

<sup>1</sup>Current address: RIKEN 2-1 Hirosawa, Wako, Saitama, Japan.

<sup>2</sup>Also at Radboud University, Houtlaan 4, Nijmegen, Netherlands.

<sup>3</sup>Current address: SLAC National Accelerator Laboratory, 2575 Sand Hill Road, Menlo Park, CA, U.S.A.

<sup>4</sup>Also at College of Engineering, Design and Physical Sciences, Brunel University, Kingston Lane, Uxbridge, U.K.

<sup>5</sup>Current address: ATC, Royal Observatory Edinburgh, Blackford Hill, Edinburgh, U.K.

<sup>6</sup>Current address: Laurentian University, 935 Ramsey Lake Road, Sudbury, ON, Canada.

<sup>7</sup>Current address: OPERA Simulation Software, Network House, Langford Locks, Kidlington, U.K.

<sup>8</sup>Current address: CERN, Esplanade des Particules 1, Geneva, Switzerland.

<sup>9</sup>Current address: School of Physics and Astronomy, University of Manchester, Oxford Road, Manchester, U.K.

<sup>10</sup>Current address: Rutherford Building, Cavendish Laboratory, JJ Thomson Avenue, Cambridge, U.K.

<sup>11</sup>Current address: Arm, City Gate, 8 St Mary's Gate, Sheffield, U.K.

<sup>12</sup>Also at School of Physics and Astronomy, Kelvin Building, University of Glasgow, Glasgow, U.K.

<sup>13</sup>Also at Cockcroft Institute, Daresbury Laboratory, Sci-Tech Daresbury, Keckwick Ln, Daresbury, Warrington, U.K.

<sup>14</sup>Current address: TNG Technology Consulting, Beta-Strasse 13A, Unterföhring, Germany.

<sup>15</sup>Current address: Department of Physics and Astronomy, University of Sheffield, Hounsfield Rd, Sheffield, U.K.

<sup>16</sup>Current address: Defence Science and Technology Laboratory, Porton Down, Salisbury, U.K.

<sup>17</sup>Current address: Macquarie Group, 50 Martin Place, Sydney, Australia.





**R.B.S. Gardener,<sup>z,18</sup> P. Kyberd,<sup>z</sup> J.J. Nebrensky,<sup>z</sup> M. Palmer,<sup>aa</sup> H. Witte,<sup>aa</sup> D. Adey,<sup>ab,19</sup>  
**A.D. Bross,<sup>ab</sup> D. Bowring,<sup>ab</sup> P. Hanlet,<sup>ab</sup> A. Liu,<sup>ab,20</sup> D. Neuffer,<sup>ab</sup> M. Popovic,<sup>ab</sup>  
**P. Rubinov,<sup>ab</sup> A. DeMello,<sup>ac</sup> S. Gourlay,<sup>ac</sup> A. Lambert,<sup>ac</sup> D. Li,<sup>ac</sup> T. Luo,<sup>ac</sup> S. Prestemon,<sup>ac</sup>  
**S. Virostek,<sup>ac</sup> B. Freemire,<sup>ad,20</sup> D.M. Kaplan,<sup>ad</sup> T.A. Mohayai,<sup>ad,21</sup> D. Rajaram,<sup>ad,22</sup>  
**P. Snopok,<sup>ad</sup> Y. Torun,<sup>ad</sup> L.M. Cremaldi,<sup>ae</sup> D.A. Sanders,<sup>ae</sup> D.J. Summers,<sup>ae,23</sup>  
**L.R. Coney,<sup>af,24</sup> G.G. Hanson<sup>af</sup> and C. Heidt<sup>af,25</sup>************

<sup>a</sup>*Department of Atomic Physics, St. Kliment Ohridski University of Sofia,  
 5 James Bourchier Blvd, Sofia, Bulgaria*

<sup>b</sup>*Institute of High Energy Physics, Chinese Academy of Sciences,  
 19 Yuquan Rd, Shijingshan District, Beijing, China*

<sup>c</sup>*Sichuan University, 252 Shuncheng St, Chengdu, China*

<sup>d</sup>*Sezione INFN Milano Bicocca and Dipartimento di Fisica G. Occhialini,  
 Piazza della Scienza 3, Milano, Italy*

<sup>e</sup>*Sezione INFN Napoli and Dipartimento di Fisica, Università Federico II,  
 Complesso Universitario di Monte S. Angelo, Via Cintia, Napoli, Italy*

<sup>f</sup>*Sezione INFN Pavia and Dipartimento di Fisica, Università di Pavia, Via Agostino Bassi 6, Pavia, Italy*

<sup>g</sup>*Sezione INFN Roma Tre and Dipartimento di Matematica e Fisica, Università Roma Tre,  
 Via della Vasca Navale 84, Roma, Italy*

<sup>h</sup>*Osaka University, Graduate School of Science, Department of Physics,  
 1-1 Machikaneyamacho, Toyonaka, Osaka, Japan*

<sup>i</sup>*High Energy Accelerator Research Organization (KEK), Institute of Particle and Nuclear Studies,  
 Tsukuba, Ibaraki, Japan*

<sup>j</sup>*Department of Physics, UNIST, 50 UNIST-gil, Ulsan, South Korea*

<sup>k</sup>*Nikhef, Science Park 105, Amsterdam, Netherlands*

<sup>l</sup>*Radboud University, Houtlaan 4, Nijmegen, Netherlands*

<sup>m</sup>*Institute of Physics, University of Belgrade, Pregrevica 118, Belgrade, Serbia*

<sup>n</sup>*Faculty of Sciences, University of Novi Sad, Trg Dositeja Obradovića 3, Novi Sad, Serbia*

<sup>o</sup>*CERN, Esplanade des Particules 1, Geneva, Switzerland*

<sup>p</sup>*DPNC, Section de Physique, Université de Genève, 24 Quai Ernest-Ansermet, Geneva, Switzerland*

<sup>q</sup>*STFC Daresbury Laboratory, Keckwick Ln, Daresbury, Cheshire, U.K.*

<sup>r</sup>*STFC Rutherford Appleton Laboratory, Harwell Campus, Didcot, U.K.*

<sup>s</sup>*School of Physics and Astronomy, Kelvin Building, University of Glasgow, Glasgow, U.K.*

<sup>t</sup>*Department of Physics, University of Liverpool, Oxford St, Liverpool, U.K.*

<sup>u</sup>*Department of Physics, Blackett Laboratory, Imperial College London, Exhibition Road, London, U.K.*

<sup>v</sup>*Department of Physics, University of Oxford, Denys Wilkinson Building, Keble Rd, Oxford, U.K.*

<sup>w</sup>*Department of Physics and Astronomy, University of Sheffield, Hounsfield Rd, Sheffield, U.K.*

<sup>18</sup>Current address: Inawisdom, Columba House, Adastral park, Martlesham, Ipswich, U.K.

<sup>19</sup>Current address: Institute of High Energy Physics, Chinese Academy of Sciences, 19 Yuquan Rd, Shijingshan District, Beijing, China.

<sup>20</sup>Current address: Euclid Techlabs, 367 Remington Blvd, Bolingbrook, IL, U.S.A.

<sup>21</sup>Current address: Fermilab, Kirk Rd and Pine St, Batavia, IL, U.S.A.

<sup>22</sup>Current address: KLA, 2350 Green Rd, Ann Arbor, MI, U.S.A.

<sup>23</sup>Deceased.

<sup>24</sup>Current address: European Spallation Source ERIC, Partikelgatan 2, Lund, Sweden.

<sup>25</sup>Current address: Swish Analytics, Oakland, CA, U.S.A.

\*Corresponding author.

<sup>x</sup>*SUPA and the Department of Physics, University of Strathclyde, 107 Rottenrow, Glasgow, U.K.*

<sup>y</sup>*Department of Physics, University of Warwick, Gibbet Hill Road, Coventry, U.K.*

<sup>z</sup>*College of Engineering, Design and Physical Sciences, Brunel University, Kingston Lane, Uxbridge, U.K.*

<sup>aa</sup>*Brookhaven National Laboratory, 98 Rochester St, Upton, NY, U.S.A.*

<sup>ab</sup>*Fermilab, Kirk Rd and Pine St, Batavia, IL, U.S.A.*

<sup>ac</sup>*Lawrence Berkeley National Laboratory, 1 Cyclotron Rd, Berkeley, CA, U.S.A.*

<sup>ad</sup>*Illinois Institute of Technology, 10 West 35th St, Chicago, IL, U.S.A.*

<sup>ae</sup>*University of Mississippi, University Ave, Oxford, MS, U.S.A.*

<sup>af</sup>*University of California, 900 University Ave, Riverside, CA, U.S.A.*

*E-mail: [p.franchini@imperial.ac.uk](mailto:p.franchini@imperial.ac.uk)*

**ABSTRACT:** Muon beams of low emittance provide the basis for the intense, well-characterised neutrino beams of a neutrino factory and for multi-TeV lepton-antilepton collisions at a muon collider. The international Muon Ionization Cooling Experiment (MICE) has demonstrated the principle of ionization cooling, the technique by which it is proposed to reduce the phase-space volume occupied by the muon beam at such facilities. This paper documents the performance of the detectors used in MICE to measure the muon-beam parameters, and the physical properties of the liquid hydrogen energy absorber during running.

**KEYWORDS:** Accelerator Applications; Accelerator modelling and simulations (multi-particle dynamics, single-particle dynamics); Accelerator Subsystems and Technologies; Beam-line instrumentation (beam position and profile monitors, beam-intensity monitors, bunch length monitors)

**ARXIV EPRINT:** [2106.05813](https://arxiv.org/abs/2106.05813)

---

## Contents

<b>1</b>	<b>Introduction</b>	<b>1</b>
<b>2</b>	<b>Time-of-flight detectors</b>	<b>3</b>
<b>3</b>	<b>Cherenkov detectors</b>	<b>5</b>
<b>4</b>	<b>KLOE-light calorimeter</b>	<b>7</b>
<b>5</b>	<b>Electron muon ranger</b>	<b>9</b>
<b>6</b>	<b>Tracking</b>	<b>11</b>
6.1	Trackers	11
6.2	Beam-based detector alignment	14
<b>7</b>	<b>Liquid hydrogen absorber</b>	<b>17</b>
<b>8</b>	<b>Summary and conclusions</b>	<b>21</b>

---

## 1 Introduction

Stored muon beams have been proposed as the basis of a facility capable of delivering lepton-antilepton collisions at very high energy [1, 2] and as the source of uniquely well-characterised neutrino beams [3–5]. In the majority of designs for such facilities the muons are produced from the decay of pions created when an intense proton beam strikes a target. The phase-space volume occupied by the tertiary muon beam must be reduced (cooled) before the beam is accelerated and subsequently injected into a storage ring. The times taken to cool the beam using techniques that are presently in use at particle accelerators (synchrotron-radiation cooling [6], laser cooling [7–9], stochastic cooling [10], electron cooling [11] and frictional cooling [12]) are long when compared with the lifetime of the muon. Ionization cooling [13, 14], in which a muon beam is passed through a material (the absorber) where it loses energy, and is then re-accelerated, occurs on a timescale short compared with the muon lifetime. Ionization cooling is therefore the only technique available to cool the muon beam at a neutrino factory or muon collider. The international Muon Ionization Cooling Experiment (MICE) provided the proof-of-principle demonstration of the ionization-cooling technique [15].

MICE operated at the ISIS Neutron and Muon Source at the STFC Rutherford Appleton Laboratory. The ISIS synchrotron accelerates pulses of protons to a kinetic energy of 800 MeV at 50 Hz. For MICE operation, a titanium target was dipped into the halo of the proton beam at 0.78 Hz. Pions created in the interaction of the beam and target were captured in a quadrupole triplet (see figure 1). A beam line composed of dipole, solenoid, and quadrupole magnets captured muons produced through pion decay and transported the resulting muon beam to the MICE apparatus. The

momentum of the muon beam was determined by the settings of the two dipole magnets D1 and D2. Beams having muon central momenta between  $140 \text{ MeV}/c$  and  $240 \text{ MeV}/c$  were used for ionisation cooling studies. The emittance of the beam injected into the experiment was tuned using a set of adjustable diffusers, some made of tungsten and some of brass. The cooling cell was composed of a liquid hydrogen or lithium hydride absorber placed inside a focus coil (FC) module, sandwiched between two scintillating-fibre trackers (TKU, TKD) placed in superconducting solenoids (SSU, SSD). Together, SSU, FC, and SSD formed the magnetic channel. The MICE coordinate system is such that the  $z$ -axis is coincident with the beam direction, the  $y$ -axis points vertically upwards, and the  $x$ -axis completes a right-handed coordinate system.

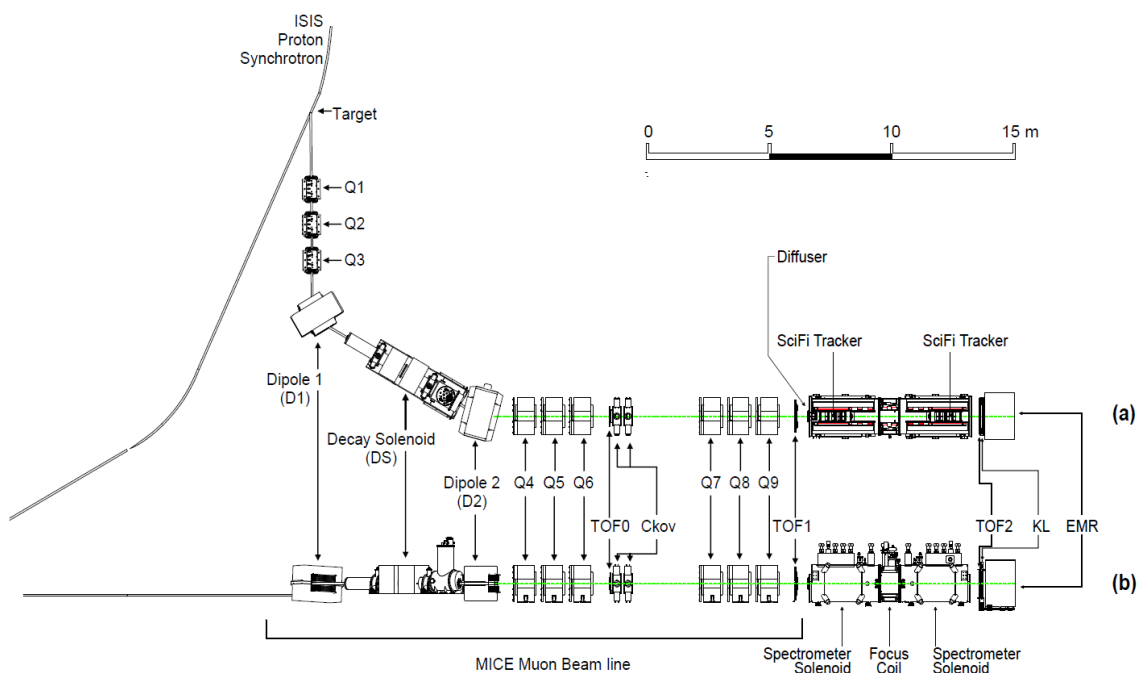


**Figure 1.** MICE, top (a) and side (b) views, showing the full beam line starting from the target position on the proton synchrotron with the quadrupoles and dipoles (Q1 to Q9, D1, D2), the Decay Solenoid, and instrumented magnetic channel elements (including the trackers upstream, TKU, and downstream, TKD, of the cooling channel, placed inside superconducting solenoids, respectively SSU and SSD) with all the other PID detectors (three TOF stations, two Ckov detectors, KL and the EMR). The cooling cell, defined to be the liquid hydrogen absorber vessel inside the focus coil (FC), is shown in figure 17.

MICE measured the passage of single particles through the apparatus which were aggregated into a beam offline. This paper documents the performance, during 2015-2017, of the instrumentation which was used to fully characterise the beam and its evolution along the magnetic channel, and quantifies the physical properties of the liquid hydrogen absorber. The beam instrumentation consisted of three time-of-flight detectors (TOF0, TOF1, TOF2) discussed in section 2, two threshold Cherenkov counters (CkovA, CkovB) discussed in section 3, a sampling calorimeter (KL) discussed in section 4, a tracking calorimeter (EMR) discussed in section 5, and the scintillating-fibre trackers discussed in section 6. The properties of the liquid hydrogen absorber are described in section 7.

## 2 Time-of-flight detectors

Three scintillator hodoscopes were used: to measure the time of flight (TOF) of the particles that made up the beam; to measure the transverse position at which the particle crossed each of the detectors; and to provide the trigger for the experiment. TOF0 and TOF1 [16–18] were placed upstream of the magnetic channel, while TOF2 [19] was located downstream of the channel, mounted in front of the KL pre-shower detector (see figure 1). At 240 MeV/ $c$ , the difference in the TOF for a muon and a pion between TOF0 and TOF1 was about 1.3 ns. The system was therefore designed to measure the TOF with a precision of 100 ps. This allowed the TOF between the first pair of TOF stations to be used to discriminate between pions, muons, and electrons, contained within the beam, with near 100% efficiency [20]. In addition, by assuming a mass hypothesis for each particle, the TOF measurement was used to infer the particle momentum. The TOF detectors, which operated smoothly during the running periods, were essential for all the measurements that were performed [15, 20–24].

Each TOF station was made of two planes of 1 inch thick scintillator bars oriented along the  $x$  and  $y$  directions. The bars of TOF0 (TOF1, TOF2) were made of Bricon BC-404 (BC-420) plastic scintillators. A simple fishtail light-guide was used to attach each end of each bar to Hamamatsu R4998 fast photomultiplier tubes (PMTs). Each PMT was enclosed in an assembly that included the voltage divider chain and a 1 mm thick  $\mu$ -metal shield. For TOF1 and TOF2 an additional soft iron (ARMCO) local shield was also used [25, 26]. The shield was required to reduce the stray magnetic field within the PMT to a negligible level [18]. To increase the count-rate stability, active dividers were used. One TOF detector is illustrated in figure 2.

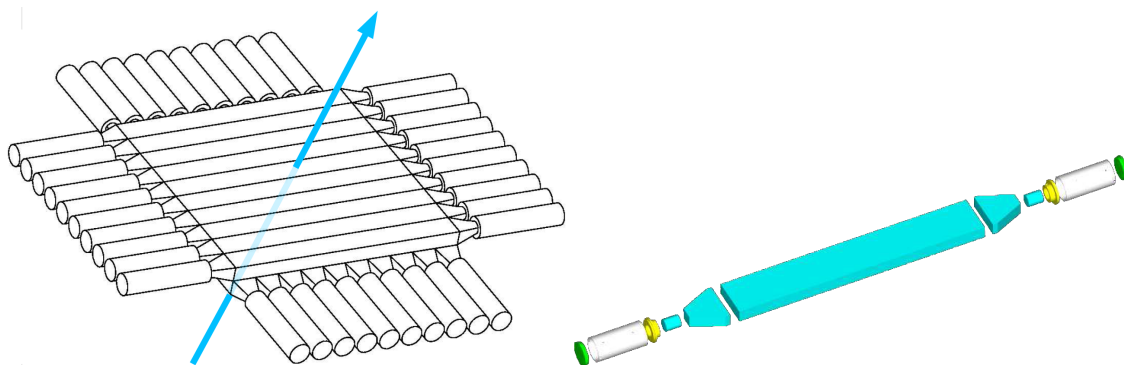


**Figure 2.** The structure of the time-of-flight detectors [16, 18] showing the horizontal and vertical layers of slabs (left) and an exploded view of each slab (right). The components of each slab are the central scintillator bar, two fishtail, clear plastic light-guides coupled to clear plastic matching pieces, and two PMTs. The beam direction is represented by the blue arrow perpendicular to the slabs.

The active areas of the three hodoscopes were  $40 \times 40 \text{ cm}^2$  (TOF0),  $42 \times 42 \text{ cm}^2$  (TOF1), and  $60 \times 60 \text{ cm}^2$  (TOF2). Each of the planes in TOF0 and TOF2 had 10 slabs while those in TOF1 had 7. A passive splitter was used to take the signal from each of the PMTs to a LeCroy 4115 leading-edge discriminator followed by a CAEN V1290 TDC for time measurement and to a CAEN V1724 FADC for pulse-height measurement. A local readout trigger was issued if the signals from each of the two PMTs on a single slab crossed a specific threshold and overlapped. TOF1 was used to trigger the readout of the experiment for most of the data taking.

**Calibration.** The intensity of the scintillation light produced when a particle crossed the plastic scintillator rose rapidly before decaying with a characteristic time of 1.8 ns. The scintillation light travelled from the particle-crossing point to each end of the scintillator slab. The light’s travel time depended on the distance of the particle crossing from the PMT. The propagation speed of the light pulse along the slabs was determined to be 13.5 cm/ns.

The local readout-trigger signal was distributed to all TDC boards and was used as the reference time. The time between a particle hit in a TOF slab and the time when the trigger was generated varied with the position of the hit along the slab. As a consequence, the reference time had an offset dependent on the crossing position, an effect referred to as the readout-trigger signal delay. To compensate for this, the final time measurement in each station was an average of the times recorded for each channel above threshold.

Further delay was introduced by the signal-transit time of each PMT and of the cable that led the signal to the readout electronics. These signal-transit times were unique for each individual readout channel and were determined by dedicated measurements. The use of a linear, leading-edge discriminator led to a correlation between the total charge in the pulse and the time at which the discriminator fired. This correlation, referred to as the time-walk, introduced a systematic offset in the time recorded by the TDC that was dependent on the pulse height.

Precise determination of the TOF required a calibration procedure that allowed channel-by-channel variations in the response of the system to be accounted for. The calibration procedure described in [27] accounted for each of the effects identified above.

**Reconstruction.** A particle crossing a TOF station passed through two orthogonal slabs. Signals from each PMT were corrected for time-walk, readout-trigger signal delay, and the channel-specific delays. The slab-crossing time was taken to be the average of the corrected PMT times. Two slab signals were taken to have been produced by the passage of a particle if their slab-crossing times were within a 4 ns window. These two *matched* slabs were used to define a pixel of area given by the width of the slabs. The particle-crossing time was then determined as the average of the slab-crossing times and the approximate position of the particle crossing was refined using the PMT signals in the two orthogonal slabs.

**Performance.** The difference,  $\Delta t$ , between the slab-crossing times for *matched* slabs was used to determine the intrinsic time resolution,  $\sigma_t$  of the TOF system. The  $\Delta t$  resolution,  $\sigma_{\Delta t}$ , is given by  $\sigma_{\Delta t} = 2\sigma_t$ , assuming that the intrinsic resolution is the same in each of the planes that make up a particular TOF station. Figure 3 shows the distributions of  $\Delta t$  for TOF0, TOF1, and TOF2 for a representative set of data taken in 2017. The RMS width of the distributions are 114 ps, 126 ps, and 108 ps for TOF0, TOF1, and TOF2 respectively. The distributions are similar, and the RMS of each distribution is consistent with the measured intrinsic resolution of approximately 60 ps [18].

Figure 4 shows an example distribution of the measured TOF between TOF0 and TOF1. The TOF peaks characteristic of electrons, muons, and pions are clearly separated. The width of the electron peak is approximately 0.10 ns, consistent with the spread calculated from a naive quadrature addition of the timing resolution of the individual TOF stations.

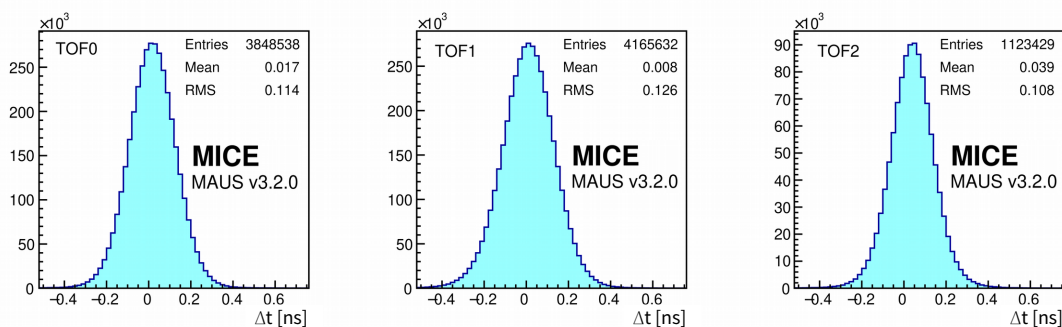


**Figure 3.** Slab  $\Delta t$  distributions. Total width of the distribution is due to the resolution of the individual channels and due to the offsets in their  $\Delta t$  distributions.

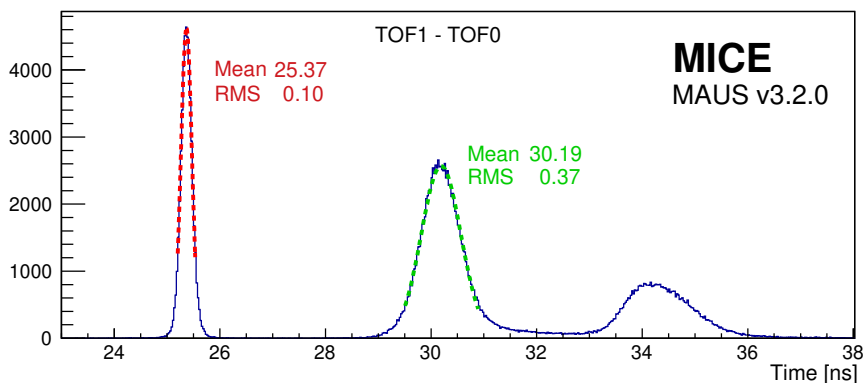


**Figure 4.** Time of flight between TOF0 and TOF1 after all corrections have been applied. The electron (left-most peak, shown in red), the muon (central peak, shown in green), and the pion (right-most peak, shown in blue) peaks are clearly separated.

### 3 Cherenkov detectors

The threshold Cherenkov counters were designed to distinguish muons from pions at particle momenta  $\gtrsim 200 \text{ MeV}/c$ , where the precision of the time-of-flight measurement was not sufficient for conclusive identification. Two high-density silica aerogel Cherenkov detectors with refractive indices  $n=1.07$  (CkovA) and  $n=1.12$  (CkovB) were used [28]. The structure of the detectors is shown in figure 5. Light was collected in each counter by four eight-inch, UV-enhanced PMTs and recorded using CAEN V1731 FADCs [29]. The two detectors were placed directly one after the other in the beamline and located just after TOF0.

The refractive indices of CkovA and CkovB result in detection thresholds for muons of approximately  $280 \text{ MeV}/c$  and  $210 \text{ MeV}/c$  respectively. For pions, the thresholds are approximately  $367 \text{ MeV}/c$  (CkovA) and  $276 \text{ MeV}/c$  (CkovB). MICE was designed to operate using beams with a central momentum between  $140 \text{ MeV}/c$  and  $240 \text{ MeV}/c$ . The Cherenkov counters' thresholds were chosen to provide muon identification for beams of  $210 \text{ MeV}/c$  and above, while the TOFs provide muon identification for beam below  $210 \text{ MeV}/c$ . Unambiguous identification of particle species using the Cherenkovs exploited the momentum measurement provided by the trackers.

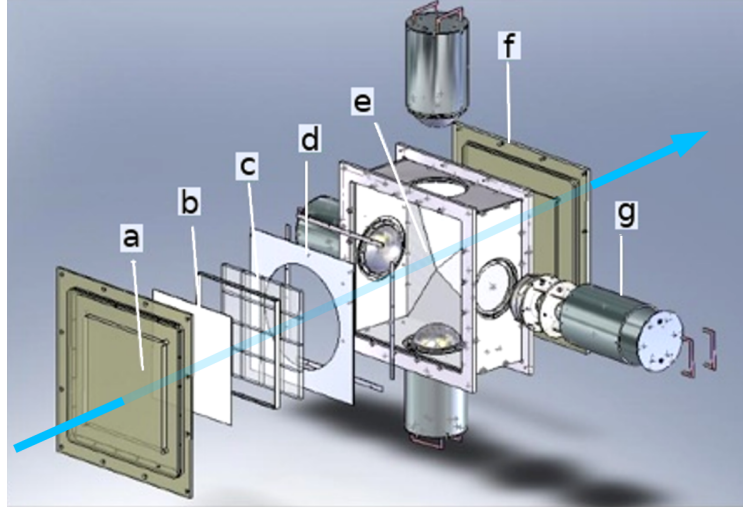


**Figure 5.** MICE aerogel Cherenkov counter: a) entrance window, b) mirror, c) aerogel mosaic, d) acetate window, e) GORE DRP reflector panel, f) exit window and g) eight-inch PMT in iron shield. The beam direction is represented by the blue arrow traversing the detector.

**Performance.** The performance of the detectors was determined using beams for which the momentum range was broad enough to observe the turn-on points and to allow the asymptotic light yields (as the particle velocity divided by the speed of light,  $\beta$ , approaches 1) to be obtained from fits to the data. The normalised photo-electron yields observed in CkovA and CkovB are plotted as a function of  $\beta\gamma$  (where  $\gamma = (1 - \beta^2)^{-\frac{1}{2}}$ ) in figure 6. The pedestal in the photo-tube response arising from background photons has been subtracted. The approximate turn-on points for CkovA and CkovB were found at  $\beta\gamma \approx 2.6$  and  $\approx 2.1$  respectively, corresponding to refractive indices of  $n \approx 1.07$  and  $\approx 1.11$  which are in broad agreement with the properties of the aerogel radiators.

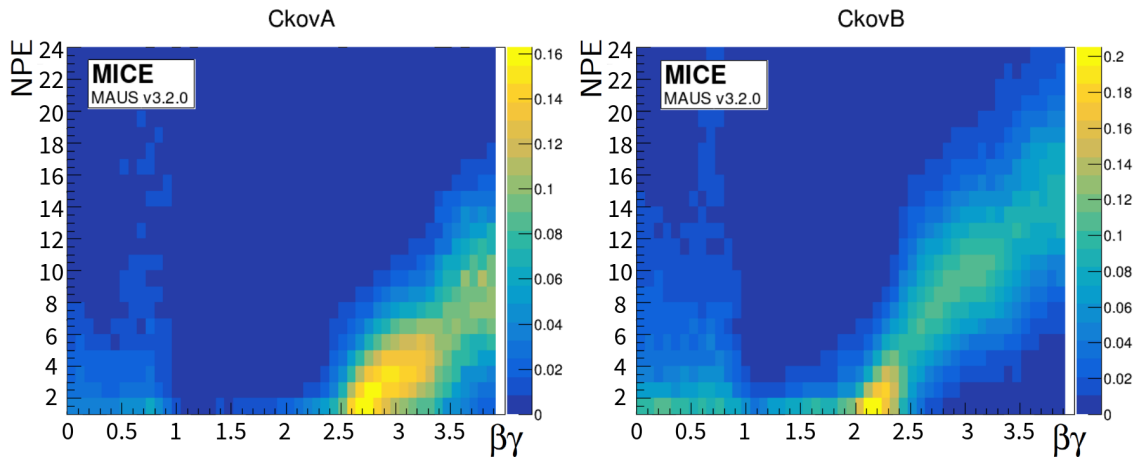


**Figure 6.** Photoelectron yields versus  $\beta\gamma$  in CkovA and CkovB, where  $\beta c$  is the particle velocity and  $\gamma = (1 - \beta^2)^{-\frac{1}{2}}$ .



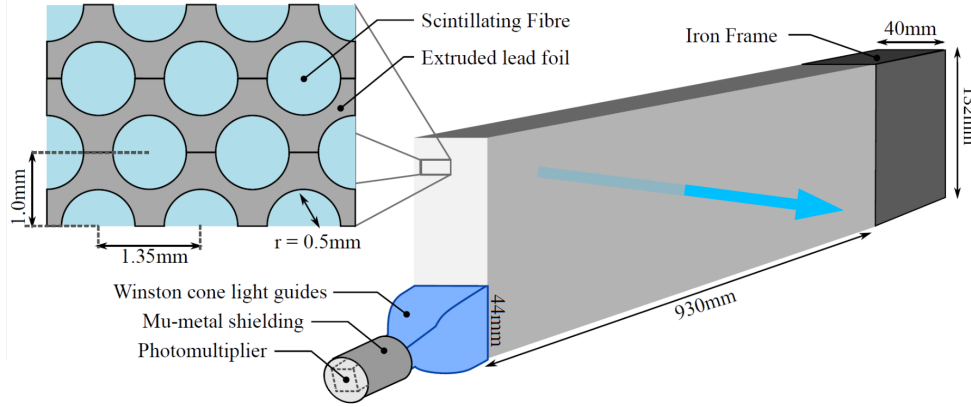


**Figure 7.** Single slab design of MICE KLOE-Light Calorimeter [31]; only one of the six PMT assemblies is shown. The beam direction is represented by the blue arrow traversing the slab.

#### 4 KLOE-light calorimeter

The KLOE-Light (KL) pre-shower sampling calorimeter was composed of extruded lead foils in which scintillating fibres were placed. At normal incidence the thickness of the detector was 2.5 radiation lengths. The detector provided energy deposition and timing information and was used to distinguish muons from decay electrons [20]. The KL consisted of a series of layers of 1 mm diameter BICRON BCF-12 scintillating fibres embedded in an appropriately shaped lead sheets (see figure 7). Each fibre was separated by 1.35 mm from its neighbours within a layer and the distance between the centres of the fibres in adjacent layers was 0.98 mm. One layer was shifted by half the fibre pitch with respect to the next. The volume ratio of scintillator to lead was approximately 2:1, “lighter” than the ratio of 1:1 used in the similar calorimeter of the KLOE experiment [30]. Lead/scintillator layers were stacked into slabs, 132 mm in depth. A total of 7 slabs formed the whole detector, which had an active volume of 93 cm×93 cm×4 cm. Scintillation light was guided from each slab into a total of six PMTs (three at each end). Iron shields were fitted to each photomultiplier to mitigate the effect of stray magnetic fields. The signal from each PMT was sent to a shaping amplifier module that stretched the signal in time to match the sampling rate of the CAEN 1724 FADCs.

**Performance.** To study the response of the KL, the particle momentum was determined from the measured time-of-flight between TOF0 and TOF1. To compensate for the effect of attenuation the performance was evaluated in terms of the “ADC product” given by:

$$\text{ADC}_{\text{prod}} = \frac{2 \times \text{ADC}_{\text{left}} \times \text{ADC}_{\text{right}}}{(\text{ADC}_{\text{left}} + \text{ADC}_{\text{right}})}; \quad (4.1)$$

where  $\text{ADC}_{\text{left}}$  and  $\text{ADC}_{\text{right}}$  are the signals from the two ends of a slab and the factor of 2 is present for normalisation. Data was taken with no field in the spectrometer solenoids or the focus coil at beam-momentum settings chosen to span the range of momenta used during MICE running. The resulting momentum distributions were centred at 140, 170, 200, 240, and 300 MeV/c. The response of the KL to muons and pions was observed to increase with beam momentum.

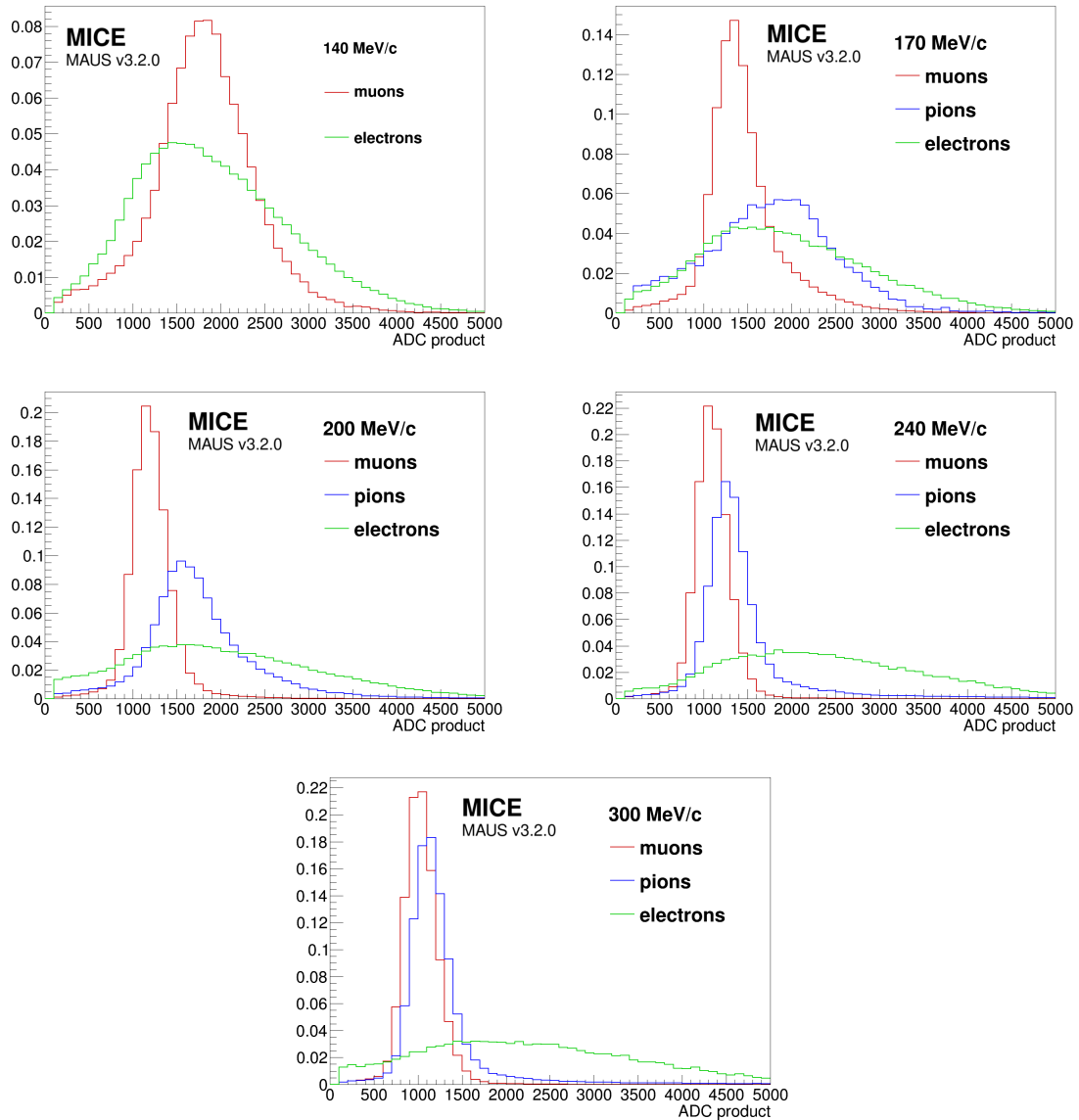


**Figure 8.** Comparison of ADC products of muons (red), pions (blue) and electrons (green) traversing the KL, at 140 MeV/c (top left), 170 MeV/c (top right), 200 MeV/c (middle left), 240 MeV/c (middle right) and 300 MeV/c (bottom).

Figure 8 presents a comparison of the response to muons, pions and electrons for various beam momentum settings. At high momentum, for example 300 MeV/c, the ADC product distributions for muons and pions are similar. At lower momentum the distributions become increasingly dissimilar, the pions having a broader distribution arising from hadronic interactions. The difference between the detector’s response to pions and muons has been exploited to determine the pion contamination in the muon beams used for the MICE cooling measurements [20].

The ADC product distribution measured using a 300 MeV/c beam is compared to the MAUS [32] simulation of the detector response in figure 9. The simulation takes into account

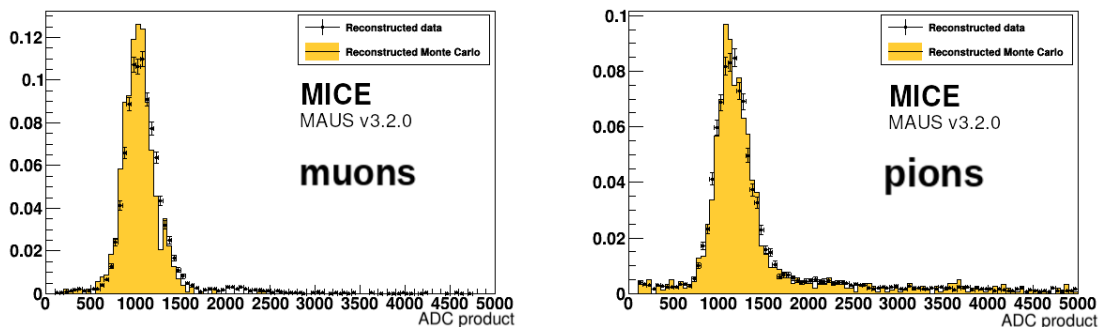


**Figure 9.** Comparison between data and Monte Carlo simulation of KL response to muons (left) and pions (right) at  $300 \text{ MeV}/c$ .

the light production distribution of the scintillating fibres, and the response of the PMTs for which the gain was approximately  $2 \times 10^6$ . The data is well described by the simulation.

## 5 Electron muon ranger

The EMR was a fully-active scintillator detector [33] with a granularity that allowed track reconstruction. The EMR consisted of extruded triangular scintillator bars arranged in planes. Each plane contained 59 bars and covered an area of  $1.27 \text{ m}^2$ . Figure 10 shows the bar cross section and the arrangement of the bars in a plane. Triangular bars were chosen so that tracks moving parallel to the detector axis could not travel along the gaps between bars. Successive planes were mounted perpendicularly, so that hits in neighbouring planes defined a position. A single “X-Y module” was a pair of orthogonal planes. The scintillation light was collected using a wavelength shifting (WLS) fibre glued inside each bar. At each end, the WLS fibre was coupled to clear fibres that transported the light to a PMT. All the WLS fibres from one edge of a plane were read out using one single-anode PMT (SAPMT) so that an integrated charge measurement could be used to determine the energy deposited in the plane. The signals from the fibres emerging from the other edge of the plane were recorded individually using multi-anode PMTs (MAPMTs). The full detector was made up of 24 X-Y modules giving a total active volume of approximately  $1 \text{ m}^3$ .

Measurements of the performance of the completed detector demonstrated an efficiency per plane of  $99.73 \pm 0.02\%$  [33, 34]. The level of crosstalk was within acceptable values for the type of MAPMT used, with an average of  $0.20 \pm 0.03\%$  between adjacent channels and a mean amplitude equivalent to  $4.5 \pm 0.1\%$  of the primary signal. Only four dead bars were present.

The primary purpose of the EMR was to distinguish between a muon that crossed the entire magnetic channel and those which decayed in flight producing an electron. Muons and electrons exhibited distinct behaviours in the detector. A muon produced a single straight track before either stopping or exiting the scintillating volume. Electrons showered in the lead of the KL and created a broad cascade of secondary particles. Two main geometric variables, the “plane density” and the “shower spread”, were used to differentiate them. The detector was capable of identifying electrons with an efficiency of  $98.6\%$ , providing a purity for the MICE beam that exceeds  $99.8\%$ .

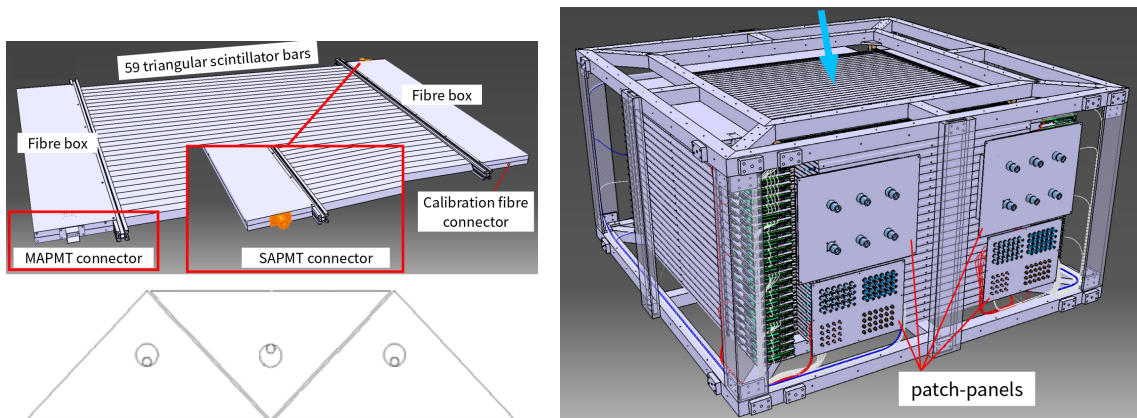


**Figure 10.** Drawing of one EMR plane (top left), cross section of the arrangement of 3 bars and their wavelength shifting fibres (bottom left) and drawing of the full detector and its supporting structure from a top perspective (right). The beam direction is represented by the blue arrow perpendicular to the detector.

The EMR also proved to be a powerful tool for the reconstruction of muon momenta in the range 100–280 MeV/ $c$  [23].

**Performance.** A full description of the detector and the reconstruction algorithms used may be found in reference [23]. Here the performance of the EMR detector over the course of the experiment is summarised.

To measure the performance of the EMR the MICE beamline was set to deliver a nominal momentum of 400 MeV/ $c$ . This maximised the muon transmission to the EMR and its range in the detector. In this configuration the beamline produced pions and muons in comparable quantities, as well as a smaller number of electrons. Time-of-flight between TOF1 and TOF2 was used to identify particle species and only particles compatible with the muon hypothesis were included in the analysis. Particles entering the muon sample had a momentum larger than 350 MeV/ $c$  at the upstream surface of TOF2 and were expected to cross both TOF2 and the KL and penetrate the EMR.  $99.62 \pm 0.03\%$  of the particles entering TOF2 were observed to produce hits in the EMR. The small inefficiency may be attributed to pions in the muon sample that experienced hadronic interactions in the KL. If hits were produced in the detector, an  $(x, y)$  pair, defining a space point, was reconstructed  $98.56 \pm 0.06\%$  of the time.

To evaluate the efficiency of the scintillator planes, only the muons that traversed the entire detector were used. Muons were selected which produced a hit in the most downstream plane. For these events a hit was expected in at least one bar in each plane on its path. The mode of the hit-multiplicity distribution per plane was one, in  $3.26 \pm 0.02\%$  of cases a plane traversed by a muon did not produce a signal in the MAPMT, and the probability that the track was not observed in the SAPMT was  $1.88 \pm 0.01\%$ .

**Electron rejection.** A broad range of beamline momentum settings was used to characterise the electron-rejection efficiency. Particle species were characterised upstream of the EMR using the time-of-flight between TOF1 and TOF2. For each momentum setting, a fit was carried out to determine the position of the muon and electron time-of-flight peaks and events were selected

accordingly to form muon and electron-template samples. Particles with a time-of-flight larger than the upper limit of the muon sample were either pions or slow muons and were rejected.

To distinguish the muon tracks from the electron-induced showers, two particle-identification variables were defined based on the distinct characteristics of the two particle species. The first is the plane density,  $\rho_p$ :

$$\rho_p = \frac{N_p}{Z_p + 1}, \quad (5.1)$$

where  $N_p$  is the number of planes hit and  $Z_p$  the number of the most downstream plane [23]. A muon deposits energy in every plane it crosses until it stops, producing a plane density close to one. An electron shower contains photons that may produce hits deep inside the fiducial volume without leaving a trace on their path, reducing the plane density. The second variable is the normalised  $\hat{\chi}^2$  of the fitted straight track given by

$$\hat{\chi}^2 = \frac{1}{N - 4} \sum_{i=1}^N \frac{\text{res}_{x,i}^2 + \text{res}_{y,i}^2}{\sigma_x^2 + \sigma_y^2}, \quad (5.2)$$

where  $N$  is the number of space points (one per bar hit),  $\text{res}_{q,i}$  the residual of the space point with respect to the track in the  $qz$  projection and  $\sigma_q$  the uncertainty on the space point in the  $qz$  projection,  $q = x, y$  [35]. This quantity represents the transverse spread of the hits produced by the particle in the EMR. A muon produced a single track giving  $\hat{\chi}^2$  close to one, while an electron shower produced a larger value. The two discriminating variables can be combined to form a statistical test on the particle hypothesis. Dense and narrow events will be tagged as muons while non-continuous and wide showers will not. The quality of this statistical test was characterised in terms of the fraction of the muon sample that is rejected,  $\alpha$ , and the fraction of the electron sample that is selected,  $\beta$ .

The momentum of the particles was measured by the downstream tracker and this information used to determine the momentum dependence of the contamination and loss in the range 100–300 MeV/ $c$ . Figure 11 shows the loss,  $\alpha$ , and the contamination,  $\beta$ , as a function of the momentum measured in TKD.  $\alpha$  increases towards low muon momentum. This is due both to an increase in the decay probability between TOF2 and the EMR and a decrease in the number of muons that cross the KL to reach the EMR.

## 6 Tracking

The MICE instrumentation allowed individual particles to be tracked from TOF0 to the EMR, a distance of more than 15 m. High-resolution particle tracking was provided by two scintillating-fibre trackers (section 6.1). The precise relative alignment of the time-of-flight hodoscopes and the trackers was obtained by combining the measurements of both detector systems (section 6.2).

### 6.1 Trackers

The two high-precision scintillating-fibre trackers each had a sensitive volume that was 110 cm in length and 30 cm in diameter [36]. Each tracker was composed of five stations (labelled 1 to 5, with station 1 being closest to the cooling cell) held in position using a carbon-fibre space-frame. Adjacent stations were separated by different distances ranging from 20 cm to 35 cm. The

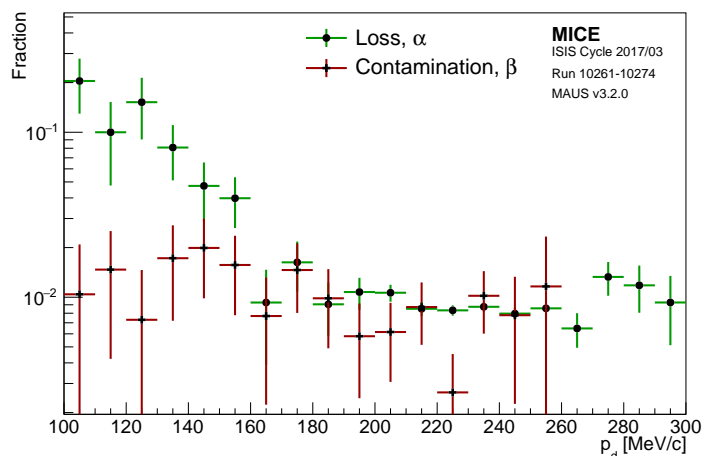


**Figure 11.** Percentage of electron contamination,  $\beta$ , and muon loss,  $\alpha$ , for different ranges of momentum measured in the downstream tracker,  $p_d$ . The error bars are based on the statistical uncertainty in a bin, and the bin width set by the resolution of the measurement.



**Figure 12.** Photograph, with UV-filtered light, of one of the MICE trackers, showing the five stations. Each station has three doublet planes of scintillating fibres, each plane at  $120^\circ$  to the next (the central fibres of each plane can be seen as darker lines traversing the station).

separations were chosen to ensure that the azimuthal rotation of track position did not repeat from one station to the next. This property was exploited in the ambiguity-resolution phase of the pattern recognition. Each tracker was instrumented with an internal LED calibration system and four 3-axis Hall probes to monitor the field. A photograph of one of the trackers on the bed of the coordinate measuring machine used to verify the mechanical alignment of the stations is shown in figure 12.

Each tracker station consisted of three doublet layers of  $350\ \mu\text{m}$  scintillating fibres; these layers were arranged such that each was set at an angle of  $120^\circ$  with respect to the next. This arrangement ensured that there were no inactive regions between adjacent fibres. Fibres were grouped into one bundle of seven for each readout channel, to match the resolution to that imposed by multiple scattering and reduce the overall number of readout channels. This resulted in a spatial resolution per doublet layer of  $470\ \mu\text{m}$  and a measured light yield of approximately 10 photo-electrons [36].

The light from the seven scintillating fibres was coupled into a single clear fibre which took it to a visible light photon counter (VLPC) [37]. The signals from the VLPCs were digitised using electronics developed by the D0 collaboration [38].

**Reconstruction.** The reconstruction software for the trackers is described in [39]. Each of the 15 doublet layers provided 214 readout channels. Calibration data taken without beam was used to determine the pedestal and the gain of each channel. These calibrations were used to correct the number of photoelectrons (NPE) corresponding to the signal recorded by the tracker electronics. The first step in the reconstruction was to record the unique channel number associated with each NPE value in a “digit”. Digit profiles were used to identify hot or dead channels which were masked from the reconstruction to reduce the rate of ambiguities that had to be resolved in the pattern recognition and to ensure the accuracy of the calibration. The reconstruction proceeded to create “spacepoints” from the intersection of digits in adjacent doublet layers. Spacepoints were constructed from clusters from all three planes (a triplet spacepoint) or from any two out of the three planes (a doublet spacepoint). The pattern-recognition algorithm searched for spacepoints from neighbouring stations that were consistent with the helical trajectory of a charged particle in the solenoidal field. In the final stage of the tracker reconstruction the track parameters were estimated using a Kalman filter.

**Noise.** Digits above a certain NPE threshold were admitted to the spacepoint-finding algorithm. Noise in the electronics arising from, for example, the thermal emission of electrons, could give rise to digits passing the threshold. Any digit not caused by the passage of a charged particle was classified as noise. To isolate noise from signal during beam-on data collection, events containing a track which included a spacepoint in each of the five tracker stations were selected. All digits corresponding to the track were removed from the total set of digits and the remainder were considered to be noise. The average noise rate per channel per event was then calculated as the total number of digits above the NPE threshold divided by the number of active channels and the number of events in the sample. The result of this calculation was that, for an NPE threshold of 2, the fraction of digits arising from noise was 0.18% in the upstream tracker and 0.06% in the downstream tracker.

**Track-finding efficiency.** The track-finding efficiency was determined using a sample of events for which the time-of-flight determined from hits in TOF1 and TOF2 was consistent with passage of a muon. This requirement ensured that the particle had been transmitted successfully through the magnetic channel, crossing both trackers. The track-finding efficiency was defined to be the number of events in which a track was successfully reconstructed divided by the total number of events in the sample. The results of the efficiency analysis are tabulated in table 1 for a range of nominal beam momentum and emittance settings. The track-finding efficiency obtained in this way averaged over beam conditions was 98.70% for the upstream tracker and 98.93% for the downstream tracker. The spacepoint-finding efficiency, defined as the number of spacepoints found divided by the number of space points expected, was also determined. The spacepoint-finding efficiency is summarised for a range of beam conditions in table 2.

The efficiency of the trackers over the data taking period was evaluated by selecting events with a measured time-of-flight between TOF1 and TOF2 consistent with the passage of a muon. Events were required to contain at least one hit within the fiducial volume of the tracker. An event was added to the numerator of the efficiency calculation if it contained a single space point in each of

**Table 1.** The track finding efficiency for the upstream and downstream trackers for 140 MeV/ $c$  and 200 MeV/ $c$  beams, and for 3, 6 and 10 mm nominal emittances.

Momentum	Emittance	Upstream tracks found	Downstream tracks found
200 MeV/ $c$	3 mm	98.38%	99.19%
200 MeV/ $c$	6 mm	99.42%	96.07%
140 MeV/ $c$	6 mm	98.37%	99.16%
140 MeV/ $c$	10 mm	98.47%	98.93%
Average		98.70%	98.21%

**Table 2.** The spacepoint-finding efficiency, in the presence of a track, for the upstream and downstream trackers for 140 MeV/ $c$  and 200 MeV/ $c$  beams, and for 3, 6 and 10 mm nominal emittances.

Momentum	Emittance	Upstream spacepoints found	Downstream spacepoints found
200 MeV/ $c$	3 mm	98.04%	97.41%
200 MeV/ $c$	6 mm	99.41%	94.63%
140 MeV/ $c$	6 mm	97.99%	99.16%
140 MeV/ $c$	10 mm	98.07%	97.44%
Average		98.44%	97.01%

the five tracker stations. The evolution of the tracking efficiency in the upstream and downstream trackers is shown in figure 13. The efficiency is shown separately for data taken in the presence of a magnetic field (“helical”) and with the solenoids turned off (“straight”). The data shows that the efficiency was generally greater than 99.0%. Water vapour ingress to the cold end of the VLPC cassettes caused the loss of channels and contributed to a reduction in the tracking efficiency. This was recovered by warming and drying the VLPCs.

**Track-fit performance.** Monte Carlo simulation with realistic field, beam conditions and detector geometry was used to estimate the performance of the track fit. A beam centred at 140 MeV/ $c$  with 10 mm nominal emittance, representing a typical data set, was used for the study. Results are presented in figure 14 for the upstream tracker and figure 15 for the downstream tracker. The resolution in the total momentum and transverse momentum is observed to be  $\sim 1.1$  MeV/ $c$  independent of momentum in the range 120 MeV/ $c$  to 160 MeV/ $c$ . The small bias in the transverse and the total momentum did not give rise to significant effects in the analysis and was considered in systematic error studies.

## 6.2 Beam-based detector alignment

A beam-based alignment algorithm was developed to improve the resolution on the position of the scintillating-fibre trackers relative to the time-of-flight hodoscopes. The starting point for the beam-based alignment was the geometrical survey of the detectors in the MICE Hall which was performed using laser geodesy. Survey monuments on the TOF frames were surveyed with respect



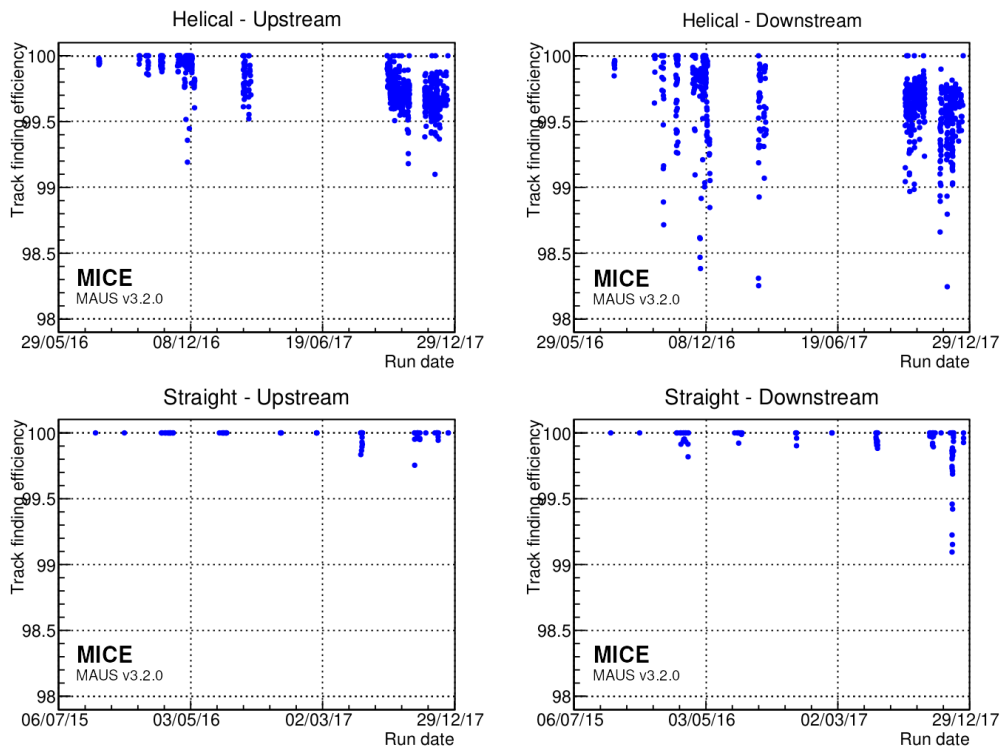


**Figure 13.** Evolution of the straight and helical track finding efficiencies over time for: the upstream (left); and downstream (right) trackers during the key periods of data taking since 2015. Each dot represents a single data taking run between 10 minutes and 3 hours long.

to the MICE Hall survey network. The trackers had been dowelled in position in the bores of the spectrometer solenoids. The dowels were used to locate each tracker precisely with respect to the axis of the warm bore of its solenoid. The position of the trackers along the beam line was inferred from the measurement of survey monuments mounted on the spectrometer-solenoid cryostats outer jackets. The beam-based alignment was used to determine the azimuthal orientation of the trackers with a resolution of  $6 \text{ mrad}/\sqrt{N}$  and their position transverse to the beamline with a resolution of  $20 \text{ mm}/\sqrt{N}$ , where  $N$  is the number of tracks used in the analysis [40].

**Analysis method.** The position of each tracker in the MICE Hall coordinate system was described using the location of its centre and a set of three angles corresponding to rotation about the  $x$  axis ( $\alpha$ ), the  $y$  axis ( $\beta$ ) and the  $z$  axis ( $\phi$ ). The rotation of the tracker about the  $z$  axis has a negligible effect on the alignment since  $\phi$  was determined precisely at installation. An initial estimate for the position of each tracker along the beamline had been inferred from the survey. The surveyed location of the TOFs was used as the reference for the tracker alignment. The line that joins the centre of TOF1 with the centre of TOF2 was chosen as the reference axis. A deviation from this axis was considered to be due to misalignment of the trackers. The alignment could not be determined on a single-particle basis due to multiple Coulomb scattering in the absorber and other material present on the beamline. Therefore, the mean residuals in position ( $x$  and  $y$ ) and angle ( $\alpha$  and  $\beta$ ) of the trackers with respect to the TOF1-TOF2 axis were evaluated to determine the alignment constants.

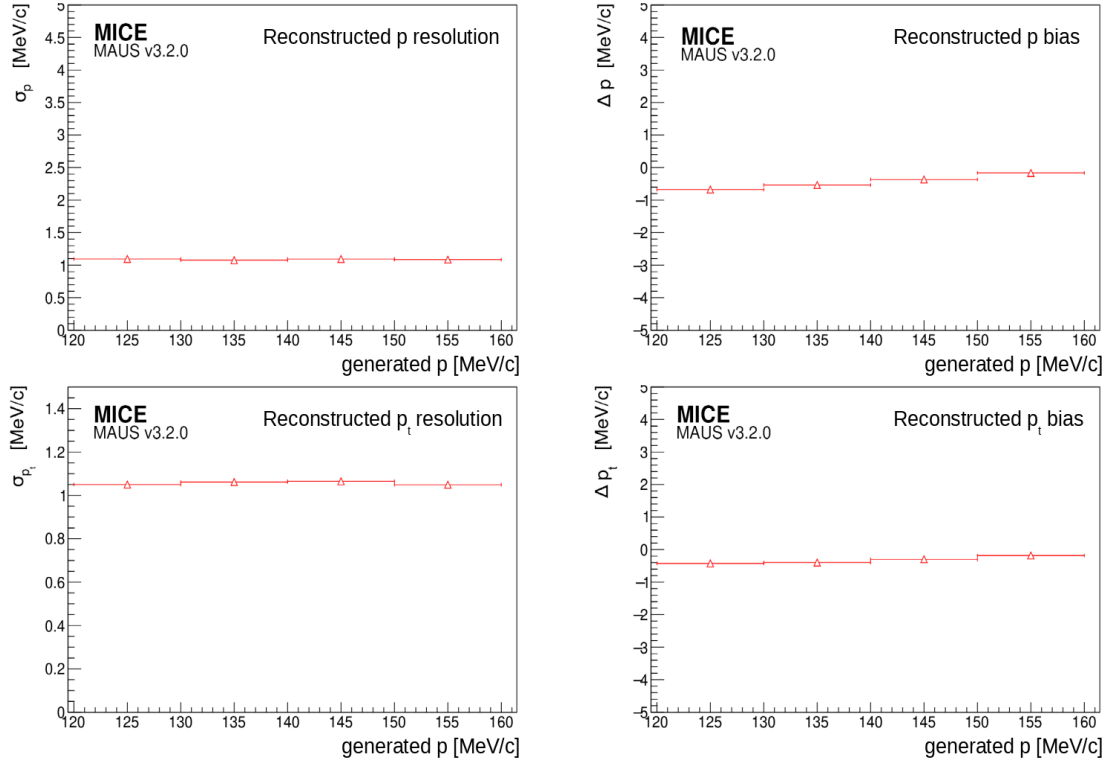


**Figure 14.** Momentum reconstruction resolution (left) and bias (right) for the total momentum (top) and transverse momentum component (bottom) in the upstream tracker.

Each TOF provided a single spacepoint in the Hall coordinate system. In Hall coordinates, on average, the track reconstructed between TOF1 and TOF2 should agree with the track reconstructed in each tracker, i.e. the mean residuals in  $x$ ,  $y$ ,  $\alpha$ , and  $\beta$  should be zero. Applying this reasoning to the unknown offset and angles leads to a system of equations for the four unknown constants [40]. The measurement of four residual distributions per tracker yields the alignment constants. The main source of bias was the scattering in the material between TOF1 and TOF2. If the beam was not perfectly centred, particles preferentially scraped out on one side of the magnet bore, anisotropically truncating the tail of the residual distribution. A fiducial cut was applied to the upstream sample in order to remove this effect.

Data were recorded with the superconducting magnets turned off. High momentum beams were used to reduce the RMS scattering angle and to maximise transmission. Each data set was processed independently. Figure 16 shows the alignment parameters determined for each run during a specific data taking period. The measurements are in good agreement with one another and show no significant discrepancy: an agreement between the independent fits guaranteed an unbiased measurement of the alignment constants. The constant-fit  $\chi^2/\text{ndf}$  was close to unity for each fit, indicating that there were no additional sources of significant uncertainty. The optimal parameters are summarised in table 3.

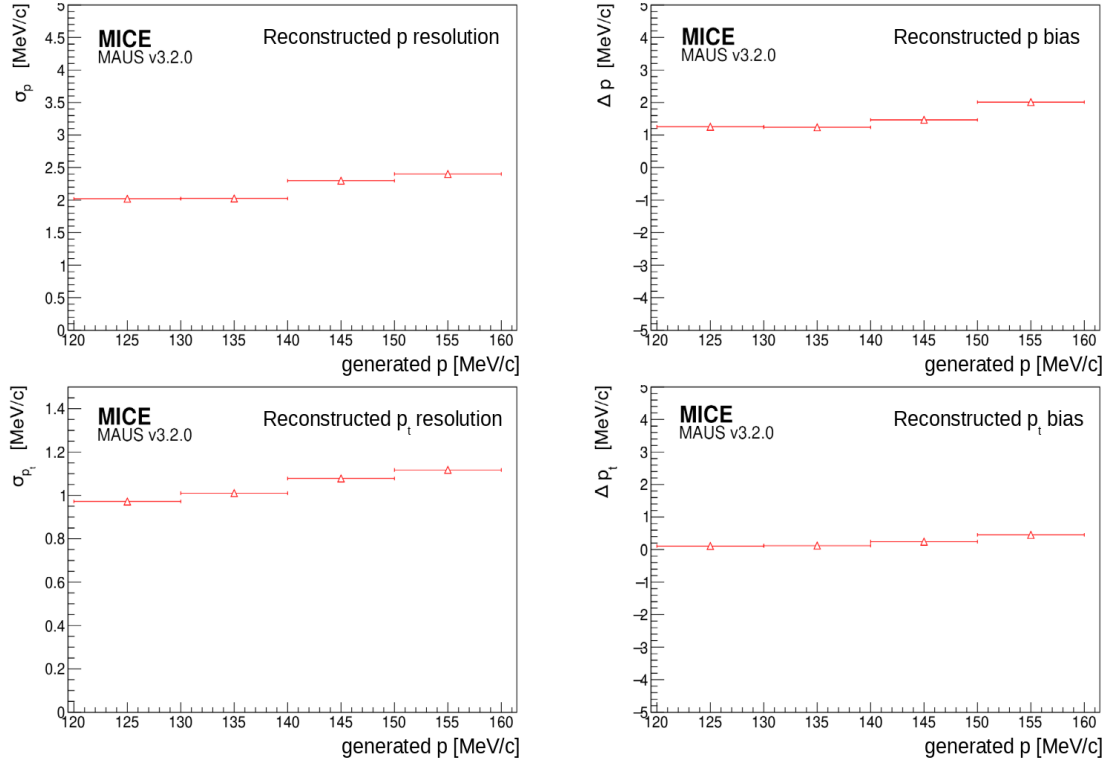


**Figure 15.** Momentum reconstruction resolution (left) and bias (right) for the total momentum (top) and transverse momentum component (bottom) in the downstream tracker.

**Table 3.** Optimal alignment constants measured in the high-momentum straight-track data acquired during May 2017 (summarised from figure 16).

	x [mm]	y [mm]	$\alpha$ [mrad]	$\beta$ [mrad]
<b>TKU</b>	$-0.032 \pm 0.094$	$-1.538 \pm 0.095$	$3.382 \pm 0.030$	$0.412 \pm 0.029$
<b>TKD</b>	$-2.958 \pm 0.095$	$2.921 \pm 0.096$	$-0.036 \pm 0.030$	$1.333 \pm 0.030$

## 7 Liquid hydrogen absorber

The accurate characterisation of the properties of the liquid hydrogen absorber was a critically-important contribution to the study of ionisation cooling. The instrumentation used for this purpose and its performance are presented in this section.

The absorber vessel consisted of a cylindrical aluminium body sealed with two thin aluminium end windows, as shown in figure 17. The absorber vessel contained 22 l of liquid. The body of the absorber had an inner diameter of 300 mm and the end flanges were separated by a distance of 230 mm. The vessel was surrounded by a second pair of safety windows. The length along the central axis, between the two domes of the end windows, was 350 mm [41].

**Variation of the density of liquid hydrogen due to varying temperature and pressure.** The energy lost by a muon travelling through the liquid hydrogen absorber depends on the path length and

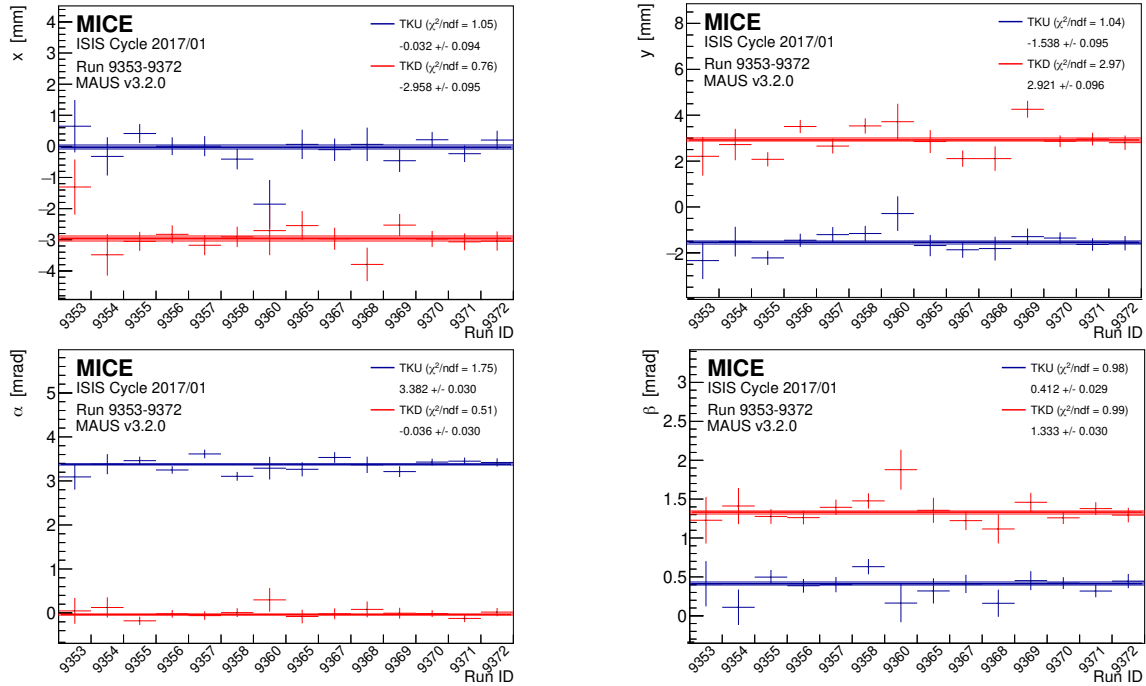


**Figure 16.** Consistency of the alignment algorithm results for upstream (blue) and downstream (red) trackers across runs acquired during the 2017/01 ISIS user cycle. The quantities  $x$ ,  $y$ ,  $\alpha$ , and  $\beta$  are defined in the text.

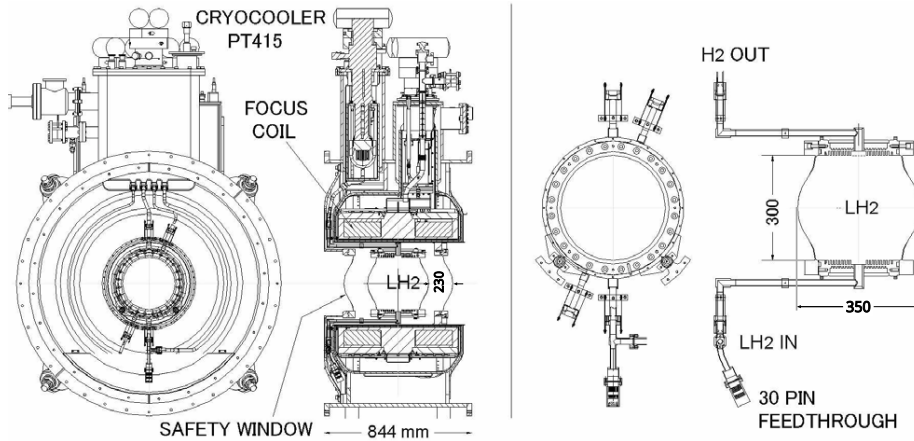


**Figure 17.** Left panel: drawing of the focus coil (FC) module showing the principal components. Right panel: detail of the liquid hydrogen absorber vessel [41].

on the density of the liquid hydrogen. The density of liquid hydrogen is a function of temperature and pressure. The temperature of the vessel was measured by eight LakeShore Cernox 1050 SD sensors, but with the values truncated for storage at a granularity of 0.1 K. Four of the sensors were used solely as temperature sensors, while the other four were also used as level sensors to ensure the liquid hydrogen reached the top of the vessel. The sensors were arranged in pairs, with two mechanically clamped at the top of the vessel, two at a polar angle of  $45^\circ$  to vertical from the top of the vessel, two at a polar angle of  $45^\circ$  to the bottom of the vessel, and a final two at the bottom of the vessel.

Cooldown and liquefaction were completed slowly over eight days at a pressure of 1105 mbar after which the vessel's pressure was lowered to 1085 mbar [41]. The vessel then remained in this steady state during the 21 day period of data taking, after which the vessel was vented. For the venting process, the cryocooler used to liquefy hydrogen was switched off and heaters were switched on to deliver a nominal power of 50 W to the absorber vessel. This resulted in an increase in pressure to 1505 mbar until the temperature stabilised at the boiling point. A rapid increase in temperature was observed once all the liquid hydrogen had boiled off.

The temperature sensors had a typical accuracy of  $\pm 9$  mK and a long-term stability of  $\pm 12$  mK at 20 K. The magnetic-field dependent temperature error,  $\Delta T/T$ , at 2.5 T is 0.04%, equivalent to  $\pm 8$  mK at 20 K [42]. These uncertainties were quoted by the manufacturer of the sensors. Magnetic fields caused reversible calibration shifts on the temperature measurements. To reduce the uncertainty in the liquid hydrogen density a calibration procedure was devised that used the boiling point, as observed during the venting process. A correction to the observed temperature reading was obtained by applying a cut-off correction, a correction for the effect of the magnetic field based on the current in the focus coil and its polarity, a correction for the non-linearity of the sensors, and a boiling point scaling factor [43].

The boiling point of hydrogen at 1085 mbar is 20.511 K. The sensors had a total uncertainty of 17 mK (9 mK accuracy, 12 mK stability, 8 mK magnetic). The deviation from the non-linearity of the sensors [42] added, on average, 0.03 K to the uncertainty. The temperature scaling and magnet-current correction factors also had an associated uncertainty as they were derived based on the 0.1 K resolution of the retrieved, truncated, values. For example, a calibrated sensor at boiling temperature and 1505 mbar should read 21.692 K, but we can only retrieve a value of 21.65 K (21.6 K truncated plus 0.05 K cut-off correction [43]) i.e. off by 0.042 K. The pressure sensors had an uncertainty of  $\pm 5$  mbar which equated to  $\pm 0.016$  K during steady state. The pressure uncertainty ( $\pm 5$  mbar) added another uncertainty to the temperature calibration constants of  $\pm 0.014$  K. Collectively, all these uncertainties summed in quadrature to 0.2 K for each sensor.

While in the steady state condition the liquid hydrogen was close to the boiling temperature of liquid parahydrogen [43] (density of  $70.53 \text{ kg/m}^3$ ): the average temperature of the eight sensors was  $(20.51 \pm 0.07)$  K at 1085 mbar (figure 18) allowing us to determine the uncertainty in the density over this period as  $0.08 \text{ kg/m}^3$ .

**Contraction of the absorber vessel due to cooling.** The absorber was cooled from room temperature to the operating temperature of the experiment (20.51 K), contracting the vessel. The linear contraction of Al-6061 as it is cooled from 293 K is given by:

$$\alpha = -4.1277 \times 10^{-3}T - 3.0389 \times 10^{-6}T^2 + 8.7696 \times 10^{-8}T^3 - 9.9821 \times 10^{-11}T^4 \quad (7.1)$$

where  $T$  is the operating temperature [44]. The equation is the result of a fit to data collated by the National Institute of Standards and Technology (NIST) and has an associated curve fit error of 4%. At the MICE operating temperature, this corresponds to a linear contraction of the vessel along each plane of 0.415%. As a result the length of the bore contracted by  $(1.45 \pm 0.05)$  mm. The vessel was suspended within the warm bore of the focus coil and was therefore free to contract in each plane without restriction.

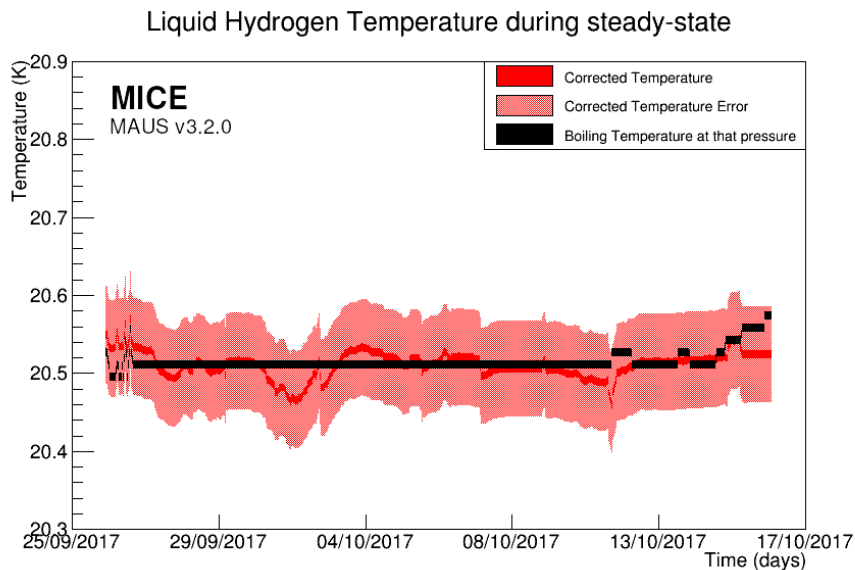


**Figure 18.** Average liquid hydrogen temperature recorded by the sensors during the steady state period. After applying all the correction factors the temperature remains at or close to the boiling point temperature.

**Deflection of absorber vessel windows due to internal pressure.** To minimise energy loss and Coulomb scattering by the absorber vessel, the window thickness was minimised. The liquid hydrogen circuit was pressurised above atmospheric pressure to prevent air ingress [41, 45]. The vessel was designed to withstand at least 2500 mbar internally. The internal pressure was limited by the 1.5 bar relief valve to atmosphere, whilst the vessel was surrounded by vacuum.

The pressure at which the absorber operated resulted in deflection of the absorber windows. These deflections were modelled using ANSYS [46], and the uncertainty in the window deflection derived from this model was 20%. The model showed a linear dependence of the window deflection on pressure up to 2 Bar when the windows begin to yield. The pressure sensors were accurate to  $\pm 5$  mbar (0.25% of 2 Bar). At  $(1085 \pm 5)$  mbar, the typical MICE operating pressure, this corresponded to a deflection of  $(0.5374 \pm 0.1076)$  mm (model uncertainty)  $\pm 0.0022$  mm (sensor uncertainty) at the centre of the absorber window.

**Variation of the absorber vessel window thicknesses.** On its passage through the absorber a muon would lose energy in the aluminium of the pair of hydrogen-containment windows, the two aluminium safety windows, and the liquid hydrogen itself. At the centre of the absorber, the total amount of aluminium the muon beam passed through was  $(785 \pm 13)$   $\mu\text{m}$ , producing a variance of 1.68%. However, as the windows were thin, the effects on energy loss were negligible. A 200 MeV/c muon passing along the central axis of an empty absorber lost 0.345 MeV, introducing a 0.006 MeV uncertainty on energy loss.

**Total systematic uncertainty on energy loss.** The principal contributions to the systematic uncertainty on energy loss in the liquid hydrogen absorber are: the uncertainty in the contraction of the absorber vessel, the uncertainty in the deflection of the hydrogen-containment windows due to internal pressure, and the uncertainty in the variation of the window thickness. The impact of the

contraction of vessel and the deflection of the windows resulted in a reduction of the length of the vessel on axis of  $(0.4 \pm 0.2)$  mm. The change in the combined thicknesses of the absorber windows on axis is  $13 \mu\text{m}$ . The average temperature during the steady state period of the experiment when the pressure remained constant at  $(1085 \pm 5)$  mbar is  $(20.51 \pm 0.07)$  K corresponding to a liquid hydrogen density of  $(70.53 \pm 0.08)$   $\text{kg/m}^3$ .

During the MICE data taking, muon beams with nominal momenta of 140, 170, 200 and 240 MeV/c were used. The energy loss and its uncertainty were calculated. The calculation used a central bore length of  $(349.6 \pm 0.2)$  mm, a total window thickness of  $(0.785 \pm 0.013)$  mm and a liquid hydrogen density of  $(70.53 \pm 0.08)$   $\text{kg/m}^3$ . For a 140 MeV/c muon this corresponds to an energy loss of  $(10.88 \pm 0.02)$  MeV, while for a 200 MeV/c muon particle this corresponds to an energy loss of  $(10.44 \pm 0.02)$  MeV. For a muon travelling along the centre axis of the absorber the systematic uncertainty in the energy loss is 0.2%.

## 8 Summary and conclusions

A complete set of particle detectors has permitted the full characterisation and study of the evolution of the phase space of a muon beam through a section of a cooling channel in the presence of liquid hydrogen and lithium hydride absorbers, leading to the first measurement of ionization cooling. The PID performance of the detectors is summarised in table 4 and table 5 and is fully compatible with the specification of the apparatus [47].

**Table 4.** Summary of the performance of the MICE PID detectors.

Detector	Characteristic	Performance
Time-of-Flight	time resolution	0.10 ns
KLOE-Light	muon PID efficiency	99%
Electron Muon Ranger	electron PID efficiency	98.6%

**Table 5.** Summary of the MICE PID detector performance for different beam settings.

Momentum	KL efficiency			EMR efficiency		Track finding efficiency					
	electrons	muons	pions	electrons	muons	3 mm		6 mm		10 mm	
						US	DS	US	DS	US	DS
<b>140 MeV/c</b>	95%	97%	n.a.	98%	35%			98%	99%	98%	99%
<b>170 MeV/c</b>	95%	99%	89%	99%	99%						
<b>200 MeV/c</b>	94%	99%	95%	100%	99%	99%	96%	99%	96%		
<b>240 MeV/c</b>	96%	99%	97%	99%	99%						
<b>300 MeV/c</b>	95%	99%	98%	n.a.	99%						

All the different elements of the MICE instrumentation have been used to characterise the beam and the measurement of the cooling performance for a different variety of beam momenta, emittance, and absorbers. The measurement of the physical properties of the liquid hydrogen

absorber have been fully described here. The experiment has thus demonstrated a technique critical for a muon collider and a neutrino factory and brings those facilities one step closer.

## Acknowledgments

The work described here was made possible by grants from the Department of Energy and National Science Foundation (U.S.A.), the Istituto Nazionale di Fisica Nucleare (Italy), the Science and Technology Facilities Council (U.K.), the European Community under the European Commission Framework Programme 7, the Japan Society for the Promotion of Science and the Swiss National Science Foundation, in the framework of the SCOPES programme. We gratefully acknowledge all sources of support. We acknowledge the use of Grid computing resources deployed and operated by GridPP in the U.K. [48]. We are also grateful to the staff of ISIS for the reliable operation of ISIS.

The MAUS software used to reconstruct and analyse the MICE data is available at [49].

## References

- [1] D.V. Neuffer and R.B. Palmer, *A high-energy high-luminosity  $\mu^+\mu^-$  collider*, *Conf. Proc. C* **940627** (1995) 52.
- [2] R.B. Palmer, *Muon colliders*, *Rev. Accel. Sci. Tech.* **7** (2014) 137.
- [3] S. Geer, *Neutrino beams from muon storage rings: characteristics and physics potential*, *Phys. Rev. D* **57** (1998) 6989 [Erratum *ibid.* **59** (1999) 039903] [[hep-ph/9712290](#)].
- [4] ISS PHYSICS WORKING GROUP collaboration, *Physics at a future neutrino factory and super-beam facility*, *Rept. Prog. Phys.* **72** (2009) 106201 [[arXiv:0710.4947](#)].
- [5] M. Apollonio et al., *Oscillation physics with a neutrino factory*, [hep-ph/0210192](#).
- [6] S.Y. Lee, *Accelerator physics*, third edition, **World Scientific**, Singapore (2012).
- [7] S. Schröder et al., *First laser cooling of relativistic ions in a storage ring*, *Phys. Rev. Lett.* **64** (1990) 2901.
- [8] J.S. Hangst, M. Kristensen, J.S. Nielsen, O. Poulsen, J.P. Schiffer and P. Shi, *Laser cooling of a stored ion beam to 1 mK*, *Phys. Rev. Lett.* **67** (1991) 1238.
- [9] P.J. Channell, *Laser cooling of heavy-ion beams*, *J. Appl. Phys.* **52** (1981) 3791.
- [10] J. Marriner, *Stochastic cooling overview*, *Nucl. Instrum. Meth. A* **532** (2004) 11 [[physics/0308044](#)].
- [11] V.V. Parkhomchuk and A.N. Skrinsky, *Electron cooling: 35 years of development*, *Phys. Usp.* **43** (2000) 433 [*Usp. Fiz. Nauk* **170** (2000) 473].
- [12] A. Antognini et al., *Demonstration of muon-beam transverse phase-space compression*, *Phys. Rev. Lett.* **125** (2020) 164802 [[arXiv:2003.11986](#)].
- [13] A.N. Skrinsky and V.V. Parkhomchuk, *Cooling methods for beams of charged particles* (in Russian), *Sov. J. Part. Nucl.* **12** (1981) 223 [*Fiz. Elem. Chast. Atom. Yadra* **12** (1981) 557].
- [14] D. Neuffer, *Principles and applications of muon cooling*, *Part. Accel.* **14** (1983) 75.
- [15] MICE collaboration, *Demonstration of cooling by the Muon Ionization Cooling Experiment*, *Nature* **578** (2020) 53 [[arXiv:1907.08562](#)].
- [16] M. Bonesini, *The design of MICE TOF0 detector*, [MICE note 145](#), (2006), accessed 14 May 2021.



- [17] R. Bertoni et al., *The construction and laboratory tests for MICE TOF0/1 detectors*, [MICE note 241](#), (2008), accessed 14 May 2021.
- [18] MICE collaboration, *The design and commissioning of the MICE upstream time-of-flight system*, [Nucl. Instrum. Meth. A](#) **615** (2010) 14 [[arXiv:1001.4426](#)].
- [19] R. Bertoni et al., *The construction of the MICE TOF2 detector*, [MICE note 286](#), (2010), accessed 14 May 2021.
- [20] MICE collaboration, *Pion contamination in the MICE muon beam*, [2016 JINST](#) **11** P03001 [[arXiv:1511.00556](#)].
- [21] MICE collaboration, *The MICE muon beam on ISIS and the beam-line instrumentation of the Muon Ionization Cooling Experiment*, [2012 JINST](#) **7** P05009 [[arXiv:1203.4089](#)].
- [22] MICE collaboration, *Characterisation of the muon beams for the Muon Ionisation Cooling Experiment*, [Eur. Phys. J. C](#) **73** (2013) 2582 [[arXiv:1306.1509](#)].
- [23] MICE collaboration, *Electron-muon ranger: performance in the MICE muon beam*, [2015 JINST](#) **10** P12012 [[arXiv:1510.08306](#)].
- [24] MICE collaboration, *First particle-by-particle measurement of emittance in the Muon Ionization Cooling Experiment*, [Eur. Phys. J. C](#) **79** (2019) 257 [[arXiv:1810.13224](#)].
- [25] M. Bonesini, R. Bertoni, A. de Bari and M. Rossella, *Behaviour in magnetic fields of fast conventional and fine-mesh photomultipliers*, [Nucl. Instrum. Meth. A](#) **693** (2012) 130 [[arXiv:1207.4909](#)].
- [26] M. Bonesini et al., *The TOF1 local shielding*, [MICE note 455](#), (2015), accessed 14 May 2021.
- [27] Y. Karadzhov et al., *TOF detectors time calibration*, [MICE note 251](#), (2009), accessed 14 May 2021.
- [28] L. Cremaldi, D.A. Sanders, P. Sonnek, D.J. Summers and J. Reidy Jr, *A Cherenkov radiation detector with high density aerogels*, [IEEE Trans. Nucl. Sci.](#) **56** (2009) 1475 [[arXiv:0905.3411](#)].
- [29] L. Cremaldi et al., *Progress on Cherenkov reconstruction in MICE*, [MICE note 473](#), (2015), accessed 14 May 2021.
- [30] F. Ambrosino et al., *Calibration and performances of the KLOE calorimeter*, [Nucl. Instrum. Meth. A](#) **598** (2009) 239.
- [31] E. Overton, *Studies and developments within the Muon Ionisation Cooling Experiment*, Ph.D. thesis, [Sheffield U.](#), Sheffield, U.K. (2014).
- [32] R. Asfandiyarov et al., *MAUS: the MICE Analysis User Software*, [2019 JINST](#) **14** T04005 [[arXiv:1812.02674](#)].
- [33] R. Asfandiyarov et al., *The design and construction of the MICE electron-muon ranger*, [2016 JINST](#) **11** T10007 [[arXiv:1607.04955](#)].
- [34] F. Drielsma, *Electron-muon ranger: hardware characterization*, master's thesis, Geneva U., Geneva, Switzerland (2014) [[arXiv:1710.06946](#)].
- [35] F. Drielsma, *Measurement of the increase in phase space density of a muon beam through ionization cooling*, Ph.D. thesis, [Geneva U.](#), Geneva, Switzerland (2018)
- [36] M. Ellis et al., *The design, construction and performance of the MICE scintillating fibre trackers*, [Nucl. Instrum. Meth. A](#) **659** (2011) 136 [[arXiv:1005.3491](#)].
- [37] M. Petroff and M. Stapelbroek, *Photon-counting solid-state photomultiplier*, [IEEE Trans. Nucl. Sci.](#) **36** (1989) 158.

- [38] D0 collaboration, *The upgraded D0 detector*, *Nucl. Instrum. Meth. A* **565** (2006) 463 [[physics/0507191](#)].
- [39] A. Dobbs et al., *The reconstruction software for the MICE scintillating fibre trackers*, *2016 JINST* **11** T12001 [[arXiv:1610.05161](#)].
- [40] F. Drielsma, *Beam-based detector alignment in the MICE muon beam line*, [arXiv:1805.06623](#).
- [41] MICE collaboration, *The liquid-hydrogen absorber for MICE*, *2018 JINST* **13** T09008 [[arXiv:1807.03019](#)].
- [42] *Temperature measurement and control catalog*, [https://www.lakeshore.com/docs/default-source/product-downloads/lakeshoretc\\_1.pdf](https://www.lakeshore.com/docs/default-source/product-downloads/lakeshoretc_1.pdf), accessed 2 October 2018.
- [43] C. Brown et al., *Systematic uncertainties in the liquid hydrogen absorber*, *MICE note 524*, (2018), accessed 14 May 2021.
- [44] G. Hardin, *Aluminum 6061-T6 (UNS AA96061)*, <https://www.nist.gov/mml/acmd/aluminum-6061-t6-uns-aa96061>, accessed 3 October 2018.
- [45] S. Ishimoto, S. Suzuki, M. Yoshida, M.A. Green, Y. Kuno and W. Lau, *Liquid hydrogen absorber for MICE*, *Conf. Proc. C* **100523** (2010) 421.
- [46] M. Green et al., *Does one know the properties of a MICE solid or liquid absorber to better than 0.3 percent?*, *MICE note 155*, (2006), accessed 14 May 2021.
- [47] MICE collaboration, *Proposal to the Rutherford Appleton Lab: an international Muon Ionization Cooling Experiment (MICE)*, *MICE note 21*, (2003), accessed 14 May 2021.
- [48] D. Britton et al., *GridPP: the U.K. grid for particle physics*, *Phil. Trans. Roy. Soc. A* **367** (2009) 2447.
- [49] MICE collaboration, *Source code of MAUS — the MICE Analysis User Software*, [10.17633/rd.brunel.8337542.v2](https://doi.org/10.17633/rd.brunel.8337542.v2), (2019).



## Radon variability due to floor level in two typical residential buildings in Serbia

Vladimir Udovicic ,  
Nikola Veselinovic,  
Dimitrije Maletic,  
Radomir Banjanac,  
Aleksandar Dragic,  
Dejan Jokovic,  
Mihailo Savic,  
David Knezevic,  
Maja Eremic Savkovic

**Abstract.** It is well known that one of the factors that influence the indoor radon variability is the floor level of the buildings. Considering the fact that the main source of indoor radon is radon in soil gas, it is expected that the radon concentration decreases at higher floors. Thus at higher floors the dominant source of radon is originating from building materials, and in some cases there may be deviations from the generally established regularity. In such sense, we chose one freestanding single-family house with loft and other 16-floor high-rise residential building for this study. The indoor radon measurements were performed by two methods: passive and active. We used passive devices based on track-etched detectors: Radtrak<sup>2</sup> Radonova. For the short-term indoor radon measurements, we used two active devices: SN1029 and SN1030 (manufactured by Sun Nuclear Corporation). The first device was fixed in the living room at the ground level and the second was moved through the floors of the residential building. Every measuring cycle at the specified floor lasted seven days with the sampling time of 2 h. The results show two different indoor radon behaviours regarding radon variability due to floor level. In the single-family house with loft we registered intense difference between radon concentration in the ground level and loft, while in the high-rise residential building the radon level was almost the same at all floors, and hence we may conclude that radon originated mainly from building materials.

**Keywords:** Radon variability • Time series

### Introduction

Radon sources in the buildings are primarily from soil, building materials and water. Considering the nature of the occurrence and all the sources, the concentration of radon is higher in the ground-floor rooms compared with that in the higher floors of the dwellings in apartments. In the literature one can find a lot of papers dealing with the influence of various factors, including the floor levels, on the radon concentration and variability. In one group of the articles, investigation of the indoor radon concentration distribution due to floor levels of the buildings is the part of the data analysis which was drawn from the national or regional radon surveys [1–6] and others are dedicated to these specific studies [7–11]. In the case of the big buildings with a several number of floors a deviation from the general regularity can be observed, since the dominant source of indoor radon at higher floors is building materials. On the other hand, the radon variability due to floor level, especially in big cities with a much higher number of high-rise buildings and population density compared with rural environments, may have an impact on the assessments of the effective dose from radon exposure at the national level. Usually, the indoor radon map represents the arithmetic mean value of indoor radon concentration on the ground floor, and thus it is not

V. Udovicic✉, N. Veselinovic, D. Maletic, R. Banjanac,  
A. Dragic, D. Jokovic, M. Savic, D. Knezevic  
Institute of Physics Belgrade  
University of Belgrade  
Pregrevica 118 St., 11080 Belgrade, Serbia  
E-mail: udovicic@ipb.ac.rs

M. Eremic Savkovic  
Serbian Radiation and Nuclear Safety and Security  
Directorate  
Masarikova 5 St., 11000 Belgrade, Serbia

Received: 30 November 2019  
Accepted: 17 January 2020

representative of the radon exposure to all citizens since most people do not live on the ground floor. So, it is necessary to convert indoor radon map to a dose map. One of the examples is presented as a plan to develop models that allow correction from ground-floor dwellings to the real situation, accounting data from the national buildings database [12]. In Serbia, national typology of residential buildings is based on the results from the monography “National typology of residential buildings of Serbia” by a group of authors from the Faculty of Architecture [13]. There are six types of the residential buildings in Serbia: two for family housing – freestanding single-family house and single-family house in a row and four types for multifamily housing – freestanding residential building and residential building (lamella) (apartment block with repeated multiple lamellar cores and separate entrances), residential building in a row, and high-rise residential building. Distribution of buildings by type at the national level shows that 97% of all residential buildings are family housing. Also, for all defined types of buildings, number of floors ranges from one to eight above the ground level. Freestanding family houses are mostly ground floor (37%) or ground floor with loft in use (26%), while there is a very low representation of houses that have more than two floors (5%), with average floor level of family buildings of 1.4 [13]. In such sense, we chose one freestanding single-family house with loft with well-known radon characteristics [14] and one 16-floor high-rise residential building for this study.

## Materials and methods

Two housing units were selected, one from the family housing group and one high-rise residential building from the collective housing group. The family house has a characteristic construction style in which the house has been built for several years with constant upgrading, which can potentially be a source of radon entry into such houses. The house has a basement and is made of standard materials (brick block, concrete, plaster). Finally, insulation was made using 5-cm thick styrofoam. Long-term measurements of radon concentrations have been carried out in this house by various methods, and several scientific papers have been published so far [14–16].

From the group of residential buildings for collective housing, we chose high-rise building in New Belgrade. It was built in the 1960s as block type. The soliter has a basement, while on the ground floor there are outlets and business premises. The apartments are located in the first floor upward. The soliter has 16 floors. One of the important parameters in the selection of building in municipality New Belgrade is the fact that this municipality is the most populated in Serbia.

The long-term radon measurements were performed with passive device Radtrak<sup>2</sup> Radonova based on CR-39 track detector. The detectors were exposed for three months from March to June. In the high-rise building, passive radon detectors were deployed at some of the floors in one or several apartments. Time series of measured radon concentrations in the studied residential buildings were obtained using two active devices: SN1029 with the following characteristics declared by the manufacturer – the measurement ranging from 1 Bq·m<sup>-3</sup> to 99.99 kBq·m<sup>-3</sup>, accuracy equal to ±25%, sensitivity of 0.16 counts/h/Bq·m<sup>-3</sup> and SN1030 with the following characteristics – the measurement ranging from 1 Bq·m<sup>-3</sup> to 99.99 kBq·m<sup>-3</sup>, accuracy equal to ±20%, sensitivity of 0.4 counts/h/Bq·m<sup>-3</sup>. SN1029 device were calibrated at the accredited metrological Lab (SUJCHBO Kamenna, Czech Republic) in 2015 and model SN1030 were calibrated by the manufacturer in 2017. The both instruments participated in 2018 NRPI Intercomparisons of radon gas continuous monitors and also, SN1029 device participated in 2015 NRPI Intercomparisons of radon gas measurement devices at SURO v.v.i. Institute, Prague, Czech Republic within the IAEA Technical Cooperation Projects RER 9153 and RER 9127, with excellent results. These are measuring devices of simple construction and practical application. It is a counter with the addition of a sensor for measuring meteorological parameters. The operator can adjust the time sequences from 0.5 h to 24 h. One measurement cycle can take 1000 h or a total of 720 time sequences (the number of successive measurements, i.e. points in a time series). The devices were set to operate in a 2-h time sequence. One was fixed in the downstairs living room and the other was fixed in repositioning floors in apartment buildings. Each measurement cycle on a given floor lasted seven days.

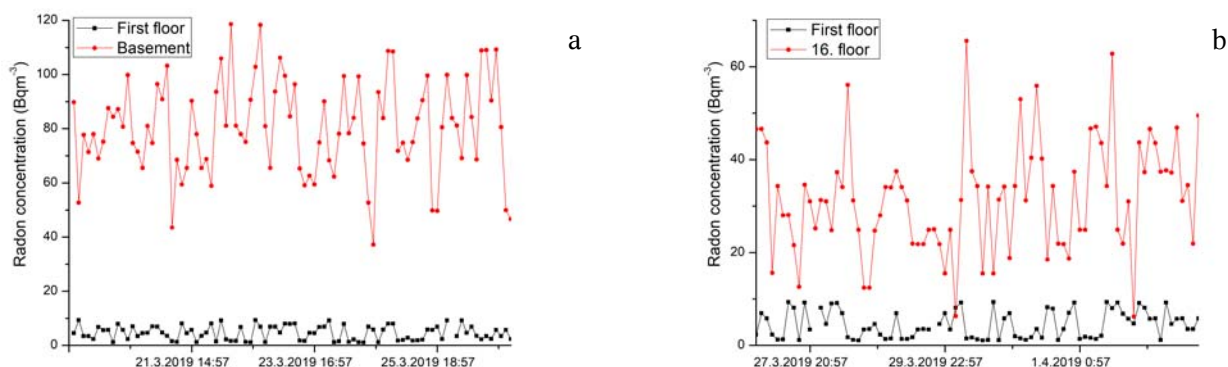


**Fig. 1.** The time series of the radon concentrations at the first floor vs. basement (a) and 16th floor (b) in the big residential building.

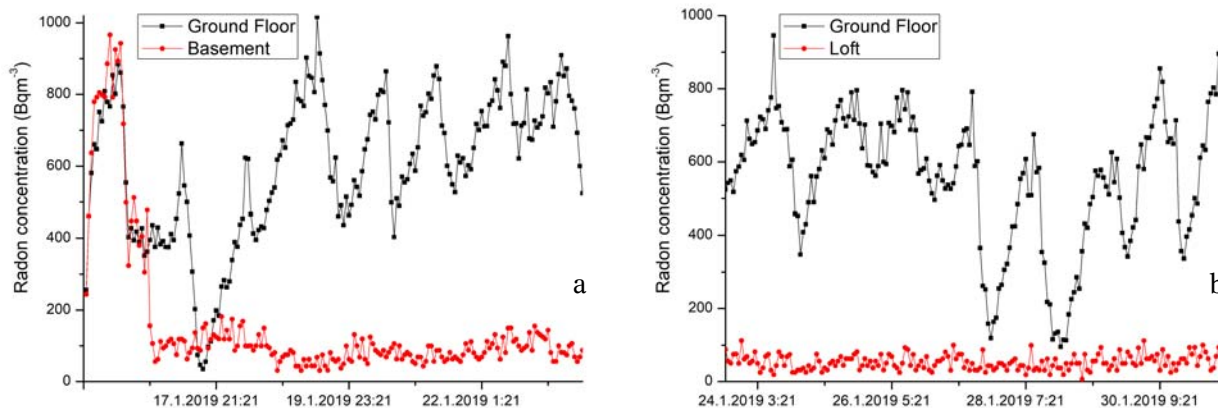


Fig. 2. The time series of the radon concentrations at the first floor vs. basement (a) and loft (b) in the single-family house.

Table 1. Results of indoor radon measurements in the high-rise residential building using passive (Radtrak<sup>2</sup> Radonova) and active radon devices

Floor level	Radon concentration/ Passive device (Radtrak <sup>2</sup> ) [Bq·m <sup>-3</sup> ]	Average radon concentration per floor level (Radtrak <sup>2</sup> ) [Bq·m <sup>-3</sup> ]	Arithmetic mean (standard deviation) radon concentration over measuring cycle [Bq·m <sup>-3</sup> ]
Basement	52 ± 10	53.5	81(17)
	69 ± 12		
	38 ± 10		
	55 ± 10		
1	<10	14	5(3)
	14 ± 8		
2	17 ± 8	17	24(9)
3			25(10)
4	21 ± 8	20.5	26(11)
	20 ± 8		
5	11 ± 8	19	
	27 ± 10		
6	22 ± 8	17	
	12 ± 8		
7	17 ± 8		
	23 ± 8		
8	22 ± 8	22	
9	15 ± 8	17.7	24(10)
	16 ± 8		
10	22 ± 8	17.5	
	15 ± 8		
11	20 ± 8	16	
12	<10	<10	
14	16 ± 8	18.5	29(9)
	17 ± 8		
15	15 ± 8	15.5	
	16 ± 8		
16	31 ± 8	31	32(12)
Overall mean	24	21.6	30

Results and discussions

Figure 1 shows the illustrative examples that show radon time series from high-rise building, and Fig. 2 originates from the observed single-family house.

The arithmetic mean radon concentrations obtained from long- and short-term measurements are shown in Tables 1 and 2 for high-rise building and single-family house with loft, respectively.

In the family house, it is possible to notice marked variations in radon concentration with 1-day periodicity. Also interesting is the ratio of radon concentration on the ground floor to the basement of the house, which is the opposite of the usual situation in houses with a basement. This inverse behaviour can be explained by the fact that the basement does not cover the whole ground floor but a smaller part of it. The rest of the ground floor is covered by a concrete slab as a substrate, but cracks and poor joint with the walls are potential sources of elevated radon. Also, the differences in the results between two methods, passive and active devices, are due to the fact that presented radon values are measured in different seasons. With high-rise residential building, the situation is the opposite and it can be considered from the first floor that the dominant source of radon is the building material. There may even be a slight increase in the mean radon concentration on the higher floors. Also, the results show very low radon level on the first floor (well below the outdoor values) in the apartment. In such sense, we performed test intercomparison radon measurements for two active devices SN1029 and SN1030 in well-defined and controlled radon atmosphere (radon concentration below 30 Bq·m<sup>-3</sup>) in the Underground Low-background Laboratory in the Institute of Physics Belgrade [17, 18]. Additional testing includes the same place and time of the measurements but different sampling time set to 1, 2, 4, 8 and 12 h. The results are shown in Table 3.

In the above performed measurements, both devices show significant differences in the low-level radon range, which may originate from individual instruments characteristics presented in the “Materials and methods” section.

**Table 2.** Results of indoor radon measurements in the single-family house with loft using passive (Radtrak<sup>2</sup> Radonova) and active radon devices

Floor level	Radon concentration/Passive device (Radtrak <sup>2</sup> ) [Bq·m <sup>-3</sup> ]	Arithmetic mean (standard deviation) radon concentration over measuring cycle [Bq·m <sup>-3</sup> ]
Basement		160(202)
Ground level	330 ± 50	579(194)
Loft	18 ± 8	53(21)

**Table 3.** Test intercomparison indoor radon measurements with active radon devices SN1029 and SN1030

	Arithmetic mean (standard deviation) radon concentration over measuring cycle [Bq·m <sup>-3</sup> ]				
Sampling time [h]	1	2	4	8	12
SN1029	28(12)	28(11)	27(7)	23(6)	32(14)
SN1030	12(6)	14(7)	10(3)	12(5)	14(6)

## Conclusions

The results show that the radon behaviour in two different residential buildings is diametrically opposite. In the single-family house with loft we registered intense difference between radon concentration in the ground level and loft, while in the high-rise residential building the radon level was almost the same at all floors and hence we may conclude that radon originated mainly from building materials. However, the results from the high-rise building can be predicted on the basis of work of a group of authors who have determined the internal exposure from construction material used in Serbia which originates from the exhalation of radon and thoron [19] and the study presented in this article [10]. We can expect similar results in any other multistorey buildings in Serbia. In the future work, we will focus on the additional radon measurements in the typical residential buildings from other types of houses.

**Acknowledgments.** The authors acknowledge funding provided by the Institute of Physics Belgrade through the grant by the Ministry of Education, Science and Technological Development of the Republic of Serbia.

## ORCID

V. Udovicic  <http://orcid.org/0000-0002-7839-1537>

## References

- Bochicchio, F., Campos-Venuti, G., Piermattei, S., Nucetelli, C., Risica, S., Tommasino, L., Torri, G., Magnoni, M., Agnesod, G., Sgorbati, G., Bonomi, M., Minach, L., Trotti, F., Malisan, M. R., Maggiolo, S., Gaidolfi, L., Giannardi, C., Rongoni, A., Lombardi, M., Cherubini, G., D'Ostilio, S., Cristofaro, C., Pugliese, M., Martucci, V., Crispino, A., Cuzzocrea, P., Sansone Santamaria, A., & Cappai, M. (2005). Annual average and seasonal variations of residential radon concentration for all the Italian Regions. *Radiat. Meas.*, *40*, 686–694.
- Friedmann, H. (2005). Final results of the Austrian Radon Project. *Health Phys.*, *89*(4), 339–348.
- Du, L., Prasauskas, T., Leivo, V., Turunen, M., Pekkonen, M., Kiviste, M., Aaltonen, A., Martuzevicius, D., & Haverinen-Shaughnessy, U. (2015). Assessment of indoor environmental quality in existing multi-family buildings in North-East Europe. *Environ. Int.*, *79*, 74–84.
- Cucoş (Dinu), A., Cosma, C., Dicu, T., Begy, R., Moldovan, M., Papp, B., Niță, D., Burgehele, B., & Sainz, C. (2012). Thorough investigations on indoor radon in Băița radon-prone area (Romania). *Sci. Total Environ.*, *431*, 78–83.
- Yarmoshenko, I., Vasilyev, A., Malinovsky, G., Bossew, P., Žunić, Z. S., Onischenko, A., & Zhukovsky, M. (2016). Variance of indoor radon concentration: Major influencing factors. *Sci. Total Environ.*, *541*, 155–160.
- Kropat, G., Bochud, F., Jaboyedoff, M., Laedermann, J. P., Murith, C., Palacios, M., & Baechler, S. (2014). Major influencing factors of indoor radon concentrations in Switzerland. *J. Environ. Radioact.*, *129*, 7–22.
- Borgoni, R., De Francesco, D., De Bartolo, D., & Tzavidis, N. (2014). Hierarchical modeling of indoor radon concentration: how much do geology and building factors matter? *J. Environ. Radioact.*, *138*, 227–237.
- Xie, D., Liao, M., & Kearfott, K. J. (2015). Influence of environmental factors on indoor radon concentration levels in the basement and ground floor of a building – A case study. *Radiat. Meas.*, *82*, 52–58.
- Man, C. K., & Yeung, H. S. (1999). Modeling and measuring the indoor radon concentrations in high-rise buildings in Hong Kong. *Appl. Radiat. Isot.*, *50*, 1131–1135.
- Vukotić, P., Zekić, R., Antović, N. M., & Andjelić, T. (2019). Radon concentrations in multi-story buildings in Montenegro. *Nucl. Technol. Radiat. Prot.*, *34*, 165–174.
- Lorenzo-González, M., Ruano-Ravina, A., Peón, J., Piñeiro, M., & Barros-Dios, J. M. (2017). Residential radon in Galicia: a cross-sectional study in a radon-prone area. *J. Radiol. Prot.*, *37*(3), 728–741.
- Elío, J., Cinelli, G., Bossew, P., Gutiérrez-Villanueva, J. L., Tollefsen, T., De Cort, M., Nogarotto, A., & Braga, R. (2019). The first version of the Pan-European Indoor Radon Map. *Nat. Hazards Earth Syst. Sci.*, *19*, 2451–2464.
- Jovanović Popović, M., Ignjatović, D., Radivojević, A., Rajčić, A., Čuković Ignjatović, N., Đukanović, Lj., & Nedić, M. (2013). *National typology of residential*

- buildings in Serbia*. Belgrade: Faculty of Architecture University of Belgrade.
14. Udovičić, V., Maletić, D., Banjanac, R., Joković, D., Dragić, A., Veselinović, N., Živanović, J., Savić, M., & Forkapić, S. (2018). Multiyear indoor radon variability in a family house—A case study in Serbia. *Nucl. Technol. Radiat. Prot.*, 33(2), 174–179.
  15. Maletić, D., Udovičić, V., Banjanac, R., Joković, D., Dragić, A., Veselinović, N., & Filipović, J. (2014). Comparison of multivariate classification and regression methods for indoor radon measurements. *Nucl. Technol. Radiat. Prot.*, 29, 17–23.
  16. Filipović, J., Maletić, D., Udovičić, V., Banjanac, R., Joković, D., Savić, M., & Veselinović, N. (2016). The use of multivariate analysis of the radon variability in the underground laboratory and indoor environment. *Nukleonika*, 61(3), 357–360. DOI: 10.1515/nuka-2016-0059.
  17. Udovičić, V., Aničin, I., Joković, D., Dragić, A., Banjanac, R., Grabež, B., & Veselinović, N. (2011). Radon time-series analysis in the Underground Low-level Laboratory in Belgrade, Serbia. *Radiat. Prot. Dosim.*, 145(2/3), 155–158.
  18. Udovičić, V., Filipović, J., Dragić, A., Banjanac, R., Joković, D., Maletić, D., Grabež, B., & Veselinović, N. (2014). Daily and seasonal radon variability in the underground low-background laboratory in Belgrade, Serbia. *Radiat. Prot. Dosim.*, 160(1/3), 62–64.
  19. Ujić, P., Čeliković, I., Kandić, A., Vukanac, I., Đurašević, M., Dragosavac, D., & Žunić, Z. S. (2010). Internal exposure from building materials exhaling  $^{222}\text{Rn}$  and  $^{220}\text{Rn}$  as compared to external exposure due to their natural radioactivity content. *Appl. Radiat. Isot.*, 68, 201–206.

OPEN ACCESS

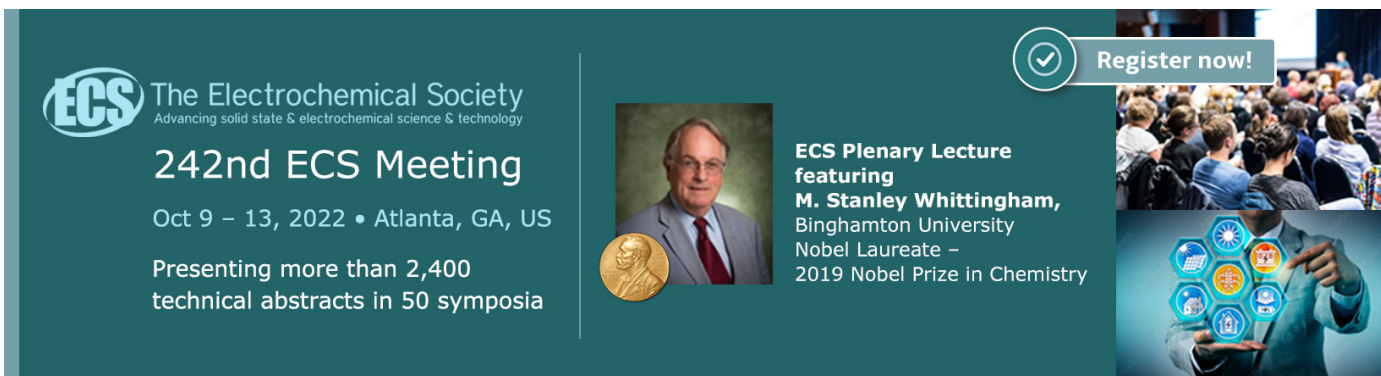
# The magnet of the scattering and neutrino detector for the SHiP experiment at CERN

To cite this article: C. Ahdida *et al* 2020 *JINST* 15 P01027

View the [article online](#) for updates and enhancements.

## You may also like

- [Pileup mitigation at CMS in 13 TeV data](#)  
A.M. Sirunyan, A. Tumasyan, W. Adam et al.
- [Fast simulation of muons produced at the SHiP experiment using Generative Adversarial Networks](#)  
C. Ahdida, R. Albanese, A. Alexandrov et al.
- [ATLAS data quality operations and performance for 2015–2018 data-taking](#)  
G. Aad, B. Abbott, D.C. Abbott et al.




**ECS** The Electrochemical Society  
Advancing solid state & electrochemical science & technology



## 242nd ECS Meeting

Oct 9 – 13, 2022 • Atlanta, GA, US

Presenting more than 2,400 technical abstracts in 50 symposia

 **ECS Plenary Lecture featuring M. Stanley Whittingham**, Binghamton University Nobel Laureate – 2019 Nobel Prize in Chemistry

 Register now!





# The magnet of the scattering and neutrino detector for the SHiP experiment at CERN



## The SHiP collaboration

C. Ahcida,<sup>44</sup> R. Albanese,<sup>14,d,h</sup> A. Alexandrov,<sup>14</sup> A. Anokhina,<sup>39</sup> S. Aoki,<sup>18</sup> G. Arduini,<sup>44</sup>  
 E. Atkin,<sup>38</sup> N. Azorskiy,<sup>29</sup> J.J. Back,<sup>54</sup> A. Bagulya,<sup>32</sup> F. Baaltasar Dos Santos,<sup>44</sup> A. Baranov,<sup>40</sup>  
 F. Bardou,<sup>44</sup> G.J. Barker,<sup>54</sup> M. Battistin,<sup>44</sup> J. Bauche,<sup>44</sup> A. Bay,<sup>46</sup> V. Bayliss,<sup>51</sup>  
 G. Bencivenni,<sup>15</sup> A.Y. Berdnikov,<sup>37</sup> Y.A. Berdnikov,<sup>37</sup> I. Berezkina,<sup>32</sup> M. Bertani,<sup>15</sup>  
 C. Betancourt,<sup>47</sup> I. Bezshyiko,<sup>47</sup> O. Bezshyyko,<sup>55</sup> D. Bick,<sup>8</sup> S. Bieschke,<sup>8</sup> A. Blanco,<sup>28</sup>  
 J. Boehm,<sup>51</sup> M. Bogomilov,<sup>1</sup> K. Bondarenko,<sup>27,57</sup> W.M. Bonivento,<sup>13</sup> J. Borburgh,<sup>44</sup>  
 A. Boyarsky,<sup>27,55</sup> R. Brenner,<sup>43</sup> D. Breton,<sup>4</sup> R. Brundler,<sup>47</sup> M. Bruschi,<sup>12</sup> V. Büscher,<sup>10</sup>  
 A. Buonaura,<sup>47</sup> S. Buontempo,<sup>14</sup> S. Cadeddu,<sup>13</sup> A. Calcaterra,<sup>15</sup> M. Calviani,<sup>44</sup>  
 M. Campanelli,<sup>53</sup> M. Casolino,<sup>44</sup> N. Charitonidis,<sup>44</sup> P. Chau,<sup>10</sup> J. Chauveau,<sup>5</sup> A. Chepurinov,<sup>39</sup>  
 M. Chernyavskiy,<sup>32</sup> K.-Y. Choi,<sup>26</sup> A. Chumakov,<sup>2</sup> P. Ciambone,<sup>15</sup> L. Congedo,<sup>11,a</sup>  
 K. Cornelis,<sup>44</sup> M. Cristinziani,<sup>7</sup> A. Crupano,<sup>14,d</sup> G.M. Dallavalle,<sup>12</sup> A. Datwyler,<sup>47</sup>  
 N. D'Ambrosio,<sup>16</sup> G. D'Appollonio,<sup>13,c</sup> J. De Carvalho Saraiva,<sup>28</sup> G. De Lellis,<sup>14,34,44,d</sup>  
 M. de Magistris,<sup>14,l</sup> A. De Roeck,<sup>44</sup> M. De Serio,<sup>11,a</sup> D. De Simone,<sup>14,d</sup> L. Dedenko,<sup>39</sup>  
 P. Dergachev,<sup>34</sup> A. Di Crescenzo,<sup>14,d</sup> C. Dib,<sup>2</sup> H. Dijkstra,<sup>44</sup> P. Dipinto,<sup>11,a</sup> V. Dmitrenko,<sup>38</sup>  
 S. Dmitrievskiy,<sup>29</sup> L.A. Dougherty,<sup>44</sup> A. Dolmatov,<sup>30</sup> D. Domenici,<sup>15</sup> S. Donskov,<sup>35</sup>  
 V. Drohan,<sup>55</sup> A. Dubreuil,<sup>45</sup> M. Ehlert,<sup>6</sup> T. Enik,<sup>29</sup> A. Etenko,<sup>33,38</sup> F. Fabbri,<sup>12</sup> L. Fabbri,<sup>12,b</sup>  
 A. Fabich,<sup>44</sup> O. Fedin,<sup>36</sup> F. Fedotovs,<sup>52</sup> G. Felici,<sup>15</sup> M. Ferro-Luzzi,<sup>44</sup> K. Filippov,<sup>38</sup> R.A. Fini,<sup>11</sup>  
 P. Fonte,<sup>28</sup> C. Franco,<sup>28</sup> M. Fraser,<sup>44</sup> R. Fresa,<sup>14,i,h</sup> R. Froeschl,<sup>44</sup> T. Fukuda,<sup>19</sup> G. Galati,<sup>14,d</sup>  
 J. Gall,<sup>44</sup> L. Gatignon,<sup>44</sup> G. Gavrillov,<sup>38</sup> V. Gentile,<sup>14,d</sup> S. Gerlach,<sup>6</sup> B. Goddard,<sup>44</sup>  
 L. Golinka-Bezshyyko,<sup>55</sup> A. Golovatiuk,<sup>14,d</sup> D. Golubkov,<sup>30</sup> A. Golutvin,<sup>52</sup> P. Gorbounov,<sup>44</sup>  
 D. Gorbunov,<sup>31</sup> S. Gorbunov,<sup>32</sup> V. Gorkavenko,<sup>55</sup> Y. Gornushkin,<sup>29</sup> M. Gorshenkov,<sup>34</sup>  
 V. Grachev,<sup>38</sup> A.L. Grandchamp,<sup>46</sup> G. Granich,<sup>32</sup> E. Graverini,<sup>46</sup> J.-L. Grenard,<sup>44</sup> D. Grenier,<sup>44</sup>  
 V. Grichine,<sup>32</sup> N. Gruzinskii,<sup>36</sup> A. M. Guler,<sup>48</sup> Yu. Guz,<sup>35</sup> G.J. Haefeli,<sup>46</sup> C. Hagner,<sup>8</sup>

H. Hakobyan,<sup>2</sup> I.W. Harris,<sup>46</sup> E. van Herwijnen,<sup>44</sup> C. Hessler,<sup>44</sup> A. Hollnagel,<sup>10</sup> B. Hosseini,<sup>52</sup> M. Hushchyn,<sup>40</sup> G. Iaselli,<sup>11,a</sup> A. Iuliano,<sup>14,d</sup> V. Ivantchenko,<sup>32</sup> R. Jacobsson,<sup>44</sup> D. Joković,<sup>41</sup> M. Jonker,<sup>44</sup> I. Kadenko,<sup>55</sup> V. Kain,<sup>44</sup> B. Kaiser,<sup>8</sup> C. Kamiscioglu,<sup>49</sup> K. Kershaw,<sup>44</sup> M. Khabibullin,<sup>31</sup> E. Khalikov,<sup>39</sup> G. Khaustov,<sup>35</sup> G. Khorauli,<sup>10</sup> A. Khotyantsev,<sup>31</sup> S.H. Kim,<sup>22</sup> Y.G. Kim,<sup>23</sup> V. Kim,<sup>36,37</sup> N. Kitagawa,<sup>19</sup> J.-W. Ko,<sup>22</sup> K. Kodama,<sup>17</sup> A. Kolesnikov,<sup>29</sup> D.I. Kolev,<sup>1</sup> V. Kolosov,<sup>35</sup> M. Komatsu,<sup>19</sup> N. Kondrateva,<sup>32</sup> A. Kono,<sup>21</sup> N. Konovalova,<sup>32,34</sup> S. Kormannshaus,<sup>10</sup> I. Korol,<sup>6</sup> I. Korol'ko,<sup>30</sup> A. Korzenev,<sup>45</sup> V. Kostyukhin,<sup>7</sup> E. Koukovini Platia,<sup>44</sup> S. Kovalenko,<sup>2</sup> I. Krasilnikova,<sup>34</sup> Y. Kudenko,<sup>31,38,g</sup> E. Kurbatov,<sup>40</sup> P. Kurbatov,<sup>34</sup> V. Kurochka,<sup>31</sup> E. Kuznetsova,<sup>36</sup> H.M. Lacker,<sup>6</sup> M. Lamont,<sup>44</sup> G. Lanfranchi,<sup>15</sup> O. Lantwin,<sup>47</sup> A. Lauria,<sup>14,d</sup> K.S. Lee,<sup>25</sup> K.Y. Lee,<sup>22</sup> J.-M. Lévy,<sup>5</sup> V.P. Loschiavo,<sup>14,k</sup> L. Lopes,<sup>28</sup> E. Lopez Sola,<sup>44</sup> V. Lyubovitskij,<sup>2</sup> J. Maalmi,<sup>4</sup> A. Magnan,<sup>52</sup> V. Maleev,<sup>36</sup> A. Malinin,<sup>33</sup> Y. Manabe,<sup>19</sup> A.K. Managadze,<sup>39</sup> M. Manfredi,<sup>44</sup> S. Marsh,<sup>44</sup> A.M. Marshall,<sup>50</sup> A. Mefodev,<sup>31</sup> P. Mermod,<sup>45</sup> A. Miano,<sup>14,d</sup> S. Mikado,<sup>20</sup> Yu. Mikhaylov,<sup>35</sup> D.A. Milstead,<sup>42</sup> O. Mineev,<sup>31</sup> V. Minutolo,<sup>j</sup> A. Montanari,<sup>12</sup> M.C. Montesi,<sup>14,d</sup> K. Morishima,<sup>19</sup> S. Movchan,<sup>29</sup> Y. Muttoni,<sup>44</sup> N. Naganawa,<sup>19</sup> M. Nakamura,<sup>19</sup> T. Nakano,<sup>19</sup> S. Nasybulin,<sup>36</sup> P. Ninin,<sup>44</sup> A. Nishio,<sup>19</sup> A. Novikov,<sup>38</sup> B. Obinyakov,<sup>33</sup> S. Ogawa,<sup>21</sup> N. Okateva,<sup>32,34</sup> B. Opitz,<sup>8</sup> J. Osborne,<sup>44</sup> M. Ovchynnikov,<sup>27,55</sup> N. Owtscharenko,<sup>7</sup> P.H. Owen,<sup>47</sup> P. Pacholek,<sup>44</sup> A. Paoloni,<sup>15</sup> B.D. Park,<sup>22</sup> S.K. Park,<sup>25</sup> G. Passeggio,<sup>14</sup> A. Pastore,<sup>11</sup> M. Patel,<sup>52</sup> D. Pereyma,<sup>30</sup> A. Perillo-Marccone,<sup>44</sup> G.L. Petkov,<sup>1</sup> K. Petridis,<sup>50</sup> A. Petrov,<sup>33</sup> D. Podgrudkov,<sup>39</sup> V. Poliakov,<sup>35</sup> N. Polukhina,<sup>32,34,38</sup> J. Prieto Prieto,<sup>44</sup> M. Prokudin,<sup>30</sup> A. Prota,<sup>14,d</sup> A. Quercia,<sup>14,d</sup> A. Rademakers,<sup>44</sup> A. Rakai,<sup>44</sup> F. Ratnikov,<sup>40</sup> T. Rawlings,<sup>51</sup> F. Redi,<sup>46</sup> S. Ricciardi,<sup>51</sup> M. Rinaldesi,<sup>44</sup> Volodymyr Rodin,<sup>55</sup> Viktor Rodin,<sup>55</sup> P. Robbe,<sup>4</sup> A.B. Rodrigues Cavalcante,<sup>46</sup> T. Roganova,<sup>39</sup> H. Rokujo,<sup>19</sup> G. Rosa,<sup>14,d</sup> T. Rovelli,<sup>12,b</sup> O. Ruchayskiy,<sup>3</sup> T. Ruf,<sup>44</sup> V. Samoylenko,<sup>35</sup> V. Samsonov,<sup>38</sup> F. Sanchez Galan,<sup>44</sup> P. Santos Diaz,<sup>44</sup> A. Sanz Ull,<sup>44</sup> A. Saputi,<sup>15</sup> O. Sato,<sup>19</sup> E.S. Savchenko,<sup>34</sup> J.S. Schliwinski,<sup>6</sup> W. Schmidt-Parzefall,<sup>8</sup> N. Serra,<sup>47</sup> S. Sgobba,<sup>44</sup> O. Shadura,<sup>55</sup> A. Shakin,<sup>34</sup> M. Shaposhnikov,<sup>46</sup> P. Shatalov,<sup>30</sup> T. Shchedrina,<sup>32,34</sup> L. Shchutska,<sup>55</sup> V. Shevchenko,<sup>33</sup> H. Shibuya,<sup>21</sup> L. Shihora,<sup>6</sup> S. Shirobokov,<sup>52</sup> A. Shustov,<sup>38</sup> S.B. Silverstein,<sup>42</sup> S. Simone,<sup>11,a</sup> R. Simoniello,<sup>10</sup> M. Skorokhvatov,<sup>38,33</sup> S. Smirnov,<sup>38</sup> J.Y. Sohn,<sup>22</sup> A. Sokolenko,<sup>55</sup> E. Solodko,<sup>44</sup> N. Starkov,<sup>32,34</sup> L. Stoel,<sup>44</sup> B. Storaci,<sup>47</sup> M.E. Stramaglia,<sup>46</sup> D. Sukhonos,<sup>44</sup> Y. Suzuki,<sup>19</sup> S. Takahashi,<sup>18</sup> J.L. Tastet,<sup>3</sup> P. Teterin,<sup>38</sup> S. Than Naing,<sup>32</sup> I. Timiryasov,<sup>46</sup> V. Tioukov,<sup>14</sup> D. Tommasini,<sup>44</sup> M. Torii,<sup>19</sup> N. Tosi,<sup>12</sup> D. Treille,<sup>44</sup> R. Tsenov,<sup>1,29</sup> S. Ulin,<sup>38</sup> A. Ustyuzhanin,<sup>40</sup> Z. Uteshev,<sup>38</sup> G. Vankova-Kirilova,<sup>1</sup> F. Vannucci,<sup>5</sup> P. Venkova,<sup>6</sup> V. Venturi,<sup>44</sup> S. Vilchinski,<sup>55</sup> M. Villa,<sup>12,b</sup> Heinz Vincke,<sup>44</sup> Helmut Vincke,<sup>44</sup> C. Visone,<sup>14,d</sup> K. Vlasik,<sup>38</sup> A. Volkov,<sup>32,33</sup> R. Voronkov,<sup>32</sup> S. van Waasen,<sup>9</sup> R. Wanke,<sup>10</sup> P. Wertelaers,<sup>44</sup> J.-K. Woo,<sup>24</sup> M. Wurm,<sup>10</sup> S. Xella,<sup>3</sup> D. Yilmaz,<sup>49</sup> A.U. Yilmazer,<sup>49</sup> C.S. Yoon,<sup>22</sup> P. Zarubin,<sup>29</sup> I. Zarubina<sup>29</sup> and Yu. Zaytsev<sup>30</sup>

<sup>1</sup>Faculty of Physics, Sofia University, Sofia, Bulgaria

<sup>2</sup>Universidad Técnica Federico Santa María and Centro Científico Tecnológico de Valparaíso, Valparaíso, Chile

<sup>3</sup>Niels Bohr Institute, University of Copenhagen, Copenhagen, Denmark

<sup>4</sup>LAL, Univ. Paris-Sud, CNRS/IN2P3, Université Paris-Saclay, Orsay, France

<sup>5</sup>LPNHE, IN2P3/CNRS, Sorbonne Université, Université Paris Diderot, F-75252 Paris, France

<sup>6</sup>Humboldt-Universität zu Berlin, Berlin, Germany

- <sup>7</sup>*Physikalisches Institut, Universität Bonn, Bonn, Germany*
- <sup>8</sup>*Universität Hamburg, Hamburg, Germany*
- <sup>9</sup>*Forschungszentrum Jülich GmbH (KFA), Jülich, Germany*
- <sup>10</sup>*Institut für Physik and PRISMA Cluster of Excellence, Johannes Gutenberg Universität Mainz, Mainz, Germany*
- <sup>11</sup>*Sezione INFN di Bari, Bari, Italy*
- <sup>12</sup>*Sezione INFN di Bologna, Bologna, Italy*
- <sup>13</sup>*Sezione INFN di Cagliari, Cagliari, Italy*
- <sup>14</sup>*Sezione INFN di Napoli, Napoli, Italy*
- <sup>15</sup>*Laboratori Nazionali dell'INFN di Frascati, Frascati, Italy*
- <sup>16</sup>*Laboratori Nazionali dell'INFN di Gran Sasso, L'Aquila, Italy*
- <sup>17</sup>*Aichi University of Education, Kariya, Japan*
- <sup>18</sup>*Kobe University, Kobe, Japan*
- <sup>19</sup>*Nagoya University, Nagoya, Japan*
- <sup>20</sup>*College of Industrial Technology, Nihon University, Narashino, Japan*
- <sup>21</sup>*Toho University, Funabashi, Chiba, Japan*
- <sup>22</sup>*Physics Education Department & RINS, Gyeongsang National University, Jinju, Korea*
- <sup>23</sup>*Gwangju National University of Education,<sup>e</sup> Gwangju, Korea*
- <sup>24</sup>*Jeju National University,<sup>e</sup> Jeju, Korea*
- <sup>25</sup>*Korea University, Seoul, Korea*
- <sup>26</sup>*Sungkyunkwan University,<sup>e</sup> Suwon-si, Gyeong Gi-do, Korea*
- <sup>27</sup>*University of Leiden, Leiden, The Netherlands*
- <sup>28</sup>*LIP, Laboratory of Instrumentation and Experimental Particle Physics, Portugal*
- <sup>29</sup>*Joint Institute for Nuclear Research (JINR), Dubna, Russia*
- <sup>30</sup>*Institute of Theoretical and Experimental Physics (ITEP) NRC 'Kurchatov Institute', Moscow, Russia*
- <sup>31</sup>*Institute for Nuclear Research of the Russian Academy of Sciences (INR RAS), Moscow, Russia*
- <sup>32</sup>*P.N. Lebedev Physical Institute (LPI), Moscow, Russia*
- <sup>33</sup>*National Research Centre 'Kurchatov Institute', Moscow, Russia*
- <sup>34</sup>*National University of Science and Technology "MISIS", Moscow, Russia*
- <sup>35</sup>*Institute for High Energy Physics (IHEP) NRC 'Kurchatov Institute', Protvino, Russia*
- <sup>36</sup>*Petersburg Nuclear Physics Institute (PNPI) NRC 'Kurchatov Institute', Gatchina, Russia*
- <sup>37</sup>*St. Petersburg Polytechnic University (SPbPU),<sup>f</sup> St. Petersburg, Russia*
- <sup>38</sup>*National Research Nuclear University (MEPhI), Moscow, Russia*
- <sup>39</sup>*Skobeltsyn Institute of Nuclear Physics of Moscow State University (SINP MSU), Moscow, Russia*
- <sup>40</sup>*Yandex School of Data Analysis, Moscow, Russia*
- <sup>41</sup>*Institute of Physics, University of Belgrade, Serbia*
- <sup>42</sup>*Stockholm University, Stockholm, Sweden*
- <sup>43</sup>*Uppsala University, Uppsala, Sweden*
- <sup>44</sup>*European Organization for Nuclear Research (CERN), Geneva, Switzerland*
- <sup>45</sup>*University of Geneva, Geneva, Switzerland*
- <sup>46</sup>*École Polytechnique Fédérale de Lausanne (EPFL), Lausanne, Switzerland*
- <sup>47</sup>*Physik-Institut, Universität Zürich, Zürich, Switzerland*
- <sup>48</sup>*Middle East Technical University (METU), Ankara, Turkey*
- <sup>49</sup>*Ankara University, Ankara, Turkey*

<sup>50</sup>*H.H. Wills Physics Laboratory, University of Bristol, Bristol, United Kingdom*

<sup>51</sup>*STFC Rutherford Appleton Laboratory, Didcot, United Kingdom*

<sup>52</sup>*Imperial College London, London, United Kingdom*

<sup>53</sup>*University College London, London, United Kingdom*

<sup>54</sup>*University of Warwick, Warwick, United Kingdom*

<sup>55</sup>*Taras Shevchenko National University of Kyiv, Kyiv, Ukraine*

<sup>a</sup>*Università di Bari, Bari, Italy*

<sup>b</sup>*Università di Bologna, Bologna, Italy*

<sup>c</sup>*Università di Cagliari, Cagliari, Italy*

<sup>d</sup>*Università di Napoli “Federico II”, Napoli, Italy*

<sup>e</sup>*Associated to Gyeongsang National University, Jinju, Korea*

<sup>f</sup>*Associated to Petersburg Nuclear Physics Institute (PNPI), Gatchina, Russia*

<sup>g</sup>*Also at Moscow Institute of Physics and Technology (MIPT), Moscow Region, Russia*

<sup>h</sup>*Consorzio CREATE, Napoli, Italy*

<sup>i</sup>*Università della Basilicata, Potenza, Italy*

<sup>j</sup>*Università della Campania “Luigi Vanvitelli”, Caserta, Italy*

<sup>k</sup>*Università del Sannio, Benevento, Italy*

<sup>l</sup>*Università di Napoli Parthenope, Napoli, Italy*

*E-mail:* [m.demagistris@unina.it](mailto:m.demagistris@unina.it), [aquercia@unina.it](mailto:aquercia@unina.it)

**ABSTRACT:** The Search for Hidden Particles (SHiP) experiment proposal at CERN demands a dedicated dipole magnet for its scattering and neutrino detector. This requires a very large volume to be uniformly magnetized at  $B > 1.2$  T, with constraints regarding the inner instrumented volume as well as the external region, where no massive structures are allowed and only an extremely low stray field is admitted. In this paper we report the main technical challenges and the relevant design options providing a comprehensive design for the magnet of the SHiP Scattering and Neutrino Detector.

**KEYWORDS:** Acceleration cavities and magnets superconducting (high-temperature superconductor; radiation hardened magnets; normal-conducting; permanent magnet devices; wigglers and undulators); Large detector systems for particle and astroparticle physics; Neutrino detectors

**ARXIV EPRINT:** [1910.02952](https://arxiv.org/abs/1910.02952)

---

## Contents

<b>1</b>	<b>Introduction</b>	<b>1</b>
<b>2</b>	<b>Experimental requirements</b>	<b>2</b>
<b>3</b>	<b>Magnet design</b>	<b>3</b>
3.1	Analytical formulae	5
3.2	Integrated magnet design	8
3.2.1	Yoke	8
3.2.2	Coil	9
3.2.3	Thermal shield	11
3.3	3-D field maps	13
<b>4</b>	<b>Mechanical issues</b>	<b>16</b>
4.1	Forces and stresses analysis	16
4.1.1	Analytical models	16
4.1.2	3-D analysis	17
4.2	Some functional issues	18
4.2.1	Structural dowels design	18
4.2.2	Opening force and deformations	19
<b>5</b>	<b>Conclusions</b>	<b>20</b>

---

## 1 Introduction

Given the absence of direct experimental evidence for Beyond the Standard Model (BSM) physics at the high-energy frontier and the lack of unambiguous experimental hints for the scale of new physics in precision measurements, it might well be that the shortcomings of the Standard Model (SM) have their origin in new physics involving very weakly interacting, relatively light particles. As a consequence of the extremely feeble couplings and the typically long lifetimes, the low mass scales for hidden particles are far less constrained [1]. In several cases, the present experimental and theoretical constraints from cosmology and astrophysics indicate that a large fraction of the interesting parameter space was beyond the reach of previous searches, but it is open and accessible to current and future facilities. While the mass range up to the kaon mass has been the subject of intensive searches, the bounds on the interaction strength of long-lived particles above this scale are significantly weaker. The recently proposed Search for Hidden Particles (SHiP) beam-dump experiment [2] at the CERN Super Proton Synchrotron (SPS) accelerator is designed to both search for decay signatures by full reconstruction and particle identification of SM final states and to search for scattering signatures of Light Dark Matter by the detection of recoil of atomic electrons or nuclei.

The Beam Dump Facility (BDF) where SHiP operates is well described in ref. [3]: the most upstream BDF part is a proton target followed by a 5 m long hadron absorber. In addition to absorbing the hadrons and the electromagnetic radiation, the iron of the hadron absorber is magnetised over a length of 4 m. Its dipole field makes up the first section of the active muon shield [4] which is optimised to sweep out of acceptance muons of the entire momentum spectrum, up to 350 GeV/c. The remaining part of the muon shield follows immediately downstream of the hadron absorber in the experimental hall and consists of a chain of iron core magnets which extends over a length of about 30 m.

The SHiP experiment incorporates two complementary apparatuses. The detector system immediately downstream of the muon shield is optimised both for recoil signatures of hidden sector particle scattering and for neutrino physics. It is based on a hybrid detector with a concept similar to what was developed by the OPERA Collaboration [5] with alternating layers of nuclear emulsion films with high-density  $\nu$ -target plates and electronic trackers. In addition, the detector is located in a magnetic field for charge sign and momentum measurement of hadronic final states. The detector  $\nu$ -target mass totals about 10 tons. The emulsion spectrometer is followed by a muon identification system. It also acts as a tagger for interactions in its passive layers which may produce long-lived neutral mesons entering the downstream decay volume and whose decay may mimic signal events. The second detector system aims at measuring the visible decays of Hidden Sector particles to both fully reconstructible final states and to partially reconstructible final states with neutrinos. The detector consists of a 50 m long decay volume followed by a large spectrometer with a rectangular acceptance of 5 m in width and 10 m in height [3]. The spectrometer is designed to accurately reconstruct the decay vertex, the mass, and the impact parameter of the hidden particle trajectory at the proton target. A calorimeter and a muon identification system provide particle identification. A dedicated timing detector with  $\sim 100$  ps resolution provides a measure of coincidence in order to reject combinatorial backgrounds. The decay volume is surrounded by background taggers to identify neutrino and muon inelastic scattering in the vacuum vessel walls. The muon shield and the SHiP detector systems are housed in a  $\sim 120$  m long underground experimental hall at a depth of  $\sim 15$  m.

In this paper we report the design and the expected performance of the SND magnet, which contains the hybrid apparatus of the Scattering and Neutrino Detector. The work is organized as follows. In section 2 the experimental requirements at the basis of the overall design constraints are presented. In section 3 the full electromagnetic design is considered, from analytical models to 3-D numerical simulations, defining a viable design option. In section 4 the problem of mechanical forces and stresses are tackled, along with functional issues relevant to the final mechanical structure of the SND magnet. Finally section 5 draws the conclusions.

## 2 Experimental requirements

The design of the SHiP SND magnet follows the need for a significantly large, uniformly magnetized volume, in order to accommodate the  $\nu$ -target and the spectrometer trackers. This results in a magnetized volume of about  $10 \text{ m}^3$  with a magnetic field of at least 1.2 T. The lower bound on the field strength comes from the requirement to measure the charge sign and momentum of hadrons up to 10 GeV/c in a very compact structure, the so-called Compact Emulsion Spectrometer (CES) [6],

made of 3 emulsion films interleaved with air over a total thickness of 3 cm. At the same time, the stray field outside the magnet has to be sufficiently low (at the percent level of the inner value) to avoid disturbing the flux of muons swept out by the muon shield. This sets severe constraints on the shape and size of the magnet. In particular the magnet yoke, beside its fundamental magnetic role (increasing efficiency, homogenizing and straightening up the field) and the mechanical one (contrasting the strong magnetic expanding force acting on the coil), is expected to sufficiently shield the field outside the magnet. Such a requirement strongly affect the magnet design constraints and goals. The detector mass and its operating temperature as well as the accessibility for the detector installation and maintenance provide further challenges for the overall design. In particular, the CES is supposed to be replaced every few weeks in order to limit the total integrated flux of background muons, thus suppressing the combinatorial background in the track matching required for the sagitta measurement. That imply that the magnet has to be designed so that it can be frequently opened, approximately once a fortnight.

The required flux density over such a significant gap size requires a power of about 1 MW. In the past, at CERN, experimental magnets of comparable or even higher power consumption (e.g. LHCb [7–9] is 4.2 MW) were designed resistive to favour a much easier operation. Furthermore, in this specific case, the CES will have to be replaced every few weeks and this will require easy human accessibility, certainly more difficult in presence of helium and of a cryogenic infrastructure. The resistive design reported here would however consume only one fourth of the LHCb magnet, making the drawbacks of a superconducting version, including constructional difficulties, far more remarkable. This is why for the baseline design we adopt a reliable and well-established design with resistive coils. However, the study of a superconducting magnet will also be carried out, as an option to the baseline design. One of the directions we intend to explore is an innovative concept of cryogen free magnet [10] using HTS conductors, or alternatively LTS coils indirectly cooled with a small inventory of liquid helium. This goes beyond the scope of this paper.

The power converter system and more generally any ancillary equipment have to comply with CERN standard specifications. Table 1 reports the main specifications of the magnet.

**Table 1.** Magnet Specifications.

internal volume (detectors + ancillary equipment)		[m <sup>3</sup> ]	$1 \times 1.6 \times 5.4$
overall external size		[m <sup>3</sup> ]	$2.4 \times 4.0 \times 7.2$
internal volume temperature		[°C]	18
reference field (internal volume)	$B$	[T]	$> 1.2$
spatial field homogeneity (internal volume)	$ \Delta B/B $	[%]	$\approx 1$
temporal field stability (internal volume)	$ \Delta B/B $	[ppm]	$< 10^3$
maximum external stray field	$B_{\text{stray max}}$	[mT]	$\leq 10$

### 3 Magnet design

Figure 1a shows the simulated profile of the muon flux distribution in the transverse plane of the region where the SND detector is located. Such distribution sets the fundamental constraint on the transverse shape of the magnet that does not have to intercept the muon flux. From this feature,

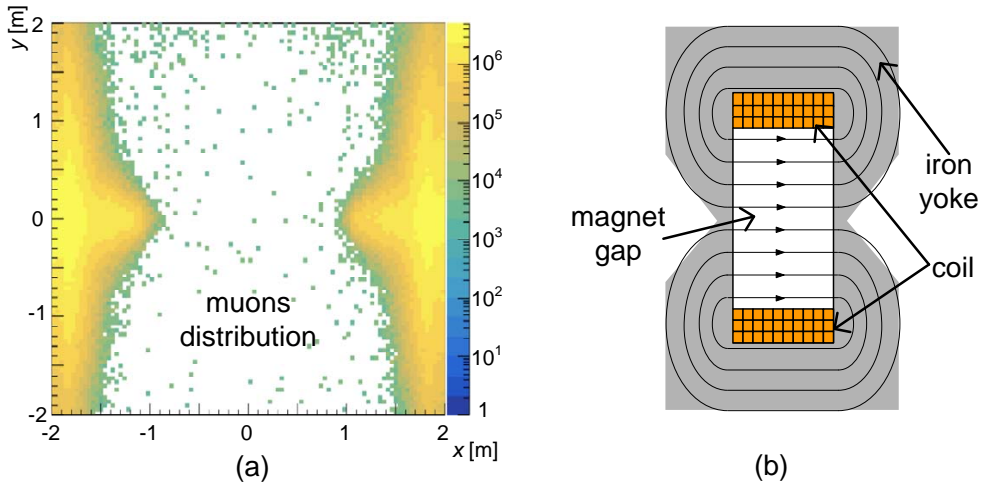


**Figure 1.** (a) Simulated muons flux at the SND magnet position of the beam line. (b) Sketch of the magnet's cross-section.

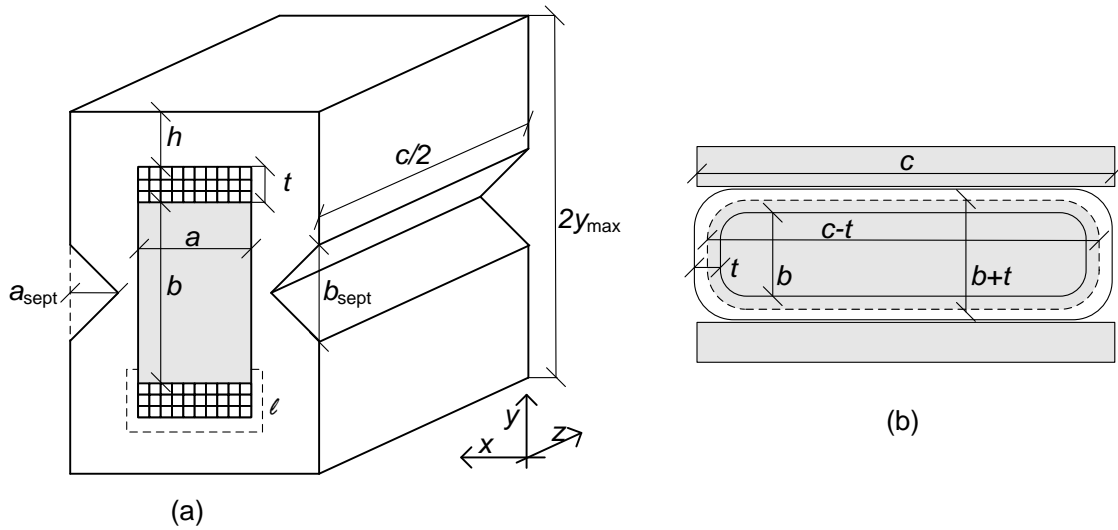


**Figure 2.** (a) Schematic representation of one half of the magnet, showing the cross-section  $z = 0$  and the corresponding geometrical parameters. The point  $x = y = z = 0$  represents the centre of the magnet. The total magnet length along the direction of the beam (the  $z$  direction) is equal to  $c$ . (b) Schematic  $x = 0$  cross-section, showing the areas (gray) considered for the flux balance.

the magnet coil can be developed longitudinally, thus providing a horizontal field and the inner magnetised volume can be taller than wider. A conceptual design of the magnet is shown in figure 1b where the yoke shape is tapered according to the muon flux. Figure 2 shows a sketch of the magnet structure, with the definition of major geometrical parameters.



### 3.1 Analytical formulae

We describe now the procedure to get an approximate analytical magnetic model, providing the basis for sizing the magnet. The results of such analysis are then employed as the starting guess for the detailed analysis that is performed in section 3.2, including the electrical and thermal coil design.

The standard design technique which seeks the optimal current density, leading to total cost minimization [11], cannot be adopted here. In fact, we have a prescription on the maximum possible total magnet height, which is fixed at  $2y_{\max} \cong 4$  m. This is determined by the muons profile, which also sets the maximum tolerable external field  $B_{\text{stray max}}$  (table 1). The following analysis aims at determining design solutions that satisfy the (internal and external) dimensional constraints and the stray field specification, while minimizing the power.

With reference to figure 2 we recognize the following fundamental geometric constraint involving the coil and yoke thickness  $t$  and  $h$

$$\frac{b}{2} + t + h = y_{\max} \quad (3.1)$$

where  $b = 1.6$  m is the total height of the magnetized volume and  $c = 7.2$  m is the magnet longitudinal length.

By neglecting the stray flux, which is a reasonable assumption for a well designed yoke, the flux is balanced when the internal flux  $\phi_{\text{int}}$ , that is the sum of the fluxes corresponding to the gap and to the coil, is equal to the flux into the yoke  $\phi_{\text{Fe}}$ . That is easily done by considering the  $x = 0$  cross-section of the magnet (figure 2b). The flux density in the coil decays approximately linearly, from the value  $B$  at the internal edge to zero at the outer edge. The flux in the coil, per unit length, is hence given by product  $Bt/2$ . One then gets  $\phi_{\text{int}} = (c - t)(b + t)B$ , where the product  $(c - t)(b + t)$  is an average area that takes into account the non uniformity of the flux density in the coil. The flux balance equation  $\phi_{\text{int}} = \phi_{\text{Fe}}$  then reads as

$$(c - t)(b + t)B = 2hcB_{\text{Fe max}}, \quad (3.2)$$

where  $B_{\text{Fe max}}$  is the maximum value of the flux density, attained in the top (and bottom) part of the yoke.

At this point we need to introduce the main figures of merit of the design, that are magnet efficiency, electrical power, magneto-motive force and stray field.

The magnet efficiency is defined as the ratio between the magnetic tension over the gap and the magneto-motive force (MMF), or formally [12, 13]

$$\eta = \frac{aB/\mu_0}{NI} = \frac{\int_{\text{gap}} \mathbf{H} \cdot d\boldsymbol{\ell}}{\int_{\text{gap}} \mathbf{H} \cdot d\boldsymbol{\ell} + \int_{\text{iron}} \mathbf{H} \cdot d\boldsymbol{\ell}} = \frac{1}{1 + \frac{1}{\mu_r(B_{\text{Fe max}})} \frac{B_{\text{Fe max}}}{B} \frac{\ell}{a}} \quad (3.3)$$

from which the following expression for the flux density  $B$  is obtained

$$B = \frac{\eta\mu_0 NI}{a} = \eta\mu_0 f t J, \quad (3.4)$$

being  $N$  the number of coil turns,  $I$  the current per turn and  $J$  the current density,  $f = \frac{S_{\text{active}}}{at}$  the total filling factor,  $S_{\text{active}}$  being the area of the coil cross-section occupied by the conductor,  $\mathbf{H}$  the magnetic field and  $\mu_r$  the nonlinear yoke relative permeability. Finally  $\ell$  is the length of the line depicted in figure 2 corresponding to the region where  $H$  is not negligible with respect to  $H(B_{\text{Fe max}})$ . This, for low carbon steel yoke materials, yields  $\ell \cong a + 2t$ .

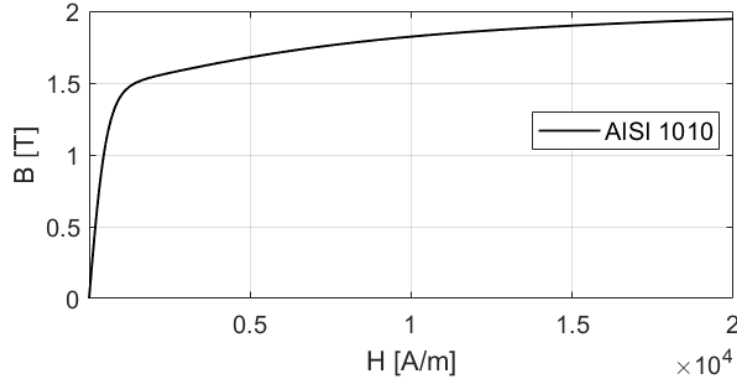


**Figure 3.** Reference AISI 1010  $H$ - $B$  curve.

The above eq. (3.4) allows to express both the MMF  $\mathcal{F}$  and current density  $J$  as a function of the flux density  $B$ . In particular, the former could be represented as

$$\mathcal{F} = NI = \frac{\mathcal{F}_{\min}}{\eta}, \quad \mathcal{F}_{\min} = \frac{aB}{\mu_0} \quad (3.5)$$

where  $\mathcal{F}_{\min}$  is the minimum value needed to get the expected  $B$  ( $\eta = 1$ ). From eq. (3.3) it is easy to realize that efficiency depends on the effective magnet's working condition and, for a well-designed magnet, its values lie in a range  $\eta \approx 0.95$ – $0.98$  [13].

A key point is the estimation of the electrical power  $P$  as a fundamental figure of merit of the electromagnet, which can easily be evaluated as follows. The volumetric power density and the net volume occupied by the electrical conductor are  $\rho J^2$  and  $\Omega = fatl_t$ , respectively, where  $\rho$  is the electrical resistivity of the conductor and  $l_t \approx 2(b+c)$  is the mean turns length. Then, by using eq. (3.4) one gets

$$P = \int_{\Omega} \rho J^2 d\Omega = \frac{\rho}{\eta^2 \mu_0^2} \frac{al_t}{ft} B^2 \approx \frac{2\rho}{\eta^2 \mu_0^2} \frac{a(b+c)}{ft} B^2. \quad (3.6)$$

The maximum stray field value, attained at the surface of the yoke, is estimated by applying the continuity of the tangential component of  $\mathbf{H}$  at the symmetry point  $x = 0$ ,  $y = y_{\max}$ ,  $z = 0$ , which reads as

$$B_{\text{stray max}} = \mu_0 H_{\text{stray max}} = \mu_0 H_{\text{Fe max}} = \frac{B_{\text{Fe max}}}{\mu_r(B_{\text{Fe max}})} = \frac{1-\eta}{\eta} \frac{a}{\ell} B \quad (3.7)$$

where the rightmost equality follows from eq. (3.3).

Having defined the above quantities, the task is now the estimation of iron and corresponding coil thickness such that the geometric and physical constraints specified in table 1, are fulfilled, after a certain choice for the iron material is made. As basic reference we consider a typical AISI 1010  $H$ - $B$  curve, shown in figure 3.

By solving eqs. (3.1)–(3.2) while assuming  $h$  as parameter, one gets  $t = y_{\max} - b/2 - h$ ,  $B_{\text{Fe max}} = (c-t)(b+t)B/(2hc)$ . In turn, eqs. (3.3), (3.5)–(3.7) and the mentioned  $H$ - $B$  curve we get  $\eta$ ,  $NI$ ,  $P$  and  $B_{\text{stray max}}$ . The analysis has been carried out by assuming  $B = 1.25$  T, the geometrical parameters as described above, leading to the plots shown in figure 4.

From the inspection of the curves it is easily realized that the stray field decreases with increasing  $h$ . Conversely, the MMF shows weak variations with  $h$  and tends toward its limit value

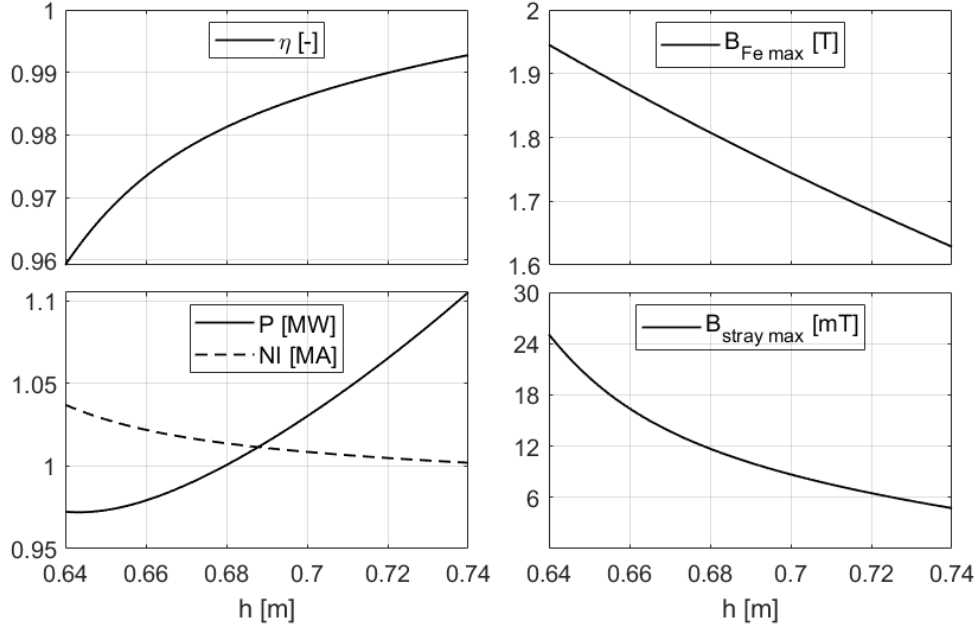


**Figure 4.** Dependence of efficiency, maximum iron flux density, power, total current and maximum stray flux density, as a function of the yoke thickness  $h$ , as predicted by the model (3.1)–(3.3), (3.5)–(3.7).

(about 1 MA, eq. (3.5)). The power is evaluated by assuming the following values for copper resistivity  $\rho = 1.87 \cdot 10^{-8} \Omega\text{m}$  (@  $T = 42.5^\circ\text{C}$ ), and the filling factor,  $f = 0.65$ , which is a reasonable value in the coil design. The corresponding curve shows a minimum for a specific value of the iron thickness, which provides a significant information to be exploited for the design. Minimising the stray field and the power at the same time results as conflicting goals.

Notice that one normally expects a completely different behaviour of the power, namely a reduction of  $P$  when  $NI$  gets reduced. In our case we have  $P \propto 1/(\eta^2 t)$ , which is the product of a decreasing ( $1/\eta^2$ ) and of an increasing ( $1/t$ ) function of  $h$ , respectively. The result is a power function that has a minimum and then increases with  $h$ , instead of decreasing. This is due to the dimensional constraint (3.1), a specific peculiarity of the present design.

Within the considered model the  $B_{\text{stray}} \leq 10 \text{ mT}$  constraint is achieved with  $h = 0.7 \text{ m}$  ( $B_{\text{stray}} = 8.7 \text{ mT}$ ), which yields to  $\eta = 0.986$ ,  $P = 1.03 \text{ MW}$ ,  $\mathcal{F} = 1.01 \text{ MA}$  and  $B_{\text{Fe max}} = 1.74 \text{ T}$ . However, it should be outlined that such quantities are highly sensitive to parameters variations. In particular, from eqs. (3.2), (3.7) the stray field sensitivity to variation of the yoke thickness  $h$  can be expressed as

$$\frac{dB_{\text{stray max}}/B_{\text{stray max}}}{dh/h} = -\frac{c'b' + h^2}{(c' + h)(b' - h)} \frac{\mu_r(B_{\text{Fe max}})}{\mu_{r \text{ diff}}(B_{\text{Fe max}})} \approx -10 \quad (3.8)$$

where  $c' = c + \frac{b}{2} - y_{\text{max}} = 6 \text{ m}$ ,  $b' = \frac{b}{2} + y_{\text{max}} = 2.8 \text{ m}$ ,  $\mu_{r \text{ diff}}$  is the differential relative permeability and  $h \approx 0.7$ . The sensitivity resulting by considering different  $H$ - $B$  curves will be shown in next sections.

Finally it should be outlined that both copper and aluminum [11] were considered as materials for the conductor coil. However, since the limit in the coil size  $t$  given by equation (3.1), the higher electrical resistivity of aluminium and the linear dependence of the power on  $\rho$ , a much

larger dissipated power results from aluminum choice, which is not compatible with current CERN standards. For this reason, all the discussions carried out hereafter will refer to copper coils.

### 3.2 Integrated magnet design

This section describes the magnet design with due detail. It includes yoke, coil and thermal shield detailed design, with the main goal of trying to keep the ohmic power  $P$  as low as possible while taking into account geometrical, electrical and thermal aspects. In particular: i) the yoke design accounting for specific iron magnetic properties; ii) the full electrical and cooling coil design, with constraints from integration of power supply according to CERN standards and iii) the integrated design of the thermal conditioning achieving the required temperature of the detector region. The due verification of the compatibility of such design option with mechanical loads, forces and stresses is treated in the following section 4.

#### 3.2.1 Yoke

As stated in previous section, three geometrical parameters are specified by the design constraints, namely:

- total longitudinal magnet length  $c = 7.20$  m;
- horizontal gap  $a = 1.00$  m
- total height  $2y_{\max} = 4.00$  m

The simplified analytical model shows (figure 4) that the limiting factor is the requirement to keep the stray field outside the magnet within the threshold  $B_{\text{stray}} \leq 10$  mT specified in section 2, yielding a yoke thickness  $h = 0.70$  m.

Moreover, this choice for the yoke thickness provides a good magnet efficiency  $\eta = 0.986$  and a power  $P = 1.03$  MW, which is not far from the unconstrained minimum of  $P = 0.97$  MW. As for the geometrical parameters of the triangular septum  $b_{\text{sept}}$  and  $a_{\text{sept}}$  illustrated in figure 2 they are selected so as to minimize the interaction with the muons, whose distribution is depicted in figure 1a, as triangular septum height  $b_{\text{sept}} = 1.44$  m, and triangular septum width  $a_{\text{sept}} = 0.50$  m.

Some further considerations are due in terms of yoke material properties. Among yoke material types used at CERN there are, ordered by performances (and cost), low carbon steels, such as AISI 1010, special grade low carbon steels of relatively high purity, such as ARMCO<sup>®</sup> grade 4, and cobalt iron. Ref. [14] reports  $H$ - $B$  curves of materials used as magnetic steel as they are obtained from measured samples, in particular different heats of 1010 steel and a special grade one. We consider their upper and lower bounds, that is the curves having the largest and lower  $B$  strengths, which are labelled ARMCO ATLAS and ST 1010 ATLAS in ref. [14]. In the region of interest, corresponding to  $B_{\text{Fe max}} = 1.75$  T, the working point is identified by  $H(B_{\text{Fe max}}) = 6.02$  kA/m and  $H(B_{\text{Fe max}}) = 9.15$  kA/m for the two bounding materials, respectively.

Figure 5 shows the results obtained with the model (3.1)–(3.3), (3.5)–(3.7) and such bounds for iron characteristics. There is a clear evidence of the sensitivity with respect to the material. In particular, the variation of  $P$  and  $B_{\text{stray max}}$  is relevant in the region of interest. From now on we assume the ST1010 ATLAS as material for the yoke, being the most conservative choice. It is clear there is room for improvement by using better materials.

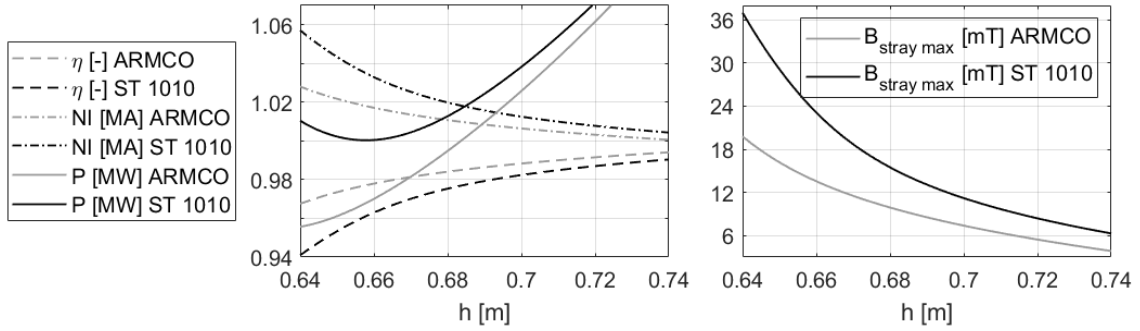


**Figure 5.** Dependence of efficiency, total current, power and maximum stray flux density, as a function of the yoke thickness  $h$ , as predicted by the model (3.1)–(3.3), (3.5)–(3.7), for yoke material curves corresponding to the considered upper and lower bounds, see text.

### 3.2.2 Coil

After the yoke has been determined in its size, shape and material we can afford the detailed design of the coil. It has to comply with the following additional constraints or criteria:

1. *Coil cross-section.* The total height of the magnetized volume  $b = 1.60$  m is specified (table 1). Therefore, the total thickness is  $t = y_{\text{max}} - b/2 - h = 0.5$  m. However, the gross area  $at$  is not fully available to the coil (see figure 6). The coil thickness  $t_{\text{coil}}$  is less than  $t$  to accommodate thermal shield, insulating laminates, mechanical supporting laminate in about 8 cm (figure 6c). Similarly, the coil width  $a_{\text{coil}}$  is less than  $a$ , so as to leave about 4 cm of lateral space for the tie-rods that fix the coil to the iron and for thermal insulation [14].
2. *Winding type.* A continuous double pancake coil configuration is assumed, so that all electrical and water pipe junctions are external to the magnet.
3. *Voltage.* The electric voltage  $V$  at coil terminals should be as close as possible to 100 V so as to exploit synergy for power converters used at CERN.
4. *Current.* The electrical current  $I$  should be less than 14.4 kA (so as to have no more than two standard 8 kA converter modules with a 10 % margin for control).
5. *Cooling water temperature.* The inlet temperature  $T_{\text{in}} = (29 \pm 1)^\circ\text{C}$  is specified by the CERN EN-CV-INJ Department, whereas the outlet temperature  $T_{\text{out}}$  should not exceed  $60^\circ\text{C}$  to avoid damage to the resin.
6. *Cooling water speed.* To avoid erosion, corrosion and impingements, the speed  $w$  should not exceed 3 m/s.
7. *Reynolds number.* To get a moderately turbulent flow, the condition  $2000 < Re < 10^5$  should be satisfied.
8. *Pressure drop.* In the water circuit, the pressure drop  $\Delta p$  should not exceed the limit of 10 bar.

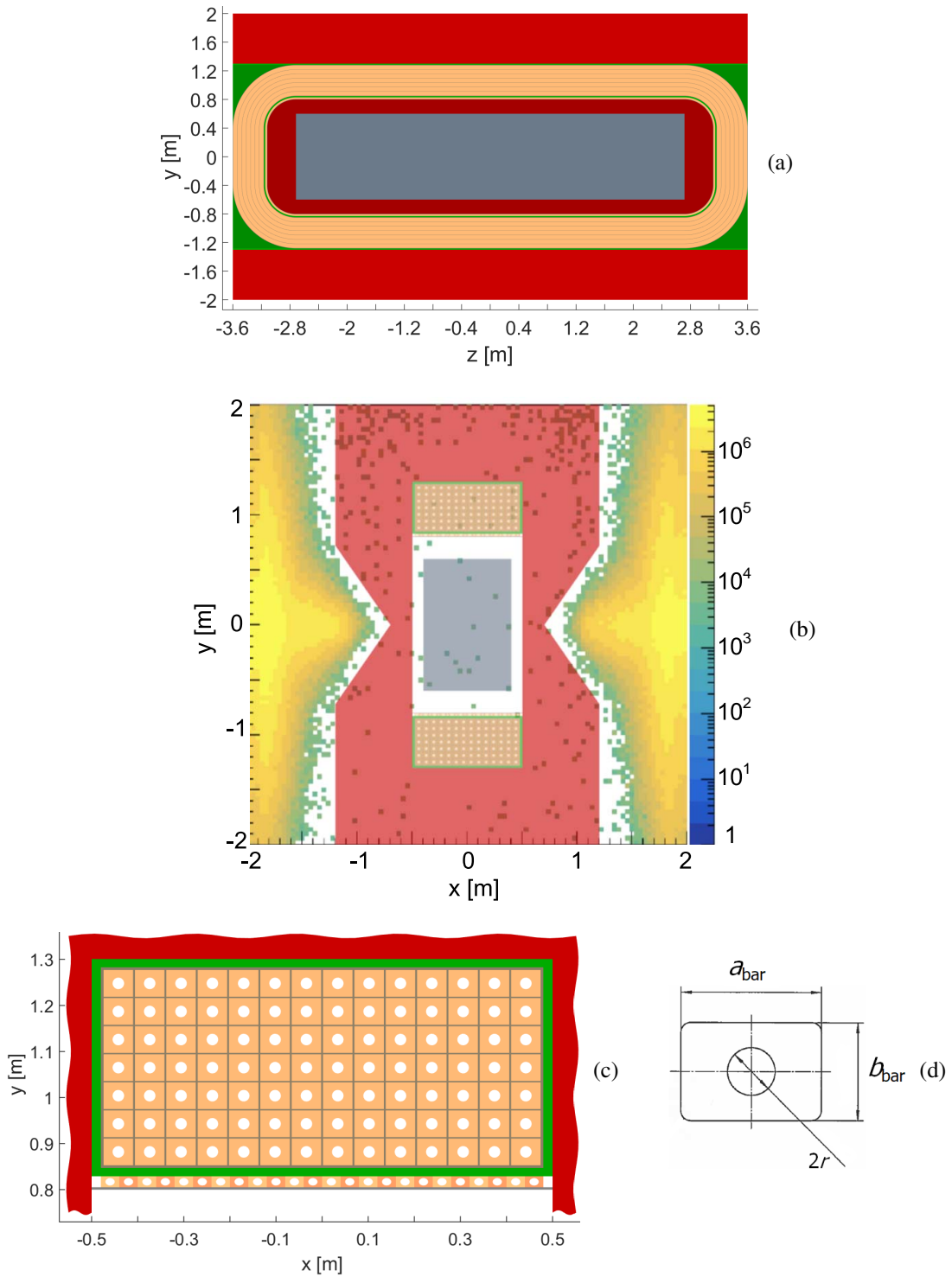


**Figure 6.** Cross-sections of the SND magnet: (a) in the plane  $x = 0$ ; (b) in the plane  $z = 0$ , superimposed to the simulated muons flux distribution in the transverse plane immediately downstream of the last sweeper magnet [15]; (c) cut-out of the upper part in the plane  $z = 0$ ; (d) particular of the hollow bar type used as coil conductor. The gray box in (a–b) represents the instrumented region, where the mean flux density is specified as  $B = 1.25$  T.

The magnetomotive force  $\mathcal{F} = NI$  of about 1 MA has been estimated in section 3.1 since, for the magnetic structure and materials considered, it mainly depends on the desired field  $B$  and the horizontal gap size  $a$ . The effective cross-section of the coils and the value of the magnetomotive force are almost fixed by the above considerations. Therefore, as stated in section 3.1, the aluminum option is discarded in order to minimize the ohmic power  $P$ , which for a copper coil and a realistic filling factor  $f = 0.65$  is about 1 MW. The requirement of a total coil voltage  $V$  of about 100 V leads to a current  $I = P/V$  of about 10 kA, hence to a number of turns  $N = \mathcal{F}/I$  of about 100. The opportunity to have cooling pipes of circular cross-section (hence coil turns of nearly square cross-section) and the ratio between  $a_{\text{coil}}$  and  $t_{\text{coil}}$ , which is about 2, lead to select  $N_a = 14$  pancakes with  $N_b = 7$  turns each. That yields to  $N = N_a N_b = 98 \approx 100$ . It is worth noticing that:

- $N_a = 14$ , an even number, is compatible with the double pancake configuration;
- greater values of the number of turns, e.g.  $N_a = 16$  with  $N_b = 8$ , would make the design of the cooling system more cumbersome and increase  $V$  above 100 V;
- the lower value of the number of turns  $N = 72$ , with  $N_a = 12$  and  $N_b = 6$ , still compatible with the constraint  $I < 14.4$  kA, would unnecessarily reduce the voltage well below 100 V, while increasing the cross-section of the single turns, which might yield problems when bending the conductor.

The next step is to specify the cross-section of the hollow bars, followed by the design of the cooling system. This design started from a first guess of the parameters and it went through a few iterations exploiting the results of more accurate numerical electrical and thermal analyses, as it will be shown in the next section. The selected design configuration is then reported in table 2 in comparison with the LHCb magnet. The 3-D analyses reported in the next section show that all constraints are satisfied. As expected, the value of the ohmic power  $P = 1.02$  MW is not far from the figure provided by the procedure based on lumped parameters. However, it is worth noticing that the ohmic power might further be optimized. Indeed, a significant reduction (about 10%) can be obtained by relaxing the stray field limit to 15 mT, while selecting a different magnetic material and a variable thickness of the yoke (different values of top and side thickness).

Finally in table 3 we compare main design figures calculated with the analytical model of section 3.1 and the accurate numerical model. Such comparison assumes iron ST 1010 ATLAS choice, a mean turns length  $l_t = 16.6$  m and a filling factor  $f = 0.62$  as accurately determined with the numerical model and reported in table 2. A very good agreement can be recognized.

### 3.2.3 Thermal shield

Figure 6c shows that the coil is thermally insulated. The proposed insulator is Vulkollan® or a similar product, which has excellent mechanical properties, including elastic ones, to accommodate the different thermal expansion of the yoke. The inner and outer insulator thickness shown in green is taken as 18 mm, while the side one is 20 mm. The insulation layer plays also the role of reducing the temperature of the yoke, preventing magnetic ageing issues [14].

The additional single-layer copper circuit shown in the lower part of figure 6c, in contact with the inner coil insulation and with a supporting 5 mm thick non-magnetic steel laminate, is a thermal

**Table 2.** Reference design configuration of the detector and comparison with the main parameters of the LHCb magnet.

			SND	LHCb [7–9]
<b>General magnet properties</b>				
total power	$P$	[MW]	1.03	4.2
magnet efficiency	$\eta$	[-]	.981	
internal usable space along $z$	$c_i$	[m]	5.43	
yoke thickness	$h$	[cm]	70	
max top stray field	$B_{\text{stray max}}$	[mT]	10	
max side stray field <sup>†</sup>		[mT]	9	
total iron mass		[t]	356	≈ 1500
<b>Coil</b>				
hollow bar material			Cu	Al-99.7
n. of pancakes	$N_a$	[-]	14	2 · 15
turns per pancake	$N_b$	[-]	7	15
total turns	$N = N_a N_b$	[-]	98	2 · 225
hollow bar width	$a_{\text{bar}}$	[mm]	64	50
hollow bar height	$b_{\text{bar}}$	[mm]	58	50
water hole diameter	$2r$	[mm]	25.5	25
average turns length	$l_t$	[m]	16.6	19.3
total winding length	$l_{\text{tot}}$	[km]	1.6	8.7
total hollow bar mass	$m_{\text{tot}}$	[t]	46	≈ 2 · 25
coil thickness	$t_{\text{coil}}$	[cm]	43.6	
total thickness	$t$	[cm]	50.1	
insulator/holes ratio	$S_i/(N\pi r^2)$	[-]	1.12	
coil fill factor	$f_{\text{coil}} = S_{\text{active}}/(a_{\text{coil}}t_{\text{coil}})$	[-]	.75	
total fill factor	$f = S_{\text{active}}/(at)$	[-]	.62	
<b>Electrical and magnetic properties</b>				
magnetomotive force	$\mathcal{F} = NI$	[MA]	1.014	2 · 1.3
current per turn	$I$	[kA]	10.3	5.85 (6.6 max)
voltage	$V$	[V]	99	730
current density	$J$	[A/mm <sup>2</sup> ]	3.2	2.9
total resistance	$R$	[mΩ]	9.6 @ 42.5 °C	130 @ 20 °C
inductance	$L$	[H]	0.18	1.3
stored magnetic energy	$W_m$	[MJ]	9.7	32
<b>Double pancake configuration and cooling</b>				
continuous bar length	$l_{\text{wc}} = 2N_b l_t$	[m]	233	290 <sup>‡</sup>
parallel water circuits	$N_{\text{wc}} = N_a/2$	[-]	7	
inlet-outlet temperature raise	$\Delta T$	[°C]	25	25
total cooling flow	$q_{\text{tot}}$	[m <sup>3</sup> /h]	35	150
water speed	$w$	[m/s]	2.7	
Reynolds number	$Re/1000$	[-]	98	
pressure drop	$\Delta p$	[bar]	6.8	11

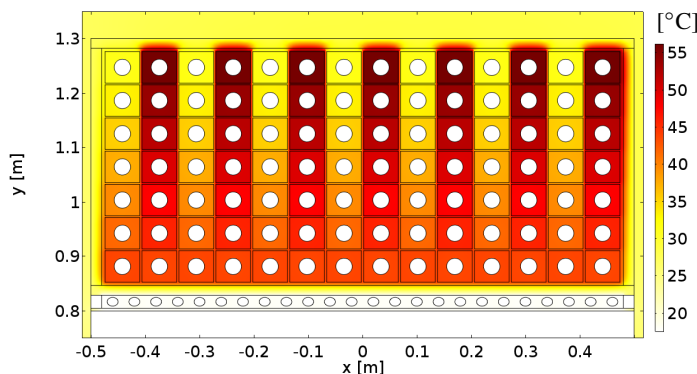
<sup>†</sup> attained at  $x = a/2$ ,  $y = 1.1$  m (see figure 10c).

<sup>‡</sup> the LHCb magnet has a single pancake configuration.



**Table 3.** Comparison of the main design parameters from different modeling approaches.

		Analytical	FEM 3-D
$B$	[T]	1.25	1.25
$NI$	[MA]	1.01	1.014
$B_{\text{Fe}}$	[T]	1.75	1.73
$B_{\text{stray max}}$	[mT]	11	10

**Figure 7.** 2-D thermal numerical simulation for the reference configuration (table 2). The maximum temperature raise,  $\Delta T = 25^\circ\text{C}$ , occurs between the outermost turns of odd and even pancakes. A differential thermal expansion of about 3 mm is calculated along the major magnet length  $c$ .

shield, hence not fed with any electric current, used to insulate the instrumented region, and keeps it at about  $18^\circ\text{C}$ . Such shield is made of copper hollow bars with rectangular cross-section with the following characteristics: two continuous even/odd parallel water circuits, each made of 12 turns and 181 m long, with corresponding inlet water pipes connected at opposite sides ( $x \approx \pm 0.5$  m), to achieve a uniform temperature; total mass 2.3 t; input thermal power (from coil) about 6 kW; inlet/outlet water temperature  $17/19^\circ\text{C}$ ; cross-section area  $40 \times 24 \text{ mm}^2$ ; elliptic cooling hole with major/minor diameter equal to  $20/16 \text{ mm}^2$  and hydraulic diameter  $d_h = 17.7 \text{ mm}$ ; water speed 1.56 m/s; Reynolds number about 38000; pressure drop 3.1 bar. The hydraulic diameter is given by four times the area divided by the perimeter of the (wetted) pipe cross-section. In the case of elliptic cross-section the perimeter can easily be calculated by means of standard special functions [19].

Figure 7 reports the result of a 2-D thermal numerical simulation for the design option of table 2. The double pancake configuration implies that the maximum temperature difference,  $\Delta T = 25^\circ\text{C}$ , is attained between the outermost turns of odd and even pancakes. The consequent differential thermal expansion along the major magnet length,  $c$ , is about 3 mm. The resin encapsulating the coil will have to withstand such differential expansion.

### 3.3 3-D field maps

We report here the results of a detailed 3-D simulation of the electromagnetic problem, after the definition of the reference design as described in previous sections. Sizes and specifications are reported in table 2. In figure 8 the structure of the FEM model is sketched, with core and coil details. The magnetic curve ST 1010 ATLAS fit shown in figure 5 is assumed as reference iron

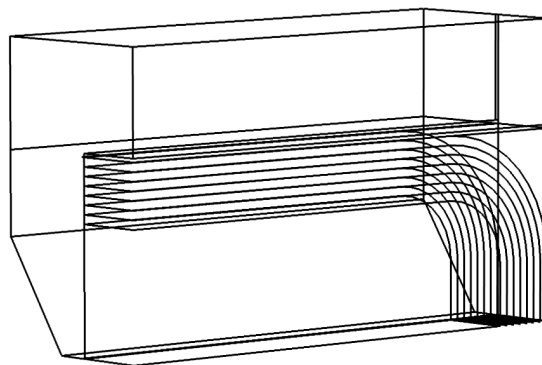


**Figure 8.** The 3-D model of the reference design.

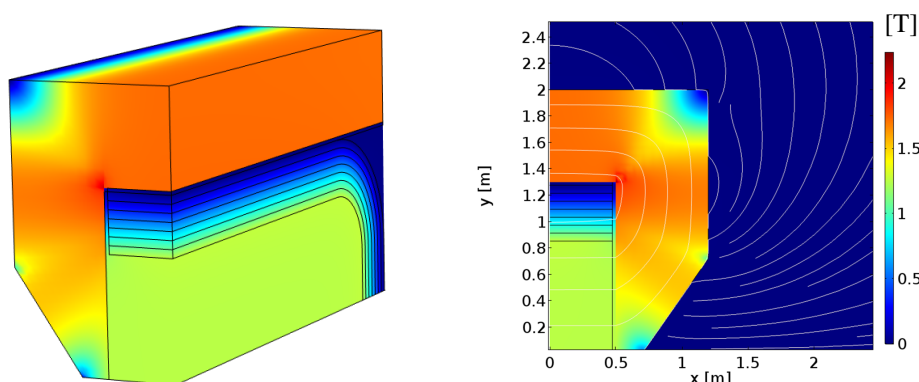


**Figure 9.**  $|B|$  mapping within the magnet and outside: 3-D view (left), 2-D section at  $z = 0$  (right). The point  $(0, 0, 0)$  is the center of the magnet.

model. Due to the symmetry only one eighth of the entire structure is simulated, hereafter named block; on the corresponding cut boundaries the symmetry condition is imposed, as well as the magnetic insulation at the external region boundaries. Such block is meshed with a total of about 239000 nodes, of which about 102000 for the air gap region, 55000 for the iron yoke, 12600 for the coil and the remaining for the external region.

The FEM simulation for the set of used parameters is reported in figure 9, where the modulus of flux density  $B$  is given in a 3-D view and 2-D section, respectively. The complete mapping of the field allows to evaluate the field uniformity within the detector region, and provide some local information at specified section/lines. Figure 10a reports the value of  $B_x$  at the  $z = 0$  section for different horizontal lines. Figures 10(a-b) show that the field uniformity  $|\Delta B/B|$  in the internal region is limited to  $\pm 1\%$ , in agreement with the requirements. Figure 10c shows the external field  $B_{\text{stray}}$  as a function of  $x$  at the  $z = 0$  section for different horizontal lines, starting 1 mm away from the yoke. The line at  $y = 0$  starts at lower  $x$  values because of the septum shape. The limit  $B_{\text{stray max}} < 10 \text{ mT}$  is fully accomplished as expected. Finally, in figure 10d a suggestive picture of the  $\sqrt{B_{\text{stray}x}^2 + B_{\text{stray}y}^2}$  field map is given at a vertical section immediately upstream of the magnet, 2 cm outside. Table 4 reports stray field values at relevant yoke surface locations.

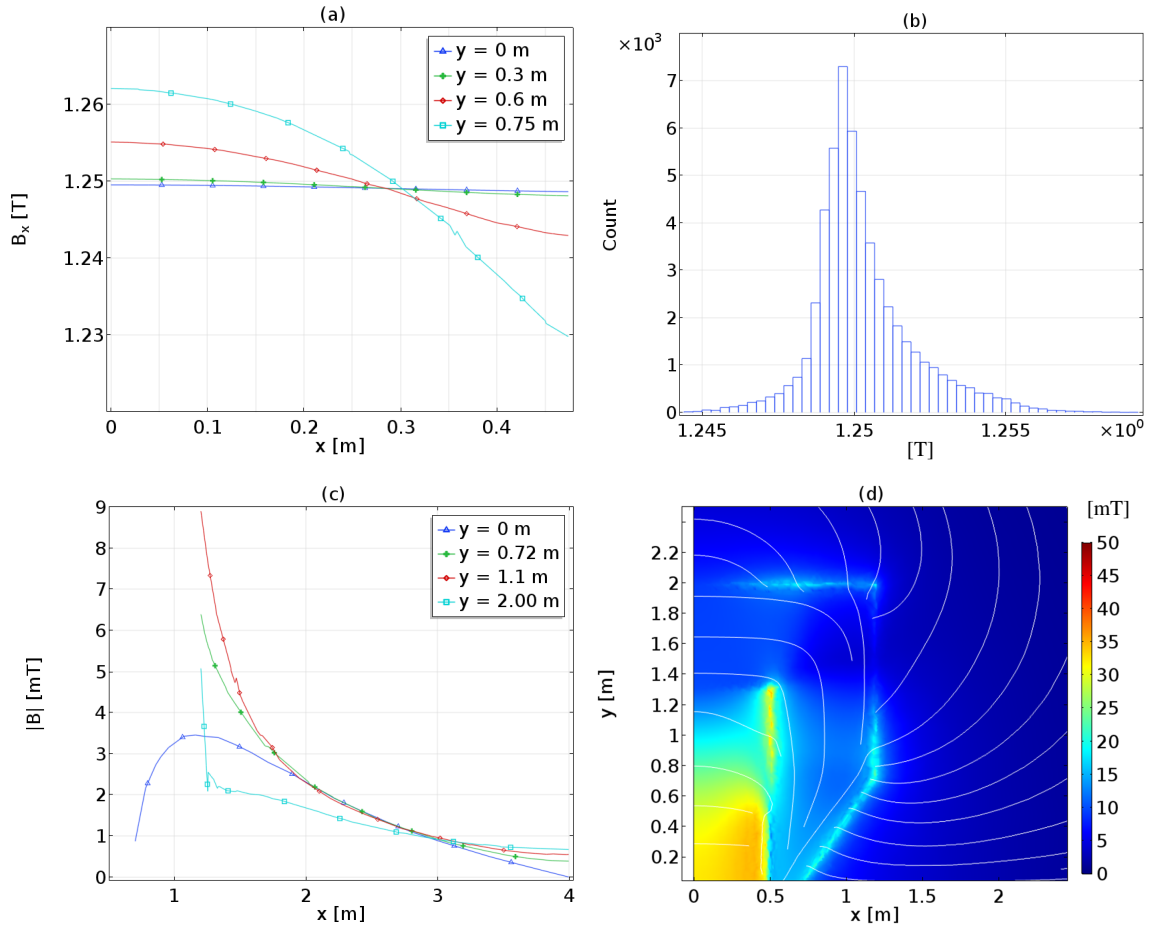


**Figure 10.** (a)  $B_x$  as a function of the horizontal axis  $x$  at the  $z = 0$  section, for different horizontal lines at  $y = 0$ ,  $y = 0.3$ ,  $y = 0.6$ ,  $y = 0.75$  m. (b) Distribution of the  $|B|$  values on the mesh points in the detector region. (c)  $|B_{\text{stray}}|$  as a function of  $x$  at the  $z = 0$  section, for different horizontal lines at  $y = 0$ ,  $y = 0.72$ ,  $y = 1.1$ ,  $y = 2.00$  m. (d) Stray field map  $\sqrt{B_{\text{stray},x}^2 + B_{\text{stray},y}^2}$  at the sections  $z = \pm(c/2 + 2 \text{ cm})$ , namely 2 cm upstream/downstream of the magnet.

**Table 4.** 3-D FEM analysis. Stray field at various  $z = \text{constant}$  cross-sections and relevant yoke surface locations.  $z = 0$  and  $z = 2.7$  m correspond to the center and the end of the detector region (the gray box in figure 6a).

$x$ y yoke surface location	$z$	[m]	0	1.35	2.7
@ top ( $x = 0$ , $y = y_{\text{max}}$ )	$B_{\text{stray max}}$	[mT]	10	10	10
@ side ( $x = a/2$ , $y = 1.10$ m)	$B_{\text{stray}}$	[mT]	9	8	7.5
@ septum ( $x = 1.00$ m, $y = 0.43$ m)	$B_{\text{stray}}$	[mT]	5	5	4.5
@ max muons flux ( $x = 1.80$ m, $y = 0$ )	$B_{\text{stray}}$	[mT]	3	3	3

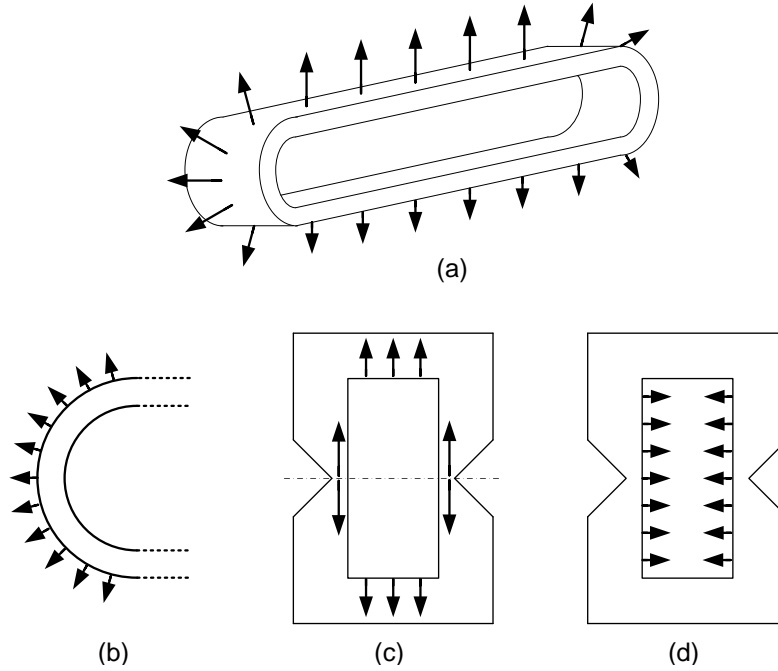


**Figure 11.** a) Magnetic coil self-force. b) Self-force stress at the coil edges. c) Iron stress induced by the coil vertical force. d) Horizontal magnetic force on the iron.

## 4 Mechanical issues

### 4.1 Forces and stresses analysis

In order to complete the design, we have to consider the problem of the magnetic force and the corresponding induced stresses [16], due to Lorentz force on the coil that tend to burst the coil radially outward and crush it axially. In figure 11 a visual representation of such effects is given.

A fair evaluation of the total force can be obtained as that produced by an infinitely thin current sheet carrying the total current. In this way, following Maxwell's stress tensor method [17], the magnetic force can easily be calculated by means of the magnetic pressure at the internal coil boundary as:

$$p_{\text{mag}} = \frac{B^2}{2\mu_0}, \quad (4.1)$$

where  $B$  is the reference induction field within the chamber volume. This expression remains valid for the case of thick conductors, for which it can be thought as the difference at the inner and outer edges of the coil. Equation (4.1) consents to calculate the stress on the coil bent section, as well as the stresses on the straight sections transmitted to the iron, without dealing with the distributed body forces. Also the horizontal force pulling the vertical iron arms inward, and the corresponding induced stress, can be directly estimated by means of the magnetic pressure concept.

#### 4.1.1 Analytical models

The evaluation of the coil stress at the bent edges is done by treating the coil as a thick-walled cylinder supporting the corresponding internal pressure of a gas. Using Lamé equations [18],

which give the stresses for thick-walled cylinders as a function of the radius  $r$ , and neglecting the external air pressure compared to the internal one, the tangential stress  $\sigma_t$  is expressed as:

$$\sigma_t = p_{\text{mag}} \frac{r_i^2}{r_e^2 - r_i^2} \left( 1 + \frac{r_e^2}{r^2} \right) \quad (4.2)$$

where  $r_i = 0.8$  m and  $r_e = 1.3$  m are the inner and outer coil radii, respectively.

The maximum tangential stress, that is the greatest magnitude of direct stress, amounts to 1 MPa, therefore well below the yield strength of the copper of about 50 MPa at 40°C. It has to be remarked that the real profile of the coil edge will slightly differ from the semi-cylindrical one in order to increase the inner volume available for the detectors. Nevertheless, the corresponding stresses are not expected to vary significantly. A more detailed analysis will be presented in section 4.1.2.

To evaluate the vertical force transmitted to the iron by the horizontal sections of the coil, the internal magnetic pressure has to be multiplied by the proper surface. The total resulting force on the upper part of the yoke will be the magnetic one reduced by the weights of the upper horizontal sections of both iron yoke and coil. Such force, equally distributed between the two vertical arms of the yoke, produces a maximum stress of about 1.5 MPa at the minimal iron thickness in the septum, that is well below the yield strength  $\sigma_y = 300$  MPa, which is the typical yield strength for standard iron.

The horizontal force pulling inward the vertical iron arms, and the corresponding induced stress, are also calculated via Maxwell's stress tensor method. In this case the magnetic pressure (4.1) is pulling the vertical inner yoke surface because the magnetic field is nearly perpendicular in the air side. Then the bending moment is evaluated by assuming the vertical iron arm as a simply supported plate under bending where one dimensional model can be used, due to the typical ratio between the longitudinal  $z$  and transversal  $y$  dimension. The bending moment is then calculated with respect to a supported beam subject to the distributed horizontal load given by the magnetic pressure. Using the flexure formula, under the conservative assumption that the beam thickness coincides with the minimal section at the yoke septum, the maximum stress results in about 20 MPa, more than one order of magnitude below  $\sigma_y$ .

#### 4.1.2 3-D analysis

The main mechanical stress on the structures is here analysed with 3-D FEM simulations. Sizes and specifications are reported in table 2.

Coupled magnetic-structural finite element 3-D analysis allows a more detailed assessment of the stresses due to the electromagnetic forces acting on both the coil and the iron yoke. In particular, the analysis returns the forces as distributed body loads overcoming the simplification of the magnetic pressure employed in the preliminary analysis. The coil has been modeled as a "racetrack" neglecting all the insulating layers whereas the iron yoke has been considered as a single piece. Note that, due to the presence of the floor, the bottom horizontal surface of the iron has been considered fixed along  $y$ . Therefore, for the mechanical case, the simulation cannot be restricted to 1/8 of the structure.

Figure 12a shows that the equivalent stress within the coil, evaluated according to the von Mises criterion,  $\sigma_M$ , reaches a maximum value of about 3.4 MPa in relatively small regions of the bent end. Compared to the analytic result, this is roughly a factor of 2 worse since the profile of the coil edge slightly differs from the semi-cylindrical one through a straight vertical section.

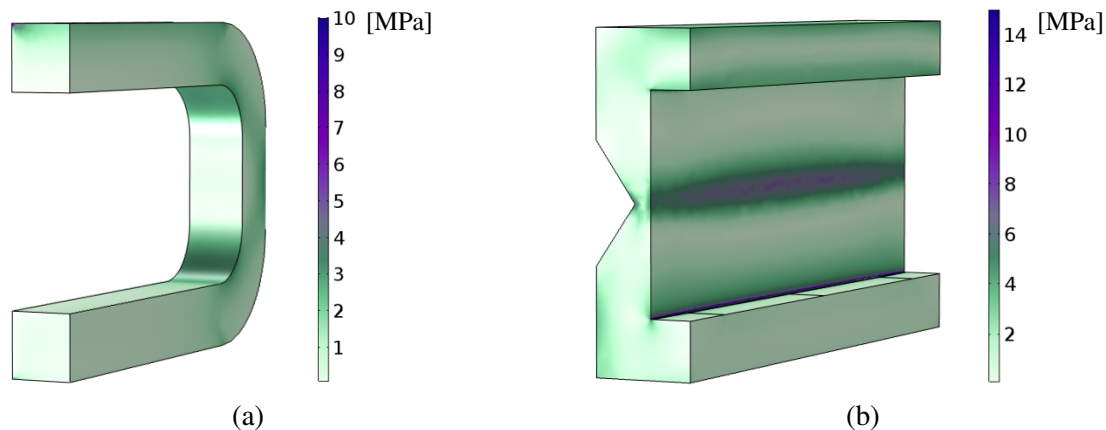


**Figure 12.** The 3-D model of copper (a) and iron (b) stress.

Figure 12b shows that the equivalent stress  $\sigma_M$  within the iron yoke, reaches a value of about 8.3 MPa at the septum corresponding to the minimum iron section. This value is about one third of that previously estimated with the conservative assumption of considering for the whole vertical iron arm the minimum iron thickness of the septum.

## 4.2 Some functional issues

We finally discuss some additional issues that, although not essential in the overall design as described above, are still relevant for more detailed design. It has to be recalled here that, beside the normal operation regime, the inner magnet volume as described in section 2 requires to be accessed for the detector installation and maintenance. Some opening mechanism needs to be defined, allowing reliable, simple and fast operations.

Different schemes can be considered, that are compatible with the presented design. The significant amount of work needed for their detailed exploration and comparison largely exceed the scope of this paper. Nevertheless we would like to show some possible solution here, accomplishing the requirements, giving some insight to the related mechanical issues. Such proposed segmentation and opening scheme is depicted in figure 13, where the iron yoke is split in independent parts, and a side opening is considered for each slab. The side slabs are coupled to the whole structure by means of dowels, and a undercarriage allows the lateral sliding. We consider in the following the problem of sizing the coupling dowels, the opening force due to residual iron magnetization and the possible deformation of the structure when a prescribed number of slabs is removed.

### 4.2.1 Structural dowels design

We tackle here the dimensioning of the dowels connecting the vertical iron arms to the upper and lower horizontal tracts of the yoke. They have to resist to the shear stress induced by the vertical force coming from the coil. The same assumptions (already considered in section 4.1.1) that the magnetic pressure internal to the chamber produces the force bursting the coil allow us to study the vertical force acting on the iron. Assuming that the magnetic pressure is uniform within the chamber, the force acting on the upper horizontal section of the iron yoke is evaluated as the product

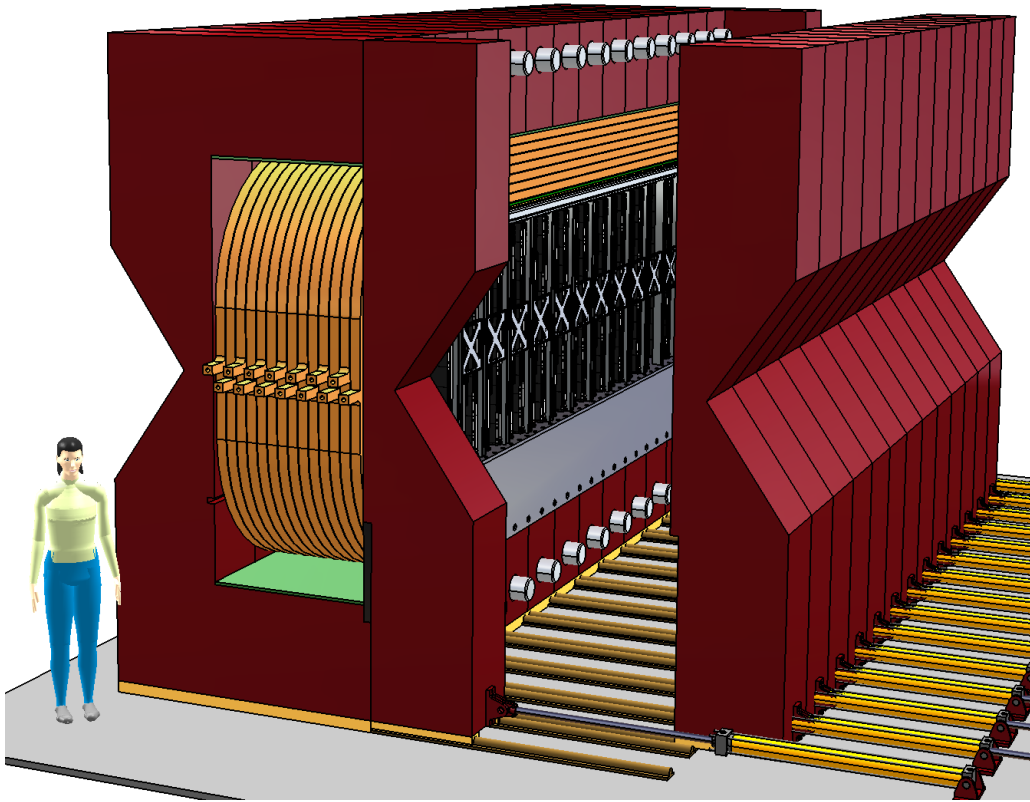


**Figure 13.** Overall structure of the SND magnet, with partial view of the internal detectors.

of pressure and surface. The total force will be the difference between the bursting force just calculated and the weights of the upper horizontal sections of both iron yoke and coil.

In order to find the dowel section able to withstand the vertical force acting on the iron we consider only the upper part of the iron yoke modeling the horizontal section as an isostatic beam. Therefore, the mobile part of the iron yoke has to balance the main force with a total constraint reaction of about 1740 kN. This reaction has to be sustained by dowels of proper cross-section. Assuming for the iron a  $K_t$  (corrected yield strength) of 50 N/mm<sup>2</sup> (“low strength” iron), it is possible to find a total minimum surface of  $35 \cdot 10^3$  mm<sup>2</sup> needed for the whole dowels. For a 15 sections solution with the one dowel (see figure 13), 15 slabs, the diameter of the single dowel can be assumed to be 160 mm (including safety factors).

#### 4.2.2 Opening force and deformations

The force required to open the magnet when the current is turned off (see section 2) can approximately be calculated as follows. Before opening the magnet, a current ramp down is performed, at the end of which the  $B$  field pattern can be assumed to be qualitatively the same as the one corresponding to operation. The condition  $I = 0$  implies  $aH + \ell H_{Fe} = NI = 0$ . Combining this equation with the flux balance equation (3.2), while assuming  $h \approx 0.7$  m,  $t \approx 0.5$  m,  $\ell \approx 3a$ , provides  $B_{Fe} = -\mu_0(c-t)(b+t)/(2hc)(\ell/a)H_{Fe} \approx -4\mu_0 H_{Fe}$ , which is a line in the second quadrant of the plane  $(H_{Fe}, B_{Fe})$ . The worst-case condition is evaluated by assuming  $H_{Fe} \approx H_c \approx 200$  A/m,

where  $H_c$  is the coercive field. That gives  $B_{Fe} \approx 1$  mT, and in turn a force per unit surface  $B_{Fe}^2/(2\mu_0) \approx 0.5$  N/m<sup>2</sup>, which is negligible.

Finally, as for reference, we calculated the worst case deformation of the structure when all the slabs are completely open, except for the two terminal ones, as shown in figure 13. The stress and deformation analyses for the open structure have been carried out with 3-D mechanical simulations, assuming an attachment boundary condition between the upper horizontal surface of the coil and the iron yoke. The maximum displacement for such case, attained at the top center of the structure on the opened face, is limited to about 30  $\mu$ m, and the maximum Von Mises stress to about 6 MPa. Such values are fully compliant with admitted deformation of any involved structure and with the yield strength for both iron and copper.

The above analysis suggests no evident structural problem in the sectioning and opening scheme, at the considered detail level. The actual number of slabs as well as the opening scheme will be better specified and optimised in further design phases, according to specific requirements of the detector structure as well as to mechanical and manufacturing issues.

## 5 Conclusions

A realistic design of the magnet for the SND detector of the SHiP experiment, fully compliant with specifications and constraints has been provided. Different options have been preliminarily considered, defining the normal conducting copper solution as best suited to the problem for different order of reasons, from structural ones to resilience, reliability and maintenance.

Due to limitations in size and shape for the coil and yoke, the design task, basically played between the conflicting goals of high magnetic efficiency and minimal power consumption, revealed the need for some deepening of standard analytical design tools. The design optimization steps have been defined and described in detail, trying to give deep insight in the process.

Such developments have been the guidance for the 3-D FEM analysis, that has assessed the figures of merit and the general quality of the established design option. In particular a detailed design set of design parameters is given, fulfilling all the requirements and constraints.

Finally, beside the fundamental electromagnetic, thermal and mechanical analysis, some basic manufacturing issues related to the required accessibility of the SND along with realistic solutions have been described.

## Acknowledgments

The Authors wish to thank Gilles Le Godec and Serge Deleval for their extensive support concerning standards and best design practice, with reference to power converters and cooling, respectively. The Authors are grateful to Attilio Milanese, Rosario Principe, Vittorio Parma, Pierre-Ange Giudici, Vitalii Zhiltsov, Jakub Kurdej, Isabel Bejar Alonso and Marco Buzio for fruitful discussion and useful suggestions. This work is supported by a Marie Skłodowska-Curie Innovative Training Network Fellowship of the European Commissions Horizon 2020 Programme under contract number 765710 INSIGHTS.



## References

- [1] S. Alekhin et al., *A facility to Search for Hidden Particles at the CERN SPS: the SHiP physics case*, *Rept. Prog. Phys.* **79** (2016) 124201 [[arXiv:1504.04855](#)].
- [2] SHiP collaboration, *A facility to Search for Hidden Particles (SHiP) at the CERN SPS*, [arXiv:1504.04956](#).
- [3] SHiP collaboration, *The experimental facility for the Search for Hidden Particles at the CERN SPS*, 2019 *JINST* **14** P03025 [[arXiv:1810.06880](#)].
- [4] SHiP collaboration, *The active muon shield in the SHiP experiment*, 2017 *JINST* **12** P05011 [[arXiv:1703.03612](#)].
- [5] R. Acquafredda et al., *The OPERA experiment in the CERN to Gran Sasso neutrino beam*, 2009 *JINST* **4** P04018.
- [6] C. Fukushima et al., *A thin emulsion spectrometer using a compact permanent magnet*, *Nucl. Instrum. Meth. A* **592** (2008) 56.
- [7] J. André et al., *Status of the LHCb magnet system*, *IEEE Trans. Appl. Supercond.* **12** (2002) 366.
- [8] J. André, et al, *Status of the LHCb dipole magnet*, *IEEE Trans. Appl. Supercond.* **14** (2004) 509.
- [9] M. Losasso et al., *Tests and Field Map of LHCb Dipole Magnet*, *IEEE Trans. Appl. Supercond.* **16** (2006) 1700.
- [10] D. Tommasini, private communication.
- [11] M.A. Green, *Use of Aluminum Coils Instead of Copper Coils in Accelerator Magnet Systems*, *IEEE Trans. Nucl. Sci.* **14** (1967) 398.
- [12] J.T. Tanabe, *Iron Dominated Electromagnets: Design, Fabrication, Assembly And Measurements*, World Scientific (2005).
- [13] D. Tommasini, *Practical Definitions and Formulae for Normal conducting Magnets*, *CERN Internal Note 2011-18* (2011).
- [14] S. Sgobba, *Physics and measurements of magnetic materials*, in *Proceedings, 2009 CAS-CERN Accelerator School: Specialised course on Magnets*, Bruges, Belgium, 16–25 June 2009 (2011) [[arXiv:1103.1069](#)].
- [15] SHiP collaboration, *SHiP Experiment — Progress Report*, *CERN-SPSC-2019-010*, *SPSC-SR-248* (2019).
- [16] D.B. Montgomery, *Solenoid magnet design: the magnetic and mechanical aspects of resistive and superconducting systems*, Wiley (1969).
- [17] J.A. Stratton, *Electromagnetic Theory*, McGraw-Hill Book Company, Inc. (1941).
- [18] S. Timoshenko, *Strength of Materials*, Part II, Art. 70, D. Van Nostrand, Princeton, N.J. (1956).
- [19] F.W.J. Olver, D.W. Lozier, R.F. Boisvert and C.W. Clark, *NIST Handbook of Mathematical Functions*, National Institute of Standards and Technology and Cambridge University Press (2010) [<https://dlmf.nist.gov/>].

OPEN ACCESS

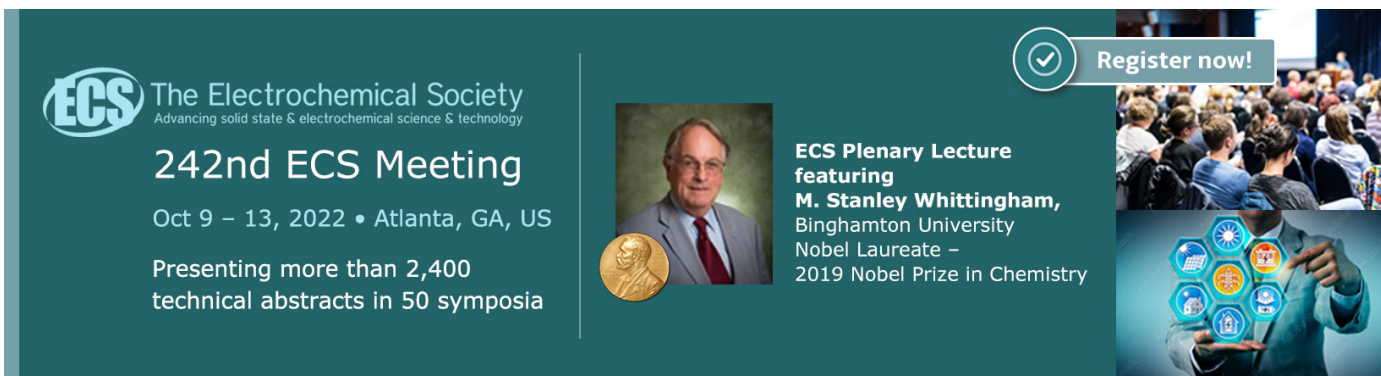
# Fast simulation of muons produced at the SHiP experiment using Generative Adversarial Networks

To cite this article: C. Ahdida *et al* 2019 *JINST* **14** P11028

View the [article online](#) for updates and enhancements.

## You may also like

- [Pileup mitigation at CMS in 13 TeV data](#)  
A.M. Sirunyan, A. Tumasyan, W. Adam et al.
- [ATLAS data quality operations and performance for 2015–2018 data-taking](#)  
G. Aad, B. Abbott, D.C. Abbott et al.
- [Performance of the reconstruction and identification of high-momentum muons in proton-proton collisions at  \$s = 13\$  TeV](#)  
A.M. Sirunyan, A. Tumasyan, W. Adam et al.



**ECS** The Electrochemical Society  
Advancing solid state & electrochemical science & technology


## 242nd ECS Meeting

Oct 9 – 13, 2022 • Atlanta, GA, US

Presenting more than 2,400 technical abstracts in 50 symposia

 **ECS Plenary Lecture featuring M. Stanley Whittingham,** Binghamton University Nobel Laureate – 2019 Nobel Prize in Chemistry

 Register now!



# Fast simulation of muons produced at the SHiP experiment using Generative Adversarial Networks



## The SHiP collaboration

C. Ahdida,<sup>44</sup> R. Albanese,<sup>14,d,h</sup> A. Alexandrov,<sup>14</sup> A. Anokhina,<sup>39</sup> S. Aoki,<sup>18</sup> G. Arduini,<sup>44</sup>  
 E. Atkin,<sup>38</sup> N. Azorskiy,<sup>29</sup> J.J. Back,<sup>54</sup> A. Bagulya,<sup>32</sup> F. Baaltasar Dos Santos,<sup>44</sup> A. Baranov,<sup>40</sup>  
 F. Bardou,<sup>44</sup> G.J. Barker,<sup>54</sup> M. Battistin,<sup>44</sup> J. Bauche,<sup>44</sup> A. Bay,<sup>46</sup> V. Bayliss,<sup>51</sup>  
 G. Bencivenni,<sup>15</sup> A.Y. Berdnikov,<sup>37</sup> Y.A. Berdnikov,<sup>37</sup> I. Berezkina,<sup>32</sup> M. Bertani,<sup>15</sup>  
 C. Betancourt,<sup>47</sup> I. Bezshyiko,<sup>47</sup> O. Bezshyyko,<sup>55</sup> D. Bick,<sup>8</sup> S. Bieschke,<sup>8</sup> A. Blanco,<sup>28</sup>  
 J. Boehm,<sup>51</sup> M. Bogomilov,<sup>1</sup> K. Bondarenko,<sup>27,55</sup> W.M. Bonivento,<sup>13</sup> J. Borburgh,<sup>44</sup>  
 A. Boyarsky,<sup>27,55</sup> R. Brenner,<sup>43</sup> D. Breton,<sup>4</sup> R. Brundler,<sup>47</sup> M. Bruschi,<sup>12</sup> V. Büscher,<sup>10</sup>  
 A. Buonauro,<sup>47</sup> S. Buontempo,<sup>14</sup> S. Cadeddu,<sup>13</sup> A. Calcaterra,<sup>15</sup> M. Calviani,<sup>44</sup>  
 M. Campanelli,<sup>53</sup> M. Casolino,<sup>44</sup> N. Charitonidis,<sup>44</sup> P. Chau,<sup>10</sup> J. Chauveau,<sup>5</sup> A. Chepurinov,<sup>39</sup>  
 M. Chernyavskiy,<sup>32</sup> K.-Y. Choi,<sup>26</sup> A. Chumakov,<sup>2</sup> P. Ciambone,<sup>15</sup> L. Congedo,<sup>11,a</sup>  
 K. Cornelis,<sup>44</sup> M. Cristinziani,<sup>7</sup> A. Crupano,<sup>14,d</sup> G.M. Dallavalle,<sup>12</sup> A. Datwyler,<sup>47</sup>  
 N. D'Ambrosio,<sup>16</sup> G. D'Appollonio,<sup>13,c</sup> J. De Carvalho Saraiva,<sup>28</sup> G. De Lellis,<sup>14,34,44,d</sup>  
 M. de Magistris,<sup>14,d</sup> A. De Roeck,<sup>44</sup> M. De Serio,<sup>11,a</sup> D. De Simone,<sup>14,d</sup> L. Dedenko,<sup>39</sup>  
 P. Dergachev,<sup>34</sup> A. Di Crescenzo,<sup>14,d</sup> N. Di Marco,<sup>16</sup> C. Dib,<sup>2</sup> H. Dijkstra,<sup>44</sup> P. Dipinto,<sup>11,a</sup>  
 V. Dmitrenko,<sup>38</sup> S. Dmitrievskiy,<sup>29</sup> L.A. Dougherty,<sup>44</sup> A. Dolmatov,<sup>30</sup> D. Domenici,<sup>15</sup>  
 S. Donskov,<sup>35</sup> V. Drohan,<sup>55</sup> A. Dubreuil,<sup>45</sup> M. Ehlert,<sup>6</sup> T. Enik,<sup>29</sup> A. Etenko,<sup>33,38</sup> F. Fabbri,<sup>12</sup>  
 L. Fabbri,<sup>12,b</sup> A. Fabich,<sup>44</sup> O. Fedin,<sup>36</sup> F. Fedotovs,<sup>52</sup> G. Felici,<sup>15</sup> M. Ferro-Luzzi,<sup>44</sup>  
 K. Filippov,<sup>38</sup> R.A. Fini,<sup>11</sup> P. Fonte,<sup>28</sup> C. Franco,<sup>28</sup> M. Fraser,<sup>44</sup> R. Fresa,<sup>14,i</sup> R. Froeschl,<sup>44</sup>  
 T. Fukuda,<sup>19</sup> G. Galati,<sup>14,d</sup> J. Gall,<sup>44</sup> L. Gagnon,<sup>44</sup> G. Gavrilo, <sup>38</sup> V. Gentile,<sup>14,d</sup> S. Gerlach,<sup>6</sup>  
 B. Goddard,<sup>44</sup> L. Golinka-Bezshyyko,<sup>55</sup> A. Golovatiuk,<sup>14,d</sup> D. Golubkov,<sup>30</sup> A. Golutvin,<sup>52</sup>  
 P. Gorbounov,<sup>44</sup> D. Gorbunov,<sup>31</sup> S. Gorbunov,<sup>32</sup> V. Gorkavenko,<sup>55</sup> Y. Gornushkin,<sup>29</sup>  
 M. Gorshenkov,<sup>34</sup> V. Grachev,<sup>38</sup> A.L. Grandchamp,<sup>46</sup> G. Granich,<sup>32</sup> E. Graverini,<sup>46</sup>  
 J.-L. Grenard,<sup>44</sup> D. Grenier,<sup>44</sup> V. Grichine,<sup>32</sup> N. Gruzinskii,<sup>36</sup> A. M. Guler,<sup>48</sup> Yu. Guz,<sup>35</sup>  
 G.J. Haefeli,<sup>46</sup> C. Hagner,<sup>8</sup> H. Hakobyan,<sup>2</sup> I.W. Harris,<sup>46</sup> E. van Herwijnen,<sup>44</sup> C. Hessler,<sup>44</sup>  
 A. Hollnagel,<sup>10</sup> B. Hosseini,<sup>52</sup> M. Hushchyn,<sup>40</sup> G. Iaselli,<sup>11,a</sup> A. Iuliano,<sup>14,d</sup> V. Ivantchenko,<sup>32</sup>

R. Jacobsson,<sup>44</sup> D. Joković,<sup>41</sup> M. Jonker,<sup>44</sup> I. Kadenko,<sup>55</sup> V. Kain,<sup>44</sup> B. Kaiser,<sup>8</sup>  
 C. Kamiscioglu,<sup>49</sup> K. Kershaw,<sup>44</sup> M. Khabibullin,<sup>31</sup> E. Khalikov,<sup>39</sup> G. Khaustov,<sup>35</sup>  
 G. Khoraiuli,<sup>10</sup> A. Khotyantsev,<sup>31</sup> S.H. Kim,<sup>22</sup> Y.G. Kim,<sup>23</sup> V. Kim,<sup>36,37</sup> N. Kitagawa,<sup>19</sup>  
 J.-W. Ko,<sup>22</sup> K. Kodama,<sup>17</sup> A. Kolesnikov,<sup>29</sup> D.I. Kolev,<sup>1</sup> V. Kolosov,<sup>35</sup> M. Komatsu,<sup>19</sup>  
 N. Kondrateva,<sup>32</sup> A. Kono,<sup>21</sup> N. Konovalova,<sup>32,34</sup> S. Kormannshaus,<sup>10</sup> I. Korol,<sup>6</sup> I. Korol'ko,<sup>30</sup>  
 A. Korzenev,<sup>45</sup> V. Kostyukhin,<sup>7</sup> E. Koukovini Platia,<sup>44</sup> S. Kovalenko,<sup>2</sup> I. Krasilnikova,<sup>34</sup>  
 Y. Kudenko,<sup>31,38,g</sup> E. Kurbatov,<sup>40</sup> P. Kurbatov,<sup>34</sup> V. Kurochka,<sup>31</sup> E. Kuznetsova,<sup>36</sup>  
 H.M. Lacker,<sup>6</sup> M. Lamont,<sup>44</sup> G. Lanfranchi,<sup>15</sup> O. Lantwin,<sup>52</sup> A. Lauria,<sup>14,d</sup> K.S. Lee,<sup>25</sup>  
 K.Y. Lee,<sup>22</sup> J.-M. Lévy,<sup>5</sup> V.P. Loschiavo,<sup>14,h</sup> L. Lopes,<sup>28</sup> E. Lopez Sola,<sup>44</sup> V. Lyubovitskij,<sup>2</sup>  
 J. Maalmi,<sup>4</sup> A. Magnan,<sup>52</sup> V. Maleev,<sup>36</sup> A. Malinin,<sup>33</sup> Y. Manabe,<sup>19</sup> A.K. Managadze,<sup>39</sup>  
 M. Manfredi,<sup>44</sup> S. Marsh,<sup>44</sup> A.M. Marshall,<sup>50</sup> A. Mefodev,<sup>31</sup> P. Mermod,<sup>45</sup> A. Miano,<sup>14,d</sup>  
 S. Mikado,<sup>20</sup> Yu. Mikhaylov,<sup>35</sup> D.A. Milstead,<sup>42</sup> O. Mineev,<sup>31</sup> A. Montanari,<sup>12</sup> M.C. Montesi,<sup>14,d</sup>  
 K. Morishima,<sup>19</sup> S. Movchan,<sup>29</sup> Y. Muttoni,<sup>44</sup> N. Naganawa,<sup>19</sup> M. Nakamura,<sup>19</sup> T. Nakano,<sup>19</sup>  
 S. Nasybulin,<sup>36</sup> P. Ninin,<sup>44</sup> A. Nishio,<sup>19</sup> A. Novikov,<sup>38</sup> B. Obinyakov,<sup>33</sup> S. Ogawa,<sup>21</sup>  
 N. Okateva,<sup>32,34</sup> B. Opitz,<sup>8</sup> J. Osborne,<sup>44</sup> M. Ovchynnikov,<sup>27,55</sup> N. Owtscharenko,<sup>7</sup>  
 P.H. Owen,<sup>47</sup> P. Pacholek,<sup>44</sup> A. Paoloni,<sup>15</sup> B.D. Park,<sup>22</sup> S.K. Park,<sup>25</sup> A. Pastore,<sup>11</sup> M. Patel,<sup>52</sup>  
 D. Pereyma,<sup>30</sup> A. Perillo-Marccone,<sup>44</sup> G.L. Petkov,<sup>1</sup> K. Petridis,<sup>50</sup> A. Petrov,<sup>33</sup> D. Podgrudkov,<sup>39</sup>  
 V. Poliakov,<sup>35</sup> N. Polukhina,<sup>32,34,38</sup> J. Prieto Prieto,<sup>44</sup> M. Prokudin,<sup>30</sup> A. Prota,<sup>14,d</sup>  
 A. Quercia,<sup>14,d</sup> A. Rademakers,<sup>44</sup> A. Rakai,<sup>44</sup> F. Ratnikov,<sup>40</sup> T. Rawlings,<sup>51</sup> F. Redi,<sup>46</sup>  
 S. Ricciardi,<sup>51</sup> M. Rinaldesi,<sup>44</sup> Volodymyr Rodin,<sup>55</sup> Viktor Rodin,<sup>55</sup> P. Robbe,<sup>4</sup>  
 A.B. Rodrigues Cavalcante,<sup>46</sup> T. Roganova,<sup>39</sup> H. Rokujo,<sup>19</sup> G. Rosa,<sup>14,d</sup> T. Rovelli,<sup>12,b</sup>  
 O. Ruchayskiy,<sup>3</sup> T. Ruf,<sup>44</sup> V. Samoylenko,<sup>35</sup> V. Samsonov,<sup>38</sup> F. Sanchez Galan,<sup>44</sup>  
 P. Santos Diaz,<sup>44</sup> A. Sanz Ull,<sup>44</sup> A. Saputi,<sup>15</sup> O. Sato,<sup>19</sup> E.S. Savchenko,<sup>34</sup> J.S. Schliwinski,<sup>6</sup>  
 W. Schmidt-Parzefall,<sup>8</sup> N. Serra,<sup>47</sup> S. Sgobba,<sup>44</sup> O. Shadura,<sup>55</sup> A. Shakin,<sup>34</sup>  
 M. Shaposhnikov,<sup>46</sup> P. Shatalov,<sup>30</sup> T. Shchedrina,<sup>32,34</sup> L. Shchutska,<sup>46</sup> V. Shevchenko,<sup>33</sup>  
 H. Shibuya,<sup>21</sup> L. Shihora,<sup>6</sup> S. Shirobokov,<sup>52</sup> A. Shustov,<sup>38</sup> S.B. Silverstein,<sup>42</sup> S. Simone,<sup>11,a</sup>  
 R. Simoniello,<sup>10</sup> M. Skorokhvatov,<sup>38,33</sup> S. Smirnov,<sup>38</sup> J.Y. Sohn,<sup>22</sup> A. Sokolenko,<sup>55</sup>  
 E. Solodko,<sup>44</sup> N. Starkov,<sup>32,33</sup> L. Stoel,<sup>44</sup> B. Storaci,<sup>47</sup> M.E. Stramaglia,<sup>46</sup> D. Sukhonos,<sup>44</sup>  
 Y. Suzuki,<sup>19</sup> S. Takahashi,<sup>18</sup> J.L. Tastet,<sup>3</sup> P. Teterin,<sup>38</sup> S. Than Naing,<sup>32</sup> I. Timiryasov,<sup>46</sup>  
 V. Tioukov,<sup>14</sup> D. Tommasini,<sup>44</sup> M. Torii,<sup>19</sup> N. Tosi,<sup>12</sup> D. Treille,<sup>44</sup> R. Tsenov,<sup>1,29</sup> S. Ulin,<sup>38</sup>  
 A. Ustyuzhanin,<sup>40</sup> Z. Uteshev,<sup>38</sup> G. Vankova-Kirilova,<sup>1</sup> F. Vannucci,<sup>5</sup> P. Venkova,<sup>6</sup> V. Venturi,<sup>44</sup>  
 S. Vilchinski,<sup>55</sup> M. Villa,<sup>12,b</sup> Heinz Vincke,<sup>44</sup> Helmut Vincke,<sup>44</sup> C. Visone,<sup>14,d</sup> K. Vlasik,<sup>38</sup>  
 A. Volkov,<sup>32,33</sup> R. Voronkov,<sup>32</sup> S. van Waasen,<sup>9</sup> R. Wanke,<sup>10</sup> P. Wertelaers,<sup>44</sup> J.-K. Woo,<sup>24</sup>  
 M. Wurm,<sup>10</sup> S. Xella,<sup>3</sup> D. Yilmaz,<sup>49</sup> A.U. Yilmazer,<sup>49</sup> C.S. Yoon,<sup>22</sup> P. Zarubin,<sup>29</sup> I. Zarubina<sup>29</sup>  
 and Yu. Zaytsev<sup>30</sup>

<sup>1</sup>Faculty of Physics, Sofia University, Sofia, Bulgaria

<sup>2</sup>Universidad Técnica Federico Santa María and Centro Científico Tecnológico de Valparaíso, Valparaíso, Chile

<sup>3</sup>Niels Bohr Institute, University of Copenhagen, Copenhagen, Denmark

<sup>4</sup>LAL, Univ. Paris-Sud, CNRS/IN2P3, Université Paris-Saclay, Orsay, France

<sup>5</sup>LPNHE, IN2P3/CNRS, Sorbonne Université, Université Paris Diderot, F-75252 Paris, France

<sup>6</sup>Humboldt-Universität zu Berlin, Berlin, Germany

<sup>7</sup>Physikalisches Institut, Universität Bonn, Bonn, Germany

- <sup>8</sup>*Universität Hamburg, Hamburg, Germany*
- <sup>9</sup>*Forschungszentrum Jülich GmbH (KFA), Jülich, Germany*
- <sup>10</sup>*Institut für Physik and PRISMA Cluster of Excellence, Johannes Gutenberg Universität Mainz, Mainz, Germany*
- <sup>11</sup>*Sezione INFN di Bari, Bari, Italy*
- <sup>12</sup>*Sezione INFN di Bologna, Bologna, Italy*
- <sup>13</sup>*Sezione INFN di Cagliari, Cagliari, Italy*
- <sup>14</sup>*Sezione INFN di Napoli, Napoli, Italy*
- <sup>15</sup>*Laboratori Nazionali dell'INFN di Frascati, Frascati, Italy*
- <sup>16</sup>*Laboratori Nazionali dell'INFN di Gran Sasso, L'Aquila, Italy*
- <sup>17</sup>*Aichi University of Education, Kariya, Japan*
- <sup>18</sup>*Kobe University, Kobe, Japan*
- <sup>19</sup>*Nagoya University, Nagoya, Japan*
- <sup>20</sup>*College of Industrial Technology, Nihon University, Narashino, Japan*
- <sup>21</sup>*Toho University, Funabashi, Chiba, Japan*
- <sup>22</sup>*Physics Education Department & RINS, Gyeongsang National University, Jinju, Korea*
- <sup>23</sup>*Gwangju National University of Education,<sup>e</sup> Gwangju, Korea*
- <sup>24</sup>*Jeju National University,<sup>e</sup> Jeju, Korea*
- <sup>25</sup>*Korea University, Seoul, Korea*
- <sup>26</sup>*Sungkyunkwan University,<sup>e</sup> Suwon-si, Gyeong Gi-do, Korea*
- <sup>27</sup>*University of Leiden, Leiden, The Netherlands*
- <sup>28</sup>*LIP, Laboratory of Instrumentation and Experimental Particle Physics, Portugal*
- <sup>29</sup>*Joint Institute for Nuclear Research (JINR), Dubna, Russia*
- <sup>30</sup>*Institute of Theoretical and Experimental Physics (ITEP) NRC 'Kurchatov Institute', Moscow, Russia*
- <sup>31</sup>*Institute for Nuclear Research of the Russian Academy of Sciences (INR RAS), Moscow, Russia*
- <sup>32</sup>*P.N. Lebedev Physical Institute (LPI), Moscow, Russia*
- <sup>33</sup>*National Research Centre 'Kurchatov Institute', Moscow, Russia*
- <sup>34</sup>*National University of Science and Technology "MISIS", Moscow, Russia*
- <sup>35</sup>*Institute for High Energy Physics (IHEP) NRC 'Kurchatov Institute', Protvino, Russia*
- <sup>36</sup>*Petersburg Nuclear Physics Institute (PNPI) NRC 'Kurchatov Institute', Gatchina, Russia*
- <sup>37</sup>*St. Petersburg Polytechnic University (SPbPU),<sup>f</sup> St. Petersburg, Russia*
- <sup>38</sup>*National Research Nuclear University (MEPhI), Moscow, Russia*
- <sup>39</sup>*Skobeltsyn Institute of Nuclear Physics of Moscow State University (SINP MSU), Moscow, Russia*
- <sup>40</sup>*Yandex School of Data Analysis, Moscow, Russia*
- <sup>41</sup>*Institute of Physics, University of Belgrade, Serbia*
- <sup>42</sup>*Stockholm University, Stockholm, Sweden*
- <sup>43</sup>*Uppsala University, Uppsala, Sweden*
- <sup>44</sup>*European Organization for Nuclear Research (CERN), Geneva, Switzerland*
- <sup>45</sup>*University of Geneva, Geneva, Switzerland*
- <sup>46</sup>*École Polytechnique Fédérale de Lausanne (EPFL), Lausanne, Switzerland*
- <sup>47</sup>*Physik-Institut, Universität Zürich, Zürich, Switzerland*
- <sup>48</sup>*Middle East Technical University (METU), Ankara, Turkey*
- <sup>49</sup>*Ankara University, Ankara, Turkey*
- <sup>50</sup>*H.H. Wills Physics Laboratory, University of Bristol, Bristol, U.K.*

<sup>51</sup>*STFC Rutherford Appleton Laboratory, Didcot, U.K.*

<sup>52</sup>*Imperial College London, London, U.K.*

<sup>53</sup>*University College London, London, U.K.*

<sup>54</sup>*University of Warwick, Warwick, U.K.*

<sup>55</sup>*Taras Shevchenko National University of Kyiv, Kyiv, Ukraine*

<sup>a</sup>*Università di Bari, Bari, Italy*

<sup>b</sup>*Università di Bologna, Bologna, Italy*

<sup>c</sup>*Università di Cagliari, Cagliari, Italy*

<sup>d</sup>*Università di Napoli “Federico II”, Napoli, Italy*

<sup>e</sup>*Associated to Gyeongsang National University, Jinju, Korea*

<sup>f</sup>*Associated to Petersburg Nuclear Physics Institute (PNPI), Gatchina, Russia*

<sup>g</sup>*Also at Moscow Institute of Physics and Technology (MIPT), Moscow Region, Russia*

<sup>h</sup>*Consorzio CREATE, Napoli, Italy*

<sup>i</sup>*Università della Basilicata, Potenza, Italy*

E-mail: [alex.marshall@cern.ch](mailto:alex.marshall@cern.ch)

**ABSTRACT:** This paper presents a fast approach to simulating muons produced in interactions of the SPS proton beams with the target of the SHiP experiment. The SHiP experiment will be able to search for new long-lived particles produced in a 400 GeV/c SPS proton beam dump and which travel distances between fifty metres and tens of kilometers. The SHiP detector needs to operate under ultra-low background conditions and requires large simulated samples of muon induced background processes. Through the use of Generative Adversarial Networks it is possible to emulate the simulation of the interaction of 400 GeV/c proton beams with the SHiP target, an otherwise computationally intensive process. For the simulation requirements of the SHiP experiment, generative networks are capable of approximating the full simulation of the dense fixed target, offering a speed increase by a factor of  $O(10^6)$ . To evaluate the performance of such an approach, comparisons of the distributions of reconstructed muon momenta in SHiP’s spectrometer between samples using the full simulation and samples produced through generative models are presented. The methods discussed in this paper can be generalised and applied to modelling any non-discrete multi-dimensional distribution.

**KEYWORDS:** Detector modelling and simulations I (interaction of radiation with matter, interaction of photons with matter, interaction of hadrons with matter, etc); Simulation methods and programs

ARXIV EPRINT: [1909.04451](https://arxiv.org/abs/1909.04451)

---

## Contents

<b>1</b>	<b>Introduction</b>	<b>1</b>
<b>2</b>	<b>The SHiP experiment</b>	<b>2</b>
<b>3</b>	<b>The SHiP simulation</b>	<b>3</b>
<b>4</b>	<b>Generative adversarial networks</b>	<b>4</b>
<b>5</b>	<b>GANs for the SHiP experiment</b>	<b>6</b>
5.1	Pre-processing	6
5.2	Figure of merit	6
5.3	Network optimisation and GAN architecture	7
<b>6</b>	<b>GAN performance</b>	<b>8</b>
<b>7</b>	<b>Reconstructing GAN generated muons</b>	<b>10</b>
<b>8</b>	<b>Benchmarking</b>	<b>12</b>
<b>9</b>	<b>Conclusion</b>	<b>13</b>

---

## 1 Introduction

Generative networks are a class of machine learning algorithms designed to generate samples according to a multidimensional function, given a randomly distributed input sample. Generative networks have been studied in the machine learning community primarily for the purpose of image generation. Each image in a training set is made up of a multitude of pixels, corresponding to a data point in a high dimensional space. Within this space, underlying features of the set of images are encoded through dependencies between pixels. Generative networks attempt to model the characteristics that define a specific set of training images. These models can then be used to generate images that are faithful emulations of the original training set. Generative networks have been successfully employed for a variety of applications such as: generating high quality images that obey fundamental features of training set images; the generation of images from descriptive text [1]; modelling image captions [2]; producing photo realistic super resolution images [3]; and generating high resolution images from semantic mapping [4, 5].

Searches for physics beyond the Standard Model often involve looking for rare signatures and must therefore be able to suppress background processes which can be many orders of magnitude more abundant than the signal. In order to optimise the design of the detectors, develop reconstruction algorithms and understand the efficiency of the selection criteria, large samples of

simulated background events are required. Dedicated software packages such as GEANT4 [6] model the transport of particles through the material and the detector response. In many cases, the CPU requirements to simulate these interactions with matter prohibit the production of large numbers of background events due to the computationally expensive procedure. Therefore, the computing demands of the simulation of high energy physics experiments are increasing exponentially [7]. Recent algorithmic improvements that take advantage of high performance computing resources aim at reducing simulation time, resulting in an order of magnitude increase in speed [8]. This improvement is not sufficient to meet the demands of future particle physics experiments, such as those at the High Luminosity LHC, for large simulation samples [7]. Generative neural networks offer an alternative approach to simulation by modelling non-analytical functions in a computationally efficient way [9].

The use of generative networks for particle physics originally focused on image based generation. Examples of their application include: the development of Location Aware Generative Adversarial Networks for the production of images of jets [10]; the simulation of reconstructed cosmic ray induced air showers [11], and of showers in electromagnetic calorimeters [12]; the fast simulation of Cherenkov detectors [13]. More recently, generative approaches have also been adopted to simulate the kinematics of final state particles emerging from physical exclusive two-to-two processes, such as  $Z$  or top-quark production at the LHC [14, 15]. In ref. [16], generative networks were used to simulate the detector reconstruction of the  $Z \rightarrow \mu^+ \mu^-$  process at the LHC.

This paper describes the use of generative networks to emulate the kinematics of muons produced through the interactions of high energy protons with the dense target designed for the Search for Hidden Particles (SHiP) experiment [17]. This approach offers a gain of multiple orders of magnitude in the computational efficiency of such processes. In contrast to the aforementioned use of generative networks to approximate a single exclusive process, this work employs four different generative networks to model the kinematics of muons originating from a multitude of processes, including muons from secondary interactions or particle showers in SHiP’s target. Large samples of generative based muons can then be passed through the GEANT4 based simulation of the rest of the SHiP experiment, offering a precise modelling of its detector response and reconstruction.

This paper is organised as follows: sections 2 and 3 describe the SHiP detector and its simulation framework respectively; section 4 discusses the generative models used in this analysis, while section 5 details how these networks are trained and optimised for the SHiP experiment. Section 6 and 7 then present the performance of the generative models in simulating muons produced through interactions of high energy protons with the SHiP target, compared to the Pythia8 [18] and GEANT4 frameworks. Finally, section 8 discusses the computational time required to produce muons through generative networks.

## 2 The SHiP experiment

The Search for Hidden Particles experiment (SHiP) is a proposed experiment that will operate at the the prospective general purpose fixed target facility at the CERN Super Proton Synchrotron (SPS) accelerator. The SHiP experiment aims to search for long-lived exotic particles with masses between a few hundred  $\text{MeV}/c^2$  and a few  $\text{GeV}/c^2$ . These particles are expected to be produced in the decays of heavy hadrons. The facility is therefore designed to maximise the production rate and detection



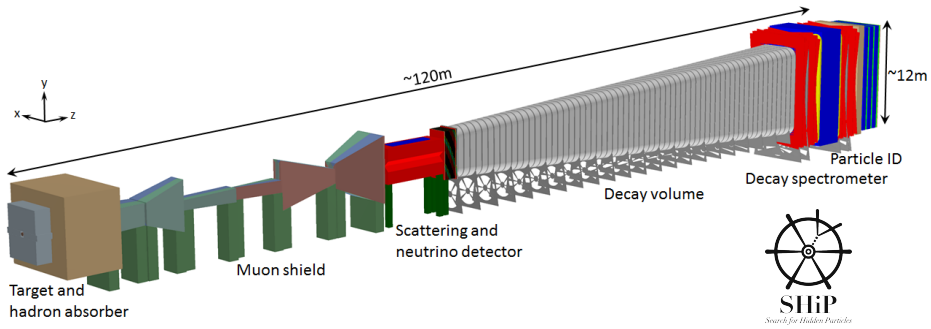


**Figure 1.** SHiP facility layout [19].

efficiency for charm and beauty mesons and their decay products, while maintaining the lowest possible background rate. The 400 GeV/c proton beam extracted from the SPS will be dumped on a high density W/Mo target with the aim of accumulating  $2 \times 10^{20}$  protons on target during 5 years of operation. The charm production at SHiP will exceed that of any existing or planned facility. The SHiP detector, shown in figure 1, incorporates two complementary apparatuses, the Scattering and Neutrino Detector (SND), and the Decay Spectrometer (DS). The SND will be used to search light dark matter particles, and perform neutrino physics measurements. The DS aims at measuring the visible decays of hidden sector particles by reconstructing their decay vertices in a 50 m long decay volume, making use of a magnetic spectrometer, veto systems and particle identification detectors. Further details of the design of the detector can be found in ref. [19]. Such a setup will allow the SHiP experiment to probe a variety of models that predict light long-lived exotic particles.

Since particles originating in charm and beauty meson decays are produced with a significant transverse momentum with respect to the beam axis,<sup>1</sup> the detector is placed as close as possible to the target. The high flux of muons produced in the target represents a serious background in searches for hidden particles. A critical component of the SHiP experiment is the muon shield [20], which deflects muons produced in the target away from the detector placed downstream of the target. The SHiP detector is designed to reconstruct the exclusive decays of hidden particles and to reduce the background to less than 0.1 events in the full five year period of operation.

### 3 The SHiP simulation

The simulation of the various physics processes of the response of the SHiP detector are handled by the FairShip software suite, which is based on the FairRoot software framework [21]. Within FairShip, primary collisions of protons are generated with Pythia8 and the subsequent propagation and interactions of particles are simulated with GEANT4. Neutrino interactions are simulated with GENIE [22], while heavy flavour production and inelastic muon interactions with Pythia6 [23] and GEANT4. Secondary heavy flavour production in cascade interactions of hadrons originating from the initial proton collision with the SHiP target is also taken into account [24]. The pattern recognition algorithms used to reconstruct tracks from the hits on the strawtubes of the DS are described in [25], and the algorithms for particle identification are presented in [26].

<sup>1</sup>In the SHiP coordinate system the z-axis is along the beam line and the y-axis is pointing upward.

In order to optimise the design of the active muon shield, and develop the reconstruction and selection algorithms of the SHiP experiment, a large simulation campaign was undertaken. Muons produced in the SHiP target were simulated with momentum  $p > 10 \text{ GeV}/c$  and a sample corresponding to approximately  $10^{11}$  protons on target was produced. In order to enhance this sample with muons likely to enter the DS, the cross-section of muons produced from decays of  $\rho^0$ ,  $\omega$ ,  $\eta$  and  $\eta'$  mesons was enhanced by a factor of 100. Similarly, the cross-section for photon conversions into muon pairs was also enhanced by the same factor. The full simulation of this sample, corresponding to a fraction of the  $4 \times 10^{13}$  protons-on-target SPS spill, required months of running on dedicated CPU farms. An order of magnitude increase of this sample could be achieved by exploiting symmetries of the system, such as that in the azimuthal plane of the collision. However, generating even larger samples commensurate to the  $2 \times 10^{20}$  SPS protons on target expected during the lifetime of the experiment is impossible using conventional particle simulation methods. The simulation of the initial proton interaction with the SHiP target, including the subsequent secondary interactions of particles with the target and the hadron absorber, requires significant computing power. Methods such as SMOTE [27] and ADASYN [28] could be used to synthesise a sample of muons that is larger than the original fully simulated sample. These methods rely on producing muons whose position and momentum vectors take values that lie in between those of existing muons in the fully simulated sample. Generative adversarial networks can offer an alternative way of producing orders of magnitude larger samples with minimal expense to the fidelity of the generated muons.

#### 4 Generative adversarial networks

Neural networks model functions that map an  $n$ -dimensional input parameter space into an  $m$ -dimensional output, and are widely employed in the particle physics community. A traditional neural network is built up of multiple *layers*: an input layer, one or more intermediate hidden layers, and an output layer. Layers are built from many individual *nodes*, and a pattern of connections joins nodes in adjacent layers. Each node has an associated tunable *bias* term that acts as an activation threshold of the node, and each connection has an associated tunable *weight* representing the strength of the connection. The simplest pattern of connections between layers is one where the nodes in one layer are fully connected with nodes in the adjacent layer. In this configuration the output value of each node is calculated by firstly calculating the sum of the output values of each node from the previous layer, weighted by the strength of each connection. This weighted sum is then shifted by the bias term and passed through an activation function that modulates the output of a node. Depending on the layer that a particular node belongs to, different types of activation functions can be used. For instance, hidden layers often make use of the so called “leaky rectified linear unit” function [29] and in the final layer a sigmoid function could be used to transform the output into a value between 0 and 1. This choice would be appropriate in a binary classification network, whose output is an estimate of whether the input sample originated from one out of two classes of samples.

A neural network must be trained in order for it to successfully approximate a function. The training process involves tuning and updating the weight and bias parameters of the network, with “supervised learning” being the most traditional approach to training. In the first stage of a

binary classification problem, labelled data are passed through the network. Output values are then recorded and compared to the true labels through the use of a *loss function*. The loss function provides a quantitative measure of the network's performance on a set of input training samples. A large value of the loss function indicates that the network is unable to distinguish between the two classes of samples. The value of the loss function is used in a process called *back-propagation* to update the weight and bias parameters across the network in an effort to improve the network's performance [30]. Neural networks are trained in steps, where in each step a small *batch* of training data is used, the loss function is then evaluated using this batch of data, and the weight and bias parameters of the network are updated for the next step.

Generative Adversarial Networks (GANs) employ two competing neural networks, one acting as a generator and the other as a discriminator [31]. The generator  $\hat{G}$  is trained to map an input vector of random noise  $z$  to an output generated vector  $G(z; \theta_g)$ , where  $\theta_g$  are parameters of the network and the dimensionality of  $z$  is typically larger than that of  $G(z; \theta_g)$ . The discriminator  $\hat{D}$ , with trainable parameters  $\theta_d$ , is trained to map an input vector  $x$  to an output prediction  $D(x; \theta_d)$ , which is a value between 0 and 1. In the study presented in this paper  $G(z; \theta_g)$  and  $x$  represent the momentum and position vector of the muons. The value of  $D(x; \theta_d)$  represents the probability that  $x$  originated from the training sample. A value of  $D(x; \theta_d)$  closer to 0 indicates that  $\hat{D}$  expects the sample to have been generated by  $\hat{G}$ , whereas if  $D(x; \theta_d)$  is closer to 1  $\hat{D}$  is predicting that the sample originated from the training data.

The discriminator and generator networks are trained using an iterative approach. Firstly, the discriminator is trained to distinguish between generated and training samples via a binary crossentropy loss function  $L_d$ . This is a common loss function for training classifier networks and is defined as

$$L_d = -[y_{\text{true}} \log(y_{\text{pred}}) + (1 - y_{\text{true}}) \log(1 - y_{\text{pred}})], \quad (4.1)$$

where  $y_{\text{true}}$  takes the values of 1 or 0 for the training or generated label of the sample respectively, and  $y_{\text{pred}}$  is the predicted label by the discriminator given by  $y_{\text{pred}} = D(x; \theta_d)$ . The value of this loss function increases rapidly the further  $y_{\text{pred}}$  is from the  $y_{\text{true}}$ . Large values of the loss function bring significant changes in the values of trainable parameters  $\theta_d$  in the network.

The generator network is then trained in a stacked model which directly connects the output  $x_{\text{gen}}$  of  $\hat{G}$  to the discriminator prediction  $D(x_{\text{gen}}; \theta_d)$ . This is the adversarial component of the GAN, it is only the feedback of  $\hat{D}$  that influences the training of  $\hat{G}$ . The  $x_{\text{gen}}$  never directly affects the training of  $\hat{G}$ . In this stacked model all training parameters of the discriminator,  $\theta_d$ , are fixed to the values obtained from the previous training step of  $\hat{D}$ . The trainable parameters,  $\theta_g$ , of the generator are updated based on the loss function,  $L_g$ , whose value depends on the output of the discriminator and is defined as

$$L_g = -\log(D(x_{\text{gen}}; \theta_d)). \quad (4.2)$$

Low values of  $D(x_{\text{gen}}; \theta_d)$  indicate that the discriminator is confident that the sample  $x_{\text{gen}}$  originated from the generator, leading to a large value of  $L_g$ . Generated samples that closely resemble training samples will return higher values of  $D(x_{\text{gen}}; \theta_d)$  and consequently lower values of  $L_g$  as the discriminator is successfully tricked into guessing a sample originated from the training sample.

The training of the discriminator and generator is repeated using the samples generated by the previous step. The training of the GAN is completed when generated samples  $G(z; \theta_g)$  are

indistinguishable from training samples. Different approaches are employed to determine the end of the training. In this paper the metric used to monitor the quality of the training is discussed in section 5.2. The overall accuracy of the generator depends on how well the discriminator is trained to distinguish between generated and training samples.

## 5 GANs for the SHiP experiment

The GAN is trained on a sample of  $3.4 \times 10^8$  muons passing through the target and hadron absorber in the full simulation campaign discussed in section 3. As mentioned, this training sample is artificially enriched with muons from rare processes. Therefore, in order to obtain a physical admixture of muons from various sources, batches of muons are extracted from the training sample according to a probability that corrects for this enhancement.

Training is performed on the position  $\mathbf{r}$  and momentum  $\mathbf{p}$  vectors of these muons at their point of production. Therefore, the GAN generates position and momentum vectors of muons at their production point within the target. Subsequently, they are propagated through the active muon shield and the Decay Spectrometer, relying on GEANT4 to simulate muon interactions with matter. This procedure allows for a fast production of large muon samples, while maintaining the flexibility to optimise the magnetic shield and downstream detector elements of SHiP, as well as the ability to correct for effects due to the spatial distribution of the proton beam impinging on the target.

Four separate GANs are trained, separated by muon charge and prompt or displaced origin. The  $x$ - and  $y$ -coordinates of muons originating from prompt decays of mesons such as the  $\rho^0$ ,  $\phi$  and  $J/\psi$  are always the same. This is a consequence of the training sample that relies on Pythia with no smearing of the proton-beam distribution. As such, muons from prompt sources are treated separately from muons originating from other sources. Therefore, the GANs trained on prompt muons generate four features ( $z$ ,  $\mathbf{p}$ ), and the GANs for non-prompt muons generate six ( $\mathbf{r}$ ,  $\mathbf{p}$ ). In this approach correlations between muons produced in pairs from, for example, vector-meson decays are ignored. Muons are generated individually and any correlation is assumed to be lost via the multiple scattering of the muons through the hadron absorber and muon shield.

### 5.1 Pre-processing

The distribution of the  $x$ - and  $y$ - coordinates of muons from non-prompt sources is extremely peaked around the interaction point. Therefore, each value of the  $x$  ( $y$ ) distribution  $x^i$  ( $y^i$ ) is transformed as

$$x_{\text{trans}}^i = \begin{cases} -\sqrt{|x^i - \bar{x}|} & \text{if } x^i < 0, \\ \sqrt{|x^i - \bar{x}|} & \text{if } x^i > 0, \end{cases} \quad (5.1)$$

before training the GANs. This transformation widens the distributions, which proves easier for the GANs to model. The distributions of all the input features are then normalised to values between -1 and 1. This transformation is reversed to obtain physical values of the generated output.

### 5.2 Figure of merit

An important requirement of the full simulation of the SHiP detector is to accurately model the flux of muons reaching the Decay Spectrometer. This flux crucially depends on the momentum

distribution of the muons entering the muon shield of the SHiP experiment. Therefore, muons generated through the GAN approach must closely match the kinematic distributions of the muons produced in the target using the full simulation.

In order to optimise the architecture of the networks and to quantify the quality of the training procedure a figure of merit, FoM, is developed with the following requirements. The FoM must account for how well the GAN is able to model individual features and the correlations between them. Furthermore, it is important that the FoM offers an independent metric of the quality of the training of the GAN since the discriminator and the generator of the GAN improve in tandem during the iterative training procedure. Finally, the calculation of the FoM must be fast so that it does not slow down the training process.

During the training process, small test samples are generated to test the progress of the procedure. As the number of muon features can span a six dimensional space, a small generated sample of muons results in a sparsely populated feature space. Therefore, traditional binned goodness of fit methods, such as  $\chi^2$ -tests, break down as almost all bins in this space have a low occupancy. Boosted decision trees can overcome this issue [32] and satisfy the aforementioned requirements on the FoM.

A gradient boosted decision tree, BDT, is trained periodically to distinguish between generated and fully simulated muon samples. The BDT uses 100,000 muons generated from the latest GAN configuration and 100,000 randomly selected, fully simulated muons. Half of the muons in each sample are used for training and the other half for testing. The resulting performance of the BDT is quantified through the area under the receiver operating characteristic curve (ROC AUC). A generated sample that is indistinguishable from a fully simulated sample would return an ROC AUC value of 0.5.

### 5.3 Network optimisation and GAN architecture

All networks are trained with a mini-batch gradient descent approach [33] and at each training step the networks use a sub-sample of training data. The generators and discriminators of the GANs are built using only fully connected layers, resulting in a GAN performance that is independent of the ordering of the muon parameters in the vectors of features that make up the training sample. The number of nodes, the size of the batch sub-sample, the number of layers and the learning rate of the networks are coarsely optimised through a grid search over these parameters. The four GANs are trained until the ROC AUC of the BDT based FoM described in section 5.2 flattens out, and the selected architecture is that which minimises the ROC AUC of the FoM.

As a result of this optimisation procedure, the GANs for both prompt and non-prompt muons follow the architecture shown in figure 2. Leaky rectified linear unit activation functions are used at every hidden layer. The generator and the discriminator have two hidden layers in an inverted pyramidal structure. For the prompt muon GANs, the number of nodes in each hidden layer of  $\hat{G}$  are 1536 and 3072 and for  $\hat{D}$  are 768 and 1536. For the non-prompt GANs, the number of corresponding nodes are 512 and 1024 for  $\hat{G}$  and 768 and 1536 for  $\hat{D}$ . The input to the generators relies on sampling from a latent space given by a 100 dimensional unit Gaussian distribution. The last layer of  $\hat{G}$  has a tanh activation function in accordance to the transformed range of the input features described in section 5.1. The last layer of  $\hat{D}$  has a sigmoid activation function providing an output between 0 and 1 that represents  $\hat{D}$ 's judgement on the origin of a sample. Dropout layers with

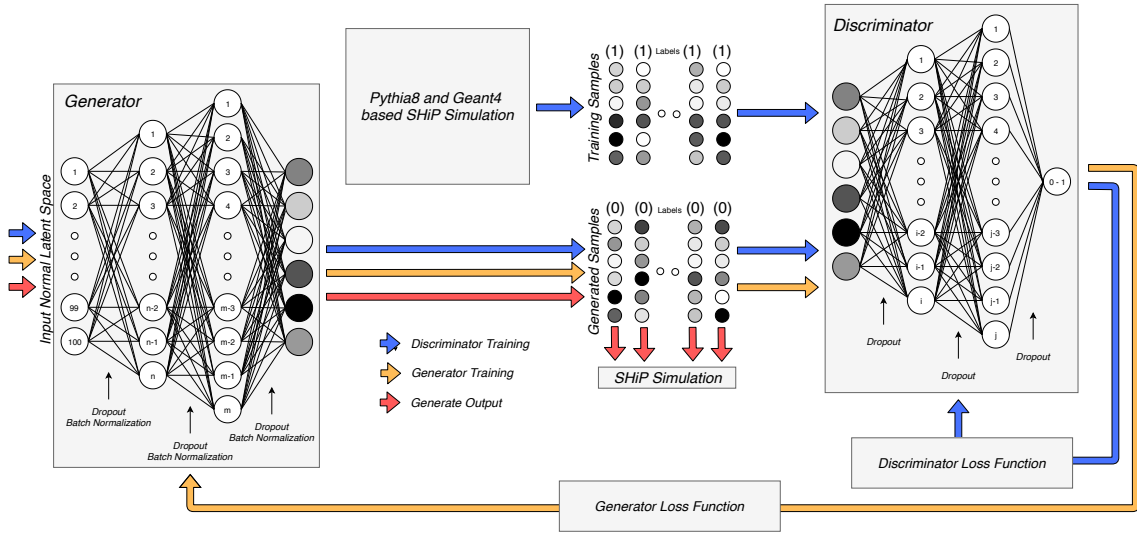


**Figure 2.** Optimal GAN architecture obtained for the simulation of muon background in SHiP. The number of nodes in each layer for prompt  $\mu$  and non-prompt  $\mu$  GANs are given in the text. Arrows indicate the flow of samples and loss information for each stage of training and generation. The features in the generated and training samples can take values between -1 and 1 as denoted by the varying shades of grey.

a dropout probability of 0.25 are added between each layer of  $\hat{G}$  and  $\hat{D}$  to prevent overfitting [34]. Batch normalisation layers are also added between layers of  $\hat{G}$  [35].

For this study the Adam optimisation algorithm [36] was used in training the networks. Employing the AMSgrad algorithm with the Adam optimiser increased the stability of our output loss and FoM progress with training [37]. A momentum parameter of Adam,  $\beta_l$ , is used with a value of 0.5 to control the progress of the gradient descent during the training of the network.

## 6 GAN performance

The progress of the FoM throughout the training of each GAN, as well as the BDT distributions of the optimal GAN models are shown in figure 3. The final FoM values for the prompt  $\mu^+$  and  $\mu^-$  GAN models are 0.57 and 0.54 respectively. Whereas, the non-prompt  $\mu^+$  and  $\mu^-$  GAN models return FoM values of 0.60 and 0.59 respectively. A more sophisticated optimisation procedure of the network architecture, such as that suggested in [38], could result in an even better GAN performance.

In order to further visualise the level of agreement between the generated and fully simulated samples, a physical sample of GAN based muons is produced by combining the output from each of the four generators according to the expected production fractions of prompt and non-prompt muons in the simulation. Figure 4 compares the one- and two-dimensional distributions of each unique pair of features between fully simulated and generated muons. The GANs can overall reproduce the correct correlations between features, although the tails of the  $(x, y, z)$  position distributions are underestimated.

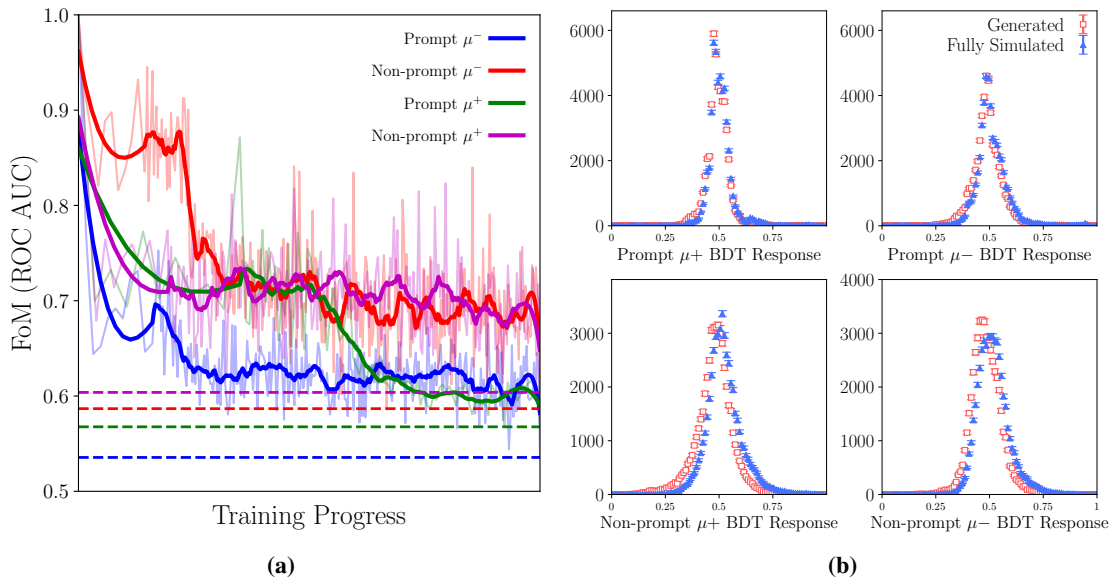


**Figure 3.** (a) Progress of the FoM ROC AUC value throughout the training of all 4 GANs, raw and smoothed data is displayed. Dashed lines indicate the FoM AUC ROC values of models chosen to generate muons in this paper. Although models were trained past this point this was the lowest FoM AUC ROC value obtained, (b) Distributions of the figure of merit BDT response for both fully simulated and GAN-based muon samples for prompt and non-prompt  $\mu^-$  and  $\mu^+$ .

Modelling of the momentum ( $p$ ) and transverse momentum ( $p_T$ ) plane accurately is crucial in order to obtain the correct flux of muons reaching the SHiP Decay Spectrometer. Figure 5 compares the ( $p$ ,  $p_T$ ) plane between the fully simulated and generated samples. The GANs can largely reproduce the correlations between these features, however they particularly underestimate the number of muons with  $p_T > 3$  GeV/ $c$ . The effect of this mismodelling on the rate and kinematics of muons reaching the Decay Spectrometer is discussed in section 7. To correct the momentum distribution of the generated muons, the three-dimensional ( $p_x$ ,  $p_y$ ,  $p_z$ ) distributions of the fully simulated and generated muons are each fit using a three-dimensional Kernel Density Estimator, for example see ref. [39]. For each generated muon, an individual correction weight is derived by taking the ratio between fully simulated over the fully generated KDEs at the corresponding ( $p_x$ ,  $p_y$ ,  $p_z$ ) muon coordinate.

This generative approach accurately models the production of muons in the SHiP target, as long as the kinematic distributions of the muons lie within the phase space covered by the fully simulated training sample. Therefore, samples of muons produced through the GAN are designed to compliment, rather than replace, existing fully simulated samples. By generating vast samples of muons through this generative approach, a better understanding of the performance of the muon shield and the detector response for muons that lie within the kinematic region of the fully simulated sample can be obtained.

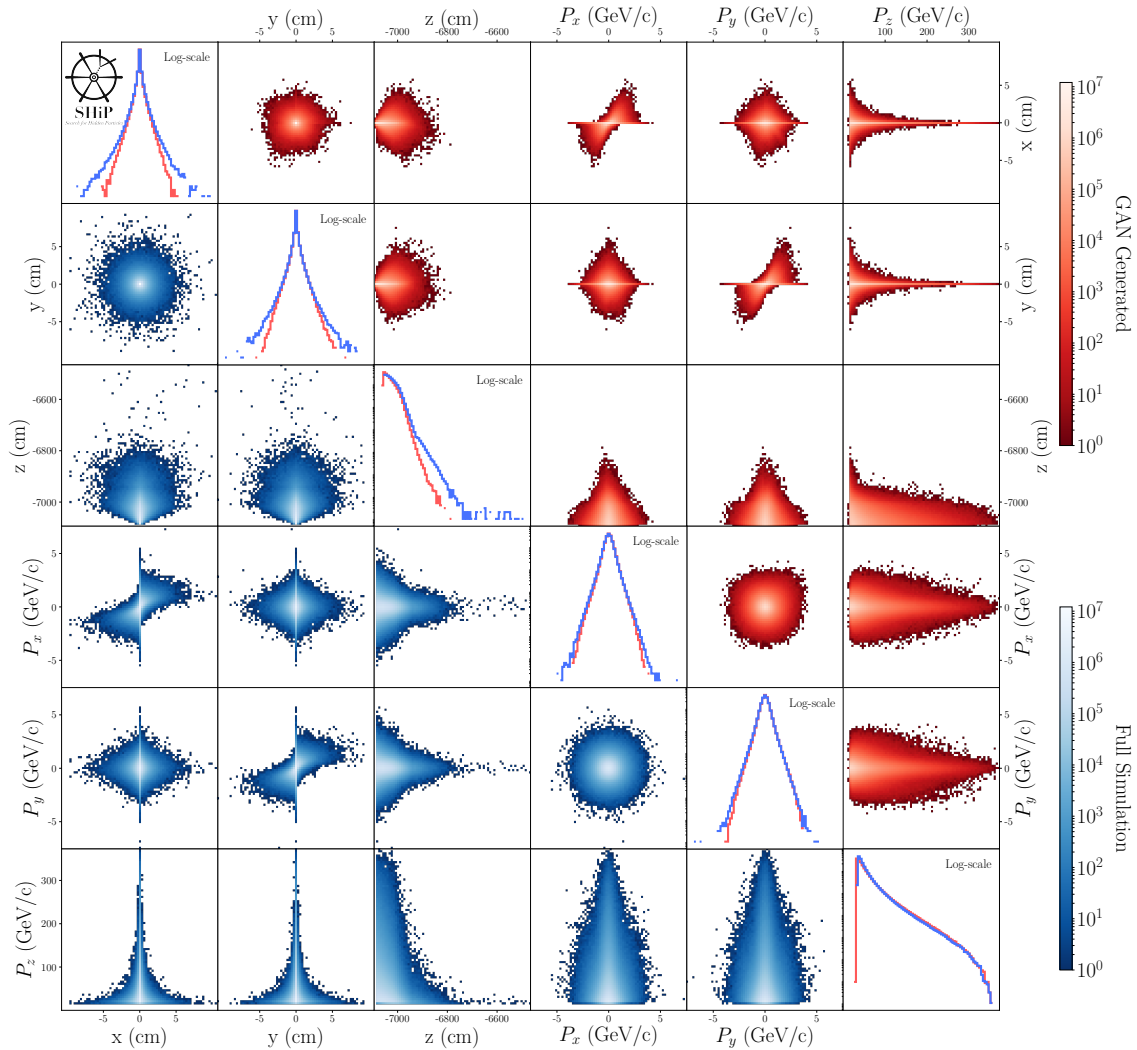


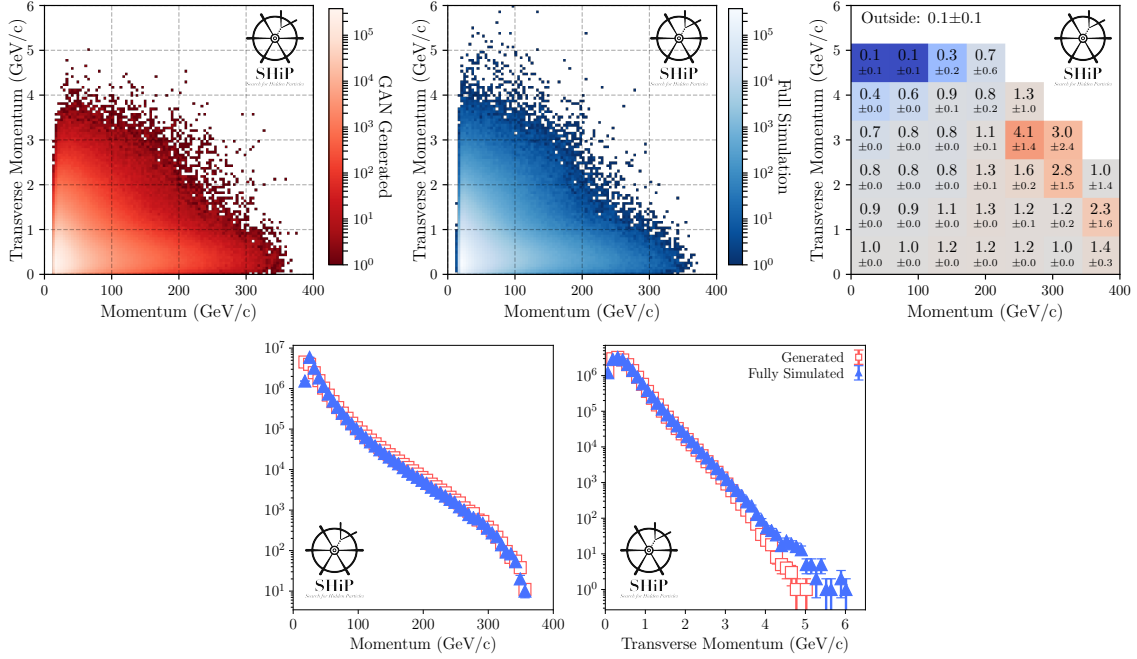
**Figure 4.** Two-dimensional distributions of all unique combinations of muon features for GAN based (upper-half) and fully simulated (lower-half) muons produced in the SHiP target. One-dimensional log scale comparisons of each feature are presented along the diagonal.

## 7 Reconstructing GAN generated muons

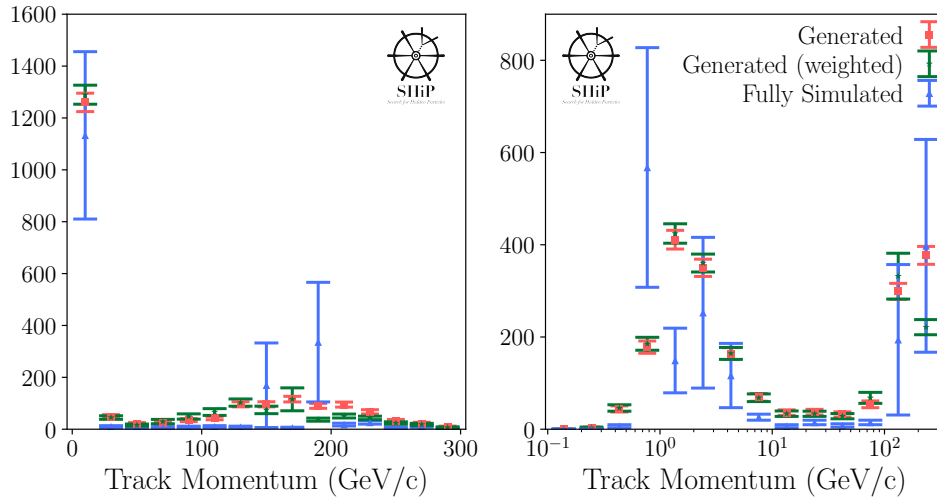
The generated muons are processed using FairShip to simulate their passage through the magnetic shield and the response of the downstream SHiP detector. Figure 6 shows the  $p$  vs  $p_T$  distribution of reconstructed muon tracks in the Decay Spectrometer of SHiP resulting from the GAN based muon sample. A comparison to the reconstructed muon tracks originating from the full simulation sample is also shown. The effect of the residual correction to the kinematics of the GAN based muon sample discussed in section 6 is found to have a small effect.

Figure 7 shows the momentum distributions at the production point of the muons, for muons that are reconstructed in the DS. The GAN based and fully simulated muons display similar features in the  $p$  vs  $p_T$  plane. The fully simulated sample exhibits localised hot-spots. These are due to the use of event weights that account for enhancement factors of particular processes that give rise to muons likely to enter the Decay Spectrometer as discussed in section 3.





**Figure 5.** Two-dimensional  $p$  vs  $p_T$  distributions for GAN based (top-left), fully simulated (top-middle) and the ratio (top-right) of muons produced in the SHiP target. The comparisons of the one dimensional projections for  $p$  (bottom-left) and  $p_T$  (bottom-right) are also shown.



**Figure 6.** Distribution in linear (left) and log-scale (right) of the reconstructed track momentum of muons in the Decay Spectrometer. The distributions of both GAN based and fully simulated muons are also shown together with the effect of the correction to the residual mismodelling of the muon kinematics from the GAN based sample. The distributions are normalised such that they correspond to the same number of protons on target.

The rate of muons that survive the magnetic shield and are reconstructed in the Decay Spectrometer is given in table 1. Both the full rate, and the rate of muons with an initial ( $p$ ,  $p_T$ ) distribution corresponding to the upper region of figure 7 agree when comparing the GAN based

and fully simulated muon samples. The correction to the kinematic distributions of the GAN based muons discussed in section 6, changes the rate of generated muons entering the Decay Spectrometer by  $\sim 4\%$ .

**Table 1.** Rates of reconstructed muons in the Decay Spectrometer. The uncertainty on the GAN based muons reflects the statistical uncertainty of the generated muon sample, given the model described in section 6.

Approach	Full Rate (kHz)	Upper Region Rate (kHz)
Full simulation	$13.9 \pm 3.4$	$4.7 \pm 2.2$
GAN	$15.8 \pm 0.3$	$5.5 \pm 0.2$
GAN (weighted)	$15.2 \pm 0.5$	$4.7 \pm 0.4$

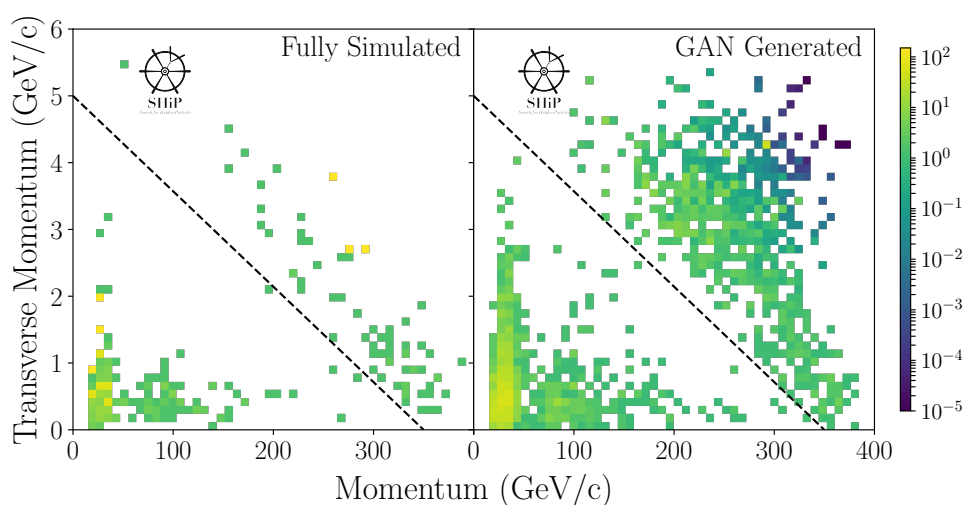


**Figure 7.** Initial momentum of muons passing through the SHiP active muon shield with well reconstructed tracks in the Decay Spectrometer. Full simulation data is presented on the left and generated data on the right. The dashed line indicates the upper region analysed in table 1.

## 8 Benchmarking

With a small expense in the fidelity between the generated and fully simulated sample, the generative approach can produce samples of muons at greater speed. Generating samples of muons from GANs on a GPU provides a speed-up of  $O(10^6)$  relative to the full Pythia8 and GEANT4 proton-on-target simulation. This test was performed using Keras(v2.1.5) on a TensorFlow backend (v1.8.0) on a single Nvidia Pascal P100 GPU card. This speed-up factor includes all the computations required to transform the output features of the generator into physical values. Generating muons using the GAN approach on a CPU is an order of magnitude slower than on a GPU.

Table 2 summarises the results of this performance test. The gain in speed using the generative approach is partly due to the small production cross-section of muons with  $p > 10 \text{ GeV}/c$ , requiring  $O(10^3)$  proton-on-target interactions to be simulated through Pythia8 in order to generate a single muon.

**Table 2.** Summary of benchmarking results.

Target simulation method	Muons produced in 5 minutes	Time to simulate single muon (s)
Pythia8 and GEANT4	$\sim 1$	$1.1 \times 10^{-1}$
GAN (CPU)	$7.5 \times 10^5$	$4.0 \times 10^{-4}$
GAN (GPU)	$3.5 \times 10^6$	$8.6 \times 10^{-5}$

## 9 Conclusion

This paper demonstrates the success of using a modern machine learning method to approximate the output of a complex and computationally intensive simulation of muons originating from SPS protons impinging on the target of the SHiP experiment. The GAN models presented in this paper produce samples that emulate the characteristics of the fully simulated sample and can approximate the kinematic correlations of the muons produced in the SHiP target. Furthermore, muons generated by these GANs correctly describe the expected flux and kinematic distributions of muons that survive the magnetic shield and are reconstructed in the Decay Spectrometer of the SHiP detector.

The generative models developed in this paper can produce muons  $\mathcal{O}(10^6)$  times faster than the current Pythia8 and GEANT4 simulation of the SHiP target. However, the muons produced by the generative model are only representative of regions of phase space populated by the full simulation of the target. These generative models are not capable of accurately extending the tails of their training distributions, and are not intended to replace the fully simulated background sample. Generated muons can be used in parallel to complement ongoing background and detector optimisation studies, where this approach can offer a vast increase in the sample size of statistically limited muon background studies at SHiP. Finally, the generative approach presented in this paper can be used to produce muons according to a model trained directly on real data, such as that from the recent muon-flux beam-test campaign of the SHiP collaboration [40]. Such an approach circumvents the challenge of tuning the multitude of parameters that control the simulation in order to match the data.

## Acknowledgments

This work was carried out using the computational facilities of the Advanced Computing Research Centre, University of Bristol — <http://www.bristol.ac.uk/acrc/>. We would like to thank the NVIDIA corporation for the donation of a Titan Xp which was used for this research.

The SHiP Collaboration wishes to thank the Castaldo company (Naples, Italy) for their contribution to the development studies of the decay vessel. The support from the National Research Foundation of Korea with grant numbers of 2018R1A2B2007757, 2018R1D1A3B07050649, 2018R1D1A1B07050701, 2017R1D1A1B03036042, 2017R1A6A3A01075752, 2016R1A2B4012302, and 2016R1A6A3A11930680 is acknowledged.

The support from the FCT — Fundação para a Ciência e a Tecnologia of Portugal with grant number CERN/FIS-PAR/0030/2017 is acknowledged. The support from the Russian Foundation for Basic Research (RFBR), grant 17-02-00607, the support from the TAEK of Turkey, and the

support from the U.K. Science and Technology Facilities Council (STFC), grant ST/P006779/1 are acknowledged.

We thank M. Al-Turany, F. Uhlig, S. Neubert and A. Gheata their assistance with FairRoot. We acknowledge G. Eulisse and P.A. Munkes for help with Alibuild.

We thank M. Daniels for his contributions to the construction of the liquid-scintillator testbeam detectors.

The muon flux and charm cross section measurements this summer would not have been possible without a significant financial contribution from CERN. In addition, several member institutes made large financial and in-kind contributions to the construction of the target and the spectrometer sub detectors, as well as providing expert manpower for commissioning, data taking and analysis. This help is gratefully acknowledged.

## References

- [1] H. Zhang et al., *Stackgan: Text to Photo-realistic Image Synthesis with Stacked Generative Adversarial Networks*, [arXiv:1612.03242](#).
- [2] Y. Pu et al., *Variational Autoencoder for Deep Learning of Images, Labels and Captions*, in *Advances in neural information processing systems. Proceedings of Neural Information Processing Systems 2016*, Barcellona Spagna (2016) [[arXiv:1609.08976](#)].
- [3] C. Ledig et al., *Photo-Realistic Single Image Super-Resolution Using a Generative Adversarial Network*, *IEEE Conf. Comput. Vis. Pattern Recognit.* **2017** (2017) 1 [[arXiv:1609.04802](#)].
- [4] T. Wang et al., *High-Resolution Image Synthesis and Semantic Manipulation with Conditional GANs*, *IEEE Conf. Comput. Vis. Pattern Recognit.* **2018** (2018) 1 [[arXiv:1711.11585](#)].
- [5] P. Isola, J. Zhu, T. Zhou and A.A. Efros, *Image-to-Image Translation with Conditional Adversarial Networks*, [arXiv:1611.07004](#).
- [6] GEANT4 collaboration, *GEANT4: A Simulation toolkit*, *Nucl. Instrum. Meth. A* **506** (2003) 250.
- [7] HEP SOFTWARE FOUNDATION collaboration, *A Roadmap for HEP Software and Computing R&D for the 2020s*, *Comput. Softw. Big Sci.* **3** (2019) 7 [[arXiv:1712.06982](#)].
- [8] P. Canal et al., *GeantV: from CPU to accelerators*, *PoS(ICHEP2016)* **177**.
- [9] M. Mirza and S. Osindero, *Conditional Generative Adversarial Nets*, [arXiv:1411.1784](#).
- [10] L. de Oliveira, M. Paganini and B. Nachman, *Learning Particle Physics by Example: Location-Aware Generative Adversarial Networks for Physics Synthesis*, *Comput. Softw. Big Sci.* **1** (2017) 4 [[arXiv:1701.05927](#)].
- [11] M. Erdmann, J. Glombitza and D. Walz, *A Deep Learning-based Reconstruction of Cosmic Ray-induced Air Showers*, *Astropart. Phys.* **97** (2018) 46 [[arXiv:1708.00647](#)].
- [12] M. Paganini, L. de Oliveira and B. Nachman, *CaloGAN: Simulating 3D high energy particle showers in multilayer electromagnetic calorimeters with generative adversarial networks*, *Phys. Rev. D* **97** (2018) 014021 [[arXiv:1712.10321](#)].
- [13] D. Derkach, N. Kazeev, F. Ratnikov, A. Ustyuzhanin and A. Volokhova, *Cherenkov Detectors Fast Simulation Using Neural Networks*, in *10th International Workshop on Ring Imaging Cherenkov Detectors (RICH 2018)*, Moscow Russia (2018) [[arXiv:1903.11788](#)].
- [14] A. Butter, T. Plehn and R. Winterhalder, *How to GAN LHC Events*, [arXiv:1907.03764](#).
- [15] S. Otten et al., *Event Generation and Statistical Sampling for Physics with Deep Generative Models and a Density Information Buffer*, [arXiv:1901.00875](#).

- [16] B. Hashemi, N. Amin, K. Datta, D. Olivito and M. Pierini, *LHC analysis-specific datasets with Generative Adversarial Networks*, [arXiv:1901.05282](#).
- [17] SHiP collaboration, *A facility to Search for Hidden Particles (SHiP) at the CERN SPS*, [arXiv:1504.04956](#).
- [18] T. Sjöstrand, S. Mrenna and P.Z. Skands, *A Brief Introduction to PYTHIA 8.1*, *Comput. Phys. Commun.* **178** (2008) 852 [[arXiv:0710.3820](#)].
- [19] SHiP collaboration, *SHiP Experiment — Progress Report*, [CERN-SPSC-2019-010](#) (2019).
- [20] SHiP collaboration, *The active muon shield in the SHiP experiment*, *2017 JINST* **12** P05011 [[arXiv:1703.03612](#)].
- [21] M. Al-Turany et al., *The FairRoot framework*, *J. Phys. Conf. Ser.* **396** (2012) 022001.
- [22] C. Andreopoulos et al., *The GENIE Neutrino Monte Carlo Generator*, *Nucl. Instrum. Meth. A* **614** (2010) 87 [[arXiv:0905.2517](#)].
- [23] T. Sjöstrand, S. Mrenna and P.Z. Skands, *PYTHIA 6.4 Physics and Manual*, *JHEP* **05** (2006) 026 [[hep-ph/0603175](#)].
- [24] H. Dijkstra and T. Ruf, *Heavy Flavour Cascade Production in a Beam Dump*, [CERN-SHiP-NOTE-2015-009](#) (2015).
- [25] E. Van Herwijnen, T. Ruf, M. Ferro-Luzzi and H. Dijkstra, *Simulation and pattern recognition for the SHiP Spectrometer Tracker*, [CERN-SHiP-NOTE-2015-002](#) (2015).
- [26] B. Hosseini and W.M. Bonivento, *Particle Identification tools and performance in the SHiP Experiment*, [CERN-SHiP-NOTE-2017-002](#) (2017).
- [27] N.V. Chawla, K.W. Bowyer, L.O. Hall and W.P. Kegelmeyer, *SMOTE: synthetic minority over-sampling technique*, *J. Artif. Intell. Res.* **16** (2002) 321 [[arXiv:1106.1813](#)].
- [28] H. He, Y. Bai, E.A. Garcia and S. Li, *ADASYN: Adaptive synthetic sampling approach for imbalanced learning*, *IEEE Int. Joint Conf. Neural Netw.* **2008** (2008) 1
- [29] A.L. Maas, A.Y. Hannun and A.Y. Ng, *Rectifier Nonlinearities Improve Neural Network Acoustic Models*, *Proc. ICML* **30** (2013) 3.
- [30] D.E. Rumelhart, G.E. Hinton and R.J. Williams, *Learning representations by back-propagating errors*, *Cognitive Modeling* **5** (1988) 1 [[Nature](#) **323** (1988) 533].
- [31] I.J. Goodfellow et al., *Generative Adversarial Networks*, [arXiv:1406.2661](#).
- [32] C. Weisser and M. Williams, *Machine learning and multivariate goodness of fit*, [arXiv:1612.07186](#).
- [33] S. Ruder, *An overview of gradient descent optimization algorithms*, [arXiv:1609.04747](#).
- [34] N. Srivastava et al., *Dropout: A Simple Way to Prevent Neural Networks from Overfitting*, *J. Mach. Learn. Res.* **15** (2014) 1929.
- [35] S. Ioffe and C. Szegedy, *Batch Normalization: Accelerating Deep Network Training by Reducing Internal Covariate Shift*, [arXiv:1502.03167](#).
- [36] D.P. Kingma and J. Ba, *Adam: A Method for Stochastic Optimization*, [arXiv:1412.6980](#).
- [37] S.J. Reddi, S. Kale and S. Kumar, *On the Convergence of Adam and Beyond*, [arXiv:1904.09237](#).
- [38] M. Jaderberg et al., *Population Based Training of Neural Networks*, [arXiv:1711.09846](#).
- [39] D.W. Scott, *Multivariate density estimation: theory, practice, and visualization*, John Wiley & Sons, New York U.S.A. (2015).
- [40] SHiP collaboration, *Alignment of the muon-flux spectrometer in FairShip using the survey measurements*, [CERN-SHiP-NOTE-2019-001](#) (2019).

**OPEN ACCESS**

# The experimental facility for the Search for Hidden Particles at the CERN SPS

To cite this article: C. Ahdida *et al* 2019 *JINST* **14** P03025

View the [article online](#) for updates and enhancements.



**IOP | ebooks™**

Bringing you innovative digital publishing with leading voices to create your essential collection of books in STEM research.

Start exploring the collection - download the first chapter of every title for free.

# The experimental facility for the Search for Hidden Particles at the CERN SPS



## The SHiP collaboration

C. Ahdida,<sup>44</sup> R. Albanese,<sup>14,a</sup> A. Alexandrov,<sup>14</sup> A. Anokhina,<sup>39</sup> S. Aoki,<sup>18</sup> G. Arduini,<sup>44</sup> E. Atkin,<sup>38</sup> N. Azorskiy,<sup>29</sup> J.J. Back,<sup>54</sup> A. Bagulya,<sup>32</sup> F. Baaltasar Dos Santos,<sup>44</sup> A. Baranov,<sup>40</sup> F. Bardou,<sup>44</sup> G.J. Barker,<sup>54</sup> M. Battistin,<sup>44</sup> J. Bauche,<sup>44</sup> A. Bay,<sup>46</sup> V. Bayliss,<sup>51</sup> G. Bencivenni,<sup>15</sup> A.Y. Berdnikov,<sup>37</sup> Y.A. Berdnikov,<sup>37</sup> I. Berezkina,<sup>32</sup> M. Bertani,<sup>15</sup> C. Betancourt,<sup>47</sup> I. Bezshyiko,<sup>47</sup> O. Bezshyyko,<sup>55</sup> D. Bick,<sup>8</sup> S. Bieschke,<sup>8</sup> A. Blanco,<sup>28</sup> J. Boehm,<sup>51</sup> M. Bogomilov,<sup>1</sup> K. Bondarenko,<sup>27,57</sup> W.M. Bonivento,<sup>13</sup> J. Borburgh,<sup>44</sup> A. Boyarsky,<sup>27,55</sup> R. Brenner,<sup>43</sup> D. Breton,<sup>4</sup> R. Brundler,<sup>47</sup> M. Bruschi,<sup>12</sup> V. Büscher,<sup>10</sup> A. Buonaura,<sup>47</sup> S. Buontempo,<sup>14</sup> S. Cadeddu,<sup>13</sup> A. Calcaterra,<sup>15</sup> M. Calviani,<sup>44</sup> M. Campanelli,<sup>53</sup> M. Casolino,<sup>44</sup> N. Charitonidis,<sup>44</sup> P. Chau,<sup>10</sup> J. Chauveau,<sup>5</sup> A. Chepurinov,<sup>39</sup> M. Chernyavskiy,<sup>32</sup> K.-Y. Choi,<sup>26</sup> A. Chumakov,<sup>2</sup> P. Ciambone,<sup>15</sup> K. Cornelis,<sup>44</sup> M. Cristinziani,<sup>7</sup> A. Crupano,<sup>14,d</sup> G.M. Dallavalle,<sup>12</sup> A. Datwyler,<sup>47</sup> N. D'Ambrosio,<sup>16</sup> G. D'Appollonio,<sup>13,c</sup> J. De Carvalho Saraiva,<sup>28</sup> G. De Lellis,<sup>14,d</sup> M. de Magistris,<sup>14,d</sup> A. De Roeck,<sup>44</sup> M. De Serio,<sup>11,a</sup> D. De Simone,<sup>14,d</sup> L. Dedenko,<sup>39</sup> P. Dergachev,<sup>34</sup> A. Di Crescenzo,<sup>14,d</sup> N. Di Marco,<sup>16</sup> C. Dib,<sup>2</sup> H. Dijkstra,<sup>44</sup> P. Dipinto,<sup>11,a</sup> V. Dmitrenko,<sup>38</sup> S. Dmitrievskiy,<sup>29</sup> L.A. Dougherty,<sup>44</sup> A. Dolmatov,<sup>30</sup> D. Domenici,<sup>15</sup> S. Donskov,<sup>35</sup> V. Drohan,<sup>55</sup> A. Dubreuil,<sup>45</sup> J. Ebert,<sup>8</sup> T. Enik,<sup>29</sup> A. Etenko,<sup>33,38</sup> F. Fabbri,<sup>12</sup> L. Fabbri,<sup>12,b</sup> A. Fabich,<sup>44</sup> O. Fedin,<sup>36</sup> F. Fedotovs,<sup>52</sup> G. Felici,<sup>15</sup> M. Ferro-Luzzi,<sup>44</sup> K. Filippov,<sup>38</sup> R.A. Fini,<sup>11</sup> P. Fonte,<sup>28</sup> C. Franco,<sup>28</sup> M. Fraser,<sup>44</sup> R. Fresa,<sup>14,i</sup> R. Froeschl,<sup>44</sup> T. Fukuda,<sup>19</sup> G. Galati,<sup>14,d</sup> J. Gall,<sup>44</sup> L. Gagnon,<sup>44</sup> G. Gavrillov,<sup>38</sup> V. Gentile,<sup>14,d</sup> B. Goddard,<sup>44</sup> L. Golinka-Bezshyyko,<sup>55</sup> A. Golovatiuk,<sup>55</sup> D. Golubkov,<sup>30</sup> A. Golutvin,<sup>52,34</sup> P. Gorbounov,<sup>44</sup> D. Gorbunov,<sup>31</sup> S. Gorbunov,<sup>32</sup> V. Gorkavenko,<sup>55</sup> Y. Gornushkin,<sup>29</sup> M. Gorshenkov,<sup>34</sup> V. Grachev,<sup>38</sup> A.L. Grandchamp,<sup>46</sup> G. Granich,<sup>32</sup> E. Graverini,<sup>47</sup> J.-L. Grenard,<sup>44</sup> D. Grenier,<sup>44</sup> V. Grichine,<sup>32</sup> N. Gruzinskii,<sup>36</sup> A. M. Guler,<sup>48</sup> Yu. Guz,<sup>35</sup> G.J. Haefeli,<sup>46</sup> C. Hagner,<sup>8</sup> H. Hakobyan,<sup>2</sup> I.W. Harris,<sup>46</sup> E. van Herwijnen,<sup>44</sup> C. Hessler,<sup>44</sup> A. Hollnagel,<sup>10</sup> B. Hosseini,<sup>52</sup> M. Hushchyn,<sup>40</sup> G. Iaselli,<sup>11,a</sup> A. Iuliano,<sup>14,d</sup> V. Ivantchenko,<sup>32</sup> R. Jacobsson,<sup>44</sup> D. Joković,<sup>41</sup> M. Jonker,<sup>44</sup> I. Kadenko,<sup>55</sup> V. Kain,<sup>44</sup> C. Kamiscioglu,<sup>49</sup> K. Kershaw,<sup>44</sup> M. Khabibullin,<sup>31</sup> E. Khalikov,<sup>39</sup>

G. Khaustov,<sup>35</sup> G. Khorauli,<sup>10</sup> A. Khotyantsev,<sup>31</sup> S.H. Kim,<sup>22</sup> Y.G. Kim,<sup>23</sup> V. Kim,<sup>36,37</sup>  
 N. Kitagawa,<sup>19</sup> J.-W. Ko,<sup>22</sup> K. Kodama,<sup>17</sup> A. Kolesnikov,<sup>29</sup> D.I. Kolev,<sup>1</sup> V. Kolosov,<sup>35</sup>  
 M. Komatsu,<sup>19</sup> N. Kondrateva,<sup>32</sup> A. Kono,<sup>21</sup> N. Konovalova,<sup>32,34</sup> S. Kormannshaus,<sup>10</sup> I. Korol,<sup>6</sup>  
 I. Korol'ko,<sup>30</sup> A. Korzenev,<sup>45</sup> V. Kostyukhin,<sup>7</sup> E. Koukovini Platia,<sup>44</sup> S. Kovalenko,<sup>2</sup>  
 I. Krasilnikova,<sup>34</sup> Y. Kudenko,<sup>31,38,g</sup> E. Kurbatov,<sup>40</sup> P. Kurbatov,<sup>34</sup> V. Kurochka,<sup>31</sup>  
 E. Kuznetsova,<sup>36</sup> H.M. Lacker,<sup>6</sup> M. Lamont,<sup>44</sup> G. Lanfranchi,<sup>15</sup> O. Lantwin,<sup>52</sup> A. Lauria,<sup>14,d</sup>  
 K.S. Lee,<sup>25</sup> K.Y. Lee,<sup>22</sup> J.-M. Lévy,<sup>5</sup> V.P. Loschiavo,<sup>14,h</sup> L. Lopes,<sup>28</sup> E. Lopez Sola,<sup>44</sup>  
 V. Lyubovitskij,<sup>2</sup> J. Maalmi,<sup>4</sup> A. Magnan,<sup>52</sup> V. Maleev,<sup>36</sup> A. Malinin,<sup>33</sup> Y. Manabe,<sup>19</sup>  
 A.K. Managadze,<sup>39</sup> M. Manfredi,<sup>44</sup> S. Marsh,<sup>44</sup> A.M. Marshall,<sup>50</sup> A. Mefodev,<sup>31</sup> P. Mermod,<sup>45</sup>  
 A. Miano,<sup>14,d</sup> S. Mikado,<sup>20</sup> Yu. Mikhaylov,<sup>35</sup> D.A. Milstead,<sup>42</sup> O. Mineev,<sup>31</sup> A. Montanari,<sup>12</sup>  
 M.C. Montesi,<sup>14,d</sup> K. Morishima,<sup>19</sup> S. Movchan,<sup>29</sup> Y. Muttoni,<sup>44</sup> N. Naganawa,<sup>19</sup>  
 M. Nakamura,<sup>19</sup> T. Nakano,<sup>19</sup> S. Nasybulin,<sup>36</sup> P. Ninin,<sup>44</sup> A. Nishio,<sup>19</sup> A. Novikov,<sup>38</sup>  
 B. Obinyakov,<sup>33</sup> S. Ogawa,<sup>21</sup> N. Okateva,<sup>32,34</sup> B. Opitz,<sup>8</sup> J. Osborne,<sup>44</sup> M. Ovchynnikov,<sup>27,55</sup>  
 N. Owscharenko,<sup>7</sup> P.H. Owen,<sup>47</sup> P. Pacholek,<sup>44</sup> A. Paoloni,<sup>15</sup> R. Paparella,<sup>11</sup> B.D. Park,<sup>22</sup>  
 S.K. Park,<sup>25</sup> A. Pastore,<sup>12</sup> M. Patel,<sup>52</sup> D. Pereyma,<sup>30</sup> A. Perillo-Marccone,<sup>44</sup> G.L. Petkov,<sup>1</sup>  
 K. Petridis,<sup>50</sup> A. Petrov,<sup>33</sup> D. Podgrudkov,<sup>39</sup> V. Poliakov,<sup>35</sup> N. Polukhina,<sup>32,34,38</sup>  
 J. Prieto Prieto,<sup>44</sup> M. Prokudin,<sup>30</sup> A. Prota,<sup>14,d</sup> A. Quercia,<sup>14,d</sup> A. Rademakers,<sup>44</sup> A. Rakai,<sup>44</sup>  
 F. Ratnikov,<sup>40</sup> T. Rawlings,<sup>51</sup> F. Redi,<sup>46</sup> S. Ricciardi,<sup>51</sup> M. Rinaldesi,<sup>44</sup> Volodymyr Rodin,<sup>55</sup>  
 Viktor Rodin,<sup>55</sup> P. Robbe,<sup>4</sup> A.B. Rodrigues Cavalcante,<sup>46</sup> T. Roganova,<sup>39</sup> H. Rokujo,<sup>19</sup>  
 G. Rosa,<sup>14,d</sup> T. Rovelli,<sup>12,b</sup> O. Ruchayskiy,<sup>3</sup> T. Ruf,<sup>44</sup> V. Samoylenko,<sup>35</sup> V. Samsonov,<sup>38</sup>  
 F. Sanchez Galan,<sup>44</sup> P. Santos Diaz,<sup>44</sup> A. Sanz Ull,<sup>44</sup> A. Saputi,<sup>15</sup> O. Sato,<sup>19</sup> E.S. Savchenko,<sup>34</sup>  
 W. Schmidt-Parzefall,<sup>8</sup> N. Serra,<sup>47</sup> S. Sgobba,<sup>44</sup> O. Shadura,<sup>55</sup> A. Shakin,<sup>34</sup>  
 M. Shaposhnikov,<sup>46</sup> P. Shatalov,<sup>30</sup> T. Shchedrina,<sup>32,34</sup> L. Shchutska,<sup>55</sup> V. Shevchenko,<sup>33</sup>  
 H. Shibuya,<sup>21</sup> S. Shirobokov,<sup>52</sup> A. Shustov,<sup>38</sup> S.B. Silverstein,<sup>42</sup> S. Simone,<sup>11,a</sup>  
 R. Simoniello,<sup>10</sup> M. Skorokhvatov,<sup>38,33</sup> S. Smirnov,<sup>38</sup> J.Y. Sohn,<sup>22</sup> A. Sokolenko,<sup>55</sup>  
 E. Solodko,<sup>44</sup> N. Starkov,<sup>32,33</sup> L. Stoel,<sup>44</sup> B. Storaci,<sup>47</sup> M.E. Stramaglia,<sup>46</sup> D. Sukhonos,<sup>44</sup>  
 Y. Suzuki,<sup>19</sup> S. Takahashi,<sup>18</sup> J.L. Tastet,<sup>3</sup> P. Teterin,<sup>38</sup> S. Than Naing,<sup>32</sup> I. Timiryasov,<sup>46</sup>  
 V. Tioukov,<sup>14</sup> D. Tommasini,<sup>44</sup> M. Torii,<sup>19</sup> N. Tosi,<sup>12</sup> D. Treille,<sup>44</sup> R. Tsenov,<sup>1,29</sup> S. Ulin,<sup>38</sup>  
 A. Ustyuzhanin,<sup>40</sup> Z. Uteshev,<sup>38</sup> G. Vankova-Kirilova,<sup>1</sup> F. Vannucci,<sup>5</sup> P. Venkova,<sup>6</sup> V. Venturi,<sup>44</sup>  
 S. Vilchinski,<sup>55</sup> M. Villa,<sup>12,b</sup> Heinz Vincke,<sup>44</sup> Helmut Vincke,<sup>44</sup> C. Visone,<sup>14,j</sup> K. Vlasik,<sup>38</sup>  
 A. Volkov,<sup>32,33</sup> R. Voronkov,<sup>32</sup> S. van Waasen,<sup>9</sup> R. Wanke,<sup>10</sup> P. Wertelaers,<sup>44</sup> J.-K. Woo,<sup>24</sup>  
 M. Wurm,<sup>10</sup> S. Xella,<sup>3</sup> D. Yilmaz,<sup>49</sup> A.U. Yilmazer,<sup>49</sup> C.S. Yoon,<sup>22</sup> P. Zarubin,<sup>29</sup> I. Zarubina<sup>29</sup>  
 and Yu. Zaytsev<sup>30</sup>

<sup>1</sup>Faculty of Physics, Sofia University, Sofia, Bulgaria

<sup>2</sup>Universidad Técnica Federico Santa María and Centro Científico Tecnológico de Valparaíso, Valparaíso, Chile

<sup>3</sup>Niels Bohr Institute, University of Copenhagen, Copenhagen, Denmark

<sup>4</sup>LAL, Univ. Paris-Sud, CNRS/IN2P3, Université Paris-Saclay, Orsay, France

<sup>5</sup>LPNHE, IN2P3/CNRS, Sorbonne Université, Université Paris Diderot, F-75252 Paris, France

<sup>6</sup>Humboldt-Universität zu Berlin, Berlin, Germany

<sup>7</sup>Physikalisches Institut, Universität Bonn, Bonn, Germany

<sup>8</sup>Universität Hamburg, Hamburg, Germany

<sup>9</sup>Forschungszentrum Jülich GmbH (KFA), Jülich, Germany



- <sup>10</sup>*Institut für Physik and PRISMA Cluster of Excellence, Johannes Gutenberg Universität Mainz, Mainz, Germany*
- <sup>11</sup>*Sezione INFN di Bari, Bari, Italy*
- <sup>12</sup>*Sezione INFN di Bologna, Bologna, Italy*
- <sup>13</sup>*Sezione INFN di Cagliari, Cagliari, Italy*
- <sup>14</sup>*Sezione INFN di Napoli, Napoli, Italy*
- <sup>15</sup>*Laboratori Nazionali dell'INFN di Frascati, Frascati, Italy*
- <sup>16</sup>*Laboratori Nazionali dell'INFN di Gran Sasso, L'Aquila, Italy*
- <sup>17</sup>*Aichi University of Education, Kariya, Japan*
- <sup>18</sup>*Kobe University, Kobe, Japan*
- <sup>19</sup>*Nagoya University, Nagoya, Japan*
- <sup>20</sup>*College of Industrial Technology, Nihon University, Narashino, Japan*
- <sup>21</sup>*Toho University, Funabashi, Chiba, Japan*
- <sup>22</sup>*Physics Education Department & RINS, Gyeongsang National University, Jinju, Korea*
- <sup>23</sup>*Gwangju National University of Education,<sup>e</sup> Gwangju, Korea*
- <sup>24</sup>*Jeju National University,<sup>e</sup> Jeju, Korea*
- <sup>25</sup>*Korea University, Seoul, Korea*
- <sup>26</sup>*Sungkyunkwan University,<sup>e</sup> Suwon-si, Gyeong Gi-do, Korea*
- <sup>27</sup>*University of Leiden, Leiden, The Netherlands*
- <sup>28</sup>*LIP, Laboratory of Instrumentation and Experimental Particle Physics, Portugal*
- <sup>29</sup>*Joint Institute for Nuclear Research (JINR), Dubna, Russia*
- <sup>30</sup>*Institute of Theoretical and Experimental Physics (ITEP) NRC 'Kurchatov Institute', Moscow, Russia*
- <sup>31</sup>*Institute for Nuclear Research of the Russian Academy of Sciences (INR RAS), Moscow, Russia*
- <sup>32</sup>*P.N. Lebedev Physical Institute (LPI), Moscow, Russia*
- <sup>33</sup>*National Research Centre 'Kurchatov Institute', Moscow, Russia*
- <sup>34</sup>*National University of Science and Technology "MISiS", Moscow, Russia*
- <sup>35</sup>*Institute for High Energy Physics (IHEP) NRC 'Kurchatov Institute', Protvino, Russia*
- <sup>36</sup>*Petersburg Nuclear Physics Institute (PNPI) NRC 'Kurchatov Institute', Gatchina, Russia*
- <sup>37</sup>*St. Petersburg Polytechnic University (SPbPU),<sup>f</sup> St. Petersburg, Russia*
- <sup>38</sup>*National Research Nuclear University (MEPhI), Moscow, Russia*
- <sup>39</sup>*Skobeltsyn Institute of Nuclear Physics of Moscow State University (SINP MSU), Moscow, Russia*
- <sup>40</sup>*Yandex School of Data Analysis, Moscow, Russia*
- <sup>41</sup>*Institute of Physics, University of Belgrade, Serbia*
- <sup>42</sup>*Stockholm University, Stockholm, Sweden*
- <sup>43</sup>*Uppsala University, Uppsala, Sweden*
- <sup>44</sup>*European Organization for Nuclear Research (CERN), Geneva, Switzerland*
- <sup>45</sup>*University of Geneva, Geneva, Switzerland*
- <sup>46</sup>*École Polytechnique Fédérale de Lausanne (EPFL), Lausanne, Switzerland*
- <sup>47</sup>*Physik-Institut, Universität Zürich, Zürich, Switzerland*
- <sup>48</sup>*Middle East Technical University (METU), Ankara, Turkey*
- <sup>49</sup>*Ankara University, Ankara, Turkey*
- <sup>50</sup>*H.H. Wills Physics Laboratory, University of Bristol, Bristol, United Kingdom*
- <sup>51</sup>*STFC Rutherford Appleton Laboratory, Didcot, United Kingdom*
- <sup>52</sup>*Imperial College London, London, United Kingdom*

<sup>53</sup>University College London, London, United Kingdom

<sup>54</sup>University of Warwick, Warwick, United Kingdom

<sup>55</sup>Taras Shevchenko National University of Kyiv, Kyiv, Ukraine

<sup>a</sup>Università di Bari, Bari, Italy

<sup>b</sup>Università di Bologna, Bologna, Italy

<sup>c</sup>Università di Cagliari, Cagliari, Italy

<sup>d</sup>Università di Napoli “Federico II”, Napoli, Italy

<sup>e</sup>Associated to Gyeongsang National University, Jinju, Korea

<sup>f</sup>Associated to Petersburg Nuclear Physics Institute (PNPI), Gatchina, Russia

<sup>g</sup>Also at Moscow Institute of Physics and Technology (MIPT), Moscow Region, Russia

<sup>h</sup>Consorzio CREATE, Napoli, Italy

<sup>i</sup>Università della Basilicata, Potenza, Italy

<sup>j</sup>Università del Sannio, Benevento, Italy

E-mail: [Richard.Jacobsson@cern.ch](mailto:Richard.Jacobsson@cern.ch)

**ABSTRACT:** The Search for Hidden Particles (SHiP) Collaboration has shown that the CERN SPS accelerator with its 400 GeV/c proton beam offers a unique opportunity to explore the Hidden Sector [1–3]. The proposed experiment is an intensity frontier experiment which is capable of searching for hidden particles through both visible decays and through scattering signatures from recoil of electrons or nuclei. The high-intensity experimental facility developed by the SHiP Collaboration is based on a number of key features and developments which provide the possibility of probing a large part of the parameter space for a wide range of models with light long-lived super-weakly interacting particles with masses up to  $O(10)$  GeV/ $c^2$  in an environment of extremely clean background conditions. This paper describes the proposal for the experimental facility together with the most important feasibility studies. The paper focuses on the challenging new ideas behind the beam extraction and beam delivery, the proton beam dump, and the suppression of beam-induced background.

**KEYWORDS:** Large detector systems for particle and astroparticle physics; Dark Matter detectors (WIMPs, axions, etc.); Neutrino detectors

ARXIV EPRINT: [1810.06880](https://arxiv.org/abs/1810.06880)

---

## Contents

<b>1</b>	<b>Introduction</b>	<b>1</b>
<b>2</b>	<b>Experimental set-up</b>	<b>3</b>
<b>3</b>	<b>Proton beam</b>	<b>5</b>
3.1	Achievable protons on target and beam sharing	7
3.2	Extraction beam loss and activation	8
3.3	Spill harmonic content	10
3.4	Beam line to proton target	11
<b>4</b>	<b>Proton target and target complex</b>	<b>13</b>
4.1	Design constraints for the proton target	13
4.2	Preliminary design of the target complex	15
<b>5</b>	<b>Suppression of beam-induced background</b>	<b>16</b>
5.1	Active muon shield	16
5.2	Vacuum vessel	17
<b>6</b>	<b>Conclusions</b>	<b>19</b>

---

## 1 Introduction

Given the absence of direct experimental evidence for Beyond the Standard Model (BSM) physics at the high-energy frontier and the lack of unambiguous experimental hints for the scale of new physics in precision measurements, it is plausible that the shortcomings of the Standard Model (SM) may have their origin in new physics only involving very weakly interacting, relatively light particles. Even in BSM scenarios associated with high mass scales such as in supersymmetry, many models contain light particles with suppressed couplings [4]. Considering the well-established observational evidence for a Hidden Sector in the form of Dark Matter, the structure and the phenomenology of the Hidden Sector may be more complex than just sourcing gravitational effects in the Universe. Non-minimal models of the Hidden Sector introduce various interactions and multiple types of hidden matter states charged only under the hidden interactions, as well as various types of portal interactions between the visible sector of ordinary matter and the Hidden Sector ([2, 5–10] and references therein).

As a consequence of the extremely feeble couplings for the portal interactions and the typically long lifetimes for the portal mediators, the low mass scales for hidden particles are far less constrained than the visible sector [2, 10]. In several cases, the present experimental and theoretical constraints from cosmology and astrophysics indicate that a large fraction of the interesting parameter space was beyond the reach of previous searches, but is open and accessible to current and future

facilities. While the mass range up to the kaon mass has been the subject of intensive searches, the bounds on the interaction strength of long-lived particles above this scale are significantly weaker.

Experimentally, the opportunity presents itself as an exploration at the intensity frontier with largest possible luminosity to overcome the very feeble interactions, and the largest possible acceptance to account for the typically long lifetimes. Beam-dump experiments are potentially superior to collider experiments in the sensitivity to GeV-scale hidden particles with their luminosities being several orders of magnitude larger than at colliders. The large forward boost for light states, giving good acceptance despite the smaller angular coverage and allowing efficient use of filters against background between the target and the detector, makes the beam-dump configuration ideal for searching for new particles with long lifetimes.

The recently proposed Search for Hidden Particles (SHiP) beam-dump experiment [1] at the CERN Super Proton Synchrotron (SPS) accelerator is designed to both search for decay signatures by full reconstruction and particle identification of SM final states and to search for scattering signatures of Light Dark Matter by the detection of recoil of atomic electrons or nuclei in a heavy medium. Since the hidden particles, such as dark photons, dark scalars, heavy neutral leptons, and axion-like particles, are expected to be predominantly accessible through the decays of heavy hadrons and in radiative processes, the SHiP Collaboration has proposed an experimental facility which maximises their production and the detector acceptance while providing an extremely clean background environment. This paper focuses on describing the experimental facility.

The proposal for the facility is based on a set of key themes. Firstly, the full exploitation of the SPS accelerator with its present performance allows producing up to  $2 \cdot 10^{20}$  protons on target (section 3.1) in five years of nominal operation without affecting the operation of the Large Hadron Collider (LHC), and while maintaining the current level of beam usage for fixed-target facilities and test beam areas. The combination of the intensity and the 400 GeV beam energy of the SPS proton beam produces yields of different light hidden sector particles which exceed those of existing or approved future facilities [3]. At the same time, it has been found that the beam induced background flux at 400 GeV is manageable with the help of a hadron absorber and a muon shield system (section 5.1). Secondly, the unique feature of slow extraction of a de-bunched beam over a timescale of around a second (section 3.2) allows a tight control of combinatorial background, and allows diluting the large beam power deposited on the proton target both spatially and temporally.

A set of innovative technological developments makes it possible to fully profit from these features. Several new techniques to improve the beam losses and irradiation inherent with slow beam extraction have been proposed and studied (section 3.2). Improvements in these areas are also of great interest to the existing CERN fixed target programs. The preliminary design of a long, complex, high-density primary proton target has been carried out (section 4.1). This target should be capable of coping with the large beam energy, and at the same time maximising the production of charm and beauty hadrons, and the production and interactions of photons, while minimising the production of neutrinos from pions and kaons. A yield of  $\mathcal{O}(10^{18})$  charmed hadrons and  $\mathcal{O}(10^{20})$  photons above 100 MeV are expected in five years of nominal operation. The feasibility of a target complex (section 4.2) which houses the proton target together with the associated services and remote handling, fully compatible with the radiation protection and environmental considerations, has been studied in detail. Furthermore, a new type of beam splitter magnet (section 3.4), which allows switching the beam to a short new transfer line to the SHiP experimental facility, while

keeping all of the current experimental facilities in the CERN North Area operational, has been developed. The experimental configuration includes a unique design of a muon shield (section 5.1) based on magnetic deflection to reduce the flux of muons by six orders of magnitude in the detector acceptance. A  $\sim 1700\text{ m}^3$  experimental vacuum chamber (section 5.2), kept at a pressure of 1 mbar, allows suppressing residual neutrino-induced background.

Currently, CERN has no high-intensity experimental facility which is compatible with the full power of the SPS. CERN's North Area has a large space next to the SPS beam transfer lines which is for the most part free of structures and underground galleries, and which could accommodate the proposed facility. In addition, this facility is being designed with future extensions in mind.

At the energy of the SPS, the fully leptonic decays of the  $D_s$  mesons are the principal source of tau neutrinos, with an expectation of  $O(10^{16})$  tau neutrinos in five years of nominal operation. Thus, while the requirements for the experimental facility for the hidden particle search makes it unsuitable for neutrino oscillation physics, the setup allows studying interactions of tau and anti-tau neutrinos at unprecedented precision. With a ten-tonne  $\nu$ -target placed in front of the vacuum volume and equipped with suitable detectors, about  $3 \cdot 10^4$  ( $2 \cdot 10^4$ ) interactions of tau (anti-tau) neutrinos are expected within the geometrical acceptance. The first direct observation of the anti-tau neutrino and the measurement of tau neutrino and anti-tau neutrino cross-sections are among the physics goals of the proposed experiment. As charm hadron decays are also a source of electron and muon neutrinos, SHiP will also be able to study neutrino-induced charm production from all flavours with a dataset which is more than one order of magnitude larger than those collected by previous experiments.

## 2 Experimental set-up

The experimental requirements, as dictated by the phenomenologies of the different Hidden Sector models, are very similar. This allows the design of a general-purpose layout based on a global optimisation of the experimental facility and of the SHiP detector. Figure 1 shows an overview of the experimental facility from the proton target to the end of the Hidden Sector detector. The main challenges concern the requirement of a highly efficient reduction of the very large beam-induced background, and an efficient and redundant tagging of the residual background down to below 0.1 events in the projected sample of  $2 \cdot 10^{20}$  protons on target. Despite the aim to cover long lifetimes, the sensitive volume should be situated as close as possible to the proton target due to the relatively large transverse momentum of the hidden particles resulting from the limited boost of the heavy hadrons (figure 2). The minimum distance is only constrained by the need of a system to absorb the electromagnetic radiation and hadrons emerging from the proton target and to reduce the beam-induced muon flux.

The proton target, described in section 4.1, is followed by a 5 m long hadron absorber. The physical dimensions of the absorber are mainly driven by the radiological requirements. In addition to absorbing the hadrons and the electromagnetic radiation, the iron of the hadron absorber is magnetised over a length of 4 m. The applied dipole field makes up the first section of the active muon shield (section 5.1) which is optimised to sweep out of acceptance the entire spectrum of muons up to  $350\text{ GeV}/c$ . The remaining part of the muon shield follows immediately downstream

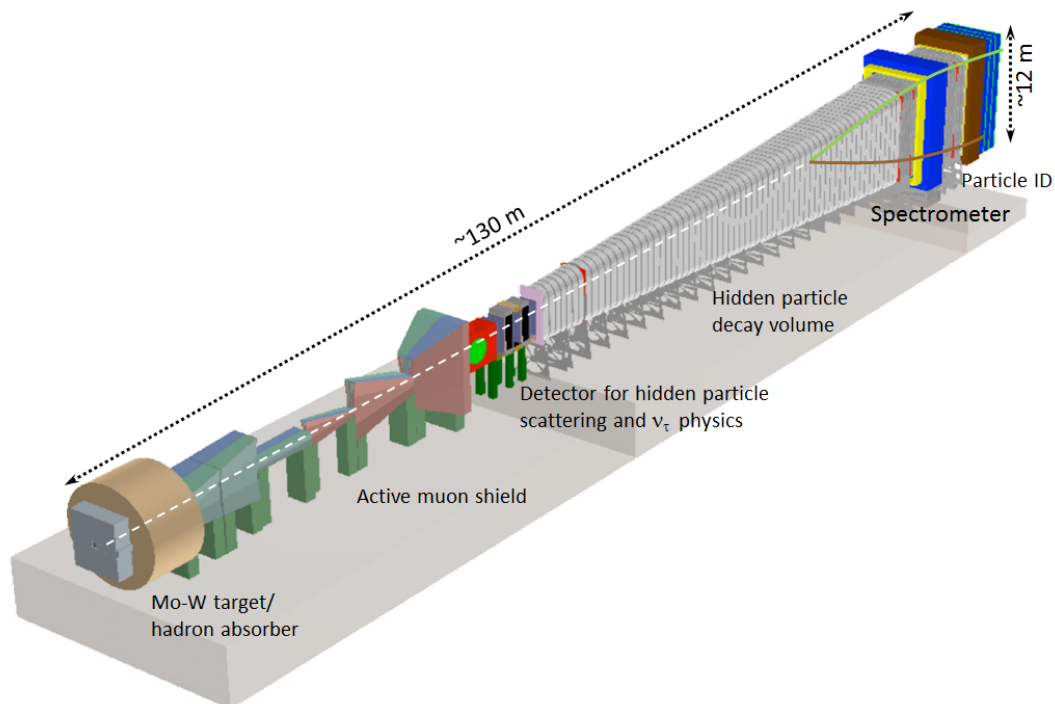


**Figure 1.** Overview of the target and experimental area for the SHiP detector as implemented in the physics simulation.

of the hadron absorber in the experimental hall and consists of a chain of magnets which extends over a length of  $\sim 40$  m.

The SHiP experiment incorporates two complementary apparatuses. The detector system immediately downstream of the muon shield is optimised both for recoil signatures of hidden sector particle scattering and for neutrino physics. It is based on a hybrid detector similar to what was developed by the OPERA Collaboration [11] with alternating layers of nuclear emulsion films and electronic trackers, and high-density  $\nu$ -target plates. In addition, the detector is located in a magnetic field for charge and momentum measurement of hadronic final states. The detector  $\nu$ -target mass totals  $O(10)$  tonnes. The emulsion spectrometer is followed by a muon identification system. This also acts as a tagger for interactions in the muon filters which may produce long-lived neutral mesons entering the downstream decay volume and whose decay may mimic signal events.

The second detector system aims at measuring the visible decays of Hidden Sector particles to both fully reconstructible final states and to partially reconstructible final states with neutrinos. The detector consists of a 50 m long decay volume (section 5.2) followed by a large spectrometer with a rectangular acceptance of 5 m in width and 10 m in height. The length of the decay volume is defined by maximising the acceptance to the hidden particle decay products (figure 2) given the transverse size of the spectrometer. In order to suppress the background from neutrinos interacting in the fiducial volume, it is maintained at a pressure of  $O(10^{-3})$  bar. The spectrometer is designed to accurately reconstruct the decay vertex, the mass, and the impact parameter of the hidden particle trajectory at the proton target. A set of calorimeters and muon stations provide particle identification. The system is optimised to detect as many final states as possible in order to be sensitive to, and

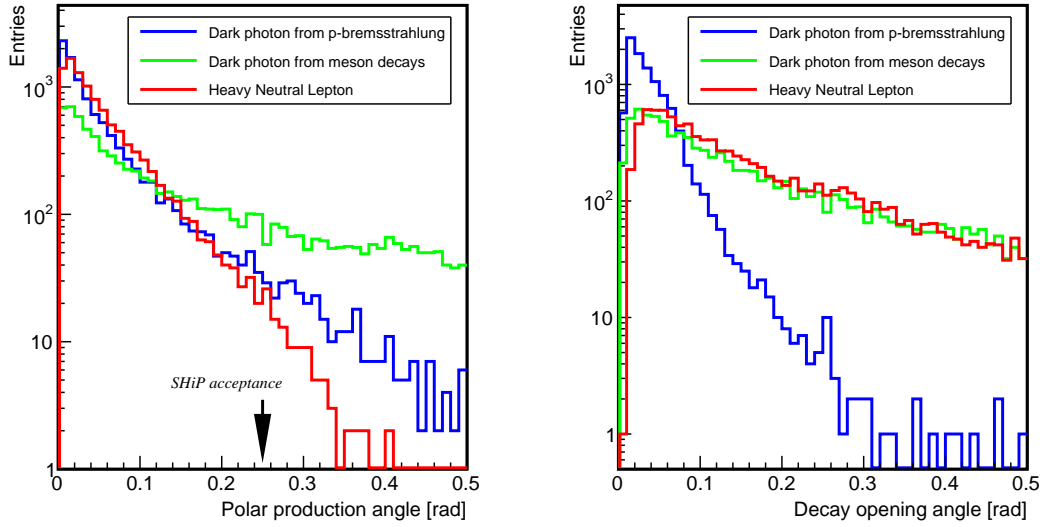


**Figure 2.** (Left) Polar production angle with a beam momentum of  $400 \text{ GeV}/c$  for dark photons ( $A$ ) produced in proton bremsstrahlung ( $m_A = 2.0 \text{ GeV}/c^2$ ) and in meson decays ( $m_A = 0.9 \text{ GeV}/c^2$ ), and for heavy neutral leptons (HNL) ( $m_{\text{HNL}} = 1.0 \text{ GeV}/c^2$ ) from decays of charm hadrons. The arrow indicates the acceptance of the SHiP fiducial volume, given by the transverse size of the decay volume (Right) Decay opening angles for two-body decays of the same three cases. The geometry of the decay volume has been optimized given the aperture of the spectrometer and the hidden particle kinematics.

discriminate between, a very wide range of models. A dedicated timing detector with  $\sim 100 \text{ ps}$  resolution provides a measure of coincidence in order to reject combinatorial backgrounds. The decay volume is surrounded by background taggers to identify neutrino and muon inelastic scattering in the vacuum vessel walls which may produce long-lived neutral SM particles, such as  $K_L$  etc. The muon shield and the SHiP detector systems are housed in a  $\sim 120 \text{ m}$  long underground experimental hall at a depth of  $\sim 15 \text{ m}$ . To minimise the background induced by the flux of muons and neutrinos interacting with material in the vicinity of the detector, no infrastructure systems are located on the sides of the detector, and the hall is  $20 \text{ m}$  wide along the entire length.

Figure 3 shows an overview of the civil engineering required for the experimental facility for SHiP. All civil engineering works are fully located within existing CERN land on the Preessin campus. This location is very well suited to house the experimental facility, owing to the stable and well understood ground conditions, accessible services and very limited interference with existing buildings, galleries and road structures. By maintaining the entire beam line horizontal and at the same level as the existing splitter region at the end of the SPS extraction line, the experimental hall is conveniently situated at a depth of about  $15 \text{ m}$ , which is compatible with the requirements from radiation protection while still allowing easy direct access from above without a shaft.

### 3 Proton beam

The proposed implementation of the SHiP experimental facility is based on minimal modifications to the SPS complex and a maximum use of the existing accelerator and beam lines. Figure 4 shows

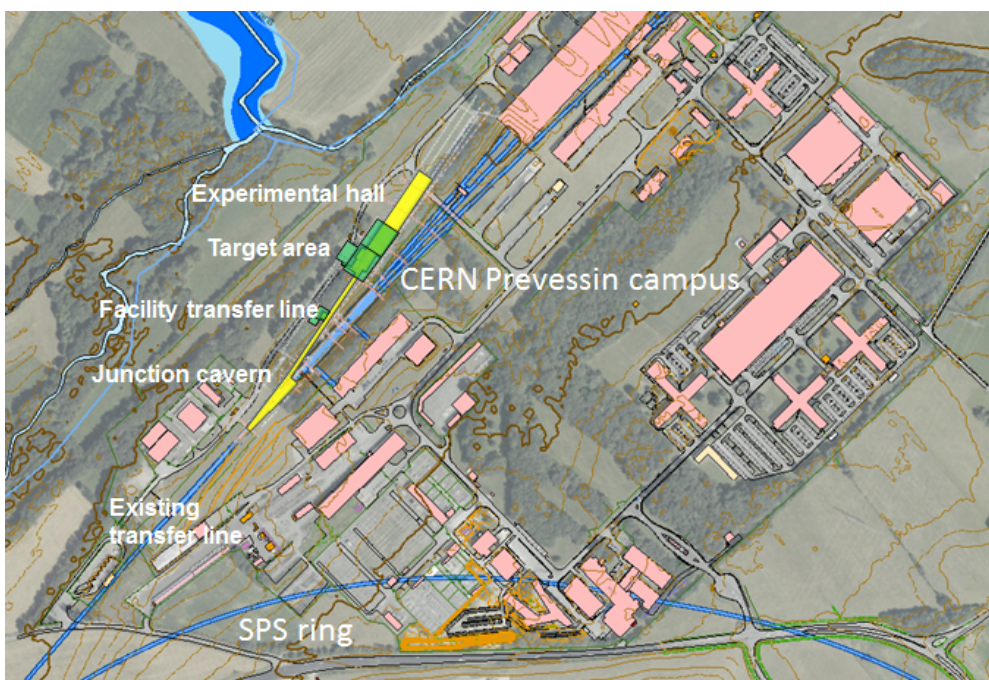


**Figure 3.** Overview of the required civil engineering for the proposed experimental facility for SHiP on the CERN Preveessin campus. The beam-axis is at a depth of about 10 m which allows trenching the entire complex from the surface. New or reworked construction in yellow (underground) and green (surface); existing tunnels in blue.

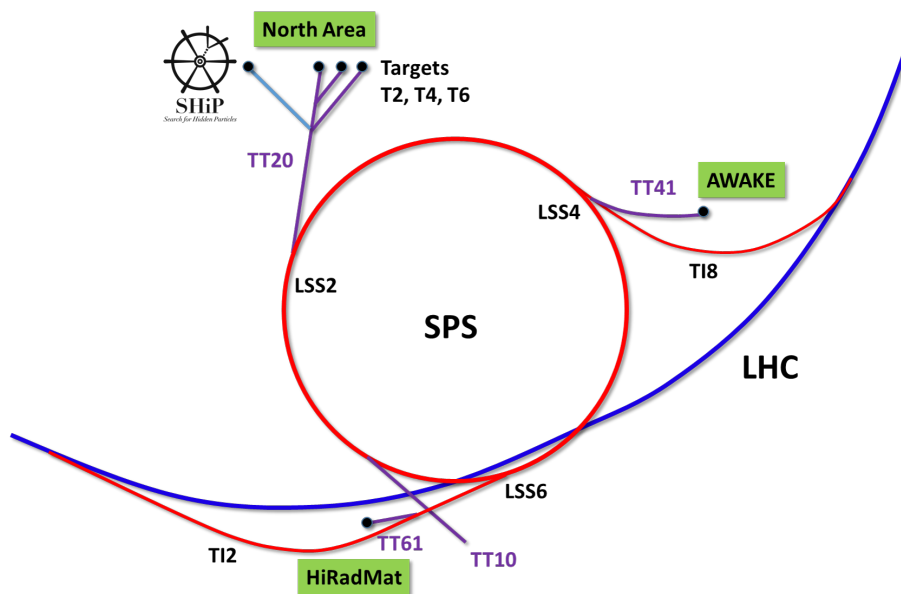


**Figure 4.** Overview of the SPS accelerator complex. The SHiP experimental facility is located in the North Area and shares the TT20 transfer line with the fixed target programs.



schematically the proposed location of the experimental facility at the CERN North Area site. The facility shares about 600 m of the existing TT20 transfer line with the other North Area facilities.

At the SPS, the most favourable experimental conditions for SHiP are obtained with a proton beam momentum of around 400 GeV/c. Based on the SPS in its current state and in view of its past performance, a nominal beam intensity of  $4 \cdot 10^{13}$  protons on target per spill is assumed for the design of the experimental facility and the detector.

In order to reduce the probability of combinatorial background events from residual muons entering the detector decay volume and to respect the limits on the instantaneous beam power deposited in the proton target, SHiP takes advantage of the SPS slow extraction used to provide beam to the CERN North Area through the Long Straight Section 2 of the SPS. The minimum SPS cycle length which is compatible with these requirements is 7.2 s. A beam cycle with a slow extraction of around one second has already been demonstrated in the studies for the experimental facility for SHiP (figure 5).

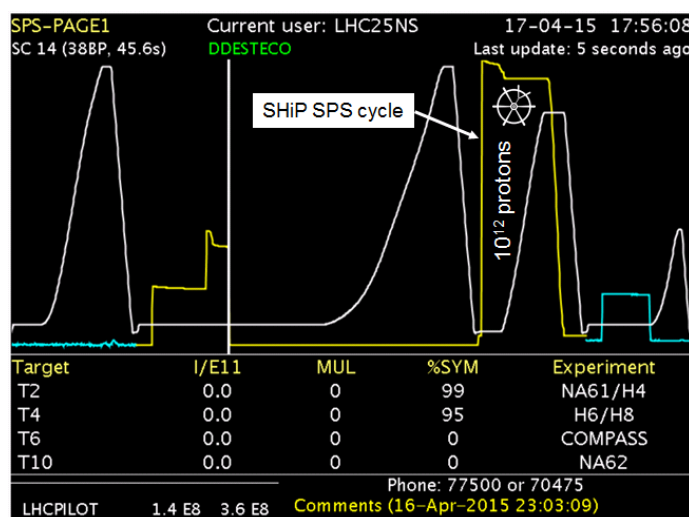


**Figure 5.** First slow beam extraction tests from the SPS for SHiP with the specific length of about 1 s. The tests were performed at low intensity of about  $10^{12}$  protons/s. The yellow line represents the proton beam intensity in the SPS and the white line represents the SPS beam energy.

### 3.1 Achievable protons on target and beam sharing

The SHiP operational scenario is based on a similar fraction of beam time as the recently completed CERN Neutrinos to Gran Sasso (CNGS) program, and assumes the operational performance of the SPS in recent years [12]. Compatibility with the existing North Area program is important, and figure 6 shows the number of protons on the current North Area targets as a function of the number of protons on the SHiP proton target for 217 days of physics, corresponding to the situation for the 2011 run. It has been assumed that 10% of the SPS scheduled physics time is devoted to run LHC pilot cycles and another 10% to run LHC nominal cycles. The assumed sharing delivers an annual yield of  $4 \cdot 10^{19}$  protons on target to the SHiP experimental facility and a total of  $1 \cdot 10^{19}$  to the other physics programs at the CERN North Area. The physics sensitivities of the experiment are

calculated based on acquiring a total of  $2 \cdot 10^{20}$  protons on target which may thus be achieved in five years of nominal operation.

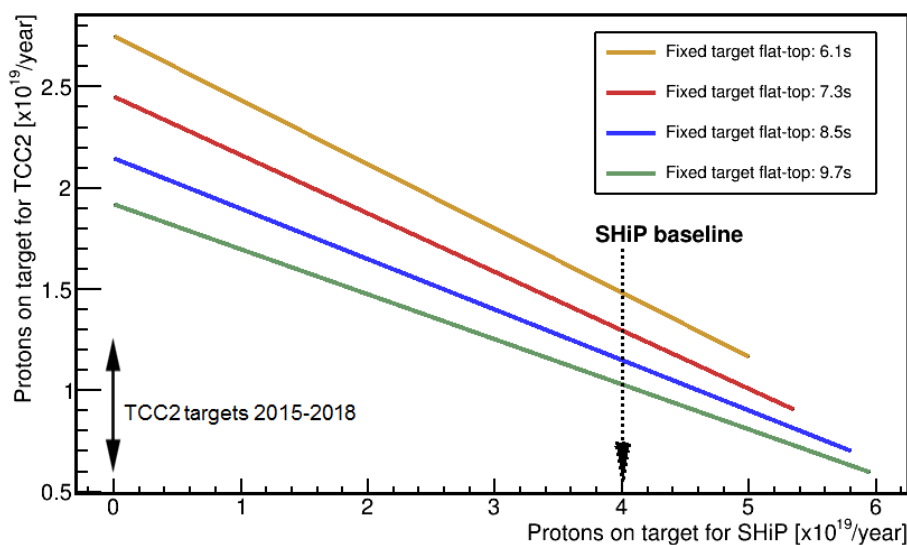


**Figure 6.** The expected number of protons on the current North Area targets (TCC2) as a function of the number of protons on target for the SHiP experimental facility with a 1.2 s spill length. The plot shows the performance for different spill durations for the current fixed target facilities between 6.1–9.7 s. The range of the numbers of protons per year delivered to the North Area targets in the years 2015–2018 is indicated. The preferred working point for SHiP is indicated by “SHiP baseline”.

### 3.2 Extraction beam loss and activation

The slow extraction from the SPS exploits a third-order resonance to achieve a controlled continuous amplitude growth of the transverse oscillations of the circulating protons. The amplitudes grow over several tens of thousands of turns until a slice of the beam crosses the wires of the electrostatic septa, and is guided into the TT20 beam line aperture continuously, as shown in figure 7, until the circulating beam in the SPS is completely extracted. The field wires have finite width and inevitably intercept a fraction of the beam, leading to beam losses of the order of 2% of the total intensity. This is an important difference with respect to CNGS operation, which used essentially loss-free fast extraction.

In addition to the increased risk of sparking and damage to the wires due to heating and vacuum pressure rise, the main consequences of beam loss are radio-activation of the extraction region, accumulated radiation damage to sensitive equipment and cables, and the increased cool-down times in case of interventions for repair or maintenance. Activation and personnel dose is already a serious issue in the SPS, and currently reach operational limits with around  $1.2 \cdot 10^{19}$  protons slowly extracted per year.

To extrapolate to the operation of the experimental facility for SHiP, the experience from operating the West Area Neutrino Facility (WANF) has been studied. Approximately half of the total integrated number of protons foreseen for SHiP was extracted to WANF with fast-slow (half-integer) extraction during a five-year period at the end of the 1990’s. More recent experience of

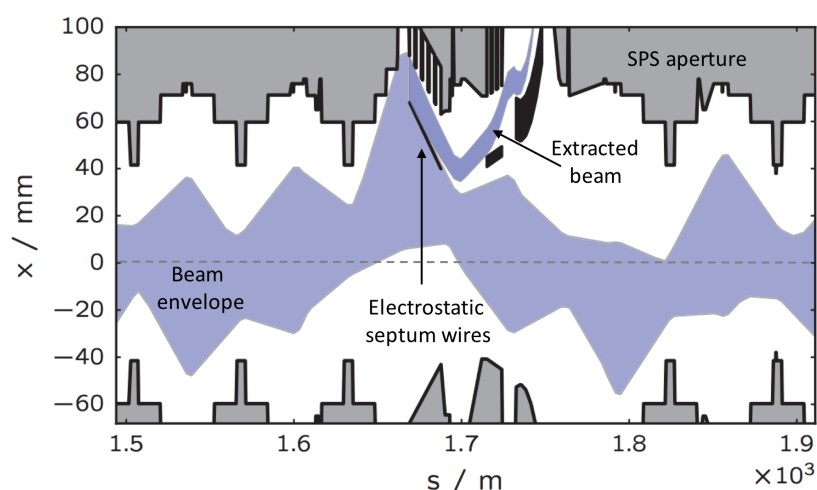


**Figure 7.** Envelope of the circulating and the extracted beam along the SPS extraction region, showing the machine aperture and the wires of the electrostatic septum. The passive diffuser or bent crystal are located just upstream of the electrostatic septum to reduce the density of protons impacting the wire.

sending beam to the North Area has also been considered, e.g. over  $2 \cdot 10^{19}$  protons were slowly extracted to the North Area during 2007. The studies show that a factor of four decrease in the potential radiation dose to personnel is required to achieve the SHiP baseline intensity of  $4 \cdot 10^{19}$  protons on target per year. This improvement will need to come from a combination of reduced beam loss, reduced activation per lost proton, and improved or remote interventions.

Extraction losses have been improved already by increasing the stability of the extraction with the help of a feed-forward system on the main quadrupole current to compensate for the ripple induced by the main electricity grid. Also, the septum wires are regularly realigned with the help of improved instrumentation and algorithms. However, a significant decrease (i.e. a factor two or more) can only be expected with substantial changes to the extraction dynamics. Studies involving two techniques based on coherent and incoherent scattering of the protons upstream of the septum (figure 7), that would otherwise hit the septum wires, are currently being tested, along with ways of modifying the transverse phase space distribution to reduce particle density at the wires.

The first technique is based on a passive beam scattering device. It consists of a short, thin blade of a high-Z material located upstream of the electrostatic septum wires. The blade intercepts a thin slice of the beam in order to generate an angular spread which reduces the transverse beam density at the wires, resulting in an overall reduction of the beam losses. Simulations show that this technique could bring up to a factor two improvement (figure 8). The device is also straightforward to deploy and operate. A prototype diffuser to benchmark the simulations with experiment is being designed and built. It will be installed in the SPS Long Straight Section 2 (LSS2 in figure 4) and tested with beam in 2018.

The second technique employs a thin bent crystal placed upstream of the septum in order to channel away the misdirected protons into the extraction aperture. Since the channeling is very sensitive to the angular alignment of the crystal, the efficiency of this technique depends strongly on the angular spread of the beam and the orbit stability. A proof-of-principle experiment with

coasting beam has already demonstrated [13] that beam can be extracted into the TT20 transfer line using a bent crystal.

Both the crystal-assisted slow extraction and the diffuser rely on stable conditions and an accurate alignment of the septum wires and the scattering device. A movement of the extraction separatrix in position and more importantly angle is, however, inherent to the SPS extraction mechanism optimised for low beam loss. Use of a dynamic extraction bump could compensate in real-time for these changes in the closed orbit. This could also permit a faster realignment of the beam with the septa, instead of the time-consuming mechanical realignment of the septa.

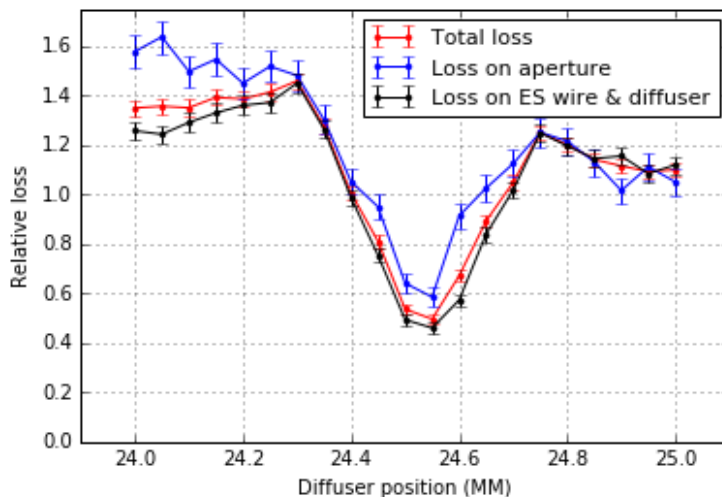


**Figure 8.** Relative loss of protons in arbitrary units as a function of the transverse position from simulation of a 3 mm long, 0.24 mm wide tungsten-rhenium diffuser. The sum of the loss on the diffuser and the electro-static septum (ES) wires is lower than the total loss with ES wires alone, because the scattering from the diffuser reduces the particle density at the ES sufficiently to result in an overall loss reduction. A factor two improvement is obtained for the optimal position.

A final set of studies focuses on manipulation of the transverse phase-space distribution, using either higher-order multipole magnets or a pair of septum elements in which the configuration of the conductor and magnetic material is used to separate the high-field region from the zero-field region without intervening physical material (“massless septa”), to reduce the particle density at the septum wires without increasing losses elsewhere in the extraction system. These approaches are being studied in simulation and proof-of-principle measurements have been planned for 2018. First studies of combining these techniques with the diffuser, or the crystal, indicate that it can potentially improve the loss reduction well beyond a factor two.

The different mitigation techniques are also complemented by studies of alternative materials for construction of septum sub-systems like titanium or carbon nanotubes to reduce activation, and developments of machine assisted intervention techniques.

### 3.3 Spill harmonic content

Suppression of combinatorial background from residual muons produced in the SHiP proton target rely on determining the time coincidence of the reconstructed tracks in the SHiP spectrometer with

the help of a timing detector. The requirement on time resolution is derived from the likelihood of coincidental muons. The likelihood is directly related to the proton interaction rate in the target, which should have minimal variations. The baseline beam parameters and the average residual muon flux in the detector acceptance requires a timing detector with a time resolution of  $O(100)$  ps. Rejection of combinatorial background is thus one of the main drivers for a highly uniform extraction of the spill.

In 2017 sample spills were generated with the SHiP beam cycle, with the encouraging result that the spill harmonic content is not worse than for the longer spills used for the North Area. Contributions are dominated at low frequency by the effect of harmonics on the main electricity grid affecting the extraction beam dynamics. To this end, improvements of the stability of the slow extraction are also aiming at improving the uniformity of the spill structure. At higher frequencies the residual radio frequency structure of the beam dominates.

### 3.4 Beam line to proton target

The location of the SHiP proton target in the North Area allows the re-use of about 600 m of the present TT20 transfer line, which has sufficient aperture for the slow-extracted beam at 400 GeV/c. The new dedicated beam transfer line to the experimental facility for SHiP branches off at the end of the TT20 transfer line with the help of a set of newly proposed bi-polar splitter magnets which replaces the existing ones. The new magnets allow both maintaining the present function of splitting the beam between the proton target for the experimental area currently hosting the COMPASS experiment [14] and the rest of the existing North Area facilities, and to alternatively switch the entire spill to the dedicated transfer line for SHiP, on a cycle-by-cycle basis. The present magnet is an in-vacuum Lambertson septum with a yoke machined from solid iron, with the coil based on a water-cooled lead of copper with an insulation of compacted MgO powder [15]. For the new magnets a laminated yoke is required in order to rapidly perform the polarity switch between SPS cycles, which implies ramping the field reliably in about 2 s. The new magnets, shown in figure 9, must also have a larger horizontal aperture, as the beam is deflected to different sides of the magnet axis for SHiP and for North Area operation. R&D and prototyping of the laminated yoke is underway to study the very tight mechanical tolerances required in the septum region in order to maintain low beam losses. Similar MgO coil technology as used in the existing splitter will provide the required radiation resistance.

A 380 m long new section of beam line is needed, which is matched to the existing TT20 transfer line (figure 10) and which brings the beam up to the new target complex. A preliminary design has been made which exploits 17 standard SPS warm bending magnets, running at a conservative field of 1.73 T producing an angular beam deflection of 8 mrad each, to increase as much as possible the distance between the new and existing beam lines. A maximum deflection angle to exit from the tunnel of the existing beam line is beneficial to reduce the longitudinal extent of the civil engineering works in the crucial junction region. The bending dipoles downstream of the splitter are grouped into a single dipole unit as early as possible, with four subsequent standard SPS half-cells of four dipoles, each separated by a quadrupole. The powering scheme for the TT20 transfer line remains largely unchanged up to the switch element with cycle-to-cycle rematching of the last nine quadrupoles before the splitter and steering, to allow the entire beam cross-section to pass

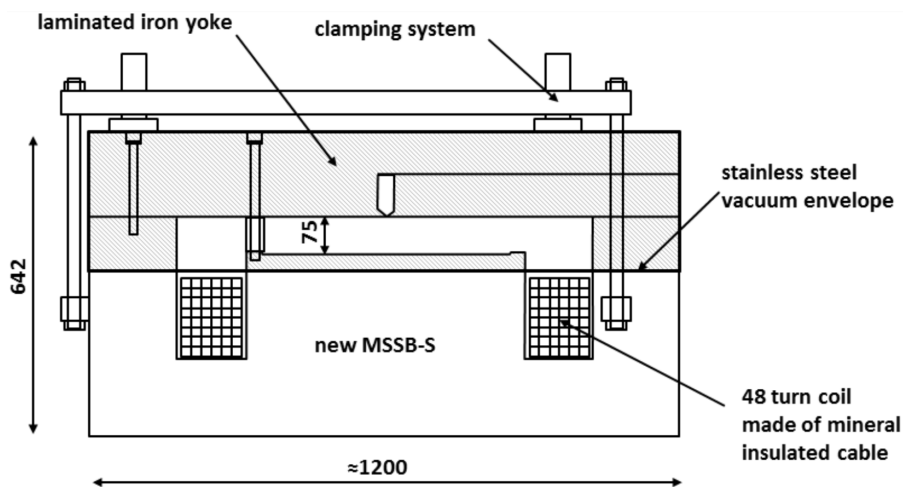


**Figure 9.** Cross-section of the new “MSSB-S” splitter magnet. The cycle-to-cycle polarity switching requires a laminated iron yoke. The 7.5 mm beam gap is made significantly wider than in the original splitter and extends to both sides of the septum to accommodate both the deflection of the SHiP beam to one side and alternatively splitting the beam between the other North Area facilities on the other side. All dimensions are in mm.

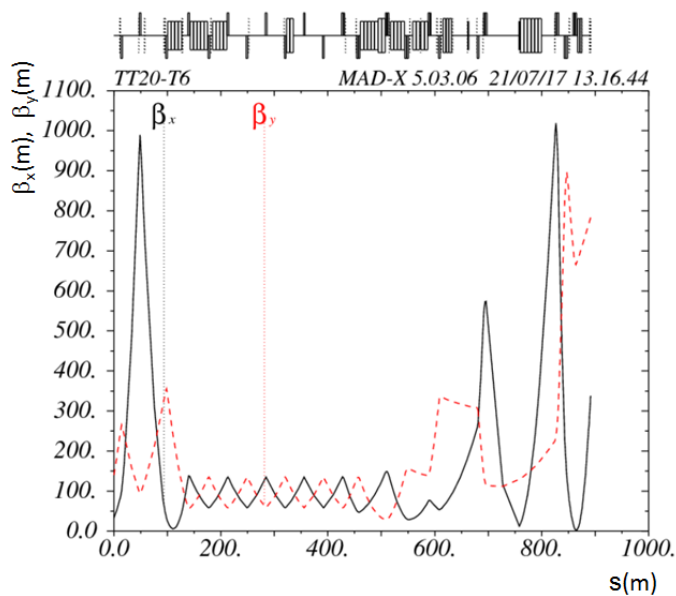


**Figure 10.** Optics shown by the beta function in the horizontal (black solid line) and vertical plane (red dashed line) along the entire length of the beam line from the SPS extraction ( $s = 0$  m) in LSS2 to the SHiP proton target located at around  $s = 900$  m. The new section of beam line is matched to the existing TT20 line to give the required beam size at the target.

through the dipole aperture with very low losses. The quadrupoles in TT20 are already laminated and suited to cycle-to-cycle switching.

For the new beam line, around six new corrector dipoles are assumed. In addition, five standard SPS quadrupole magnets will be required to control the vertical beam size through the dipole apertures, and provide flexibility and tunability of the beam spot size and dispersion at the proton target. In order to produce sufficient dilution of the beam power in the SHiP proton target, the slow extraction is combined with a beam spot of at least 6 mm root-mean square in both planes and a large sweep of the beam over the target surface. The beam sweep is implemented with two orthogonal kicker magnets located after the last bending dipole magnet at 120 m upstream of the target, with Lissajous powering functions to produce a circular sweep. With a free drift length for the beam of about 120 m and a bending angle of 0.25 mrad per plane, it is possible to achieve a sweep radius of 30 mm. Since the survival of the proton target relies critically on the beam dilution, the SPS beam is interlocked with the beam dilution system and the instantaneous loss rate at the target.

The overall layout and clearances allow civil engineering to take place along the entire experimental facility starting from the middle of the new transfer line and up to the end of the experimental hall during beam operation for the other North Area facilities.

## 4 Proton target and target complex

### 4.1 Design constraints for the proton target

The physics scope of the SHiP experiment requires a proton target which maximises the production of  $D$  and  $B$  mesons, and photons. At the same time, the proton interactions give rise to copious direct production of short-lived meson resonances, as well as pions and kaons. While a hadron absorber of a few meters of iron is sufficient to absorb the hadrons and the electromagnetic radiation emerging from the target, the decays of the pions, kaons and short-lived meson resonances result in a large flux of muons and neutrinos. In order to reduce the flux of neutrinos, in particular the flux of muon neutrinos and the associated muons, the pions and kaons should be stopped as efficiently as possible before they decay. The target should thus be made of a material with the highest possible atomic mass and atomic charge. It should be sufficiently long to intercept virtually all of the proton intensity and to contain the majority of the hadronic shower with minimum leakage. Simulation [16] shows that re-interactions of primary protons and interactions of secondaries produced in the nuclear cascades also contribute with a significant amplification of the signal yields. For instance, in the case of charm production, the cascade processes contribute by more than doubling the yield as compared to what is expected from only the primary proton-nucleus interactions.

The very high instantaneous beam power of  $\sim 2.56$  MW per spill of 1.2 s and the average deposited power of  $\sim 355$  kW over consecutive spills spaced by the SPS cycle of 7.2 s make the design of the proton target, its radiological protection, and its cooling very challenging aspects of the facility. Studies show that the required performance may be achieved with a longitudinally segmented hybrid target consisting of blocks of four nuclear interaction lengths (58 cm) of titanium-zirconium doped molybdenum alloy (TZM, density  $10.22$  g/cm<sup>3</sup> as compared to  $10.28$  g/cm<sup>3</sup> for pure Mo) in the core of the proton shower, followed by six nuclear interaction lengths (58 cm) of pure tungsten (density  $19.3$  g/cm<sup>3</sup>). A medium-density material is required in the first half of the

target in order to reduce the energy density and create acceptable stresses in the blocks. The blocks are all interleaved with 5 mm wide slots for water cooling. Tantalum alloy cladding of the TZM and the tungsten blocks is considered in order to prevent corrosion and erosion by the high flow rate of the water cooling. In order to respect the material limits derived from thermo-mechanical stresses, the thickness of each block together with the location of each cooling slot has been optimised to provide a relatively uniform energy deposition and sufficient energy extraction. Using FLUKA Monte Carlo simulations [17] and ANSYS finite element analyses, the preliminary target design has been shown to limit the peak power density in the target blocks to below  $850 \text{ J/cm}^3/\text{spill}$  and compressive stresses below 300 MPa in the core of the shower for a 6 mm RMS spot size and 30 mm single-turn sweep radius. Figure 11 (top) shows the preliminary proton target as designed for the SHiP Technical Proposal [1]. The total dimensions of the target are 1.2 m in length with transverse dimensions of  $30 \times 30 \text{ cm}^2$ . Figure 11 (bottom) shows the maximum energy density per spill of  $4 \cdot 10^{13}$  protons on target.

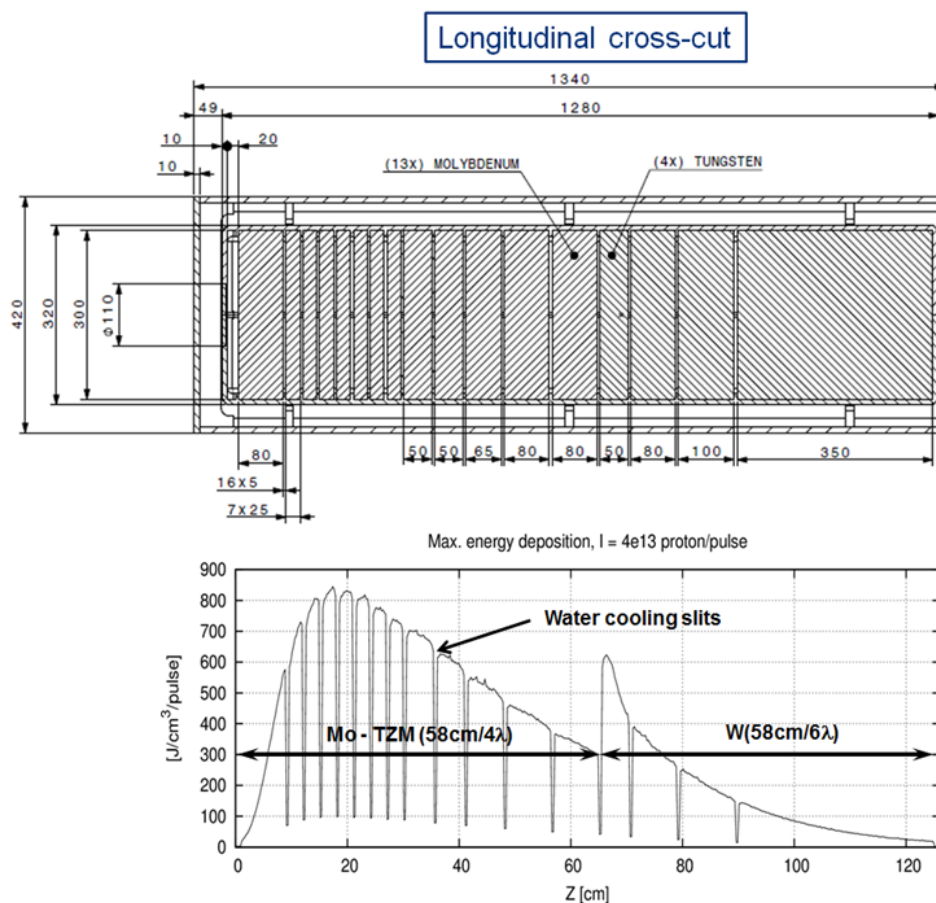


**Figure 11.** (Top) Preliminary design of the proton target configuration. All dimensions are in mm. The right-slanted hatched region in the top drawing shows the TZM blocks and the left-slanted hatched region the tungsten blocks. (Bottom) Peak energy deposition in the proton target during a spill of  $4 \cdot 10^{13}$  protons.

Over the long term, the very high proton cumulated dose alters the physical and mechanical properties of the target material such as thermal conductivity and yield strength. First estimates of



the radiation damage in terms of the displacement per atom, as well as the internal production of hydrogen and helium gas, indicate that the current target design ensures the longevity of the target, but the limited availability of data in literature call for accelerated aging studies of the materials with irradiation. A replica target is being designed and built for testing with beam in 2018.

The proton target blocks are assembled in a double-walled vessel. The inner vessel enforces the high-flow water circulation between the proton target blocks and ensures a pressurised water cooling of 15–20 bar in order to avoid water boiling in contact with the target blocks. A flow rate of  $\sim 180 \text{ m}^3/\text{h}$  is envisaged. The outer vessel acts as a safety hull to contain hypothetical leaks, and is filled with an inert gas to prevent corrosion.

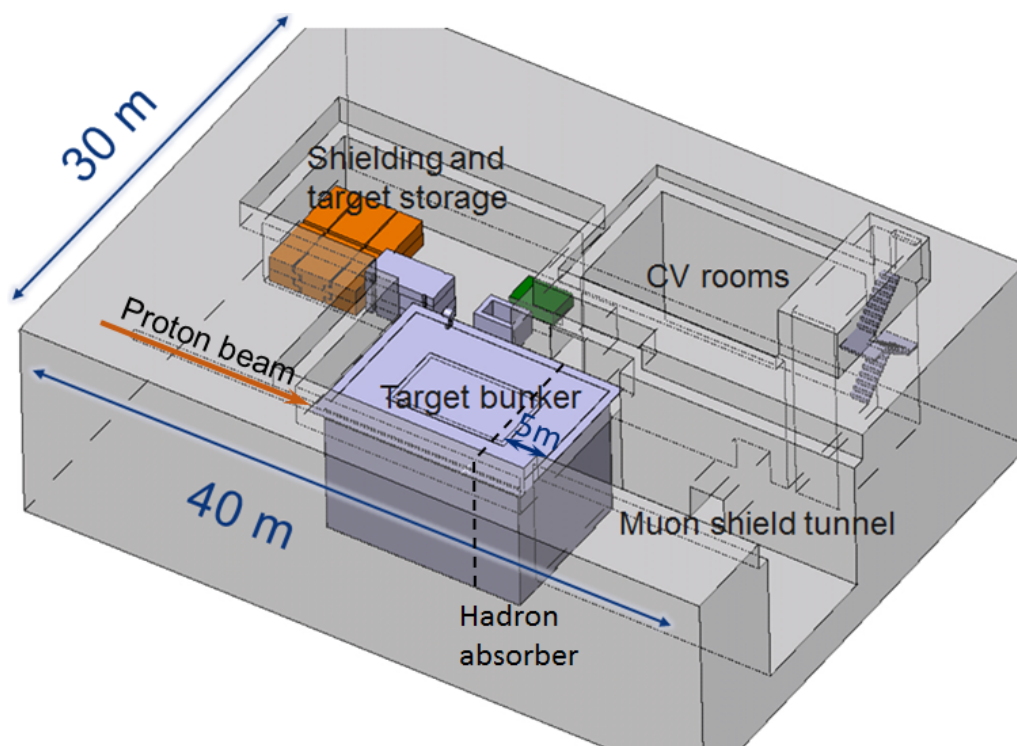


**Figure 12.** Overview of the main components of the target complex. The proton beam line arrives from the left of the target bunker. The target is located in the centre of the target bunker and the first section of the muon shield in terms of the magnetised hadron absorber is integrated in the downstream end of the bunker.

## 4.2 Preliminary design of the target complex

An overview of the target complex is shown in figure 12. In order to contain the radiation generated by the beam impacting on the proton target, the target is embedded in a  $\sim 450 \text{ m}^3$  cast-iron bunker. The inner part of the cast iron shielding ( $\sim 20 \text{ m}^3$ ) is water cooled by means of embedded stainless steel pipes in order to extract the average power of 20 kW which is leaking out of the target during operation. The outer part of the shielding is fully passive. The assembly has been designed with emphasis on reliability, remote handling and with the aim of being multi-purpose, i.e. allowing exchange of the proton target and the shielding configuration for alternative uses in future experiments. To minimise the irradiation of the primary beam line, the upstream shielding has only a

limited passage of about 20 cm in diameter for the beam vacuum chamber. The 5 m thick downstream shielding acts as a hadron absorber with the double objective of absorbing the secondary hadrons and the residual non-interacting protons emerging from the target, and significantly reducing the exposure of the downstream active muon shield to radiation. The overall shielding is designed to respect the limits from radiological and environmental protection applicable at CERN.

A helium-vessel containing high-purity helium gas (> 99%) at atmospheric pressure encloses the SHiP proton target and the entire iron shielding. This is required to protect the equipment from radiation-accelerated corrosion as well as to avoid the production of high-mass radioactive isotopes from secondary neutrons interacting with air.

## 5 Suppression of beam-induced background

### 5.1 Active muon shield

The total flux of muons emerging from the proton target with a momentum larger than 1 GeV/ $c$  amounts to  $O(10^{11})$  muons per spill of  $4 \cdot 10^{13}$  protons. In order to control the background from random combinations of muons producing fake decay vertices in the detector decay volume and from muon deep inelastic scattering producing long-lived neutral particles in the surrounding material, and to respect the occupancy limits of the sub-detectors, the muon flux in the detector acceptance must be reduced by several orders of magnitude over the shortest possible distance. To this end, a muon shield entirely based on magnetic deflection has been developed [18, 19] (figure 1).

Figure 13 shows schematically the field configuration of the muon shield magnets. The first section of the muon shield starts within the hadron absorber with the integration of a coil which magnetises the iron shielding block, and continues with a set of freestanding magnets over a length of  $\sim 20$  m. The purpose of the first section is to deflect the positively and negatively charged muons on either side of the beam axis. As shown by the trajectories of the muons in figure 13, lower momentum muons and muons with larger transverse momenta are swept out of the core field before the end of the first section. Due to the return fields, a large fraction of these muons are bent back towards the detector acceptance. For this reason, the second section serves two purposes. In addition to providing further bending power to deflect out of acceptance the higher momentum muons, it should also give the lower momentum muons another magnetic kick outwards. This 20 m section therefore consists of a series of magnets with the return field close to the  $z$ -axis. The residual muons entering the decay volume after the muon shield are mainly due to stochastic processes involving large energy losses and large angle scattering in the muon shield material.

In order to achieve a high magnetic flux of 1.7–1.8 T in the core at low current and with coils of small cross-sections, grain-oriented steel is considered as the yoke material for the freestanding magnets [18]. The actual field configuration for the entire muon shield has been optimised with the help of machine learning techniques using a large sample of muons from a full GEANT4 [20] simulation of  $2 \cdot 10^{10}$  protons on the SHiP proton target. Engineering studies are underway to study the optimal assembly techniques. The total mass of the muon shield magnets is of the order of 1500 tonnes. The current design allows reducing the rate of residual muons above 1 GeV/ $c$  reconstructed in the SHiP spectrometer to an acceptable rate of  $O(10^5)$  per spill.

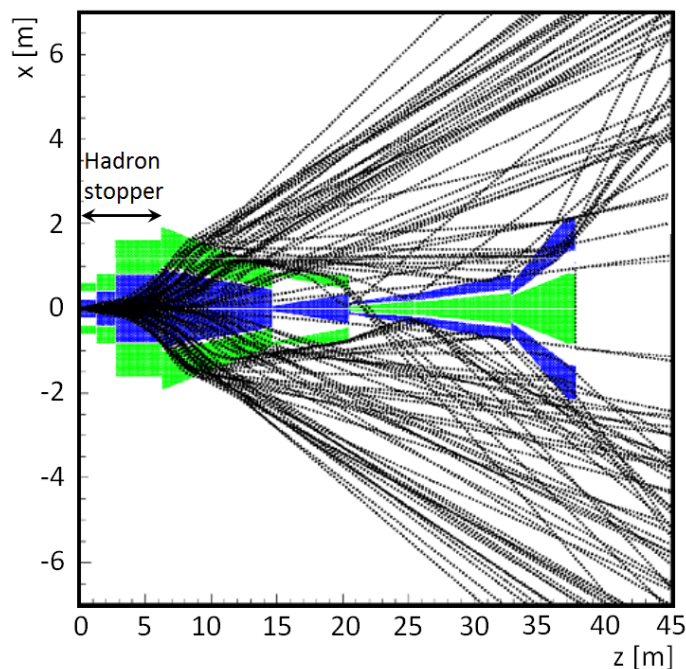


**Figure 13.** Horizontal cross-section of the muon shield magnet configuration at the level of the beam-axis. The direction up/down of the vertical magnetic field is illustrated by the blue/green colour of the iron poles of the magnets. Typical trajectories of muons across the momentum spectrum are overlaid. Reproduced from [19]. CC BY 3.0.

## 5.2 Vacuum vessel

Deep inelastic neutrino-nucleon scattering in the detector volume leads to background events through the production of  $V^0$  particles ( $K_L, K_S, \Lambda$ ) whose decay mimic the topology and modes of the hidden particle decays. With  $2 \cdot 10^{20}$  protons on target, a flux of  $\sim 4.5 \cdot 10^{18}$  neutrinos and  $\sim 3 \cdot 10^{18}$  anti-neutrinos are expected within the angular acceptance of the SHiP detector. The flux is dominated by muon neutrinos coming from the decays of pions and kaons produced in the proton target. Neutrinos from decays of charm and beauty hadrons constitute  $\sim 10\%$  of the total neutrino flux. Figure 14 (left) shows the vertex distribution of signal candidates produced by neutrino interactions assuming air at atmospheric pressure in the fiducial volume, and no surrounding vessel structure. A soft selection for heavy neutral leptons based on finding a vertex in the fiducial volume and no activity in the upstream detectors is applied. In these conditions, a total number of  $2.5 \cdot 10^3$  candidate events are expected within the acceptance for  $2 \cdot 10^{20}$  protons on target. The events are largely concentrated along the centre with small reconstructed impact parameters at the proton target. To achieve the required level of neutrino background rejection, the fiducial volume is therefore contained in a vacuum vessel (figure 1) which is evacuated down to a pressure of  $O(10^{-3})$  bar. Figure 14 (right) shows the vertex distribution of signal candidates at this pressure. In these conditions,  $1.4 \cdot 10^4$  candidate events are expected within the fiducial volume with the same soft selection for  $2 \cdot 10^{20}$  protons on target, mainly produced through neutrino interactions with the vessel walls. Even if the total number of neutrino interactions are larger due to the vessel material, almost all candidate events are in this case easily rejected by using criteria based on the reconstructed impact parameter at the

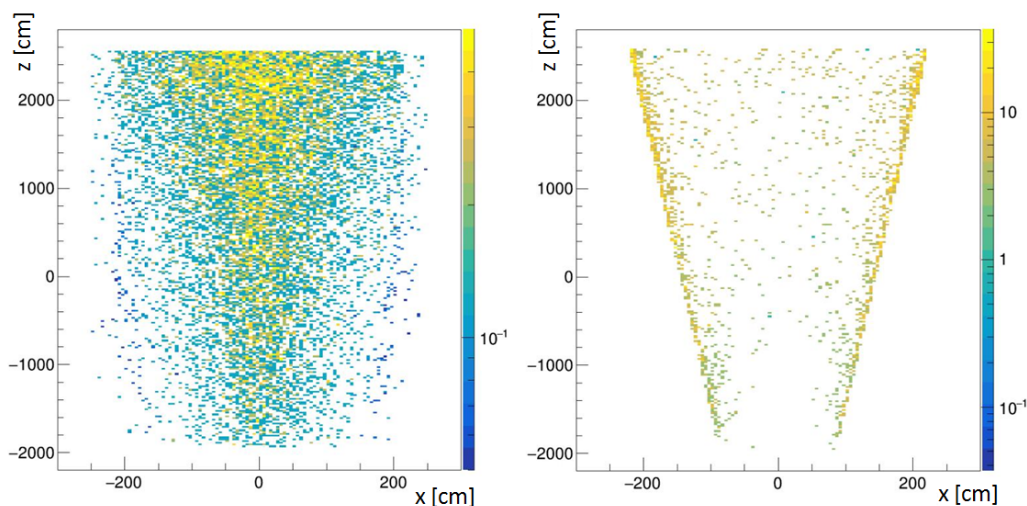


**Figure 14.** Vertex distribution of signal candidates produced by neutrino interactions from  $2 \cdot 10^{20}$  protons on target assuming air at atmospheric pressure in the fiducial volume with a soft selection for heavy neutral leptons (left), as compared to the situation with a vacuum vessel evacuated down to a pressure of  $10^{-3}$  bar (right).

proton target. In addition, residual neutrino interactions as well as muon deep inelastic interactions with the vessel structure are further suppressed by instrumenting the entire decay volume walls with a background tagger system and detecting the additional activity associated with the interactions. Simulation studies show that no background events remain after applying these criteria [1].

The SHiP decay vessel consists of the  $\sim 50$  m decay volume constructed in S355JO(J2/K2)W Corten steel with upstream outer dimensions of  $2.4 \times 4.5$  m<sup>2</sup> and downstream outer dimensions of  $5 \times 10$  m<sup>2</sup>. The design of the vessel wall is based on an optimisation aiming at producing a structure as light as possible and as slim as possible in order to stay within the boundaries of the deflected muon flux whilst maintaining the required acceptance. At the same time, the optimisation also accounts for the structural safety norms allowing access to the underground hall while under vacuum and the earthquake loads in the region. Figure 15 shows the structure of the decay volume. The preliminary design consists of a 30 mm thick continuous inner steel sheet acting as vacuum liner, supported azimuthally by welded T-shaped beams with a steel thickness of 15 mm and a height varying from 300 mm to 450 mm. The structure is further reinforced by longitudinal stiffening profiles between the azimuthal beams.

Two options are considered for the surrounding background tagger, either a liquid or a plastic scintillator. For the liquid option, the scintillator is integrated within the decay volume structure with an extra 8 mm steel sheet welded to the azimuthal beams and stiffening profiles, while for the plastic scintillator option, it is attached directly to the structure. The decay volume is directly connected to the  $\sim 10$  m downstream spectrometer vacuum section, which is made out of austenitic steel since it runs through the spectrometer magnet and houses the four tracker stations of straw tubes built using the same technology from the NA62 experiment [21]. The preliminary design considers extruded aluminum profiles with a material budget equivalent to 0.8 radiation lengths for the upstream and downstream windows.

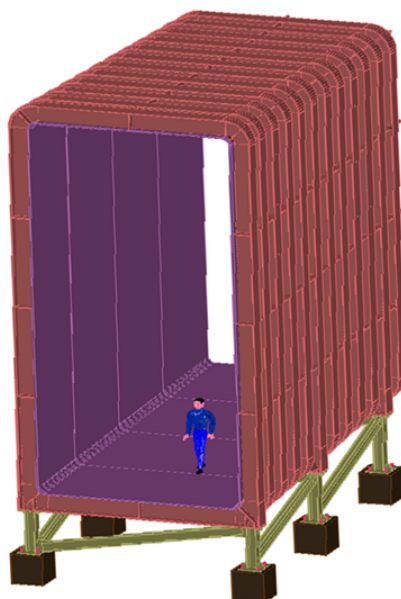


**Figure 15.** Cross-sectional view of the vacuum vessel which provides a pressure of  $O(10^{-3})$  bar in the decay volume. The design has been optimised in order for the wall to be as light and as slim as possible, and to incorporate a detector system which tags background events.

## 6 Conclusions

The SHiP experimental facility will provide a unique experimental platform for physics at the intensity frontier which is complementary to both the searches for new physics at the energy frontier and the direct searches for cosmic Dark Matter. CERN’s accelerator complex makes for an ideal siting for the experimental facility. The assumed availability of  $2 \cdot 10^{20}$  protons on target at  $400 \text{ GeV}/c$  in about five years of nominal operation and an environment of extremely low background compares favourably with the potential of other existing facilities.

The two-fold SHiP apparatus is sensitive both to decays and to scattering signatures, and is able to probe a wide variety of models with light long-lived exotic particles in a largely unexplored domain of very weak couplings and masses up to  $O(10) \text{ GeV}/c^2$ . This puts it in a unique position worldwide to resolve several of the major observational puzzles of particle physics and cosmology. In addition, the same facility enables the study of interactions of tau neutrino and anti-tau neutrinos, as well as neutrino-induced charm production by all neutrino species. A more recent investigation also shows that an additional detector on the SHiP beam line with a proton target consisting of thin wires and operating in parallel would allow a search for lepton flavour violating tau lepton decays at a sensitivity that could be highly competitive with projections of approved experiments.

The experimental facility presents a number of technological challenges to the beam delivery, the proton target system, and the reduction of beam-induced background. As reported, in-depth studies and prototyping are already well underway for all of the critical components. Taking into account the required R&D and construction, and the accelerator schedule at CERN, we plan to commission and perform the pilot run for the SHiP experiment when the SPS resumes operation after LHC’s third long shutdown for maintenance and upgrades.

## Acknowledgments

The SHiP Collaboration wishes to thank the Castaldo company (Naples, Italy) for their contribution to the development studies of the decay vessel. The support from the National Research Foundation of Korea with grant numbers of 2018R1A2B2007757, 2018R1D1A3B07050649, 2018R1D1A1B07050701, 2017R1D1A1B03036042, 2017R1A6A3A01075752, 2016R1A2B40-12302, and 2016R1A6A3A11930680 is acknowledged. The support from the Russian Foundation for Basic Research, grant 17-02-00607, and the support from the TAEK of Turkey are acknowledged.

## References

- [1] SHiP collaboration, *A facility to Search for Hidden Particles (SHiP) at the CERN SPS*, [arXiv:1504.04956](#).
- [2] S. Alekhin et al., *A facility to Search for Hidden Particles at the CERN SPS: the SHiP physics case*, *Rept. Prog. Phys.* **79** (2016) 124201 [[arXiv:1504.04855](#)].
- [3] SHiP collaboration, *Addendum to Technical Proposal: A Facility to Search for Hidden Particles (SHiP) at the CERN SPS*, [CERN-SPSC-2015-040](#) (2015).
- [4] G.F. Giudice and R. Rattazzi, *Theories with gauge mediated supersymmetry breaking*, *Phys. Rept.* **322** (1999) 419 [[hep-ph/9801271](#)].
- [5] I. Yu. Kobzarev, L.B. Okun and I. Ya. Pomeranchuk, *On the possibility of experimental observation of mirror particles*, *Sov. J. Nucl. Phys.* **3** (1966) 837.
- [6] R. Foot, H. Lew and R.R. Volkas, *A Model with fundamental improper space-time symmetries*, *Phys. Lett.* **B 272** (1991) 67.
- [7] R. Foot and X.-G. He, *Comment on Z-Z-prime mixing in extended gauge theories*, *Phys. Lett.* **B 267** (1991) 509.
- [8] B. Patt and F. Wilczek, *Higgs-field portal into hidden sectors*, [hep-ph/0605188](#).
- [9] R. Essig et al., *Working Group Report: New Light Weakly Coupled Particles*, in *Proceedings of the 2013 Community Summer Study on the Future of U.S. Particle Physics*, Snowmass on the Mississippi, Minneapolis, MN, U.S.A., 29 July–6 August, 2013, [arXiv:1311.0029](#), <http://www.slac.stanford.edu/econf/C1307292/docs/IntensityFrontier/NewLight-17.pdf>.
- [10] J. Alexander et al., *Dark Sectors 2016 Workshop: Community Report*, [arXiv:1608.08632](#), FERMILAB-CONF-16-421 (2016).
- [11] OPERA collaboration, *The OPERA experiment in the CERN to Gran Sasso neutrino beam*, [2009 JINST 4 P04018](#).
- [12] E. Gschwendtner et al., *CNGS, CERN Neutrinos to Gran Sasso, five years of running a 500 kilowatt neutrino beam facility at CERN*, in *Proceedings of IPAC2013*, Shanghai, China, 12–17 May 2013, pp. 211–213.
- [13] K. Elsener, G. Fidecaro, M. Gyr, W. Herr, J. Klem, U. Mikkelsen et al., *Proton extraction from the CERN SPS using bent silicon crystals*, *Nucl. Instrum. Meth.* **B 119** (1996) 215.
- [14] COMPASS collaboration, <http://wwwcompass.cern.ch/>.
- [15] L.R. Evans et al., *The steel septum magnets for beam splitting at the CERN SPS*, in *Proceedings of the 6<sup>th</sup> International Conference on Magnet Technology (MT-6)*, Bratislava, Slovakia, 29 August–2 September 1977 [[CERN-SPS-ABT-77-13](#)].

- [16] H. Dijkstra and T. Ruf, *Heavy Flavour Cascade Production in a Beam Dump*, [CERN-SHiP-NOTE-2015-009](#) (2015).
- [17] A. Ferrari, P.R. Sala, A. Fasso and J. Ranft, *FLUKA: A multi-particle transport code (Program version 2005)*, [CERN-2005-010](#), SLAC-R-773, INFN-TC-05-11 (2005).
- [18] V. Bayliss, M. Courthold and T. Rawlings, *Active Muon Shield - Preliminary Design Report*, [CERN-SHiP-NOTE-2015-003](#) (2015).
- [19] SHiP collaboration, *The active muon shield in the SHiP experiment*, [2017 JINST 12 P05011](#) [[arXiv:1703.03612](#)].
- [20] GEANT4 collaboration, *GEANT4: A Simulation toolkit*, *Nucl. Instrum. Meth. A* **506** (2003) 250.
- [21] G. Anelli et al., *Proposal to measure the rare decay  $K^+ \rightarrow \pi^+ \nu \bar{\nu}$  at the CERN SPS*, [CERN-SPSC-2005-013](#) (2005).

## MULTIYEAR INDOOR RADON VARIABILITY IN A FAMILY HOUSE – A CASE STUDY IN SERBIA

by

**Vladimir I. UDOVIČIĆ<sup>1\*</sup>, Dimitrije M. MALETIĆ<sup>1</sup>, Radomir M. BANJANAC<sup>1</sup>,  
Dejan R. JOKOVIĆ<sup>1</sup>, Aleksandar L. DRAGIĆ<sup>1</sup>, Nikola B. VESELINOVIĆ<sup>1</sup>,  
Jelena Z. ŽIVANOVIĆ<sup>1</sup>, Mihailo R. SAVIĆ<sup>1</sup>, and Sofija M. FORKAPIĆ<sup>2</sup>**

<sup>1</sup>Institute of Physics, University of Belgrade, Belgrade, Serbia

<sup>2</sup>Department of Physics, Faculty of Science, University of Novi Sad, Novi Sad, Serbia

Scientific paper

<http://doi.org/10.2298/NTRP1802174U>

The indoor radon behavior has complex dynamics due to the influence of the large number of different parameters: the state of indoor atmosphere (temperature, pressure, and relative humidity), aerosol concentration, the exchange rate between indoor and outdoor air, construction materials, and living habits. As a result, indoor radon concentration shows variation, with the usual periodicity of one day and one year. It is well-known that seasonal variation of the radon concentration exists. It is particularly interesting to investigate indoor radon variation at the same measuring location and time period, each year, due to estimation of individual annual dose from radon exposure. The long-term indoor radon measurements, in a typical family house in Serbia, were performed. Measurements were taken during 2014, 2015, and 2016, in February and July, each year. The following measuring techniques were used: active and charcoal canisters methods. Analysis of the obtained results, using multivariate analysis methods, is presented.

*Key words: radon variability, multivariate regression analysis, multi-seasonal radon measurements, indoor radon*

### INTRODUCTION

The research of the dynamics of radon in various environments, especially indoors, is of great importance in terms of protection against ionizing radiation and in designing of measures for its reduction. Published results and development of many models to describe the behavior of indoor radon, indicates the complexity of this research, especially with models for prediction of the variability of radon [1-3]. This is because the variability of radon depends on a large number of variables such as local geology, permeability of soil, building materials used for the buildings, the state of the indoor atmosphere (temperature, pressure and relative humidity), aerosol concentration, the exchange rate between indoor and outdoor air, construction materials, as well as the living habits of people. It is known that the indoor radon concentration variation has periodicity of one day and one year. It is also well-known that the seasonal variation of the radon concentration exists. This is why it is particularly interesting to investigate indoor radon variation at the same measuring location and time period, year after

year, in order to estimate the individual annual dose from radon exposure. In that sense, we performed long-term indoor radon measurements in a typical family house in Serbia. Measurements were taken during the 2014, 2015, and 2016, in February and July, each year. We used the following measuring techniques: active and charcoal canisters methods. The detailed analysis of the obtained results using multivariate analysis (MVA) methods is presented in this paper.

First, MVA methods were tested on the radon variability studies in the Underground Low Background Laboratory in the Institute of Physics, Belgrade [4, 5]. Several climate variables: air temperature, pressure, and humidity were considered. Further advance was made by using all the publicly available climate variables monitored by nearby automatic meteorological station. In order to analyze the dependence of radon variation on multiple variables, multivariate analysis needs to be used. The goal was to find an appropriate method, out of the wide spectrum of multivariate analysis methods that are developed for the analysis of data from high-energy physics experiments, to analyze the measurements of variations of radon concentrations in indoor spaces. Previous

\* Corresponding author; e-mail: [udovicic@ipb.ac.rs](mailto:udovicic@ipb.ac.rs)



analysis were done using the maximum of 18 climate parameters and use and comparison of 8 different multivariate methods. In this paper the number of variables is reduced to the most important ones and new derived variables, like vapor pressure, simple modeled solar irradiance and simple modeled precipitation, which were introduced in the multivariate analysis.

## INDOOR RADON MEASUREMENTS METHODS

Depending on the integrated measurement time, methods of measurement of the indoor radon concentrations may be divided into long-term and short-term ones. The device for the performed short-term radon measurements is SN1029 radon monitor (manufactured by the Sun Nuclear Corporation, NRSB approval-code 31822) with the following characteristics: the measurement range from  $1 \text{ Bqm}^{-3}$  to  $99.99 \text{ kBqm}^{-3}$ , accuracy equal to  $\pm 25 \%$ , sensitivity of  $0.16 \text{ counts hour per Bqm}^{-3}$ . The device consists of two diffused junction photodiodes as the radon detector which is furnished with sensors for temperature, barometric pressure, and relative humidity. The sampling time was set to 2 h. The method for Charcoal Canister used is: EERF Standard Operating Procedures for Radon-222 Measurement Using Charcoal Canisters [6], also used by major laboratories which conduct radon measurements in Serbia [7]. Exposure time of the charcoal canisters was 48 h. The connection between short term and long term measurements has attracted some interest previously [8].

The family house, selected for the measurements and analysis of variations of radon concentrations, is a typical house in Belgrade residential areas, with requirement of existence of cellar. House is built on limestone soil. Radon measurements were carried out in the living room of the family house, which is built of standard materials (brick, concrete, mortar) and isolated with styrofoam. During the period of measurements (winter-summer 2014, 2015, and 2016), the house was naturally ventilated and air conditioning was used in heating mode at the beginning of the measurement period. During the winter period measurements, the electrical heating was used in addition to air conditioning. Measured radon concentrations, room temperature ( $T_{id}$ ), atmospheric pressure ( $P_{id}$ ) and relative humidity ( $H_{id}$ ) inside the house, were obtained using radon monitor. Values of meteorological variables, in the measurement period, were obtained from an automatic meteorological station, located near the house in which the measurement was performed. We used the following meteorological variables: external air temperature ( $T$ ), also at height of 5cm, pressure ( $P$ ) and humidity ( $H$ ), solar irradiation, wind speed, precipitation, temperature of the soil at depths of 10 cm, 20 cm and 50 cm. The natural ventilation routine was not monitored. Since the ventilation is of

crucial importance for the level of radon indoors [9], Multivariate regression analysis was used mainly for winter periods.

## MULTIVARIATE REGRESSION ANALYSIS

In many fields of physics, especially in high-energy physics, there is the demand for detailed analyses of a large amount of data. For this purpose, the data analysis environment ROOT [10], is developed. ROOT is modular scientific software framework, which provides all the functionalities needed to deal with big data processing, statistical analysis, visualization and storage. A specific functionality gives the developed Toolkit for Multivariate Analysis (TMVA) [11]. The TMVA provides an environment for the processing, parallel evaluation and application of multivariate regression techniques.

TMVA is used to create, test and apply all available regression multivariate methods, implemented in ROOT, in order to find methods which are the most appropriate and yield maximum information on the dependence of indoor radon concentrations on the multitude of meteorological variables. Regression methods are used to find out which regression method can, if any, on the basis of input meteorological variables only, give an output that would satisfactorily close match the observed variations of radon concentrations. The output of usage of multivariate regression analysis methods has mapped functional behavior, which can be used to evaluate the measurements of radon concentrations using input meteorological variables only. All the methods make use of training events, for which the desired output is known and is used for training of Multivariate regression methods, and test events, which are used to test the MVA methods outputs.

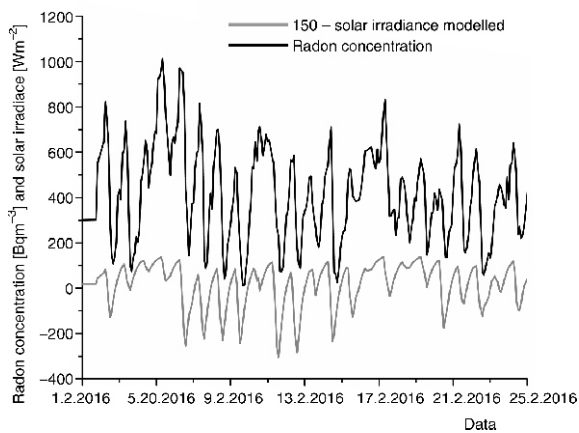
## RESULTS

Measurements were performed during February and July in 2014, 2015, and 2016 using radon monitor and charcoal canister measurements. The descriptive results are summarized in tab. 1. The measurements using radon monitor and charcoal canisters are in good agreement.

Previous work done by researchers from the Low Background Laboratory, Institute of Physics, Belgrade, using the MVA analysis in search of connections between radon concentration and meteorological variables, included only one period of measurement, February or July 2014 [4]. Now the MVA analysis is using all the measured data February/July 2014-2016. New variables introduced in MVA analysis are modeled solar irradiance, modeled precipitation and vapor

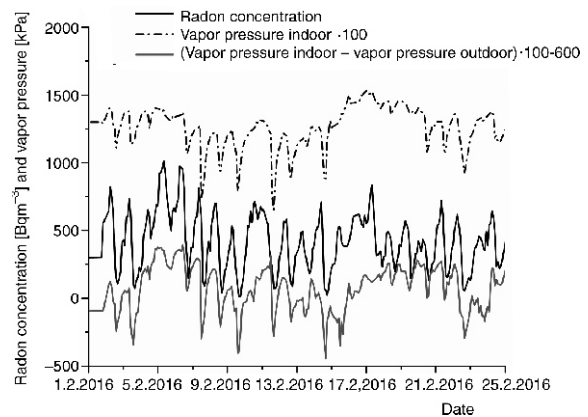
**Table 1. Descriptive results of February and July 2014, 2015, and 2016 measurements, using radon monitor and charcoal canisters (only in February)**

Results of measurements	2014		2015		2016	
	Feb.	July	Feb.	July	Feb.	July
Minimal radon activity using radon monitor [ $\text{Bqm}^{-3}$ ]	15	0	28	0	12	3
Maximal radon activity using radon monitor [ $\text{Bqm}^{-3}$ ]	1000	286	915	88	1013	262
Median radon activity using radon monitor [ $\text{Bqm}^{-3}$ ]	418	25	524	22	412	28
Arithmetic mean of radon activity using radon monitor (standard deviation) [ $\text{Bqm}^{-3}$ ]	402 (216)	40 (41)	508 (207)	27 (18)	423 (214)	39 (32)
Room temperature using radon monitor (standard deviation) [ $^{\circ}\text{C}$ ]	20.4 (0.8)	24.7 (0.9)	21.2 (0.6)	24.9 (0.8)	22.3 (0.6)	24.6 (0.8)
Relative humidity using radon monitor (standard deviation) [%]	67.4 (5.7)	67.8 (4.8)	68.2 (4.8)	51.5 (4.7)	64.0 (6.4)	58.9 (7.5)
Radon activity using charcoal canister (standard deviation) [ $\text{Bqm}^{-3}$ ]	432 (10)	/	518 (6)	/	407 (5)	/

**Figure 1. Modeled solar irradiance in comparison with measured radon concentration during February 2016**

pressure. In order to make use of intensity of solar irradiance during the whole day and night, the solar irradiance is modeled so that it includes 80 % of solar irradiance value from the previous measurement (previous hour) with addition of solar irradiance value for the actual hour of measurement (fig. 1). The value of 80 % is chosen so that the modeled solar irradiation has the best correlation with the radon measurements. Similar model of precipitation was used in this analysis. The next new variable is vapor pressure. The vapor pressure variable is calculated using the slope  $s(T)$ , of the relationship between saturation vapor pressure and air temperature and is given by [12, 13], so that the vapor pressure equals relative humidity times saturation vapor pressure, fig. 2.

Before the start of training of Multivariate regression methods using TMVA toolkit in ROOT, the description of input meteorological variables is performed, mainly by looking into inter-correlations of input variables and their connections with the measured radon concentrations. The MVA is using all the measured data. Table 2 presents the meteorological variables and their module value of correlation with the measured radon concentrations (target), which is indicative in finding linear dependence of radon mea-

**Figure 2. Vapor pressure in comparison with measured radon concentration during February 2016**

surements and input variables. The second column in tab. 2 presents us with correlation ratio values which indicate if there are some functional dependence (not only linear) between input variables and radon concentration, and the last column presents the mutual information which indicates if there is a non-functional dependence of input variables and radon measurements [11].

From tab. 2 it can be noticed that linear correlated values are not the only ones which can be used in MVA analysis, for example variable solar irradiance has high mutual information with the radon measurements.

In the data preparation for MVA training the whole dataset is consisting of many events. An event includes time of measurement, radon measurement and meteorological variables. The dataset is randomly split in two halves, one half of the events will be used for training of multivariate regression methods, and the other half of events for testing of methods, mainly to compare the measured and MVA evaluated values for radon concentration.

It turns out that the methods best suited for our purpose is the Boosted Decision Trees (BDT) method. This means that BDT gives the smallest difference be-

**Table 2. Input variable rank and values for correlation, correlation ratio and mutual information, all with the measured radon concentrations (target) for February and July 2014-2016 measurements**

Variable	Correlation with target		Correlation ratio		Mutual information	
	Rank	Value	Rank	Value	Rank	Value
Soil temperature depth 20 cm [°C]	1	0.87	1	0.60	13	1.48
Soil temperature depth 50 cm [°C]	2	0.86	2	0.57	14	1.31
Soil temperature depth 10 cm [°C]	3	0.82	3	0.54	9	1.84
Temperature outdoor [°C]	4	0.82	5	0.53	8	1.85
Vapor indoor – vapor od [mbar]	5	0.81	9	0.41	11	1.73
Temperature od – temperature id [°C]	6	0.80	4	0.53	6	1.92
Temperature height 5 cm [°C]	7	0.77	8	0.48	7	1.91
Vapor od [mbar]	8	0.76	10	0.41	5	1.92
Temperature id [°C]	9	0.75	7	0.49	17	1.16
Solar irradiance [Wm <sup>-2</sup> ]	10	0.61	6	0.50	2	2.23
Humidity indoor [%]	11	0.45	11	0.26	1	2.26
Humidity outdoor [%]	12	0.31	13	0.20	10	1.76
Air pressure outdoor [mbar]	13	0.27	17	0.07	12	1.55
Wind speed [ms <sup>-1</sup> ]	14	0.22	16	0.01	16	1.28
Air pressure indoor [mbar]	15	0.17	18	0.04	15	1.31
Humidity od – Humidity id [%]	16	0.10	14	0.19	4	2.11
Precipitation [Lm <sup>-2</sup> ]	17	0.01	15	0.19	18	1.13
Vapor indoor [mbar]	18	0.002	12	0.02	3	2.17

tween the measured radon concentration from test sample and the evaluation of value of radon concentration using input variables only. This can be seen in fig. 3, which shows the distribution of BDT and BDTG regression method outputs (evaluated values) in comparison with the measured radon concentration during February 2016.

Since TMVA has 12 different regression methods implemented, only some of those will give useful results when evaluating the radon concentration measurements. Table 4 summaries the results of MVA analysis. It shows the MVA methods RMS of difference of evaluated and measured radon concentration. Also, tab. 4 shows the mutual information of measured and MVA evaluated radon concentration. Besides

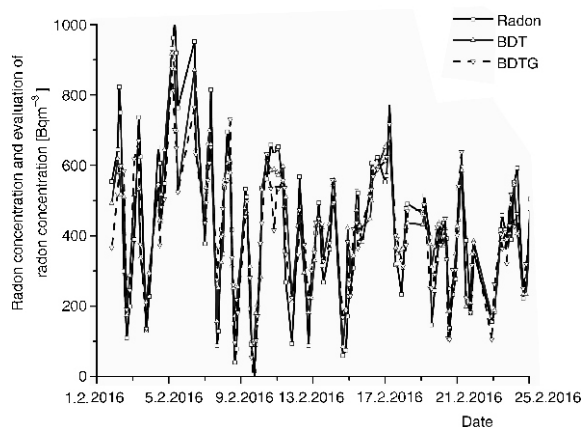


**Figure 3. Comparison of MVA evaluated radon concentration and measured one from the test sample of events during February 2016**

BDT, the Multi-Layer Perceptron (MLP) [10], an implementation of Artificial Neural Network multivariate method, also gives good results.

The MVA regression analysis results in mapped functional behavior and, as opposed to possible existence of theoretical modeling, which is independent of the number of measurements, MVA depends on the number of events. More events, the better mapped function we get as a result. In this sense, if the number of measurements is not great, multivariate analysis can be used only as help, to indicate which variables are more important to be used in theoretical modeling, for comparison of mapped and modeled functions, and modeled function test.

## CONCLUSION

Indoor radon variation at one location in the same periods (February and July), was investigated for three years. Long-term indoor radon measurements show intense seasonal variation. The results obtained with different measuring methods are in good agreement. The radon behavior in the house is almost the same and shows good reproducibility year by year. The small variations in the year by year dynamics are originated mostly from the variations in meteorological variables during winter seasons and mostly due to ventilation habits during summer season. Ventilation habits were not monitored nor taken into account in MVA regression analysis. The preliminary results using multivariate analysis methods in TMVA are shown. Main output of Multivariate regression analy-

**Table 3. Input variable correlation with the measured radon concentrations for February and July 2016**

Correlation with target			
February 2016		July 2016	
Variable	Value	Variable	Value
Vapor id-vapor od [mbar]	0.58	Soil temperature depth 20 cm [°C]	0.46
Humidity id [%]	0.54	Soil temperature depth 50 cm [°C]	0.42
Vapor id [mbar]	0.52	Solar irradiance	0.32
Solar irradiance [Wm <sup>-2</sup> ]	0.48	Temperature id [°C]	0.30
Temperature od – temperature id [°C]	0.46	Soil temperature depth 10 cm [°C]	0.24
Temperature [°C]	0.44	Temperature od [°C]	0.21
Soil temperature depth 10 cm [°C]	0.43	Humidity od [%]	0.20
Soil temperature depth 20 cm [°C]	0.42	Humidity id [%]	0.19
Humidity [%]	0.38	Air pressure [mbar]	0.17
Temperature height 5 cm [°C]	0.32	Precipitation [Lm <sup>-2</sup> ]	0.17
Temperature id [°C]	0.29	Temperature od – temperature id [°C]	0.16
Air pressure od [mbar]	0.23	Air pressure id [mbar]	0.16
Air pressure id [mbar]	0.21	Humidity od – humidity id [%]	0.14
Soil temperature depth 50 cm [°C]	0.20	Wind speed [ms <sup>-2</sup> ]	0.13
Precipitation [Lm <sup>-2</sup> ]	0.19	Temperature height 5 cm [°C]	0.12
Humidity od – humidity id [%]	0.15	Vapor id [mbar]	0.06
Vapor od [mbar]	0.08	Vapor od [mbar]	0.03
Wind speed [ms <sup>-1</sup> ]	0.05	Vapor id – vapor od [mbar]	0.02

**Table 4. RMS of MVA method's evaluation error and mutual information; February/July 2014-2016**

MVA method	RMS [Bqm <sup>-3</sup> ]	Mutual information
BDT	85.5	1.477
BDTG	92.1	1.614
MLP	101	1.401

sis is the initial version of *mapped* function of radon concentration dependence on multitude of meteorological variables. Simplification of MVA methods can be made by choosing only the most important input variables and exclude the other variables.

#### ACKNOWLEDGEMENTS

The authors acknowledge the financial support of the Ministry of Science, Technology and Development of Serbia within the projects: Nuclear Methods Investigations of Rare Processes and Cosmic Rays (grant number 171002) and Biosensing Technologies and Global System for Continuous Research and Integrated Management (grant number 43002).

#### AUTHORS' CONTRIBUTIONS

The idea for this paper came as a result of discussions of V. I. Udovičić, R. M. Banjanac, D. R. Joković, A. L. Dragić, and D. M. Maletić. Gathering climate data and MVA analysis was done by D. M. Maletić and V. I. Udovičić. Performed indoor radon measurements were done by V. I. Udovičić and S. M. Forkapić. Writing of the paper was done by D. M. Maletić and V. I. Udovičić. A. L. Dragić gave idea about using MVA

methods in cosmic and radon measurements. N. B. Veselinović and M. R. Savić analyzed and validated climate data. J. Z. Živanović helped with MVA analysis. D. R. Joković helped with data analysis and paper technical preparation.

#### REFERENCES

- [1] Collignan, B., *et al.*, Development of a Methodology to Characterize Radon Entry in Dwellings, *Building and Environment*, 57 (2012), Nov., pp. 176-183
- [2] Li, F., Baixeras, C., The RAGENA Dynamic Model of Radon Generation, Entry and Accumulation Indoors, *Science of the Total Environment*, 307 (2003), 1-3, pp. 55-69
- [3] Jelle, B. P., *et al.*, Development of a Model for Radon Concentration in Indoor Air, *Science of the Total Environment*, 416 (2012), Jan., pp. 343-350
- [4] Maletić, D., *et al.*, Comparison of Multivariate Classification and Regression Methods for Indoor Radon Measurements, *Nucl Technol Radiat*, 29 (2014), 1, pp. 17-23
- [5] Udovičić, V., *et al.*, Radon Problem in an Underground Low-Level Laboratory, *Radiation Measurements*, 44 (2009), 9-10, pp. 1009-1012
- [6] \*\*\*, EPA 520/5-87-005, Gray D.J, Windham S.T, United States Environmental Protection Agency, Montgomery, 1987
- [7] Živanović, M. Z., *et al.*, Radon Measurements with Charcoal Canisters, *Nucl Technol Radiat*, 31 (2016), 1, pp. 65-72
- [8] Stojanovska, Z., *et al.*, Prediction of Long-Term Indoor Radon Concentrations Based on Short-Term Measurements, *Nucl Technol Radiat*, 32 (2017), 1, pp. 77-84
- [9] Nikolić, M. D., *et al.*, Modelling Radiation Exposure in Homes from Siporex Blocks by Using Exhalation Rates of Radon, *Nucl Technol Radiat*, 30 (2015), 4, pp. 301-305
- [10] Brun, R., Rademakers, F., ROOT – An Object Oriented Data Analysis Framework, *Nucl. Inst. Meth. in Phys. Res., A* 389 (1997), 1-2, pp. 81-86

- [11] Hoescker, A., et al., TMVA – Toolkit for Multivariate Data Analysis, PoS ACAT 040, arXiv:physics/070303, 2007
- [12] Murray, F. W., On the Computation of Saturation Vapor Pressure, *J. Applied Meteorology*, 6 (1967), 1, pp. 203-204

- [13] Tetens, O., About Some Meteorological Aspects (in German), *Z. Geophys*, 6 (1930), pp. 207-309

Received on October 6, 2018

Accepted on June 8, 2018

---

**Владимир И. УДОВИЧИЋ, Димитрије М. МАЛЕТИЋ, Радомир М. БАЊАНАЦ,  
Дејан Р. ЈОКОВИЋ, Александар Л. ДРАГИЋ, Никола Б. ВЕСЕЛИНОВИЋ,  
Јелена З. ЖИВАНОВИЋ, Михаило Р. САВИЋ, Софија М. ФОРКАПИЋ**

**СТУДИЈА СЛУЧАЈА ВИШЕГОДИШЊЕ ВАРИЈАБИЛНОСТИ РАДОНА  
У ПОРОДИЧНОЈ КУЋИ У СРБИЈИ**

Понашање радона у затвореном простору има сложену динамику због утицаја великог броја различитих параметара који утичу на његову варијабилност: метеоролошких (температура, притисак и релативна влажност), концентрације аеросола, брзине размене између унутрашњег и спољашњег ваздуха, грађевинских материјала и животних навика. Као резултат, концентрација радона у затвореним просторијама показује варијацију, уз стандардну периодичност од једног дана и једне године. Годишња варијабилност је добро позната сезонска варијација концентрације радона. Посебно је интересантно пратити вишегодишње варијације концентрације радона на истој мерној локацији и временском периоду, пре свега због процене индивидуалних годишњих доза од изложености радону. У типичној породичној кући у Србији извршена су дуготрајна мерења радона у дневном боравку. Мерења су рађена током 2014, 2015, и 2016. године, у фебруару и јулу, сваке године. Коришћене су следеће мерне технике: активна и метода коришћења угљених канистера. Добијени резултати анализирани су коришћењем мултиваријантне регресионе анализе.

*Кључне речи: варијабилност радона, мултиваријантна регресиона анализа, радон у затвореним просторијама, вишегодишње мерење радона*



## Lattice design and expected performance of the Muon Ionization Cooling Experiment demonstration of ionization cooling

M. Bogomilov,<sup>1</sup> R. Tsenov,<sup>1</sup> G. Vankova-Kirilova,<sup>1</sup> Y. Song,<sup>2</sup> J. Tang,<sup>2</sup> Z. Li,<sup>3</sup> R. Bertoni,<sup>4</sup> M. Bonesini,<sup>4</sup> F. Chignoli,<sup>4</sup> R. Mazza,<sup>4</sup> V. Palladino,<sup>5</sup> A. de Bari,<sup>6</sup> G. Cecchet,<sup>6</sup> D. Orestano,<sup>7</sup> L. Tortora,<sup>7</sup> Y. Kuno,<sup>8</sup> S. Ishimoto,<sup>9</sup> F. Filthaut,<sup>10</sup> D. Jokovic,<sup>11</sup> D. Maletic,<sup>11</sup> M. Savic,<sup>11</sup> O. M. Hansen,<sup>12</sup> S. Ramberger,<sup>12</sup> M. Vretenar,<sup>12</sup> R. Asfandiyarov,<sup>13</sup> A. Blondel,<sup>13</sup> F. Drielsma,<sup>13</sup> Y. Karadzhov,<sup>13</sup> G. Charnley,<sup>14</sup> N. Collomb,<sup>14</sup> K. Dumbell,<sup>14</sup> A. Gallagher,<sup>14</sup> A. Grant,<sup>14</sup> S. Griffiths,<sup>14</sup> T. Hartnett,<sup>14</sup> B. Martlew,<sup>14</sup> A. Moss,<sup>14</sup> A. Muir,<sup>14</sup> I. Mullacrane,<sup>14</sup> A. Oates,<sup>14</sup> P. Owens,<sup>14</sup> G. Stokes,<sup>14</sup> P. Warburton,<sup>14</sup> C. White,<sup>14</sup> D. Adams,<sup>15</sup> R. J. Anderson,<sup>15</sup> P. Barclay,<sup>15</sup> V. Bayliss,<sup>15</sup> J. Boehm,<sup>15</sup> T. W. Bradshaw,<sup>15</sup> M. Courthold,<sup>15</sup> V. Francis,<sup>15</sup> L. Fry,<sup>15</sup> T. Hayler,<sup>15</sup> M. Hills,<sup>15</sup> A. Lintern,<sup>15</sup> C. Macwaters,<sup>15</sup> A. Nichols,<sup>15</sup> R. Preece,<sup>15</sup> S. Ricciardi,<sup>15</sup> C. Rogers,<sup>15</sup> T. Stanley,<sup>15</sup> J. Tarrant,<sup>15</sup> M. Tucker,<sup>15</sup> A. Wilson,<sup>15</sup> S. Watson,<sup>16</sup> R. Bayes,<sup>17</sup> J. C. Nugent,<sup>17</sup> F. J. P. Soler,<sup>17</sup> R. Gamet,<sup>18</sup> G. Barber,<sup>19</sup> V. J. Blackmore,<sup>19</sup> D. Colling,<sup>19</sup> A. Dobbs,<sup>19</sup> P. Dornan,<sup>19</sup> C. Hunt,<sup>19</sup> A. Kurup,<sup>19</sup> J.-B. Lagrange,<sup>19,\*</sup> K. Long,<sup>19</sup> J. Martyniak,<sup>19</sup> S. Middleton,<sup>19</sup> J. Pasternak,<sup>19</sup> M. A. Uchida,<sup>19</sup> J. H. Cobb,<sup>20</sup> W. Lau,<sup>20</sup> C. N. Booth,<sup>21</sup> P. Hodgson,<sup>21</sup> J. Langlands,<sup>21</sup> E. Overton,<sup>21</sup> M. Robinson,<sup>21</sup> P. J. Smith,<sup>21</sup> S. Wilbur,<sup>21</sup> A. J. Dick,<sup>22</sup> K. Ronald,<sup>22</sup> C. G. Whyte,<sup>22</sup> A. R. Young,<sup>22</sup> S. Boyd,<sup>23</sup> P. Franchini,<sup>23</sup> J. R. Greis,<sup>23</sup> C. Pidcott,<sup>23</sup> I. Taylor,<sup>23</sup> R. B. S. Gardener,<sup>24</sup> P. Kyberd,<sup>24</sup> J. J. Nebrensky,<sup>24</sup> M. Palmer,<sup>25</sup> H. Witte,<sup>25</sup> A. D. Bross,<sup>26</sup> D. Bowring,<sup>26</sup> A. Liu,<sup>26</sup> D. Neuffer,<sup>26</sup> M. Popovic,<sup>26</sup> P. Rubinov,<sup>26</sup> A. DeMello,<sup>27</sup> S. Gourlay,<sup>27</sup> D. Li,<sup>27</sup> S. Prestemon,<sup>27</sup> S. Virostek,<sup>27</sup> B. Freemire,<sup>28</sup> P. Hanlet,<sup>28</sup> D. M. Kaplan,<sup>28</sup> T. A. Mohayai,<sup>28</sup> D. Rajaram,<sup>28</sup> P. Snopok,<sup>28</sup> V. Suezaki,<sup>28</sup> Y. Torun,<sup>28</sup> Y. Onel,<sup>29</sup> L. M. Cremaldi,<sup>30</sup> D. A. Sanders,<sup>30</sup> D. J. Summers,<sup>30</sup> G. G. Hanson,<sup>31</sup> and C. Heidt<sup>31</sup>

(The MICE collaboration)

<sup>1</sup>*Department of Atomic Physics, St. Kliment Ohridski University of Sofia, Sofia 1164, Bulgaria*

<sup>2</sup>*Institute of High Energy Physics, Chinese Academy of Sciences, Beijing 100039, China*

<sup>3</sup>*Sichuan University, Sichuan Sheng 610000, China*

<sup>4</sup>*Sezione INFN Milano Bicocca, Dipartimento di Fisica G. Occhialini, Milano 20126, Italy*

<sup>5</sup>*Sezione INFN Napoli and Dipartimento di Fisica, Università Federico II, Complesso Universitario di Monte S. Angelo, Napoli 80126, Italy*

<sup>6</sup>*Sezione INFN Pavia and Dipartimento di Fisica, Pavia 27100, Italy*

<sup>7</sup>*INFN Sezione di Roma Tre and Dipartimento di Matematica e Fisica, Università Roma Tre, 00146 Roma, Italy*

<sup>8</sup>*Osaka University, Graduate School of Science, Department of Physics, Toyonaka, Osaka 565-0871, Japan*

<sup>9</sup>*High Energy Accelerator Research Organization (KEK), Institute of Particle and Nuclear Studies, Tsukuba 305-0801, Ibaraki, Japan*

<sup>10</sup>*Nikhef, Amsterdam, The Netherlands and Radboud University, Nijmegen 1098, The Netherlands*

<sup>11</sup>*Institute of Physics, University of Belgrade, Belgrade 11080, Serbia*

<sup>12</sup>*CERN, Geneva 1217, Switzerland*

<sup>13</sup>*DPNC, Section de Physique, Université de Genève, Geneva 1205, Switzerland*

<sup>14</sup>*STFC Daresbury Laboratory, Daresbury, Cheshire WA4 4AD, United Kingdom*

<sup>15</sup>*STFC Rutherford Appleton Laboratory, Harwell Oxford, Didcot OX11 0QX, United Kingdom*

<sup>16</sup>*STFC Rutherford UK Astronomy Technology Centre, Royal Observatory, Edinburgh, Blackford Hill, Edinburgh EH9 3HJ, United Kingdom*

<sup>17</sup>*School of Physics and Astronomy, Kelvin Building, The University of Glasgow, Glasgow G12 8SU, United Kingdom*

<sup>18</sup>*Department of Physics, University of Liverpool, Liverpool L69 7ZE, United Kingdom*

<sup>19</sup>*Department of Physics, Blackett Laboratory, Imperial College London, London SW7 2BB, United Kingdom*

<sup>20</sup>*Department of Physics, University of Oxford, Denys Wilkinson Building, Oxford OX1 3PJ, United Kingdom*

<sup>21</sup>*Department of Physics and Astronomy, University of Sheffield, Sheffield S10 2TN, United Kingdom*

<sup>22</sup>*SUPA and the Department of Physics, University of Strathclyde, Glasgow G1 1XQ, United Kingdom and Cockcroft Institute, United Kingdom*

<sup>23</sup>*Department of Physics, University of Warwick, Coventry CV4 7AL, United Kingdom*

<sup>24</sup>*Brunel University, Uxbridge UB8 3PH, United Kingdom*

<sup>25</sup>*Brookhaven National Laboratory, New York NY 11967, USA*

<sup>26</sup>*Fermilab, Batavia, Illinois 60510, USA*

<sup>27</sup>*Lawrence Berkeley National Laboratory, Berkeley, California 94720, USA*<sup>28</sup>*Illinois Institute of Technology, Chicago, Illinois 60616, USA*<sup>29</sup>*Department of Physics and Astronomy, University of Iowa, Iowa City, Iowa 52242, USA*<sup>30</sup>*University of Mississippi, Oxford, Mississippi 38677, USA*<sup>31</sup>*University of California, Riverside, California 92521, USA*

(Received 30 January 2017; published 19 June 2017)

Muon beams of low emittance provide the basis for the intense, well-characterized neutrino beams necessary to elucidate the physics of flavor at a neutrino factory and to provide lepton-antilepton collisions at energies of up to several TeV at a muon collider. The international Muon Ionization Cooling Experiment (MICE) aims to demonstrate ionization cooling, the technique by which it is proposed to reduce the phase-space volume occupied by the muon beam at such facilities. In an ionization-cooling channel, the muon beam passes through a material in which it loses energy. The energy lost is then replaced using rf cavities. The combined effect of energy loss and reacceleration is to reduce the transverse emittance of the beam (transverse cooling). A major revision of the scope of the project was carried out over the summer of 2014. The revised experiment can deliver a demonstration of ionization cooling. The design of the cooling demonstration experiment will be described together with its predicted cooling performance.

DOI: [10.1103/PhysRevAccelBeams.20.063501](https://doi.org/10.1103/PhysRevAccelBeams.20.063501)

## I. INTRODUCTION

Stored muon beams have been proposed as the source of neutrinos at a neutrino factory [1,2] and as the means to deliver multi-TeV lepton-antilepton collisions at a muon collider [3,4]. In such facilities the muon beam is produced from the decay of pions generated by a high-power proton beam striking a target. The tertiary muon beam occupies a large volume in phase space. To optimize the muon yield while maintaining a suitably small aperture in the muon-acceleration system requires that the muon beam be “cooled” (i.e., its phase-space volume reduced) prior to acceleration. A muon is short-lived, decaying with a lifetime of  $2.2 \mu\text{s}$  in its rest frame. Therefore, beam manipulation at low energy ( $\leq 1 \text{ GeV}$ ) must be carried out rapidly. Four cooling techniques are in use at particle accelerators: synchrotron-radiation cooling [5]; laser cooling [6–8]; stochastic cooling [9]; and electron cooling [10]. Synchrotron-radiation cooling is observed only in electron or positron beams, owing to the relatively low mass of the electron. Laser cooling is limited to certain ions and atomic beams. Stochastic cooling times are dependent on the bandwidth of the stochastic-cooling system relative to the frequency spread of the particle beam. The electron-cooling time is limited by the available electron density and the electron-beam energy and emittance. Typical cooling times are between seconds and hours, long compared with the muon lifetime. Ionization cooling proceeds by passing a muon beam through a material, the absorber, in which it

loses energy through ionization, and subsequently restoring the lost energy in accelerating cavities. Transverse and longitudinal momentum are lost in equal proportions in the absorber, while the cavities restore only the momentum component parallel to the beam axis. The net effect of the energy-loss/reacceleration process is to decrease the ratio of transverse to longitudinal momentum, thereby decreasing the transverse emittance of the beam. In an ionization-cooling channel the cooling time is short enough to allow the muon beam to be cooled efficiently with modest decay losses. Ionization cooling is therefore the technique by which it is proposed to cool muon beams [11–13]. This technique has never been demonstrated experimentally and such a demonstration is essential for the development of future high-brightness muon accelerators.

The international Muon Ionization Cooling Experiment (MICE) collaboration proposes a two-part process to perform a full demonstration of transverse ionization cooling. First, the “Step IV” configuration [14] will be used to study the material and beam properties that determine the performance of an ionization-cooling lattice. Second, a study of transverse-emittance reduction in a cooling cell that includes accelerating cavities will be performed.

The cooling performance of an ionization-cooling cell depends on the emittance and momentum of the initial beam, on the properties of the absorber material and on the transverse betatron function ( $\beta_{\perp}$ ) at the absorber. These factors will be studied using the Step IV configuration. Once this has been done, “sustainable” ionization cooling must be demonstrated. This requires restoring energy lost by the muons as they pass through the absorber using rf cavities. The experimental configuration with which the MICE collaboration originally proposed to study ionization cooling was presented in [15]. This configuration was revised to accelerate the timetable on which a demonstration of ionization cooling could be delivered and to reduce

\*[j.lagrange@imperial.ac.uk](mailto:j.lagrange@imperial.ac.uk)

cost. This paper describes the revised lattice proposed by the MICE collaboration for the demonstration of ionization cooling and presents its performance.

## II. COOLING IN NEUTRINO FACTORIES AND MUON COLLIDERS

At production, muons occupy a large volume of phase space. The emittance of the initial muon beam must be reduced before the beam is accelerated. A neutrino factory [16] requires the transverse emittance to be reduced from 15–20 mm to 2–5 mm. A muon collider [17] requires the muon beam to be cooled in all six phase-space dimensions; to achieve the desired luminosity requires an emittance of  $\sim 0.025$  mm in the transverse plane and  $\sim 70$  mm in the longitudinal direction [18,19].

Ionization cooling is achieved by passing a muon beam through a material with low atomic number ( $Z$ ), in which it loses energy by ionization, and subsequently accelerating the beam. The rate of change of the normalized transverse emittance,  $\varepsilon_{\perp}$ , is given approximately by [12,20,21]:

$$\frac{d\varepsilon_{\perp}}{dz} \simeq -\frac{\varepsilon_{\perp}}{\beta^2 E_{\mu}} \left\langle \frac{dE}{dz} \right\rangle + \frac{\beta_{\perp} (13.6 \text{ MeV}/c)^2}{2\beta^3 E_{\mu} m_{\mu} X_0}; \quad (1)$$

where  $z$  is the longitudinal coordinate,  $\beta c$  is the muon velocity,  $E_{\mu}$  the energy,  $\langle \frac{dE}{dz} \rangle$  the mean rate of energy loss per unit path-length,  $m_{\mu}$  the mass of the muon,  $X_0$  the radiation length of the absorber and  $\beta_{\perp}$  the transverse betatron function at the absorber. The first term of this equation describes “cooling” by ionization energy loss and the second describes “heating” by multiple Coulomb scattering. Equation (1) implies that the equilibrium emittance, for which  $\frac{d\varepsilon_{\perp}}{dz} = 0$ , and the asymptotic value of  $\frac{d\varepsilon_{\perp}}{dz}$  for large emittance are functions of muon-beam energy.

In order to have good performance in an ionization-cooling channel,  $\beta_{\perp}$  needs to be minimized and  $X_0 \langle \frac{dE}{dz} \rangle$

maximised. The betatron function at the absorber is minimized using a suitable magnetic focusing channel (typically solenoidal) [22,23] and  $X_0 \langle \frac{dE}{dz} \rangle$  is maximized using a low- $Z$  absorber such as liquid hydrogen ( $\text{LH}_2$ ) or lithium hydride ( $\text{LiH}$ ) [24].

## III. THE MUON IONIZATION COOLING EXPERIMENT

The muons for MICE come from the decay of pions produced at an internal target dipping directly into the circulating proton beam in the ISIS synchrotron at the Rutherford Appleton Laboratory (RAL) [25,26]. A beam line of 9 quadrupoles, 2 dipoles and a superconducting “decay solenoid” collects and transports the momentum-selected beam into the experiment [27]. The small fraction of pions that remain in the beam may be rejected during analysis using the time-of-flight hodoscopes and Cherenkov counters that are installed in the beam line upstream of the experiment [28]. A diffuser is installed at the upstream end of the experiment to vary the initial emittance of the beam. Ionization cooling depends on momentum through  $\beta$ ,  $E_{\mu}$  and  $\langle \frac{dE}{dz} \rangle$  as shown in Eq. (1). It is therefore proposed that the performance of the cell be measured for momenta in the range 140 MeV/ $c$  to 240 MeV/ $c$  [15].

### A. The configuration of the ionization-cooling experiment

The configuration proposed for the demonstration of ionization cooling is shown in Fig. 1. It contains a cooling cell sandwiched between two spectrometer-solenoid modules. The cooling cell is composed of two 201 MHz cavities, one primary (65 mm) and two secondary (32.5 mm) LiH absorbers placed between two superconducting “focus-coil” (FC) modules. Each FC has two separate windings that can be operated either with the same or in opposed polarity.

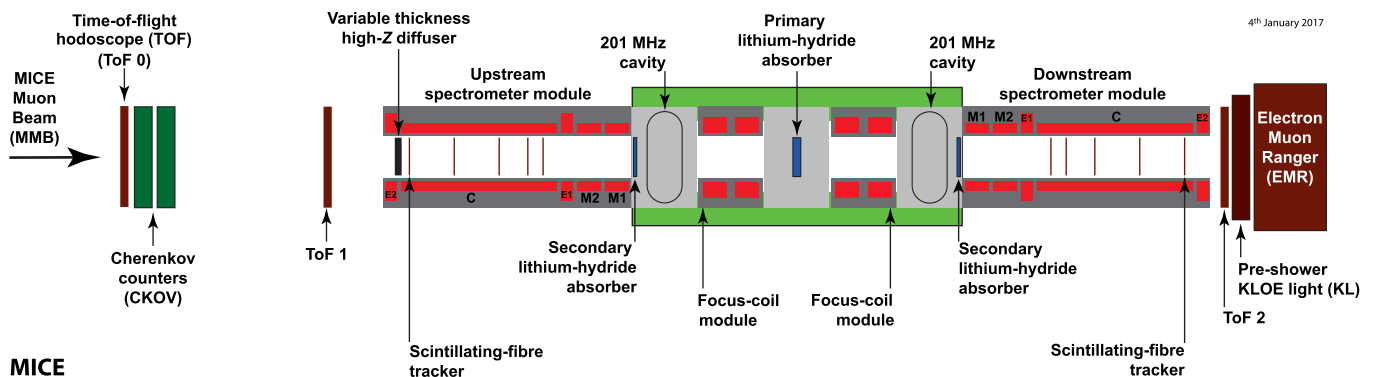


FIG. 1. Layout of the lattice configuration for the cooling demonstration. The red rectangles represent the solenoids. The individual coils in the spectrometer solenoids are labeled E1, C, E2, M1 and M2. The ovals represent the rf cavities and the blue rectangles the absorbers. The various detectors (time-of-flight hodoscopes [29,30], Cherenkov counters [31], scintillating-fibre trackers [32], KLOE Light (KL) calorimeter [27,33], electron muon ranger [34]) used to characterize the beam are also represented. The green-shaded box indicates the cooling cell.



The emittance is measured upstream and downstream of the cooling cell using scintillating-fiber tracking detectors [32] immersed in the uniform 4 T magnetic field provided by three superconducting coils (E1, C, E2). The trackers are used to reconstruct the trajectories of individual muons at the entrance and exit of the cooling cell. The reconstructed tracks are combined with information from instrumentation upstream and downstream of the spectrometer modules to measure the muon-beam emittance at the upstream and downstream tracker reference planes. The instrumentation upstream and downstream of the spectrometer modules serves to select a pure sample of muons. Time-of-flight hodoscopes are used to determine the time at which the muon crosses the rf cavities. The spectrometer-solenoid magnets also contain two superconducting “matching” coils (M1, M2) that are used to match the optics between the uniform field region and the neighboring FC.

The secondary LiH absorbers (SAs) are introduced between the cavities and the trackers to minimize the exposure of the trackers to “dark-current” electrons originating from the rf cavities. Experiments at the MuCool Test Area (MTA) at Fermilab [35] have observed that the rate of direct x-ray production from the rf cavities can be managed to ensure it does not damage the trackers [36]. The SAs are introduced to minimize the exposure of the trackers to energetic dark-current electrons that could produce background hits. The SAs are positioned between the trackers and the cavities such that they can be removed to study the empty channel. The SAs increase the net transverse-cooling effect since the betatron functions at these locations are small.

Retractable lead radiation shutters will be installed on rails between the spectrometer solenoids and the rf modules to protect the trackers against dark-current induced radiation during cavity conditioning. The SAs will be mounted on a rail system similar to that which will be used for the lead shutters and will be located between the cavities and the lead shutters. Both mechanisms will be moved using linear piezoelectric motors that operate in vacuum and magnetic field. The design of both the radiation shutter and the movable SA inside the vacuum chamber is shown in Fig. 2.

The rf cavities are 201 MHz “pillbox” resonators, 430 mm in length, operating in the  $TM_{010}$  mode with large diameter apertures to accommodate the high emittance beam. The apertures are covered by thin (0.38 mm) beryllium windows to define the limits for the accelerating rf fields whilst minimizing the scattering of muons. The cavity is excited by two magnetic-loop couplers on opposite sides of the cavity. At the particle rate expected in MICE there is no beam-loading of the rf fields. An effective peak field of 10.3 MV/m is expected for a drive power of 1.6 MW to each cavity. This estimate was used to define the gradient in the simulations described below.

The original configuration of the MICE cooling cell described in [15] was composed of three focus-coil modules, each of which housed a liquid-hydrogen absorber, and two,

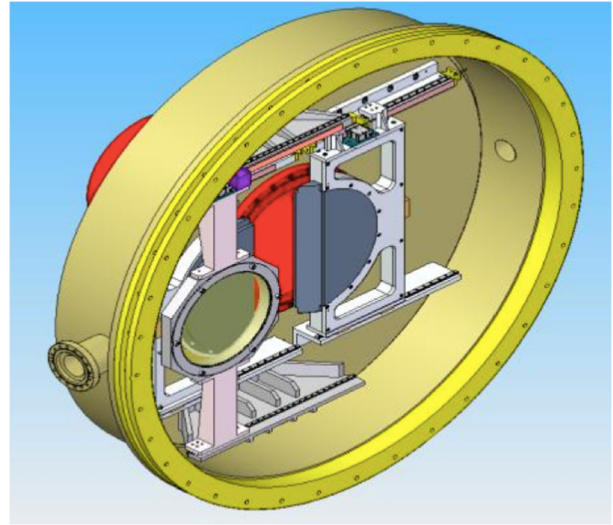


FIG. 2. Design of the movable frame for the secondary absorber (front) and the lead radiation shutter (back). The half discs of the lead shutter (grey) can be seen together with the rails (white) inside the vacuum chamber (yellow).

four-cavity, linac modules. Each linac module incorporated a large, superconducting “coupling coil” to transport the beam. The configuration described in this paper was developed to simplify the lattice described in [15] such that the coupling coils are not required and acceleration is provided by two single-cavity modules. The revision of the magnetic lattice substantially reduces the technical risks associated with the implementation of the experiment since all of the superconducting solenoids required to transport and focus the beam have been commissioned on the beam line. Further, by reducing the number of cavities from eight to two and reconfiguring the rf-power-distribution system the cost of implementing the experiment has been reduced and the timetable on which the experiment can be mounted has been advanced. The present configuration was optimized to maximize its cooling performance as described in Sec. IV. The performance of the optimized lattice, though reduced compared to that described in [15], is sufficient for the principle of ionization-cooling to be demonstrated (see Sec. VI).

## IV. LATTICE DESIGN

### A. Design parameters

The lattice has been optimized to maximize the reduction in transverse emittance. The optimum is obtained by matching the betatron function to a small value in the central absorber while minimizing its maximum values in the FC modules; limiting the size of the betatron function in the FCs helps to reduce the influence of nonlinear terms in the magnetic-field expansion. The matching accounts for the change in energy of the muons as they pass through the cooling cell by adjusting currents in the upstream and

downstream FCs and in the matching coils in the spectrometer solenoids independently while maintaining the field in the tracking volumes at 4 T. In this configuration, it is also possible to keep the betatron function relatively small at the position of the secondary absorbers whilst maintaining an acceptable beam size at the position of the cavities.

Chromatic aberrations caused by the large momentum spread of the beam ( $\sim 5\%$  rms) lead to a chromatic mismatch of the beam in the downstream solenoid unless the phase advance across the cooling cell (i.e., the rate of rotation of the phase-space ellipse) is chosen appropriately. The phase advance of the cell is obtained by integrating the inverse of the beta-function along the beam axis from the reference plane in the upstream spectrometer-solenoid to the reference plane in the downstream spectrometer-solenoid. Such a mismatch reduces the effective transverse-emittance reduction through the chromatic decoherence that results from the superposition of beam evolutions for the different betatron frequencies that result from the range of momenta in the beam. For beams with a large input emittance, spherical aberrations may lead to phase-space filamentation. The chromatic and spherical aberrations were studied by tracking samples of muons through the lattice using the ‘‘MICE Analysis User Software’’ (MAUS, see Sec. V). The betatron-function and emittance evolution of a 200 MeV/ $c$  beam with the

TABLE I. General parameters of the initial beam conditions used in the simulations.

Parameter	Value
Particle	muon $\mu^+$
Number of particles	10000
Longitudinal position [mm]	-4612.1
Central energy (140 MeV/ $c$ settings) [MeV]	175.4
Central energy (200 MeV/ $c$ settings) [MeV]	228.0
Central energy (240 MeV/ $c$ settings) [MeV]	262.2
Transverse Gaussian distribution:	
$\alpha_{\perp}$	0
$\beta_{\perp}$ (140 MeV/ $c$ settings) [mm]	233.5
$\varepsilon_{\perp}$ (140 MeV/ $c$ settings) [mm]	4.2
$\beta_{\perp}$ (200 MeV/ $c$ settings) [mm]	339.0
$\varepsilon_{\perp}$ (200 MeV/ $c$ settings) [mm]	6.0
$\beta_{\perp}$ (240 MeV/ $c$ settings) [mm]	400.3
$\varepsilon_{\perp}$ (240 MeV/ $c$ settings) [mm]	7.2
Longitudinal Gaussian distribution:	
Longitudinal emittance [mm]	20
Longitudinal $\beta$ [ns]	11
Longitudinal $\alpha$	-0.7
rms momentum spread (140 MeV/ $c$ settings)	4.8%
rms time spread (140 MeV/ $c$ settings) [ns]	0.40
rms momentum spread (200 MeV/ $c$ settings)	4.0%
rms time spread (200 MeV/ $c$ settings) [ns]	0.34
rms momentum spread (240 MeV/ $c$ settings)	3.6%
rms time spread (240 MeV/ $c$ settings) [ns]	0.31

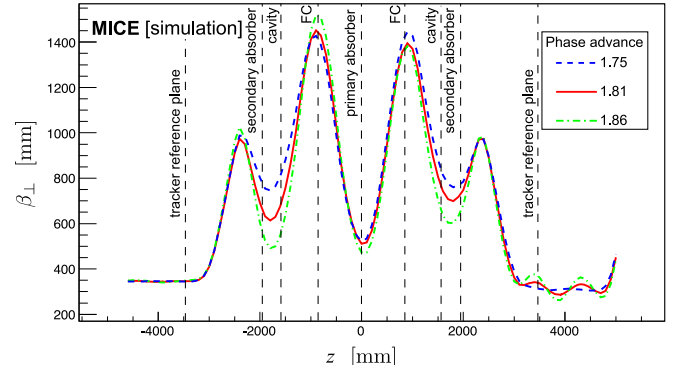


FIG. 3. Transverse 4D beta-function versus longitudinal coordinate  $z$  in the cooling-demonstration lattice for 200 MeV/ $c$  settings with a phase advance of  $2\pi \times 1.75$  (dashed blue line),  $2\pi \times 1.81$  (solid red line) and  $2\pi \times 1.86$  (dot-dashed green line). The vertical dashed lines with labels show the positions of the tracker reference planes and the centers of the absorbers, rf cavities, and focus coil modules.

initial parameters given in Table I are shown, for different phase advances, in Figs. 3 and 4, respectively. The phase advance of  $2\pi \times 1.81$  showed the largest transverse-emittance reduction and was therefore chosen. The lattice parameters for this phase advance are presented in Table II.

The currents that produce the optimum magnetic lattice were obtained using the procedure described above for three momentum settings: 140 MeV/ $c$ , 200 MeV/ $c$ , and 240 MeV/ $c$ . The magnetic field on axis for each of these settings is shown in Fig. 5. The fields in the downstream FC and spectrometer are opposite to those in the upstream FC and spectrometer, the field changing sign at the primary absorber. Such a field flip is required in an ionization cooling channel to reduce the build-up of canonical angular momentum [37]. The currents required to produce the magnetic fields shown in Fig. 5 are listed in Table III. All currents are within the proven limits of operation for the

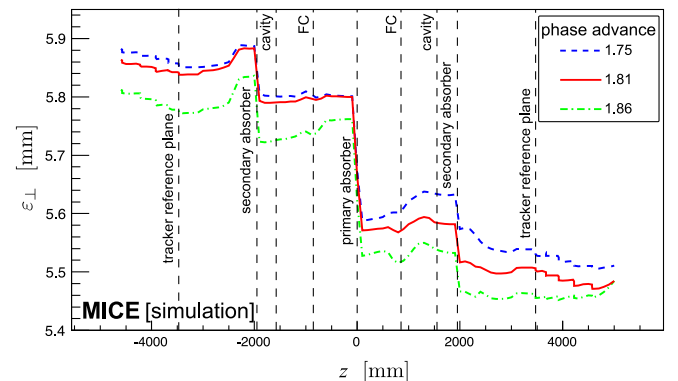


FIG. 4. 4D emittance evolution in the cooling-demonstration lattice for 200 MeV/ $c$  settings with a phase advance of  $2\pi \times 1.75$  (dashed blue line),  $2\pi \times 1.81$  (solid red line) and  $2\pi \times 1.86$  (dot-dashed green line). The vertical dashed lines with labels show the positions of the tracker reference planes and the centers of the absorbers, rf cavities, and focus coil modules.

TABLE II. Parameters of the cooling-demonstration lattice.  $L_{SS \rightarrow FC}$  is the distance between the center of the spectrometer solenoid and the center of the neighboring FC,  $L_{FC \rightarrow FC}$  the distance between the centers of the FCs, and  $L_{RF \text{ module} \rightarrow FC}$  the distance between the rf module and the neighboring FC.

Parameter	Value
Length $L_{SS \rightarrow FC}$ [mm]	2607.5
Length $L_{FC \rightarrow FC}$ [mm]	1678.8
Length $L_{rf \text{ module} \rightarrow FC}$ [mm]	784.0
rf Gradient [MV/m]	10.3
Number of rf cavities	2
Number of primary absorbers	1
Number of secondary absorbers	2

individual coil windings. The magnetic forces acting on the coils have been analyzed and were found to be acceptable. Configurations in which there is no field flip can also be considered.

Figure 6 shows matched betatron functions versus longitudinal position for beams of different initial momentum. These betatron functions are constrained, within the fiducial-volume of the trackers, by the requirements on the Courant-Snyder parameters  $\alpha_{\perp} = 0$  and  $\beta_{\perp} = \frac{2p_z}{eB_z}$  (where  $p_z$  is the mean longitudinal momentum of the beam,  $e$  the elementary charge and  $B_z$  the longitudinal component of the magnetic field). A small betatron-function “waist” in the central absorber is achieved. Betatron-function values at relevant positions in the different configurations are summarized in Table IV.

## V. SIMULATION

Simulations to evaluate the performance of the lattice have been performed using the official MICE simulation

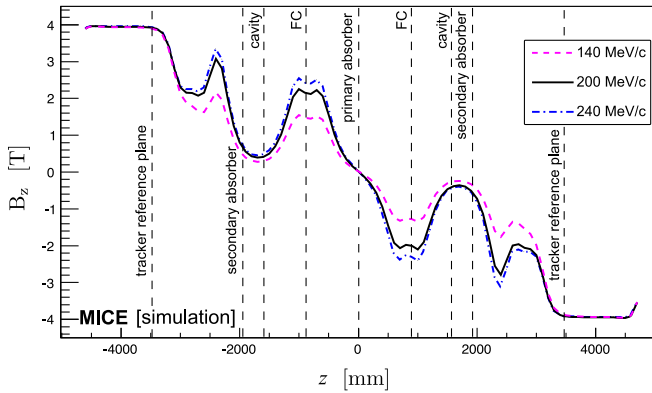


FIG. 5. Magnetic field  $B_z$  on-axis versus the longitudinal coordinate  $z$  for the cooling-demonstration lattice design for 200 MeV/c (solid black line), 140 MeV/c (dashed purple line), and 240 MeV/c (dot-dashed blue line) settings. The vertical dashed lines with labels show the positions of the tracker reference planes and the centres of the absorbers, rf cavities, and focus coil modules.

TABLE III. Coil currents used for 140 MeV/c, 200 MeV/c, and 240 MeV/c lattice settings.

Coil	140 MeV/c Lattice [A]	200 MeV/c Lattice [A]	240 MeV/c Lattice [A]
Upstream E2	+253.00	+253.00	+253.00
Upstream C	+274.00	+274.00	+274.00
Upstream E1	+234.00	+234.00	+234.00
Upstream M2	+126.48	+155.37	+163.50
Upstream M1	+175.89	+258.42	+280.72
Upstream FC-coil 1	+54.14	+79.35	+89.77
Upstream FC-coil 2	+54.14	+79.35	+89.77
Downstream FC-coil 1	-47.32	-74.10	-85.35
Downstream FC-coil 2	-47.32	-74.10	-85.35
Downstream M1	-140.43	-231.60	-261.71
Downstream M2	-100.12	-149.15	-159.21
Downstream E1	-234.00	-234.00	-234.00
Downstream C	-274.00	-274.00	-274.00
Downstream E2	-253.00	-253.00	-253.00

and reconstruction software MAUS (MICE Analysis User Software) [38]. In addition to simulation, MAUS also provides a framework for data analysis. MAUS is used for offline analysis and to provide fast real-time detector reconstruction and data visualisation during MICE running. MAUS uses GEANT4 [39,40] for beam propagation and the simulation of detector response. ROOT [41] is used for data visualisation and for data storage.

Particle tracking has been performed for several configurations. The parameters of the initial beam configurations used for the simulations are summarized in Table I.

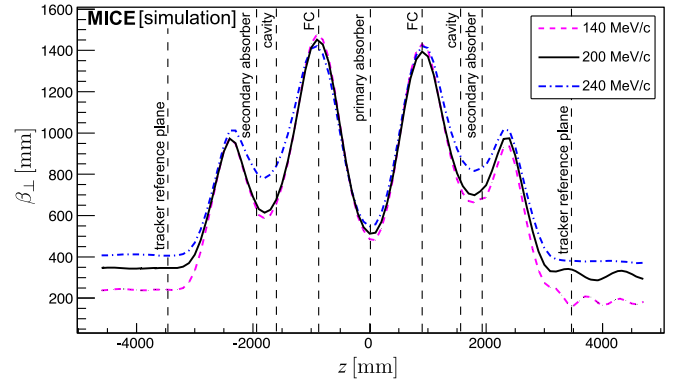


FIG. 6.  $\beta_{\perp}$  versus the longitudinal coordinate  $z$  for 200 MeV/c (solid black line), 140 MeV/c (dashed purple line) and 240 MeV/c (dot-dashed blue line) in the cooling-demonstration lattice. The vertical dashed lines with labels show the positions of the tracker reference planes and the centers of the absorbers, rf cavities, and focus coil modules.

TABLE IV. Beta-function values at relevant positions for an initial beam at 140 MeV/c, 200 MeV/c, and 240 MeV/c in the cooling-demonstration lattice design.

Parameter	Value for 140 MeV/c	Value for 200 MeV/c	Value for 240 MeV/c
$\beta_{\perp}$ at primary absorber [mm]	480	512	545
$\beta_{\perp}$ at upstream secondary absorber [mm]	660	710	840
$\beta_{\perp}$ at downstream secondary absorber [mm]	680	740	850
$\beta_{\perp \text{ max}}$ at FC [mm]	1480	1450	1430

The simulation of the beam starts at a point between the diffuser and the first plane of the tracker. The beam is generated by a randomizing algorithm with a fixed seed. The number of particles launched for each simulation is a compromise between the statistical uncertainty required ( $\approx 1\%$ ) and computing time. Each cavity is simulated by a TM<sub>010</sub> ideal cylindrical pillbox with a peak effective gradient matched to that expected for the real cavities. The reference particle is used to set the phase of the cavities so that it is accelerated “on crest.” The initial distributions defined in Table I are centred on the reference particle in both time and momentum. Table V lists the acceptance criteria applied to all analyses presented here. Trajectories that fail to meet the acceptance criteria are removed from the analysis.

The normalized transverse emittance is calculated by taking the fourth root of the determinant of the four-dimensional phase-space covariance matrix [20,21]. The MICE collaboration plans to take data such that the statistical uncertainty on the relative change in emittance for a particular setting is 1%. The MICE instrumentation was designed such that the systematic uncertainty related to the reconstruction of particle trajectories would contribute at the  $\sim 0.3\%$  level to the overall systematic uncertainty [15]; such uncertainties would thus be negligible.

## VI. PERFORMANCE

Figure 7 shows the evolution of the mean energy of a muon beam as it traverses the lattice. Beams with initial normalised transverse emittance  $\epsilon_{\perp} = 4.2$  mm,

TABLE V. Acceptance criteria for analysis.

Parameter	Acceptance condition
Particle	muon $\mu^+$
Transmission: pass through two planes	$z = -4600$ mm and $z = 5000$ mm
Radius at $z = -4600$ mm	$\leq 150.0$ mm
Radius at $z = 5000$ mm	$\leq 150.0$ mm

$\epsilon_{\perp} = 6$  mm, and  $\epsilon_{\perp} = 7.2$  mm for initial muon beam momenta of 140 MeV/c, 200 MeV/c, and 240 MeV/c respectively are shown. The initial normalized transverse emittance is chosen such that the geometrical emittance of the three beams is the same. A 200 MeV/c muon passing through two 32.5 mm thick secondary LiH absorbers and one 65 mm thick primary LiH absorber loses an energy of 18.9 MeV. Including losses in the scintillating-fiber

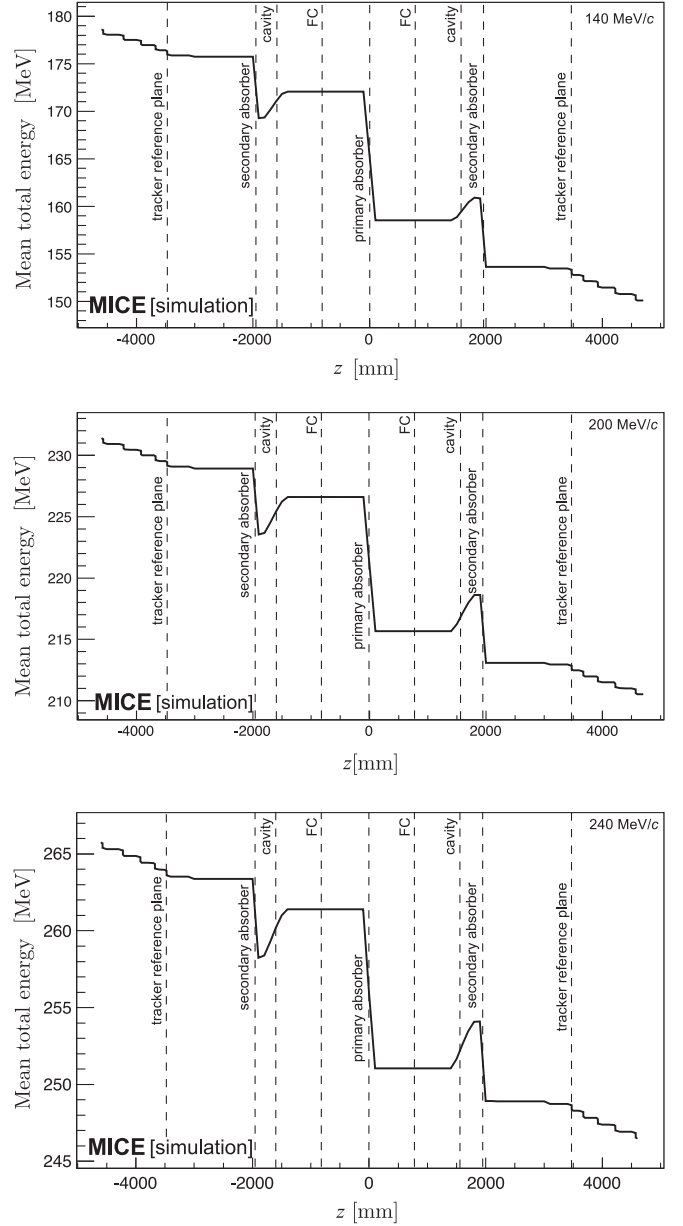


FIG. 7. Mean energy of the beam versus longitudinal coordinate ( $z$ ) in the cooling-demonstration lattice. Top: the 140 MeV/c configuration for initial emittance  $\epsilon_{\perp} = 4.2$  mm. Middle: the 200 MeV/c configuration for initial emittance  $\epsilon_{\perp} = 6$  mm. Bottom: the 240 MeV/c configuration for initial emittance  $\epsilon_{\perp} = 7.2$  mm. The vertical dashed lines with labels show the positions of the tracker reference planes, and the centers of the absorbers, rf cavities, and focus coil modules.

trackers and windows, this increases to 24.3 MeV. The accelerating gradient that can be achieved in each of the two cavities is constrained by the available rf power and is insufficient to replace all the lost energy. Therefore, a comparison of beam energy with and without acceleration is required. With acceleration an energy

deficit of  $\langle \Delta E \rangle = 19$  MeV will be observed. This measurable difference will be used to extrapolate the measured cooling effect to that which would pertain if all the lost energy were restored.

The evolution of normalized transverse emittance across the lattice is shown in Fig. 8. The beam is subject to nonlinear effects in regions of high  $\beta_{\perp}$ , which cause the normalized transverse emittance to grow, especially in the 140 MeV/c configuration. This phenomenon can be seen in three different regions of the lattice: a moderate increase in emittance is observed at  $z \approx -2500$  mm and  $z \approx 1000$  mm while a larger increase is observed at  $z \approx 3000$  mm. The nonlinear effects are mainly chromatic in origin, since they are greatly lessened when the initial momentum spread is reduced. This is illustrated for the 140 MeV/c case for which the evolution of normalized emittance for beams with an rms momentum spread of 6.7 MeV/c and 2.5 MeV/c are shown. Nonetheless, in all cases a reduction in emittance is observed between the upstream and downstream trackers ( $z = \pm 3473$  mm). The lattice is predicted to achieve an emittance reduction between the tracker reference planes of  $\approx 8.1\%$ ,  $\approx 5.8\%$  and  $\approx 4.0\%$  in the 140 MeV/c, 200 MeV/c, and 240 MeV/c cases, respectively. A reduction as large as  $\approx 10\%$  can be reached in the 140 MeV/c configuration with an rms momentum spread of 1.4%.

The transmission of the cooling-demonstration lattice for beams of mean momentum 140 MeV/c, 200 MeV/c, and 240 MeV/c is shown in Fig. 9. Transmission is computed as the ratio of the number of particles that satisfy the acceptance criteria observed downstream of the cooling cell divided by the number that enter the cell. This accounts

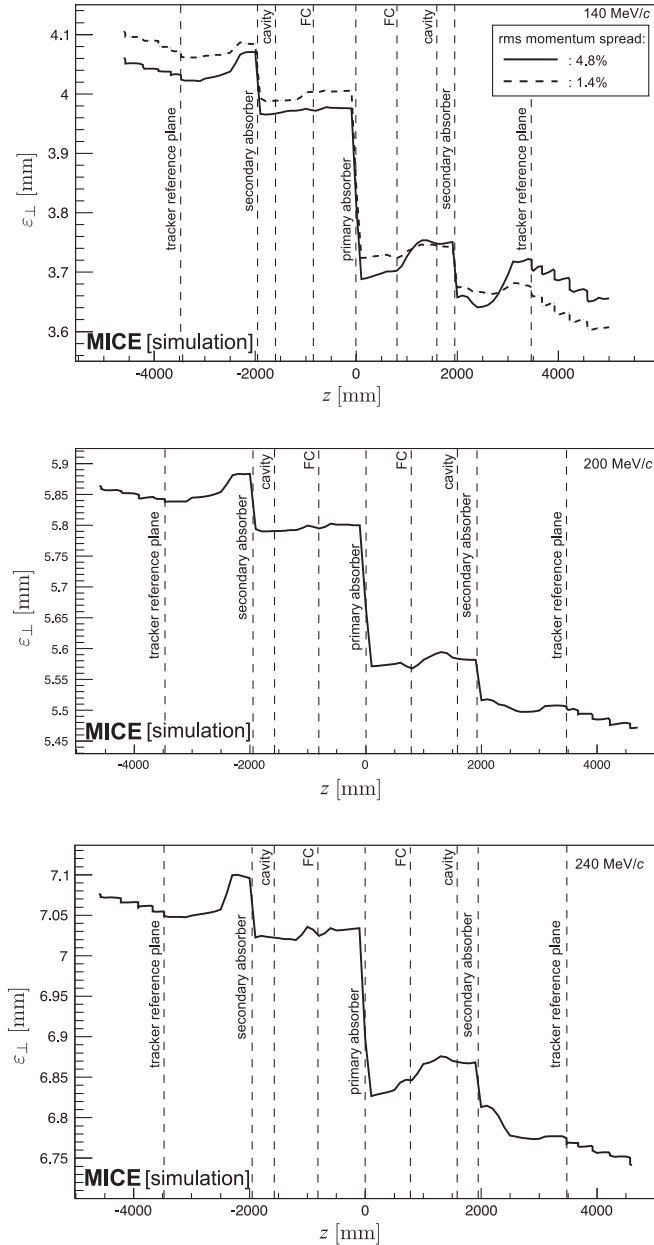


FIG. 8. Emittance variation versus the longitudinal coordinate ( $z$ ) for the cooling-demonstration lattice design. Top: 140 MeV/c beam with initial  $\varepsilon_{\perp} = 4.2$  mm with an rms momentum spread of 6.7 MeV/c (rms spread 4.8%, solid line) and 2.5 MeV/c (rms spread 1.8%, dashed line). Middle: 200 MeV/c beam with initial  $\varepsilon_{\perp} = 6$  mm (rms spread 4.0%). Bottom: 240 MeV/c beam with initial  $\varepsilon_{\perp} = 7.2$  mm (rms spread 3.6%). The vertical dashed lines with labels show the positions of the tracker reference planes, and the centers of the absorbers, rf cavities, and focus coil modules.

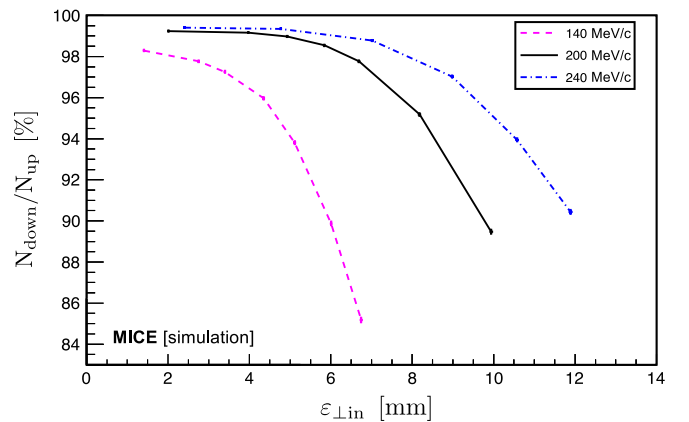


FIG. 9. Transmission (defined as the ratio of good muons observed downstream of the cooling cell,  $N_{\text{down}}$ , to those observed upstream,  $N_{\text{up}}$ ) in percent versus initial emittance ( $\varepsilon_{\perp,\text{in}}$ ) for the cooling-demonstration lattice. The transmission of the 140 MeV/c, 200 MeV/c, and 240 MeV/c lattices are shown as the purple-dashed, solid black, and dot-dashed blue lines respectively. The error bars indicate the statistical precision that would be achieved using a sample of 100,000 muons.

for decay losses and implies that, in the absence of scraping or acceptance losses, the maximum transmission for beams of mean momentum 140 MeV/c, 200 MeV/c, and 240 MeV/c is 98.9%, 99.2%, and 99.5%, respectively. The lattice delivers transmission close to the maximum for 200 MeV/c and 240 MeV/c beams with input emittance below  $\approx 5$  mm and  $\approx 7$  mm, respectively. For beams of larger input emittance, the transmission gradually decreases with increasing initial emittance due to the scraping of high amplitude muons. The beam is subject to chromatic effects in regions of high  $\beta_{\perp}$ , which causes nonlinear emittance growth and limits the transmission. The behavior of the transmission for the various beam energies results from the different geometrical emittance values of the beam for the same initial normalised emittance and the energy dependence of the energy loss and scattering in the material through which the beam passes.

The fractional change in normalized transverse emittance with respect to the input emittance for beams of mean momentum 140 MeV/c, 200 MeV/c, and 240 MeV/c is shown in Fig. 10. The different values of the equilibrium emittance and the asymptote at large emittance for each momentum are clearly visible in Fig. 10. A maximum cooling effect of 15%, 8%, and 6% can be observed for beams with 140 MeV/c, 200 MeV/c, and 240 MeV/c, respectively.

The performance of the configuration proposed here is comparable to that described in [15]. In the ‘‘Step V’’ configuration, that incorporated two liquid-hydrogen absorbers each placed within a focus-coil module capable of providing a value  $\beta_{\perp}$  smaller than that which can be achieved with the present lattice, the maximum cooling effect with an input momentum and emittance of

200 MeV/c and 10 mm respectively, was  $\sim 10\%$ . Figures 9 and 10 show the statistical uncertainties that will result from the reconstruction of a sample of 100,000 muons [42] with the configuration proposed in this paper. The instrumentation was specified to ensure that no single source of systematic uncertainty would contribute more than one third of the statistical uncertainty on the fractional change in emittance [15]. All of the instrumentation has been commissioned on the beam-line and performs to specification. The emittance-change evolution presented in Fig. 10 can therefore be measured with high significance.

## VII. CONCLUSION

An experiment by which to demonstrate ionization cooling has been described that is predicted by simulations to exhibit cooling over a range of momentum. The demonstration is performed using lithium-hydride absorbers and with acceleration provided by two 201 MHz cavities. The equipment necessary to mount the experiment is either in hand (the superconducting magnets and instrumentation), or at an advanced stage of preparation. The configuration of the demonstration of ionization cooling has been shown to deliver the performance required for the detailed study of the ionization-cooling technique.

The demonstration of ionization cooling is essential to the future development of muon-based facilities that would provide the intense, well characterized low-emittance muon beams required to elucidate the physics of flavor at a neutrino factory or to deliver multi-TeV lepton-antilepton collisions at a muon collider. The successful completion of the MICE programme would therefore herald the establishment of a new technique for particle physics.

## ACKNOWLEDGMENTS

The work described here was made possible by grants from the Science and Technology Facilities Council (UK), the Department of Energy and National Science Foundation (USA), the Instituto Nazionale di Fisica Nucleare (Italy), the Bulgarian Academy of Sciences, the Chinese Academy of Sciences, the Dutch National Science Foundation, the Ministry of Education, Science and Technological Development of the Republic of Serbia, the European Community under the European Commission Framework Programme 7 (AIDA project, Grant Agreement No. 262025, TIARA project, Grant Agreement No. 261905, and EuCARD), the Japan Society for the Promotion of Science and the Swiss National Science Foundation in the framework of the SCOPES programme. We gratefully acknowledge all sources of support. We are grateful to the support given to us by the staff of the STFC Rutherford Appleton and Daresbury Laboratories. We acknowledge the use of Grid computing resources deployed and operated by GridPP in the UK, <http://www.gridpp.ac.uk/>.

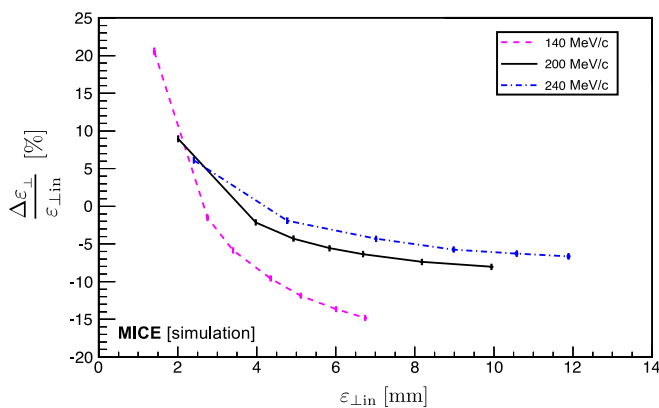


FIG. 10. Fractional change in emittance versus initial emittance ( $\epsilon_{\perp in}$ ) for the cooling-demonstration lattice design measured at the tracker reference planes. The fractional change in emittance of the 140 MeV/c, 200 MeV/c, and 240 MeV/c lattices are shown as the purple-dashed, solid black, and dot-dashed blue lines, respectively. The error bars indicate the statistical precision that would be achieved using a sample of 100,000 muons.

- [1] S. Geer, Neutrino beams from muon storage rings: Characteristics and physics potential, *Phys. Rev. D* **57**, 6989 (1998).
- [2] M. Apollonio *et al.*, Oscillation Physics with a Neutrino Factory, [arXiv:hep-ph/0210192](https://arxiv.org/abs/hep-ph/0210192).
- [3] D. V. Neuffer and R. B. Palmer, A high-energy high-luminosity  $\mu^+\mu^-$  collider in *Proceedings of the Fourth European Particle Accelerator Conference EPAC 94, London, England* (World Scientific, River Edge, NJ, 1994), p. 52.
- [4] R. B. Palmer, Muon colliders, *Rev. Accel. Sci. Technol.* **07**, 137 (2014).
- [5] S. Y. Lee, *Accelerator Physics*, 3rd ed., edited by S. Y. Lee (World Scientific, Singapore, 2012).
- [6] S. Schröder *et al.*, First laser cooling of relativistic ions in a storage ring, *Phys. Rev. Lett.* **64**, 2901 (1990).
- [7] J. S. Hangst, M. Kristensen, J. S. Nielsen, O. Poulsen, J. P. Schiffer, and P. Shi, Laser cooling of a stored ion beam to 1 mK, *Phys. Rev. Lett.* **67**, 1238 (1991).
- [8] P. J. Channell, Laser cooling of heavy ion beams, *J. Appl. Phys.* **52**, 3791 (1981).
- [9] J. Marriner, Stochastic cooling overview, *Nucl. Instrum. Methods Phys. Res., Sect. A* **532**, 11 (2004).
- [10] V. V. Parkhomchuk and A. N. Skrinsky, Electron cooling: 35 years of development, *Phys. Usp.* **43**, 433 (2000).
- [11] A. N. Skrinsky and V. V. Parkhomchuk, Cooling methods for beams of charged particles, *Fiz. Elem. Chastits At. Yadra* **12**, 557 (1981) [*Sov. J. Part. Nucl.* **12**, 223 (1981)].
- [12] D. Neuffer, Principles and applications of muon cooling, in *Proceedings, 12th International Conference on High-Energy Accelerators, HEACC 1983: Fermilab, Batavia, 1983*, Vol. C830811 (Fermi National Accelerator Laboratory, Batavia, 1983), p. 481–484.
- [13] D. Neuffer, Principles and applications of muon cooling, *Part. Accel.* **14**, 75 (1983).
- [14] D. Rajaram and V. C. Palladino, The status of MICE Step IV, in *Proceedings, 6th International Particle Accelerator Conference (IPAC 2015): Richmond, Virginia, USA, 2015* (JACoW, Geneva, 2015), p. 4000.
- [15] MICE Collaboration, MICE: An International Muon Ionization Cooling Experiment, <http://mice.iit.edu/micenotes/public/pdf/MICE0021/MICE0021.pdf> (2003), MICE Note 21.
- [16] M. Apollonio *et al.* (ISS Accelerator Working Group Collaboration), Accelerator design concept for future neutrino facilities, *J. Instrum.* **4**, P07001 (2009).
- [17] C. M. Ankenbrandt *et al.*, Status of muon collider research and development and future plans, *Phys. Rev. ST Accel. Beams* **2**, 081001 (1999).
- [18] M. M. Alsharoa *et al.* (Neutrino Factory and Muon Collider Collaboration), Recent progress in neutrino factory and muon collider research within the Muon collaboration, *Phys. Rev. ST Accel. Beams* **6**, 081001 (2003).
- [19] R. B. Palmer, J. S. Berg, R. C. Fernow, J. C. Gallardo, H. G. Kirk, Y. Alexahin, D. Neuffer, S. A. Kahn, and D. Summers, A complete scheme of ionization cooling for a muon collider, in *Proceedings of the 22nd Particle Accelerator Conference, PAC-2007, Albuquerque, NM* (IEEE, New York, 2007), p. 3193.
- [20] G. Penn and J. S. Wurtele, Beam Envelope Equations for Cooling of Muons in Solenoid Fields, *Phys. Rev. Lett.* **85**, 764 (2000).
- [21] C. Rogers, Ph.D. dissertation, Imperial College of London, 2008.
- [22] D. Stratakis and R. B. Palmer, Rectilinear six-dimensional ionization cooling channel for a muon collider: A theoretical and numerical study, *Phys. Rev. ST Accel. Beams* **18**, 031003 (2015).
- [23] D. Neuffer, H. Sayed, T. Hart, and D. Summers, Final Cooling for a High-Energy High-Luminosity Lepton Collider, [arXiv:1612.08960](https://arxiv.org/abs/1612.08960).
- [24] A. V. Tollestrup and J. Monroe, Fermi National Accelerator Laboratory Technical Report No. FERMILAB-MUCOOL-176, 2000.
- [25] C. N. Booth *et al.*, The design, construction and performance of the MICE target, *J. Instrum.* **8**, P03006 (2013).
- [26] C. N. Booth *et al.*, The design and performance of an improved target for MICE, *J. Instrum.* **11**, P05006 (2016).
- [27] M. Bogomilov *et al.* (MICE Collaboration), The MICE Muon Beam on ISIS and the beam-line instrumentation of the Muon Ionization Cooling Experiment, *J. Instrum.* **7**, P05009 (2012).
- [28] D. Adams *et al.* (MICE Collaboration), Characterisation of the muon beams for the Muon Ionisation Cooling Experiment, *Eur. Phys. J. C* **73**, 2582 (2013).
- [29] R. Bertoni *et al.*, The design and commissioning of the MICE upstream time-of-flight system, *Nucl. Instrum. Methods Phys. Res., Sect. A* **615**, 14 (2010).
- [30] R. Bertoni, M. Bonesini, A. de Bari, G. Cecchet, Y. Karadzhev, and R. Mazza, The construction of the MICE TOF2 detector, <http://mice.iit.edu/micenotes/public/pdf/MICE0286/MICE0286.pdf> (2010).
- [31] L. Cremaldi, D. A. Sanders, P. Sonnek, D. J. Summers, and J. Reidy, Jr., A Cherenkov radiation detector with high density aerogels, *IEEE Trans. Nucl. Sci.* **56**, 1475 (2009).
- [32] M. Ellis *et al.*, The design, construction and performance of the MICE scintillating fibre trackers, *Nucl. Instrum. Methods Phys. Res., Sect. A* **659**, 136 (2011).
- [33] F. Ambrosino *et al.*, Calibration and performances of the KLOE calorimeter, *Nucl. Instrum. Methods Phys. Res., Sect. A* **598**, 239 (2009).
- [34] R. Asfandiyarov *et al.*, The design and construction of the MICE Electron-Muon Ranger, *J. Instrum.* **11**, T10007 (2016).
- [35] M. Leonova *et al.*, MICE cavity installation and commissioning/operation at MTA, in *Proceedings, 6th International Particle Accelerator Conference (IPAC 2015): Richmond, Virginia, USA, 2015* (JACoW, Geneva, 2015), p. 3342–3344.
- [36] Y. Torun *et al.*, Final commissioning of the MICE RF module prototype with production couplers, in *Proceedings, 7th International Particle Accelerator Conference (IPAC 2016): Busan, Korea, 2016* (JACoW, Geneva, 2016), p. 474.
- [37] R. C. Fernow and R. B. Palmer, Solenoidal ionization cooling lattices, *Phys. Rev. ST Accel. Beams* **10**, 064001 (2007).
- [38] C. D. Tunnell and C. T. Rogers, MAUS: MICE Analysis User Software, in *Proceedings of the 2nd International Particle Accelerator Conference, San Sebastián, Spain* (EPS-AG, Spain, 2011), p. 850.

- 
- [39] S. Agostinelli *et al.* (GEANT4 Collaboration), GEANT4: A simulation toolkit, *Nucl. Instrum. Methods Phys. Res., Sect. A* **506**, 250 (2003).
- [40] J. Allison *et al.*, Geant4 developments and applications, *IEEE Trans. Nucl. Sci.* **53**, 270 (2006).
- [41] R. Brun and F. Rademakers, ROOT: An object oriented data analysis framework, *Nucl. Instrum. Methods Phys. Res., Sect. A* **389**, 81 (1997).
- [42] C. Hunt, Ph.D. dissertation, Imperial College of London, 2017.



S01-NPNE-001 / **Invited talk**

## **Applications of Geant4 simulation methods in studies of nuclear processes**

**Author:** Dejan Joković<sup>1</sup><sup>1</sup> *Institute of Physics, University of Belgrade, Pregrevica 118, 11080 Belgrade, Serbia***Presenter:** D. Joković (yokovic@ipb.ac.rs)

Geant4 is a toolkit for Monte Carlo simulations of the particle transport through matter. It has a complete set of routines for modelling particle trajectories and interactions: geometry and materials, physical processes, event generation, detector response and analysis and visualisation. It has been used in wide range of applications in high energy, nuclear and accelerator physics, as well as in studies in medical and space science.

The low-background underground laboratory at the Institute of Physics Belgrade is a facility for gamma-ray spectroscopy measurements and for measurements of the cosmic-ray muon intensity. Related to the two research objectives, studies of the cosmic-ray muon induced background in gamma-ray spectroscopy is of particular interest. In these experiments various Monte Carlo based simulations (Geant4, CORSIKA) have been extensively used.

Continuous measurements of the cosmic-ray muon intensity at the ground and the underground levels have been done since 2002, by means of plastic scintillation detectors. The detector response, interpretation of the experimental spectra and their calibration have been done and verified using Geant4 based simulation. The results of the simulations were used for calculation of the muon fluxes at the ground and the underground levels [1].

The scintillation detector in the underground laboratory can operate in coincidence with HPGe gamma-ray detector. A simulation of the coincident response of the two detectors to the cosmic-ray muons has been made in order to determine the muon contribution to the background spectrum of the HPGe detector [2]. The cosmic-ray muons contribute to the background through production of particles in detector surroundings. In low-level gamma spectroscopy, neutrons are produced in the lead shielding of an HPGe detector. The Geant4 simulation of the muon induced neutron production in lead has been developed. It can also be used for the simulation of production of nuclei in rock or soil.

The Geant4 toolkit has been widely applied in efficiency calibration of HPGe detectors in gamma-ray spectroscopy measurements. The main problem with this method is an imprecise detector description; the detector parameters initially are not well defined and certain parameters deteriorate with time. Therefore the simulation models need to be optimised in order to obtain the best possible agreement with experimental results. Several studies on uses of the Geant4 based simulations in calculation of efficiency of HPGe detectors have been performed, applied to different detector assemblies [3,4].

**Presenter:** S. Stojku (stefans@ipb.ac.rs)

Through analytical arguments, numerical calculations and comparison with experimental data, we show that the ratio of high  $p_{\perp}$  observables  $v_2/(1 - R_{AA})$  reaches a well-defined saturation value at high  $p_{\perp}$ , which depends on the spatial anisotropy of quark-gluon plasma formed in ultrarelativistic heavy ion collisions. By using our recently developed DREENA framework, which can accommodate any temperature profile, we calculate this ratio for various temperature evolutions and demonstrate that it is robustly related to the time-averaged anisotropy of the evolving QGP, as seen by jets. With the future reduction of experimental errors, our method will provide a way to constrain an important bulk property of the medium – spatial anisotropy of QGP – directly from high pt experimental data.

S01-NPNE-109 / Oral presentation

## HPGe detector characterisation by means of Monte Carlo simulation through application of Geant4 toolkit

**Author:** Milos Travar<sup>1</sup>

**Co-authors:** Jovana Nikolov<sup>1</sup>; Natasa Todorovic<sup>1</sup>; Andrej Vranicar<sup>1</sup>; Dejan Jokovic<sup>2</sup>; Igor Celikovic<sup>3</sup>; Tamara Milanovic<sup>3</sup>; Peter Völgyesi<sup>4</sup>; Dosa Gergely<sup>4</sup>; Peter Kirchknopf<sup>4</sup>; Krisztian Soós<sup>4</sup>

<sup>1</sup> Faculty of Sciences, University of Novi Sad, Serbia

<sup>2</sup> Institute for Physics, University of Belgrade, Serbia

<sup>3</sup> University of Belgrade, Institute for Nuclear Sciences Vinca, Serbia

<sup>4</sup> Centre for Energy Research, Nuclear Security Department, Hungary

**Presenter:** M. Travar (travarmilos@gmail.com)

Over the years High Purity Germanium (HPGe) detectors proved to be an excellent practical tool and as such have established their today's wide use in low background  $\gamma$ -spectrometry. One of the advantages of gamma ray spectrometry is its easy sample preparation as chemical processing and separation of the studied subject is not required. Thus, with a single measurement one can simultaneously perform both qualitative and quantitative analysis. One of the most prominent features of HPGe detectors, besides their excellent efficiency is their superior resolution. This feature virtually allows researcher to perform a thorough analysis by discriminating photons of similar energies in the studied spectra where otherwise they would superimpose within a single-energy peak and as such could potentially scathe analysis and produce wrongly assessed results. Naturally, this feature is of great importance when identification of radionuclides, as well as their activity concentrations, is being practiced where high precision comes as a necessity. In measurements of this nature, in order to be able to reproduce good and trustworthy results, one has to have initially performed an adequate full energy peak (FEP) efficiency calibration of the used equipment. However, experimental determination of the response i.e. efficiency curves for a given detector-sample configuration and its geometry is not

always easy and requires a certain set of reference calibration sources in order to account for and cover broader energy ranges of interest. With the goal of overcoming these difficulties, a lot of researches turned towards the application of different software toolkits that implement Monte Carlo method (e.g. MCNP, FLUKA, PENLOPE, Geant4, etc.), as it has proven time and time again to be a very powerful tool. In the process of creating a reliable model, one has to have a well-established and described specifications of the detector. Unfortunately, the documentation that manufacturers provide alongside of the equipment are rarely sufficient enough for this purpose. Furthermore, certain parameters tend to evolve and change over time, especially with older equipment. Deterioration of these parameters consequently decrease the active volume of the crystal and can thus affect the efficiencies by a large margin if they're not properly taken into account. In this study, the optimisation method of two HPGe detectors through implementation of Geant4 toolkit developed by CERN is described, with the goal of further improving simulation accuracy in calculations of FEP efficiencies by investigating the influence of certain detector variables (e.g. crystal-to-window distance, dead layer thicknesses, inner crystal's void dimensions, etc.). Detectors on which the optimisation procedures were carried out were a standard traditional co-axial extended range detector (XtRa HPGe, CANBERRA) and a broad energy range planar detector (BEGe, CANBERRA). Optimised models were verified through comparison with experimentally obtained data from measurements of a set of point-like radioactive sources. Acquired results of both detectors displayed good agreement with experimental data that falls under an average statistical uncertainty of  $\sim 4.6\%$  for XtRa and  $\sim 1.8\%$  for BEGe detector within the energy range of 59.4–1836.1 [keV] and 59.4–1212.9 [keV], respectively.

S01-NPNE-200 / **Poster presentation (virtual)**

## **Uncertainty estimation in Individual Monitoring – Part I**

**Authors:** Irma Bërdufi<sup>1</sup>; Erjon Spahiu<sup>2</sup>; Manjola Shyti<sup>1</sup>

<sup>1</sup> *University of Tirana, Institute of Applied Nuclear Physics, Tirana, Albania*

<sup>2</sup> *University of Tirana, Faculty of Natural Sciences, Department of Physics, Tirana, Albania*

**Presenter:** I. Bërdufi (irmaberdufi@gmail.com)

To achieve a good determination of the equivalent dose for occupational exposure workers from the whole body dosimeter an overall uncertainty associated with the measurement needs to be estimated. The work reported here is focused to estimate the absolute standard uncertainty that arises for Reader Calibration Factor (RFC), Element Correction Coefficient (ECC), and Zero Dose Reading. In this study, the thermoluminescence dosimeters are used and measured with Harshaw4500 Reader at Personal Dosimetry Laboratory in the Institute of Applied Nuclear Physics, Tirana, Albania and irradiated in the Secondary Standard Dosimetry Laboratory (SSDL) in place. In this study we estimated the uncertainties coming from the measurements, and didn't take into consideration those which might arise from the users. The method used in this study is based on Guide to the Expression of Uncertainty in

## Nucleosynthesis

80

**The radiogenic heating of planets and the 40K question****Author:** Georgios Perdikakis<sup>1</sup><sup>1</sup> *Central Michigan University***Corresponding Author:** perdi1g@cmich.edu

The quantity of radioactive isotopes in a planet's mantle and the evolution of its heating due to the isotopes' radioactive decay determines the capability of that planet to develop geological features associated with a habitable environment, such as surface crust and plate tectonics. When our solar system was formed, large quantities of Potassium (K), a major element available in the interstellar medium at the time, got subsequently deposited inside our planet's mantle and crust. Potassium's long-lived radioactive isotope <sup>40</sup>K is still present in large quantities inside the planet. The beta particles that it emits heat up earth's mantle for the last several billions of years and largely contribute to the habitable nature of Earth. Predicting the amount of <sup>40</sup>K enrichment in the solar system of a given exoplanet would be fundamental for a reliable calculation of the planet's heating evolution and would allow us to make estimates on the likely existence of a habitable environment. Potassium, however, has a complex production and (destruction) mechanism in the cosmos. From a nucleosynthesis point of view, the uncertainty in the abundance of <sup>40</sup>K is associated with the reactions that create and destroy 40K in stellar nucleosynthesis processes and the corresponding reaction rates. In my talk, I will discuss the importance of potassium in the context of exoplanet-related research, the origin of potassium in stars, the nuclear physics aspects that affect the existence of <sup>40</sup>K, and current experimental efforts to constrain the relevant reaction rates.

**Length of presentation requested:**

Oral presentation: 25 min + 5 min questions (Review-type talk)

**Please select between one and three keywords related to your abstract:**

Nuclear physics - experimental

**2nd keyword (optional):**

Nucleosynthesis

**3rd keyword (optional):**

Habitability, Exoplanets

81

**Simulation of production of the cosmogenic radionuclides in loess**

**Authors:** Nikola Veselinovic<sup>None</sup>; Dimitrije Maletic<sup>None</sup>; Mihailo Savic<sup>1</sup>; Aleksandar Dragić<sup>1</sup>; Dejan Jokovic<sup>2</sup>; Radomir Banjanac<sup>3</sup>; David Knežević<sup>4</sup>; Vladimir Udovičić<sup>5</sup>

<sup>1</sup> *Institute of Physics Belgrade*<sup>2</sup> *Institute of Physics, University of Belgrade*<sup>3</sup> *Institute of physics Belgrade*<sup>4</sup> *Institute of physics Belgrade*

<sup>5</sup> *Institute of Physics Belgrade*

**Corresponding Authors:** veselinovic@ipb.ac.rs, maletic@ipb.ac.rs, yokovic@ipb.ac.rs, banjanac@ipb.ac.rs, davidk@ipb.ac.rs, udovicic@ipb.ac.rs, dragic@ipb.ac.rs, msavic@ipb.ac.rs

Development of a Geant4 application which models propagation and interaction of cosmic rays with the soil - loess, including the simulation of creation of cosmogenic radionuclides in soil is reported. CORSIKA is used to simulate the propagation of cosmic rays through atmosphere to the ground. The distribution of concentration of produced radionuclides by depth from simulation is presented thus allowing alternative method of study loess geomorfology but also to study cosmic ray flux modulated by the sun activity on long-term scale. The possibility of detection using laboratory equipment of these cosmogenic radionuclides created in soil is discussed.

**Length of presentation requested:**

Oral presentation: 8 min + 2 min questions (Poster-type talk)

**Please select between one and three keywords related to your abstract:**

Cosmic Rays

**2nd keyword (optional):**

Nuclear physics - experimental

**3rd keyword (optional):**

82

## Spectroscopy of $^{48}\text{Cr}$ by the $^{50}\text{Cr}(p, t)^{48}\text{Cr}$ reaction

**Authors:** Philip Adsley<sup>1</sup>; Sifundo Binda<sup>2</sup>

<sup>1</sup> *Texas A&M University*

<sup>2</sup> *WITS/iTL*

**Corresponding Authors:** padsley@tamu.edu, 1395463@students.wits.ac.za

The radioactive nucleus  $^{44}\text{Ti}$  is thought to be produced in Core-Collapse Supernovae (CCSNe) with the amount produced being sensitive to internal dynamics of the explosion. As such,  $^{44}\text{Ti}$  is a potential diagnostic tool for understanding the behaviour of these stellar explosions.

The amount of  $^{44}\text{Ti}$  produced depends not only on the production reactions but also on the destruction reactions, most notably the  $^{44}\text{Ti}(\alpha, p)^{47}\text{V}$  reaction which proceeds through states in the compound nucleus  $^{48}\text{Cr}$ . This reaction is usually treated through statistical models (see, for example, the recent study by Chipps and collaborators Phys. Rev. C 102, 035806) but it is not clear that this is valid given the limitations of the levels which can be populated in  $^{44}\text{Ti}+\alpha$  fusion (natural parity, isoscalar) and the influence of  $\alpha$ -particle clustering behaviour on other  $\alpha$ -particle induced reactions.

Spectroscopy in the Gamow Window of the  $^{44}\text{Ti}(\alpha, p)^{47}\text{V}$  reaction has been performed using the  $^{50}\text{Cr}(p, t)^{48}\text{Cr}$  reaction with the K600 magnetic spectrometer at iThemba LABS in South Africa. A number of excited states have been observed, many for the first time, giving insights into the validity of statistical models for the  $^{44}\text{Ti}(\alpha, p)^{47}\text{V}$  reaction.

**Length of presentation requested:**

Oral presentation: 8 min + 2 min questions (Poster-type talk)

**Please select between one and three keywords related to your abstract:**

Nuclear physics - experimental

## **The study of atmospheric effects on cosmic ray muons in the Low Background Laboratory for Nuclear Physics at the Institute of Physics Belgrade**

**Mihailo Savić, Nikola Veselinović, Aleksandar Dragić, Dimitrije Maletić,  
Dejan Joković, Vladimir Udovičić, Radomir Banjanac and David Knežević**

*Institute of Physics Belgrade, University of Belgrade, Pregrevica 118, 11080  
Belgrade, Serbia  
Email: msavic@ipb.ac.rs*

Galactic cosmic rays are being modulated in the heliosphere by different processes on the Sun. Upon arriving at Earth, they interact with nuclei in the atmosphere and produce secondary cosmic rays. Changing conditions in the atmosphere affect the propagation of secondary cosmic rays, especially the muon component. To increase the effectiveness of ground-based muon detectors these atmospheric effects need to be decoupled from non-atmospheric ones, and corrected for. To this end, in the Low Background Laboratory for Nuclear Physics at the Institute of Physics Belgrade, we are using several existing techniques but have also developed two new empirical methods for modeling and correction of barometric and temperature effects on cosmic ray muons. Newly developed methods proved to be equally or more effective than the most widely used ones. Such results allow for more precise study of solar modulation and more reliable long term monitoring of galactic cosmic ray flux, and could provide further insight into the relationship between atmospheric parameters and propagation of secondary cosmic rays in the atmosphere.

## **New insights from cross-correlation studies between solar activity indices and cosmic-ray fluxes during Forbush decreases**

**Nikola Veselinović, Mihailo Savić, Aleksandar Dragić, Dimitrije Maletić, Radomir Banjanac, Dejan Joković, David Knežević and Vladimir Udovičić**

*Institute of Physics Belgrade, University of Belgrade, Pregrevica 118,  
11080 Belgrade, Serbia*

Observed galactic cosmic rays intensity can be subjected to transient decrease, called Forbush decreases, which can be driven by solar activity and shockwaves in Heliosphere with solar origin, in terms of flares and coronal mass ejections (Miteva et al., 2018 [1]). By combining in-situ measurements, using space borne instruments, of solar energetic particles with ground-based observations we investigate the relationship between solar activity indices, as well as event-integrated spectra of solar energetic particles (Belov et al, 2021 [2]) with intensity measurements of cosmic rays during these strong transient decreases. We present cross-correlation studies ( Veselinović et al, 2021 [3]) using data from the SOHO/ERNE measurements at 19 energy thresholds between 1.6 and 90 MeV/n, neutron monitors and solar observatories collected during strongest Forbush decreases over last two solar cycles.

### **References**

- [1] Miteva, R., Samwel, S.W. & Costa-Duarte, M.V. The *Wind*/EPACT Proton Event Catalog (1996 – 2016). *Sol Phys* **293**, 27 (2018).  
<https://doi.org/10.1007/s11207-018-1241-5>
- [2] Belov A. *et al* 2021 *ApJ* **908** 5. <https://doi.org/10.3847/1538-4357/abd724>
- [3] Veselinović, N., Savić, M., Dragić, A. *et al*. Correlation analysis of solar energetic particles and secondary cosmic ray flux. *Eur. Phys. J. D* **75**, 173 (2021). <https://doi.org/10.1140/epjd/s10053-021-00172-x>

## CORRELATION ANALYSIS OF SOLAR WIND PARAMETERS AND SECONDARY COSMIC RAYS FLUX

NIKOLA VESELINOVIĆ, MIHAILO SAVIĆ, ALEKSANDAR DRAGIĆ,  
DIMITRIJE MALETIĆ, DEJAN JOKOVIĆ, RADOMIR BANJANAC,  
VLADIMIR UDOVIČIĆ and DAVID KNEŽEVIĆ

*Institute of Physics Belgrade  
Pregrevica 118, Belgrade, Serbia  
E-mail veselinovic@ipb.ac.rs*

**Abstract.** Galactic cosmic rays (GCRs) entering the heliosphere are disturbed by solar wind and Sun's magnetic field, see Potgieter 2013 Coronal mass ejections (CMEs) structure and shockwave can additionally modulate GCRs, which could result in a transient decrease followed by a gradual recovery in the observed galactic cosmic ray intensity, known as Forbush decrease (FD) see Maričić et al.2014. CMEs are regularly observed via in-situ measurements of plasma and magnetic field in near-Earth space so it is important to understand the relationship between the FDs and near-Earth particles flux associated with these CMEs.

During last 24th Solar cycle, unprecedented extent of heliospheric observations has been achieved thanks to the several new satellites in orbit and CMEs can be observed throughout the heliosphere from the Sun to the Earth, allowing us to relate ground observations to remote sensing data, for Mars see Freiherr von Forstner et al. 2019. We analyzed the dynamics of the variation of galactic cosmic rays (GCR) combining in situ measurement of the particles species present in solar wind with ground observations (worldwide neutron monitor (NM) network and Belgrade's muon detector). This dynamics compared for several CMEs induced FD events. Variations in interplanetary plasma and field parameters during, before, and after the Forbush decreases were examined. Correlation between the 1-hour variations of GCR and several different one-hour averaged particle fluxes was found during FDs and it depends on energy of the particles of the solar wind as well as cut-off rigidities of secondary cosmic rays detectors on ground. These correlations were compared with correlation between same parameters during quiet period of the solar activity. This cross-correlation analysis can help in better understanding of Earth-affecting CMEs and space weather but also to predict GCR flux during extreme solar events.

### References

- Freiherr von Forstner, J. L. et al. : 2019, *Space Weather*, **17**, 586– 598.  
Maričić, D., Vršnak, B., Dumbović, M. et al. : 2014, *Sol Phys* **289**, 351–368.  
Potgieter, M. S.: 2013, *Living Rev. Sol. Phys.* **10**, 3 (2013).



## SIMULACIJA PRODUKCIJE NEUTRONA MIONIMA IZ KOSMIČKOG ZRAČENJA U OLOVNOJ ZAŠTITI GERMANIJUMSKOG DETEKTORA

**Dejan JOKOVIĆ, Dimitrije MALETIĆ, Vladimir UDOVIČIĆ,  
Radomir BANJANAC, Aleksandar DRAGIĆ, Mihailo SAVIĆ,  
Nikola VESELINOVIĆ i David KNEŽEVIĆ**

*Institut za fiziku u Beogradu, Univerzitet u Beogradu, Beograd, Srbija,  
[yokovic@ipb.ac.rs](mailto:yokovic@ipb.ac.rs), [maletic@ipb.ac.rs](mailto:maletic@ipb.ac.rs), [udovicic@ipb.ac.rs](mailto:udovicic@ipb.ac.rs), [banjanac@ipb.ac.rs](mailto:banjanac@ipb.ac.rs),  
[dragic@ipb.ac.rs](mailto:dragic@ipb.ac.rs), [msavic@ipb.ac.rs](mailto:msavic@ipb.ac.rs), [veselinovic@ipb.ac.rs](mailto:veselinovic@ipb.ac.rs), [davidk@ipb.ac.rs](mailto:davidk@ipb.ac.rs)*

### SADRŽAJ

*Zbog svojih osobina, olovo se uobičajeno koristi kao materijal za zaštitu germanijumskih detektora. Mioni iz kosmičkog zračenja u interakcijama sa olovom proizvode sekundarno zračenje, koje doprinosi ukupnom fonu detektora. Značajan deo ove komponente fona čine neutroni proizvedeni u interakcijama miona u olovnoj zaštiti. Neutroni mogu biti poseban problem u eksperimentima u dubokim podzemnim laboratorijama. U podzemnoj laboratoriji u Institutu za fiziku u Beogradu, germanijumski detektor, koji se nalazi u olovnoj zaštiti, može raditi u koincidenciji sa mionskim detektorom. U ovom režimu rada mogu se proučavati različiti efekti u germanijumskom detektoru izazvani mionima, posebno efekti koji potiču od neutrona proizvedenih mionima. Ovde su predstavljeni rezultati Geant4 simulacija produkcije neutrona u olovu mionima iz kosmičkog zračenja. Rezultat ovih simulacija je procena prinosa neutrona – broja proizvedenih neutrona u olovu po jedinici dužine puta – u interakcijama miona. Pored toga, određena je raspodela multipliciteta neutrona, kao broja proizvedenih neutrona u jednoj interakciji.*

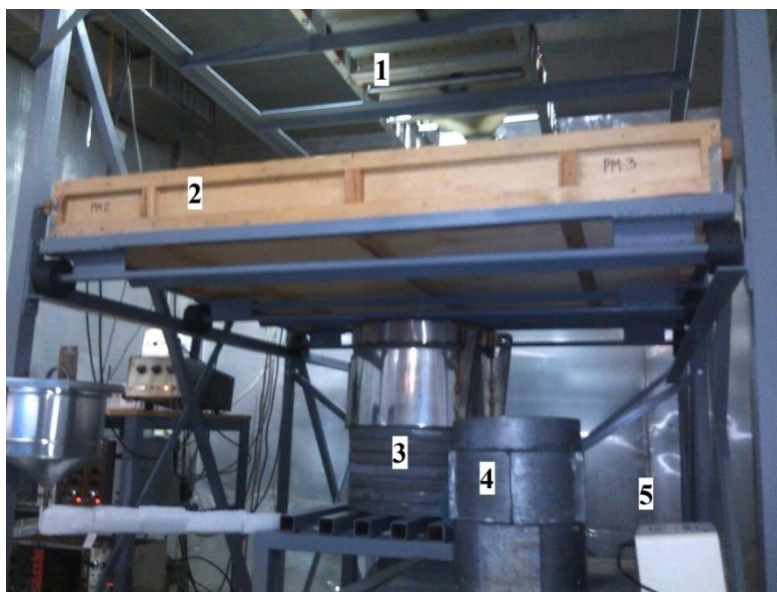
### 1. Uvod

U eksperimentima u kojima se traže retki događaji glavni problem je redukcija fonskog zračenja. Zato se ovi eksperimenti vrše u podzemnim laboratorijama, gde je fon u odnosu na površinu Zemlje znatno niži. Međutim, mioni iz kosmičkog zračenja su veoma prodorne čestice, prisutne i u dubokim podzemnim laboratorijama, i zato čine važan izvor fonskog zračenja u ovakvim osetljivim eksperimentima. Poseban problem je mionima indukovano sekundarno zračenje u detektorima i njihovoj okolini (detektorskoj zaštiti, zidovima, itd). Značajan doprinos fonu potiče od neutrona proizvedenih u interakcijama miona sa materijalom u okolini detektora [1].

U Niskofonskoj laboratoriji Instituta za fiziku u Beogradu intenzitet kosmičkog zračenja kontinuirano se meri od 2002. godine [2,3]. Geografski položaj laboratorije je takav da se kosmičko zračenje koje se detektuje u osnovi sastoji od mionske tvrde komponente, uz izvestan procenat meke elektromagnetne komponente. Laboratorija se sastoji od nadzemnog i plitko ukopanog podzemnog dela na dubini od 12 m ispod površine. Zemljište (les) iznad podzemne laboratorije ima gustinu približno  $2,0 \text{ g/cm}^3$  – efektivni apsorpcioni sloj iznosi približno  $25 \text{ hg/cm}^3$  ( $25 \text{ m.w.e.}$ ). Na toj dubini prisutna je praktično samo mionska komponenta kosmičkog zračenja. Zbog svojih niskofonskih karakteristika, laboratorija je osposobljena za izučavanja različitih pojava generisanih kosmičkim zračenjem, pre svega događaja indukovanih mionima iz kosmičkog zračenja u germanijumskim detektorima, kao i u pasivnoj zaštiti detektora.

U podzemnoj laboratoriji nalazi se HPGe detektor deklarisanе aktivne zapremine  $149 \text{ cm}^3$  i relativne efikasnosti 35 %. Podzemna pozicija detektora, zajedno sa olovnom

zaštitom debljine 12 cm, daje značajno smanjenje fonskog zračenja. Pored pasivne zaštite, za aktivnu veto zaštitu germanijumskog detektora mogu se koristiti postojeći scintilacioni detektori kosmičkog zračenja. Plastični scintilacioni detektor nalazi se neposredno iznad olovne zaštite; dimenzije detektora su 100 cm × 100 cm × 5 cm. Oba detektora – HPGe i scintilacioni – vezani su za analogno-digitalni konvertor, koji omogućava snimanje i čuvanje svih detektovanih događaja. Svi događaji analiziraju se *off-line*. Uz odgovarajuće selekzione kriterijume mogu se izdvojiti svi koincidentni i/ili antikoincidentni događaji u scintilacionom i HPGe detektoru [4,5].



**Slika 1. Ekperimentalna konfiguracija u podzemnoj laboratoriji: scintilacioni detektori (1,2) i germanijumski detektor u olovnoj zaštiti (3).**

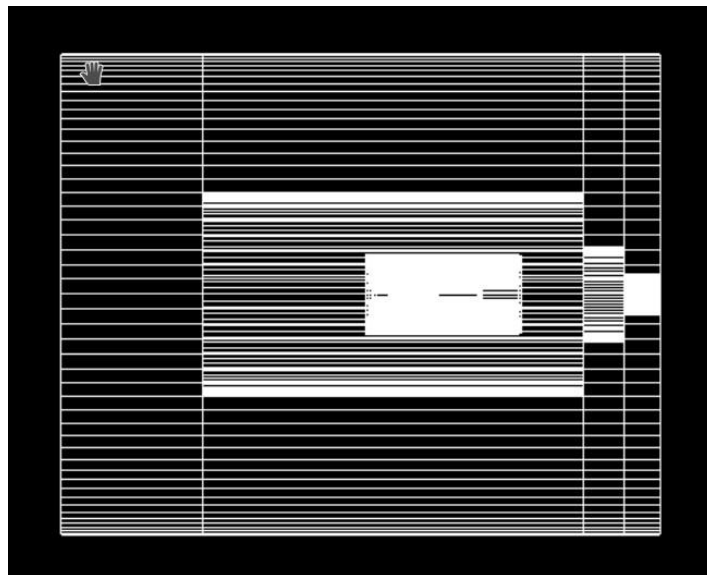
Prvi rezultati merenja produkcije neutrona mionima iz kosmičkog zračenja u olovnoj zaštiti HPGe detektora objavljeni su 2013. godine. Podaci su snimani tokom više od 400 dana merenja, u koincidentnom režimu rada scintilator-HPGe detektor. Analizom ovih podataka dobijen je rezultat za fluks neutrona proizvedenih mionima, na dubini naše podzemne laboratorije [6]. Merenja su kontinuirano nastavljena, sa većom statistikom snimljenih događaja; analiza ovih podataka je u toku. Pored eksperimentalnih merenja, uporedo su urađene Monte Carlo simulacije produkcije neutrona u olovnoj zaštiti, bazirane na Geant4 *framework*-u. Ovde su predstavljeni prvi rezultati simulacija: procena prinosa neutrona (broj neutrona po jedinici dužine) u interakcijama miona, kao i raspodela multipliciteta proizvedenih neutrona.

### 2. Metod

Geant4 je softverski paket za Monte Carlo simulacije transporta i interakcija čestica sa materijom [7]. On sadrži kompletan alat za modelovanje geometrije detektora, fizičkih procesa, primarnih i sekundarnih događaja, kao i odziva detektora. Na osnovi Geant4 platforme razvijena je posebna aplikacija za simulacije odziva germanijumskog i scintilacionih detektora u laboratoriji. Aplikacija je fleksibilna i omogućuje simulacije pojedinačnih i koincidentnih režima rada detektora. Prethodno je korišćena u različitim

slučajevima koji su zahtevali precizne simulacije scintilacionih i germanijumskih detektora [2,4,8,9].

Olovna zaštita je geometrije šupljeg cilindra, unutar kojeg se nalazi germanijumski detektor. Visina cilindra je 51 cm, prečnik osnove 41 cm, a debljina olovnog zida je 12 cm. Detektor je konstruisan prema specifikaciji proizvođača. Skica detektora i olovnog cilindra prikazana je na slici 2.



**Slika 2. Skica olovne zaštite germanijumskog detektora.**

Primarni događaji generisani su definisanjem incidentne čestice, njene pozicije, pravca kretanja i energije. Incidentne čestice su pozitivni i negativni mioni; odnos broja pozitivnih i broja negativnih miona je 1,3. Početne pozicije miona na površini olovnog cilindra određene su na sledeći način: prvo se odabere gornja horizontalna strana ili vertikalna strana cilindra, prema verovatnoći da kosmički mion pogodi horizontalnu ili vertikalnu stranu, a zatim se odabere pozicija na datoj površini iz uniformne raspodele. Pravac kretanja miona simpliran je iz raspodele miona po pravcima, u funkciji od zenitnog ugla  $\theta$ , koja je proporcionalna  $\cos^{1.55}\theta$ . Energija miona određena je iz energijske raspodele miona na površini Zemlje, pri čemu se uzimaju oni mioni koji uspeju da prođu kroz 12 m zemljišta. Detaljnija procedura generisanja primarnih događaja i izvođenje raspodele miona po pravcima i energijama može se videti u [4].

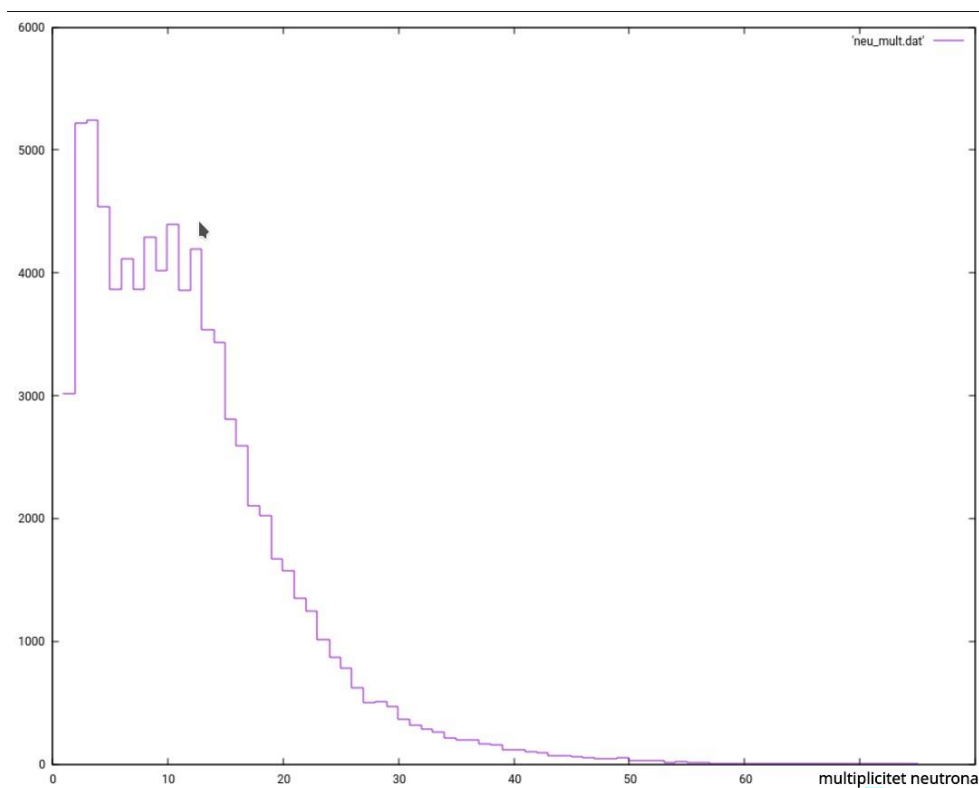
Fizički procesi u kojima učestvuju mioni – elektromagnetni i nuklearni – uključeni su u simulaciju kroz predefinisane Geant4 klase QGSP\_BERT\_HP; ova klasa omogućava simulacije interakcija čestica sa velikom preciznošću.

### **3. Rezultati i diskusija**

Prvi cilj simulacije bio je da se odredi broj proizvedenih neutrona u interakcijama miona sa jezgrom olova, po jedinici dužine puta, pri njihovom prolasku kroz olovnu zaštitu germanijumskog detektora. Generisanih primarnih događaja bilo je  $10^8$ ; ovaj broj može biti povezan sa vremenom eksperimentalnih merenja, uzimajući u obzir fluks miona u podzemnoj laboratoriji.

Ukupan broj proizvedenih neutrona bio je 934 000. Odavde je određen prinos neutrona, kao odnos broja neutrona i proizvoda gustine olova i srednje dužine puta miona kroz

olovo. Srednja dužina puta miona je 26,6 cm, a proizvod gustine olova i srednje dužine puta iznosi  $302 \text{ g/cm}^3$ . Dobijena vrednost za prinos neutrona je  $3,1 \times 10^{-5} \text{ neut./}(g\text{cm}^{-2})$ . Pored prinosa neutrona, određena je raspodela multipliciteta neutrona – broja neutrona proizvedenih u interakciji jednog miona sa olovom. Mion može proizvesti više od jednog neutrona na svom putu kroz olovo, što za rezultat ima više neutronske fonske događaja u detektoru koji potiču od jednog miona. Događaji su vremenski razdvojeni, odnosno detektuju se sa vremenskim razmakom, u zavisnosti od trenutka i mesta produkcije neutrona. Ovi događaji registruju se u detektoru kao signali sa vremenskim kašnjenjem, unutar definisanog vremenskog prozora mionskog događaja. To može poslužiti za selekciju fonskih događaja koji potiču od neutrona indukovanih mionima. Raspodela multipliciteta neutrona prikazana je na slici 3. Najveći broj miona proizvede manje od 10 neutrona u kaskadi, dok srednji multiplicitet neutrona iznosi 11,5. Dobijena raspodela slaže se sa rezultatima ranijih sličnih simulacija [10].



**Slika 3. Raspodela multipliciteta neutrona proizvedenih mionima iz kosmičkog zračenja u olovnoj zaštiti HPGE detektora.**

Rezultati simulacije pokazali su da ovaj metod može biti koristan za procenu produkcije neutrona mionima iz kosmičkog zračenja. On može dati detaljniji uvid u mehanizam produkcije neutrona. Osim toga, rezultati simulacije mogu pomoći u analizi podataka eksperimentalnih merenja, njihovom boljem razumevanju i evaluaciji.

#### 4. Zahvalnica

Ovaj rad finansiran je od Instituta za fiziku u Beogradu kroz projekat Ministarstva prosvete, nauke i tehnološkog razvoja Republike Srbije.

**5. Literatura**

- [1] D. Mei, A. Hime. Muon-induced background study for underground laboratories. *Phys. Rev. D* 73, 2006, 053004.
- [2] A. Dragić, D. Joković, R. Banjanac, V. Udovičić, B. Panić, J. Puzović, I. Aničin. Measurement of cosmic ray muon flux in the Belgrade ground level and underground laboratories. *Nucl. Instr. Meth. A* 591, 2008, 470-475.
- [3] M. Savić, A. Dragić, D. Maletić, N. Veselinović, R. Banjanac, D. Joković, V. Udovičić. A novel method for atmospheric correction of cosmic-ray data based on principal component analysis. *Astropart. Phys.* 109, 2019, 1-11.
- [4] D. Joković, A. Dragić, V. Udovičić, R. Banjanac, J. Puzović, I. Aničin. Monte Carlo simulations of the response of a plastic scintillator and an HPGe spectrometer in coincidence. *Appl. Radiat. Isot.* 67, 2009, 719-722.
- [5] A. Dragić, V. Udovičić, R. Banjanac, D. Joković, D. Maletić, N. Veselinović, M. Savić, J. Puzović, I. Aničin. The new set-up in the Belgrade low-level and cosmic-ray laboratory. *Nucl. Techn. Radiat. Prot.* 26, 2011, 181-192.
- [6] A. Dragić, I. Aničin, R. Banjanac, V. Udovičić, D. Joković, D. Maletić, M. Savić, N. Veselinović, J. Puzović. Neutrons produced by muons at 25 mwe. *J. Phys.: Conf. Ser.* 409, 2013 012054.
- [7] S. Agostinelli et al. Geant4 – a simulation toolkit. *Nucl. Instr. Meth. A* 506, 2003, 250-303.
- [8] M. Krmar, J. Hansman, N. Jovančević, N. Lalović, J. Slivka, D. Joković, D. Maletić. A method to estimate a contribution of Ge(n,n') reaction to the low-energy part of gamma spectra of HPGe detectors. *Nucl. Instr. Meth. A* 709, 2013, 8-11.
- [9] J. Nikolić, T. Vidmar, D. Joković, M. Rajačić, D. Todorović. Calculation of HPGe efficiency for environmental samples: comparison of EFFTRAN and GEANT4. *Nucl. Instr. Meth. A* 763, 2014, 347-353.
- [10] L. Reichhart et al. Measurement and simulation of the muon-induced neutron yield in lead. *Astropart. Phys.* 47, 2017, 67-76.

### MONTE CARLO SIMULATION OF THE COSMIC RAY MUON INDUCED NEUTRON PRODUCTION IN THE LEAD SHIELD OF THE GERMANIUM DETECTOR

**Dejan JOKOVIĆ, Dimitrije MALETIĆ, Vladimir UDOVIČIĆ,  
Radomir BANJANAC, Aleksandar DRAGIĆ, Mihailo SAVIĆ,  
Nikola VESELINOVIĆ and David KNEŽEVIĆ**

*Institute of Physics Belgrade, University of Belgrade, Belgrade, Serbia,  
[yokovic@ipb.ac.rs](mailto:yokovic@ipb.ac.rs), [maletic@ipb.ac.rs](mailto:maletic@ipb.ac.rs), [udovicic@ipb.ac.rs](mailto:udovicic@ipb.ac.rs), [banjanac@ipb.ac.rs](mailto:banjanac@ipb.ac.rs),  
[dragic@ipb.ac.rs](mailto:dragic@ipb.ac.rs), [msavic@ipb.ac.rs](mailto:msavic@ipb.ac.rs), [veselinovic@ipb.ac.rs](mailto:veselinovic@ipb.ac.rs), [davidk@ipb.ac.rs](mailto:davidk@ipb.ac.rs)*

#### ABSTRACT

Lead is usually used as a common shielding material for germanium detectors. Cosmic ray muons produce secondary particles in their interactions with lead nuclei, which contribute to overall background radiation detected by germanium detectors. Neutrons produced in muon interactions in lead shield make a significant part of this background component. Cosmic ray induced neutrons are a particular problem in experiments carried out in deep underground laboratories.

In the low-level underground laboratory at Institute of Physics Belgrade, a germanium detector and a muon detector operate in coincidence. This provides studying of different effects in the germanium detector induced by cosmic rays, especially effects originated from the cosmic ray induced neutrons.

Here, the results of Geant4 simulations of the cosmic ray muon induced neutron production in the lead shield of the germanium detector are presented. Estimate of the neutron yield – number of neutrons produced per unit path length – in muon interactions is obtained. The result is  $3.1 \times 10^{-5}$  neutrons/(gcm<sup>-2</sup>). Also, the neutron multiplicity distribution is determined, as a distribution of number of neutrons produced per muon interaction. The average multiplicity is 11.5.

## DISTRIBUCIJA KONCENTRACIJE RADONA PO SPRATNOSTI STAMBENIH ZGRADA

**Vladimir UDOVIČIĆ<sup>1</sup>, Dimitrije MALETIĆ<sup>1</sup>, Aleksandar DRAGIĆ<sup>1</sup>,  
Radomir BANJANAC<sup>1</sup>, Dejan JOKOVIĆ<sup>1</sup>, Nikola VESELINOVIĆ<sup>1</sup>,  
Mihailo SAVIĆ<sup>1</sup>, David KNEŽEVIĆ<sup>1</sup> i Maja EREMIĆ-SAVKOVIĆ<sup>2</sup>**

- 1) *Institut za fiziku u Beogradu, Institut od nacionalnog značaja za Republiku Srbiju, Beograd, Srbija, [udovic@ipb.ac.rs](mailto:udovic@ipb.ac.rs), [maletic@ipb.ac.rs](mailto:maletic@ipb.ac.rs), [dragic@ipb.ac.rs](mailto:dragic@ipb.ac.rs), [banjanac@ipb.ac.rs](mailto:banjanac@ipb.ac.rs), [yokovic@ipb.ac.rs](mailto:yokovic@ipb.ac.rs), [veselinovic@ipb.ac.rs](mailto:veselinovic@ipb.ac.rs), [msavic@ipb.ac.rs](mailto:msavic@ipb.ac.rs), [davidk@ipb.ac.rs](mailto:davidk@ipb.ac.rs)*
- 2) *Direktorat za radijacionu i nuklearnu sigurnost i bezbednost Srbije, Beograd, Srbija, [eremic.savkovic@srbatom.gov.rs](mailto:eremic.savkovic@srbatom.gov.rs)*

### SADRŽAJ

*Dobro je poznato da je jedan od faktora koji utiče na varijabilnost radona u zatvorenom prostoru spratnost stambenih zgrada. Imajući u vidu činjenicu da glavni izvor radona u zatvorenim prostorijama potiče iz zemljišta, očekuje se smanjenje koncentracije radona na višim spratovima. Na višim spratovima dominantan izvor radona potiče od građevinskog materijala, a u nekim slučajevima može doći do odstupanja od ove opšte utvrđene pravilnosti. S druge strane, varijabilnost radona zbog spratnosti, posebno u velikim gradovima, sa mnogo većim brojem visokih zgrada i gustom naseljenosti u poređenju sa ruralnim sredinama, može uticati na procenu kolektivne doze koja potiče od radona. U tom smislu, a u svrhu naših istraživanja, izabrali smo jednu tipičnu porodičnu kuću sa potkrovljem i jedan šesnaestospratni soliter. Merenje koncentracije radona u odabranim stambenim objektima izvršeno je sa dva aktivna uređaja. Jedan je bio fiksiran u dnevnoj sobi u prizemlju, a drugi je menjao poziciju po spratovima u stambenim zgradama. Svaki merni ciklus na datom spratu trajao je sedam dana uz vreme uzorkovanja od dva sata. U ovom radu detaljno je urađena analiza dobijenih rezultata.*

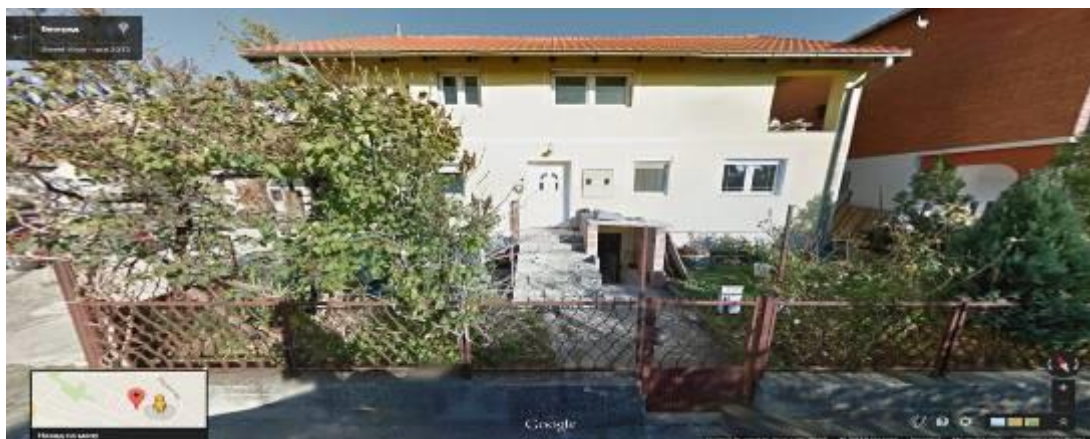
### 1. Uvod

Izvori radona u stambenim i poslovnim zgradama su, pre svega iz zemljišta, građevinskog materijala i vode. S obzirom na prirodu nastanka i svih pomenutih izvora, koncentracija radona je veća u prizemnim prostorijama u odnosu na stanove na višim spratovima stambenih objekata. U literaturi se može pronaći dosta radova koji se bave uticajem raznih faktora na nivo i varijabilnost radona u zatvorenim prostorijama, pa između ostalih i uticajem spratnosti [1-4]. U slučaju velikih stambenih objekata sa većim brojem spratova, može se uočiti odstupanje od opšte pravilnosti, jer je na višim spratovima dominantan izvor radona građevinski materijal, te se mogu uočiti povećane koncentracije radona u odnosu na situaciju na nižim spratovima. U tom smislu, urađena su merenja radona u dva tipična stambena objekta. Izbor zgrada je baziran na rezultatima iz monografije „Nacionalna tipologija stambenih zgrada Srbije“ grupe autora sa Arhitektonskog fakulteta [5]. S obzirom na specifičnosti gradnje u Srbiji, broj

tipova zgrada je tako sveden na šest kategorija, dve za porodično stanovanje i četiri kategorije za kolektivno stanovanje; porodično stanovanje: 1. slobodnostojeća kuća, 2. kuća u nizu i kolektivno stanovanje: 3. slobodnostojeća zgrada, 4. zgrada u nizu, 5. zgrada u nizu tipa lamele (ponavlja se više zgrada rađenih po istom projektu, zgrada sa više ulaza...) i 6. soliter (slobodnostojeća zgrada velike spratnosti). Pokazuje se da više od 97% svih stambenih zgrada čine samostojeće porodične kuće. Takođe, za sve definisane tipove zgrada broj spratova se kreće od jednog do osam, pri čemu su samostojeće porodične kuće uglavnom prizemne (37%) ili prizemne sa potkrovljem (26%), dok je veoma niska zastupljenost kuća koje imaju više od dva sprata (5%), sa prosečnom visinom porodičnih zgrada od 1,4 [5].

### 2. Eksperimentalna postavka

Izabrana su dva stambena objekta, jedan iz grupe za porodično stanovanje i jedan soliter iz grupe za kolektivno stanovanje. Porodična kuća (slika 1) ima karakterističan stil gradnje u kome se kuća gradi više godina uz konstantno dograđivanje i nadogradnju, što potencijalno može biti izvor ulaska radona u takve kuće. Kuća ima podrum i izgrađena je od standardnih materijala (cigla-blok, beton, malter). Na kraju je urađena i izolacija korišćenjem stiropora debljine 5 cm. U kući su već vršena višegodišnja merenja koncentracije radona različitim metodama, o čemu je do sada publikovano nekoliko naučnih radova [6-8].



Slika 1. Tipična porodična kuća u Beogradu.

Iz grupe stambenih zgrada za kolektivno stanovanje izabran je soliter na Novom Beogradu (slika 2). Izgrađen je šezdesetih godina prošlog veka, blokovskog tipa. Soliter ima podrum, dok se u prizemlju nalaze lokali i poslovne prostorije. Stanovi se nalaze od prvog sprata pa naviše. Soliter ima 16. spratova.





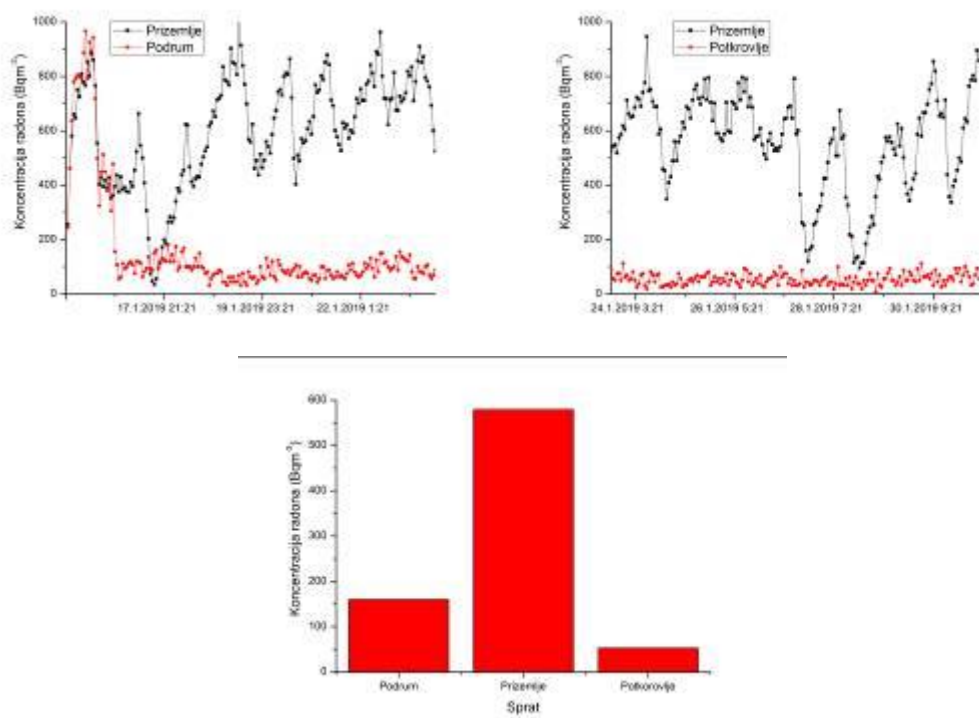
**Slika 2. Soliter na Novom Beogradu.**

Vremenske serije merenih koncentracija radona u ispitivanim stambenim objektima dobijene su pomoću dva aktivna uređaja SN1029 i SN1030 (proizvođača Sun Nuclear Corporation). To su merni uređaji jednostavne konstrukcije i primene u praksi. U suštini, radi se o brojaču sa dodatkom senzora za merenje meteoroloških parametara. Nedostatak uređaja je nemogućnost merenja koncentracije radona u zemljištu i vodi. Operater može podesiti vremenske sekvence od 0,5 do 24 sati. Jedan ciklus merenja može trajati 1000 sati ili ukupno 720 vremenskih sekvenci (broj sukcesivnih merenja, odnosno tačaka u vremenskoj seriji). Uređaji su bili podešeni da rade u vremenskoj sekvenci od 2 sata. Jedan je bio fiksiran u dnevnoj sobi u prizemlju, a drugi je menjao poziciju po spratovima u stambenim zgradama. Svaki merni ciklus na datom spratu trajao je sedam dana.

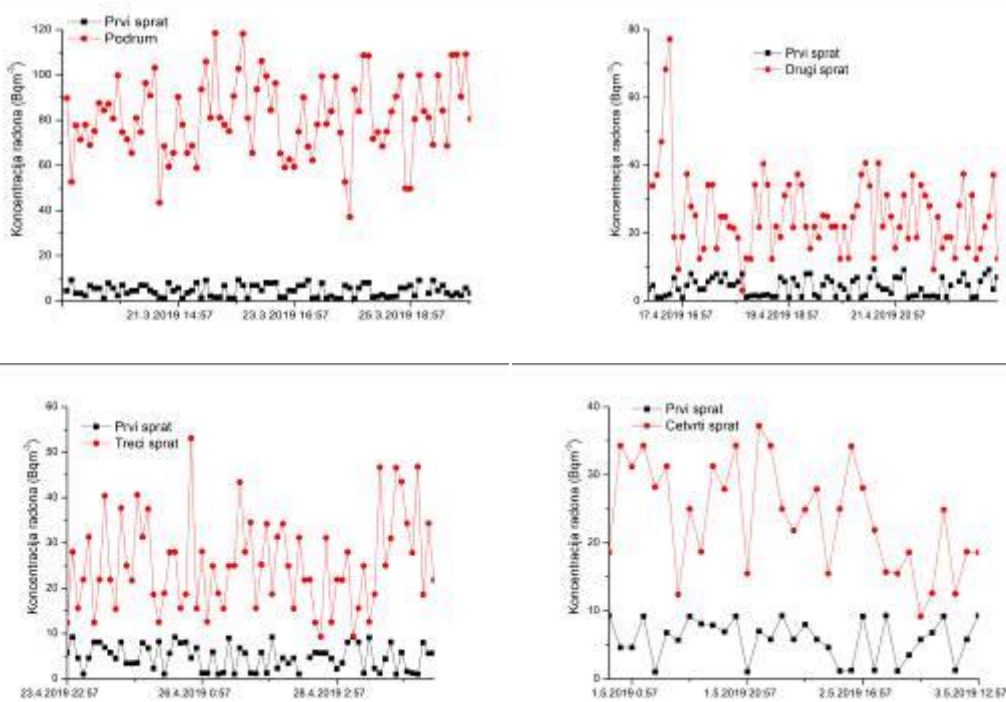
### **3. Rezultati i diskusija**

Na slikama 3 i 4 su prikazani dobijeni rezultati merenja, kako vremenske serije tako i usrednjene koncentracije radona u ispitivanim stambenim objektima za zadati ciklus merenja od sedam dana.

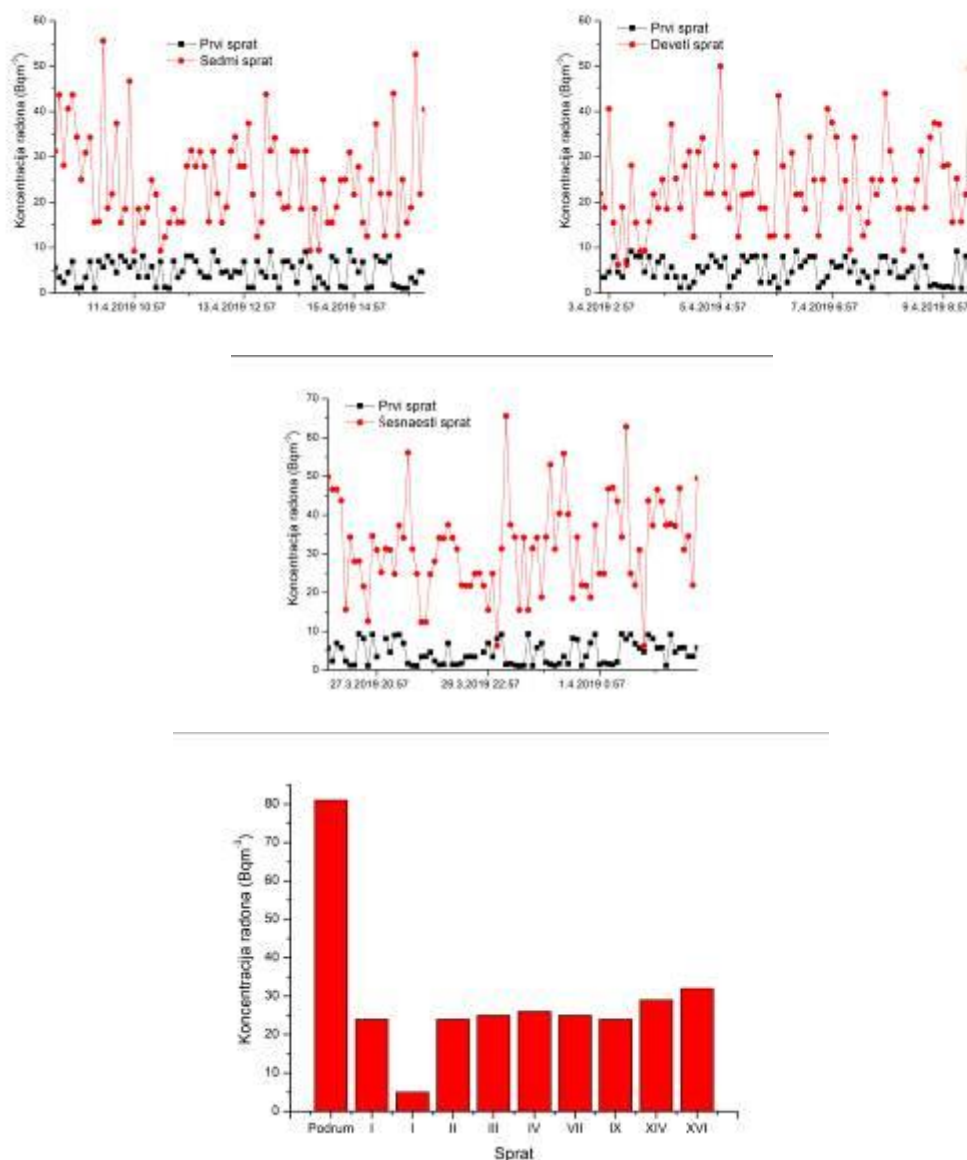
S obzirom da je detektor koji je sve vreme stajao u prizemlju solitera pokazao neobično niske vrednosti za koncentraciju radona, uradili smo uporedno merenje sa drugim detektorom u susednom, kao i u stanu u kome se nalazio fiksirani detektor. Dobijeni rezultati pokazuju izvesnu razliku, ali s obzirom da se radi o domenu izrazito niskih nivoa radona, pretpostavka je da su i merne nesigurnosti velike.



Slika 3. Vremenske serije i srednja koncentracija radona po spratovima u porodičnoj kući.



Slika 4. Vremenske serije i srednja koncentracija radona po spratovima u soliteru.



Slika 4. Nastavak.

#### 4. Zaključak

Dobijeni rezultati pokazuju da je ponašanje radona u dva različita stambena objekta dijametralno suprotno. U porodičnoj kući je moguće uočiti izrazite varijacije koncentracije radona uz jednodnevnu periodiku. Takođe, interesantan je odnos koncentracije radona u prizemlju, u odnosu na podrum kuće, koji je suprotan od uobičajene situacije kod kuća sa podrumom. Ovo inverzno ponašanje može se protumačiti činjenicom da podrum ne prekriva celo prizemlje već njegov manji deo. Ostali deo prizemlja je pokriven betonskom pločom kao podlogom, ali sa pukotinama i lošim spojem sa zidovima predstavlja potencijalni izvor povišenog radona. Kod solitera je situacija suprotna i može se smatrati da već od prvog sprata dominantan izvor radona je građevinski materijal. Čak se može uočiti blagi rast srednje koncentracije radona na

višim spratovima. No, dobijeni rezultati u soliteru se mogu predvideti, a na osnovu rada grupe autora koji su odredili interno izlaganje iz građevinskog materijala, koji se koristi u Srbiji, a koje potiče od eshalacije radona i torona [9].

### 5. Zahvalnica

Ovaj rad je realizovan uz podršku Ministarstva prosvete, nauke i tehnološkog razvoja Republike Srbije u okviru projekta pod brojem III43002.

### 6. Literatura

- [1] F. Bochicchio, G. Campos-Venuti, S. Piermattei, C. Nuccetelli, S. Risica, L. Tommasino, G. Torri, M. Magnoni, G. Agnesod, G. Sgorbati, M. Bonomi, L. Minach, F. Trotti, M.R. Malisan, S. Maggiolo, L. Gaidolfi, C. Giannardi, A. Rongoni, M. Lombardi, G. Cherubini, S. D'Ostilio, C. Cristofaro, M. Pugliese, V. Martucci, A. Crispino, P. Cuzzocrea, A. Sansone Santamaria, M. Cappai. Annual average and seasonal variations of residential radon concentration for all the Italian Regions. *Radiat. Meas.* 40, 2005, 686-694.
- [2] H. Friedmann. Final Results of the Austrian Radon Project. *Health Phys.* 89(4), 2005, 339-348.
- [3] R. Borgoni, D. De Francesco, D. De Bartolo, N. Tzavidis. Hierarchical modeling of indoor radon concentration: how much do geology and building factors matter? *J. Environ. Radioact.* 138, 2014, 227-237.
- [4] M. Lorenzo-González, A. Ruano-Ravina, J. Peón, M. Piñeiro, J. Miguel Barros-Dios. Residential radon in Galicia: a cross-sectional study in a radon-prone area. *J. Radiol. Prot.* 37(3), 2017, 728-741.
- [5] M. Jovanović Popović, D. Ignjatović, A. Radivojević, A. Rajčić, N. Ćuković Ignjatović, Lj. Đukanović, M. Nedić. National Typology of Residential Buildings in Serbia, Faculty of Architecture University of Belgrade, Belgrade, 2013, ISBN 978-86-7924-102-3.
- [6] V. Udovičić, D. Maletić, R. Banjanac, D. Joković, A. Dragić, N. Veselinović, J. Živanović, M. Savić, S. Forkapić. Multiyear Indoor Radon Variability in a Family House – a Case Study in Serbia. *Nucl. Tech. Radiat. Protect.* XXXIII (2), 2018, 174-179.
- [7] D. Maletić, V. Udovičić, R. Banjanac, D. Joković, A. Dragić, N. Veselinović, J. Filipović. Comparison of multivariate classification and regression methods for indoor radon measurements. *Nucl. Tech. Radiat. Protect.* 29, 2014, 17-23.
- [8] J. Filipović, D. Maletić, V. Udovičić, R. Banjanac, D. Joković, M. Savić, N. Veselinović. The use of multivariate analysis of the radon variability in the underground laboratory and indoor environment. *Nukleonika* 61(3), 2016, 357-360.
- [9] P. Ujić, I. Ćeliković, A. Kandić, I. Vukanac, M. Đurašević, D. Dragosavac, Z. S. Žunić. Internal exposure from building materials exhaling  $^{222}\text{Rn}$  and  $^{220}\text{Rn}$  as compared to external exposure due to their natural radioactivity content. *Appl. Radiat. Isot.* 68, 2010, 201–206.

---

## INDOOR RADON DISTRIBUTION DUE TO FLOOR LEVEL IN THE RESIDENTIAL BUILDINGS

**Vladimir UDOVICIC<sup>1</sup>, Nikola VESELINOVIC<sup>1</sup>, Dimitrije MALETIC<sup>1</sup>,  
Radomir BANJANAC<sup>1</sup>, Aleksandar DRAGIC<sup>1</sup>, Dejan JOKOVIC<sup>1</sup>,  
Mihailo SAVIC<sup>1</sup>, David KNEZEVIC<sup>1</sup> and Maja EREMIC-SAVKOVIC<sup>2</sup>**

*1) Institute of Physics Belgrade, University of Belgrade, Belgrade, Serbia,  
udovicic@ipb.ac.rs, maletic@ipb.ac.rs, dragic@ipb.ac.rs, banjanac@ipb.ac.rs,  
yokovic@ipb.ac.rs, veselinovic@ipb.ac.rs, msavic@ipb.ac.rs, davidk@ipb.ac.rs*

*2) Serbian Radiation and Nuclear Safety and Security Directorate, Belgrade,  
Serbia, eremic.savkovic@srbatom.gov.rs*

### ABSTRACT

It is well known that one of the factors influencing indoor radon variability is the floor level of residential buildings. Bearing in mind the fact that the main source of indoor radon is from radon in soil gas, a radon concentration on upper floors is expected to decrease. On the upper floors, the dominant source of radon originates from building materials, and in some cases there may be deviations from this generally established regularity. On the other hand, radon variability due to floor level, especially in large cities, with a much larger number of high buildings and density of population compared to rural areas, can affect the estimation of the collective dose derived from radon. In this sense, and for the purpose of our research, we chose a typical family house with a loft and sixteen high-rise building. Indoor radon measurements in selected residential buildings were done with two active devices. One was fixed in the living room on the ground floor, while the other was changing the position on the floors in residential buildings. Each measuring cycle on the floor lasted for seven days with a sampling time of two hours. In this paper, an analysis of the obtained results has been done in detail.

# PROCENA TEMPERATURSKOG PROFILA ATMOSFERE NA OSNOVU DETEKTOVANOG FLUKSA KOSMIČKIH MIONA

Mihailo SAVIĆ, Vladimir UDOVIČIĆ, Dimitrije MALETIĆ,  
Aleksandar DRAGIĆ, Radomir BANJANAC, Dejan JOKOVIĆ,  
Nikola VESELINOVIĆ i David KNEŽEVIĆ

Institut za fiziku u Beogradu, Institut od nacionalnog značaja za Republiku Srbiju,  
Beograd, Srbija, [msavic@ipb.ac.rs](mailto:msavic@ipb.ac.rs), [udovicic@ipb.ac.rs](mailto:udovicic@ipb.ac.rs), [maletic@ipb.ac.rs](mailto:maletic@ipb.ac.rs),  
[dragic@ipb.ac.rs](mailto:dragic@ipb.ac.rs), [banjanac@ipb.ac.rs](mailto:banjanac@ipb.ac.rs), [yokovic@ipb.ac.rs](mailto:yokovic@ipb.ac.rs), [veselinovic@ipb.ac.rs](mailto:veselinovic@ipb.ac.rs),  
[davidk@ipb.ac.rs](mailto:davidk@ipb.ac.rs)

## SADRŽAJ

*Uticaj atmosferskih parametara na intenzitet mionske komponente sekundarnog kosmičkog zračenja dobro je poznat. Dominantan doprinos varijaciji fluksa kosmičkih miona usled atmosferskih parametara daju dva meteorološka efekta - barometarski (usled varijacije atmosferskog pritiska) i temperaturski (usled varijacije temperature atmosfere). Postoji više teorijskih i empirijskih modela koji dobro opisuju ove zavisnosti. Obično se na osnovu ovih modela vrši korekcija kako bi se eliminisala varijacija fluksa kosmičkih miona atmosferskog porekla.*

*Obrnuto, osetljivost mionskih detektora na varijacije atmosferskih parametara može se iskoristiti da se na osnovu poznatih parametara modela i poznatog odbroja kosmičkih miona odredi temperatura različitih nivoa atmosfere. U ovom radu ćemo demonstrirati ovaj pristup na osnovu podataka merenih mionskim monitorima Niskofonske laboratorije za nuklearnu fiziku Instituta za fiziku u Beogradu i primenom empirijskog modela meteoroloških efekata, zasnovanog na tehnici dekompozicije na osnovne komponente.*

## 1. Uvod

Intenzitet pljusкова sekundarnog kosmičkog zračenja zavisi od atmosferskih meteoroloških parametara. To se naročito odnosi na mionsku komponentu sekundarnog kosmičkog zračenja. Dva efekta dominantno utiču na fluks sekundarnih miona: barometarski koji opisuje antikorelaciju fluksa kosmičkih miona sa atmosferskim pritiskom [1] i temperaturski koji se odnosi na uticaj varijacije atmosferske temperature na detektovani intenzitet miona [2].

Osim fundamentalnog, detaljno poznavanje meteoroloških efekata ima značaj u proceduri korekcije na date efekte, čime se povećava osetljivost zemaljskih detektora kosmičkog zračenja na varijacije neatmosferskog porekla. Alternativno, dobar model meteoroloških efekata bi u principu omogućio predviđanje atmosferskih parametara na osnovu merenja fluksa miona. Ovo je potencijalno značajno za određivanje temperatura pojedinih slojeva atmosfere u slučaju da su druge metode nedostupne.

Postoji više predloženih metoda za predikciju atmosferskih meteoroloških parametara na osnovu merenja intenziteta kosmičkog zračenja zemaljskim detektorima. Mogu se

bazirati na merenju različitih komponenti fluksa kosmičkih miona [3, 4], simultanom merenju neutronske i mionske komponente [5] ili upotrebi mionskog teleskopa sposobnim da meri ugaonu distribuciju intenziteta [6]. Sve pomenute metode karakteriše relativna kompleksnost eksperimentalne postavke i analize. Takođe, zajedničko svim pomenutim metodama je da se u proceduri određivanja atmosferskih temperatura oslanjaju na teorijski izračunate koeficijente za opisivanje zavisnosti inenziteta miona od temperaturskog profila atmosfere. Ovaj pristup ima određenih ograničenja usled nužno aproksimativnog karaktera i neprilagođenosti konkretnom detektorskom sistemu.

U ovom radu, mi ćemo demonstrirati upotrebljivost jednostavnije eksperimentalne postavke i primenu empirijskog modela meteoroloških efekata na određivanje temperaturskog profila atmosfere.

### 2. Eksperimentalni podaci i obrada

U Niskofonskoj laboratoriji za nuklearnu fiziku Instituta za fiziku u Beogradu mionski fluks se meri kontinualno od 2009. godine, na nivou zemlje i na dubini od 25 m.w.e. Eksperimentalna postavka se sastoji od scintilacionog detektora i sistema za akviziciju. Detektor je plastični scintilator dimenzija  $100\text{cm}\times 100\text{cm}\times 5\text{cm}$  sa četiri fotomultiplikatora postavljena na čoškove. U srcu sistema za akviziciju nalazi se brzi analogno-digitalni konverter sposoban da u realnom vremenu precizno određuje vreme detekcije i amplitudu signala [7]. U ovoj analizi korišćeni su podaci snimljeni detektorom na nivou zemlje u periodu od 01.06.2010. do 31.05.2011. godine.

Za opisivanje meteoroloških efekata na kosmičke mione, u okviru Niskofonske laboratorije razvijen je empirijski model baziran na tehnici dekompozicije na osnovne komponente (Principal Component Analysis - PCA) [8]. Metod se zasniva na ideji da se u analizi meteoroloških efekata sa skupa visoko korelisanih meteoroloških parametara pređe na skup linearno nezavisnih promenljivih, kao i potencijalno smanji dimenzionalnost problema zadržavanjem samo statistički značajnih osnovnih komponenti u analizi. Koeficijenti zavisnosti detektovanog odbroja miona od tako određenih osnovnih komponenti su pouzdaniji, jer su manje podložni statističkim fluktuacijama. Ovde ćemo primeniti ovaj model kako bismo na osnovu odbroja miona merenog u nadzemnoj laboratoriji odredili temperature različitih nivoa atmosfere.

Neka je  $C_X$  matrica tipa  $n\times m$  koja predstavlja  $m$  merenja  $n$  različitih meteoroloških parametara. Dekompozicijom na osnovne komponente se sa skupa  $n$  meteoroloških varijabli prelazi na skup  $n$  osnovnih komponenti, čije vrednosti su reprezentovane matricom  $C_Y$ , takođe tipa  $n\times m$ . Ova relacije se može predstaviti jednačinom:

$$C_Y = PC_X, \quad (1)$$

gde je  $P$  matrica transformacije čiji redovi predstavljaju kompoziciju osnovnih komponenti.

Na slici 1 prikazana je kompozicija prvih 9 osnovnih komponenti. Na x-osi su meteorološke promenljive: pritisak, temperature 24 izobarna nivoa (10, 20, 30, 50, 70, 100, 150, 200, 250, 300, 350, 400, 450, 500, 550, 600, 650, 700, 750, 800, 850, 900, 925 i 975 mb) i temperatura na nivou tla. Na y-osi su prikazane vrednosti kosinusa uglova rotacije pri prelasku sa skupa meteoroloških varijabli na skup osnovnih komponenti.

Na osnovu statističke i korelacione analize zaključeno je da su za meteorološke efekte od značaja samo pet osnovnih komponenti, i to komponente 1, 3, 4, 5 i 6 [8].

Zavisnost varijacije detektovanog odbroja miona od ovih komponenti, usled meteoroloških efekata, data je jednačinom:

$$\delta N_{PC} = \sum_i k_i PC_i, \quad i=1,3,4,5,6 \quad (2)$$

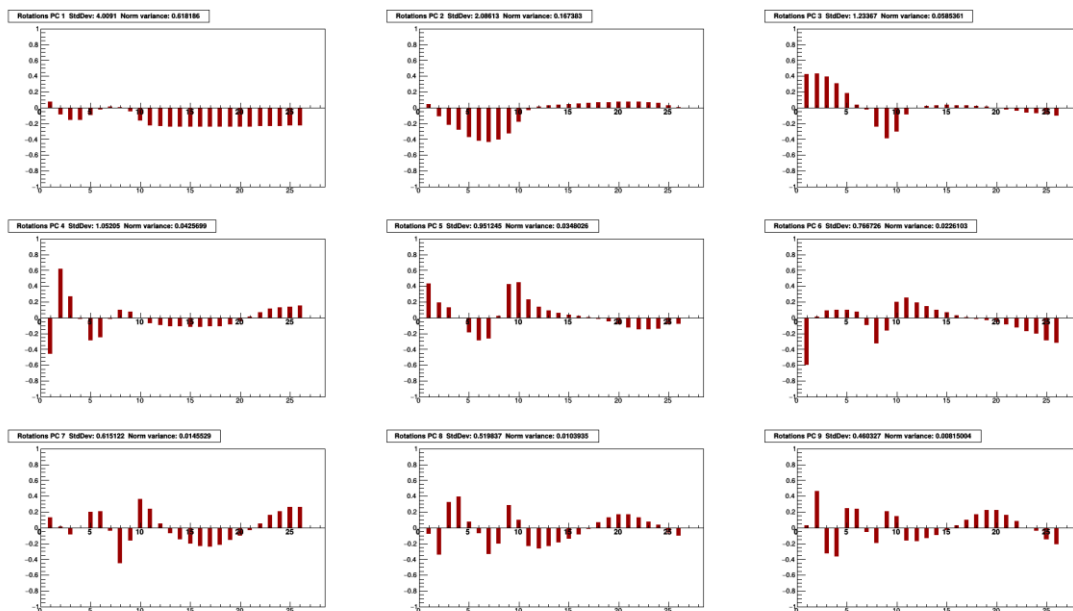
gde su  $PC_i$  osnovne komponente a  $k_i$  odgovarajući koeficijenti.

Pomoću ove relacije u principu je moguće proceniti vrednosti osnovnih komponenti na osnovu poznatog odbroja.

Dalje, transformišući jednačinu 1 kao:

$$C_X = P^{-1} C_Y = P^T C_Y \quad (3)$$

na osnovu procenjenih vrednosti osnovnih komponenti sada je moguće odrediti procenjene vrednosti meteoroloških parametara.



**Slika 1. Kompozicija prvih devet osnovnih komponenti.** Na x-osi su meteorološke promenljive: pritisak, temperatura 24 izobarna nivoa (10, 20, 30, 50, 70, 100, 150, 200, 250, 300, 350, 400, 450, 500, 550, 600, 650, 700, 750, 800, 850, 900, 925 i 975 mb) i temperatura na nivou tla. Na y-osi su prikazane vrednosti uglova rotacije.

### 3. Rezultati i diskusija

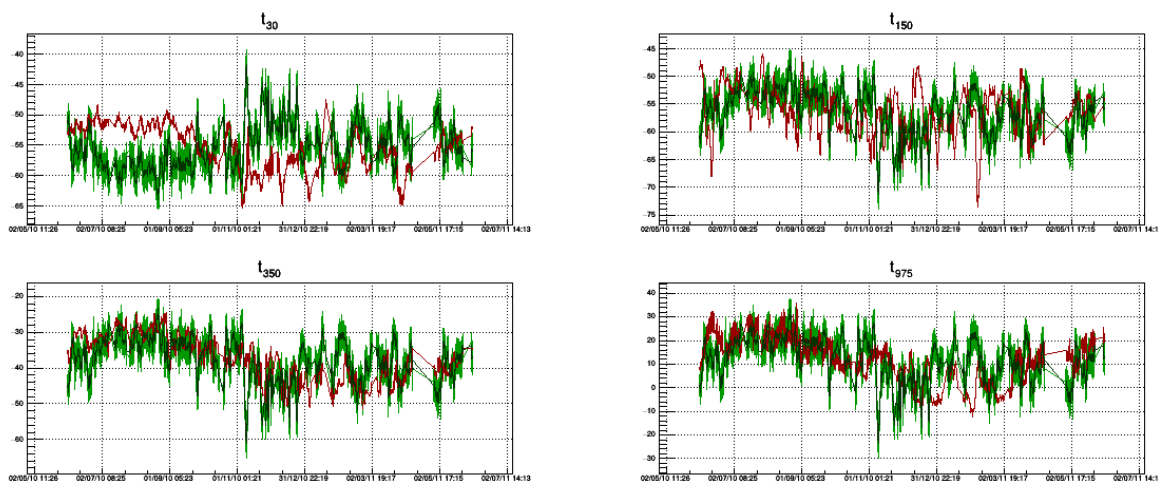
Za pomenuti referentni period određeni su koeficijenti u jednačini 2, uzimajući u obzir samo geomagnetno mirne dane [8]. Pomoću ovako određenih koeficijenata i merenog odbroja određene su procenjene vrednosti za pet signifikantnih osnovnih komponenti za ceo referentni period. Zatim su na osnovu jednačine 3 određene procenjene vrednosti meteoroloških parametara. Na slici 2 prikazane su vremenske serije merenih i procenjenih vrednosti meteoroloških parametara za izabrane izobarne nivoe.



Zbog preglednosti, prikazani su grafici za četiri različita nivoa. Kao referentni izabrani su nivoi od 30 mb (stratosfera), 150 mb (tropopauza/gornja troposfera), 350 mb (troposfera) i 975 mb (u blizini zemlje). Na plotovima crvenom linijom prikazane su merene vrednosti a svetlo zelenom vrednosti procenjene na osnovu merenog odbroja miona. Takođe, kako bi se dala jasnija slika i smanjio efekat fluktuacija merenog odbroja, vremenska serija predviđenih vrednosti je smutovana (*smoothing*) i prikazana na graficima tamno zelenom bojom.

Na slici 3 prikazana je raspodela razlika merenih i procenjenih vrednosti meteoroloških parametara.

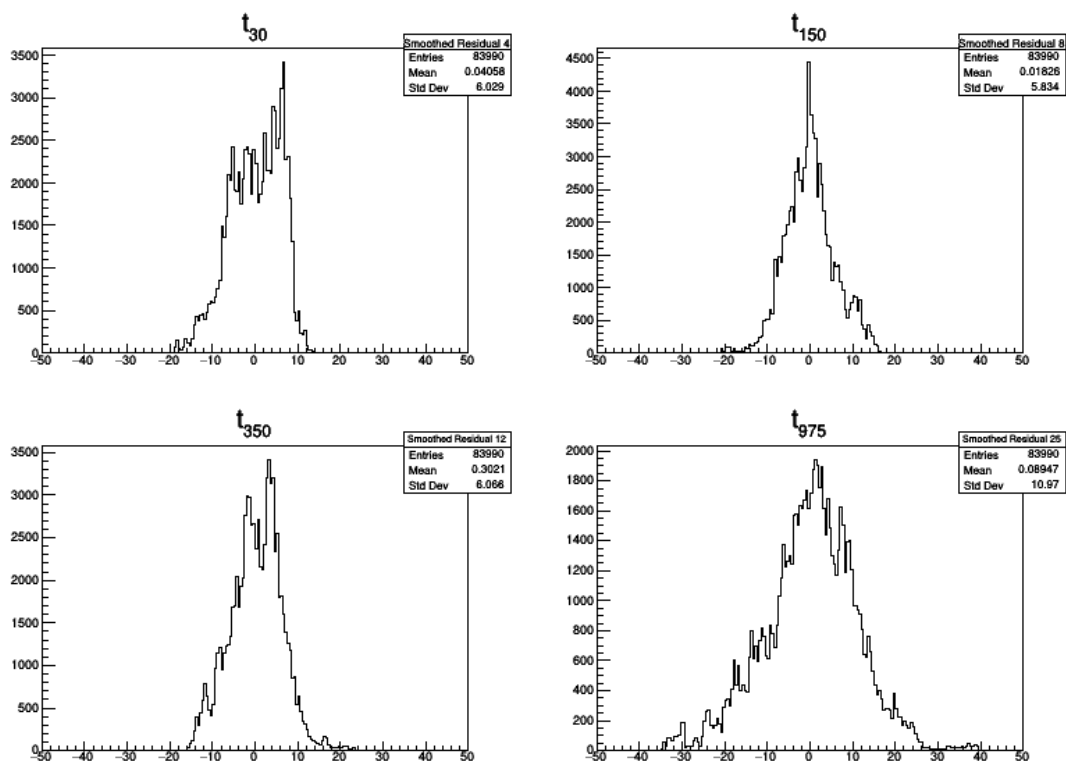
Osim analize vremenskih serija, još jedan kriterijum za određivanje efikasnosti predviđanja temperature pojedinih nivoa mogao bi biti na osnovu širine prikazanih raspodela. Međutim, varijacija temperatura različitih nivoa nije ista tako da ovo može dati nepotpunu sliku. Stoga su u tabeli 1 prikazane vrednosti standardnih devijacija ovih raspodela, standardnih devijacija merenih vrednosti, kao i relativan odnos ove dve veličine koji daje bolji uvid u efikasnost predikcije temperatura pojedinih nivoa atmosfere.



**Slika 2. Vremenske serije merenih i procenjenih vrednosti meteoroloških parametara za izabrane nivoje od 30, 150, 350 i 975 mb. Merene vrednosti - crvena linija, procenjene - svetlo zelena linija i smutovane procenjene - tamno zelena linija.**

Na osnovu predstavljenih grafika i tabela možemo videti da se najbolje slaganje dobija za sloj atmosfere od 300 do 600 mb. Nešto slabije slaganje dobija se za nivoje u blizini tla, što je u skladu sa kompleksnijom dinamikom temperatura u ovih slojevima, kao i za slojeve od 100 do 200 mb, u kojima dominantno dolazi do produkcije miona. Ovaj drugi podatak je moguća posledica činjenice da je za mione detektovane na površini zemlje značajniji negativni temperaturski efekat, asociran sa jonizacionim gubicima i verovatnoćom raspada miona u nižim slojevima atmosfere, dok pozitivni temperaturski efekat u vezi sa verovatnoćom nastanka miona u sloju između 100 i 200 mb ima manji doprinos. Najslabije slaganje dobija se za neke od nivoa u stratosferi i tropopauzi, što se može videti na primeru temperature nivoa od 30 mb koji je u značajnom delu godine antikorelisan sa procenjenom temperaturom. Ovo je možda uslovljeno manjim varijacijama temperature na ovim nivoima kao i činjenicom da postoji značajna

varijacija temperature ovih nivoa koja nije korelisana sa intenzitetom kosmičkih miona, sadržana u osnovnoj komponenti 2 (slika 1).



Slika 3. Raspodela razlika merenih i procenjenih vrednosti meteoroloških parametara za izobarne nivoe od 30, 150, 350 i 975 mb.

Tabela 1. Standardna devijacija raspodela razlika merenih i procenjenih vrednosti ( $\sigma_r$ ), raspodele vrednosti merenih temperatura ( $\sigma_t$ ) i relativan odnos ove dve vrednosti ( $\sigma_r/\sigma_t$ ).

	t <sub>10</sub>	t <sub>20</sub>	t <sub>30</sub>	t <sub>50</sub>	t <sub>70</sub>	t <sub>100</sub>	t <sub>150</sub>	t <sub>200</sub>	t <sub>250</sub>	t <sub>300</sub>	t <sub>350</sub>	t <sub>400</sub>
$\sigma_r$	9,314	5,246	6,029	3,645	3,940	4,032	5,834	7,455	5,761	5,679	6,066	6,297
$\sigma_t$	7,154	4,844	3,669	3,320	2,862	3,055	4,012	5,754	5,111	5,658	6,237	6,460
$\sigma_r/\sigma_t$	1,302	1,083	1,643	1,098	1,377	1,320	1,454	1,296	1,127	1,004	0,973	0,975

t <sub>450</sub>	t <sub>500</sub>	t <sub>550</sub>	t <sub>600</sub>	t <sub>650</sub>	t <sub>700</sub>	t <sub>750</sub>	t <sub>800</sub>	t <sub>850</sub>	t <sub>900</sub>	t <sub>925</sub>	t <sub>975</sub>	t <sub>ground</sub>
6,386	6,415	6,389	6,387	6,504	6,863	7,340	8,085	8,985	9,956	10,40	10,97	11,20
6,518	6,510	6,466	6,415	6,428	6,616	6,841	7,253	7,793	8,456	8,810	9,444	9,523
0,980	0,985	0,988	0,996	1,012	1,037	1,073	1,115	1,153	1,177	1,181	1,161	1,176

### 4. Zaključak

Preliminarna analiza je pokazala da postoji dosta dobro slaganje merenih i procenjenih atmosferskih temperatura za veći broj nivoa. Procenjene temperature imaju uglavnom konzistentne vremenske serije i dobro opisuju godišnju varijaciju. Najbolje slaganje sa merenim vrednostima dobija se u višim slojevima troposfere. Stoga, prikazani rezultati predstavljaju dobru polaznu osnovu za dalju analizu.

### 5. Zahvalnica

Ovaj rad je realizovan uz podršku Ministarstva prosvete, nauke i tehnološkog razvoja Republike Srbije u okviru projekta pod brojem OI 171002.

### 6. Literatura

- [1] L. Myssowsky, L. Tuwim. Unregelmäßige Intensitätsschwankungen der Höhenstrahlung in geringer Seehöhe. *Zeitschrift für Physik* 39, 1926, 2-3.
- [2] A Duperier. The Temperature Effect on Cosmic-Ray Intensity and the Height of Meson Formation. *Proc. Phys. Soc.* 61, 1948, 34-40.
- [3] Y. Miyazaki, M. Wada. Simulation of cosmic ray variation due to temperature effect. *Acta phys. Acad. Sci. hung.* 29, 1970, 591-595.
- [4] T. Kohno, K. Imai, A. Inue, M. Kodama, M. Wada. Estimation of the Vertical Profile of Atmospheric Temperature from Cosmic-Ray Components. *Proceedings of the 17th International Cosmic Ray Conference, held in Paris, France.* Volume 10., p.289.
- [5] L.I. Dorman. *Cosmic Rays in the Earth's Atmosphere and Underground*, Springer 2004.
- [6] V.V. Borog, O.V. Belonosova, A.S. Davydov, G.M. Kruchenitskii, S.P. Perov, V.G. Yanke. Study of Atmospheric Temperature at Different Altitudes using Muon Angular Distribution at Sea Level. *29th International Cosmic Ray Conference Pune, 2005*, 381-384.
- [7] A. Dragić, V. Udović, R. Banjanac, D. Joković, D. Maletić, N. Veselinović, M. Savić, J. Puzović. The New Setup in the Belgrade Low-Level and Cosmic-Ray Laboratory. *Nucl. Tech. Radiat. Protect.* 26, 2011, 181-192.
- [8] M. Savić, A. Dragić, D. Maletić, N. Veselinović, R. Banjanac, D. Joković, V. Udović. A novel method for atmospheric correction of cosmic-ray data based on principal component analysis. *Astropart. Phys.* 109, 2019, 1-11.

**ATMOSPHERIC TEMPERATURE PROFILE ESTIMATION  
BASED ON MEASURED COSMIC RAY MUON FLUX**

**Mihailo SAVIĆ, Vladimir UDOVIČIĆ, Dimitrije MALETIĆ,  
Aleksandar DRAGIĆ, Radomir BANJANAC, Dejan JOKOVIĆ,  
Nikola VESELINOVIĆ and David KNEŽEVIĆ**

*Institute of Physics Belgrade, University of Belgrade, Belgrade, Serbia,  
msavic@ipb.ac.rs, udovicic@ipb.ac.rs, maletic@ipb.ac.rs, dragic@ipb.ac.rs,  
banjanac@ipb.ac.rs, yokovic@ipb.ac.rs, veselinovic@ipb.ac.rs,  
davidk@ipb.ac.rs*

**ABSTRACT**

The effect of atmospheric parameters in secondary cosmic ray muon component is well known. This is mainly through two dominant meteorological effects - barometric (due to atmospheric pressure variation) and temperature (due to atmospheric temperature variation). There are several theoretical and empirical models that describe these effects well. Usually this knowledge is used to correct for secondary cosmic ray variations due to atmospheric effects.

Alternatively, once model parameters are established, sensitivity of cosmic ray muon detectors to variations of atmospheric origin can be used to estimate temperatures for different layers of the atmosphere. In this work we will demonstrate this procedure using cosmic ray data measured in Low Background Laboratory for Nuclear Physics at Institute of Physics Belgrade, combined with parameters of empirical model for meteorological effects based on principal component analysis.

## New empirical methods for correction of meteorological effects on cosmic ray muons

M. Savić,<sup>a,\*</sup> A. Dragić,<sup>a</sup> D. Maletić,<sup>a</sup> N. Veselinović,<sup>a</sup> D. Joković,<sup>a</sup> R. Banjanac,<sup>a</sup> V. Udovičić<sup>a</sup> and D. Knežević<sup>a</sup>

<sup>a</sup>*Institute of Physics Belgrade,  
Pregrevica 118, 11080 Belgrade, Serbia  
E-mail: [msavic@ipb.ac.rs](mailto:msavic@ipb.ac.rs)*

Flux of muon component of secondary cosmic rays is affected by varying conditions in the atmosphere. Dominant effects are barometric and temperature effect, which reflect variations of atmospheric pressure and atmospheric temperature respectively. Precise modelling and correction for these meteorological effects significantly increases sensitivity of Earth-based muon detectors to variations of primary cosmic ray flux. We are presenting two recently developed empirical methods for correction of meteorological effects on cosmic ray muons. First method is based on principal component analysis, while second employs multivariate analysis using machine learning techniques. Both methods are applied for correction of barometric and temperature effects, but can easily be generalised to take more atmospheric parameters into account. We apply these corrections to muon count rates measured by Belgrade cosmic ray station and study their effect on sensitivity of detection of periodic and aperiodic flux variations of primary cosmic rays. Comparison with the most widely used method for correction of meteorological effects – integral method, as well as with neutron monitor data, demonstrates very high effectiveness of presented methods.

*37<sup>th</sup> International Cosmic Ray Conference (ICRC 2021)  
July 12th – 23rd, 2021  
Online – Berlin, Germany*

---

\*Presenter

## 1. Introduction

Cosmic ray muons (hard component of secondary cosmic rays) are affected by variations of atmospheric parameters as they propagate toward Earth. There are a number of meteorological effects that affect cosmic ray muon flux, most prominent being the *barometric (pressure) effect* and the *temperature effect*, which depend on atmospheric pressure and atmospheric temperature respectively. Apart from fundamental, precise modelling of these effects also has practical importance, as it allows for correction that significantly increases the sensitivity of ground based muon monitors to variations of primary cosmic rays.

A number of methods for correction of barometric and temperature effect have been developed over the years. Some (i.e. method of effective level of generation [1]) are empirical in nature, while others (most notably integral method) rely on the theory of meteorological effects, developed by Dorman [2] among others. All these methods are at least in some part approximative, but for all intents and purposes we have decided to use the integral method as a reference in our analysis, as it gives the most complete treatment of the problem.

The idea behind the work presented here is to try and develop a new, easy to use empirical method, less approximative in nature, compare it to the reference integral method, and investigate whether a more precise model of meteorological effects can be constructed, and possibly some additional information extracted. In order to most completely treat the meteorological effects, both atmospheric pressure and full atmospheric temperature profile need to be taken into account. For analysis that involves that many potentially highly correlated input variables, we have decided to employ modern techniques used for decorrelation and dimensionality reduction, and introduce two new methods for modelling and correction of meteorological effects - *PCA method* based on principal component analysis (PCA), and *MVA method* based on multivariate analysis (MVA) via use of machine learning. Though these two are somewhat similar in nature, a more "hands on" approach of the PCA method can offer a somewhat different insight than the more "blackbox" machine learning approach.

## 2. Data

### 2.1 CR data

Muon count rates used in this analysis were measured in the Ground Level Laboratory (GLL) of the Low Background Laboratory for Nuclear Physics, at the Institute of Physics Belgrade [3]. More detailed description of the laboratory and current detector system can be found in some of our previous work [4]. Muon count rates can have arbitrary time resolution but five-minute and hour sums were used in the analysis. For quality and consistency of data reasons, and to remove potential biases due to annual variation, data for a period of one year (from 01.06.2010 to 31.05.2011) were selected.

### 2.2 Meteo data

This analysis requires information about both atmospheric pressure and vertical atmospheric temperature profile. Data about atmospheric pressure is readily available from the Republic Hydro-meteorological Servis of Serbia. As for the vertical temperature profile data, temperatures for 24

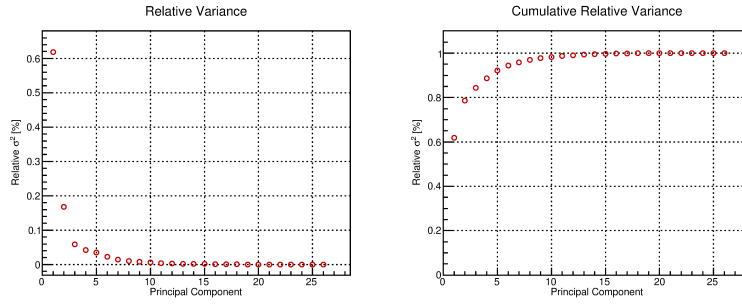


**Figure 1:** Relative variance (left) and cumulative relative variance (right) for all 26 principal components.

isobaric levels modelled by the Global Forecast System (GFS) [5] were used, starting from the top layer of the atmosphere (10 mb), to the level just above ground level (975 mb). For the above ground layer, locally measured temperature was used as the model was performing poorly there. More details about the preparation of meteorological data is available elsewhere [7].

### 3. Methodology

#### 3.1 PCA method

Principal component analysis is a well established technique for dimensionality reduction of complex problems that involve large number of correlated variables, and as such very well suited for application to our problem. Using principal component decomposition we have transformed the initial set of correlated meteorological variables (locally measured atmospheric pressure, 24 modelled temperatures, and locally measured ground temperature) to a set of 26 uncorrelated principal components.

Using a series of tests typically used in such analysis (cumulative percentage rule, modified Kaiser's rule, mean eigenvalue rule, ...), we have determined that the first six components (responsible for close to 95% of total variance, as seen on Figure 1) are significant. Composition of the these components is shown on Figure 2, where variables on the x-axis are atmospheric pressure followed by atmospheric temperatures, starting from the top layer of the atmosphere.

Correlative analysis of muon count rate and significant principal components showed practically no correlation between measured muon count rate and the second principal component, further reducing the set of principal components to five. This is an interesting results as this component, mainly composed of lower stratosphere and upper troposphere temperatures, is responsible for close to 17% of total variation of meteorological variables.

Finally, we have determined the muon count rate corrected for meteorological effects according to formula:

$$N_{\mu}^{(corr)} = N_{\mu} - \langle N_{\mu} \rangle \sum_i k_i PC_i, \quad i = 1, 3, 4, 5, 6 \quad (1)$$

where  $N_{\mu}^{(corr)}$  is corrected,  $N_{\mu}$  measured and  $\langle N_{\mu} \rangle$  mean muon count rate, while  $k_i$ , that correspond to principal components  $PC_i$ , are coefficients determined by linear regression, as shown on Figure 3. Full analysis and results are presented in more detail in our other work [8].

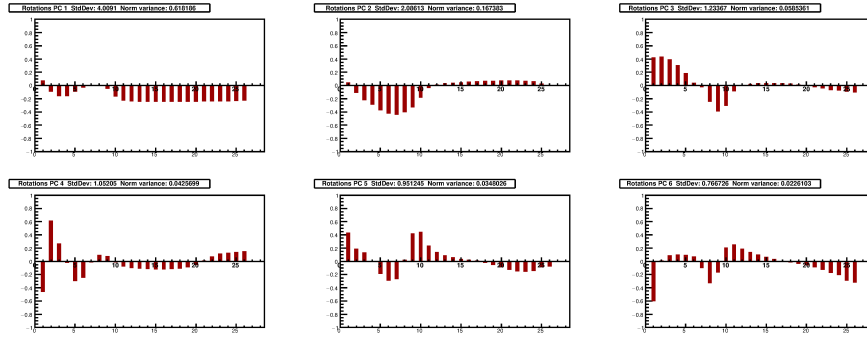


**Figure 2:** Composition for six most significant principal components. Meteorological variables are on the x-axis, first one being atmospheric pressure, followed by atmospheric temperatures (starting with the top layer of the atmosphere and ending with the ground level).

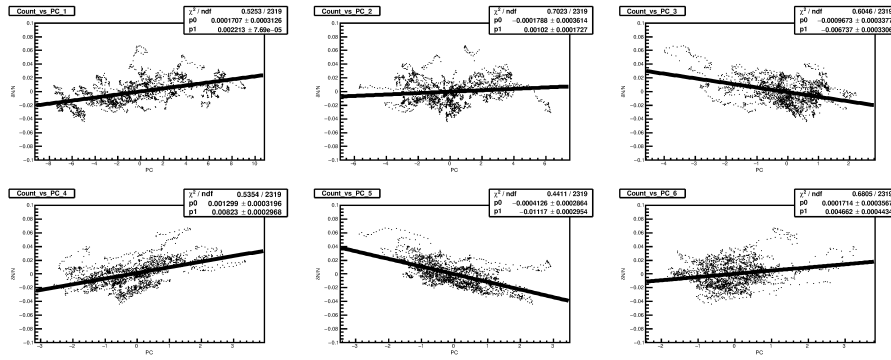


**Figure 3:** Muon count rate dependence on principal components for six most significant components, distributions fitted with linear function.

### 3.2 MVA method

Multivariate analysis utilising machine learning techniques can be a powerful tool for modelling of highly correlated systems. We have tested a number of algorithms implemented in Toolkit for Multivariate Data Analysis (TMVA), which has been successfully used for classification and regression problems in particle physics. For us, regression application is of greater interest, as the idea is to train and test multivariate algorithms on a subset of data (for geomagnetically quiet days), where most of the variation can be attributed to atmospheric effects, using meteorological variables as input and muon count rate as the target value. Trained algorithms can be then used on a full data set to predict the muon count rate (which would ideally depend only on meteorological parameters), and corrected muon count rate can be calculated using the formula:

$$N_{\mu}^{(corr)} = \Delta N_{\mu} + \langle N_{\mu} \rangle, \quad \Delta N_{\mu} = N_{\mu}^{(mod)} - N_{\mu}, \quad (2)$$

where  $N_{\mu}^{(corr)}$  is corrected,  $N_{\mu}$  measured,  $N_{\mu}^{(mod)}$  modelled, and  $\langle N_{\mu} \rangle$  is mean muon count rate.

Minimal average quadratic deviation of modelled from measured value was the only criterion used for optimisation of algorithm parameters in the training phase, so a series of tests have been



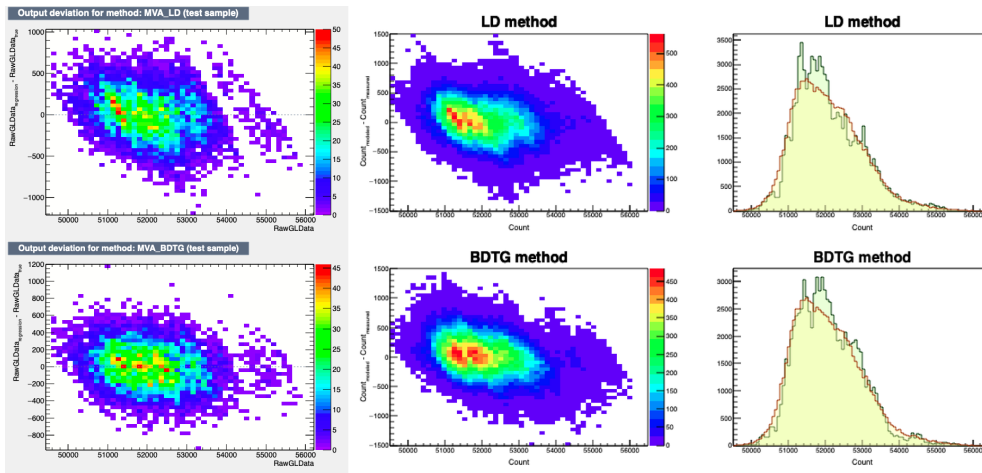


**Figure 4:** Modelled count rate and its deviation from measured count rate as a function of measured count rate for LD (top) and BDTG (bottom) algorithms. Deviation distributions for test data set are on left, for the full data set are in the middle, while distributions of modelled count rate (compared with the measured one) are on the right.

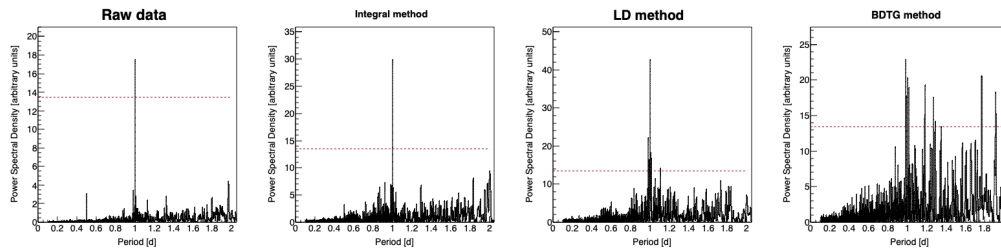


**Figure 5:** Power spectra for periods in the interval [0, 2] days, for measured data (far left), and data corrected using integral (central left), LD (central right) and BDTG (far right) methods.

devised in order to investigate the consistency of application of trained algorithms and minimise the possibility of artificial features being introduced.

Some of the tests included comparison of distributions of residual deviation of modelled from measured data for the test and full data set, or looking for anomalous features in distributions of modelled count in comparison with measured count distribution (both types of distributions for selected algorithms shown in Figure 4).

Based on these tests, the best performing algorithm proved to be LD (Linear Discriminant method), which is closely related to PCA approach. The second best potential candidate was BDTG (Gradient Boosted Decision Tree method), but there are probably some limits to its applicability, as indicated by spectral analysis (Figure 5). From the remaining tested methods, algorithms based on probability density techniques performed more poorly, which was not that surprising as the problem analysed here involves highly linear dependencies, but poor performance of methods based on neural networks was not expected, and possibly some improvement can be made there.

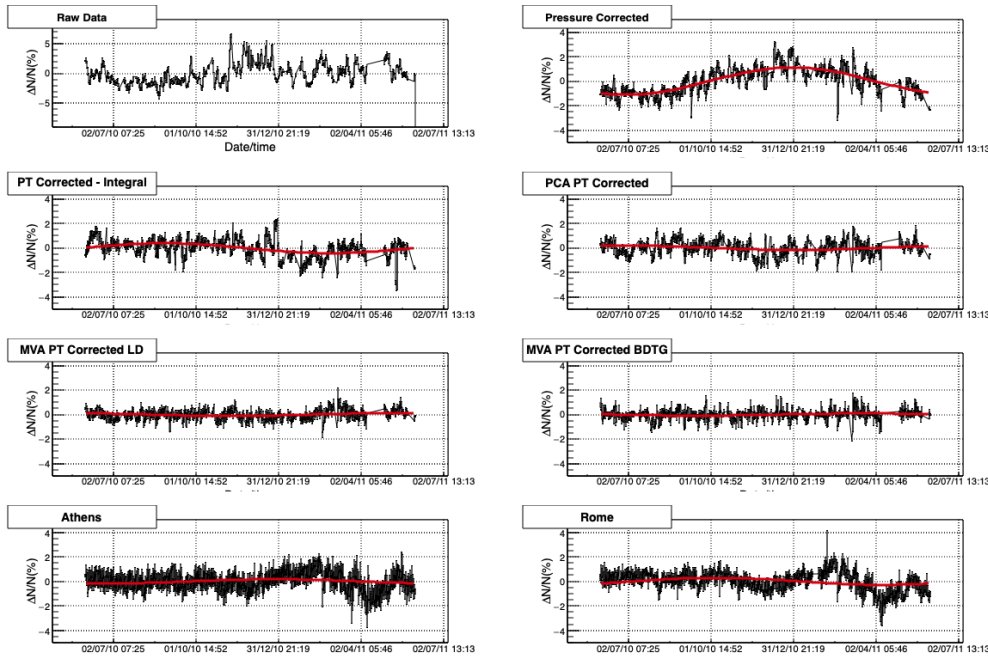


**Figure 6:** Muon count rate time series and reference neutron monitor data for the period of one year (01.06.2010-31.05.2011), fitted with sine function with a period of one year.

## 4. Results

### 4.1 Effect of corrections on periodic CR variations

One way to assess the performance of different methods for correction of meteorological effects could be to compare the efficiency with which they remove the annual variation due to temperature variation. In order to determine this variation, we have fitted pressure corrected data with a sine function, with a period of one year. Amplitude determined from such fit is then used as an estimate of magnitude of the annual variation. The same procedure was used to determine the residual annual variation after the correction via use of different methods (Figure 6). As neutron monitor count rates are usually considered to negligibly depend on atmospheric temperature (at least in the first approximation), we can treat their time series the same way in order to estimate the expected annual variation magnitude.

Table 1 shows amplitudes for the annual variation calculated based on plots in Figure 6, as well as reduction in annual variation relative to pressure corrected data. As can be seen, values for PCA and LD methods are closer to the estimates based on the neutron monitor data than the integral method value, while for BDTG method the value is somewhat smaller.

### 4.2 Effect of corrections on aperiodic CR variations

To study the effect of corrections on aperiodic variations we have selected the most intense Forbush decrease event in the one year period used for the analysis. For the event that occurred on 18.02.2011, we determined the amplitude of decrease for data corrected via different methods and reference neutron monitors, using procedure suggested by Barbashina et al. [9] (as shown on

Method/ Neutron monitor	P corr.	Integral	PCA	LD	BDTG	Athens	Rome
Annual amplitude [%]	1.11(9)	0.40(3)	0.18(5)	0.11(3)	0.086(9)	0.17(5)	0.29(1)
Relative reduction [% of P corrected]	-	64(10)	84(28)	90(30)	92(30)	-	-

**Table 1:** Amplitude and reduction of the amplitude of annual variation relative to pressure corrected data (P corr.) for pressure and temperature corrected data (using integral and selected multivariate methods). Athens and Rome neutron monitor data also included for reference

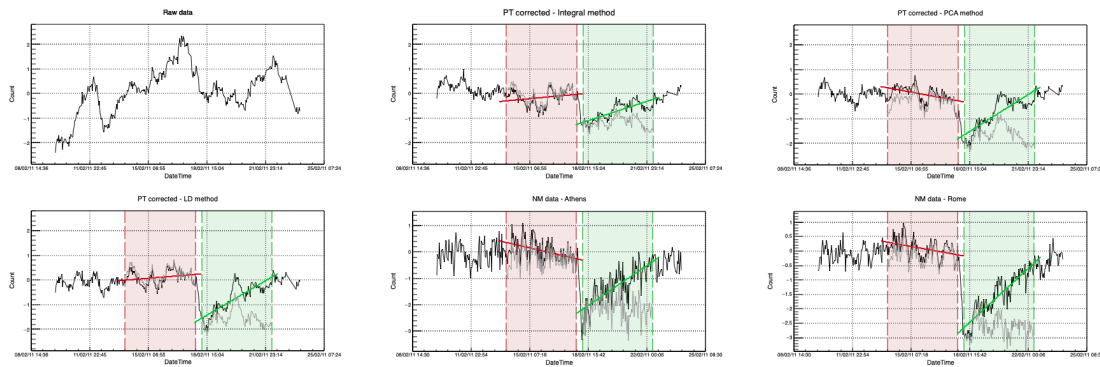


**Figure 7:** Muon count rate time series and reference neutron monitor data for the period around the Forbush decrease event of 18.02.2011. Highlighted intervals are used for detrending and calculation of decrease amplitude.

Method/ Neutron monitor	Integral	PCA	LD	BDTG	Athens	Rome
FD amplitude [%]	1.38(14)	1.52(21)	1.96(18)	1.10(13)	1.97(15)	2.68(15)
Relative FD amplitude	4.31(44)	4.90(66)	7.09(65)	4.78(56)	5.30(40)	8.65(48)

**Table 2:** Amplitudes and relative amplitudes for the Forbush decrease event of 18.02.2011 for pressure and temperature corrected muon data and reference neutron monitors

Figure 7). Additionally, as a measure of sensitivity to such events, we have introduced amplitude calculated relative to standard deviation of count rates leading up to the event.

Values for thusly calculated amplitudes and relative amplitudes are shown in Table 2. LD algorithm has values comparable to neutron monitor values, but that is at least in part due to somewhat larger calculated amplitude. This is most likely a feature pertaining to the specific event, as preliminary results for other events outside the interval used in this work show values closer to expected.

## 5. Conclusions

Two new methods for correction of meteorological effects on cosmic ray muons are introduced. Both are fully empirical, require knowledge about the atmospheric pressure and atmospheric temperature profile and can be applied to any muon monitor. The effect on reduction of the annual variation of CR data, as well as the effect on sensitivity of FD event detection was compared to the integral method and reference neutron monitor data. Their effectiveness was comparable or possibly better than for the integral method, allowing for the possibility that a part of meteorological effects is not taken into account by theory.

## References

- [1] A Duperier, "The Meson Intensity at the Surface of the Earth and the Temperature at the Production Level", in Proceedings of the Physical Society. Section A, volume 62, number 11, pages 684, year 1949, doi: 10.1088/0370-1298/62/11/302
- [2] Dorman, L. I., "On the temperature effect of the hard component of cosmic rays", in Reports of Academy of Sciences of USSR (DAN SSSR), volume 95, issue 1, pages 49 - 52, year 1954b
- [3] Low Background Laboratory for Nuclear Physics, url: <http://www.cosmic.ipb.ac.rs/>
- [4] Dragic Aleksandar, Udovicic Vladimir, Banjanac Radomir, Jokovic Dejan, Maletic Dimitrije, Veselinovic Nikola, Savic Mihailo, Puzovic Jovan, Anicin Ivan, "The New Set-Up in the Belgrade Low-Level and Cosmic-Ray Laboratory", in NUCLEAR TECHNOLOGY AND RADIATION PROTECTION, volume 26, number 3, pages 181-192, year 2011, doi: 10.2298/NTRP1103181D
- [5] GFS, url: <https://www.ncdc.noaa.gov/data-access/model-data/model-datasets/global-forecast-system-gfs>
- [6] Berkova M., Belov A., Eroshenko E., Yanke Victor, "Temperature effect of muon component and practical questions of how to take into account in real time", in Astrophysics and Space Sciences Transactions, year 2012, pages 41-44, volume 8, doi: 10.5194/astra-8-41-2012
- [7] Savic Mihailo, Dragic Aleksandar, Veselinovic Nikola, Udovicic Vladimir, Banjanac Radomir, Jokovic Dejan, Maletic Dimitrije, "Effect of pressure and temperature corrections on muon flux variability at ground level and underground", in "25th European Cosmic Ray Symposium", Torino, Italy, eprint: 1701.00164, year 2016
- [8] Savic Mihailo, Dragic Aleksandar, Maletic Dimitrije, Veselinovic Nikola, Banjanac Radomir, Jokovic Dejan, Udovicic Vladimir, "A novel method for atmospheric correction of cosmic-ray data based on principal component analysis", in ASTROPARTICLE PHYSICS, volume 109, pages 1-11, year 2019, doi: 10.1016/j.astropartphys.2019.01.006
- [9] Barbashina N., Dmitrieva Anna, Kompaniets K., Petrukhin A., Timashkov D., Shutenko V., Yakovleva Elena, Yashin, Igor, "Specific features of studying Forbush decreases in the muon flux", in Bulletin of The Russian Academy of Sciences: Physics, year 2009, pages 343-346, volume 73, doi: 10.3103/S1062873809030198